

Hi-JAK-ing The Ubiquitin System: The Design and Physicochemical Optimisation of JAK PROTACs

Rishi R. Shah

Medicine Design, GSK
University of Strathclyde

A thesis submitted for the degree of
Doctor of Philosophy

2020

Declaration of Copyright

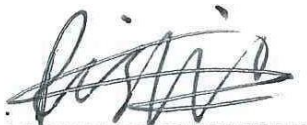
This thesis is the result of the author's original research. It has been composed by the author and has not been previously submitted for examination which has led to the award of a degree.

The copyright of this thesis belongs to the author under the terms of the United Kingdom Copyright Acts as qualified by University of Strathclyde Regulation 3.50. Due acknowledgement must always be made of the use of any material contained in, or derived from, this thesis.

Rishi Shah

Signed:

Date: 14/06/2020

A handwritten signature in black ink, appearing to read 'Rishi Shah', written over a horizontal line.

Contents

List of Abbreviations	8
Abstract.....	18
Acknowledgements.....	20
1 Introduction	22
1.1 Kinase Structure and Their Inhibitor Types.....	22
1.2 Implications of the JAK-STAT Pathway.....	26
1.2.1 Structure of the JAK Family.....	30
1.2.2 Sequence Homology of JAKs.....	31
1.3 Why Target the JAKs?	32
1.4 Non-selective JAK inhibitors.....	34
1.4.1 Ruxolitinib	34
1.4.2 Tofacitinib	37
1.4.3 Baricitinib	41
1.5 Pan JAK Inhibitors.....	43
1.5.1 Peficitinib	43
1.6 Selective JAK Inhibitors	48
1.6.1 Filgotinib.....	48
1.6.2 Upadacitinib	50
1.7 JAK3 Selective Inhibitors	52
1.7.1 Decernotinib.....	53
1.7.2 PF-06651600	56
1.8 Alternative JAK Antagonists	58
1.8.1 PF-956980	58
1.9 The Unmet Needs of Targeting The JAK-STAT Pathway	59

1.10 The Ubiquitin System	60
1.11 Early Intracellular Protein Concentration Modulators	63
1.11.1 RNA, ODNs and RNase in Protein Degradation	63
1.11.2 Heat Shock Protein 90 (HSP90) Induced Degradation	64
1.12 Utilising the Ubiquitin-Proteasome System to Degrade Target Proteins	65
1.12.1 Hydrophobic Tagging: Induced Protein Degradation Through Mimicking Protein Denaturation	65
1.12.2 Proteolysis Targeting Chimeras (PROTACs): Hijacking the Ubiquitin System	67
1.12.3 Peptide PROTACs	69
1.12.4 Small Molecule PROTACs	72
1.12.5 MDM2 PROTACs.....	72
1.12.6 IAP PROTACs	73
1.12.7 VHL PROTACs	74
1.12.8 Cereblon PROTACs	78
2 Results and Discussion	82
2.1 Aims: Can PROTAC Induced Degradation of Proximal Membrane-Bound JAK be Achieved?	82
2.2 Biological Characterisation.....	83
2.2.1 The K_m and Desensitised JAK Biochemical Assays.....	83
2.2.2 IL2 PBMC Assay	86
2.2.3 Western Blotting.....	88
2.3 Selecting a Warhead	90
2.3.1 Tofacitinib	92
2.3.2 Quinazoline Series.....	94
2.3.3 Indole Carboxamide Series	98
2.3.4 Pyrimidine series.....	100

2.3.5 Imidazotriazine series	102
2.3.6 Imidazopyridinone Series.....	104
2.3.7 Quinoxaline series.....	106
2.3.8 Thienopyrazole series	108
2.3.9 Review of the ‘Go’ Category	110
2.4 Design of Cell Penetrant JAK PROTACs	111
2.4.1 ‘Click’ Linked Pyrimidine-OH PROTACs	115
2.4.2 7C-Linked Pyrimidine-OH PROTACs	117
2.4.4 10C-Linked Pyrimidine-H PROTACs.....	120
2.4.5 4EG Pyrimidine-H PROTACs	122
2.4.6 Pyrimidine-Bn PROTACs	123
2.4.7 10C-Linked Pyrimidine-Bn PROTACs.....	126
2.4.8 16C-Linked Pyrimidine-Bn PROTACs.....	128
2.4.9 4EG Pyrimidine-Bn PROTACs.....	129
2.4.10 6EG Pyrimidine-Bn PROTACs.....	131
2.4.11 Quinoxaline Warhead Selection	132
2.4.12 4EG Quinoxaline PROTACs.....	133
2.4.13 6EG Quinoxaline PROTACs.....	135
2.4.14 10C Quinoxaline PROTACs	136
2.5 On The Synthesis of Pyrimidine Series PROTACs	138
2.5.1 Early Explorations Around the Pyrimidine Series	138
2.5.2 Retrosynthesis of Pyrimidine Series PROTACs.....	139
2.5.3 Photoredox Etherification.....	140
2.5.4 Cyanation of the Aryl Ether.....	144
2.5.5 Cyanation of 1,3-Dibromo-2,5-difluorobenzene.....	145
2.5.6 Reducing the Nitrile	148

2.5.7 S _N Ar on Trichloropyrimidine	149
2.5.8 Azide Formation	151
2.5.9 Copper ‘Click’ Chemistry	152
2.5.10 C-Linked PROTAC Synthesis	156
2.5.11 Synthesis of Pyrimidine-H PROTACs.....	158
2.5.12 Pyrimidine-Bn PROTAC Synthesis	163
2.5.13 On The Synthesis of Quinoxaline Series PROTACs	169
2.5.14 Synthesis of JP-6 Inverse; A Negative Control	184
2.6 Medicinal Chemistry of Pyrimidine Series PROTACs.....	188
2.6.1 The Pyrimidine-OH PROTAC Medicinal Chemistry.....	188
2.6.2 The Medicinal Chemistry of the Pyrimidine-H PROTACs	193
2.6.2 The Medicinal Chemistry of the Pyrimidine-Bn PROTACs: Exploiting an Alternative Vector.....	196
2.6.4 The Medicinal Chemistry of the Quinoxaline Series	201
2.7 Physicochemical Property Impact on Permeability	204
2.8 Cellular Screening of JAK PROTACs	211
2.8.1 Initial Degradation Screen.....	211
2.8.2 Exploring PROTAC-Mediated JAK Degradation	217
2.8.3 Implications of Physicochemical Properties on Degradation Efficiency	220
2.8.4 JAK PROTACs Mechanism of Action.....	221
3 Conclusions	225
4 Future Work	227
5 Experimental	229
5.1 Biological Methods.....	229
5.2 Synthetic Chemistry	231
5.2.1 General Methods	231

5.2.2 Synthesis of Novel Compounds.....	235
8 References.....	333
9 Appendix	361

List of Abbreviations

ADP	Adenosine diphosphate
AHR	Airway hyperresponsiveness
AKT	Protein kinase B
AML	Acute myeloid leukaemia
AR	Androgen receptor
ATP	Adenosine triphosphate
ATRA	All- <i>trans</i> retinoic acid
BET	Bromo- and extra-terminal
BIR	Baculovirus inhibitor of apoptosis protein repeat
BMS	Bristol-Myers Squibb
Bn	Benzyl
Boc	<i>tert</i> -Butyloxycarbonyl
BRD	Bromodomain
bRo5	Beyond the Rule of 5
CFL	Compact fluorescent light bulb
ciAP1	Cellular inhibitor of apoptosis protein 1
CKIα	Casein kinase I α
CMC	Chronic mucocutaneous candidiasis
CML	Chronic myelogenous leukemia
CRABP	Cellular retinoic acid-binding protein

CRBN	Cereblon
CRISPR/Cas9	Clustered regularly interspaced short palindromic repeats/CRISPR associated protein 9
CYP	Cytochromes P450
DC₅₀	Concentration of drug that results in 50 % protein degradation
DCM	Dichloromethane
DDB1	Damaged DNA-binding protein
DHFR	Dihydrofolate reductase
DHT	Dihydrotestosterone
DIPEA	<i>N,N</i> -Diisopropylethylamine
DMA	Dimethylacetamide
DMAP	4-Dimethylaminopyridine
DME	1,2-Dimethoxyethane
DMF	<i>N,N</i> -Dimethylformamide
DMPK	Drug metabolism and Pharmacokinetics
DMSO	Dimethyl sulfoxide
DNA	2-Deoxyribonucleic acid
dppf	1,1'-Ferrocenediyl-bis(diphenylphosphine)
DS	Desensitised
dtbby	4,4'-Di- <i>tert</i> -butyl-2,2'-bipyridyl
EDG	Electron-donating group
EDTA	Ethylenediaminetetraacetic acid

EG	Ethylene glycol
EGFR	Epidermal growth factor receptor
ELOBC-CUL2	Elongin B/C–cullin 2
EPO	Erythropoietin
ER	Estrogen receptor
ERRα	Estrogen-related receptor- α
ET	Essential thrombocythemia
Et	Ethyl
Eu-Ab	Eu-labelled anti-phospho-substrate antibody
EWG	Electron-withdrawing group
FDA	Food and Drug Administration
FERM	Region consisting of band 4.1, ezrin, radixin, moesin
FP	Fluorescence polarisation
FLINT	Fluorescence intensity
G-CSF	Granulocyte-colony stimulating factor
glyme	Dimethoxyethane
GM-CSF	Granulocyte-macrophage colony-stimulating factor
GSK	GlaxoSmithKline
GSPT1	G1 to S phase transition protein homologue
HATU	1-[Bis(dimethylamino)methylene]-1 <i>H</i> -1,2,3-triazolo[4,5 <i>b</i>]pyridinium 3-oxide hexafluorophosphate
HBA	Hydrogen bond acceptor

HBD	Hydrogen bond donor
HEK	Human embryonic kidney
HER2	Human epidermal growth factor receptor 2
HIES	Hyperimmunoglobulin E syndrome
HIF1α	Hypoxia-inducible factor 1 α
HIV	Human immunodeficiency virus
HPLC	High-performance liquid chromatography
HRMS	High resolution mass spectrometry
HRP	Horseradish peroxidase
HSC	Hematopoietic stem cells
HSP90	Heat shock protein 90
HTS	High-throughput screening
hWB	Human whole blood
IAP	Inhibitor of apoptosis protein
IBD	Inflammatory bowel disease
IC	Inhibitory concentration
IgE	Immunoglobulin E
IKZF	Ikaros family zinc finger
IL	Interleukin
IL2R	IL2 receptor
IFN	Interferon

ⁱPr	Isopropyl
IκBα	Nuclear factor of kappa light polypeptide gene enhancer in B-cells inhibitor, alpha
JAK	Janus Kinase
JH	Jak homology
K_d	Dissociation constant – an equilibrium constant that measures the propensity of a larger object to dissociate reversibly into smaller components
K_i	Inhibitor constant - an indication of how potent an inhibitor is; it is the concentration required to produce half maximum inhibition
K_m	Michaelis Constant - Substrate concentration at which the reaction rate is half its maximal value
LCMS	Liquid chromatography–mass spectrometry
LED	Light Emitting Diode
LCK	Lymphocyte-specific protein tyrosine kinase
mAbs	Monoclonal antibodies
MARK	MAP/microtubule affinity-regulating kinases
mCRPC	Metastatic castration resistant prostate cancer
MDAP	Mass directed auto purification
MDM2	Mouse double minute 2
Me	Methyl
MetAP-2	Methionine aminopeptidase 2
MF	Myelofibrosis

MPN	Myeloproliferative neoplasm
mRNA	Messenger RNA
Ms	Methanesulfonyl
MW	Molecular weight
n	Number of repeats
NIS	<i>N</i> -Iodosuccinimide
NK	Natural killer
NMR	Nuclear magnetic resonance
NrotB	Number of rotatable bonds
ns	Non-significant
NX	Normalised expression level, and values > 1 are considered expressed
ODN	Oligonucleotide
PBMC	Peripheral blood mononuclear cell
PCC	Protein-catalyzed capture agent
PD	Pharmacodynamic
PDB	Protein Data Bank
PDE	Phosphodiesterase
PEG	Polyethylene glycol
pIC₅₀	Negative natural log of the half maximal inhibitory concentration
PK	Pharmacokinetics
PMF	Primary myelofibrosis

POI	Protein of interest
Post-ET/PV MF	Myelofibrosis arising from progression of PV and ET
PPIs	Protein-protein interactions
PROTAC	Proteolysis-Targeting Chimera
PS	Proteasome
PSA	Polar surface area
pSTAT	Phosphorylated signal transducers and activators of transcription
PV	Polycythemia vera
qPCR	Quantitative polymerase chain reaction
RA	Rheumatoid arthritis
RIPA	Radioimmunoprecipitation assay buffer
RIPK2	Receptor-interacting serine/threonine-protein kinase 2
RISC	RNA-induced silencing complex
RNA	Ribonucleic acid
RNAi	RNA interference
Ro5	Rule of 5
ROC1	Regulator of cullins
RT	Room temperature
S	Substrate
SAR	Structure–activity relationship
SARM	Non-steroidal selective androgen receptor modulator

SCF	SKP1–cullin 1– F-box E3 ligase complex
SCID	Severe combined immunodeficiency
SH2	Src Homology 2
siRNA	Small interfering RNA
SKP1	S-phase kinase-associated protein 1
S_N1	Unimolecular Nucleophilic Substitution
S_N2	Bimolecular Nucleophilic Substitution
S_NAr	Nucleophilic Aromatic Substitution
SPhos	2-Dicyclohexylphosphino-2',6'-dimethoxybiphenyl
STAT	Signal transducers and activators of transcription
TBK1	TANK-binding kinase 1
TBME	<i>tert</i> -Butyl methyl ether
TBS	<i>tert</i> -Butyldimethylsilyl
Bu	Butyl
^tBu	<i>tert</i> -Butyl
TFA	Trifluoroacetic acid
Th	Helper T cells
THF	Tetrahydrofuran
THP	Tetrahydropyranyl
THPTA	Tris(3-hydroxypropyltriazolylmethyl)amine
TPO	Thrombopoietin

TRIM24	Tripartite motif-containing 24
TR-FRET	Time Resolved Fluorescence Resonance Energy Transfer
TYK2	Non-receptor tyrosine-protein kinase
U_B	Ubiquitin
UPS	Ubiquitin proteasome system
v	Reaction rate
VHL	Von Hippel–Lindau
V_{max}	Maximal enzyme velocity
WHO	World Health Organisation
XIAP	X-linked inhibitor of apoptosis protein
XPhos	2-Dicyclohexylphosphino-2',4',6'-triisopropylbiphenyl
β-TRCP	β-Transducin repeat-containing protein

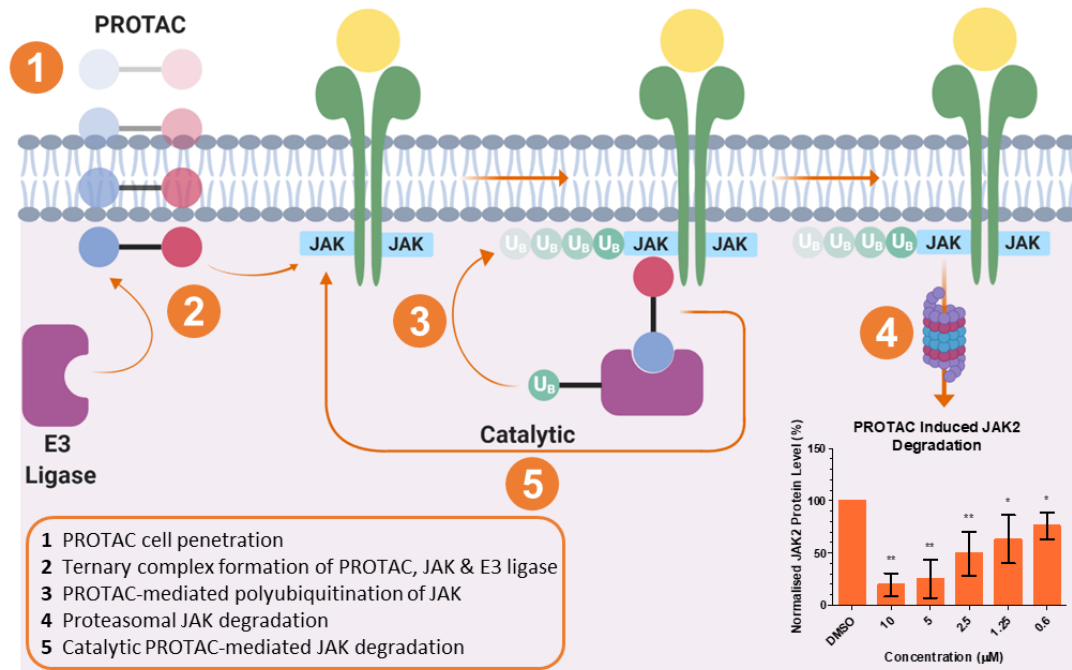
Abstract

Proteolysis-targeting chimaeras (PROTACs) have recently emerged as a novel paradigm that can hijack existing biological machinery to selectively degrade proteins of interest (POIs), in a catalytic fashion. This thesis explores the application of the PROTAC technology to members of the Janus kinase (JAK) family (JAK1 and JAK2), which have been implicated in several diseases, from inflammatory diseases to cancer. The thesis discloses the first account of PROTAC-mediated proximal membrane protein degradation.

Initial efforts focused around selecting JAK warheads (JAK inhibitors) from which to generate PROTACs. The physicochemical properties of each template were optimised to enhance cell permeation, and following the identification of two JAK warheads, the PROTACs' physicochemical properties were profiled *in silico*, prior to synthesis, as to identify a physicochemical property space optimal for JAK PROTAC cell penetration. The existing routes to the warheads were scrutinised, and more recent synthetic methodology was exploited to significantly reduce the number of steps and increase the overall yield of key intermediates.

Following PROTAC library generation, the PROTACs were evaluated within *in vitro* biochemical and cellular assays to ascertain target engagement and cell penetration. It was confirmed that the JAK PROTACs were capable of engaging JAK and accessing intracellular compartments. A subset of PROTACs was selected based on chemical diversity of the warhead, linker and ligase binder. This subset was progressed to initial western blot assays within THP-1 cells, and it was identified that only PROTACs possessing an inhibitor of apoptosis (IAP) binder were able to induce JAK1/JAK2 degradation. As such, the IAP-containing JAK PROTACs were further evaluated and six PROTACs were capable of inducing significant (up to 86 %) JAK1 and/or JAK2 degradation. To confirm the mechanism of JAK PROTAC-mediated JAK degradation to be both IAP- and proteasome-dependent, IAP competition assays were developed, which illustrated the IAP-dependent nature of JAK PROTAC-mediated degradation. Furthermore, proteasome inhibitor dosing, in combination with an active JAK PROTAC, prevented a decrease in intracellular JAK protein levels. Consequently, JAK PROTAC-mediated degradation was determined to be both IAP- and proteasome-dependent.

In summary, reported herein is the design of cell penetrant JAK PROTACs from two distinct JAK chemotypes; these novel PROTACs induce degradation of JAK1 and JAK2 at varying levels, demonstrating an extension of the cutting edge PROTAC methodology to an unprecedented class of protein targets. The JAK PROTACs could find utility as biological tool molecules or be further optimised to develop therapeutics for a variety of diseases.



Acknowledgements

First and foremost, I would like to thank my two industrial supervisors, Dr Diane Coe and Dr Jo Redmond for their continued support, training, encouragement, enthusiasm for the program even in the face of less desirable data, and passing of a wealth of knowledge and scientific rigour, throughout my PhD. Additionally, for proofing parts of my thesis at such short notice! I would also like to thank my academic supervisor, Prof John Murphy, for his guidance and advice throughout the project.

Additionally, I would like to thank Malini Menon, Andrei Mihut and Michelle Bartholomew for training me on running Westerns, in addition to them running Westerns and various JAK-associated assays, and their useful discussion around the program. I would also like to thank John Evans for running the JAK biochemical and cellular assays.

I also thank Chris Tame, Markus Queisser, Afjal Miah, Ian Smith and John Harling for their invested time regarding protein degradation at various different points of the project, which helped steer it to success. Furthermore, I am grateful to Zoë Henley, Neal Fazakerley, Chris Wellaway, Darren Poole, Joe Mason and Deborah Needham for taking the time to assist me on various aspects of science.

Additionally, I would like to thank Dr Harry Kelly and Prof Billy Kerr for setting up the program and providing the opportunity to undertake this PhD project.

Outside of science, I would like to thank my family and friends, particularly, my ma and dad, and Neil for their support and reassurance that it is almost over! I would not have made it this far without them. I would also like to thank Matt Cocks for distracting me, Shiri for zoning out whilst I ranted about PROTACs. Many thanks to Yard Sale Pizza for fuelling almost all of my writing sessions. Finally, thank you to Holly for being extra gassy.

1 Introduction

1.1 Kinase Structure and Their Inhibitor Types

Whilst kinase inhibitors have been utilised as drugs since the 1930s, it took until the 1990s for the first characterisation of kinase drugs, and since then kinases have been one of the most intensely pursued targets in drug discovery.¹ To date, 49 kinase inhibitors have been approved by the Food and Drug Administration (FDA), for disease indications ranging from cancer to inflammatory diseases such as rheumatoid arthritis (RA).²

Whilst kinases only account for ~5 % of the protein-coding genes, they play a crucial role in physiology through mediation of most cellular signal transduction and regulation of a wide variety of cellular functions such as apoptosis, immune response, transcription and nearly every other aspect in cell biology.^{3,4} As such, protein kinases represent an attractive class of drug targets, as their dysregulation results in a variety of diseases due to their involvement in numerous cellular processes. Specifically kinases catalyse the transfer of the γ -phosphate unit within adenosine triphosphate (ATP) **1** onto a wide range of hydroxy substrates such as proteins, sugars, and nucleotides (Fig 1).^{3,5} Despite possessing a myriad of cellular functions, they share a high homology sequence within their active site due to sharing a single common substrate, ATP **1**.³ As the human genome contains over 500 known protein kinase genes, achieving selectivity between the various kinases presents a significant challenge.⁶ The nature of the phosphorylated hydroxy groups conducted by these enzymes dictates their classification as serine/threonine kinases, tyrosine kinases, dual-specificity kinases, tyrosine-kinase-like, lipid kinases, sugar kinases, and nucleotide kinases.¹

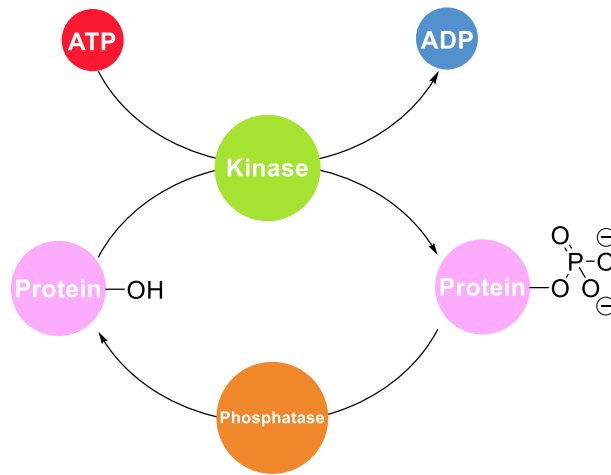


Fig 1 A schematic illustrating the ATP-dependent phosphorylation of proteins via kinases.

The catalytic domain of kinases is highly conserved in both sequence and structure. The activity of a kinase is dependent on binding of the substrate to be phosphorylated and ATP **1** to Mg^{2+} within the catalytic domain (Fig 2). The domain comprises a bilobal structure composed of an *N*-lobe which maintains a 5-stranded beta sheet and α -helix (αC), which contributes to ATP binding (Fig 3). The C-lobe is formed from multiple alpha helices, and it is in the C-lobe where the kinase substrate binds. Within the interface of the *N*- and C-lobes is the hinge region, which possesses several conserved residues and provides the catalytic machinery within the ATP binding pocket. Every kinase active site also expresses a gatekeeper residue which partially or fully blocks the hydrophobic region deep within the ATP binding site. Present in all kinases is an activation loop, marked by a conserved Asp-Phe-Gly (DFG) motif at the *N*-terminus. The flexible activation loop serves to regulate kinase activity, controlling access to ATP **1** within the active site. The activation loop can adopt two conformations, with the DFG-Asp residue pointing either in (DFG-in) or out (DFG-out) of the active site. It is dependent on this conformation as to whether the kinase is catalytically active or not; if the conformation is in its DFG-in state then the kinase is active, whereas a DFG-out conformation renders the kinase inactive. For the DFG-in state, the Asp residue coordinates to Mg^{2+} within the active site, however in the DFG-out conformation, the Asp residue no longer coordinates Mg^{2+} .⁷

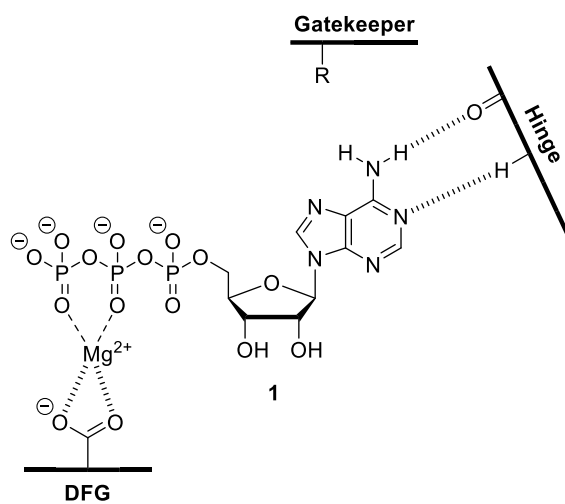


Fig 2 The chemical structure of ATP 1 highlighting the interactions of ATP 1 and the active site of a given kinase.

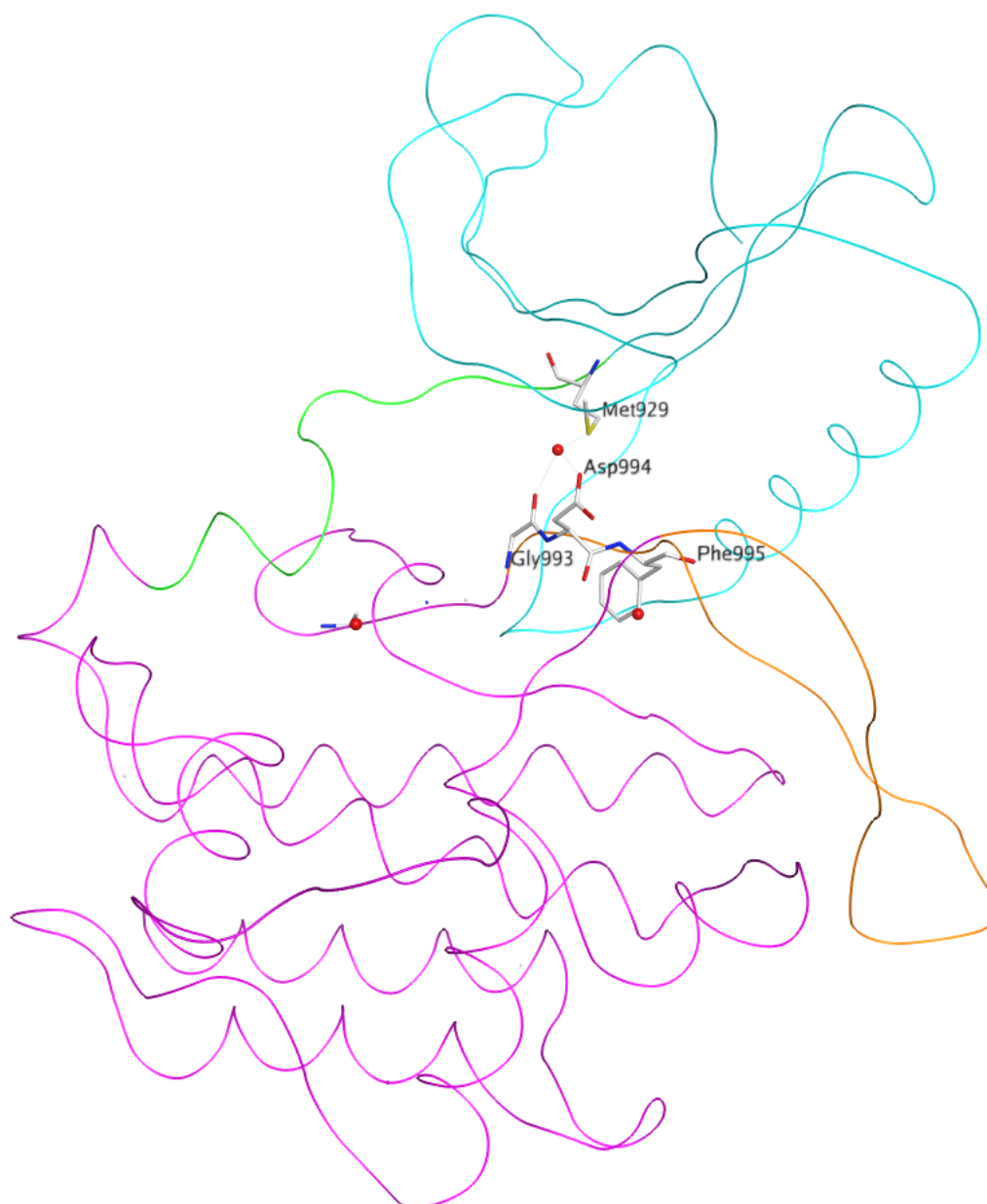


Fig 3 The crystal structure of a kinase (JAK2) illustrating the structural components. Blue ribbon = N-lobe; pink ribbon = C-lobe; orange ribbon = activation loop; green ribbon = hinge region; DFG residues in white showing a DFG-in conformation. Gatekeeper residue (Met929) in white. PDB: 6BBV, resolution: 1.80 Å.⁸

The kinase active site is not the only domain to be targeted by kinase inhibitors, and as such targeted kinase drugs are categorised as Type I – VI based on their binding mode. Drugs which inhibit the ATP domain with an active protein kinase conformation (DFG-Asp-in, α C-helix-in) are known as Type I inhibitors. Conversely, Type I½ inhibitors bind to an inactive

DFG-Asp-in conformation, whereas Type II inhibitors bind the DFG-Asp out inactive conformation. Furthermore, Type I, I½ and II inhibitors all occupy the adenine region, and form H-bonds to the hinge region of the protein. Additionally, Type III and IV inhibitors are allosteric in nature, occupying sites excluding the active site. In particular, Type III inhibitors bind within the cleft between the small and large lobes adjacent to the ATP binding site and Type IV inhibitors bind outside of the cleft and active site. If a drug occupies two different regions of the protein kinase in a bivalent fashion, they are labelled as type V inhibitors. Type I – V inhibitors are all reversible inhibitors, however, covalent kinase inhibitors are known as Type VI.⁹ A type classification does not currently exist for kinase binders that induce proteasome-mediated target kinase degradation.

1.2 Implications of the JAK-STAT Pathway

The Janus kinases or JAKs are a family of intracellular tyrosine kinases that are pivotal in both innate and adaptive immunity, and hematopoiesis, thus making them attractive targets for a number of disease indications.^{10,11,12} Since their discovery in the early 1990s, the JAKs have acquired significant interest from both academic and industrial groups alike as targets for novel chemical entities, resulting in a wealth of chemical matter, both marketed and in the clinic, for diseases spanning myeloproliferative disorders to various inflammatory diseases.¹³

Communication between cells is fundamental to cell development, host defence, and tissue and organism homeostasis. As one of the simplest architectural systems implicated in cell signalling, the Janus kinase/signal transducers and activators of transcription (JAK-STAT) pathway provides an exquisite solution to cell communication from transmembrane receptors directly to the nucleus (Fig 4).¹⁴ Seminal studies revolving around the control of gene expression through interferons resulted in the discovery of the JAK-STAT pathway,¹⁵ and it has since been shown that a multitude of cytokines, hormones and colony-stimulating factors utilise this form of signal transduction. In mammals, the JAK family comprises four members: JAK1, JAK2, JAK3 and TYK2. The cytokine receptors comprise two or more receptor subunits, each associated with a particular JAK isoform. The JAK isoforms assume their proximal-membrane bound positions, as homo and heterodimers, after ligand binding to the

cytokine receptor. Upon engagement of a ligand, activation of the JAKs occurs, prompting cross-phosphorylation and phosphorylation of tyrosines at the intracellular receptor tails. This phosphorylation event forms intracellular docking sites for latent, cytoplasmic transcription factors named signal transducers and activators of transcription (STATs). Upon binding, the STATs in turn become activated through phosphorylation, giving rise to STAT-STAT dimers which can translocate to the nucleus, directly bind DNA and regulate gene expression. Any one or more of six STAT family members (STAT1, STAT2, STAT3, STAT4, STAT5 or STAT6) may be recruited through their Src Homology 2 (SH2) domains.^{16,17} This transcriptional program controls whether the cell undergoes proliferation, differentiation, survival, or death.

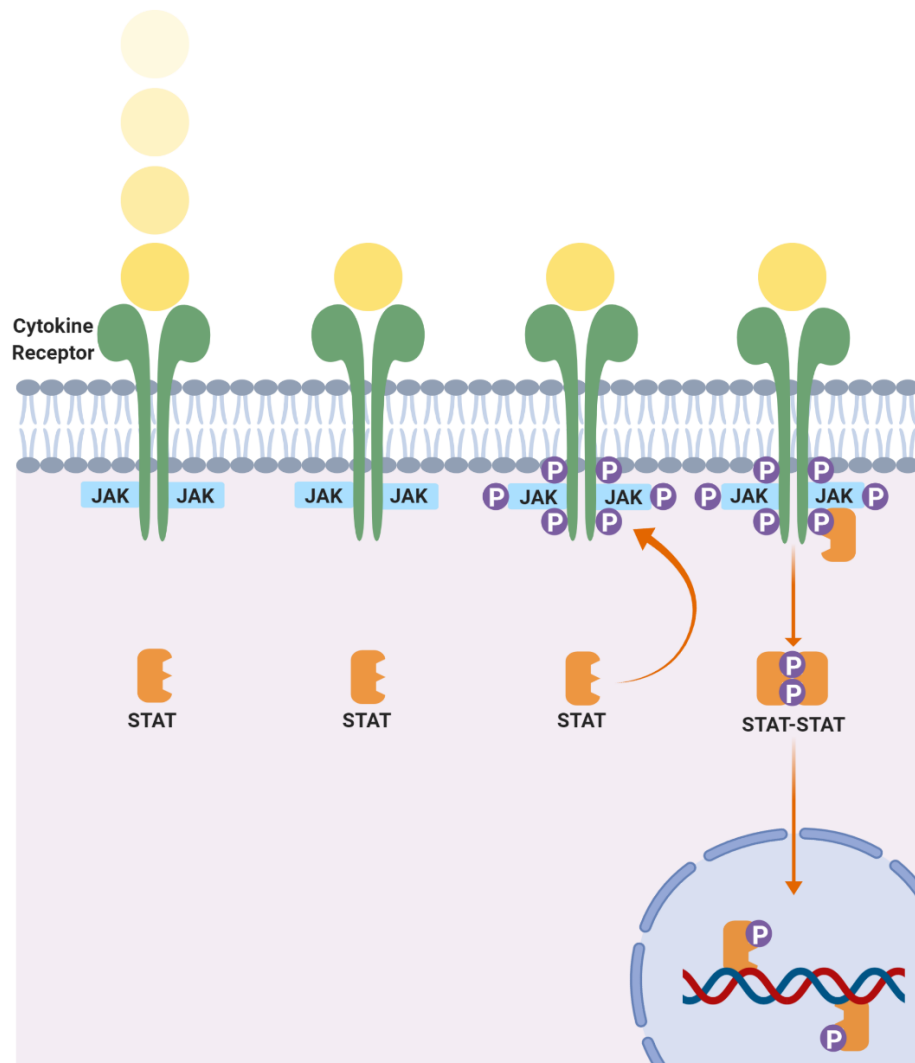


Fig 4 Through ligand (yellow) binding to the cytokine receptor, JAKs become activated, which initiates a cross-phosphorylation event (purple) to create docking sites for STATs. Phosphorylation of STATs results in STAT-STAT dimers which can translocate to the nucleus and go on to bind DNA and regulate gene expression.

Whilst strides are currently being taken to understand the etiology of inflammatory diseases and autoimmune diseases, the exact cause is not fully understood and is often a combination of genetic predispositions, and environmental and lifestyle factors. The pathogenic inflammatory state typically involves a break in T- and B-cell tolerance against self-antigens, resulting in undesirable autoimmune responses. Antigens from affected tissues are presented on antigen-presenting cells to naïve T-helper cells (Th0) along with secretion of co-stimulatory factors, cytokines, or glycoprotein signalling molecules. This leads to

activation, differentiation and expansion of Th0 cells into distinct T-helper phenotypes such as Th1 and Th2 cells. These activated T-cells further secrete cytokines that activate additional cells of the immune system, such as macrophages, natural killer (NK) cells, and neutrophils that subvert the targeted tissue, causing the damage associated with these diseases. As such, cytokines choreograph the intracellular communication process thereby cementing themselves in inflammatory response.¹⁸

As displayed by Fig 5, cytokines signal through a plethora of receptor superfamilies.¹⁹ Through binding to the extracellular domains of such receptors, cytokines instigate intracellular changes, eliciting signal transduction cascade events, culminating in gene expression changes. Protein kinases, such as JAK, are key in the signalling cascade between cytokine receptor superfamilies and gene expression. It is therefore unsurprising that many of these kinases have been targeted in attempts to regulate inflammatory response.²⁰ However, some of these kinases present themselves as better drug targets than others, as many of these signal transduction pathways can be redundant.

As mentioned previously, the JAKs associate with the intracellular domain of receptors, but more specifically, receptor subunits of type I and II receptor superfamily.²¹ Type I receptors bind ligands with a common four-helical structure, display four conserved cysteines, and possess a common WSXWS amino acid motif extracellularly, adjacent to the cell membrane (Fig 5). Whilst divergent intracellularly, they all maintain a conserved membrane proximal region for associating with the JAKs. Type II receptors are structurally related to type I receptors, and bind interferons and the IL-10 family.²² There is currently no known compensatory mechanism around the JAK-STAT pathway and thus the JAKs are critical in regulating the cytokines that signal via these pathways. Additionally, a significant proportion of cytokines that signal via type I and II cytokine receptors are directly implicated in the pathogenesis of autoimmune diseases, making the JAKs attractive drug targets.²³

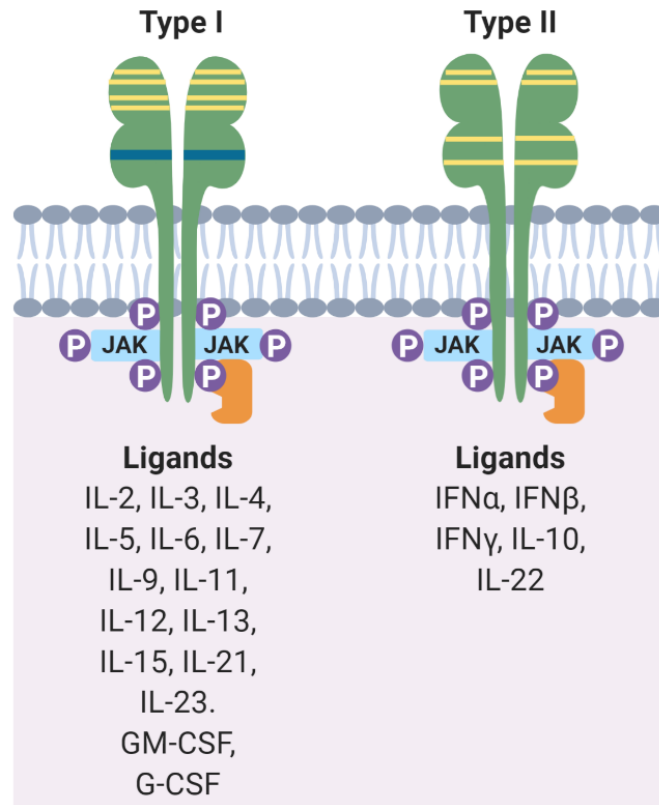


Fig 5 Type I and Type II cytokine receptors. Yellow bands on the type I receptor indicate conserved cysteine residues, and the blue band represents the WSXWS region. Type I and type 2 cytokine ligands are listed below their respective receptor.

1.2.1 Structure of the JAK Family

The four members of the JAK family consist of approximately 1150 amino acids each, and range from 120 to 130 kDa in molecular weight.²⁴ Each JAK isoform is comprised of a common domain architecture (Fig 6). The JAK isoforms possess seven regions of high homology, Jak homology 1 – 7 (JH1 – JH7). Whilst the various JH regions have been well characterised, several regions are yet to be fully elucidated.²⁵ The JH1 catalytic region plays a role in encoding the kinase, whereas the JH2 region represents a pseudokinase domain, which is likely required for JH1 catalytic activity.²⁶

JH3 – JH7 are involved in cytokine receptor association, however the exact role of JH7 remains unknown.²⁷

The *N*-terminus, which spans 550 amino acids is fairly divergent between the isoforms. The *N*-terminus appears to be required for JAK1 binding to the interferon gamma (IFN γ) receptor. The JH4 – JH7 region consists of a band 4.1, ezrin, radixin, moesin (FERM) domain and the JH3 – JH4 region shares some similarity to SH2 domains. Both regions are involved in JAK association with the cytoplasmic tail of various cytokine receptors,²⁸ through mediating protein-protein interactions (PPIs).²⁹

The four JAK isoforms are distinct from other tyrosine kinases in that they possess a pseudokinase domain.²⁵ The pseudokinase domain comprises all the structural features required for a true tyrosine kinase, however, it lacks catalytic activity. Whilst the exact nature of the pseudokinase domain remains unclear, there is increasing evidence that it regulates the activity of the kinase domain. This has been typified by deletion studies of the pseudokinase domain in JAK2, which led to hyperactivity of JAK2.^{30,31}



Fig 6 The domain structure of the JAK isoforms, comprising a FERM, SH2, pseudokinase and kinase domain.

1.2.2 Sequence Homology of JAKs

The sequence homology of the active site of each of the JAKs is near-identical, differing by only a few amino acid residues (Fig 7). The protein kinase domain of JAK3 shares 52 % sequence identity with JAK1, 62 % with JAK2 and 50 % with TYK2. Furthermore, JAK2 and JAK3 share an almost identical amino acid composition within the ATP-binding site, with two major differences; JAK1, JAK2 and TYK2 contain a Ser at position 936, whereas JAK3 displays a Cys at the equivalent position (909). Additionally, JAK3 exhibits an Ala, whereas JAK1, JAK2 and TYK2 express a Gly at the equivalent position. Achieving isoform selectivity through the

development of small-molecule JAK inhibitors is therefore not be without its challenges; however, exploitation of these subtle differences could give rise to selective JAK inhibitors.³²

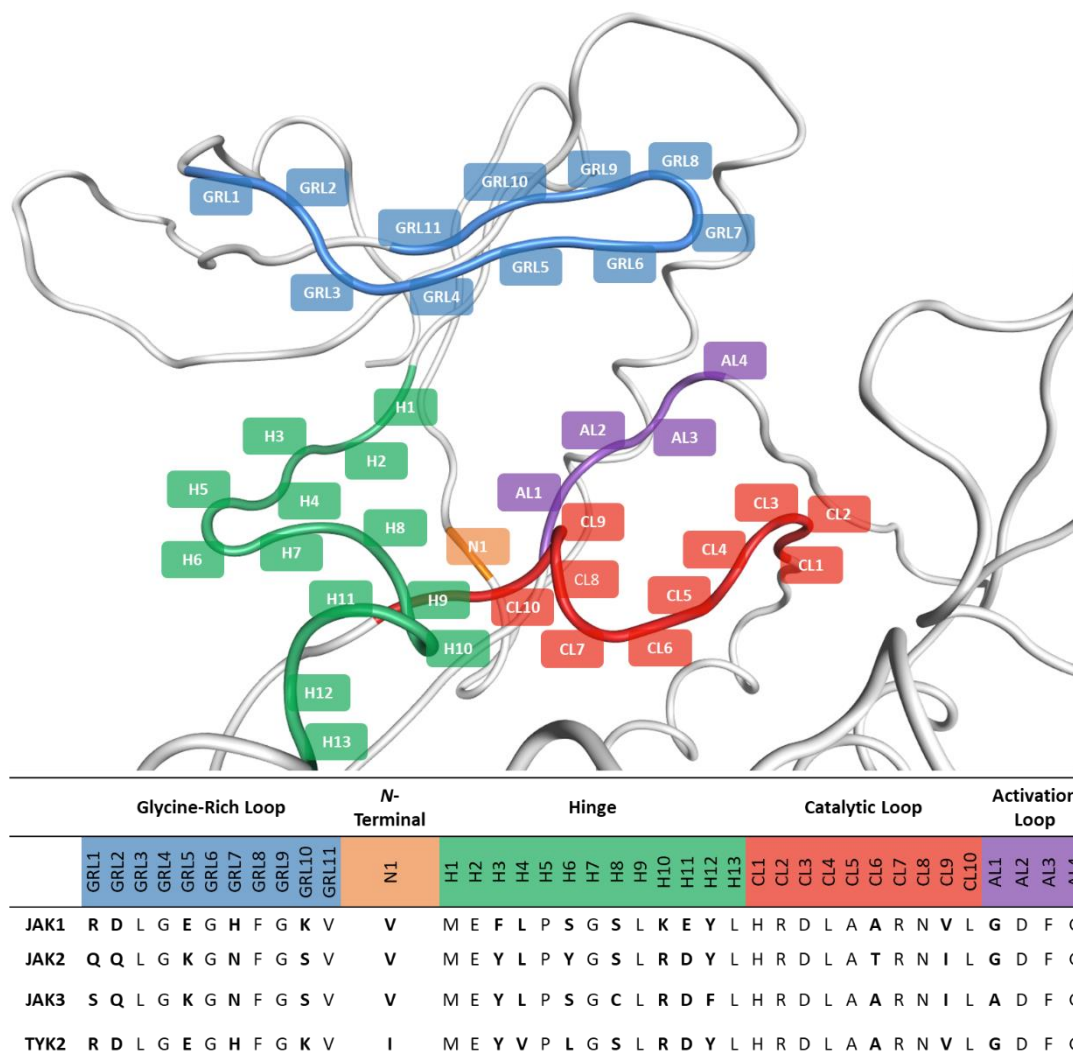


Fig 7 The amino acid alignment of regions of the ATP binding site of the JAKs. Residues in bold indicate that they are not conserved across the isoforms.

1.3 Why Target the JAKs?

Recently, the identification of various cytokines' involvement in the pathogenesis of allergic inflammatory and autoimmune diseases has led to the development of therapeutic biologics, such as monoclonal antibodies (mAbs) and recombinant proteins that target such cytokines

and cytokine receptors. Despite these therapies altering the outcomes for diseases such as asthma, psoriasis, rheumatoid arthritis, and inflammatory bowel disease (IBD),³³ a considerable proportion of the patient population do not completely respond, and few cases of long-term remission after therapy termination have been documented.³⁴ Moreover, diseases involving fibrosis and tissue destruction such as systemic sclerosis have experienced fewer advances.³⁵ Therefore, there is a growing unmet need for novel treatments for the aforementioned diseases which could potentially be addressed by small molecules, and more novel modalities for treating disease.

An alternative approach to treating cytokine-related diseases is to disrupt the downstream signalling cascade via inhibition of individual, or combinations of the JAKs, which could lead to a novel class of immunomodulatory drugs (Fig 8).

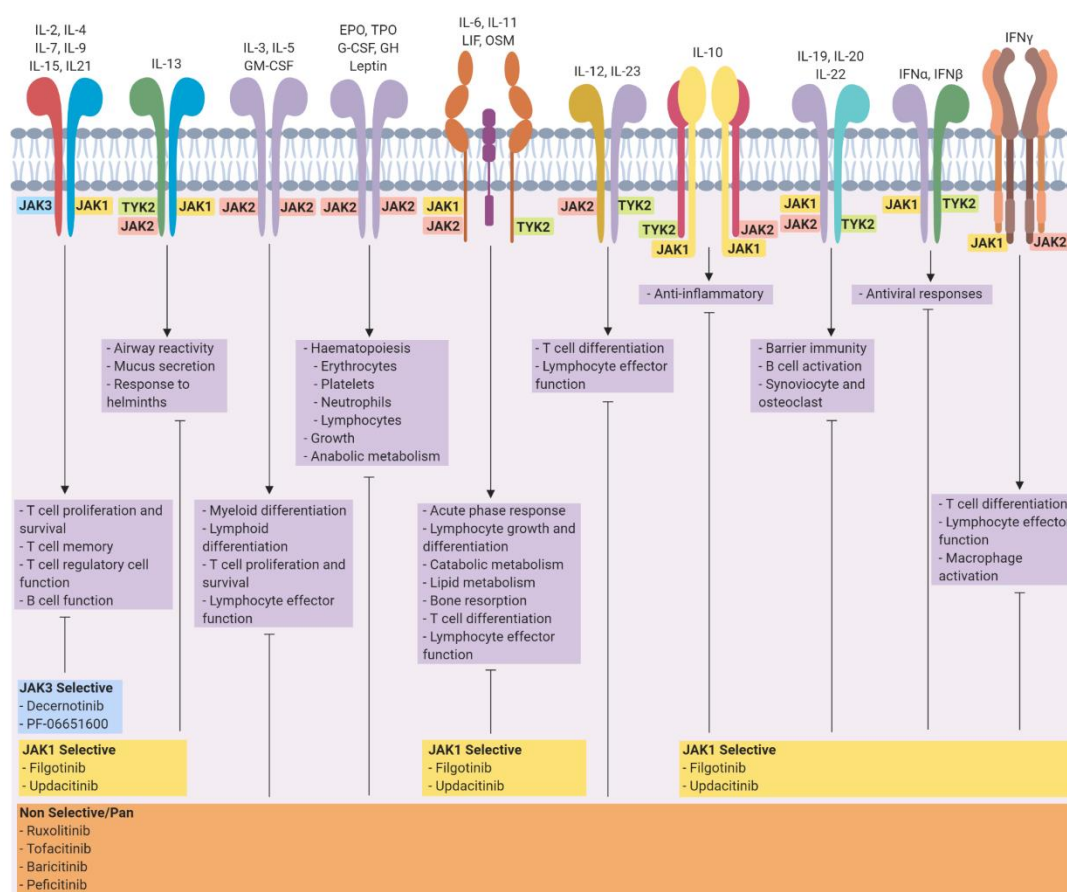


Fig 8 Effects of targeting different JAKs. Cytokine receptors associate with the JAKs which transduce downstream intracellular signals. Different cytokine receptors associate with different JAK homo- and heterodimers. Inhibition of specific JAKs can lead to a multitude of therapeutic effects.

1.4 Non-selective JAK inhibitors

1.4.1 Ruxolitinib

The first JAK inhibitor to be approved by the FDA, in 2011, was Ruxolitinib **2**, for the treatment of intermediate/high-risk myelofibrosis (MF).^{36,37} MF is a type of myeloproliferative neoplasm (MPN), which is a group of clonal hematological malignancies that originate at the level of pluripotent hematopoietic stem cells (HSC) and comprise chronic myelogenous leukemia (CML), polycythemia vera (PV), essential thrombocythemia (ET), and primary myelofibrosis (PMF). Myelofibrosis can arise from progression of PV and ET (termed post-ET/PV MF), which is clinically indistinguishable from PMF. Together, PMF and post-ET/PV MF are referred to as MF.³⁷ The mutation JAK2V617F, which is characterised by a G-to-A point mutation, leading to substitution of valine for phenylalanine at amino acid position 617 (V617F) within the pseudokinase domain, silences the autoinhibitory function of the pseudokinase domain resulting in activation of the catalytic component of JAK2.³⁸ Therefore, inhibition of dysregulated JAK2 would provide therapeutic intervention. Furthermore, disease progression appeared elevated by proinflammatory cytokines, and so JAK1 was also targeted. Additionally, patients absent of JAK2V617F also experience JAK/STAT pathway activation.

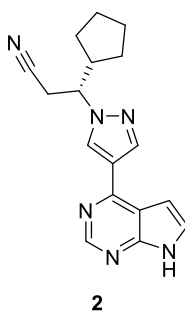


Fig 9 The chemical structure of Ruxolitinib **2**.

Ruxolitinib **2** is a potent, orally bioavailable JAK1/JAK2 inhibitor, with a pIC_{50} of 8.5 and 8.6 respectively. Ruxolitinib **2** inhibits the dysregulated JAK-STAT pathway in MF patients regardless of their *JAK2* mutational state, thus explaining its efficacy in patients possessing

the mutation or not.³⁸ Whilst ruxolitinib **2** exhibits a ~159-fold selectivity over JAK3 against JAK2, it is frequently described as a JAK1/JAK2 select inhibitor, however, ruxolitinib **2** possesses nanomolar potency at TYK2, and only displays an ~8-fold bias over TYK2 against JAK2 (Table 1). Additionally, ruxolitinib **2** displays moderate potency with both the IL6 and TPO stimulated human whole blood assays, pIC₅₀ 6.5 and 6.6, respectively.³⁹

Compound	pIC ₅₀				hWB pIC ₅₀	
	JAK1	JAK2	JAK3	TYK2	IL-6	TPO
Ruxolitinib 2	8.5	8.6	6.4	7.7	6.5	6.6

Table 1 The biochemical and cellular data associated with ruxolitinib **2**. JAK1, JAK2, JAK3 and TYK2 pIC₅₀'s measured at *K_m* ATP concentrations.

Though the literature is absent of the SAR of ruxolitinib **2**, structural binding information to JAK2 within the kinase domain is known (Fig 10). Ruxolitinib **2** possesses one H-bond donor, and forms essential donor/acceptor interactions with the hinge region of JAK2 (Glu930 and Leu932) through the pyrrolopyrimidine core. Ruxolitinib **2** is predominantly hydrophobic, and the planar pyrrolopyrimidine ring system is sandwiched between hydrophobic residues of the *N*-terminal lobe (Leu855, Val863, Ala880, Val911 and Leu983). Additionally, the methionine (Met929) gatekeeper residue forms an additional interaction with the pyrrolopyrimidine core. The nitrile forms a H-bond interaction with Asn981, within the catalytic site. As with other Type 1 kinase inhibitors, ruxolitinib **2** requires a DFG-in conformation.^{40,41}

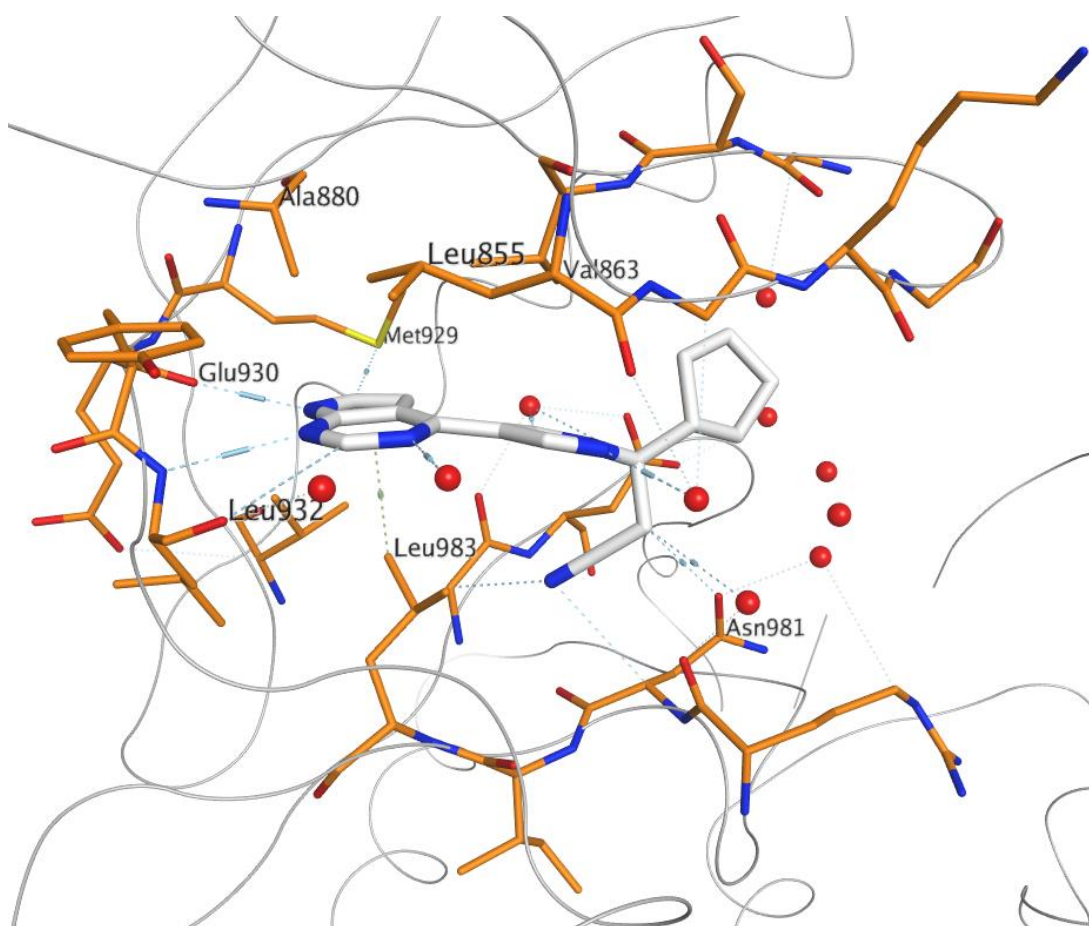


Fig 10 A crystal structure of ruxolitinib **2** bound to JAK2. In-house crystal structure, resolution: 2.22 Å.⁴²

Ruxolitinib **2** is currently being investigated in various clinical trials for differing disease indications such as vitiligo (phase II) (NCT02809976), whereby it is being administered as a topical formulation. Trials with topical ruxolitinib **2** have also demonstrated improvement in psoriasis compared with placebo or other topical approved therapies, however such improvements were not sustained after discontinuation.^{10,43} Interestingly, systemic absorption was minimal and there lacked evidence of systemic toxicity.⁴³ Topical ruxolitinib has also demonstrated efficacy in treatment of alopecia areata, however, it is yet to enter clinical trials for this indication.⁴⁴ It is important to note that ruxolitinib has been discussed widely within the literature as being associated with progressive multifocal leukoencephalopathy (PML), a rare and often fatal viral disease characterised by progressive damage or inflammation of the white matter of the brain at multiple locations. However, this was only reported in one 75-year old patient with intermediate-2-risk myelofibrosis.

Neurologic signs developed ten weeks after the initiation of ruxolitinib **2** therapy, and it should be noted that it is not yet clear whether the PML was directly related to this agent.⁴⁴

1.4.2 Tofacitinib

Tofacitinib **3** was the first orally bioavailable JAK inhibitor approved for the treatment of autoimmune diseases, such as moderate-to-severe rheumatoid arthritis (RA) and ulcerative colitis (Fig 11).³⁵ To date, it has been studied in numerous clinical trials, including six phase III trials.^{45,46,47,48,49}

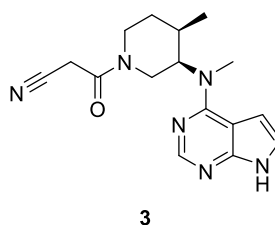


Fig 11 The chemical structure of tofacitinib **3**.

Tofacitinib **3** displays low nanomolar inhibitory pan-JAK activity, and to a lesser extent inhibits TYK2 (JAK1 pIC₅₀ = 8.5, JAK2 pIC₅₀ = 8.4, JAK3 pIC₅₀ = 8.8, TYK2 pIC₅₀ = 7.5) (Table 2).⁵⁰ Additionally, through inhibition of JAK1 and JAK3 within a cellular context, tofacitinib **3** exhibits a pIC₅₀ of 6.5. When screened against a panel of > 300 other kinases, which represents more than 50 % of the predicted human kinome, tofacitinib **3** displayed phenomenal selectivity.⁵¹

Compound	pIC ₅₀				
	JAK1	JAK2	JAK3	TYK2	IL-2
Tofacitinib 2	8.5	8.4	8.8	7.5	6.5

Table 2 The biochemical and cellular data associated with tofacitinib **2**. JAK1, JAK2, JAK3 and TYK2 pIC₅₀'s measured at K_m ATP concentrations.

As with ruxolitinib **2**, and many other pan-JAK inhibitors, tofacitinib **3** is constructed around a pyrrolopyrimidine core which functions as the hinge binder, forming donor/acceptor interactions in JAK3 with hinge residues, Glu903 and Leu905 (Fig 12). The pyrrolopyrimidine ring forms an additional H-bond to a conserved water molecule found within JAK1, JAK2 and TYK2. The piperidine ring is positioned within a hydrophobic environment, forming hydrophobic interactions with Val836, Cys909, Leu956 and Ala966. Furthermore, the methyl group appended to the piperidine ring occupies a hydrophobic pocket within the binding cavity of JAK3. It is thought that this interaction aids in the observed kinome selectivity of tofacitinib **3**, and provides an increase in potency. The nitrile interacts with the glycine-rich loop, predominantly through Gly831, Gly834, Ser835 and Val836 residues. It is thought that these interactions between the nitrile and glycine-rich loop provides tofacitinib **3** with its exquisite kinome selectivity.³² However, it should be noted that its selectivity between the JAK isoforms is not fully understood.

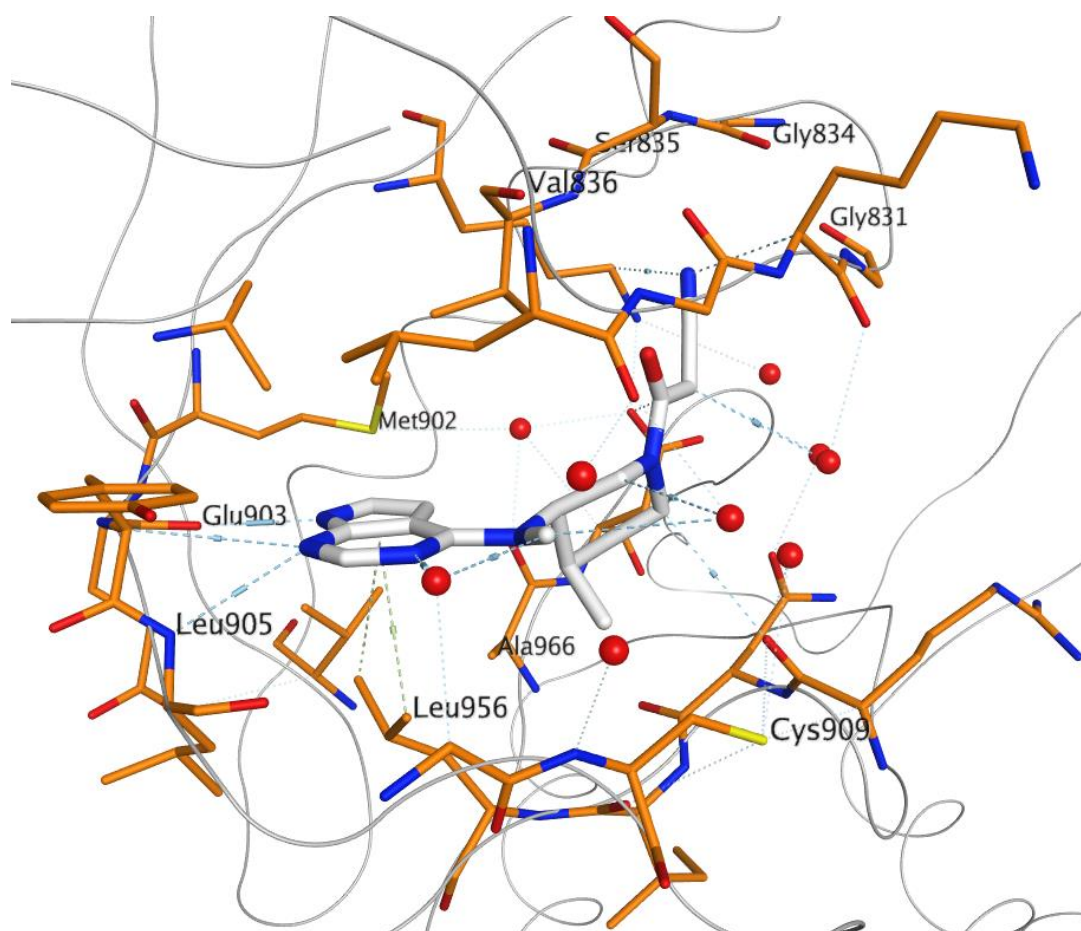


Fig 12 A crystal structure of tofacitinib **2** bound to JAK3. PDB: 3LXK, resolution: 2.00 Å.

Unlike ruxolitinib **2**, the medicinal chemistry story of tofacitinib **3** has been published. Pfizer conducted a high-throughput screen against JAK, culminating in the identification of compound **4**, which possessed a pyrrolo[2,3-d]pyrimidine pharmacophoric subunit (Fig 13). SAR was explored around the pyrrolopyrimidine ring, and since crystal structures were not available at the time of this study, the pyrrolopyrimidine ring was assumed to be the hinge binder. Attempts in switching out the pyrrolopyrimidine ring for other heterocycles, or substitution around the ring resulted in loss in potency. C-5 substituents were tolerated for JAK3 potency, however often conferred suboptimal metabolic stability within human liver microsomes and/or diminished cell potency. As such, efforts revolved around optimisation of the anilinic position. The addition of the cyclohexyl group to give compound **5** led to an increase in cell potency likely due to an increase in JAK1 activity. In the absence of crystal structures, exploration of SAR was guided by high-speed analoging (HSA) technology. The

library of compounds provided a wealth of SAR insights. The *N*-methyl group was also recognised as providing enhanced kinome selectivity. As to identify optimal stereochemistry, terpenoids such as *S*-carvone were drawn from the chiral pool resulting in all-*cis* configuration, such as compound **6**, being identified as optimal. The piperidine provided a vector to access the glycine-rich loop. A variety of analogues were prepared from the piperidine scaffold, including urea **7**, in attempts to optimise potency and improve physicochemical properties. The cyanoacetamide side-chain of tofacitinib **3** provided the best combination of potency and physicochemical properties and was therefore progressed from the > 1000 synthetic analogues produced over a three-year period.⁵⁰

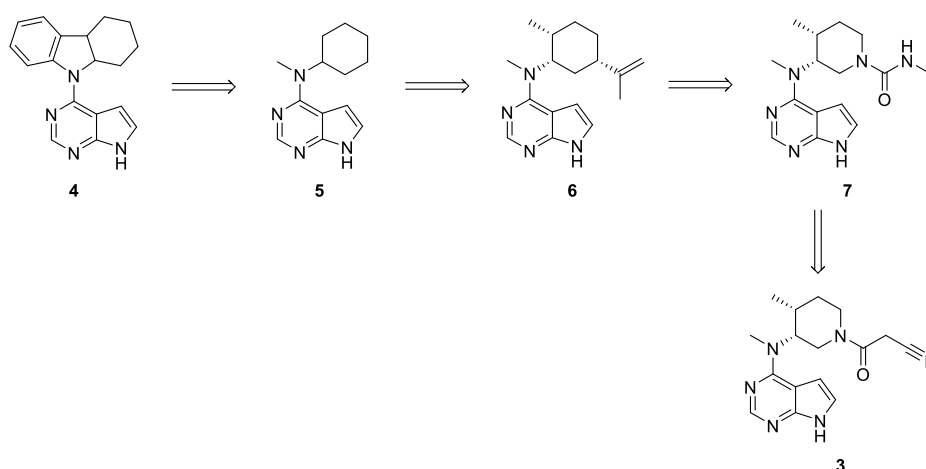


Fig 13 The key structural milestones in the development and discovery of tofacitinib **3**.

Haematopoietic growth factors such as, but not limited to, erythropoietin (EPO), signal through JAK2, and therefore inhibition of JAK2 often results in cytopenias, when patients are treated with first-generation pan-JAK inhibitors such as tofacitinib. Additionally, neutropenia and anaemia have been reported at higher doses of tofacitinib **3**.^{45,46,47,52,53} However, it should be noted that these conditions were often well tolerated and did not require treatment discontinuation.¹⁸

One additional concern with immunosuppression and treatment with tofacitinib **3** is the increased risk of malignancy. JAK inhibitors can induce inhibition of the immune response to cancer through interference with T and NK cell functions in immunosurveillance, and with the antineoplastic function of IFNs.⁵⁴ However, data derived from clinical trials centred

around tofacitinib **3** have not revealed an increased risk of haematological malignancies or solid tumors.⁵⁵ As such, further examining of patients treated with tofacitinib **3** is required to elucidate whether long-term therapy produces a risk of cancer.

1.4.3 Baricitinib

Baricitinib **8** is an oral small-molecule JAK inhibitor, initially approved in the EU and Japan for the treatment of moderate to severe RA, for use in patients that inadequately responded to other treatments (Fig 11). In contrast to tofacitinib **3**, the medicinal chemistry discovery story has not been published for baricitinib **8**. It is structurally related to ruxolitinib **2** and tofacitinib **3**, in that it shares the common pyrrolopyrimidine core, and the pyrazole motif as found in ruxolitinib **2**. Baricitinib **8** selectively and reversibly inhibits JAK1 and JAK2; however, it also inhibits JAK3 and TYK2, but to a lesser extent (Table 3).⁵⁵

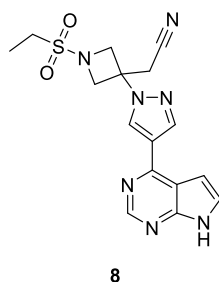


Fig 14 The chemical structure of baricitinib **8**.

Compound	pIC ₅₀				
	JAK1	JAK2	JAK3	TYK2	IL-6
Baricitinib 8	8.2	8.2	6.3	7.3	> 6.3

Table 3 The biochemical and cellular data associated with baricitinib **8**. JAK1, JAK2, JAK3 and TYK2 pIC₅₀'s measured at K_m ATP concentrations.

Whilst no crystal structures of baricitinib **8** have been reported with the JAKs, a crystal structure of baricitinib **8** bound to JAK2 was generated at GSK (Fig 15).⁴² Owing to its pyrrolopyrimidine core, baricitinib **8** binds to JAK in a similar fashion to ruxolitinib **2** and tofacitinib **3**. Baricitinib **8** forms crucial hinge interactions with Glu930 and Leu932. As with tofacitinib **3**, the pyrrolopyrimidine ring H-bonds to a conserved water molecule found within JAK1, JAK2 and TYK2. Located within a hydrophobic environment, the pyrimidine ring forms hydrophobic interactions with Val911 and Leu983. Additionally, the ethyl sulfonamide points towards the glycine-rich loop, in a similar vein as tofacitinib **3** and ruxolitinib's **2** nitrile groups, through Gly858, Gly861, Ser862 and Val863 residues.

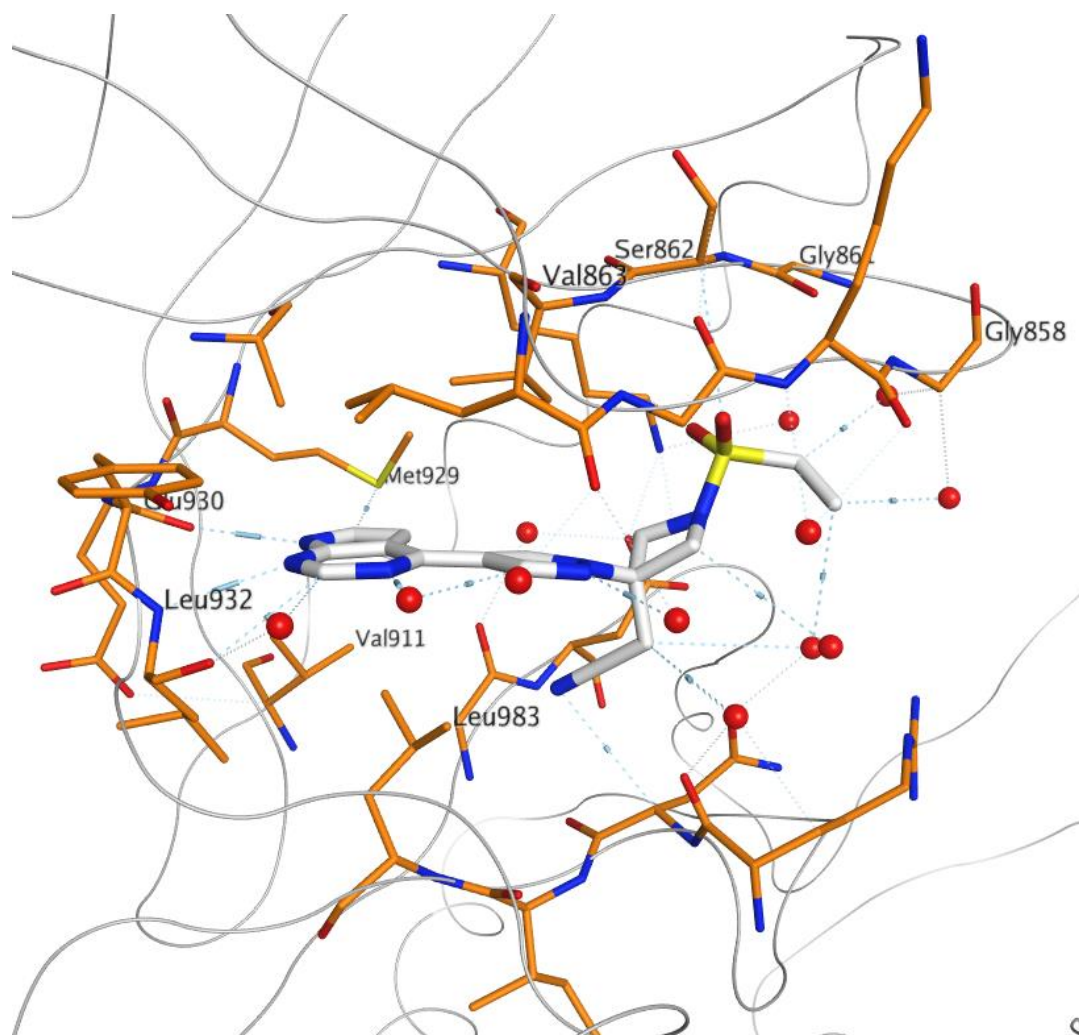


Fig 15 A crystal structure of baricitinib **8** bound to JAK2. In-house crystal structure, resolution: 1.50 Å.⁴²

Dissimilarly to its structural relatives, tofacitinib **3** and ruxolitinib **2**, baricitinib **8** is not metabolised via the cytochrome P450 (CYP) system; instead, it is cleared by the kidney.⁵⁶ The FDA initially issued a complete response letter indicating that it was not able to approve baricitinib, due to requirements of additional clinical data to determine the most appropriate dose and clarify safety concerns.⁵⁶ However, following resubmission of a new drug application, baricitinib was approved in 2019 as a once-daily 2 mg oral for the treatment of moderate to severe RA.⁵⁷

Since tofacitinib **3** is the most widely used JAK inhibitor, its safety profile is most well characterised, however, the side effects of baricitinib **8** and other non-selective JAK inhibitors are similar. This is to be expected due to similar indirect cytokine inhibition of the non-selective drugs.⁵⁷ Baricitinib **8** is associated with increased risk of herpes zoster infection, and anaemia and neutropenia were also reported.^{58,59}

Interestingly, mild thrombocytosis was observed in patients treated with baricitinib **8**, although not in those treated with tofacitinib **3**. Since JAK2 blockade is an FDA-approved treatment for essential thrombocytosis,⁶⁰ it would be expected that thrombocytopenia would be an adverse effect, not thrombocytosis, and the causes underlying treatment-associated thrombocytosis are not understood.³⁵

1.5 Pan JAK Inhibitors

1.5.1 Peficitinib

Deviating from the pyrrolopyrimidine motif of tofacitinib **3**, ruxolitinib **2** and baricitinib **8**, is peficitinib **9** which was discovered and developed by Astellas Pharma and was recently approved in Japan for the treatment of RA.^{60,61} Peficitinib **9** displays pan-JAK activity, inhibiting JAK1, JAK2, JAK3 and TYK2, albeit JAK3 biased (Table 4). Additionally, peficitinib **9**

displayed high potency within various rat and human cellular assays; peficitinib **9** inhibited IL-2 induced rat and human T cell proliferation with similar potencies ($pIC_{50} = 8.0$ and $pIC_{50} = 7.7$, respectively). Peficitinib **9** was able to prevent EPO-induced proliferation of human erythroleukemia cell line TF-1 ($pIC_{50} = 6.6$). The TF-1 assay involves signalling through JAK2, and the potency readout is 14-fold less potent than that against the human T cell proliferation. It is hypothesised that the reduction in activity against JAK2 within a cellular context may explain peficitinib's **9** alleviation of JAK2-mediated adverse hematopoietic effects displayed by other JAK inhibitors, such as ruxolitinib **2**, tofacitinib **3** and baricitinib **8**.

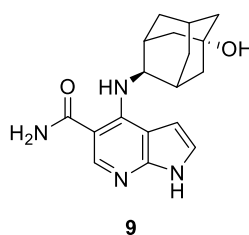


Fig 16 The chemical structure of peficitinib **9**.

Compound	pIC_{50}				Rat T Cells	Human T Cells	Human TF-1
	JAK1	JAK2	JAK3	TYK2			
Peficitinib 9	8.4	8.3	9.2	8.3	8.0	7.7	6.6

Table 4 The biochemical and cellular data associated with Peficitinib **9**. JAK1, JAK2, JAK3 and TYK2 pIC_{50} 's measured at K_m ATP concentrations.

Through compound screening against JAK1, JAK2 and JAK3, Astellas identified pyrrolopyridine **10**, which possessed low potency across JAK1, JAK2 and JAK3 (Fig 17). An SAR study was conducted which led to the discovery of carboxamide **11**, which possessed potent pan-JAK activity; however, it displayed poor metabolic stability in liver microsomes and *in*

vivo pharmacokinetic (PK) profiles due to high molecular lipophilicity.⁶² The cyclohexyl ring occupies a hydrophobic cavity within JAK3, and the group expected switching it out for an adamantyl group would increase potency. Following the synthesis of several analogous carbon-based bridged ring systems, the group discovered peficitinib **9**.⁶¹

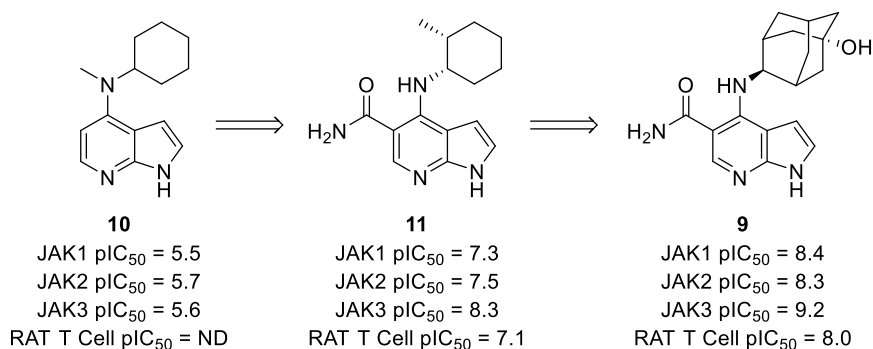


Fig 17 The discovery milestones towards the identification of peficitinib **9**, and their associated biochemical and cellular data.

Interestingly, and not reported with other JAK inhibitors, peficitinib's **9** binding mode flips depending on which JAK isoform it is bound to. Within JAK1, peficitinib **9** binds as expected (Fig 18); the pyrrolopyridine ring positions itself along the hinge region, in a similar fashion to the pyrrolopyrimidine JAK inhibitors, tofacitinib **3**, ruxolitinib **2** and baricitinib **8**. The pyrrolopyridine ring forms two H-bonds to Glu957 and Leu959. Furthermore, the carboxamide H-bonds to Leu959 and through two through-water interactions, to Pro960 and Ser963. Additionally, the carboxamide's conformation is locked via an intramolecular H-bond to the exocyclic anilinic group of the pyrrolopyridine ring. The adamantyl group occupies a hydrophobic cavity, interacting with Val889, with the hydroxy group forming a H-bond with the carbonyls of Arg1007 and Asn1008.⁶¹

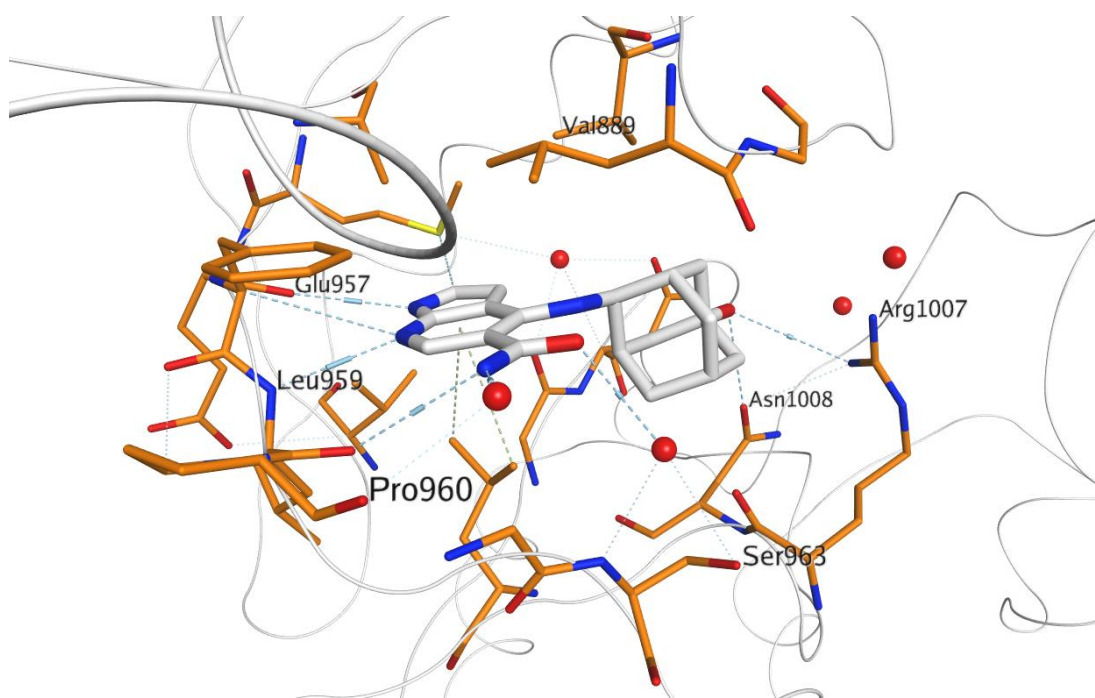


Fig 18 A crystal structure of peficitinib **9** bound to JAK1. PDB: 6AAH, resolution: 1.83 Å.

Within JAK2, the crystal structure of peficitinib **9** illustrates a flipped binding mode as compared to peficitinib **9** bound to JAK1, such that the carboxamide occupies the inside pocket, whereas the pyrrolopyridine points outside the active site (Fig 19). This flip in binding mode results in the carboxamide forming interactions with Glu930 and the pyrrolopyridine solely forming H-bonds to Leu932. Similarly to JAK1, the adamantyl group forms hydrophobic interactions with Val863. Dissimilarly, the hydroxy group is unable to interact with polar residues, and instead is located towards a solvent-exposed region of the protein.

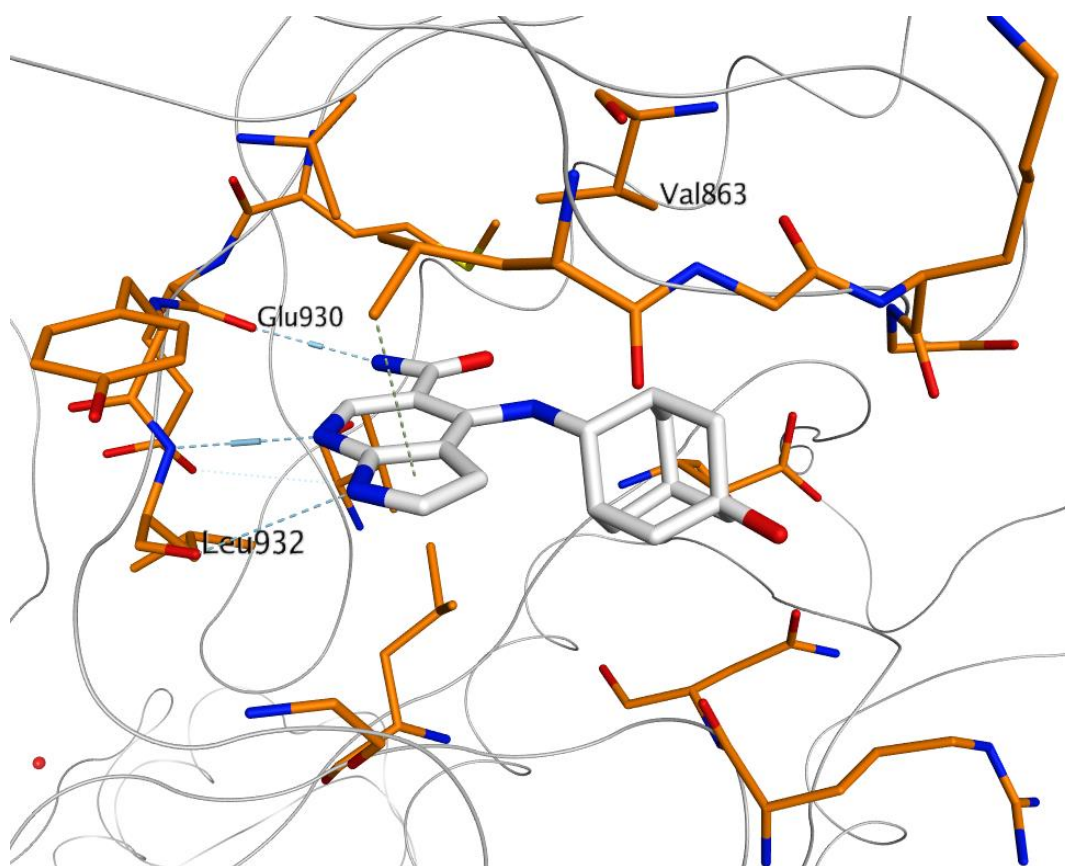


Fig 19 A crystal structure of peficitinib 9 bound to JAK2. PDB: 6AAJ, resolution: 2.37 Å.

As when bound to JAK2, peficitinib 9 exhibits a flipped binding mode when bound to JAK3. However, in contrast to the published JAK2 crystal structure with peficitinib 9 bound, the carboxamide forms a through-water interaction to Asp697, and an intramolecular H-bond to the anilinic exocyclic nitrogen of the pyrrolopyridine as observed in JAK1. Additionally, the hydroxy group of the adamantyl moiety interacts with Arg953.⁶¹

It is evident that the furthest progressed non-selective JAK inhibitors possess a distinct lack of structural diversity, revolving around a pyrrolopyrimidine or pyrrolopyridine core, with pyrazoles or anilinic sp^3 substituents emanating from the 4-position. Clearly, scope exists for non-selective, structurally distinct JAK inhibitors to occupy this space.

1.6 Selective JAK Inhibitors

Following the success of non-selective JAK inhibitors previously described, academia and industry turned their attention to targeting specific JAK isoforms in attempts to identify novel isoform-specific disease treatments. Additionally, isoform-specific JAK targeting could potentially reduce side effects such as anaemia, thrombocytopenia, and neutropenia, which arise through JAK2 inhibition. As such, selective JAK1 or JAK3 inhibition, in the absence of JAK2 inhibition could hypothetically provide access to an increased therapeutic window, and avoid dose-limiting pharmacology associated with pan JAK inhibitors. Despite the toxicity associated with JAK2, selective JAK inhibition could provide useful in the treatment of MPNs.

1.6.1 Filgotinib

Galapagos identified triazolopyridine **12** through their BioFocus kinase-focused library collection screened against a JAK1 *in vitro* biochemical assay (Fig 20).⁶³ Triazolopyridine was selected for its JAK1 potency ($pIC_{50} = 7.2$), in addition to its modular nature, enabling synthetic tractability. Moreover, triazolopyridine **12** exhibited a JAK1 bias over the other JAK isoforms (JAK2 $pIC_{50} = 6.9$; JAK3 $pIC_{50} = 6.3$; TYK2 $pIC_{50} = 6.3$). As the first JAK1-selective drug discovery program to be published, precedented SAR was unavailable, as such, discrete SAR campaigns around the amide substituent, heterocyclic core, and *para*-aryl substituent led to the discovery of filgotinib **13**. Filgotinib **13** is ubiquitously referred to as a selective JAK1 inhibitor within the literature, however filgotinib **13** falls within 10-fold of the other JAK isoforms and its alleged 'JAK1 selectivity' is not observed with the *in vitro* biochemical assays (~2-fold bias over JAK2; ~8-fold bias over JAK3 and ~5-fold bias over TYK2). Furthermore, biochemically, filgotinib **13** expresses a poorer selectivity profile for JAK1 than ruxolitinib **2**. However, assessment of filgotinib **13** within a cellular human whole blood (hWB) assay highlighted an alternative selectivity profile. Stimulation by either IL-6 or granulocyte-macrophage colony-stimulating factor (GM-CSF) to activate JAK1 or JAK2, respectively, measuring the downstream production of pSTAT1 and pSTAT5, respectively, highlighted a ~25-fold selectivity window of JAK1 over JAK2 (IL-6 hWB $pIC_{50} = 6.2$; GM-CSF hWB $pIC_{50} = 4.8$). The discrepancies between the selectivity profiles observed within the biochemical

assays and the cellular assay are thought to arise from differences in ATP concentrations of the two assays,¹⁸ and the dominance of specific JAK isoforms within heterodimeric pairs. For example, JAK1 is dominant in IL-2, IL-22 and IL-6 signalling pathways. Additionally, differing selectivity profiles of the same inhibitor is divulged when examining different cytokine pathways.^{64,64,65}

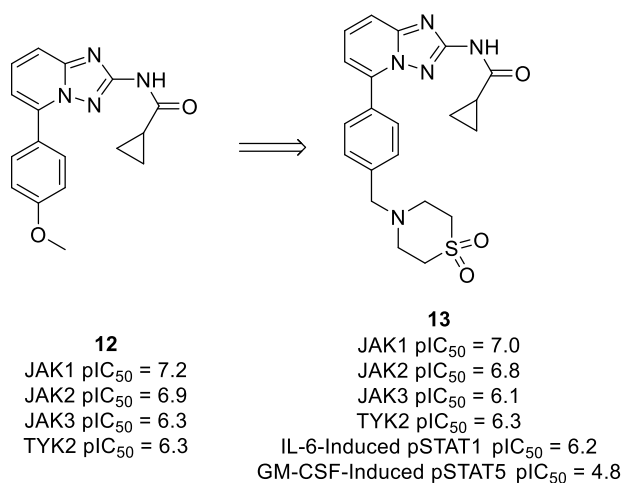


Fig 20 The development of filgotinib **13**, from the initial hit, and the associated biochemical and cellular data associated with filgotinib. JAK1, JAK2, JAK3 and TYK2 pIC₅₀'s measured at *K_m* ATP concentrations.

The cocrystal structure of filgotinib **13** within JAK2 reveals the triazolopyrimidine forms interactions with the hinge region, and forms two H-bonds to Leu932 via the endo and exocyclic nitrogen atoms (Fig 21). The phenyl ring is sandwiched within a hydrophobic region of the active site, between Val863 and Leu983. Furthermore, the thiomorpholine dioxide group interacts with the glycine-rich loop, with polar interactions formed with Gly861 and Ser862. Additionally, the thiomorpholine dioxide group interacts with the catalytic Lys882 and Asp994 of the DFG segment. Whilst this crystal structure unveils crucial interactions between filgotinib and JAK2, it provides little information regarding filgotinib's **13** apparent bias for JAK1, and perhaps a crystal structure of filgotinib **13** in JAK1 as a comparator would be more useful in unravelling its JAK1 bias.

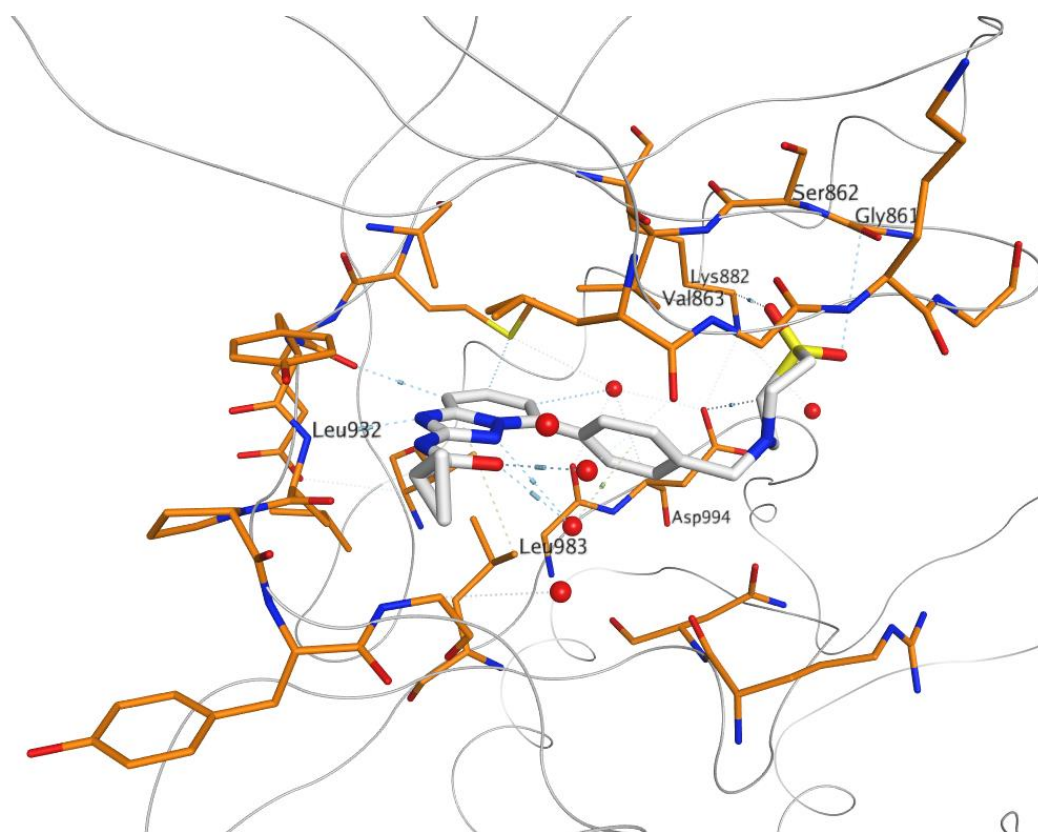


Fig 21 A crystal structure of filgotinib **13** bound to JAK2. PDB: 4P7E, resolution: 2.40 Å.

1.6.2 Upadacitinib

In contrast to filgotinib **13**, a structural hypothesis was employed to engineer the JAK1-selective inhibitor, upadacitinib **14** (Fig 22), rather than a kinase-focused library screen.^{65,66} Due to the highly conserved sequence within the kinase domain of JAK1 and JAK2 (~85 % sequence identity), the group's design strategy exploited structural differences within the active site, as opposed to specific interactions with unique residues, to achieve isoform selectivity. The glycine-rich loop was specifically targeted as it was speculated that the difference in amino acid sequence between the two isoforms resulted in a 'closed' backbone conformation in JAK1, differing from JAK2 (Fig 23). The 'closed' loop refers to His885 forming a salt bridge with Asp1003. As such, efforts were focused on identifying substituents to exploit the differences in protein conformation which stabilised the 'closed' conformation of the loop. The group predicted that a trifluoroethyl group would occupy the tight van der

Waals interaction space under the loop to provide an induced fit into JAK1, resulting in the identification of upadacitinib **14**.⁶⁵ The medicinal chemistry story and SAR surrounding upadacitinib **14** development has not been published.

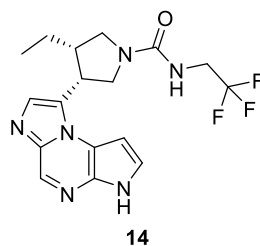


Fig 22 The chemical structure of upadacitinib **14**.

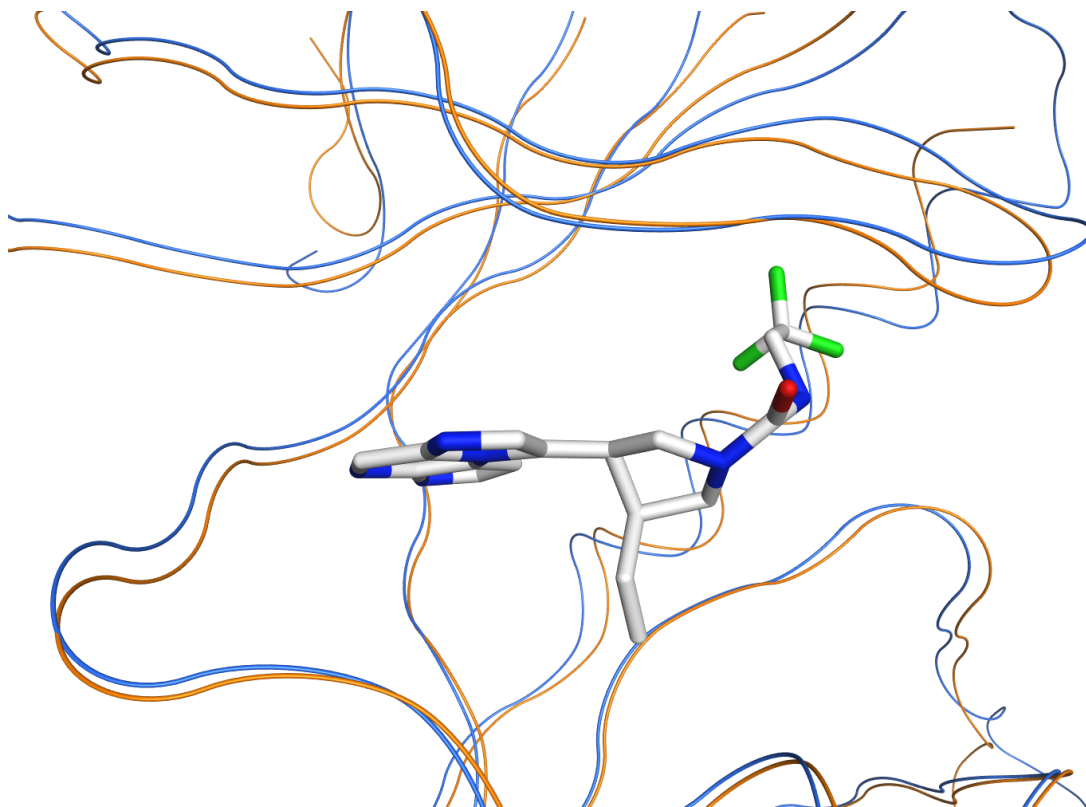


Fig 23 Upadacitinib **14** docked within the crystal structure of JAK1 (orange). JAK2 is overlaid in blue PDB: 2B7A, resolution: 2.00 Å.

Within the JAK biochemical assays, upadacitinib displays activity at JAK1 ($pIC_{50} = 7.9$) and ~2.5-fold bias over JAK2 ($pIC_{50} = 6.9$) (Table 5). Additionally, it shows a ~50-fold selectivity over JAK3 ($pIC_{50} = 5.6$) and 100-fold selectivity over TYK2 ($pIC_{50} = 5.3$). Whilst these data show JAK1 selectivity over JAK3 and TYK2, upadacitinib lacks selectivity over JAK2 within the biochemical assays. As with filgotinib **13**, this observation is contradicted through cellular assays. Within their Ba/F3 engineered cellular JAK assays, upadacitinib **14** exhibits enhanced selectivity over the other JAK isoforms; 50-fold selective against JAK2 ($pIC_{50} = 6.2$), ~158-fold selective against JAK3 ($pIC_{50} = 5.7$) and ~200-fold selective against TYK2 ($pIC_{50} = 5.6$), as compared to JAK1.⁶⁵

Compound	pIC_{50}							
	JAK1	JAK2	JAK3	TYK2	Ba/F3 Engineered Cellular Assay			
					JAK1	JAK2	JAK3	TYK2
Upadacitinib 14	7.3	6.9	5.6	5.3	7.9	6.2	5.7	5.6

Table 5 The biochemical and cellular data associated with upadacitinib **14**. JAK1, JAK2, JAK3 and TYK2 pIC_{50} 's measured at K_m ATP concentrations.

Upadacitinib **14** was approved by the FDA for the treatment of moderate-to-severe rheumatoid arthritis in 2019.⁶⁷

1.7 JAK3 Selective Inhibitors

As opposed to JAK1, JAK2 and TYK2, which each are appended to many different cytokine receptors, JAK3 only binds one subunit, the common gamma chain. The common gamma chain binds a subset of cytokines that include IL-2, IL-4, IL-7, IL-9, IL-15 and IL-21.⁶⁸ Preservation of JAK1 and JAK2 signalling via selective JAK3 inhibition is hypothesised to eliminate non-immunological adverse effects due to transmission via the common gamma chain-associated cytokines, which predominantly affect immune cells.^{68,69} As such, extensive

research has been carried out to identify JAK3 selective inhibitors, some of which are discussed below.

1.7.1 Decernotinib

Similar to many other inhibitors, decernotinib **15** was identified through a high-throughput screen of Vertex Pharmaceuticals' compound collection against a truncated form of JAK3, containing only the active site to assess JAK3 activity (Fig 24).⁷⁰ Due to the inaccuracy of JAK selectivity derived through biochemical assays of isolated kinase domains, their screening cascade was extended to include cellular assays to obtain more biologically relevant selectivity data. Namely, they utilised an IL-2-stimulated HT-2 cell assay measuring the downstream inhibition of STAT5 phosphorylation, via JAK1 and JAK3 signalling, and a GM-CSF-stimulated TF-1 cell assay measuring JAK2-mediated inhibition of STAT5 phosphorylation. Furthermore, the group utilised an IFN α -mediated STAT2 assay in HeLa cells, which is dependent on JAK1 and TYK2, to determine the compound's specificity against these JAK isoforms. Within their JAK2 and JAK3 biochemical assays, decernotinib **15** failed to display significant JAK3 selectivity (JAK2 pK_i = 7.9; JAK3 pK_i = 8.7; JAK3-bias over JAK2 = ~6-fold), likely due to the reasons discussed above. However, within the HT-2 IL-2 cell assay, signalling through JAK1 and JAK3, decernotinib **15** displayed a pIC_{50} of 7.0, which was ~25-fold selective over the TF-1 GM-CSF cell assay (JAK2 signalling) (Fig 25). Additionally, counter-screening in the HeLa IFN α assay indicated a selectivity of ~126-fold for JAK1/JAK3 signalling inhibition, indicating a lack of significant activity at JAK1 and TYK2.

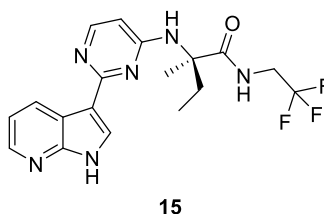


Fig 24 The chemical structure of decernotinib **15**.

From their JAK3 HTS, diaminotriazole **16** was identified which showed promising JAK3 activity, and a parallel screen discovered azaindole **17**, again with promising JAK3 activity. Crystal structure analysis of the two compounds led to a transfer of SAR between the two motifs due to similarities in binding modes to afford pyrimidine **18**, and further SAR optimisation yielded decernotinib **15**.⁷⁰

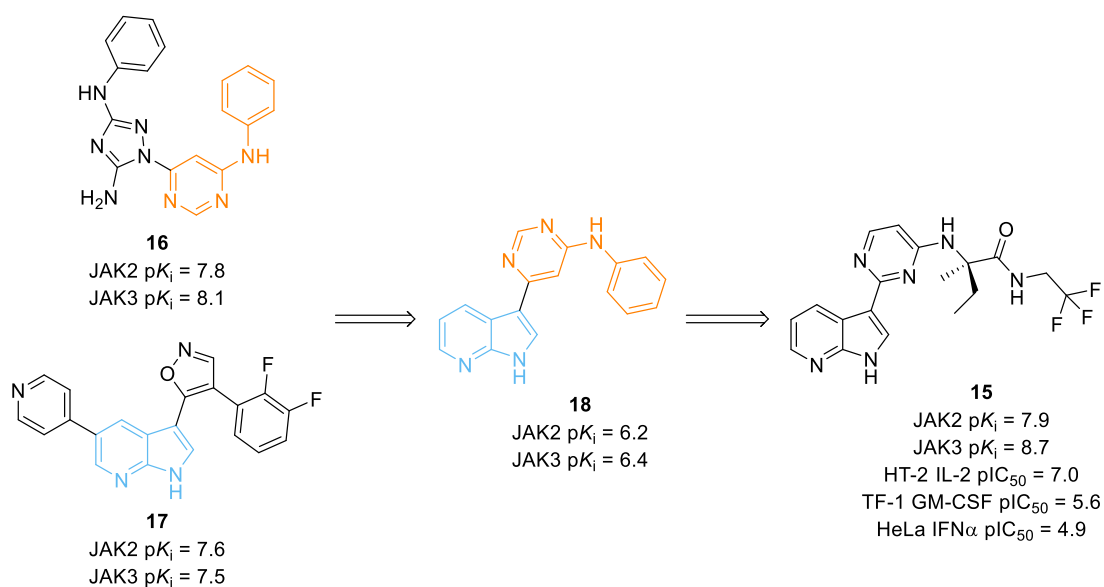


Fig 25 The initial two hits **16** and **17**, identified through a high-throughput screen, the hybridisation of the two hits (highlighted in orange and blue), and decernotinib **15**, and their associated biochemical and cellular data.

Through generation of co-crystal structures between compounds of the same class as decernotinib **15**, and decernotinib **15** itself, Vertex identified flips in binding mode even when compounds exhibited modest structural differences (Fig 26). This change in binding mode complicated SAR analysis.⁷⁰ It is not clear through structural analysis how selectivity over JAK2 is obtained.

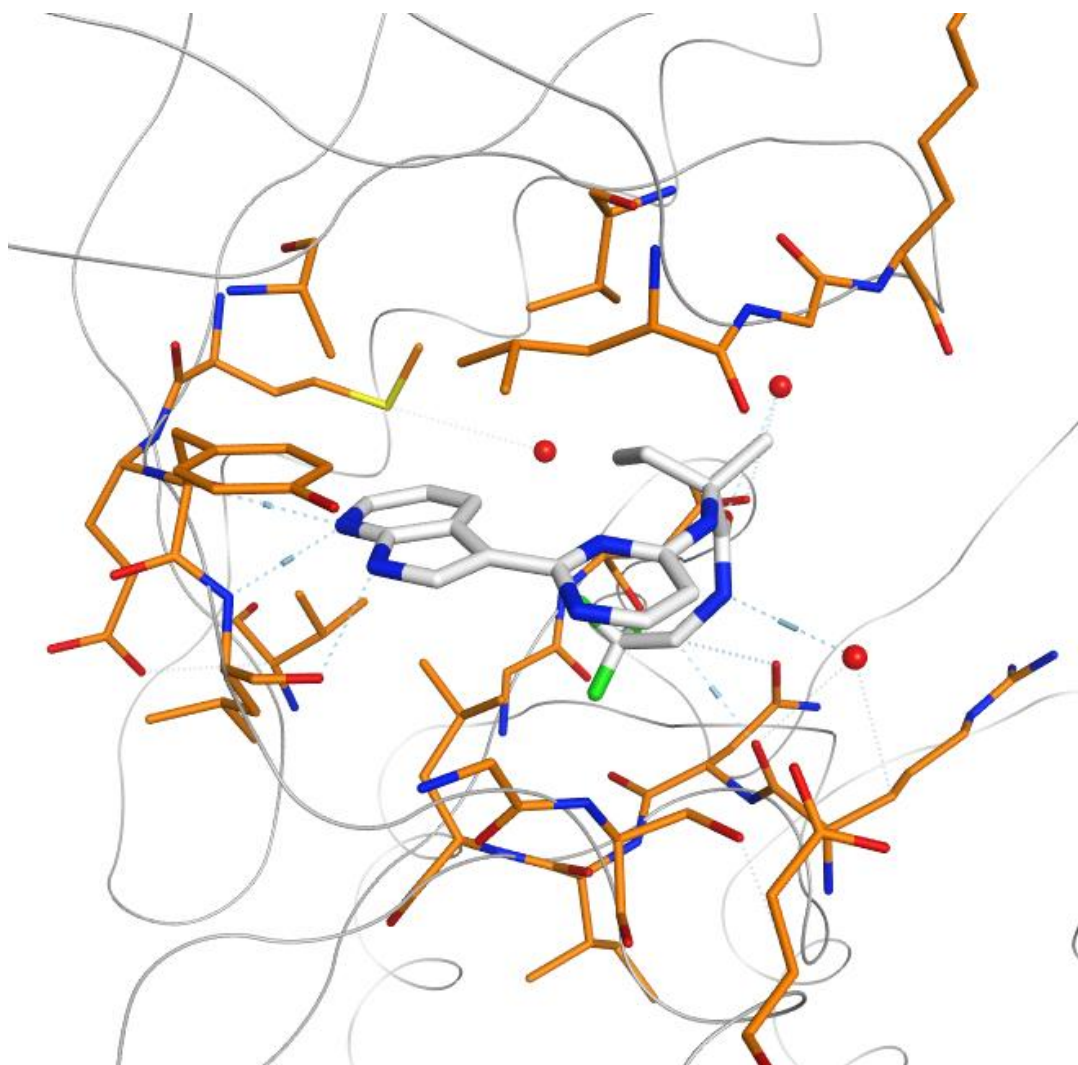


Fig 26 Crystal structure of decernotinib **15** bound to JAK2. PDB: 4YTI, resolution: 2.52 Å.

Despite decernotinib **15** being hailed as a JAK3 selective inhibitor, *in vitro* assays indicate it may have some JAK1 activity.¹⁸ Whilst the results from phase II clinical trials were encouraging, with decernotinib **15** showing comparable efficacy to tofacitinib **3**, two major concerns arose; it was reported to cause neutropenia in clinical trials, which is likely related to JAK2 inhibition.^{71,72} As such, this raised questions regarding its selectivity profile. Additionally, decernotinib **15** is the only known JAK inhibitor that is a potent inhibitor of CYP3A4. The enzyme CYP3A4 is the predominant hepatic CYP, metabolising over half of all medications currently used to treat human disease.⁷³ Therefore, this drug-drug interaction presents a huge limitation for decernotinib **15** prescription.

1.7.2 PF-06651600

Irreversible covalent inhibitors have experienced a resurgence in recent years.⁷⁴ PF-06651600 **19** is currently the only irreversible covalent JAK3 inhibitor being evaluated in clinical trials for the treatment of rheumatoid arthritis and alopecia areata, and a clinical trial for ulcerative colitis has recently been initiated (Fig 27).⁷⁵ Drawing from previously reported JAK3 covalent inhibitors developed at AbbVie,⁷⁶ Harvard Medical School and the University of Dundee,⁷⁷ Pfizer adapted tofacitinib **3** to contain a Michael acceptor motif, which could irreversibly, covalently and selectively bind JAK3, through exploitation of a Cys909 residue expressed within JAK3.⁷⁸ Binding JAK3 in a covalent fashion allows advantages over reversible inhibitors in that it has the potential for an extended pharmacodynamic (PD) effect following target inactivation. However, irreversible covalent protein modification is not without its liabilities, in that off-target reactivity could result in undesired pharmacology and non-traditional methods of clearance.

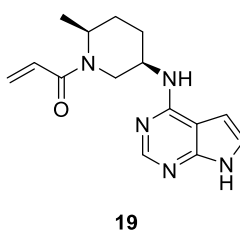


Fig 27 The chemical structure of PF-06651600 **19**.

As observed in Fig 7, JAK3 possesses three unique residues, relative to the other isoforms, which could be exploited to design selective inhibitors. Additionally, JAK3 maintains a higher ATP affinity versus the other isoforms. These two factors combined make the design of JAK3-selective inhibitors astonishingly challenging.⁷⁹ However, one of the unique residues observed with JAK3, Cys909, provides a handle for covalent targeting which overcomes limitations of high sequence homology and shape similarity with the ATP binding site.

Pfizer drew inspiration from a crystal structure of tofacitinib bound to JAK3, which enabled the design of PF-06651600 **19**. Various Michael acceptors, and ring systems protruding from

the 5-position were examined, before PF-06651600 **19** was discovered. PF-06651600 **19** displayed exquisite activity within the biochemical assays at JAK3 over the other isoforms (Table 6). The *in vitro* potency translated to the cell, where PF-06651600 **19** displayed high cellular potency within the IL-15 PBMC and hWB assays.⁷⁷

Compound	pIC ₅₀					
	JAK1	JAK2	JAK3	TYK2	IL-15 PBMC	IL-15 hWB
PF-06651600 19	< 4.0	< 4.0	7.5	< 4.0	7.3	6.7

Table 6 The biochemical and cellular data associated with PF-06651600 **19** relating to JAK1, JAK2, JAK3 and TYK2. The covalent interaction between PF-06651600 **19** and JAK3 was confirmed via a crystal structure of PF-06651600 **19** within JAK3 (Fig 28). A covalent bond between Cys909 and PF-06651600 was identified.⁷⁷

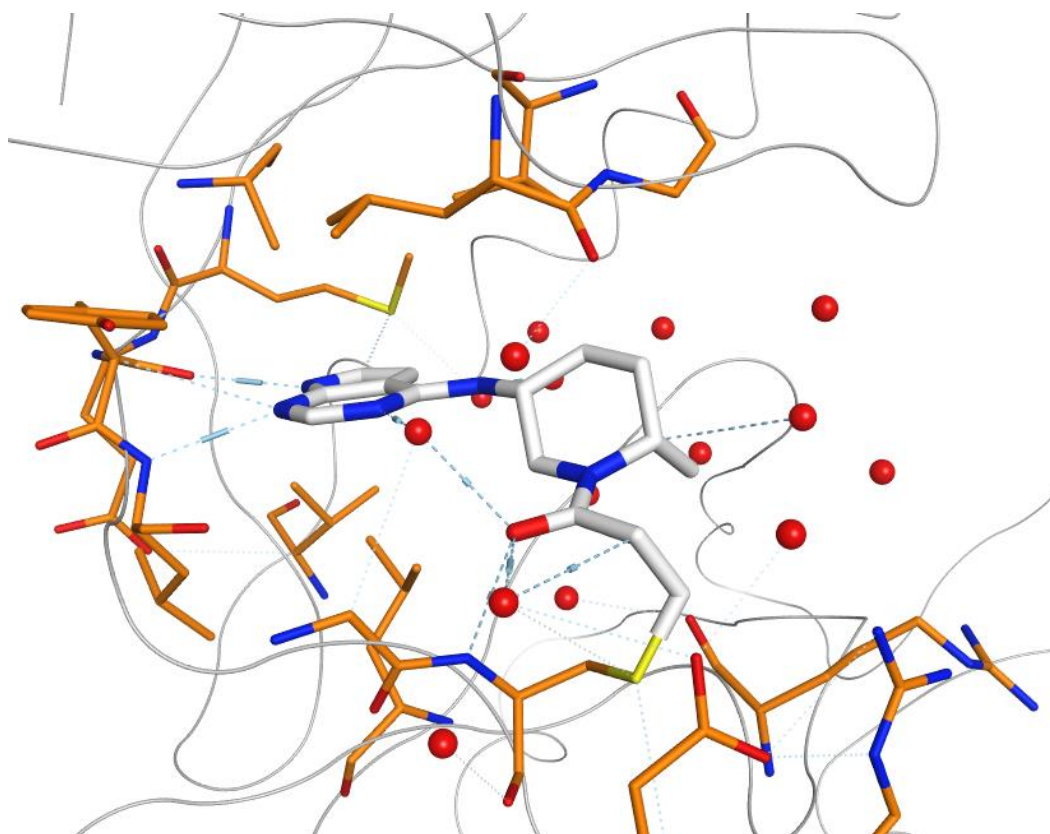


Fig 28 The crystal structure of PF-06651600 **19** covalently bound to JAK3. PDB: 5TOZ, resolution: 1.98 Å.

1.8 Alternative JAK Antagonists

1.8.1 PF-956980

An orthogonal approach to controlling JAK-mediated signalling, and thus regulated JAK-implicated diseases, would be to reduce intracellular protein levels. Jones and co-workers identified that the pan-JAK inhibitor PF-956980 **20** was able to selectively downregulate JAK2 and JAK3 mRNA, corresponding to changes at the protein level (Fig 29).⁸⁰ PF-956980 **20** displays high potency across the JAKs, with a slight bias against TYK2 (JAK1 pIC_{50} = 8.1, JAK2 pIC_{50} = 8.2, JAK3 pIC_{50} = 8.6, TYK2 pIC_{50} = 6.9) however, it is likely PF-956980 **20** ability to downregulate JAK2/JAK3 is not a consequence of JAK binding alone (Table 7). Moreover, PF-

956980 **20** displays exquisite kinome selectivity; when screened against a panel of 38 kinases and 65 proteins, JAK3 was the only protein inhibited to a significant extent at 1 μ M. However, MARK1, LCK and PDE4 were inhibited at higher concentrations. Following 22 h incubation of PF-956980 **20** in PBMC cells, a significant reduction in JAK2 and JAK3 protein levels occurred at concentrations as low as 100 nM. To elucidate the mechanism of action of PF-956980 **20**, changes in mRNA levels were determined by qPCR which identified that PF-956980 **20** significantly reduced JAK2 and JAK3 gene expression but had no effect on JAK1 and/or TYK2. The observed selectivity for JAK2 and JAK3 is not fully understood, since PF-956980 **20** engages all four isoforms.

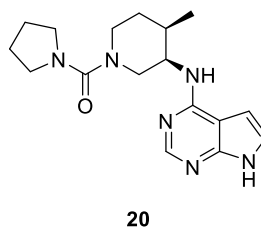


Fig 29 The chemical structure of PF-956980 **20**.

Compound	pIC_{50}			
	JAK1	JAK2	JAK3	TYK2
PF-956980 20	8.1	8.2	8.6	6.9

Table 7 The biochemical and cellular data associated with PF-956980 **20**. JAK1, JAK2, JAK3 and TYK2.

1.9 The Unmet Needs of Targeting The JAK-STAT Pathway

Currently treatments for diseases aligned to the JAK-STAT pathway typically employ non-selective small molecule reversible inhibitors, such as tofacitinib **3** and ruxolitinib **2**, with irreversible and selective inhibitors currently being evaluated in clinical trials. However, it

should be noted that these inhibitors carry a number of imperfections such as off-target side effects and thus there is a significant unmet need for novel JAK-targeting therapies that can alleviate such off-target side effects. As such, novel modes of treatment to induce JAK degradation were explored herein.

1.10 The Ubiquitin System

Cells are required to promptly adjust to environmental changes in order to maintain homeostasis or to undergo particular developmental decisions. In order to maintain homeostasis, regulated protein degradation is critical due to its role in cell signalling.⁸¹ Modifications in the transcriptome provide control over shifts in extra- or intracellular signals. However post-translational modifications of the proteome provide a more rapid mechanism for the activation or inhibition of signalling pathways. Significant control over such signalling pathways typically transpires through processes such as protein phosphorylation or ubiquitination, and these mechanisms are usually intertwined. Protein phosphatases are responsible for the reversibility of protein phosphorylation, enabled by protein kinases, allowing a particular protein to exist and interchange between two or more states depending on the signals being received. In comparison, however, protein degradation offers a less dynamic method to govern cell signalling via a specific pathway. Such regulated protein degradation occurs via the ubiquitin-proteasome system (UPS).⁸² Other routes to protein degradation also exist such as autophagy, which is largely responsible for degrading long-lived proteins and conserving amino acid levels during chronic starvation. However, its role in degrading defective proteins is equal to that of the UPS.⁸³

Ubiquitin is comprised of 76-amino acids and this small evolutionarily conserved protein adopts an almost globular conformation (Fig 30).⁸⁴ The C-terminal carboxylate of ubiquitin is appended to lysine residues within proteins via an isopeptide bond. The attached ubiquitin molecule can then operate as an additional point of chain extension through further isopeptide bonds between lysine and the C-terminus of two ubiquitin molecules. Of the seven lysine residues contained within ubiquitin, lysine-48 is the most frequent site of ubiquitin chain extension. It is thought that lysine-48 polyubiquitin chains are primarily

recognised by the proteasome.^{85,86} Other chain linkages such as lysine-63 polyubiquitin chains appear to be regulatory rather than initiating degradation.⁸⁷

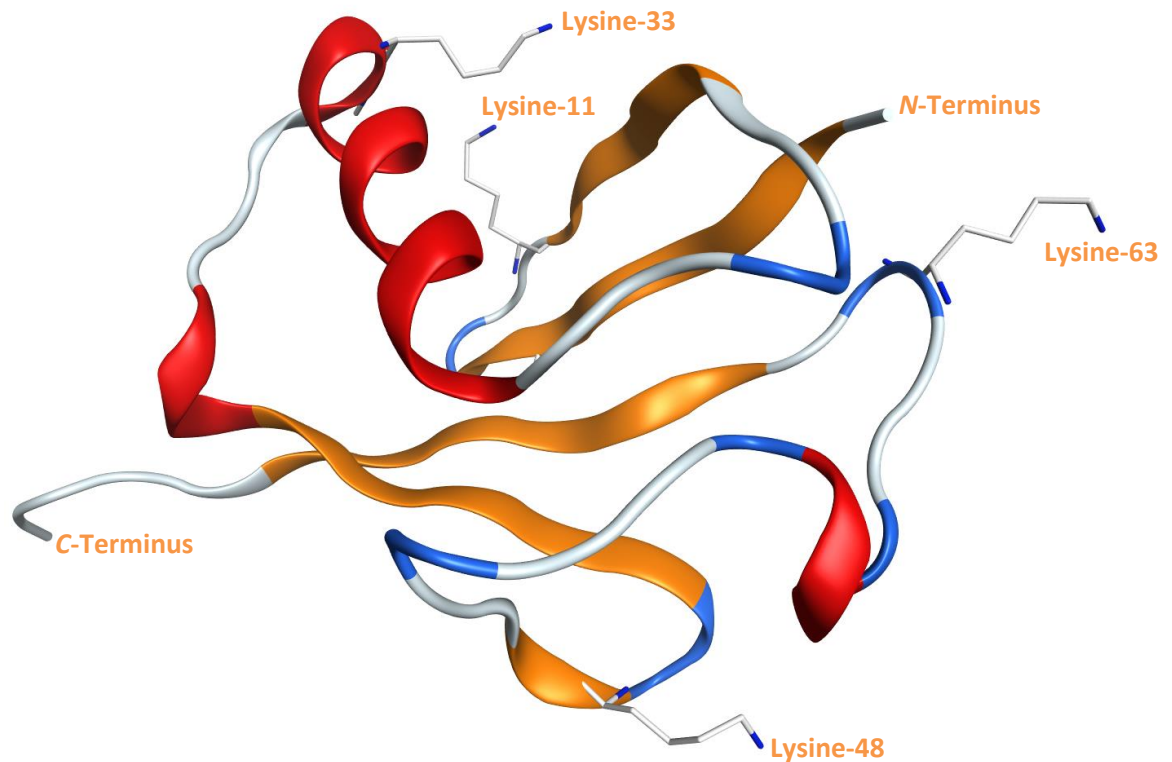


Fig 30 The crystal structure of ubiquitin in ribbon representation, highlighting lysine-11, 33, 48 and 63. PDB: 1UBQ, resolution: 1.80 Å.⁸⁴

The initial step in the highly regulated protein degradation cascade is ubiquitin activation by E1 (ubiquitin-activating enzyme) (Fig 31). This process then facilitates the transfer of ubiquitin to E2 (ubiquitin-conjugating enzyme). The construction of a complex involving E2, ubiquitin, E3 (ubiquitin ligase) and the substrate then occurs, and these early steps involve the union of E1 and E2 enzymes via thiol ester linkages between their active sites and the C-terminal carboxylate of ubiquitin. The substrate's lysine residue(s) are then ubiquitinated, eventually resulting in a polyubiquitin chain, and the polyubiquitinated substrate then disassociates from the E3. Proteasomes can identify the polyubiquitinated substrate, condemning the protein to degradation. The process occurs in an ATP-dependent manner

whereby the proteasome unfolds the substrate and removes the ubiquitin chain via ubiquitin hydrolase. The unfolded protein enters the proteasome chamber and localises within the protease active sites. Within the proteasome, the protein is degraded into peptides and amino acids, which are recycled for new protein synthesis.⁸²

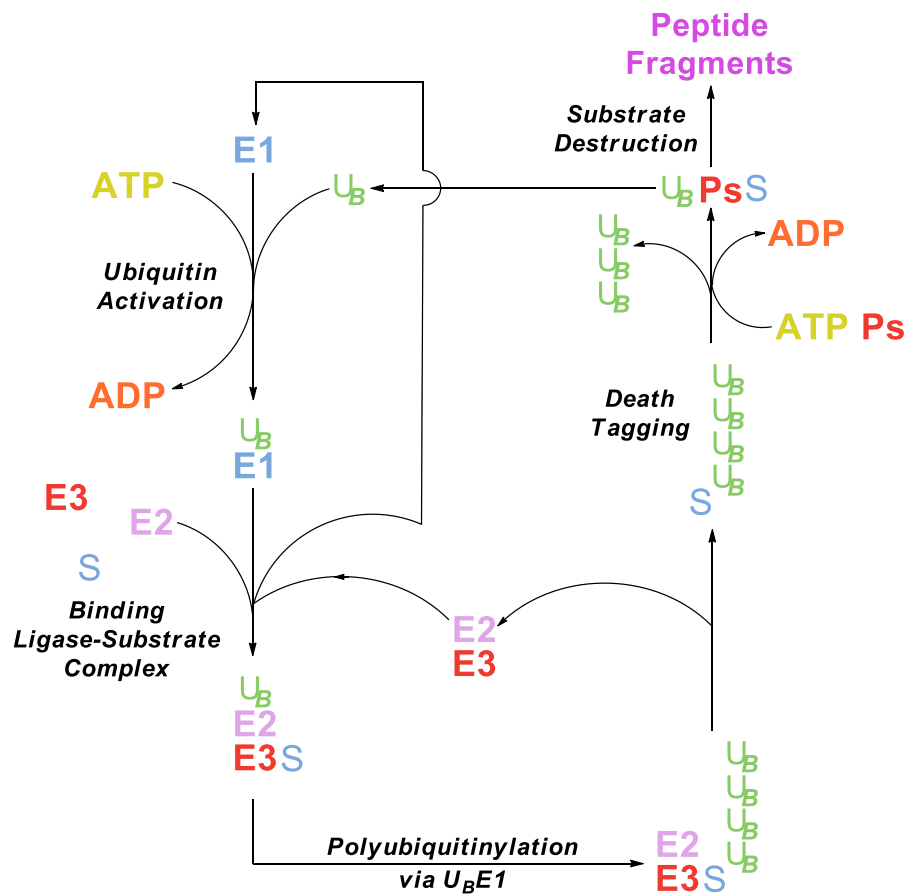


Fig 31 The protein degradation cascade beginning with ATP-dependent ubiquitin activation of E1 followed by formation of the E2 binding ligase-substrate complex and subsequent ubiquitin transfer to E2. Polyubiquitination of the substrate occurs followed by ubiquitinated substrate dissociation to the death tagging phase where the substrate is transported to the proteasome and degraded. U_B = ubiquitin, S = substrate, Ps = proteasome.

1.11 Early Intracellular Protein Concentration Modulators

1.11.1 RNA, ODNs and RNase in Protein Degradation

Early explorations in gene expression silencing were typically carried out through oligonucleotides (ODNs), which are short pieces of deoxyribonucleic acid (DNA) or ribonucleic acid (RNA), ribozymes and RNA interference (RNAi). Whilst ODNs have demonstrated success *in vitro* through hybridisation with mRNA, generating an RNA-DNA duplex and subsequent degradation by RNase, a lack of delivery mechanisms has restricted ODNs' use in *in vivo* applications. Ribozymes are catalytically active RNA and function by cleaving single-stranded RNA via transesterification or hydrolysis mechanisms.⁸⁸ They have not been extensively investigated for *in vivo* applications due to their inherent instability in serum, with half-lives lasting anywhere between ten seconds and a few minutes.⁸⁹ RNAi however, has emerged as a new paradigm for gene downregulation. RNAi is a method which targets specific mRNA degradation resulting in inhibition of encoded protein synthesis.⁹⁰ In addition to nucleases, proteins and small interfering RNA (siRNA) assemble into an RNA-induced silencing complex (RISC) in the cytosol (Fig 32). The RISC complex facilitates binding of the antisense strand of siRNA to the complementary sequence of mRNA. This binding event induces degradation of the complementary mRNA sequence, preventing encoded protein synthesis.⁹¹ The lack of an efficient delivery mechanism for siRNA to the desired target is a significant limitation for the therapeutic use of this technology. However, many groups are searching for an optimal delivery tool to allow for safe, reliable, efficient, and specific administration of this technology, such as nanoparticles.⁹²

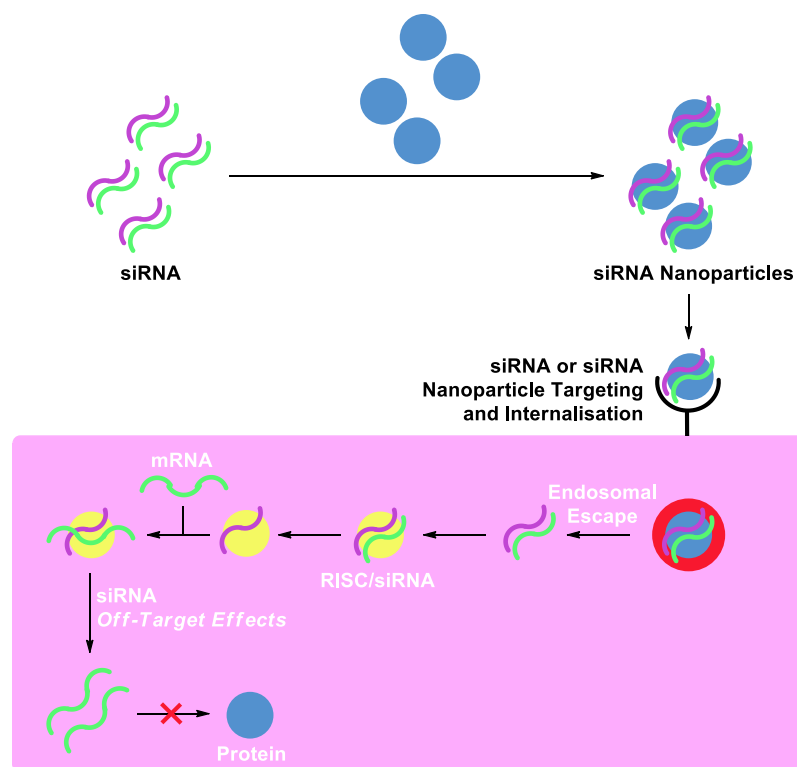


Fig 32 A scheme of small interfering RNA (siRNA) delivery and the siRNA-induced RNAi pathway. Numerous limitations exist for siRNA delivery such as: siRNA stability, siRNA nanoparticle stability, siRNA or siRNA nanoparticle targeting and internalisation, siRNA endosomal escape, and siRNA off-target effects.

1.11.2 Heat Shock Protein 90 (HSP90) Induced Degradation

Towards the latter end of the 20th century, inhibitors of the molecular chaperone heat shock protein 90 (HSP90) entered clinical trials, with currently over 30 clinical trials in progress. HSP90 assists in the correct folding of proteins, and within cancer cells HSP90 is upregulated to aid proliferation and survival pathways.⁹³ Inhibition of HSP90 within the ATP-binding domain prevents the HSP90 chaperone cycling and results in degradation of HSP90 client proteins. There are currently over 175 known client proteins, which are involved in numerous cellular processes.^{94,95} HSP90 inhibitors are not without their deficiencies, often displaying poor *in vivo* properties, such as poor solubility and low bioavailability, in addition to severe hepatotoxicity owing to their benzoquinone moiety.^{96,97,98} As a result, HSP90 inhibitors are yet to gain approval from the FDA.

1.12 Utilising the Ubiquitin-Proteasome System to Degrade Target Proteins

1.12.1 Hydrophobic Tagging: Induced Protein Degradation Through Mimicking Protein Denaturation

The traditional approach to treating disease typically transpires through modulation of the desired target via binding occupancy with small molecules. Since only approximately 25 % of the human proteome is 'druggable' using traditional small molecules, and due to a focus on binding site occupancy, the majority of human proteins encoded by the human genome such as transcription factors, scaffolding proteins and nonenzymatic proteins remain 'undruggable'.^{99,100} In addition to limiting the number of biological targets accessible to those with active sites, occupancy-based inhibitory pharmacology typically requires high doses to achieve IC_{90-95} concentrations in order to elicit a therapeutic effect. As a consequence, off-target binding frequently occurs resulting in negative side-effects. In contrast, small molecule induced protein degradation is emerging as a method to target such 'undruggable' proteins, allowing access to a variety of proteins which can be targeted, since active-site binding of the target protein is not necessarily required to induce the desired pharmacological effect.¹⁰¹

Crews *et al.* disclosed a strategy for targeted post-translational protein degradation, known as hydrophobic tagging, whereby a hydrophobic moiety appended to the surface of a protein of interest (POI) can solicit cellular quality control machinery (Fig 33). Hydrophobic tagging makes use of heterobifunctional molecules that consist of a POI binder linked to a hydrophobic group, via a linker. Once the POI binder engages the desired target, the hydrophobic tag portion mimics a partially denatured protein folding state, leading to degradation by the UPS.

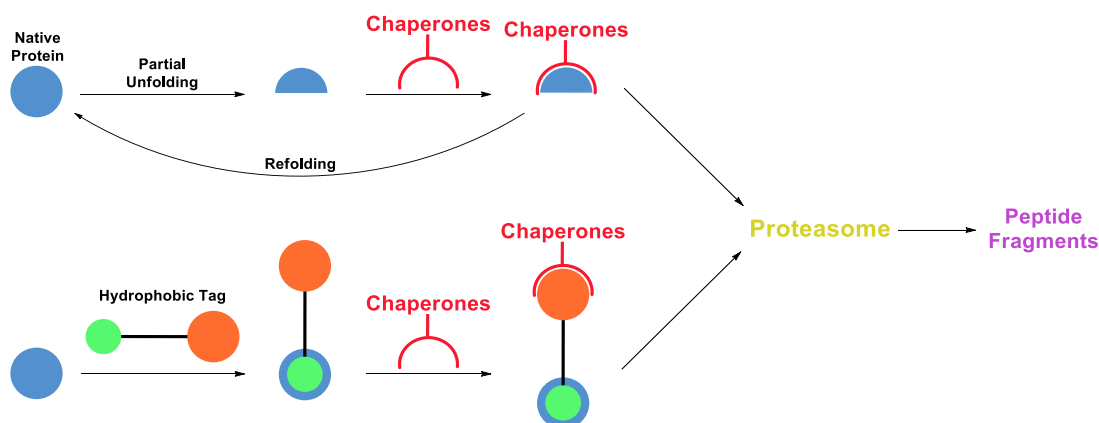


Fig 33 Cellular chaperones assist proteins that have become partially unfolded to refold back to their correct tertiary structure. Refolding may fail, resulting in the chaperones triggering degradation of the unfolded protein via the proteasome. Hydrophobic tagging of a protein's surface can mimic the partially unfolded state. Chaperones lack the ability to refold the hydrophobically tagged proteins, thus inducing targeted protein degradation.

This technology was first demonstrated by covalently attaching hydrophobic tags to engineered dehalogenase HaloTag-2 fusion proteins.^{102,103,104} Hydrophobic tagging was then extended to the degradation of *E. coli* dihydrofolate reductase (DHFR), however, using a non-covalent POI binder.¹⁰⁵ More recently, efforts have been focused towards turning this technology to degrade clinically relevant targets. Crews and colleagues designed a hydrophobic tag, based around the high-affinity androgen receptor (AR) agonist, RU59063 **3** (Fig 34).¹⁰⁶ Linking an adamantyl group via a PEG linker to RU59063 **21**, resulted in SARD279 **22**, which was capable of reducing AR protein levels by 50 % at 1 μ M (DC_{50}).¹⁰⁷ This study propelled the concept of induced protein degradation as a therapeutic strategy; however, hydrophobic tagging remains an emerging platform for therapeutic applications.

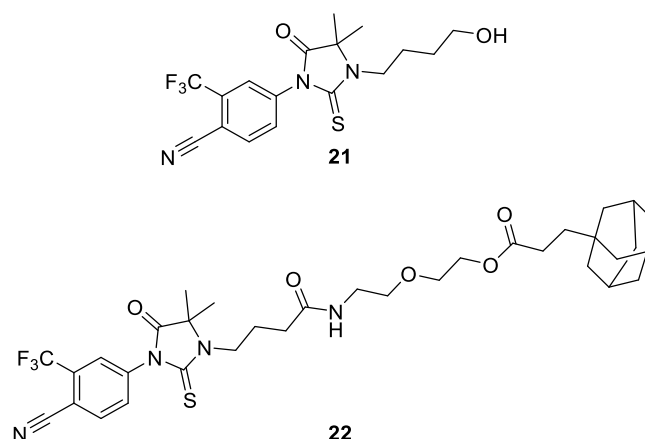


Fig 34 The chemical structures of the high affinity AR agonist, RU59063 **21** and the hydrophobically tagged degrader, SARD279 **22**.

1.12.2 Proteolysis Targeting Chimeras (PROTACs): Hijacking the Ubiquitin System

More recently, chemical knockdown strategies involving proteolysis targeting chimeras (PROTACs) have been developed by Crews and colleagues.¹⁰¹ PROTACs are heterobifunctional compounds consisting of two differing recruiting ligands joined through a linker (Fig 35). The target protein binder resides on one side of the linker, whereas an E3 ligase binder, which can recruit an E3 ligase, is appended to the other side. Upon formation of the ternary complex, the E3 ligase binder is able to hijack the biological machinery required for protein degradation and position the target protein in a spatially favourable position whereby polyubiquitination can occur, ultimately resulting in transportation of the ubiquitinated protein to the proteasome and degradation, thereby reducing target protein levels.¹⁰⁸

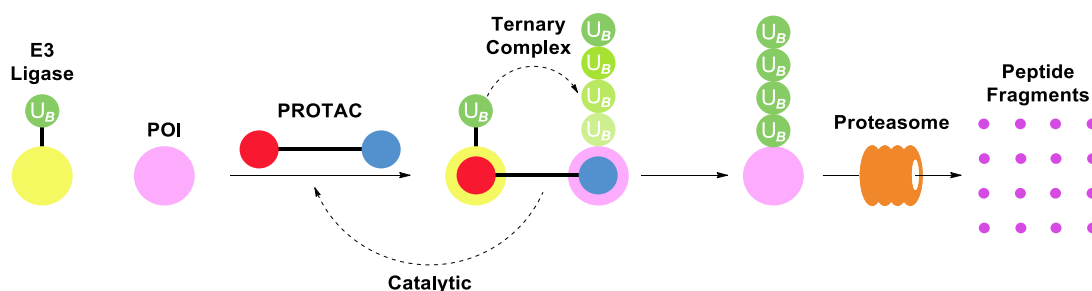


Fig 35 The binding of a PROTAC to the target protein and E3 ligase, followed by ubiquitination (U_b) and subsequent degradation.

Unlike small molecule inhibition, this process is catalytic, facilitating numerous iterations of target ubiquitination and protein degradation.¹⁰⁹ Catalytic activity arises from the formation of reversible ternary complexes between the ligase and protein of interest (POI). Once the target protein has been sufficiently ubiquitinated, the PROTAC can dissociate and form additional ternary complexes, thus repeating the degradation process. Currently, up to four turnovers of the PROTAC in the degradation of the receptor-interacting serine/threonine protein kinase 2 (RIPK2) has been observed through PROTAC-mediated degradation.¹⁰⁹ Due to their catalytic nature, high target occupancy is not required, and this phenomenon can be further exploited if target protein turnover is slow, thereby providing extended duration of action.¹¹⁰ The ability to remove target scaffolding function can result in additional efficacy as compared to inhibition of a specific function by a small molecule inhibitor. Since target protein degradation is dependent on the formation of ternary complexes, PROTACs can lack functional activity, in that they are not required to inhibit protein function, which makes them an attractive strategy for difficult targets such as transcription factors and enzymatic proteins. Interestingly, PROTACs may afford additional selectivity compared to their small molecule counterparts as different proteins may better accommodate different linker types, lengths, and ligase binders.¹¹¹ Whilst PROTACs demonstrate numerous advantages over traditional small molecules, various unique hurdles must be overcome to make the technology viable. PROTACs inherently possess significantly higher molecular weights than small molecule inhibitors, since they are comprised of two individual small molecules connected via a linker. As a result these compounds typically reside outside of Lipinski's Rule of Five (Ro5) space, which would likely impact on their bioavailability, solubility, permeability and clearance.¹¹² PROTAC-mediated ubiquitination of target proteins can also be reversed

by deubiquitinases.¹¹³ Their dose response curves are biphasic (hook effect) as a result of ternary complex formation and, as a result, the maximally efficacious concentration can prove challenging to derive (Fig 36).¹¹⁴ The PROTAC approach has been successfully applied to a plethora of different targets discussed herein; however PROTACs are yet to enter clinical trials.

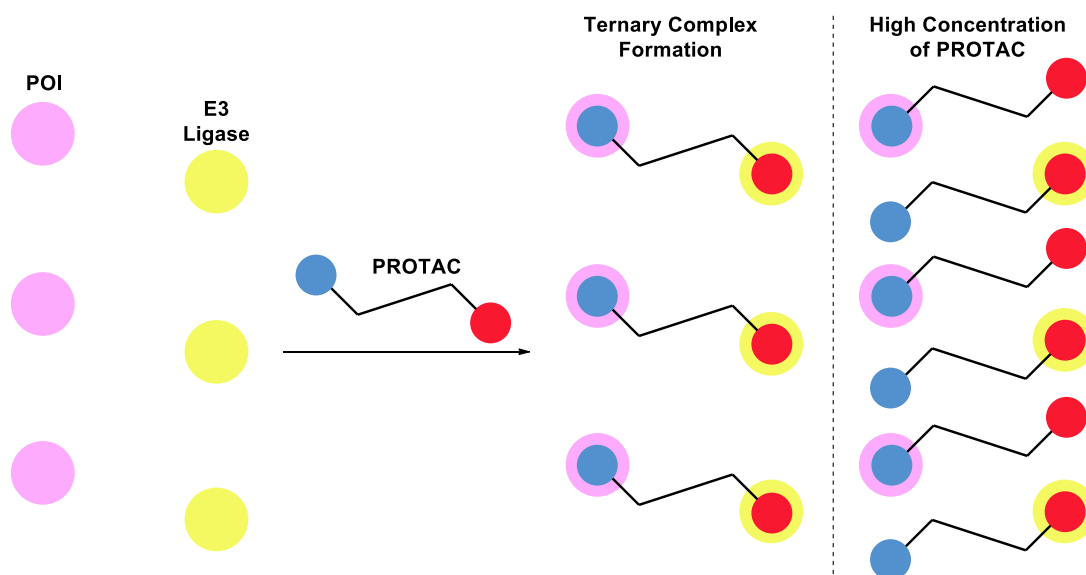


Fig 36 A diagram illustrating the hook effect. At high concentrations of PROTAC, binary complexes are formed between the POI binder and POI, and the ligase binder and E3 ligase, surpassing the formation of ternary complexes. Bypassing ternary complex formation therefore prevents POI degradation.

1.12.3 Peptide PROTACs

Crews and Deshaies published the first PROTAC proof-of-concept studies in 2001.¹¹⁵ These early PROTACs comprised of a nuclear factor of kappa light polypeptide gene enhancer in B-cells inhibitor, alpha ($I\kappa B\alpha$) phosphopeptide that can recruit the F-box protein, β -transducin repeat-containing protein (β -TRCP), a component of the S-phase kinase-associated protein 1 (SKP1)–cullin 1– F-box E3 ligase complex ($SCF^{\beta\text{-TRCP}}$). The phosphopeptide was tethered to Ovalicin **23**, a methionine aminopeptidase 2 (MetAP-2) inhibitor. Whilst the resultant degradation of MetAP-2 demonstrated proof-of-concept, these early PROTACs, compounds **24** and **25**, lacked cell permeability and had potencies in the micromolar range (Fig 37). As a result of poor cell permeability, degradation experiments were carried out using *Xenopus*

egg extract.¹¹⁵ As a consequence, these early PROTACs had limited utility as chemical probes, let alone therapeutic agents. Efforts were subsequently focused on the ligase binders, with intent to improve permeability and depart from the requirement to phosphorylate peptides.¹¹⁶

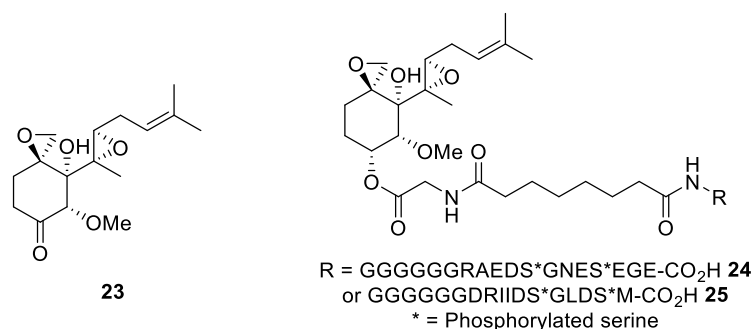


Fig 37 The chemical structures of Ovalicin **23** and the peptide-based β -TRCP-PROTACs **24** and **25**.

An early improvement was the move towards smaller peptide fragments to recruit E3 ligases without the need for phosphorylation; this led to the recruitment of the E3 ligase, von Hippel-Lindau (VHL). VHL is the substrate recognition portion of the E3 ligase complex VHL–elongin B/C–cullin 2 (VHL–ELOBC–CUL2) that mediates the transfer of ubiquitin onto hypoxia-inducible factor 1 α (HIF1 α). VHL recognises the core hydroxyproline in a seven-amino-acid sequence, ALAPYIP, of HIF1 α .^{117,118} The peptide fragment of HIF1 α was incorporated into an androgen receptor (AR) PROTAC **27** using dihydrotestosterone (DHT) **26** as the target protein binder motif (Fig 38). As with the MetAP-2 peptide-based PROTACs, it was envisaged that the incorporation of the short peptide sequence alone, when tethered to DHT **26**, confers poor cell permeability. A poly-D-arginine tag was inserted at the C-terminus, which enhanced cell permeability and prevented nonspecific proteolysis of the ligase binder. Polyarginine sequences appended to proteins aid translocation into the cell via a mechanism analogous to that of the Antennapedia and HIV Tat proteins, however the exact mechanism remains unknown.¹¹⁹ The DHT-PROTAC **27** demonstrated significant AR degradation at 25 μ M concentrations in human embryonic kidney cells 293 (HEK29).¹²⁰

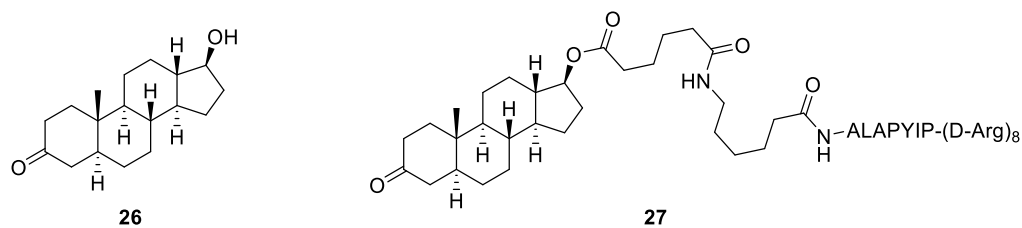


Fig 38 The chemical structures of dihydrotestosterone (DHT) **26** and peptide-based AR-PROTAC **27**.

In addition, Mohan *et al.* developed analogous PROTACs, replacing DHT **26** with oestradiol **28** generating cell-permeable oestrogen receptor (ER) PROTACs **29** and **30**. These PROTACs were capable of reducing proliferation of ER-dependent breast cancer cell lines (Fig 39).^{121,122} More recently, Heath and colleagues merged protein-catalysed capture agents (PCCs) with the HIF1 α peptide fragment to generate PROTACs which rapidly degrade protein kinase B (AKT) in cancer cells.¹²³ PCCs are high-affinity ligands that bind the POI and are assembled *in situ* through click chemistry. They are synthetic peptides that possess similarities to monoclonal antibodies but are significantly smaller and are particularly stable.¹²⁴ The addition of the ligase binder allows degradation of specific proteins in cells. However, PCCs are not intrinsically cell permeable and so small molecule binders would likely be better suited to cell penetrant PROTAC technology.¹²³ Whilst improvements to the cell permeability of the peptide ligase binders were achieved through the incorporation of poly-D-arginine tags, subsequent iterations of PROTACs were directed towards ligase-binding moieties with further enhanced cell permeability that were clinically viable, by departing from peptide fragments.

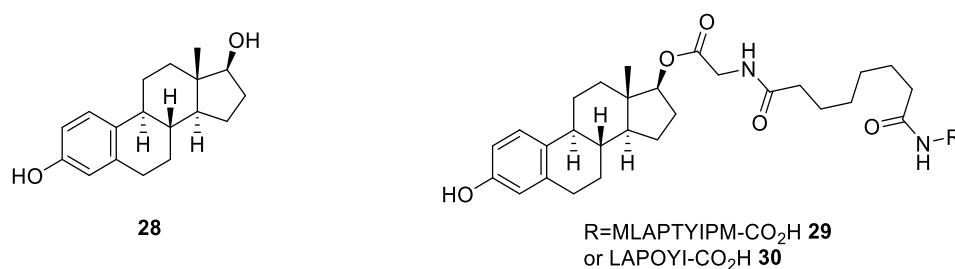


Fig 39 The chemical structures of oestradiol **28** and peptide-based ER-PROTACs **29** and **30**.

1.12.4 Small Molecule PROTACs

1.12.5 MDM2 PROTACs

The first all-small molecule PROTAC capable of target protein degradation was developed by Crews *et al.*; the PROTAC **31**, which targeted AR, consisted of a non-steroidal selective androgen receptor modulator (SARM) **32** as the POI binder, and a mouse double minute 2 (MDM2) ligand **33** known as nutlin ($IC_{50} = 0.09 \mu M$)¹²⁵ as the E3 ligase-binding moiety, bridged via a polyethylene glycol (PEG) linker (Fig 40). The PROTAC demonstrated enhanced cell permeability and AR degradation at 10 μM in cells, however, maximum AR degradation was not as high as had been observed with peptidic-based VHL PROTACs. It is possible that the reduced degradation as compared to VHL may be due to MDM2 not being the optimal ligase for AR degradation.¹⁰⁸ Since this study, more potent MDM2 ligase-binders have been developed such as idasanutlin **34**. However, cytopenias and gastrointestinal effects were reported in phase I clinical trials,^{126,127} which may limit their applicability for use within PROTACs.

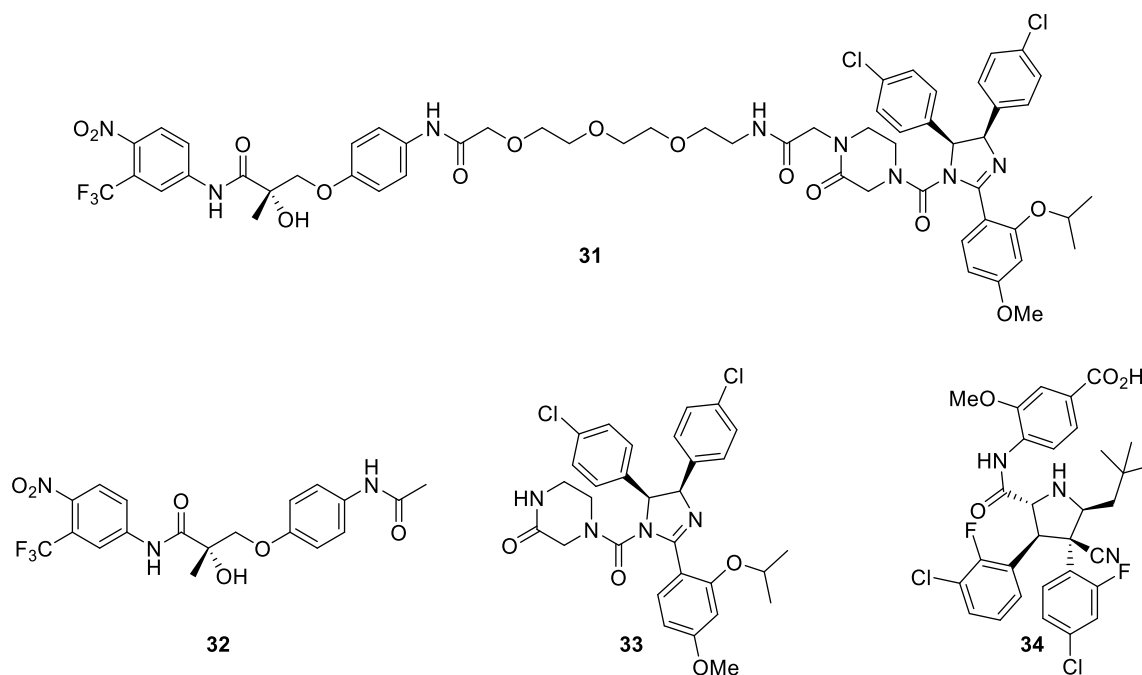


Fig 40 The chemical structures of the first all small molecule PROTAC **31**, non-steroidal selective androgen receptor modulator (SARM) **32**, nutlin **33** and the more potent MDM2 inhibitor, idasanutlin **34**.

1.12.6 IAP PROTACs

Shortly after the publication of the first all small molecule PROTACs by Crews *et al.*, Hashimoto and colleagues also reported all-small molecule PROTACs.¹²⁸ However, their efforts focused on the use of cellular inhibitor of apoptosis protein 1 (cIAP1) which resides in the inhibitor of apoptosis protein (IAP) family. cIAP1 facilitates the ubiquitination and subsequent degradation of the proteins to which it binds. The Hashimoto group adopted bestatin (ubemimex) esters **35** as their ligase-binder ligated to all-*trans* retinoic acid (ATRA) **36** as their POI binder, to form PROTAC **37** with the goal of inducing protein degradation of cellular retinoic acid-binding protein I (CRABPI) and CRABPII (Fig 41).¹²⁸ The use of bestatin has significant drawbacks in that it is non-selective and inhibits off-target proteins such as arginyl aminopeptidases and leukotriene A4 hydrolase.^{129,130} Furthermore, these bestatin-containing PROTACs promoted autoubiquitination and subsequent degradation of the recruited E3 ligase cIAP1, thus limiting the use of such PROTACs.¹³¹ In attempts to overcome such limitations, the same group developed an ‘amide-type’ IAP E3 ligase binder **38**. This demonstrated no autoubiquitination and improved selectivity over the first generation binders.¹³² In addition to CRABP degradation, cIAP PROTACs have since been adapted to degrade ER,¹³³ AR, retinoic acid receptors,¹³⁴ and transforming acidic coiled-coil-3-containing protein.¹³⁵ Due to the micromolar potency ranges and reduced selectivity of cIAP PROTACs, they have not been tested *in vivo*.

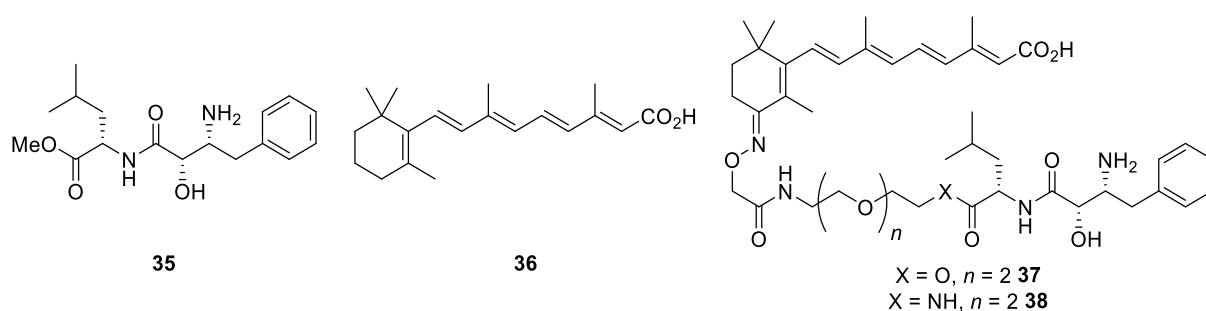


Fig 41 The chemical structures of bestatin ester **35**, ATRA **36** and PROTACs **37** and **38**.

More recently, to bypass the limitations observed with cIAP1, and the low potency with bestatin-based PROTACs, an IAP antagonist LCL161 **41** was incorporated into PROTACs (Fig

42). PROTACs containing LCL161, which primarily recruits XIAP instead of cIAP1, displayed nanomolar potency against ER α , BRD4, PDE4, and BCR-ABL. Furthermore, the group identified *in vivo* protein knockdown in a tumour model with the ER α IAP PROTAC **42**. The ER α IAP PROTAC **42** reduced protein levels in the orthotopic tumours to ~50 % within mice.

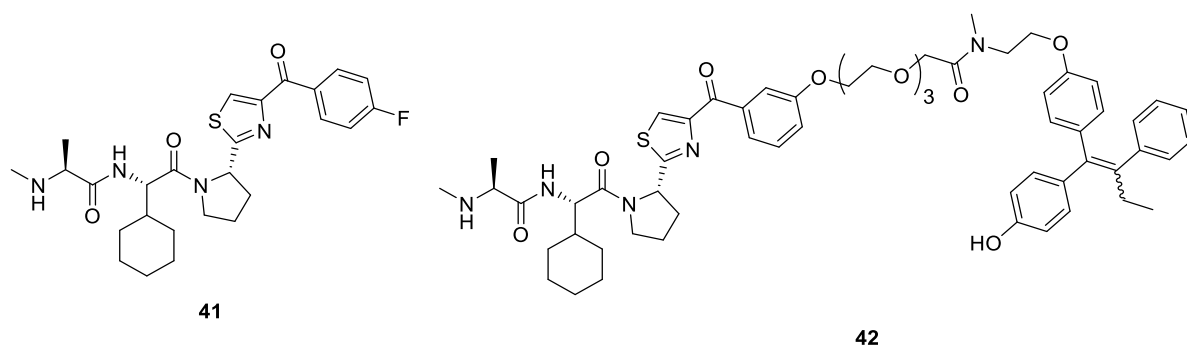


Fig 42 The chemical structures of IAP antagonist LCL161 **41** and the LCL161-based PROTAC **42**.

1.12.7 VHL PROTACs

More recently, optimisation efforts geared towards the generation of small molecule VHL inhibitors to replace the HIF1 α peptide fragment have been carried out with the objective of increasing potency, decreasing metabolic liabilities and improving cell permeability. An understanding of the key role played by the hydroxyproline motif for substrate recognition led to *in silico* and fragment based screens which afforded compounds such as **41**. Compound **41** exhibits single digit micromolar affinity ($IC_{50} = 4.1 \mu M$) for VHL (Fig 43). Whilst this compound displayed moderate potency, it exhibited very low lipophilicity due to the highly hydrophilic nature of the hydroxyproline.¹³⁶ Further structure-activity relationship (SAR) optimisation was performed,^{137,138} which ultimately led to the discovery of compound **42**. The VHL inhibitor **42**, which exhibited a K_d of 185 nM,¹³⁹ is currently the most potent published VHL inhibitor to date, and exceeds the potency of the model 10-mer HIF1 α peptide fragment.

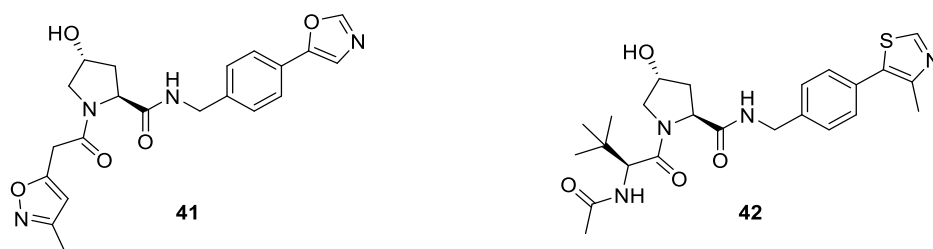


Fig 43 The chemical structures of VHL inhibitors, where compound **42** is the most potent VHL inhibitor to date.

With this improved VHL inhibitor in hand, the first all small molecule VHL PROTAC was recently described by Crews and Churcher *et al.* Both the estrogen-related receptor- α (ERR α)-VHL-PROTAC **43** and the RIPK2-VHL-PROTAC **44** demonstrated nanomolar potency for nearly complete degradation of both targets (Fig 44). Both PROTACs demonstrated catalytic activity, with the RIPK2 PROTAC **44** facilitating four rounds of protein degradation. Furthermore, degradation of ERR α *in vivo* was observed with 40 % knockdown observed in heart, kidney and tumour xenografts. Interestingly, the PROTACs also exhibited greater off-target selectivity over their parent compounds within comparative proteomic studies.¹⁰⁹

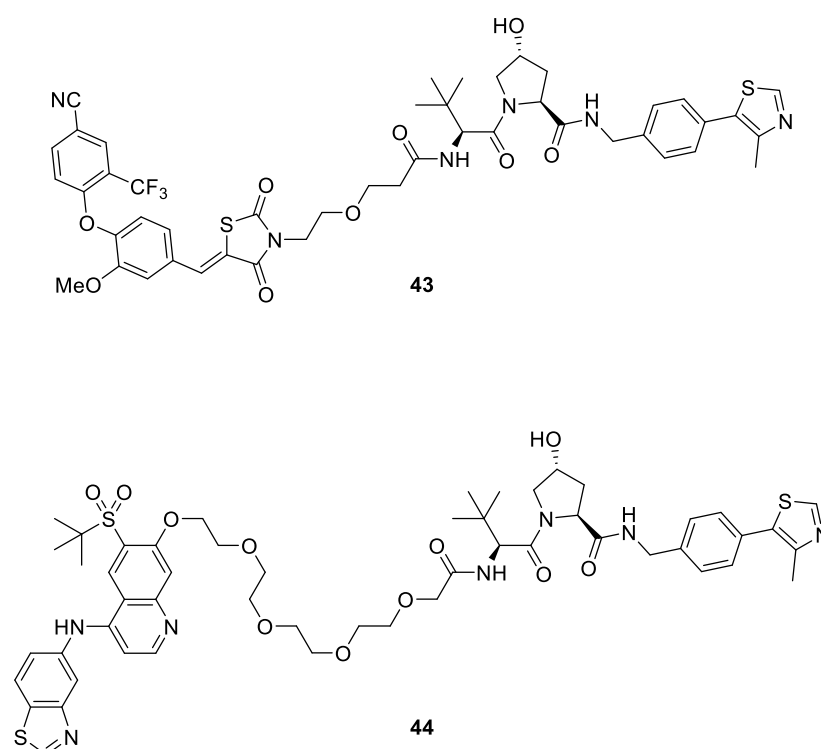


Fig 44 The chemical structures of ERR α -PROTAC **43** and RIPK2-PROTAC **44**.

A number of groups have recently reported small molecule PROTACs that degrade the bromo- and extra-terminal (BET) family of proteins. The pan-BET inhibitor, JQ1 **45**,¹⁴⁰ was ligated to VHL inhibitor **42** via a three-unit PEG linker, generating PROTAC **46**, known as MZ1, that was able to selectively degrade BRD4 over its family paralogs, BRD2 and BRD3 (Fig 45).¹¹¹

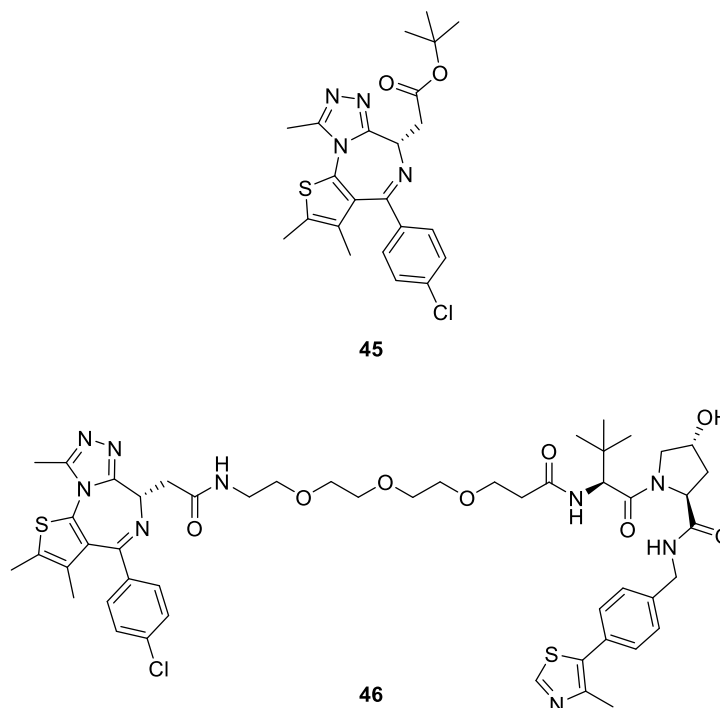


Fig 45 The chemical structures of JQ1 **45** and JQ1-VHL-PROTAC **46**.

To understand the selectivity exhibited by MZ1 **46**, Cuilli *et al.* successfully crystallised the ternary complex formed between BRD4-VHL-ElonginC-ElonginB complex (Fig 46). The crystal structure revealed numerous new intramolecular interactions in the ternary structure which suggest that isoform-specific protein-protein interactions (PPIs) may be involved in the cooperativity of the ternary complex equilibria.¹⁴¹ A ternary complex is defined as positively cooperative if interactions enhance the formation of a ternary complex compared to binary complexes ($\alpha = K_d(\text{binary})/K_d(\text{ternary}) > 1$; $\Delta pK_d = pK_d(\text{ternary}) - pK_d(\text{binary}) > 0$). On the other hand if a system is defined as negatively cooperative, the formation of a ternary complex is disfavoured ($\alpha < 1$; $\Delta pK_d < 0$), which can arise from repulsive interactions or steric hindrance between the constituents of the ternary complex.^{142,114} BRD4 ($\alpha = 18$) exhibited the greatest

cooperativity amongst all BET bromodomains, which may explain the selective degradation of BRD4 over the other isoforms.¹⁴¹

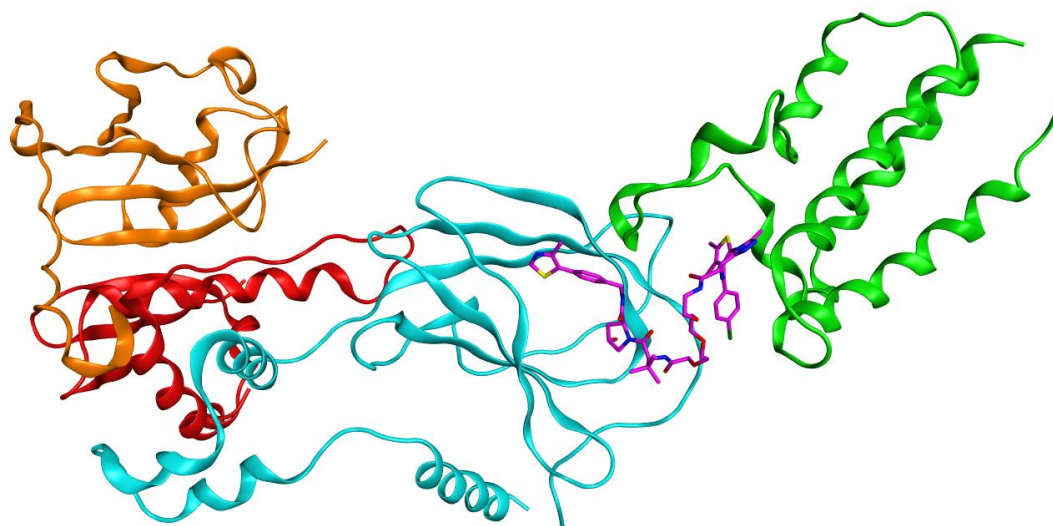


Fig 46 The crystal structure of BRD4^{BD2}-MZ1-VHL-ElonginC-ElonginB in ribbon representation. Orange = Elongin B; Red = Elongin C; Teal = VHL; Green = BRD4^{BD2}; Pink = MZ1 PROTAC. PDB: 5T35, resolution: 2.70 Å.

Additionally, generation of the crystal structure allowed the design of a novel PROTAC molecule **47** that displayed exquisite selectivity for BRD4 degradation over BRD2 and BRD3, solely depleting BRD4 levels by up to 40 %, leaving BRD2 and BRD3 protein levels untouched (Fig 47).

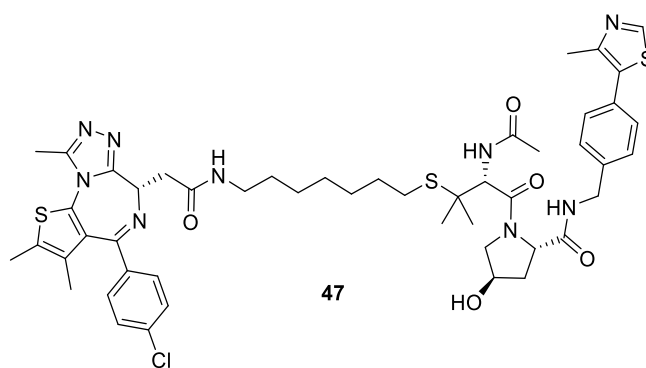


Fig 47 The chemical structure of BRD4-specific PROTAC **47**.

VHL-mediated PROTAC-induced degradation is not however limited to RIPK2, ERR α and BET. VHL-based small molecule PROTACs have also been developed to induce GFP-HaloTag fusions,¹⁴³ BCR-ABL,¹⁴⁴ TBK1,¹⁴⁵ TRIM24,¹⁴⁶ and various transmembrane receptor tyrosine kinases such as EGFR, HER2 and c-Met.¹⁴⁷

1.12.8 Cereblon PROTACs

During the late 1950s and early 1960s, thalidomide **48** was extensively prescribed in over 40 countries as a sedative to treat morning sickness in pregnant women. Its use in pregnant women during weeks 3 to 8 of gestation resulted in teratogenicity causing numerous birth defects including limb malformations in the form of severe shortening or complete absence, known as phocomelia and amelia. Hearing malfunctions also arose such as anotia, microtia and hearing loss, in addition to cardiac and gastrointestinal malfunctions. Between 8000 and 12000 children were affected before the drug was banned.^{148,149,150} Almost 50 years later, it was identified by Handa *et al.* that thalidomide's primary target for teratogenicity is cereblon (CRBN), a protein encoded by a candidate gene for mild intellectual disability. It was revealed that CRBN forms E3 ligase complexes comprising of the cullin scaffold Cul4A, damaged DNA-binding protein (DDB1) and regulator of cullins (ROC1). CRBN functions as a ubiquitin ligase through autoubiquitination, and the process can be inhibited by thalidomide **48**.¹⁵¹ Through a series of studies it was found that phthalimides such as thalidomide **48**, lenalidomide **49** and pomalidomide **50** could bind to CRBN and adapt the E3 ligase to induce degradation of

the lymphoid transcription factors Ikaros family zinc finger 1 (IKZF1) and IKZF3 (Fig 48).^{152,153,154} However, the different phthalimides possess different substrate degradation. For example, lenalidomide **49** can bring about degradation of casein kinase I α (CKI α), whereas pomalidomide **50** and thalidomide **48** are unable to induce CKI α degradation.^{155,156} A recent screening for CRBN substrates resulted in the identification of CC-885 **51**, a phthalimide derivative that binds G1 to S phase transition protein homologue (GSPT1).¹⁵⁷

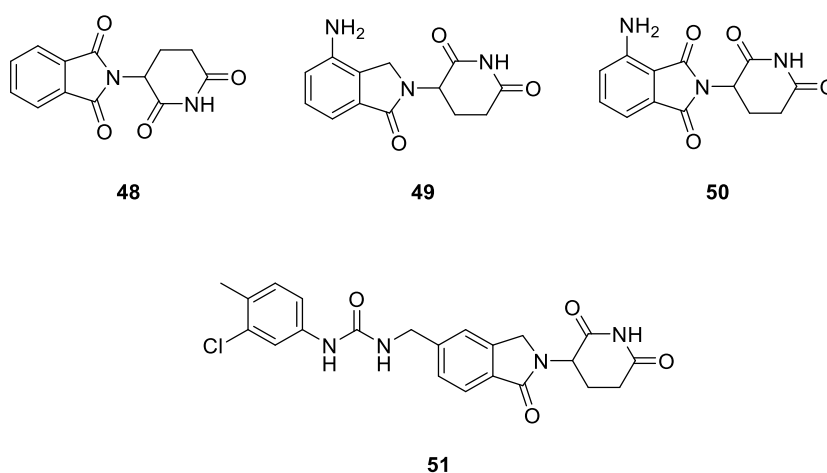


Fig 48 The chemical structures of phthalimide family: thalidomide **48**, lenalidomide **49**, pomalidomide **50** and CC-885 **51**.

The realisation of the involvement of phthalimides and CRBN in protein degradation led to the use of phthalimides to utilise CRBN for targeted protein degradation. Prior to BRD4 degradation using a VHL recruiter as discussed previously, the BRD4 inhibitor, OTX015 **52**, was tethered to pomalidomide **51** generating the first PROTAC **53** capable of degrading the epigenetic target BRD4 with picomolar potencies (Fig 49).¹⁵⁸ The CRBN-based PROTACs generated a more sustained suppression of MYC levels by preventing increased BRD4 expression resulting from BRD4 inhibition.¹⁵⁹ As a result of sustained suppression of BRD4 expression, enhanced antiproliferative and apoptotic effects against Burkitt's lymphoma cell lines were observed compared with the inhibitors alone.¹⁵⁸

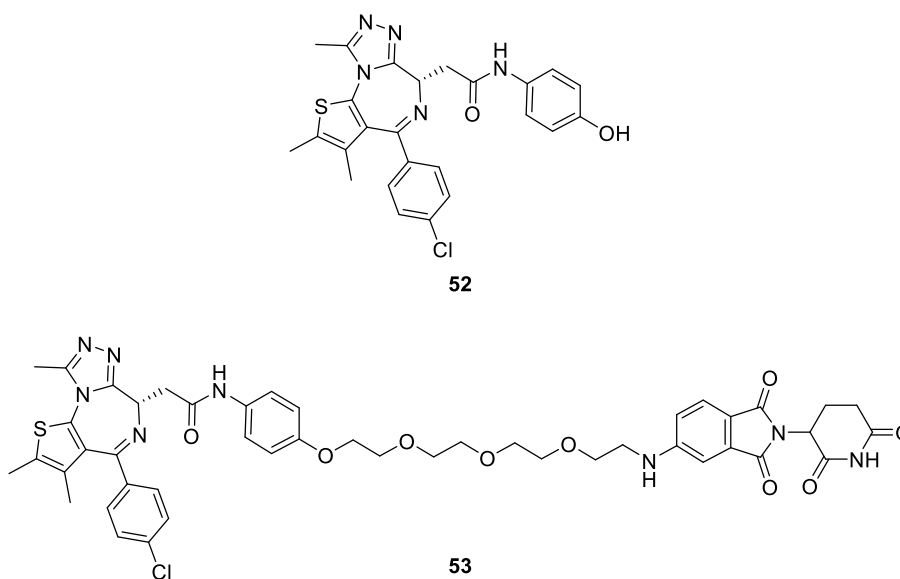


Fig 49 The chemical structures of BET inhibitor, OTX015 **52** and the derived BET PROTAC **53**.

As with the BRD4-VHL PROTAC, JQ1 **45** was also appended to a thalidomide derivative resulting in the PROTAC known as dBET1 **54** (Fig 50). In addition to inducing BRD4 degradation at low nanomolar concentrations, proteomic studies highlighted the significant reduction of MYC, BRD2, BRD3 and BRD4 with minor off-target degradation. Again, dBET1 **54** displayed a dramatic increase in potency against human acute myeloid leukaemia (AML) and lymphoma cell lines in comparison to JQ1 **45** alone. Perhaps more interestingly, dBET1 **54** showed activity in a xenograft model of AML and a disseminated leukaemia mouse model, where dBET1 **54** exceeded JQ1 **45** activity in the mouse model.¹⁶⁰ This enhanced activity of the dBET1 **54** over JQ1 **45** in preclinical models proves promising in future clinical applications.

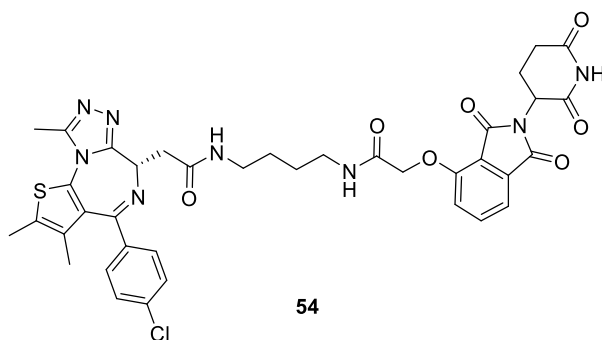


Fig 50 The chemical structure of BET PROTAC, dBET1 **54**.

PROTACs as a novel therapeutic paradigm have captured the curiosity of both academia and the pharmaceutical industry.¹⁶¹ The first PROTAC was set to advance to Phase I clinical trials in 2017,¹⁶² however, whilst this milestone was not fulfilled, the first PROTAC known as ARV-110 entered clinical trials for treating patients with metastatic castration resistant prostate cancer (mCRPC) in 2019, as an orally bioavailable PROTAC. The chemical structure of ARV-110 has not yet been published.¹⁶³ As this technology is still within its infancy, it is yet to be determined whether PROTACs embody the future of drug discovery or have a valuable role in target identification and validation.

2 Results and Discussion

2.1 Aims: Can PROTAC-Induced Degradation of Proximal Membrane-Bound JAK be Achieved?

PROTACs generated to degrade proximal membrane-bound proteins, such as JAK, have not been investigated within the literature. The degradation of the JAK family may present novel opportunities to treat a variety of diseases as discussed in the introduction, from oncology to inflammatory diseases, in addition to advancing PROTAC technology to degrading proximal membrane-bound proteins. The PROTAC approach to treating JAK-implemented diseases may provide benefits over current small molecule JAK inhibitors. For example, a reduced dose may be accessible due to the catalytic nature of the PROTAC moiety. In addition, reduced dose frequency may be accessible due to the pharmacodynamic effect of protein degradation persisting after PROTAC clearance. And finally, improved kinase selectivity could be achieved since degradation selectivity can exceed selectivity of the inhibitor alone.

The synthesis, medicinal chemistry and chemical biology of JAK PROTACs are explored herein, in attempts to design and synthesise cell penetrant PROTACs capable of inducing pan-JAK degradation. It is proposed that such PROTACs can be used to both explore the feasibility of degrading membrane proximal proteins, and to probe the degradation of JAK proteins as a potential treatment for oncology-related and inflammatory diseases.

2.2 Biological Characterisation

2.2.1 The K_m and Desensitised JAK Biochemical Assays

To discover and develop novel therapeutics it is essential to measure their biological effects. Biochemical assays utilise artificial environments in order to evaluate compound interactions with isolated biological targets. Biochemical assays have become the principal approach in conducting high throughput screening (HTS) in part due to their ability to be easily adapted to microtitre plate formats. Numerous HTS assays have been designed and developed for assessing protein interactions with compounds such as Fluorescence Intensity (FLINT), Time Resolved Fluorescence Resonance Energy Transfer (TR-FRET) and Fluorescence Polarisation (FP).¹⁶⁴

The TR-FRET assays employed within our laboratories to assess inhibition of each individual JAK isoform made use of LANCE® Ultra TR-FRET technology (Fig 51).¹⁶⁵ The assays used a proprietary Europium chelate donor dye, with *ULight*, a small molecular weight acceptor dye with a red-shifted fluorescent emission. The *ULight*-JAK-1 peptide (sequence: *ULight*-CAGAGAIETDKEYYTVKD) is derived from amino acids 1015 – 1027 of JAK1. Tyr1023, within *ULight*-JAK-1 peptide, is phosphorylated by the JAKs and the resulting phospho-peptide can bind an Eu-labelled anti-phospho-substrate antibody (Eu-Ab), bringing the Eu donor in close proximity to the *ULight* acceptor. The binding of the Eu-Ab is detected upon irradiation, at 320 or 340 nm, and the energy from the excited Eu-Ab can be transferred to the *ULight* acceptor dye, which, in turn, emits light at 665 nm. Inhibition of JAK prevents phosphorylation of Tyr1023, thus preventing binding of Eu-Ab to *ULight*-JAK-1 resulting in a diminished FRET signal.

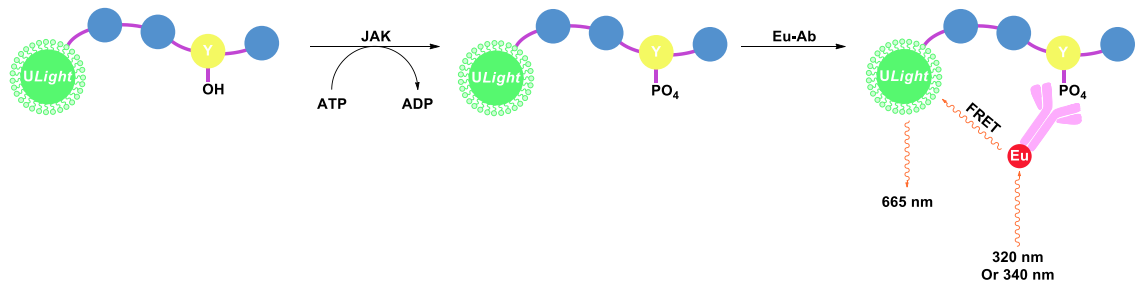


Fig 51 The LANCE® Ultra TR-FRET assays, illustrating the phosphorylation of Tyr1023, followed by binding of Eu-Ab and subsequent TR-FRET signal generation.

The FRET signal for specific compounds can then be converted into an inhibition percentage and plotted against increasing log compound concentration, generating a dose-response curve (Fig 52). From the dose response curve, a pIC_{50} , which is defined as the negative log of the concentration of a compound that is required for 50 % inhibition, can be derived.

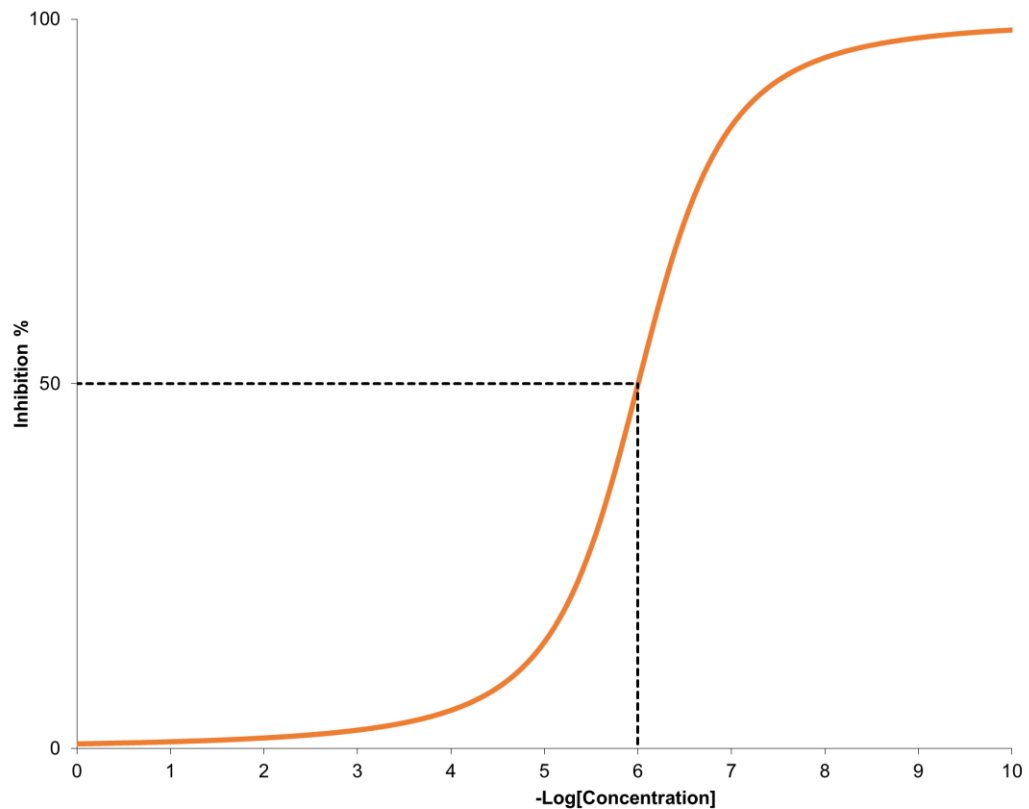


Fig 52 A dose response curve, illustrating the extrapolation of a pIC_{50} .

Within our laboratories, two variations of the JAK biochemical assays were used to assess potencies of the PROTACs and parent compounds. One of the assay formats was carried out at K_m (Michaelis-Menten constant) concentrations of ATP, whereas the desensitised biochemical (DS) JAK assays were carried out at higher ATP concentrations (Equation 1). Within the K_m assay, where K_m is the substrate concentration required to achieve half-maximal enzyme velocity (V_{max}), 50 μM of ATP is employed for JAK1, 10 μM of ATP for JAK2 and JAK3, and 30 μM of ATP is used for TYK2. The K_m assay possesses significant limitations in quantifying competitive JAK inhibitor binding affinity since the ATP concentration is significantly lower than that observed in the cell (cellular $[\text{ATP}] = 1 - 5 \text{ mM}$). To overcome this limitation, a more biologically relevant JAK biochemical assay was developed; the DS assay.

$$v = \frac{V_{max}[S]}{K_m + [S]} \quad (1)$$

Equation 1 The Michaelis-Menten equation relating reaction rate (v) to substrate concentration $[S]$.

The DS assay provides a higher concentration of ATP ($[\text{ATP}] = 2 \text{ mM}$), thereby increasing competition for active-site binding. The higher concentration of ATP observed within the DS assay is analogous to that of a cellular system. As a result of increased ATP competition, a potency drop-off is typically expected from the K_m biochemical assay to the DS assay, which can be derived from the Cheng-Prusoff equation (Equation 2 & 3) (Table 8).

$$\text{IC}_{50} = K_i \left(1 + \frac{[\text{ATP}]}{[K_{m,\text{ATP}}]} \right) \quad (2)$$

$$\text{Shift} = \frac{\text{IC}_{50\text{DS}}}{\text{IC}_{50K_m}} = \frac{\left(1 + \frac{[\text{ATP}]}{[K_{m,\text{ATP}}]} \right)}{2} \quad (3)$$

Equation 2 & 3 The Cheng-Prusoff equation (1) and a derived equation (2) to determine the theoretical potency shift between the biochemical K_m and DS assays.

Isoform	Expected Shift Δ (pIC ₅₀)	Expected Shift plus Assay Tolerance Δ (pIC ₅₀)
JAK1	1.25	1.75
JAK2	1.80	2.30
JAK3	1.83	2.33
TYK2	1.45	1.95

Table 8 A table illustrating the expected drop-off in potency when moving from the in-house GSK JAK K_m biochemical assay to the DS biochemical assay.

It should be noted that the K_m JAK biochemical assays were deemed suitable for use on this project and as such the K_m JAK biochemical assays were used exclusively to determine target engagement and JAK biochemical potency.

2.2.2 IL2 PBMC Assay

Since the isolated TR-FRET biochemical assay cannot determine the activity of JAK PROTACs within a cellular context, an interleukin 2 (IL2) peripheral blood mononuclear cell (PBMC) assay was utilised to probe the inhibitors' cellular activity. The PBMCs, which were extracted from human whole blood, consist of lymphocytes (T cells, B cells, natural killer (NK) cells) and monocytes.¹⁶⁶ These all express all four JAK enzymes. The IL2 PBMC assay quantifies the extent of JAK1 and JAK3 inhibition within a cellular environment. JAK1 and JAK3 are known to be activated upon IL2 stimulation, which results in the downstream production of interferon gamma (IFN γ) (Fig 53).

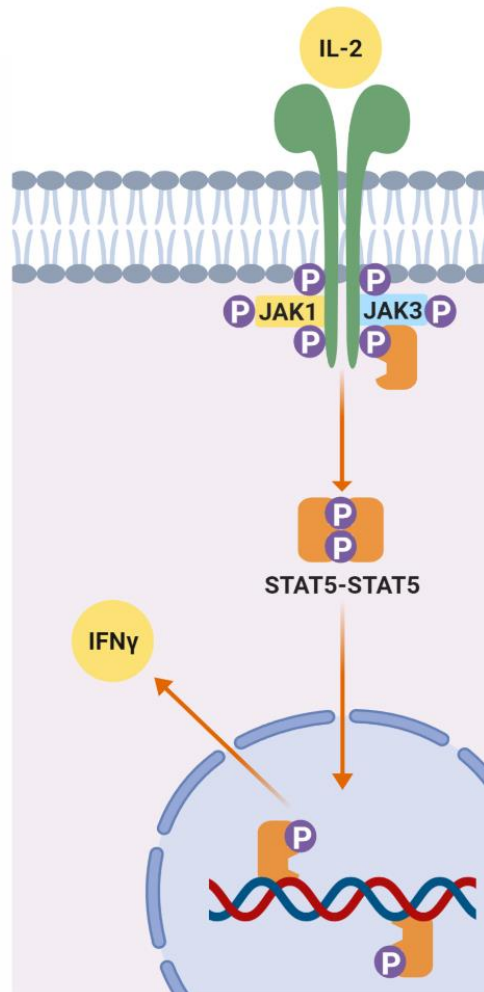


Fig 53 IL2 binds to the IL2 receptor (IL2R) which recruits JAK1 and JAK3, and triggers the phosphorylation event activating JAK1 and JAK3. The activated JAK1 and JAK3 enzymes phosphorylate STATs. Dimerisation of STAT5 occurs and the resulting dimer translocates into the nucleus where it acts as a transcription factor to induce expression of IFN γ .

Within the IL2 PBMC assay, the test compound is incubated with PBMCs for 1 h, after which the stimuli, namely IL2 and anti-human-CD3 (OKT3) are added. OKT3 antibody serves to silence IFN γ production from alternative pathways, thus allowing for the generation of IFN γ solely from IL2 stimulation. The stimuli are incubated with the PBMCs for 16 h at which point an anti-human IFN γ antibody is added to determine the extent of IFN γ inhibition. IFN γ concentration can then be plotted against log of JAK inhibitor concentration to generate a pIC₅₀ value.

Typically for small molecule inhibitors, moving from the isolated enzyme biochemical assay to a cellular environment, such as the IL2 PBMC assay, results in a drop-off in potency. This phenomenon can be attributed to numerous factors. The cellular concentrations of ATP within the IL2 PBMC assay are higher than that of the biochemical K_m assay and so competition arises between the dosed compound and ATP, resulting in loss of potency within the biochemical K_m assay. Whilst the cellular assay and DS assay share the same ATP concentration, a drop-off from the DS assay to the cellular assay is still observed. This is due to the additional complexity of a cellular environment, such as additional non-specific proteins, to which compounds can bind, which can decrease the free-compound concentration. Lastly, the compound must also traverse the cell membrane in order to access the target within the cell. Consequently, it is not uncommon for a potent compound within the biochemical K_m assay to display poor cell activity if its membrane permeability is particularly low. Compounds can also be actively effluxed out of the cell, thus decreasing their cellular concentration and so can decrease potency.¹⁶⁷

2.2.3 Western Blotting

Western blotting was employed as a means of quantifying JAK1 and JAK2 protein levels, and the extent of PROTAC-mediated JAK degradation. The technique is often utilised within PROTAC studies to detect specific proteins, from a complex mixture of proteins associated with a particular cell line.¹⁶⁸ THP-1 cells were selected as the cell line for this study since THP-1 cells have been validated as a robust cell type within other PROTAC studies.^{109,169} Furthermore, THP-1 cells express both JAK1 and JAK2,⁷⁴ and screening against these two isoforms was deemed sufficient for the initial study. Additionally, TYK2 was beyond the primary scope of this work and thus was not considered further.

To facilitate the screening of a larger number of samples, automated western blotting was carried out using a Wes system. This system automates each step within a gel- and blot-free system using a capillary based method for protein separation, immunoprobng and detection. Following incubation of a given PROTAC at varying concentrations with the THP-1 cells for the indicated time, a proteasome inhibitor (MG132) is added and western blotting is initiated through preparation of the protein sample through cell lysis with

radioimmunoprecipitation assay buffer (RIPA) buffer supplemented with Halt™ protease inhibitor cocktail and EDTA. The cell lysate was loaded onto the Wes assay plate with the other key components which are “5x Fluorescent-Master-Mix” a biotinylated ladder, a blocking agent, the primary and horseradish peroxidase (HRP)-conjugated secondary antibodies. The blocking agent serves to prevent any non-specific binding of the antibodies to the surface of the cell membrane, through covering the membrane surface, without interfering with the bound proteins. The first antibody is specific to the protein of interest, in this case JAK1 or JAK2, whereas the second antibody (HRP-conjugated secondary antibody) is specific to the host species of the primary antibody (Fig 54). The secondary antibody, which acts to amplify the signal, is conjugated to an enzyme (HRP), which when bound to the appropriate substrate, produces a detectable signal.¹⁷⁰ For each sample, the signal/peak corresponding to JAK protein levels was normalised to that of the loading control, and reported as a ratio. The individual ratios of the compound-treated samples were normalised to that of the DMSO negative control, and the data expressed as percentage.

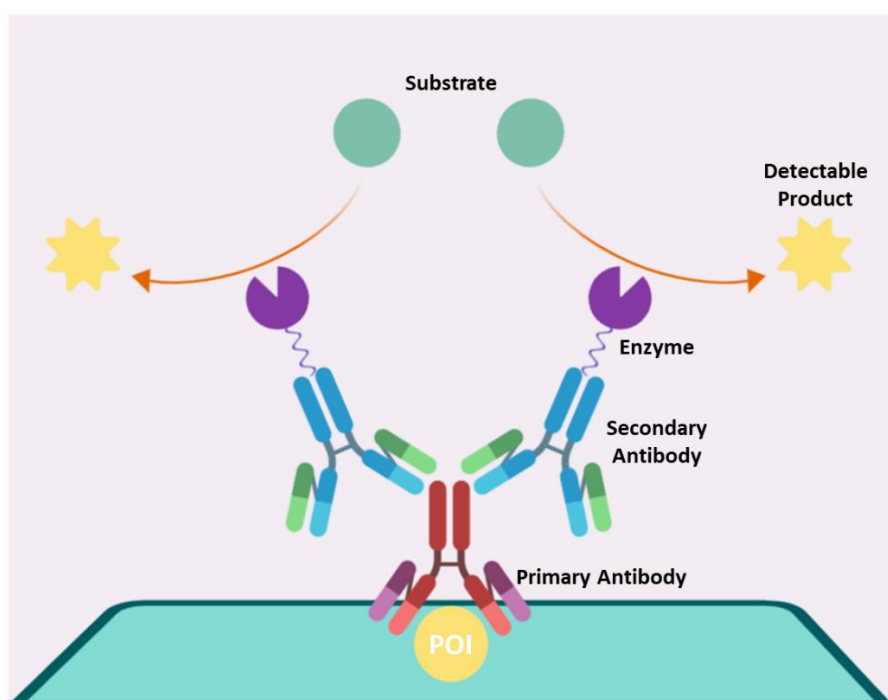


Fig 54 A schematic illustrating the western blot detection process using a primary and secondary antibody.

Compounds were evaluated within the biochemical, cellular, and western blotting assays with a number of repeats ($n \geq 2$).

2.3 Selecting a Warhead

When selecting a particular chemotype from which to generate PROTACs, it is imperative that target affinity, physicochemical properties of the warhead, and ligation vector are all adequately considered. As such, a variety of in-house GSK and published JAK inhibitors were examined on the basis of their target potency, physicochemical properties and structural binding information for progression as JAK warheads in PROTAC generation.

Whilst target inhibition is not required for PROTACs, high biochemical potency was desired across JAK1 – JAK3 from the warhead as it was indicative of target engagement. To maximise the chances of successful JAK degradation, pan-JAK inhibitors were preferred over isoform selective inhibitors. Furthermore, cellular potency readouts of the examined warheads were used to confirm target engagement upon cell penetration.

Since PROTACs typically possess molecular weights (MW) and polar surface area (PSA) values outside of those associated with efficient membrane penetration,^{171,172} the physicochemical properties of each component should be considered. As such, warheads with fewer HBDs were sought in attempts to reduce overall PROTAC polarity, and improve permeability. Additionally, a higher ChromLogD_{7.4} value, would also indicate potential improved permeability.

With relation to ligation vectors, it is critical that the linker does not disrupt essential binding interactions and is tolerated by the POI to facilitate successful ternary complex formation, and subsequent degradation. Furthermore, exploiting alternative ligation vectors will vary the nature of protein-protein interactions (PPIs) between JAK and the E3 ligase, upon forming a ternary complex, thus increasing the probability of achieving an energetically favourable and productive complex, and efficient JAK ubiquitination and degradation.^{173,174} A result of such differing PPIs may also confer alternative degradation specificity between different POI binders and ligation vectors.¹⁴⁴

With these initial parameters in mind, selection criteria parameters were developed (Table 9). The selected JAK inhibitors must have possessed a pIC₅₀ > 6.5 at JAK1 – JAK3, in addition to a pIC₅₀ > 6.5 within the cell, to ensure sufficient target engagement and cellular permeability. With respect to physicochemical space, warheads were only selected if they

possessed a HBD count of ≤ 3 or if a HBD count of ≤ 3 would be achieved following ligation or potential tolerated warhead modification to reduce HBD count. Whilst ChromLogD_{7.4}, MW and PSA were used for overall PROTAC evaluation, at this stage they were not considered as the ligase and linker strategy was unknown. Warheads lacking in structural binding information, or that of closely related analogues were immediately ruled out, and those possessing clear, achievable ligation vectors from crystal structure/computational modelling analysis against closely related analogues were progressed for further evaluation. Finally, rapid access to a library of PROTACs to assess JAK degradation aptitude was desired, and as such, synthetic tractability was essential. However, in the initial selection process, synthetic tractability was not prioritised, but reviewed to triage the penultimate set.

Selection Criteria			
Biochemical Potency (JAK1 – 3 pIC ₅₀)	Cellular Potency (pIC ₅₀)	HBD Count	Structural Binding Information
> 6.5	> 6.5	$\leq 3^*$	Requires Clear Exit Vector

Table 9 Warhead selection criteria. * = Compounds selected on the basis of ≤ 3 HBDs, including being achieved through template modification and/or subsequent ligation.

Eleven JAK inhibitors were selected for further comparison to identify warheads from which to generate PROTACs (Fig 55): namely tofacitinib **3**, a GSK quinazoline series **55**, a carbazole carboxamide **56** series developed at BMS,¹⁷⁵ an indole carboxamide series **57** discovered at Merck,¹⁷⁶ a GSK pyrimidine series **58**,¹⁷⁷ an imidazotriazine series **59**, Palau Pharma's imidazopyridinone **60**,¹⁷⁸ Novartis's quinoxaline series **61**,¹⁷⁹ and a thienopyrazole series **62**. All eleven series were placed into two distinct categories, 'go' or 'no-go', and the compounds binned within the 'go' classification were further scrutinised to determine which series to take forward into the development of JAK PROTACs. It should be noted that not all biochemical and cellular data were determined at GSK, and that literature data were compared to in-house GSK generated data across the different series.

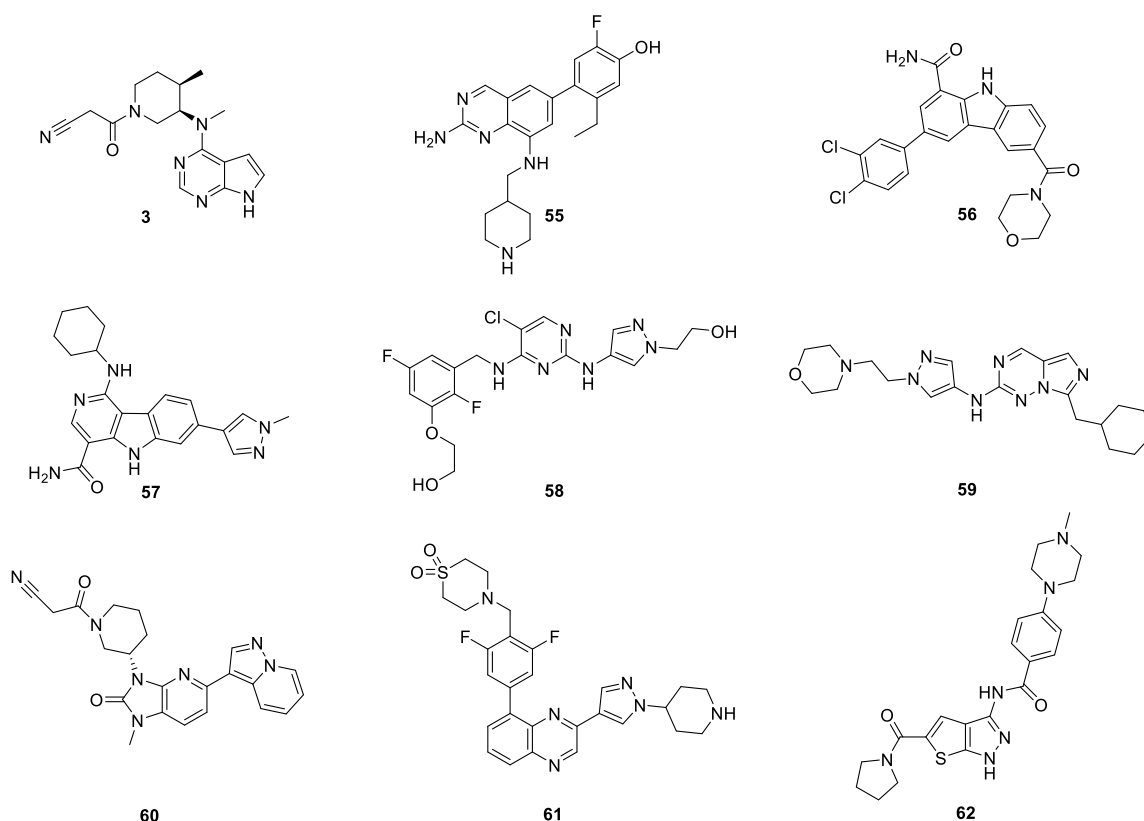
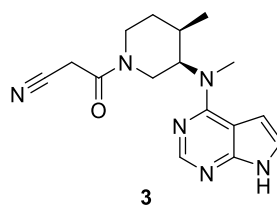


Fig 55 The selected warheads for scrutiny and characterisation within the ‘go’ and ‘no-go’ categories based on the selection criteria.

2.3.1 Tofacitinib

As discussed previously in Section 1.4.2, tofacitinib **3** confers excellent potency at each JAK isoform, and within our biochemical and cellular assays the high potency readout was confirmed (JAK1 pIC_{50} = 8.9, JAK2 pIC_{50} = 8.7, JAK3 pIC_{50} = 9.2, IL-2 PBMC pIC_{50} = 6.9) (Table 10). In addition to the contribution of 1 HBD, it was hypothesised that ligation from the *N*-methyl group would be well tolerated by the JAKs (Fig 56). Late-stage installation of the methyl group appeared challenging, therefore, late-stage addition of linkers and ligase binders via the same route would also be challenging, thus hindering rapid PROTAC access. However, due to its target potency and physicochemical properties, tofacitinib **3** was promoted to further evaluation against the other selected JAK inhibitors and placed within the ‘go’ bin.



Compound	HBD	ChromLogD _{7,4}	MW	pIC ₅₀			
				JAK1	JAK2	JAK3	IL-2 PBMC
Tofacitinib 3	1	1.79	312.38	8.9	8.7	9.2	6.9

Table 10 The physicochemical properties and binding affinities data associated with tofacitinib **3**. pIC₅₀ values are quoted as a mean of multiple, separate experiments (n ≥ 2).

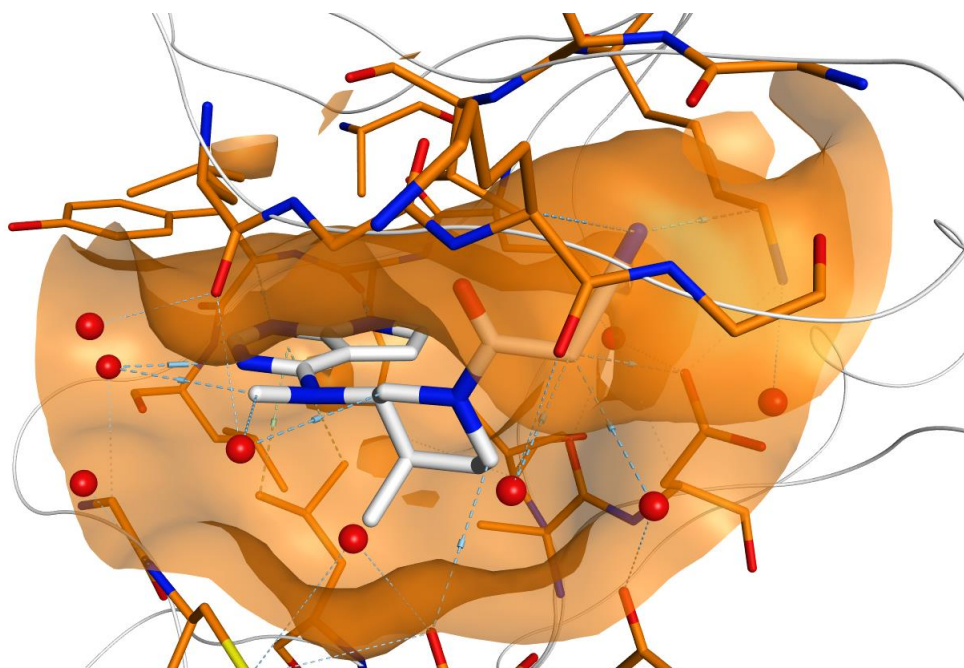
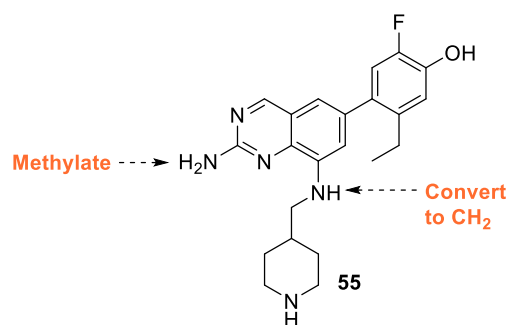


Fig 56 A crystal structure of tofacitinib **3** in JAK3, illustrating the *N*-methyl handle as a potential ligation vector. PDB = 3LXK, resolution: 2.00 Å.³²

2.3.2 Quinazoline Series

The GSK quinazoline series, as exemplified by compound **55**, possessed excellent potency across each JAK isoform within the biochemical assays (JAK1 pIC_{50} = 9.0, JAK2 pIC_{50} = 8.2, JAK3 pIC_{50} = 8.9) (Table 11).¹⁸⁰ Additionally, quinazoline **55**, displayed high potency with the IL-2 PBMC assay (pIC_{50} = 6.9). Quinazoline **55** exhibited a desirable ligation vector from the piperidine, which could likely be easily exploited, and likely tolerated by the JAKs (Fig 57). Although quinazoline **55** conferred desirable target potency and ligation vector, its physicochemical properties were suboptimal for permeability. Quinazoline **55** displays 4 HBDs, which would reduce to 3 upon ligation of the piperidine. Furthermore, it was hypothesised that switching out the secondary aniline for a carbon, and monomethylation of the exocyclic two-amino group would further reduce the HBD count to two. It was known through in-house SAR studies that modification of the phenol HBD resulted in a significant loss of JAK potency. However, the effects of the proposed modifications on potency and permeability were unknown, and the C-linked analogues could potentially complicate the synthesis, although it would only require the synthesis of one analogue to assess such alterations. As such, the quinazoline series was placed with the 'go' bin.



Compound	HBD	ChromLogD _{7.4}	MW	pIC ₅₀			
				IL2			
				JAK1	JAK2	JAK3	PBMC
Quinazoline 55	4	2.27	395.48	9.0	8.2	8.9	6.9

Table 11 The physicochemical properties and binding affinities data associated with quinazoline **55**. pIC₅₀ values are quoted as a mean of multiple, separate experiments (n ≥ 2). The potential modifications to remove HBDs are highlighted in orange.

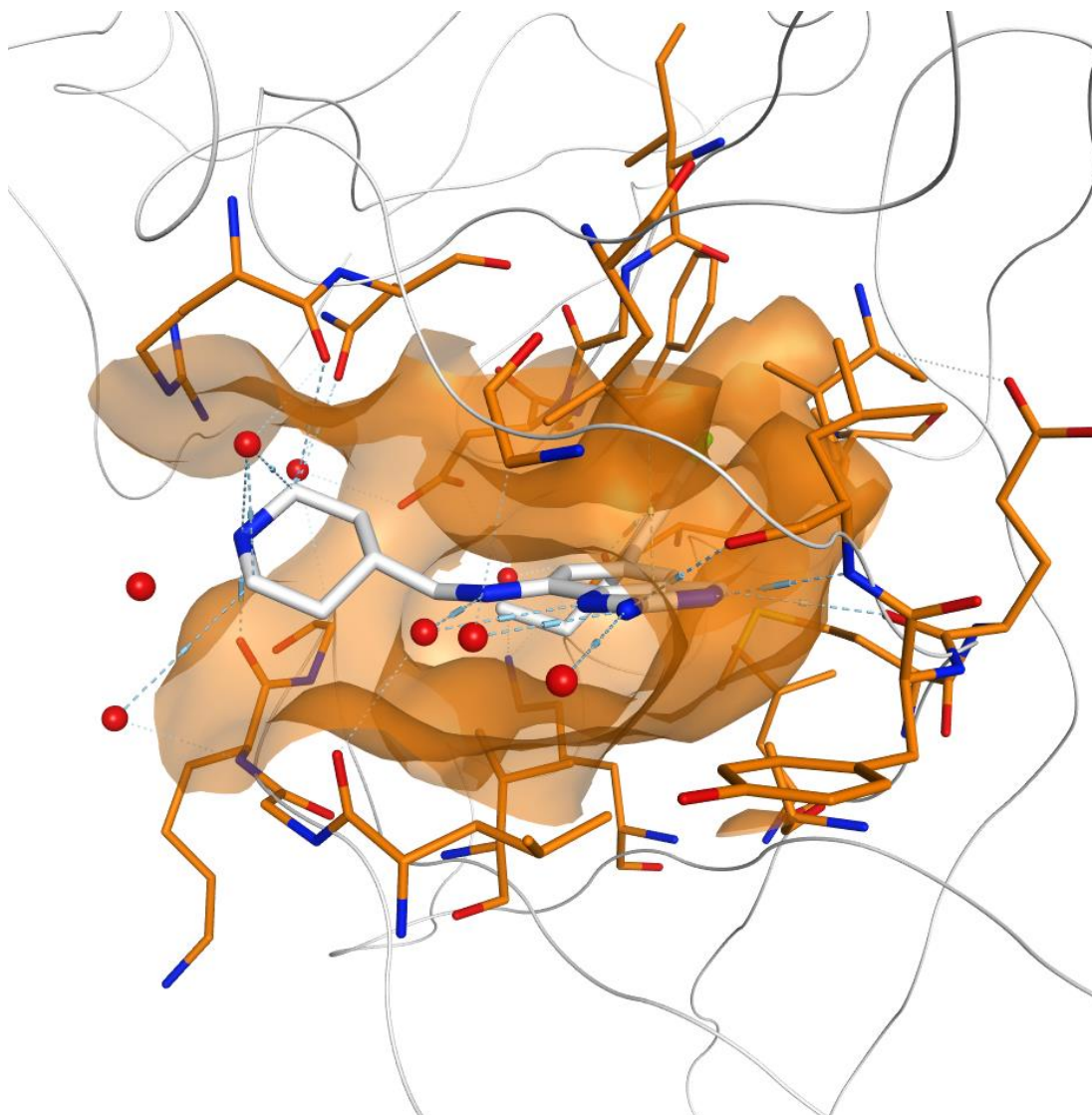
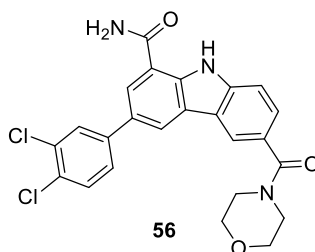


Fig 57 A in-house crystal structure of quinazoline **55** in JAK2, illustrating the clear ligation vector from the solvent exposed piperidine moiety. Resolution: 1.80 Å.⁴²

2.3.3 Carbazole Carboxamide Series

From the published JAK biochemical assay data,¹⁷⁵ carbazole carboxamide **56**, displays JAK2 biased potency over JAK1 and JAK3, albeit carbazole carboxamide **56** still displays high activity at the latter mentioned isoforms (JAK1 pIC_{50} = 7.3, JAK2 pIC_{50} = 8.6, JAK3 pIC_{50} = 6.9). Furthermore, evaluation of carbazole carboxamide **56** with a JAK2-dependent SET-2 cellular assay revealed high cellular JAK2 activity (SET-2 pIC_{50} = 6.7). A crystal structure of carbazole carboxamide **56** within JAK2 revealed the *para*-chloro to be a likely vector that could be easily

exploited and potentially tolerated (Fig 58). Furthermore, the morpholine moiety appears to point outside of the active site, which could provide a second vector. Carbazole carboxamide **56** possessed desirable physicochemical properties in relation to permeability, possessing only 2 HBDs. However, the preceded synthesis of carbazole carboxamide **56** was relatively lengthy (8 steps, involving the use of SnCl₂) and the JAK2 bias could reduce its degradation aptitude at the other JAK isoforms. Whilst carbazole carboxamide **56** exhibited favourable physicochemical properties, and ease of ligation, the lengthy synthesis of carbazole carboxamide **56** resulted in it being placed within the ‘no-go’ category, but with a view to revisit following initial PROTAC library generation.



Compound	HBD	CChromLogD _{7.4}	MW	pIC ₅₀			
				JAK1	JAK2	JAK3	SET-2
Carbazole carboxamide 56	2	3.88	468.33	7.3	8.6	6.9	6.7

Table 12 The physicochemical properties and binding affinities data associated with carbazole carboxamide **56**. pIC₅₀ values are quoted from literature values.

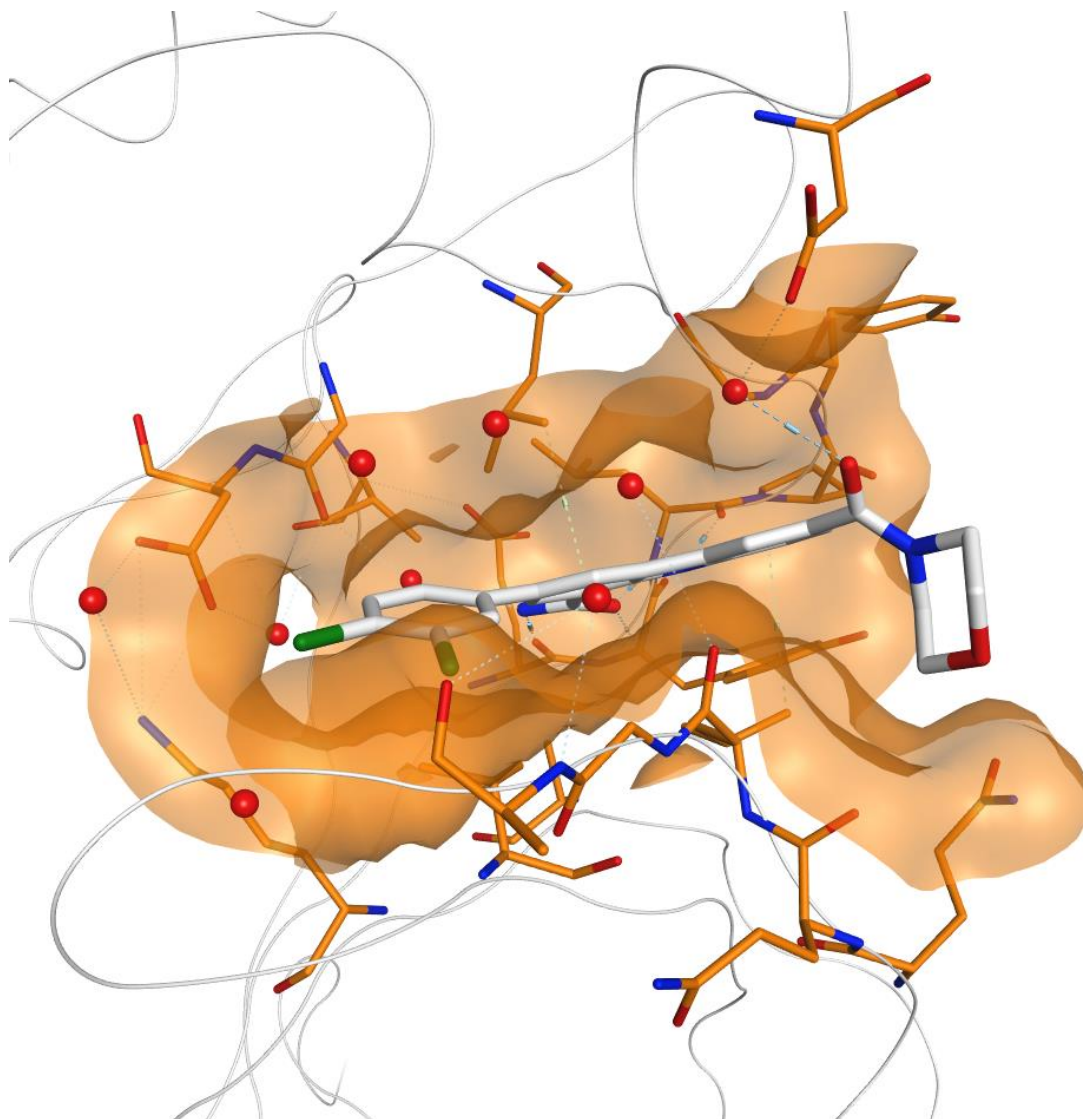
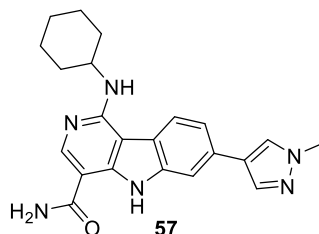


Fig 58 The crystal structure of carbazole carboxamide **56** within JAK2, illustrating the *para*-Cl and morpholine moieties which could be tethered to a linker and ligase binder. PDB = 4ZIM, resolution: 2.65 Å.¹⁷⁵

2.3.3 Indole Carboxamide Series

An indole carboxamide series exemplified by compound **57**, with only three displayed HBDs, was reported in the literature (Table 13);¹⁷⁵ although only JAK2 biochemical data ($pIC_{50} = 8.3$) was presented, and there was no disclosure of cellular data, this template was considered further due to the favourable physicochemical properties displayed and multiple ligation vectors from the pyrazole and cyclohexyl group.¹⁷⁵ However, as a synthetic route to indazole

carboxamide **57** was not published at the time of selection, a retrosynthesis of indole carboxamide **57** was carried out which exposed a potentially difficult synthesis. Therefore, the indole carboxamide series was placed within the 'no-go' category.



Compound	HBD	CChromLogD _{7,4}	MW	pIC ₅₀			
				JAK1	JAK2	JAK3	Cell Assay
Indole carboxamide 57	3	1.94	388.48	N/D	8.3	N/D	N/D

Table 13 The physicochemical properties and binding affinities data associated with indole carboxamide **57**. pIC₅₀ values are quoted from literature values.

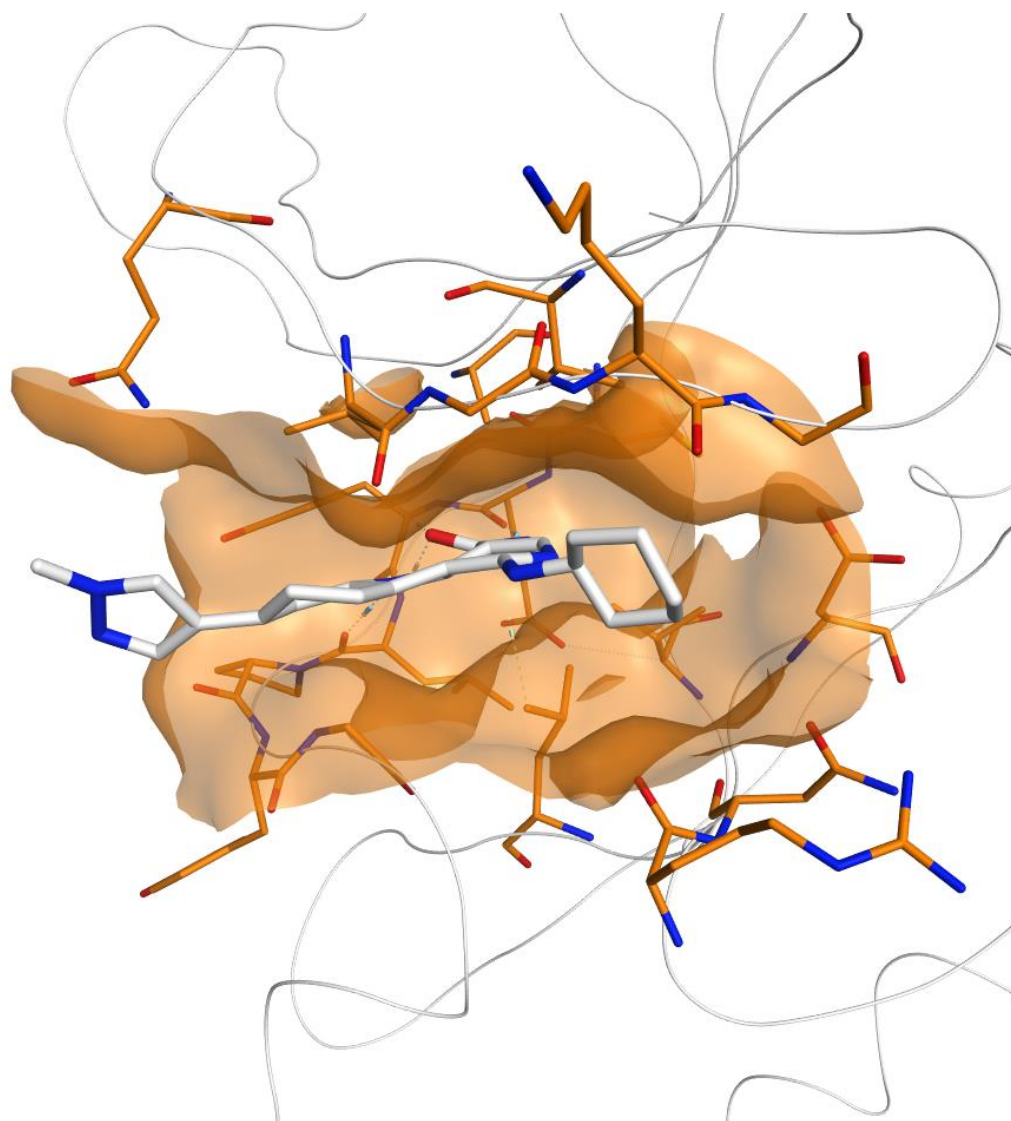
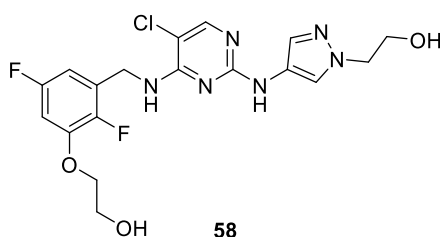


Fig 59 A crystal structure of indole carboxamide **57** within JAK2, highlighting the cyclohexyl and pyrazole vectors. PDB = 3RVG, resolution: 2.50 Å.

2.3.4 Pyrimidine series

Pyrimidine **58**, derived from GSK's in-house pyrimidine series displays a pan-JAK profile, with high potency across the JAKs within the K_m biochemical assay (Table 14).¹⁷⁷ Further assessment of pyrimidine **58** within the IL-2 PBMC assay, showed high levels of inhibition of IFN γ through JAK1/JAK3 inhibition ($pIC_{50} = 7.5$), thus, placing pyrimidine within the potency realms of the selection criteria. Somewhat displeasingly, pyrimidine **58** contains four HBDs,

however, it was envisaged that ligation at the benzylic, or pyrazole vectors would remove one HBD. Moreover, structurally related analogues within the compound collection identified that the terminal hydroxy groups were not required for potency and the compounds could be truncated to remove these HBDs if required, thereby reducing the HBD count to ≤ 3 , thus satisfying the selection criteria's physicochemical property requirements. Since the pyrimidine series was developed at GSK, considerable information of the synthesis of the template was available; however, the synthesis is relatively long (8 steps). It was hypothesised that this could be considerably shortened through integration of more recent and novel chemistries. The opportunity to exploit two distinct vectors from both hydroxy groups for ligation was particularly attractive (Fig 60), and this coupled with high pan-JAK activity and cellular potency led to pyrimidine **58** being placed within the 'go' category.



Compound	HBD	ChromLogD _{7.4}	MW	pIC ₅₀			
				JAK1	JAK2	JAK3	IL-2 PBMC
Pyrimidine-OH							
58	4	2.75	440.84	9.8	> 9.8	> 9.8	7.5

Table 14 The physicochemical properties and binding affinity data associated with pyrimidine **58**. pIC₅₀ values are quoted as a mean of multiple, separate experiments (n \geq 2).

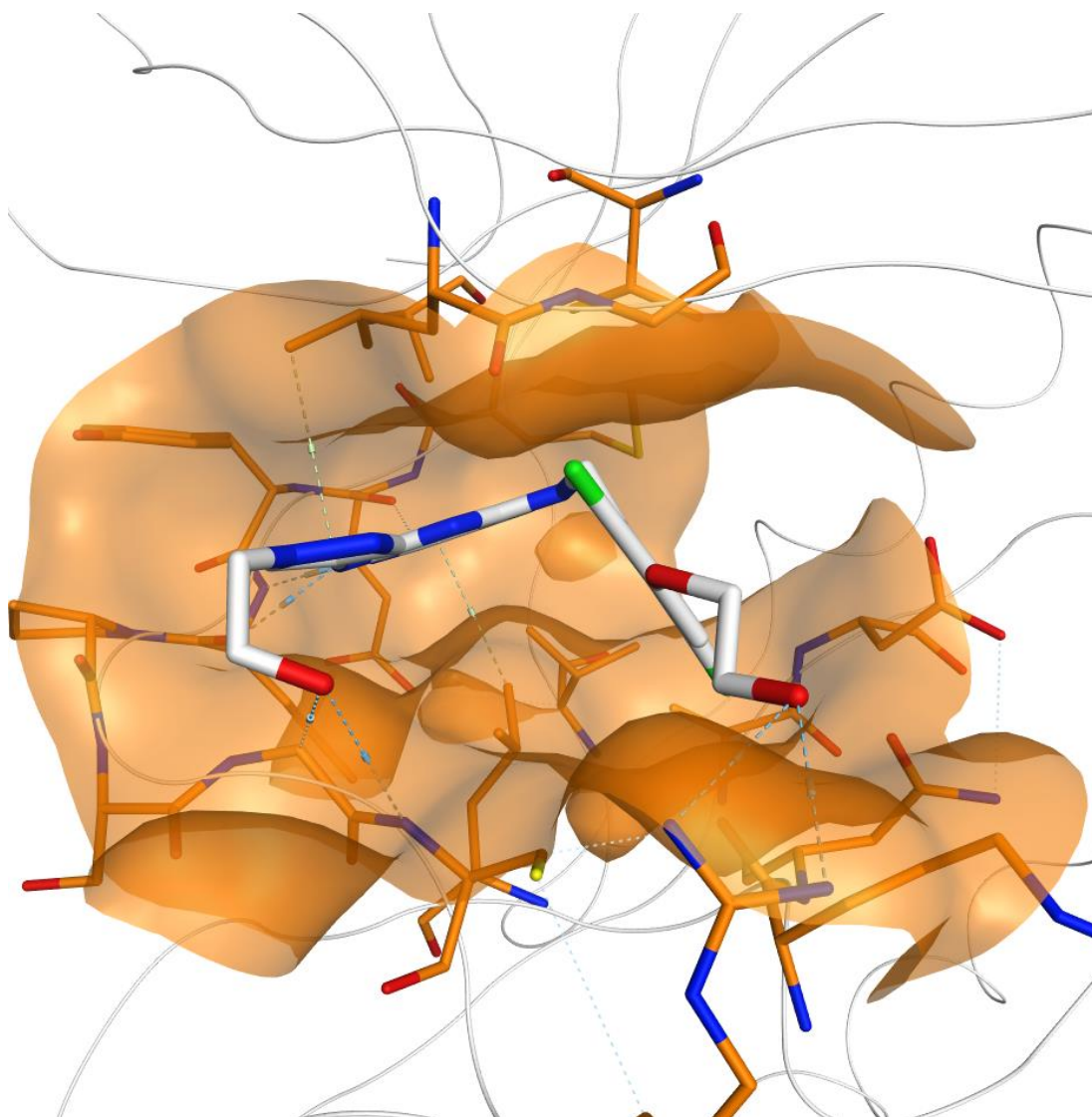
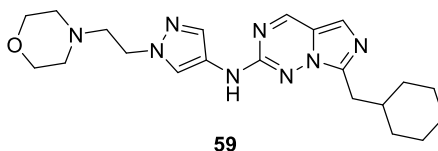


Fig 60 A docking of pyrimidine-OH **58** within JAK3, based on a closely related crystal structure, illustrating the two hydroxy ligation vectors from the pyrazole and benzyl positions.

2.3.5 Imidazotriazine series

The GSK imidazotriazine **59** was potent at each JAK isoform, sequentially increasing in potency from JAK1, to JAK2, to JAK3 within the K_m biochemical assay (JAK1 pIC_{50} = 7.1, JAK2 pIC_{50} = 8.4, JAK3 pIC_{50} = 9.2). Within a cellular context, in the IL-2 PBMC assay, imidazotriazine **59** exhibits potent JAK1/JAK3 activity (pIC_{50} = 6.7). Furthermore, imidazothiazole **59** would contribute 1 HBD to imidazotriazine-derived PROTACs. A clear exit vector was envisaged

from the morpholine moiety (Fig 61), from which a linker and ligase binder could be attached. The synthesis of imidazotriazine **59** appeared relatively simple and was well preceded. Due to these favourable characteristics, such as *in vitro* biochemical and cellular potency, physicochemical properties and structural binding information, imidazotriazine was placed in the 'go' bin.



Compound	HBD	ChromLogD _{7.4}	MW	pIC ₅₀			
				JAK1	JAK2	JAK3	IL-2 PBMC
Imidazotriazine 59	1	4.17	410.53	7.1	8.4	9.2	6.7

Table 15 The physicochemical properties and binding affinities data associated with imidazotriazine **59**. pIC₅₀ values are quoted as a mean of multiple, separate experiments (n ≥ 2).

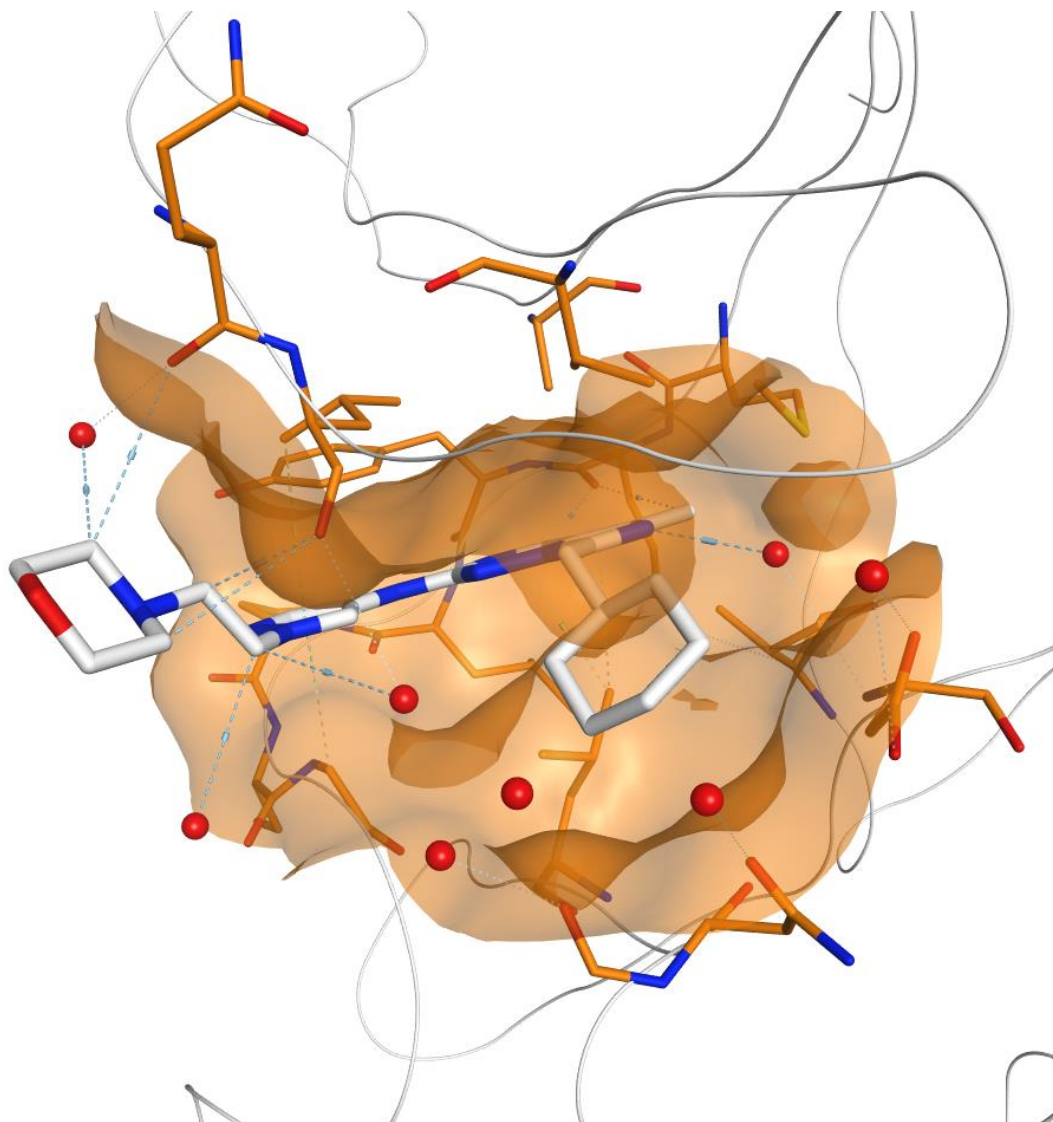
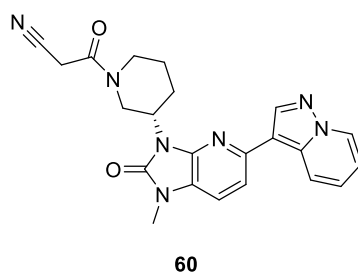


Fig 61 An in-house crystal structure of imidazotriazine **59** within JAK2, highlighting the solvent exposed morpholine ligation vector. Resolution: 1.60 Å.¹⁸¹

2.3.6 Imidazopyridinone Series

The imidazopyridinone **60** displayed high biochemical (JAK1 pIC_{50} = 9.0, JAK2 pIC_{50} = 9.5, JAK3 pIC_{50} = 9.3), and cellular potencies (IL-2 PBMC pIC_{50} = 6.9) within our assays (Table 16). Moreover, imidazopyridinone **60** possessed no HBDs, which would aid its permeability.¹⁷⁸ However, a crystal structure of imidazopyridinone **60** within JAK2 revealed it binds deeper within the active site possessing no solvent exposed groups, although ligation at the *N*-

methyl position appeared as if it may be tolerated (Fig 62). Somewhat displeasingly, the synthetic tractability assessment of imidazopyridinone **60** highlighted that rapid imidazopyridinone-PROTAC library generation may not be achievable. Although imidazopyridinone's **60** ligation vector and synthesis were suboptimal, its target potency and physicochemical properties were highly desirable and thus imidazopyridinone was placed within the 'go' category.



Compound	HBD	ChromLogD _{7.4}	MW	pIC ₅₀			
				JAK1	JAK2	JAK3	IL-2 PBMC
Imidazopyridone 60	0	3.44	415.46	9.0	9.5	9.3	6.9

Table 16 The physicochemical properties and binding affinities data associated with imidazopyridinone **60**. pIC₅₀ values are quoted as a mean of multiple, separate experiments (n ≥ 2).

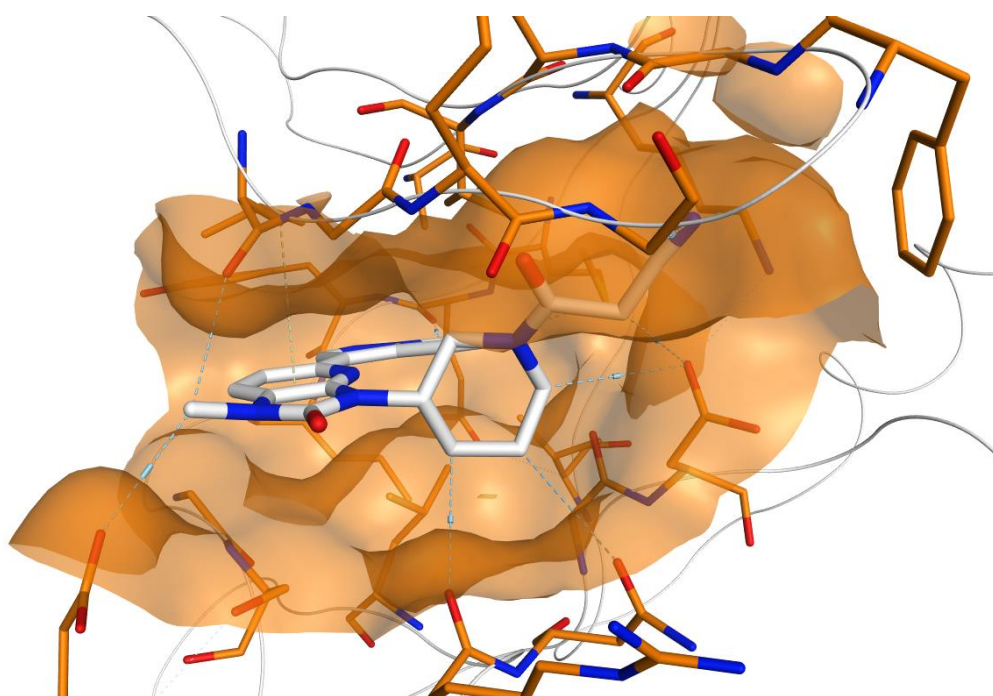
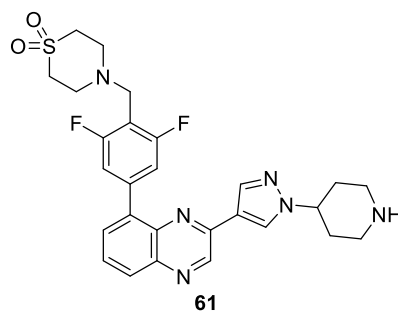


Fig 62 An in-house crystal structure of imidazopyridinone **60** within JAK2. Resolution: 1.53 Å.⁴²

2.3.7 Quinoxaline series

The quinoxaline series, exemplified by quinoxaline **61** (NVP-BSK805) was a JAK2 selective series, developed for the treatment of myeloproliferative disorders.¹⁷⁹ Characterisation within our JAK biochemical assays confirmed its JAK2 selective profile (JAK1 pIC_{50} = 7.3, JAK2 pIC_{50} = 9.5, JAK3 pIC_{50} = 7.4) (Table 17). Disappointingly, quinoxaline **61** lacked potency within the IL-2 PBMC assay (pIC_{50} = 5.7); however, this was unsurprising since the IL-2 PBMC assay measures JAK1/JAK3 inhibition, omitting JAK2, and thus this value was not considered in relation to warhead selection. Additionally, quinoxaline **61** displays one HBD which would be removed upon ligation, as a crystal structure of quinoxaline **61** bound within JAK2 identified the piperidine *N*-H would make a suitable ligation vector as it resides within a solvent exposed region of the protein (Fig 63).¹⁸² Additionally, a large-scale synthesis was published within the patent,¹⁷⁹ which would allow for significant quantities of the parent compound to be synthesised, which could then be used directly into PROTAC library synthesis through late-stage ligation. Whilst NVP-BSK805 **61** displayed a less favourable JAK2-selective profile, as opposed to pan-JAK potency, the desirable physicochemical properties, conjoined to the

suitable ligation vector and published and precedented synthetic route led to NVP-BSK805 **61** being placed within the 'go' bin.



Compound	HBD	ChromLogD _{7.4}	MW	pIC ₅₀			
				JAK1	JAK2	JAK3	IL-2 PBMC
NVP-BSK805 61	1	2.8	538.62	7.3	9.5	7.4	5.7

Table 17 The physicochemical properties and binding affinities data associated with quinoxaline **61** (NVP-BSK805). pIC₅₀ values are quoted as a mean of multiple, separate experiments (n ≥ 2). Quinoxaline **61** tested as a formic acid salt.

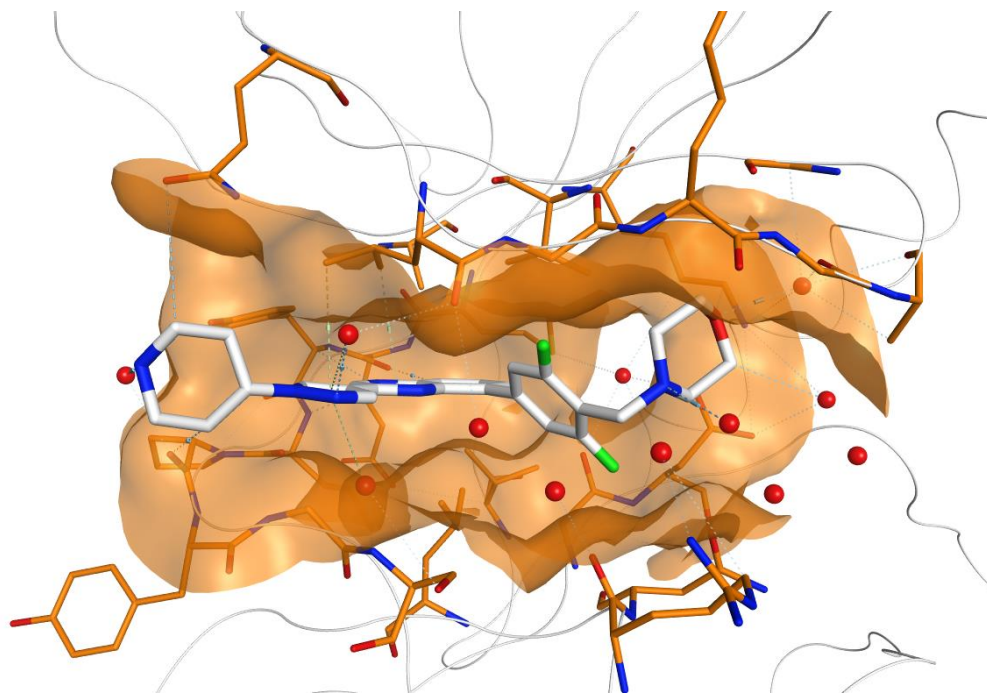
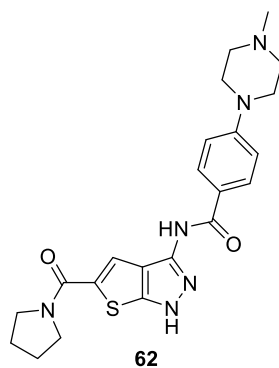


Fig 63 The crystal structure of NVP-BSK805 **61** within JAK2, highlighting the solvent exposed piperidine as a potential ligation vector. PDB = 3KRR, resolution: 1.80 Å.

2.3.8 Thienopyrazole series

The final JAK inhibitor to be scrutinised was the thienopyrazole series, exemplified by thienopyrazole **62**.¹⁶⁸ Within our biochemical assays, the thienopyrazole exemplar **62** expressed a TYK2 bias, which was unfavourable, as JAK1 – 3 degradation was desired in the first instance (JAK1 pIC₅₀ = 6.9, JAK2 pIC₅₀ = 7.1, JAK3 pIC₅₀ = 7.5, TYK2 pIC₅₀ = 8.1) (Table 18). Within the IL-2 PBMC assay, thienopyrazole **62** possessed moderate cell potency (IL-2 PBMC pIC₅₀ = 6.4). Despite undesirable target potency, thienopyrazole **62** contains two HBDs, and an easily exploited vector; it was thought that removal of the *N*-methyl group on the piperazine, would allow for easy attachment of a linker and ligase binder. Furthermore, the synthesis of thienopyrazole **62** was well preceded and relatively simple. However, due to the undesirable target potency and moderate cell potency, thienopyrazole **62** was placed within the ‘no-go’ bin.



Compound	HBD	ChromLogD _{7.4}	MW	pIC ₅₀			
				JAK1	JAK2	JAK3	IL-2 PBMC
Thienopyrazole 62	2	1.58	438.55	6.9	7.1	7.5	6.4

Table 18 The physicochemical properties and binding affinities data associated with thienopyrazole **62**. pIC₅₀ values are quoted as a mean of multiple, separate experiments (n ≥ 2).

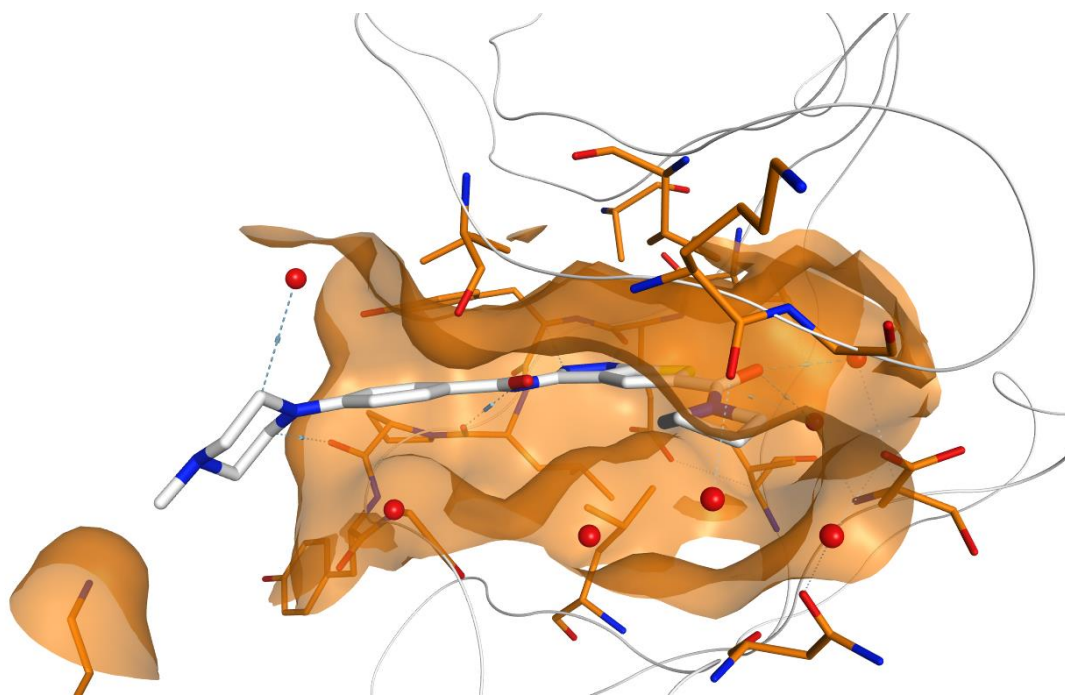


Fig 64 An in-house crystal structure of thienopyrazole **63** within JAK3, highlighting the solvent exposed piperazine ligation vector. Resolution: 1.92 Å.¹⁸¹

2.3.9 Review of the 'Go' Category

With the initial set whittled down, attention was diverted to the JAK inhibitors placed within the 'go' category, namely, tofacitinib **3**, quinazoline **55**, pyrimidine **58**, imidazopyridinone **60**, and the quinoxaline **61** series.

Tofacitinib **3** was not progressed further at this stage, as late-stage modification of the aniline to rapidly provide a library of PROTACs was not feasible following the published routes. Therefore, after linker attachment, further synthetic steps would be required to furnish the warhead.

The quinazoline **55** series was ruled out due to the significant number of structural changes to the compound which would have an unknown effect on potency and permeability. Additionally, the C-linked compounds would be challenging to synthesise. Finally, other compounds within the 'go' category were able to access the same vector as quinazoline **61**.

Due to the wealth of knowledge on the pyrimidine series and its desirable pan-JAK, and cellular potency, and multiple ligation vectors, pyrimidine **58** was progressed as a parent compound for PROTAC library synthesis and evaluation, with a view to exploiting both ligation vectors.

The synthetic tractability of imidazopyridinone **60** was not particularly attractive, and it was unknown whether the *N*-methyl would allow for rapid PROTAC generation, which would only be determined at the last step of a lengthy synthesis. Therefore, imidazopyridinone **60** was not progressed for PROTAC library generation.

Finally, the quinoxaline series' desirable physicochemical properties, preceded synthesis and the possibility of rapid PROTAC generation led to its progression, and further evaluation to identify analogous compounds pertaining to a more pan-JAK profile. As such, two quinoxaline compounds **61** and **63** were selected and progressed to synthesis for possessing more of a pan-JAK profile than analogous compounds from the series, to determine the most suitable warhead of the series for PROTAC generation (Fig 65).

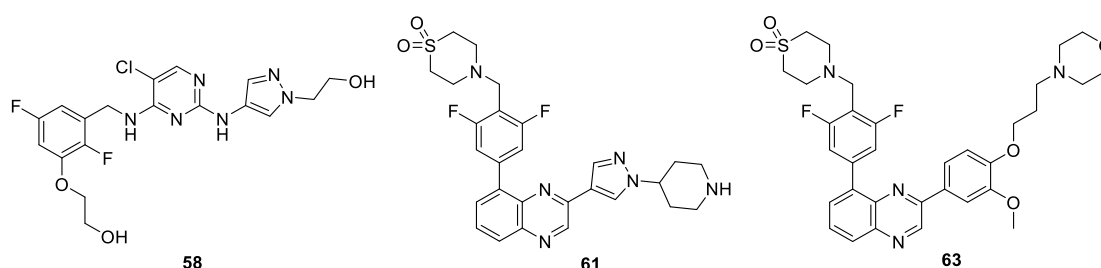


Fig 65 Selected warheads for evaluation and PROTAC generation.

2.4 Design of Cell Penetrant JAK PROTACs

PROTACs can be dissected into three distinct components: the warhead, ligase binder and linker. As such, it is crucial that the physicochemical properties of each component is evaluated when designing a PROTAC library. Therefore, prior to synthesising the library, the

physicochemical properties of each component, and the overall PROTACs were examined. We sought to vary the warhead, ligase binder and linker as to modulate the physicochemical properties of our PROTACs to evaluate our target physicochemical space.

Whilst the adoption of all-small molecule PROTACs has led to an improvement in cell permeation over their peptidic counterparts, PROTACs occasionally require high concentrations to achieve maximal protein degradation.^{183,172} Therefore PROTAC physicochemical properties should be considered prior to PROTAC synthesis.

In 1997 Lipinski *et al.* published their seminal study known as the rule of 5 (Ro5) (Table 19),¹¹² which attempted to establish a set of guidelines to decrease attrition rates of oral drug candidates. The study, which was quickly adopted as a staple of medicinal chemistry, suggested oral drug candidates should adhere to the following properties; MW \leq 500 Da, cLogP \leq 5, HBD \leq 5 and HBA \leq 10 in order to maximise probability of good bioavailability (Table 19). However, a significant number of medicinal opportunities intrinsically fall outside of the Ro5 space such as macrocycles, cyclic peptides and PROTACs, and as a consequence, a set of guidelines titled 'beyond the rule of 5' (bRo5) has been developed.¹⁸⁴ The in-depth analysis outlined the following physicochemical space for improved bioavailability; MW \leq 1000 Da, cLogP \leq -2 - \leq 5, HBD \leq 6, HBA \leq 15, PSA \leq 250 Å² and number of rotatable bonds (NRotB) \leq 20. From a critical analysis of the publication it appears if there were 6 HBDs, one HBD was always masked by an intramolecular hydrogen bond. Whilst these guidelines were generated to achieve oral absorption with larger small molecules, the boundaries of physicochemical parameters, such as H-bond donor (HBD) count (\leq 6), were selected as a surrogate to enhance cell permeation. In addition to the bRo5, GSK recommendations developed for cell-penetrant PROTACs suggested a measured ChromLogD_{7.4}, or a calculated ChromLogD_{7.4} adjusted for > 70 heavy atoms (CChromLogD_{7.4}), space of 4 – 6. Since the PROTAC approach to targeting JAK remains in its proof-of-concept stage, only HBD and ChromLogD_{7.4} were taken into account. These physicochemical properties can be modulated by altering the JAK warhead, and linker type and length. For the purposes of our work, PROTAC optimisation was focused on increasing permeability as a driver of activity in an *in vitro* cellular environment.

Guidelines	MW	LogP	HBD	HBA	PSA	NRotB	ChromLogD _{7.4}
Ro5	< 500	< 5	< 5	< 10	-	-	-
bRo5	≤ 1000	≤ -2 - ≤ 5	≤ 6	≤ 15	≤ 250 Å ²	≤ 20	-
GSK	-	-	-	-	-	-	4 - 6

Table 19 The physicochemical guidelines of Lipinski's Rule of 5, Beyond the Rule of 5 and GSK guidelines.

With the JAK chemotypes selected, and the PROTAC design criteria outlined, focus was shifted towards exploring different classes of E3 ligase binders. Three distinct E3 ligase binders were chosen: inhibitor of apoptosis protein (IAP) **64**,¹⁸⁵ Von Hippel–Lindau (VHL) **65**,¹⁸⁶ and Cereblon (CRBN) **49** (Fig 66).¹⁵² These ligase binders were selected as they were the most widely used in PROTAC technology, and target protein degradation had been exemplified by all three.

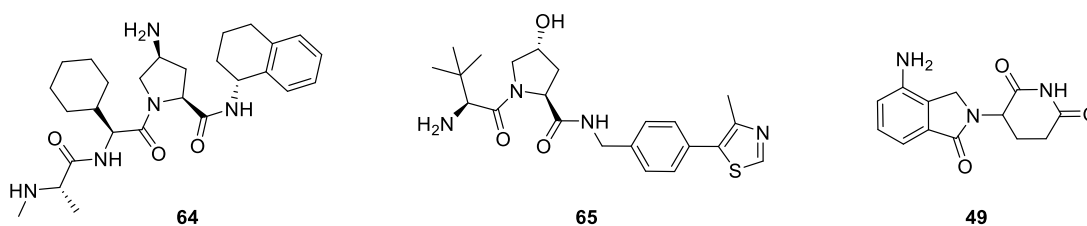
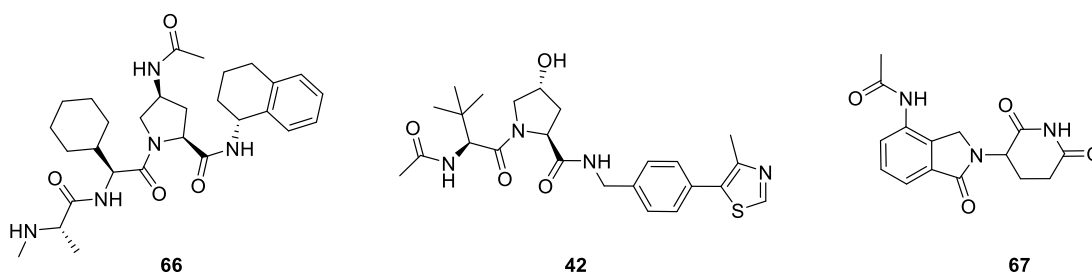


Fig 66 The three E3 ligase binders, IAP **64**, VHL **65**, and CRBN **49** selected for PROTAC generation.

In addition to possessing alternative degradation specificity,¹⁴⁴ IAP **64**, VHL **65** and CRBN **49** ligands confer differing physicochemical attributes, which can have profound effects on cell penetration. MW, PSA, ChromLogD_{7.4} and HBD count decrease from acetylated-IAP **66** (MW = 525.69, ChromLogD_{7.4} = 3.6, HBD = 4) to acetylated-VHL **42** (MW = 472.60, ChromLogD_{7.4} = 2.5, HBD = 3) to acetylated-CRBN **67** (MW = 301.30, ChromLogD_{7.4} = 0.2, HBD = 2) (Table 20).



Compound	MW	HBD	ChromLogD _{7.4}	PSA (Å ²)
Acetylated-IAP 66	525.69	4	3.6	120
Acetylated-VHL 42	472.60	3	2.5	112
Acetylated-CRBN 67	301.30	2	0.2	96

Table 20 The physicochemical data associated with acetylated-IAP **66**, acetylated-VHL **42**, and acetylated-CRBN **49**, illustrating a decrease in HBD count, ChromLogD_{7.4} and PSA moving from acetylated-IAP **66** to acetylated-VHL **42** to acetylated-CRBN **67**.

The final component of a PROTAC is the linker. The linker can have a profound effect on the PROTACs' physicochemical properties, and consequently modulate cell permeability. Since the optimum linker length and composition for JAK degradation was unknown, an assortment of all-carbon and PEG linkers was sought, varying in length from 7 – 20 atoms (Fig 67). In addition to the aforementioned linkers, a 'click' chemistry platform was being developed, which would allow rapid access to PROTACs and linkers derived from 'click' reactions. As such, the 'click' platform was incorporated into the PROTAC design.

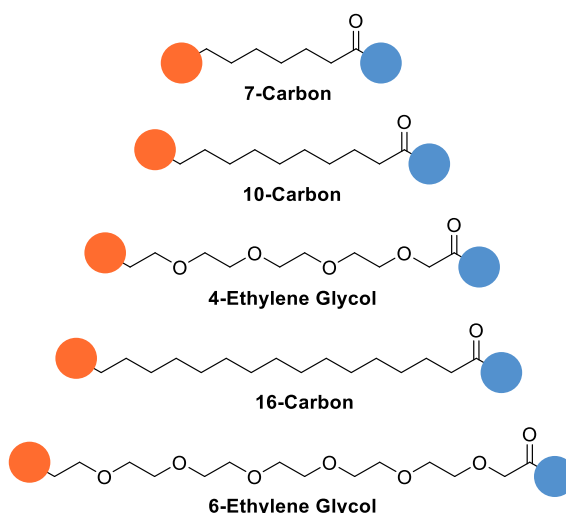


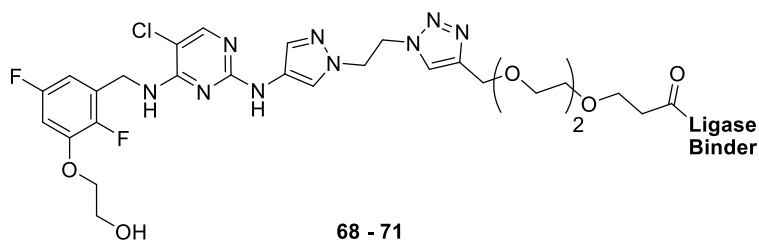
Fig 67 The 7C, 10C, 4-ethylene glycol, 16C and 6-ethylene glycol linker used to tether the JAK warhead to an E3 ligase binder. Orange circle = JAK warhead; blue circle = E3 ligase binder.

Prior to synthesis, the compounds were evaluated *in silico* with respect to their calculated physicochemical properties. Compounds that significantly exceeded the design criteria were eliminated. However, to examine the boundaries of the target physicochemical space, a wide range of physicochemical space with respect to MW, PSA, HBD count and ChromLogD_{7.4} was explored, both encompassing, and exceeding the GSK and literature guidelines.

2.4.1 'Click' Linked Pyrimidine-OH PROTACs

The 'click' linked PROTACs possessed suboptimal physicochemical properties in relation to those selected for increased permeability within an *in vitro* cellular environment (Table 21). All but the CRBN 'click' linked pyrimidine-OH PROTACs **68** – **71** possessed an MW > 1000. However, all of the PROTACs from the 'click' linked subseries maintained a HBD ≤ 6, except for the IAP 'click' linked PROTAC **68**, which contained 7 HBDs, falling outside of the design criteria. Furthermore, the only compound not to exceed the PSA guideline of ≤ 250 Å² was the CRBN 'click' linked PROTAC **69**. Whilst the CRBN 'click' linked pyrimidine-OH PROTAC **69** occupied a physicochemical region within the desired space, its PSA value was only under by 2 Å², and its MW was approaching 1000 (910.29). Additionally, an alternative VHL binder was

used within the ‘click’ subseries due to its differing physicochemical properties, exemplified by PROTAC **71**, however, this VHL binder was not used in subsequent PROTAC design. Whilst CChromLogD_{7.4} was the only parameter that all the ‘click’ linked PROTACs satisfied, it was expected that the compounds would lack efficient cell penetration due to their poor physicochemical attributes; however, they were progressed to synthesis to explore the boundaries and limitations of the physicochemical guidelines.

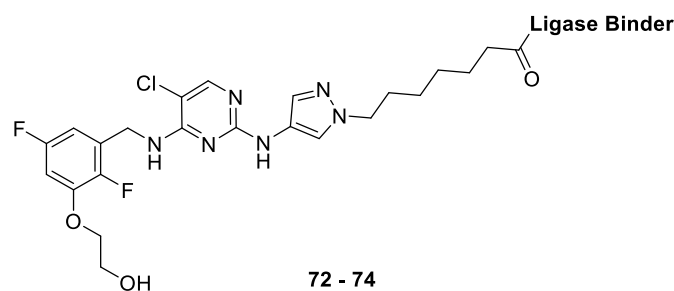


Ligase Binder	MW	HBD	CChromLogD _{7.4}	PSA (Å ²)
<p style="text-align: center;">68</p>	1147.72	7	4.0	275
<p style="text-align: center;">69</p>	910.29	4	4.0	248
<p style="text-align: center;">70</p>	1094.63	6	4.4	267
<p style="text-align: center;">71</p>	1198.74	5	5.4	268

Table 21 The *in silico* physicochemical data associated with the pyrimidine-OH ‘click’ subseries PROTACs, growing from the pyrazole vector.

2.4.2 7C-Linked Pyrimidine-OH PROTACs

It was envisaged that switching out the 'click' linker to all-carbon linkers would dramatically improve PSA, reduce MW, and increase ChromLogD_{7.4} of the analogous C-linked PROTACs. This was due to the triazole and oxygen atoms contained within the linker region of the 'click'-linked PROTACs contributing significantly to the polarity of the PROTAC and increasing its MW. This hypothesis was confirmed through *in silico* analysis of a virtual library of 7C-linked PROTACs **72 – 73** derived from the pyrimidine-OH warhead (Table 22). All PROTACs within this subseries possessed an MW < 1000, a PSA of < 250 Å² and a CChromLogD_{7.4} within the desired range of 4 – 6, which was a vast improvement on the 'click'-linked PROTACs **68 – 71**. However, the 7C-linked pyrimidine-OH series was not without its deficiencies; the HBD count exceeded 6 for the 7C-linked IAP pyrimidine-OH PROTAC **72** (HBD = 7).



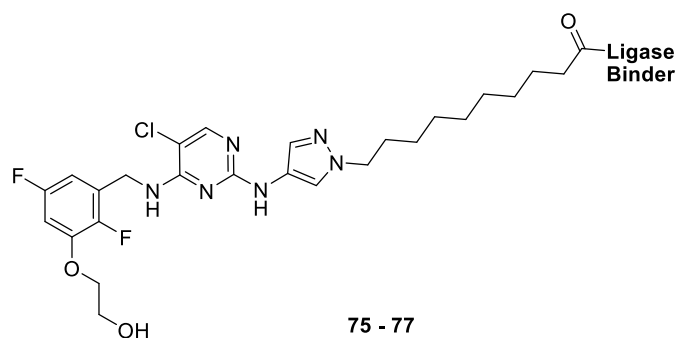
Ligase Binder	MW	HBD	CChromLogD _{7.4}	PSA (Å ²)
<p style="text-align: center;">72</p>	990.60	7	4.5	218
<p style="text-align: center;">73</p>	766.20	5	3.7	193
<p style="text-align: center;">74</p>	937.51	6	5.0	209

Table 22 The *in silico* physicochemical data associated with the pyrimidine-OH 7C-linked PROTACs, growing from the pyrazole vector.

2.4.3 10C-Linked Pyrimidine-OH PROTACs

Since the optimum linker length for JAK degradation was unknown, and to further build on the improved physicochemical space observed in the 7C-linked PROTACs **75** – **77**, a 10C-linked pyrimidine-OH subseries **75** – **77** was designed (Table 23). Since no HBDs were removed or introduced from switching out the 7C-linker to a 10C-linker, the HBD count for each PROTAC remained the same. Furthermore, no significant change in PSA was observed, however CChromLogD_{7.4} increased by approximately a log unit moving from the 7C-linked

PROTACs to the analogous 10C-linked PROTACs **75** – **77**. As expected, MW increased through changing the 7C-linker to the 10C-linker; however, all but the 10C-linked IAP pyrimidine-OH PROTAC **75** possessed an MW < 1000, and the IAP PROTAC only exceeded a MW of 1000 by 32.68.

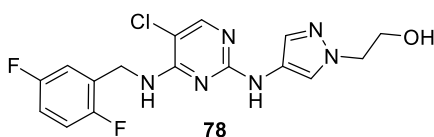


Ligase Binder	MW	HBD	CChromLogD _{7.4}	PSA (Å ²)
<p style="text-align: center;">75</p>	1032.68	7	5.4	217
<p style="text-align: center;">76</p>	808.28	5	4.5	193
<p style="text-align: center;">77</p>	979.59	6	5.9	209

Table 23 The *in silico* physicochemical data associated with the pyrimidine-OH 10C-linked PROTACs, growing from the pyrazole vector.

It was concluded that the poor physicochemical space occupied by the initial iteration of PROTACs may limit their cell permeation. Since changes to the number of HBDs of the ligase

binder would result in unknown effects in their ligase-recruiting ability, modifications to the JAK inhibitor, to reduce the HBD count, were investigated. The pyrimidine series compound database at GSK was consulted, resulting in the identification of JAK inhibitor **78** (Table 24). In addition to its potent pan-JAK profile within the biochemical assay and its particularly high efficacy within the IL-2 PBMC assay, pyrimidine-H **78** contains three HBDs, with the hydroxy H-bond being removed when ligated, therefore resulting in two HBDs arising from the JAK inhibitor. In addition, the increased ChromLogD_{7.4} of JAK inhibitor **78** juxtaposed with the pyrimidine-OH parent compound **58** may be reflected in the ChromLogD_{7.4} of the generated PROTACs, potentially resulting in greater cell permeation. As such virtual PROTAC libraries from pyrimidine-H **78** were generated *in silico* for physicochemical analysis.



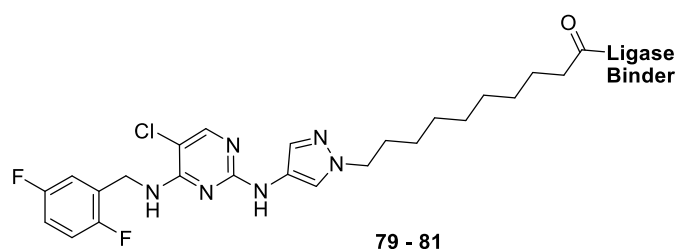
Compound	HBD	ChromLogD _{7.4}	MW	pIC ₅₀				
				IL2				
				JAK1	JAK2	JAK3	TYK2	PBMC
58	4	2.75	440	9.8	>9.8	>9.8	9.3	7.5
78	3	3.45	381	> 9.8	9.5	9.0	N/D	8.1

Table 24 The physicochemical properties and the biochemical and cell potencies associated with pyrimidine series compound **78** and pyrimidine-OH **58**. pIC₅₀ values are quoted as a mean of multiple test occasions (n ≥ 3).

2.4.4 10C-Linked Pyrimidine-H PROTACs

Physicochemical analysis of the 10C-linked pyrimidine-H subseries **79 – 81** indicated a dramatic improvement in PSA as compared to the analogous 10C-linked pyrimidine-OH subseries **75 – 77** (decreasing by ~30 Å²) (Table 25). Furthermore, removal of the ethylene glycol moiety from the pyrimidine warhead resulted in the HBD count of each PROTAC

decreasing by one, placing all of the 10C-linked pyrimidine-H PROTACs **79 – 81** within the preferred HBD count space (≤ 6). Contrary to the 10C-linked pyrimidine-OH series PROTACs **75 – 77**, each of the 10C-linked pyrimidine Bn PROTACs **79 – 81** maintains an MW < 1000 (MW = 748.23 – 972.62). Whilst physicochemical property improvements were observed across the majority of parameters related to the desired physicochemical space, the CChromLogD_{7.4} resided within, and in the case of the 10C-linked pyrimidine-H VHL PROTAC **81**, exceeded the desired ChromLogD_{7.4} range. The reduction in HBDs, MW and PSA, and an increase in ChromLogD_{7.4} was thought to provide an increase cell penetration. Despite the CChromLogD_{7.4} approaching or exceeding the upper limit of the target range, a broad exploration of physicochemical space was desired and so the compounds were progressed to synthesis.



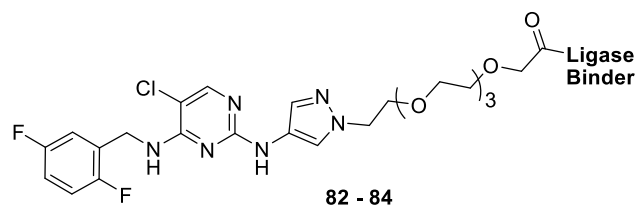
Ligase Binder	MW	HBD	CChromLogD _{7.4}	PSA (Å ²)
<p style="text-align: center;">79</p>	972.62	6	5.9	187
<p style="text-align: center;">80</p>	748.23	4	4.9	163
<p style="text-align: center;">81</p>	919.53	5	6.8	179

Table 25 The *in silico* physicochemical data associated with the pyrimidine-H 10C-linked PROTACs, growing from the pyrazole vector.

2.4.5 4EG Pyrimidine-H PROTACs

Substitution of the 10C linker for a 4EG linker decreased the CChromLogD_{7.4} of the 4EG linked pyrimidine-H PROTACs **82** – **86** as expected (Table 26), satisfying the initial ChromLogD_{7.4} guidelines of 4 – 6. Additionally, PSA increased due to the introduction of ethylene glycol units within the linker; however, PSA still remained below 250 Å². Furthermore, the

introduction of the 4EG linker led to one compound, the 4EG linked pyrimidine-H IAP PROTAC **82** exceeding the ≤ 1000 MW guideline.



Ligase Binder	MW	HBD	CChromLogD _{7.4}	PSA (Å ²)
<p style="text-align: center;">82</p>	1036.62	6	4.3	224
<p style="text-align: center;">83</p>	812.23	4	3.6	200
<p style="text-align: center;">84</p>	983.53	5	4.8	216

Table 26 The *in silico* physicochemical data associated with the pyrimidine-H 4EG PROTACs, growing from the pyrazole vector.

2.4.6 Pyrimidine-Bn PROTACs

Exploiting alternative ligation vectors from the pyrimidine series could potentially result in more favourable PPIs between the JAKs and the E3 ligase binder, upon forming the ternary complex; this may result in achieving more efficient JAK ubiquitination and increased

degradation. Therefore, PROTACs generated from the benzylic substituent of the pyrimidine series **85** were sought (Fig 68).

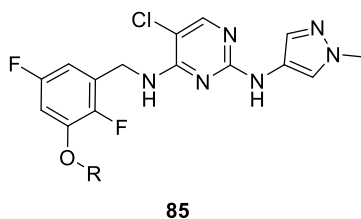
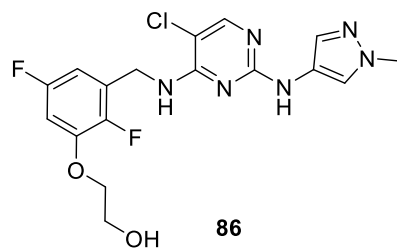


Fig 68 The Markush structure of pyrimidine-Bn PROTACs, illustrating the ligation vector as R.

The pyrimidine series database at GSK was consulted once more in an attempt to identify a parent compound that exhibited high biochemical and cellular activity, in addition to an easily exploited benzylic vector and low HBD count. Whilst identification of a suitable compound possessing these traits may be difficult to achieve, pyrimidine-Bn **86** was identified (Table 27). Pyrimidine-Bn **86** possesses two HBDs, which should aid the derived PROTAC's permeability. In addition, it displays high potency within the K_m biochemical assays across the JAKs, and good IL2 PBMC activity. It was hypothesised that the pyrimidine-Bn PROTACs could be easily accessed via ligation at the aryl ether position. Further confidence was placed in the benzylic ligation vector based on the docking of pyrimidine-OH **58**, which clearly illustrates the ethylene glycol moiety, analogous to the ethylene glycol group of pyrimidine-Bn **86** pointing towards a solvent-exposed region of the protein (Fig 69).



Compound	HBD	ChromLogD _{7.4}	MW	pIC ₅₀				
				IL2				
				JAK1	JAK2	JAK3	TYK2	PBMC
86	2	4.36	425	9.3	8.9	9.2	8.0	7.1

Table 27 The biological and physicochemical properties of pyrimidine-Bn **86**. pIC₅₀ values are quoted as a mean of multiple test occasions (n = ≥ 3).

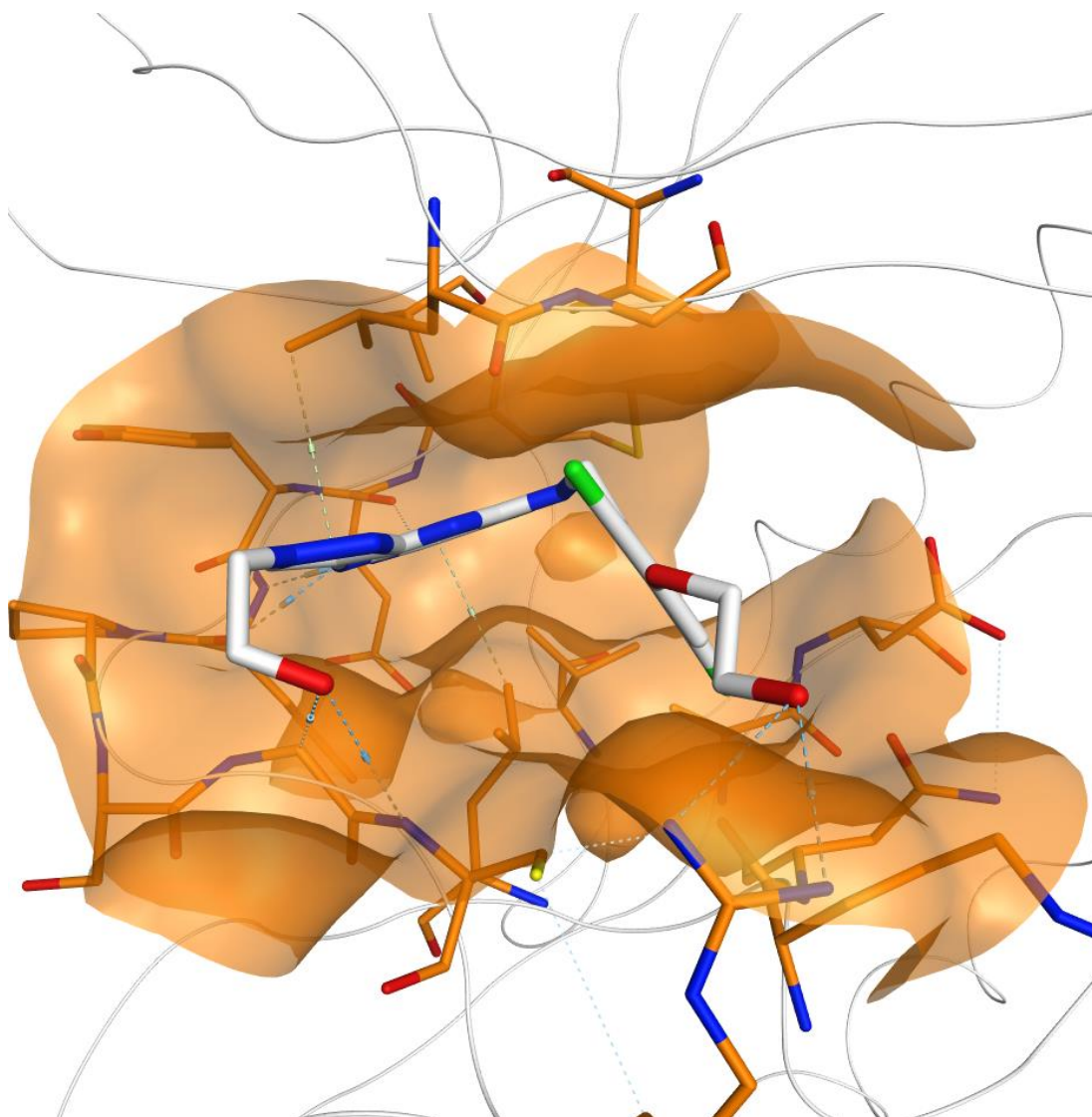
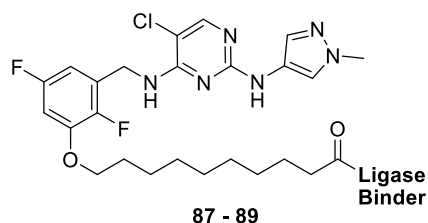


Fig 69 A docking of pyrimidine-OH **58** within JAK3, based on a closely related crystal structure, illustrating the hydroxy ligation vector the benzyl substituent.

2.4.7 10C-Linked Pyrimidine-Bn PROTACs

Therefore, to provide a direct comparison to the pyrimidine-H series, a 10C-linked pyrimidine Bn subseries **87 – 89** was designed (Table 28). As expected, *O*-linked ligation from the benzyl substituent resulted in a minor increase in PSA ($\sim 10 \text{ \AA}^2$) as compared to the matched 10C-linked pyrimidine-H series **79 – 81**. However, PSA for the 10C-linked Bn series **87 – 89**, still resided below 250 \AA^2 . Furthermore, CChromLogD_{7.4} did not change significantly between the

analogous compounds of the two series, and in the case of 10C-linked pyrimidine-Bn VHL **89** PROTAC, CChromLogD_{7.4} exceeded the upper limit of 6 by ~3-fold. As such, the 10C-linked pyrimidine-Bn series possessed favourable properties to assess the physicochemical parameters and the alternative vector and was therefore progressed to synthesis.

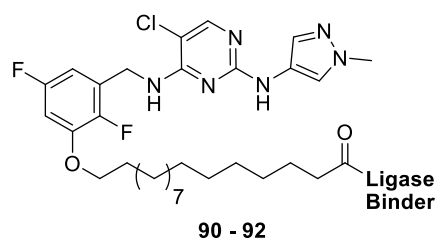


Ligase Binder	MW	HBD	CChromLogD _{7.4}	PSA (Å ²)
<p style="text-align: center;">87</p>	1002.65	6	6.04	197
<p style="text-align: center;">88</p>	778.26	4	5.2	173
<p style="text-align: center;">89</p>	949.56	5	6.5	189

Table 28 The *in silico* physicochemical data associated with the pyrimidine-Bn 10C-linked PROTACs, growing from the benzyl vector.

2.4.8 16C-Linked Pyrimidine-Bn PROTACs

A longer linker was sought since it was unknown which linker length was optimum. Within the previously discussed design strategies, whilst PEG linkers allow for increased linker length, they also increase PSA and MW, in addition to decreasing CChromLogD_{7.4}. Therefore, a subseries containing a longer linker length, but without increasing PSA was desired, that would also further exceed the upper ChromLogD_{7.4} range, and so a 16C-linked pyrimidine-Bn subseries **90 – 92** was designed (Table 29). Whilst this subseries expressed MWs in the range of 862.42 – 1086.81, their PSA was identical to the 10C-linked pyrimidine Bn series **87 – 89** (PSA = 173 – 197 Å²). Furthermore, the series maintained a HBD count of ≤ 6. However, the CChromLogD_{7.4} range was particularly high (7.3 – 8.3) which would suitably assist in exploring the upper limits.



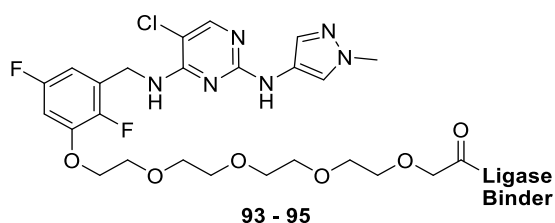
Ligase Binder	MW	HBD	CChromLogD _{7,4}	PSA (Å ²)
<p style="text-align: center;">90</p>	1086.81	6	7.8	197
<p style="text-align: center;">91</p>	862.42	4	7.3	173
<p style="text-align: center;">92</p>	1033.72	5	8.3	189

Table 29 The *in silico* physicochemical data associated with the pyrimidine-Bn 16C-linked PROTACs, growing from the benzyl vector.

2.4.9 4EG Pyrimidine-Bn PROTACs

In a similar fashion to the pyrimidine-H series, a 4EG linker was appended to the pyrimidine-Bn core, tethered to the three E3 ligase binders, and profiled *in silico* (Table 30). As expected, the PSA increased in relation to the analogous 10C- **87 – 89** and 16C-linked pyrimidine-Bn subseries **90 – 92**, although was still within the desired region. Contrary to the analogous 10C- **87 – 89** and 16C-linked pyrimidine-Bn subseries **90 – 92**, the 4EG pyrimidine-

Bn subseries **93 – 95** possessed a CChromLogD_{7.4} range (3.7 – 4.9) towards the lower end of the desired ChromLogD_{7.4} range. However, similar MWs were observed to those of the 16C-linked pyrimidine-Bn series **90 – 92**, with two PROTACs exceeding an MW of 1000 (MW = 1013.56 and 1066.65).

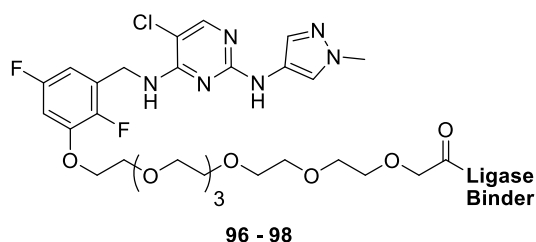


Ligase Binder	MW	HBD	CChromLogD _{7.4}	PSA (Å ²)
<p style="text-align: center;">93</p>	1066.65	6	4.4	234
<p style="text-align: center;">94</p>	842.25	4	3.7	209
<p style="text-align: center;">95</p>	1013.56	5	4.9	225

Table 30 The *in silico* physicochemical data associated with the pyrimidine-Bn 4EG PROTACs, growing from the benzyl vector.

2.4.10 6EG Pyrimidine-Bn PROTACs

Further extension of the ethylene glycol linker resulted in the design of 6EG pyrimidine-Bn subseries **96 – 98** (Table 31). Within this set the 6EG pyrimidine-Bn IAP PROTAC **96** exceeded the PSA guidelines, possessing a PSA of 252 Å². The CChromLogD_{7.4} range (4.1 – 5.2) remained within the desired range, however the MW guideline was significantly exceeded in two cases; the 6EG pyrimidine-Bn IAP PROTAC **96** displayed an MW of 1154.75, and the 6EG pyrimidine Bn IAP PROTAC **96** maintained a MW of 1101.66. However, since exploration of longer linkers at both vectors was desired, the 6EG pyrimidine-Bn subseries **96** was progressed to synthesis.



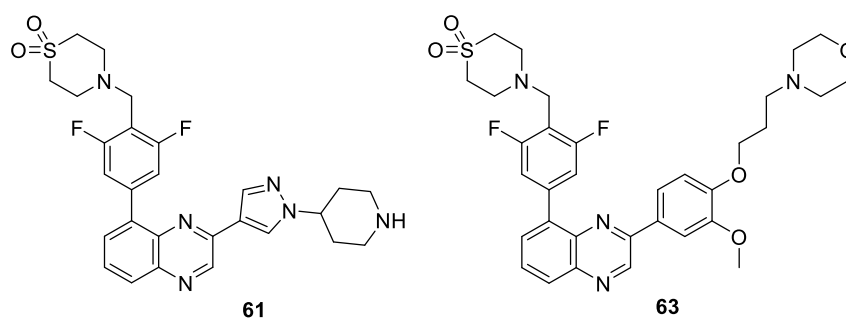
Ligase Binder	MW	HBD	CChromLogD _{7.4}	PSA (Å ²)
<p>96</p>	1154.75	6	4.6	252
<p>97</p>	930.36	4	4.1	228
<p>98</p>	1101.66	5	5.2	244

Table 31 The *in silico* physicochemical data associated with the pyrimidine-Bn 6EG PROTACs, growing from the benzyl vector.

2.4.11 Quinoxaline Warhead Selection

To determine which quinoxaline warhead to generate PROTACs from, both compounds were synthesised (synthesis outlined in Section 2.6.13) and evaluated within our biochemical and cellular assays developed at GSK (Table 32). Whilst both the pyrazole quinoxaline **61** and the morpholine quinoxaline **63** were equipotent at JAK2 (pyrazole quinoxaline **61** JAK2 pIC₅₀ = 9.5; morpholine quinoxaline **63** JAK2 pIC₅₀ = 9.6), the morpholine quinoxaline **63** maintained

elevated levels of JAK1 and JAK3 inhibition as compared to the pyrazole quinoxaline **61** (pyrazole quinoxaline **61** JAK1/JAK3 pIC₅₀ = 7.3/7.4; morpholine quinoxaline **63** JAK1/JAK3 pIC₅₀ = 8.1/8.1). Since JAK PROTACs remained in their proof-of-concept stage, a more pan-JAK profile was desirable so to not bias degradation. As the morpholine quinoxaline **63** displayed a more pan-JAK profile than its pyrazole counterpart, and possessed elevated cellular potency within the IL2 PBMC assay (~6-fold more potent), likely due to its increased activity at JAK1/JAK3, and higher ChromLogD_{7.4}, it therefore potentially better accesses the intracellular compartments. As such, morpholine quinoxaline **63** was selected as the JAK warhead for PROTAC generation.



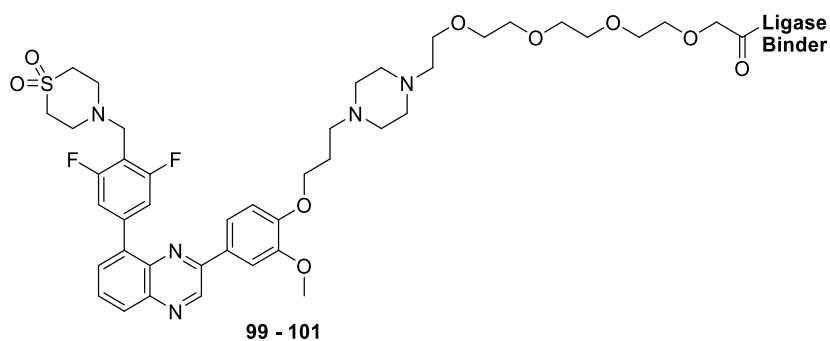
Compound	HBD	ChromLogD _{7.4}	MW	pIC ₅₀				
				IL2				
				JAK1	JAK2	JAK3	TYK2	PBMC
61	1	2.8	538.62	7.3	9.5	7.4	7.7	5.7
63	0	5.99	638.73	8.1	9.6	8.1	7.9	6.5

Table 32 The biological and physicochemical properties of quinoxaline **61** and **63**. pIC₅₀ values are quoted as a mean of multiple test occasions (n = ≥ 3). Both quinoxaline compounds were tested as formic acid salts.

2.4.12 4EG Quinoxaline PROTACs

The quinoxaline warhead **63** was conjoined to the three ligase binders via a 4EG linker and profiled *in silico*. Due to the warhead having no HBDs, the HBD count was influenced only by the ligase binders and, as such, the HBD range for the subseries **99 – 101** remained low (HBD

count: 2 – 4). Additionally, the CChromLogD_{7.4} resided towards the upper-middle range (5.0 – 5.8) of the initial desired ChromLogD_{7.4} range (4 – 6). PSA did not exceed the guidelines and fell below 250 Å². Perhaps unsurprisingly, the MW for each compound within the 4EG-linked quinoxaline subseries **99** – **101** surpassed 1000. This was a consequence of the parent quinoxaline **63** possessing a relatively high MW (638.73). Since usage of the linkers and ligase binders implemented in the pyrimidine series would inevitably increase the MW of the quinoxaline PROTACs to > 1000, the quinoxaline PROTACs were still progressed to synthesis.

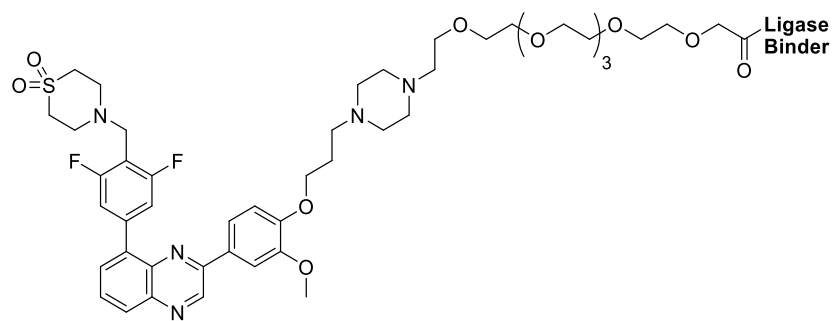


Ligase Binder	MW	HBD	CChromLogD _{7.4}	PSA (Å ²)
<p style="text-align: center;">99</p>	1337.64	4	5.7	245
<p style="text-align: center;">100</p>	1113.24	2	5.0	221
<p style="text-align: center;">101</p>	1284.55	3	5.8	237

Table 33 The *in silico* physicochemical data associated with the quinoxaline 4EG PROTACs.

2.4.13 6EG Quinoxaline PROTACs

Similarly to the pyrimidine-Bn series, switching the 4EG linker for a 6EG linker within the quinoxaline series resulted in an increase in PSA by 18 \AA^2 across each matched pair (Table 34). This caused the 6EG-linked quinoxaline IAP PROTAC **102** and the 6EG-linked quinoxaline VHL PROTAC **104** to possess PSAs of $> 250 \text{ \AA}^2$. Furthermore, MW increased by 88.10 from the analogous 4EG-linked PROTACs **99 – 101**. Interestingly, a reduction in CChromLogD_{7.4} was not observed, however, it is likely that the measured values would identify a drop in ChromLogD_{7.4} moving from the 4EG subseries **99 – 101** to the 6EG subseries **102 – 104** due to the increase in PSA and introduction of additional heteroatoms within the linker. As no HBDs were introduced from the linker, the HBD count remained constant, and the subseries was marked for synthesis.



102 - 104

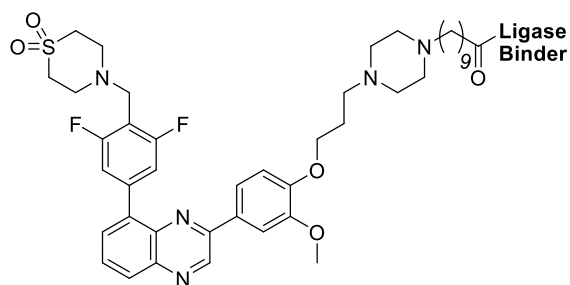
Ligase Binder	MW	HBD	CChromLogD _{7.4}	PSA (Å ²)
<p>102</p>	1425.74	4	5.6	263
<p>103</p>	1201.35	2	5.2	239
<p>104</p>	1372.65	3	5.8	255

Table 34 The *in silico* physicochemical data associated with the quinoxaline 6EG PROTACs.

2.4.14 10C Quinoxaline PROTACs

The final quinoxaline subseries to be designed was the 10C-linker set **105 – 107** (Table 35). As expected, the CChromLogD_{7.4} increased dramatically, with each PROTAC displaying a CChromLogD_{7.4} > 6. However, the addition of a carbon-based linker resulted in a sharp drop

in PSA (PSA range: 184 - 208). This reduction in PSA, coupled with the high CChromLogD_{7.4} and low HBD count, would likely aid cell penetration, and therefore the synthesis of this subseries was explored.



105 - 107

Ligase Binder	MW	HBD	CChromLogD _{7.4}	PSA (Å ²)
<p>105</p>	1273.64	4	7.2	208
<p>106</p>	1049.25	2	6.5	184
<p>107</p>	1220.55	3	7.2	200

Table 35 The *in silico* physicochemical data associated with the quinoxaline 10C-linked PROTACs.

2.5 On The Synthesis of Pyrimidine Series PROTACs

2.5.1 Early Explorations Around the Pyrimidine Series

With the PROTAC library designed and profiled *in silico*, initial efforts were focused towards synthesising PROTACs derived from the pyrimidine series (Fig 70), and the existing route to the pyrimidine compounds was scrutinised.

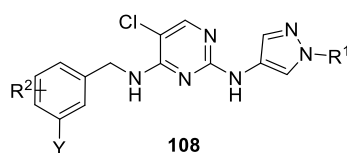
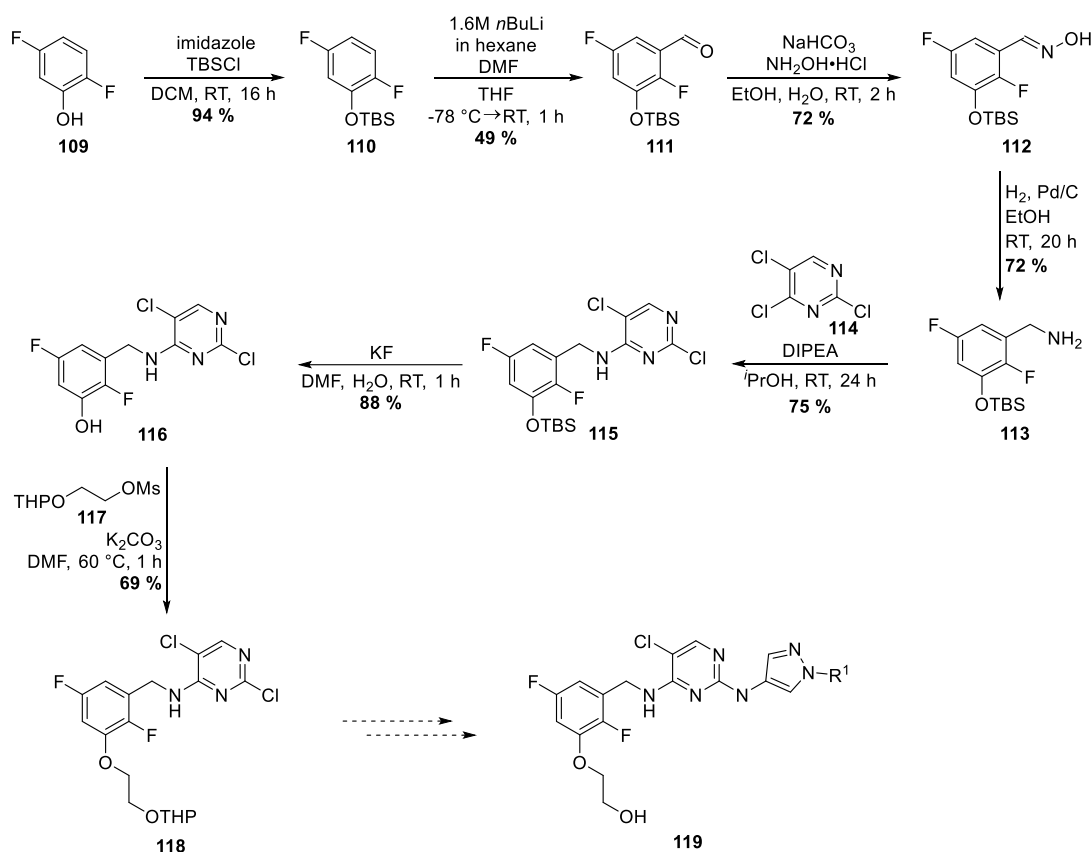


Fig 70 The Markush structure of the pyrimidine series **108**. R¹ = alkyl; R² = halogen; Y = polar group.

The current in-house route developed at GSK to pyrimidine compounds utilised difluorophenol **109** as the starting material (Scheme 1). Protection with a *tert*-butyldimethylsilyl group (TBS) afforded protected phenol **110**, which subsequently underwent a formylation and provided aldehyde **111** in a 49 % yield. Condensation of the aldehyde **111** with hydroxylamine furnished the oxime **112** in a 72 % yield and subsequent reduction gave benzylamine **113**, also in a 72 % yield. An S_NAr with trichloropyrimidine **114** generated aniline **115** which was then deprotected producing free phenol **116**, which then underwent an S_N2 with mesylate ester **117** furnishing the protected alcohol **118** in a 69 % yield.¹⁷⁷ A further S_NAr reaction with an amino-pyrazole, and removal of the protecting group afforded the target compound **119**. Whilst the current route provides access to the desired compounds, application of recently developed methodology may decrease the number of synthetic transformations and improve the efficiency of the route: for example, the three-step procedure to obtain benzylamine **113** could be avoided, the TBS protection and deprotection steps may also be negated if different starting materials were employed. Furthermore, the process utilises cryogenic conditions, which may also be avoided.



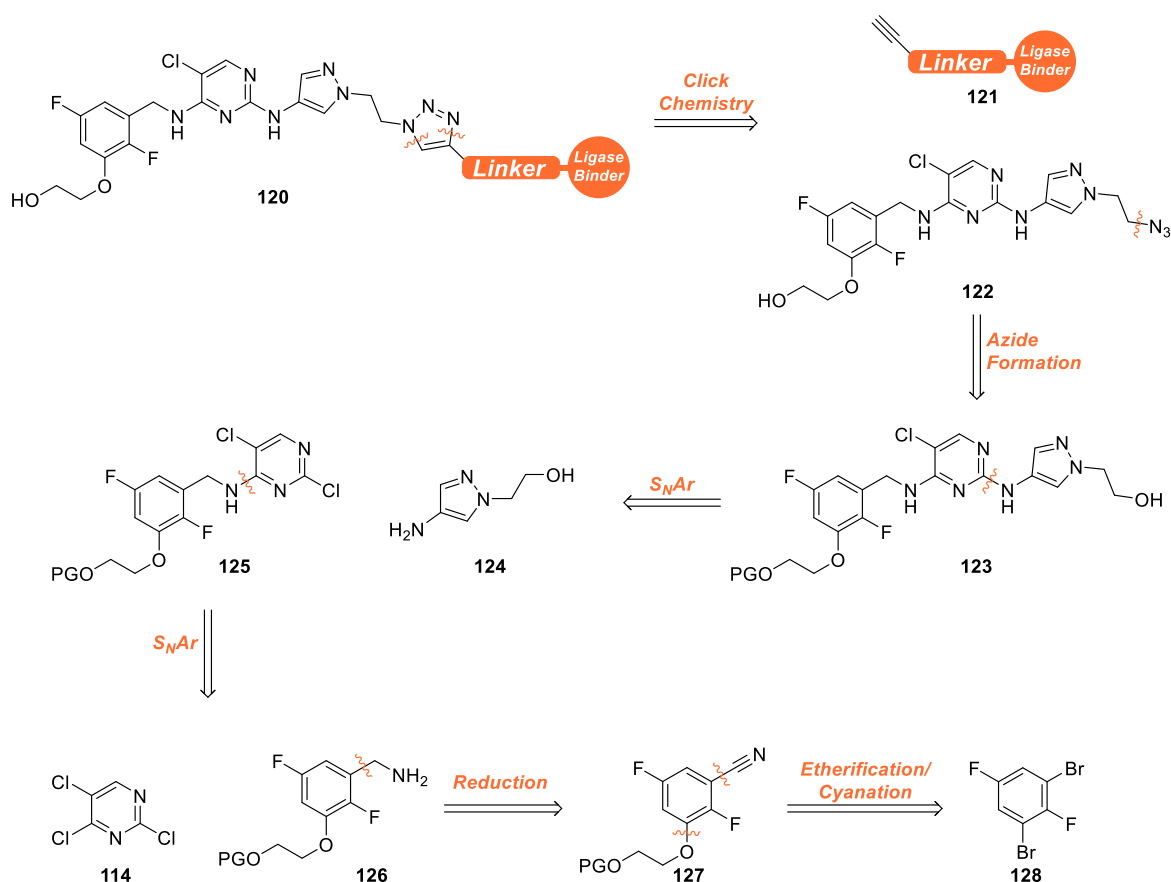
Overall Yield to Compound **118**: 11 %
 Number of Steps to Compound **118**: 8 (including synthesis of **117**)

Scheme 1 The initial route to pyrimidine series compounds **119** as carried out previously, at GSK.

2.5.2 Retrosynthesis of Pyrimidine Series PROTACs

Although a route to the pyrimidine compounds has previously been described, a retrosynthetic analysis was performed to optimise the synthetic route (Scheme 2). Drawing from previous work carried out at GSK on differing PROTAC series,¹⁸⁷ a preliminary disconnection was envisaged at the triazole of PROTAC **120** resulting in alkyne-linked ligase binder **121** and azide **122**. It was pre-empted that various E3 ligase binders with differing linker lengths could be ‘clicked’ together with azide **122**,¹⁸⁸ in an array format, resulting in an assortment of PROTACs with varying linkers and E3 ligase binders. A subsequent disconnection at the azide resulted in alcohol **123**, which in turn was traced back to aminopyrazole **124** and pyrimidine **125**. A further disconnection at the pyrimidine of compound **51** led back to trichloropyrimidine **114** and benzylamine **126**. The benzylamine

moiety could be derived from nitrile **53** via a reduction,¹⁸⁹ and two successive disconnections, generated through an etherification and cyanation, resulted in 1,3-dibromo-2,5-difluorobenzene **128**.



Scheme 2 A retrosynthetic analysis of pyrimidine series PROTAC **120** back to 1,3-dibromo-2,5-difluorobenzene **128**.

2.5.3 Photoredox Etherification

In recent years visible light photoredox catalysis has emerged as a valuable tool in organic synthesis, as it allows access to non-traditional points of reactivity, thereby providing a varied array of transformations.^{190,191,192,193,194} As such, MacMillan and colleagues have enabled the reductive elimination of Ni alkoxide complexes which proceeds via a single electron transfer event, generating Ni(III) systems from Ni(II), under photoredox conditions.¹⁹⁵ In contrast to Pd, Pt and alkyl Ni(II) systems, computational studies have confirmed Ni(II)

alkoxide reductive elimination as endothermic.^{196,197,198} Oxidation to its corresponding Ni(III) alkoxide complex allows reductive elimination via an exothermic process, thus generating a new C-O bond (Fig 71).

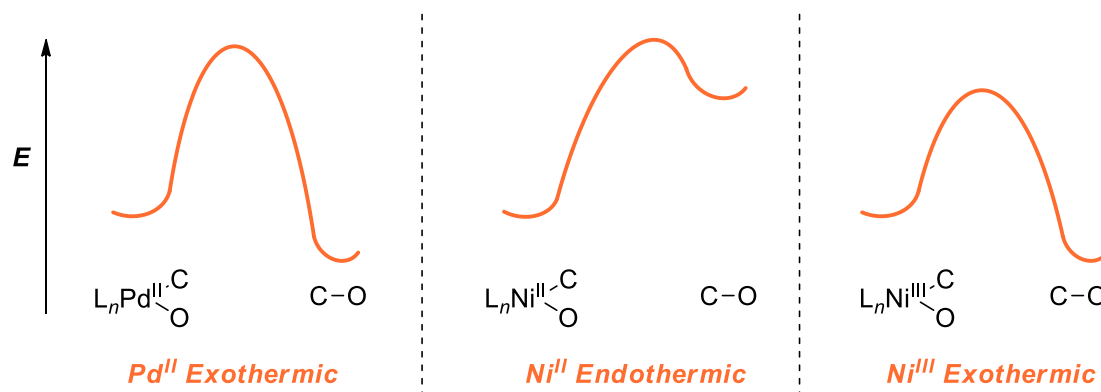
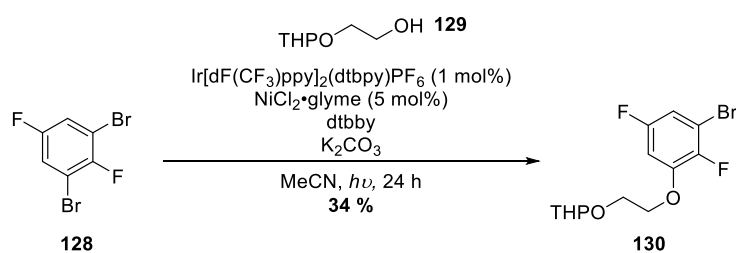


Fig 71 Energy profiles illustrating reductive elimination of Pd(II), Ni(II), and Ni(III) alkoxide complexes, highlighting the disfavoured, endothermic process of Ni(II) alkoxide complexes.

Exploratory etherification efforts were first carried out on 1,3-dibromo-2,5-difluorobenzene **128**, utilising photoredox etherification methods recently developed by MacMillan *et al.* using an Ir photocatalyst Ir[dF(CF₃)ppy]₂(dtbpy)PF₆ in the presence of NiCl₂·glyme. Reaction with 2-((tetrahydro-2H-pyran-2-yl)oxy)ethanol **129** afforded the aryl ether **130** (Scheme 3). (The reaction pathway is described in Scheme 4).



Scheme 3 Photoredox etherification of 1,3-dibromo-2,5-difluorobenzene **128** to afford aryl ether **130**.

Although MacMillan describes the use of blue LEDs as the optimal light source, initial reactions were carried out at GSK using standard compact fluorescent light bulbs (CFLs) as the light source, as it was understood that the Ir photocatalyst could absorb, and be excited by, wavelengths emitted from household CFLs. As illustrated in Table 36, utilisation of CFLs

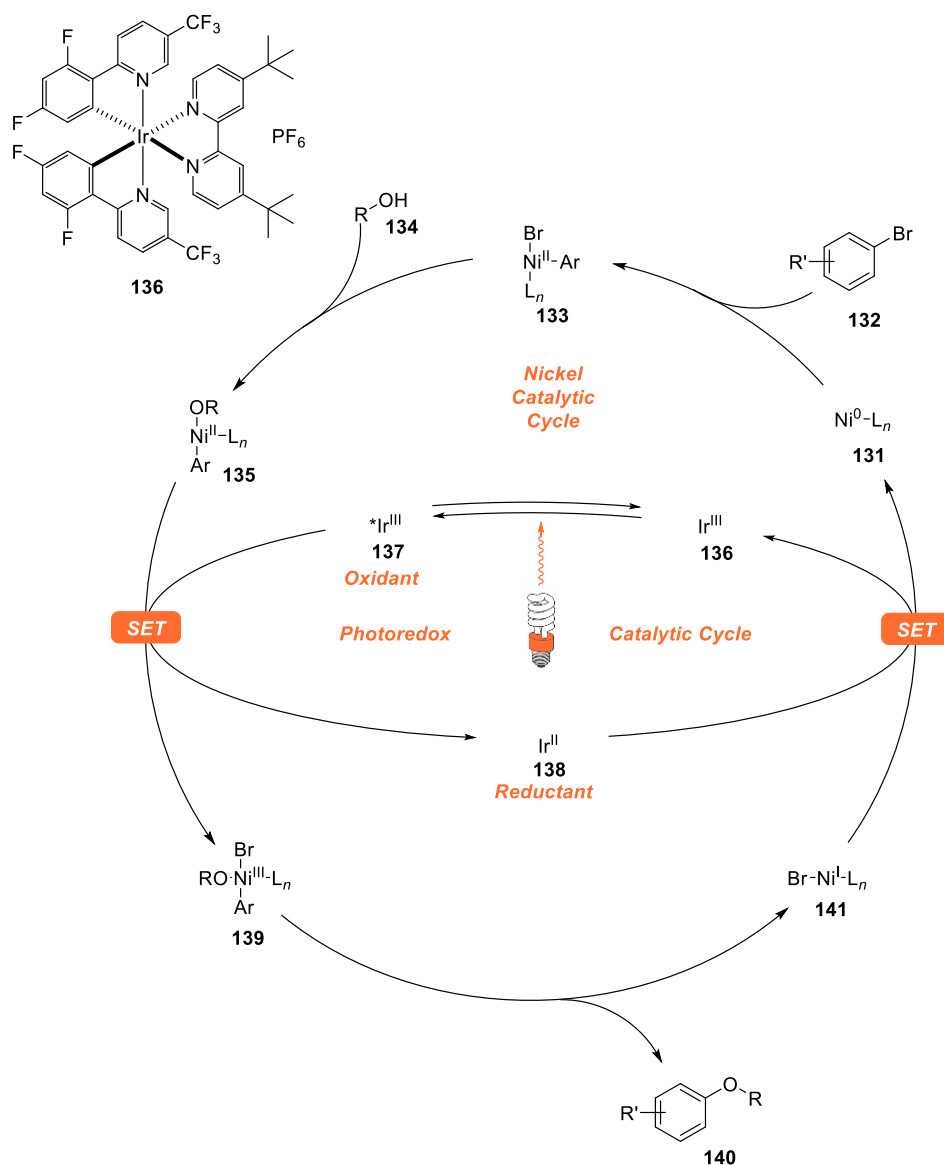
resulted in a 34 % isolated yield and 46 % conversion to product by LCMS analysis. However, when irradiated with 24 W, 12 V blue LEDs, LCMS conversion was dramatically decreased (11 %). The significant decrease in conversion was likely due to the 24 W, 12 V blue LEDs being drastically lower in intensity than the CFLs, therefore resulting in diminished light absorption by the Ir photocatalyst and hence lower turnover. It was subsequently identified that the MacMillan group typically employ Kessil A160WE Tuna Blue LEDs as standard. The use of such LEDs improved the conversion over the 24 W, 12 V blue LEDs. Surprisingly, however conversion was less than half (17 %) of that of the CFLs and numerous unknown impurities were present. It was thought that the intensity of the Kessil A160WE Tuna Blue LEDs was too great and thus resulted in various other reaction pathways being activated, and so decreasing product conversion. Not unexpectedly, decreasing the intensity of the LEDs led to a slight increase in product conversion (23 %). Since CFLs provided the greatest conversion of the light-sources investigated, they were used as standard in the subsequent reactions.

Light Source	Conversion by LCMS [isolated yield] (%)
Two 23 W, 1500 lumens, 6500 K CFLs	46 [34]
Maplin 24 W, 12 V blue LEDs	11*
Two Kessil A160WE Tuna Blue LEDs (highest intensity, full 'blue')	17*
Two Kessil A160WE Tuna Blue LEDs (lowest intensity, full 'blue')	23*

Table 36 A table illustrating the isolated yields and conversion by LCMS of various light-sources employed. *Indicates no attempts were made in isolating the desired product. 6500 K refers to the colour temperature of the light source expressed in Kelvin (K).

The proposed mechanism suggests that oxidative addition occurs with Ni(0) **131** into aryl bromide **132**, affording the Ni(II) complex **133** (Scheme 4). Subsequent displacement of the bromide with alcohol **134** generates the Ni(II) alkoxide complex **135** which would traditionally have signalled a 'dead end' in the catalytic cycle. Whilst the Ni catalytic cycle proceeds, irradiation of Ir(III) photocatalyst **136** gives the long-lived *Ir(III) **137** excited

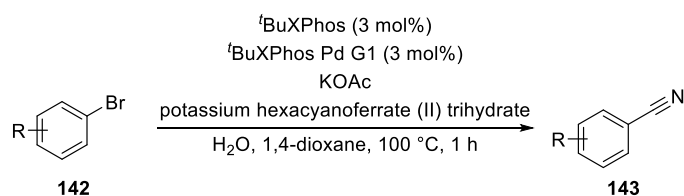
photocatalyst ($\tau = 2.3 \mu\text{s}$).¹⁹⁹ It is then assumed that a single electron transfer event, merging the two catalytic cycles, occurs to $^*\text{Ir(III)}$ **137** from the Ni(II) alkoxide complex **135**, producing Ir(II) **138** and the Ni(III) alkoxide complex **139**. This Ni(III) alkoxide complex undergoes rapid reductive elimination, giving aryl ether **140** and a Ni(I) complex **141**. It is thought that the catalytic cycles merge for a second time, whereby a second single electron transfer event reduces Ni(I) **141** to Ni(0) **131**, and oxidises Ir(II) **138** back to Ir(III) **139**, thus completing both catalytic cycles.¹⁹⁵



Scheme 4 The proposed mechanistic pathway of the photoredox nickel-iridium etherification. L = Ligand; R = alkyl; R' = EWGs.

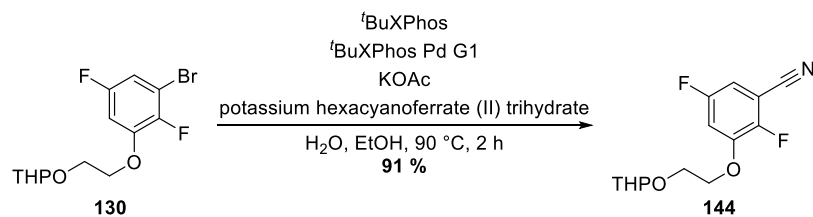
2.5.4 Cyanation of the Aryl Ether

Copious cyanation methods utilising a variety of reagents and conditions are available for the generation of aromatic nitriles. However, conventional methods such as the diazotisation of anilines, followed by a Sandmeyer reaction or the Rosenmund-von Braun reaction tend to employ harsh conditions and toxic cyanation reagents, such as copper(I) cyanide.^{200,201,202,203} Recently, Buchwald *et al.* developed a novel, catalytic cyanation reaction involving a non-toxic source of cyanide, potassium hexacyanoferrate(II) (Scheme 5). The mild reaction conditions convert aryl bromides **142** into aryl nitriles **143**, and display a wide functional group tolerance and short reaction times.²⁰⁴



Scheme 5 Reaction displaying the conversion of aryl bromides into aryl nitriles. R = EWG, EDG, alkyl.

Following etherification, aryl bromide **130** was subjected to cyanation conditions based on methodology developed by Buchwald *et al.* Whilst the literature report uses dioxane as the organic component of the solvent system, we found within our labs that ethanol typically produces comparable yields when used in place of dioxane certain cross-coupling reactions, and so was used in the reaction, furnishing the product **144** in a 91 % yield (Scheme 6). Ethanol is a preferred solvent over dioxane since ethanol is environmentally benign and exhibits low health hazards, whereas dioxane possesses significant environmental and health issues.²⁰⁵

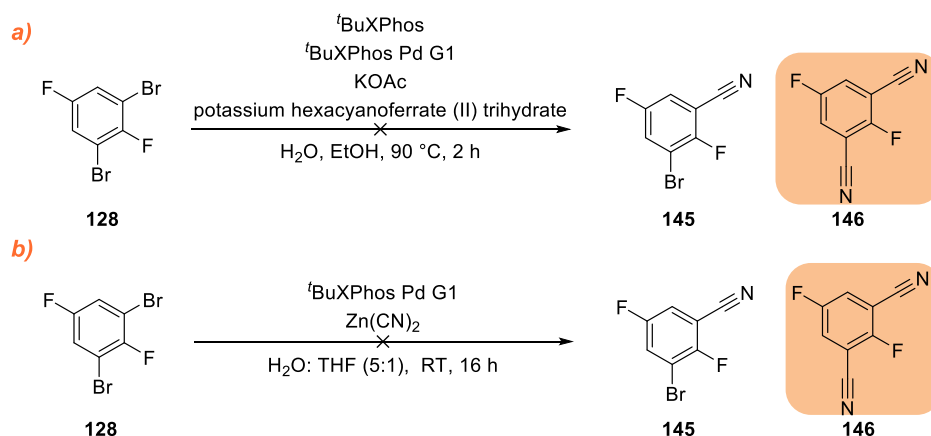


Scheme 6 The cyanation of aryl ether **130** affording the aryl nitrile **144** in 91 % yield.

Whilst the cyanation step proceeded in excellent yield, the initial etherification step was clearly limiting. Literature precedent on etherification on di- or tri-bromosubstituted phenols via alternative methods, such as Cu-catalysed reactions, presented poor isolated yields, likely due to bis-etherification. It was therefore proposed that decreasing the electron density of the ring would increase the susceptibility to oxidative addition of nickel and hence increase the yield of the etherification. Accordingly, efforts turned towards installing the nitrile prior to forming the ether.

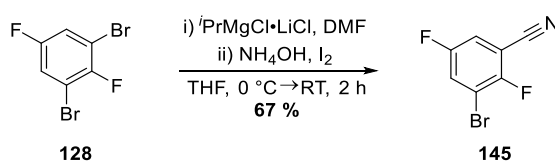
2.5.5 Cyanation of 1,3-Dibromo-2,5-difluorobenzene

Having observed some success constructing the nitrile, similar Buchwald conditions were carried out on 1,3-dibromo-2,5-difluorobenzene **128** (Scheme 7a). However, whilst the reaction progressed cleanly, only bis-cyanated product **146** was produced (82 % conversion by LCMS). Similar results were also obtained when attempting to cyanate 1,3-dibromo-2,5-difluorobenzene **128** using milder cyanating conditions, albeit much slower (33 % conversion by LCMS) (Scheme 7b).²⁰⁶ This is likely due to the addition of the nitrile group in the monosubstituted product activating the ring to oxidative addition by decreasing its electron density. Whilst undesired, the results proved encouraging in that decreasing the electron density may increase the propensity to undergo etherification.



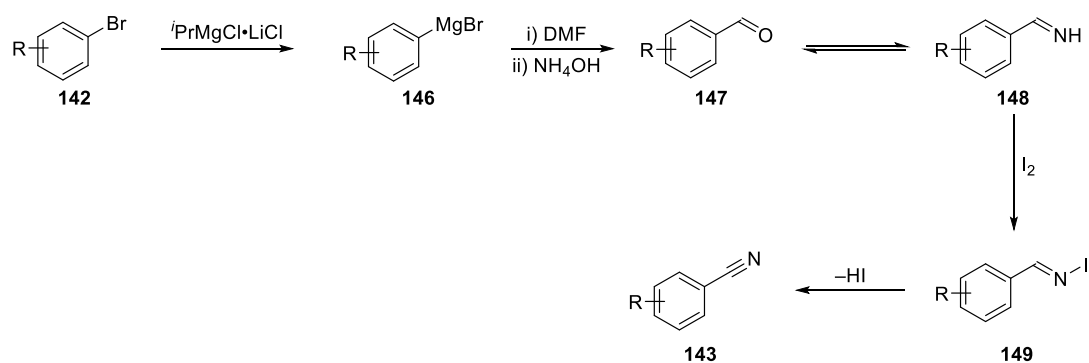
Scheme 7 The unsuccessful mono-cyanation of 1,3-dibromo-2,5-difluorobenzene **128** under Buchwald conditions. Only bis-cyanation was observed.

A recently reported one-pot procedure, documented by Ishii *et al.* described the synthesis of aryl nitriles from mono- or di-substituted aryl halides.²⁰⁷ This methodology was successfully utilised when converting 1,3-dibromo-2,5-difluorobenzene **128** into aryl nitrile **145** in good yield (67 %) (Scheme 8).



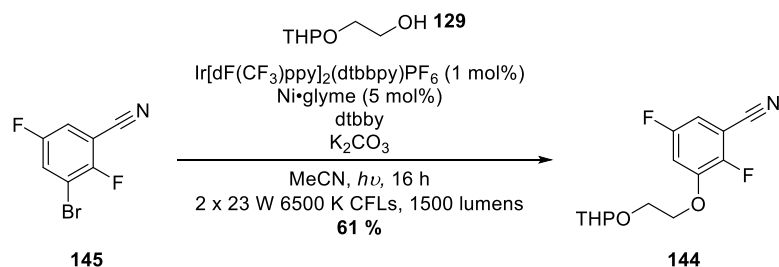
Scheme 8 One-pot aryl nitrile synthesis from 1,3-dibromo-2,5-difluorobenzene **128**.

The reaction utilised 1.1 equivalents of *i*PrMgCl·LiCl, which underwent a single Br-Mg exchange leaving the other three halides on the ring intact. The resultant aryl Grignard **146** can then be trapped with DMF, and added ammonium hydroxide to affords the aldehyde **147** (Scheme 9). Aldehyde generation was succeeded by imine **148** formation, which was subsequently oxidised in the presence of iodine to the aryl nitrile **143**.²⁰⁷ It is yet to be seen if greener iodine alternatives, such as NIS or iodobenzene diacetate may be utilised in generating the aryl nitrile from the imine.



Scheme 9 One-pot aryl nitrile **143** formation from aryl bromide **142**. R = alkyl, EDG, EWG.

Following the addition of the nitrile, MacMillan's photoredox etherification conditions were attempted on aryl nitrile **145** providing the aryl ether **144** in a 61 % yield (Scheme 10), a marked increase from the comparative reaction on 1,3-dibromo-2,5-difluorobenzene **128** (35 % yield).



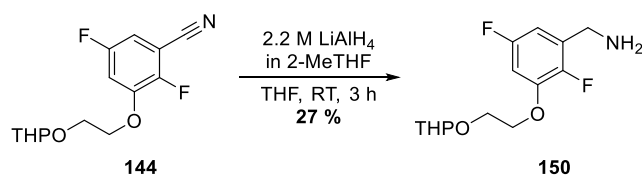
Scheme 10 The photoredox etherification of aryl bromide **145** to afford aryl ether **144**.

Whilst the reaction occurred cleanly, 25 % starting material remained, as determined by LCMS analysis. Since 1.5 equivalents of the alcohol were used, it was thought that increasing the number of equivalents to two, might result in greater conversion and greater yield; however, such a reaction was not carried out.

In contrast to the initial novel route, whereby etherification was carried out first followed by cyanation (31 % yield over two steps), a 10 % increase in overall yield of the two steps was observed, when the cyanation step preceded the etherification (41 % yield over two steps), and so this order of steps was utilised when accessing aryl ether **144**.

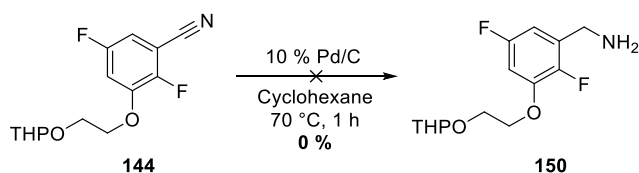
2.5.6 Reducing the Nitrile

As outlined in the retrosynthesis, following the generation of aryl ether **144**, a reduction of the nitrile group is required to afford benzylamine **150**. Early explorations of reducing the nitrile centred on the use of LiAlH_4 as the reducing agent (Scheme 11). Whilst the conversion, as determined by LCMS analysis, was excellent (85 %), it is thought that due to the troublesome isolation typified with using LiAlH_4 , a significant decrease in isolated yield was observed.



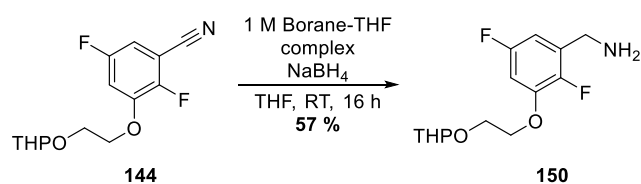
Scheme 11 The reduction of aryl nitrile **144** to benzylamine **150** using LiAlH_4 .

Although nitrile groups can be readily and efficiently reduced to their corresponding primary amines under typical hydrogenation conditions employing Pd/C as the catalyst in ethanol, it has been reported that THP groups are also cleaved under such conditions. Whilst there are no observations of THP groups being cleaved under hydrogenolytic mechanisms, deprotection is due to the presence of traces of PdCl_2 present in commercial sources of Pd/C which liberates HCl under hydrogenation conditions. It has been reported that the addition of pyridine to the reaction mixture, or switching the solvent from ethanol to cyclohexane resulted in the THP group remaining intact.²⁰⁸ This was attempted however, LCMS analysis identified only minor product formation, and major formation of a possible $\text{S}_{\text{N}}\text{Ar}$ product formed from the reaction of reduced amine **150** with the nitrile starting material **144** (Scheme 12).



Scheme 12 The attempted reduction of nitrile **144** to benzylamine **150**.

Alternatively, milder reducing conditions were examined, making use of borane-THF complex, and NaBH₄ which provided an elevated yield of 57 %, when compared to previous methods trialled (Scheme 13).



Scheme 13 The borane-THF-mediated reduction of nitrile **144** to amine **150**.

2.5.7 S_NAr on Trichloropyrimidine

Handy and Zhang revealed a method for determining the regiochemical selectivity of multi-halogenated heterocycles through ¹H NMR spectra of the respective dehalogenated substrates.²⁰⁹ The experimental method is based upon the chemical shifts of each proton, whereby the proton with the largest chemical shift implies it is appended to the most electron-deficient carbon, and thus the preferred site of nucleophilic substitution or cross-coupling.²¹⁰ The method is not without its pitfalls, however, since it does not account for steric effects or directing groups.

Pyrimidines, however, are in direct contrast to the Handy principle in that the Handy principle predicts the 2-position as the most reactive (δ 9.26 ppm) followed by the 4-position (δ 8.78 ppm) and finally the 5-position (δ 7.36 ppm) (Fig 72). Whilst the 5-position has been experimentally confirmed as the least reactive position, the 4-position typically undergoes nucleophilic substitution before the 2-position.²¹¹ Whilst the cause of selectivity for the 4-position over the 2-position is unknown, it may result from the lone pairs on the ring nitrogens hindering approach at the 2-position.

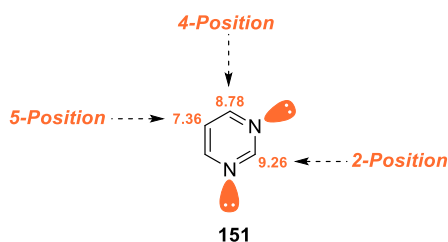
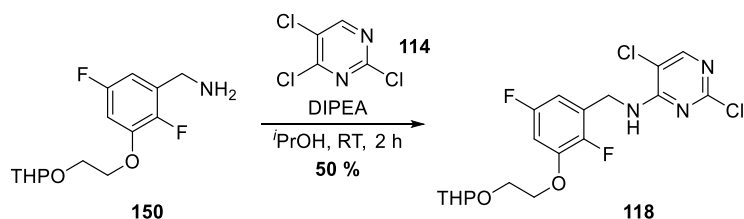


Fig 72 The calculated chemical shifts of 2-, 4- and 5-positions of pyrimidine **151** illustrating pyrimidines not adhering to the Handy principle.

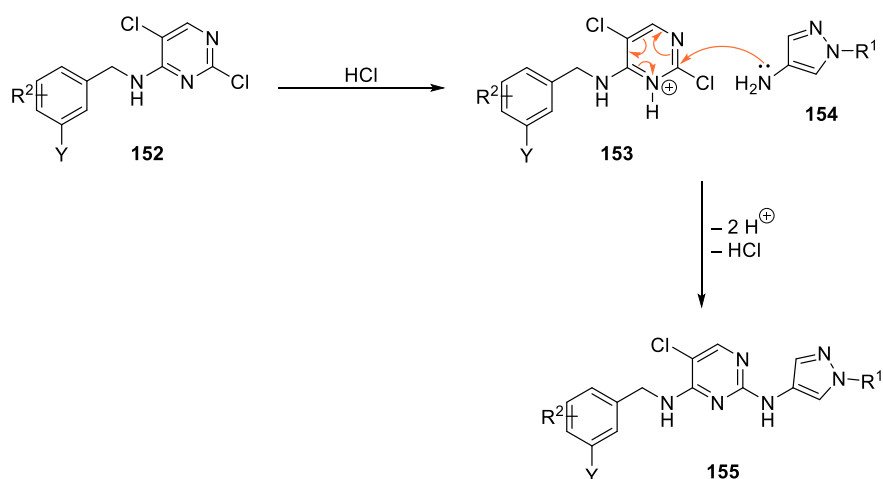
Exploiting the known reactivities of trichloropyrimidine **114**, the initial S_NAr was carried out with benzylamine **150**, where substitution at the 4-position afforded the aniline **118** in a moderate yield (50 %) (Scheme 14).



Scheme 14 The S_NAr reaction of benzylamine **150** with trichloropyrimidine **114**, highlighting selectivity for the 4-position.

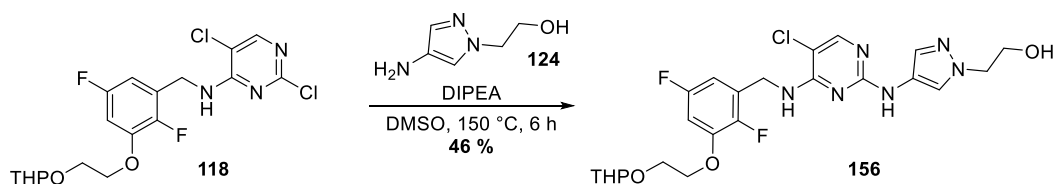
The novel, significantly shorter route (eight steps decreased to four steps), with improved overall yield (11 % optimised to 12 %) towards the common intermediate utilises more recent methodology to bypass numerous steps. The decrease in steps removes the need for protection and deprotection steps in addition to the removal of reactions requiring cryogenic control.

Following the S_NAr with benzylamine **150**, a subsequent S_NAr was carried out exploiting the reactivity of the 2-position on pyrimidine **118** with pyrazole **124**. When previously carried out at GSK, HCl has typically been added to protonate the pyrimidine,¹⁷⁷ thus activating the 2-position and facilitating addition of the poorly nucleophilic aminopyrazole **154** (Scheme 15).



Scheme 15 The S_NAr mechanism under acidic conditions, activating the 2-position to nucleophilic attack of aminopyrazole **154**.

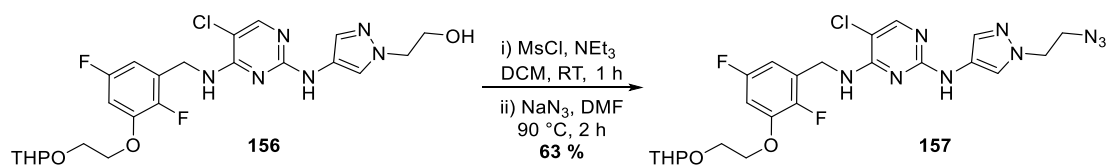
Since a THP protecting group was present, S_NAr under acidic conditions was avoided to prevent deprotection; thus, the reaction was carried out under elevated temperatures, in the presence of base and afforded the desired product in a 46 % yield (Scheme 16).



Scheme 16 The S_NAr of aminopyrazole **124** to pyrimidine **118** under basic conditions, requiring elevated temperatures and increased reaction times.

2.5.8 Azide Formation

As illustrated in the retrosynthesis, in order to carry out the ‘click’ reaction, an azide was required as one of the substrates (Scheme 2), and since the toolbox of ligase binder-appended linkers consisted of alkynes, it was required that alcohol **156** be converted to azide **157**. To achieve this, the alcohol was initially activated through generation of a mesylate which readily underwent an S_N2 reaction in the presence of sodium azide to afford azide **157** in good yield over the two steps (Scheme 17).

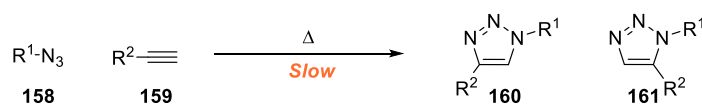


Scheme 17 Mesylation of alcohol **156**, followed by azide formation.

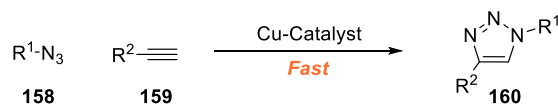
2.5.9 Copper ‘Click’ Chemistry

As one of the most widely used ‘click’ reactions to date, the copper-catalysed union of organic azides and terminal alkynes displaying a wide variety of functional groups has demonstrated drastically accelerated rate over the uncatalysed reaction (Scheme 18). This catalytic ‘click’ reaction stands apart from most other catalytic processes in that it displays exquisite functional group tolerance, often negating the use of protecting groups. A variety of organic and inorganic solvent systems can be implemented, in addition to biological media such as serum and whole blood. It functions over a broad range of temperatures (0 °C – 160 °C) and pH ranges (pH 4 – 12) alike.²¹² Purification by chromatography or recrystallisation is seldom performed, as pure products are typically isolated by filtration or extraction.²¹³

Huisgen 1,3-Dipolar Cycloaddition

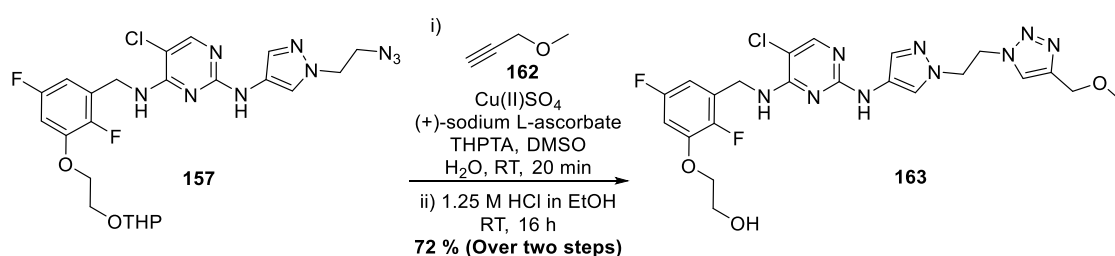


Cu-Catalysed ‘Click’ Chemistry



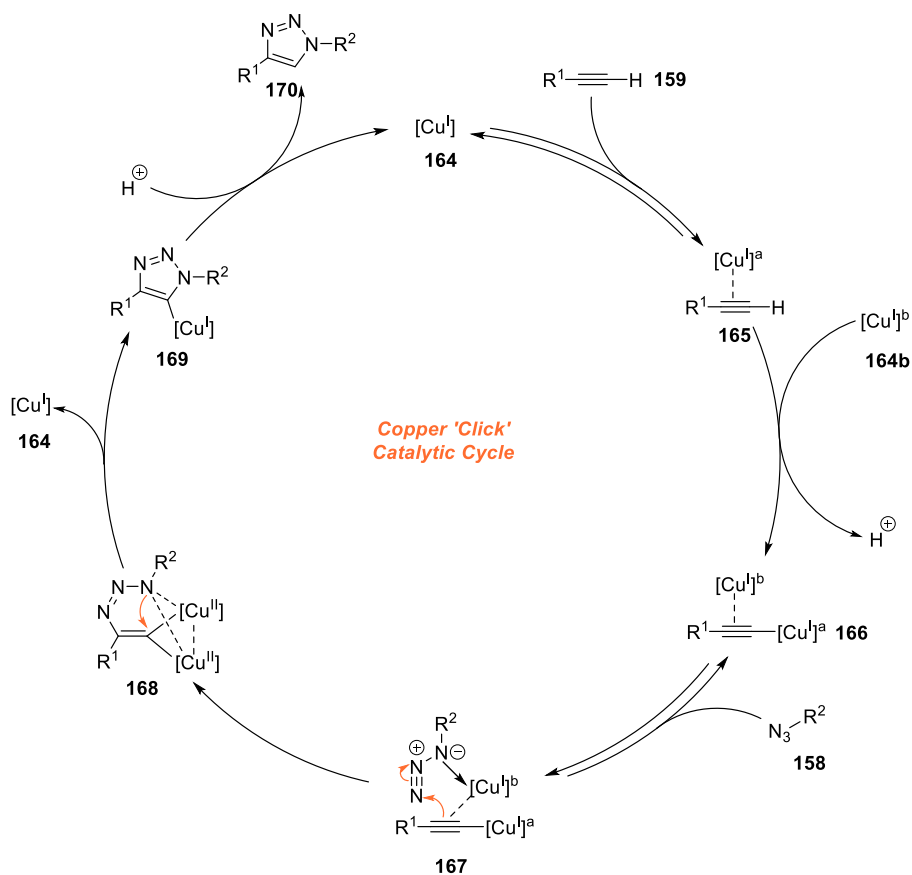
Scheme 18 A scheme illustrating the slow and unselective Huisgen’s azole synthesis, in comparison to the fast, regioselective Cu-catalysed ‘click’ reaction.

An assortment of terminal alkynes, differing in length and appended to a variety of E3 ligase binders had been prepared at GSK and were available to ‘click’ onto azide **157**.¹⁸⁷ However, before ‘clicking’ on linkers with ligase binders attached, a truncated linker **162** was first attached to assess the chemistry on azide **157** and also to determine whether a triazole is tolerated by the JAK active site (Scheme 19). Following the click reaction of azide **155** and terminal alkyne **162**, HCl was subsequently added to cleave the THP protecting group affording triazole **163** in good yield over the two steps.



Scheme 19 The Cu-catalysed ‘click’ reaction with alkyne **162** and azide **157** to afford triazole **163**.

Fokin and colleagues recently disclosed the mechanism of Cu-catalysed ‘click’ reactions,²¹⁴ and found that the process requires the two equivalents of Cu ions (Scheme 20). The mechanism is initiated by coordination of $[\text{Cu}^I]$ **164** to the alkyne **159**. A second chemically equivalent $[\text{Cu}^I]$ unit **164b** generates the σ -bonded copper acetylide species **166**. Coordination of organic azide **158** gives complex **167**. Nucleophilic attack at the azide by the β -carbon of the acetylide generates the first C-N bond **168**. Ring closure can then occur, ejecting $[\text{Cu}^I]$ **164**, exclusively affording triazole **169**. Protodemetalation can then occur affording triazole **170** and regenerates the $[\text{Cu}^I]$ catalyst **164**.

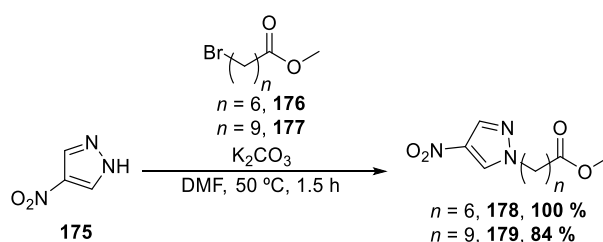


Scheme 20 The mechanism of Cu-catalysed 'click' triazole formation, involving two chemically equivalent Cu units (a and b).

Following validation of the chemistry with the truncated linker **162**, the Cu-click chemistry was then applied to generate PROTACs **68** – **71**, utilising the alkyne-linked ligase binders **171** – **174** available at GSK (Table 37). The yields obtained were typically low (18 – 25 %), however the CRBN triazole PROTAC **69** was obtained in excellent yield (97 %).

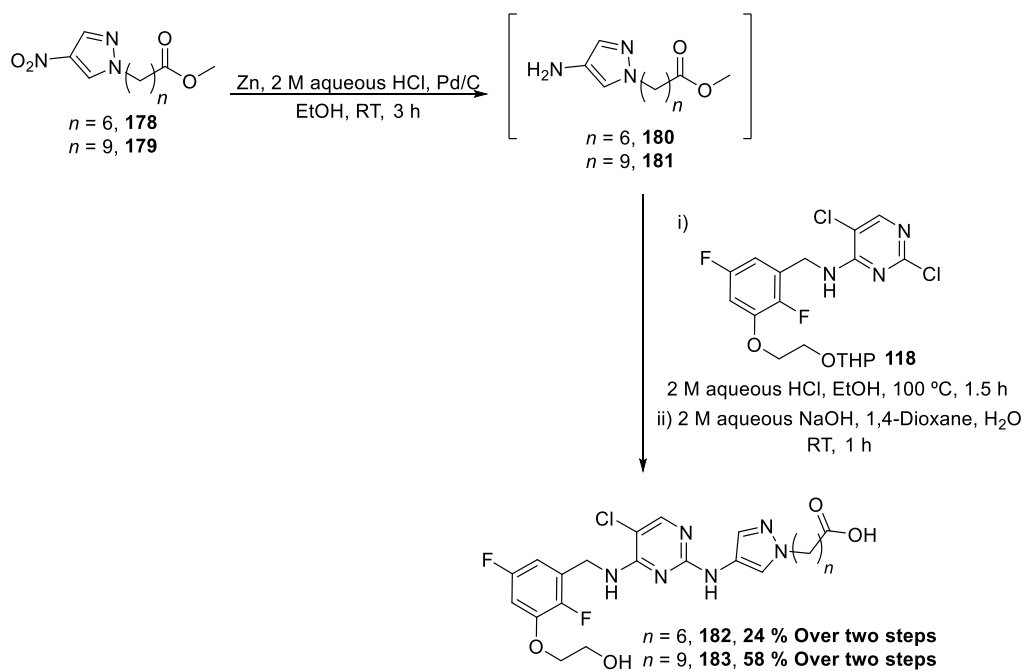
2.5.10 C-Linked PROTAC Synthesis

In order to obtain all carbon linkers, methyl 7-bromoheptanoate **176** and methyl 10-bromodecanoate **177** were tethered to nitropyrazole **175** to afford 7C pyrazole linker **179** and 10C pyrazole linker **180**, both in excellent yield (Scheme 21).



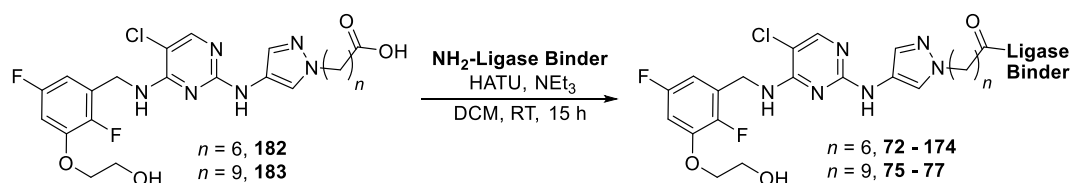
Scheme 21 The alkylation of nitropyrazole **175** with methyl 7-bromoheptanoate **176** and methyl 10-bromodecanoate **177** to afford 7C pyrazole linker **178** and 10C pyrazole linker **179**, respectively.

Following alkylation of the pyrazole, the nitro group was reduced to generate aminopyrazoles **180** and **181** (Scheme 22). Since both pyrazoles were found to be unstable and rapidly degraded to unknown entities at room temperature, attempts at isolating the aminopyrazoles proved unsuccessful. Their instability was likely due to the increased electron density placed on the pyrazole ring, making it more susceptible to electrophilic attack, or attack by O_2 . As a consequence, the aminopyrazoles were reacted without further purification. Upon reduction, the 7C linked amino pyrazole **180** and 10C linked amino pyrazole **181**, were obtained in 43 % and 76 % crude yields, respectively. As described previously in Section 2.6.7 the lone pair of the amino groups is delocalised into the pyrazole ring, with the result that it is poorly nucleophilic. Consequently, the S_NAr reaction was carried out under acidic conditions to protonate the pyrimidine and activate the ring to nucleophilic attack, and furthermore facilitate THP deprotection. For the 7C pyrazole linker **180**, the S_NAr reaction, followed by ester hydrolysis, proceeded in 24 % yield over two steps affording acid **182**, whereas S_NAr reaction with the 10C pyrazole linker **181** afforded carboxylic acid **183** in 58 % yield over two steps.



Scheme 22 The reduction of nitropyrazole linkers **178** – **179**, followed by an S_NAr onto the pyrimidine core to generate carboxylic acids **182** – **183**.

Both the 7C carboxylic acid **182** and the 10C carboxylic acid **183** were progressed to a series of amide coupling reactions with ligase binders Boc-IAP **184**, VHL **65** and CRBN **49** (Table 38). Using unoptimised amide coupling conditions with HATU, the reactions provided variable yields (8 – 70 %) depending on the ligase binder.



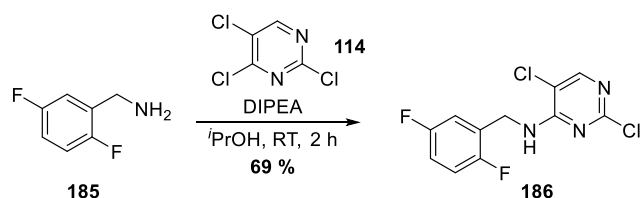
NH ₂ -Ligase Binder	PROTAC	Linker Length	Yield (%)
		7C 10C	12* 8*
		7C 10C	16 15
		7C 10C	70 36

Table 38 The synthesis of 7C- and 10C linked PROTACs **72 - 77**, and their respective yields. TFA was added to the IAP PROTAC reaction mixtures, following amide coupling to effect Boc-deprotection. * = Yield over two steps (amide coupling, followed by Boc deprotection).

2.5.11 Synthesis of Pyrimidine-H PROTACs

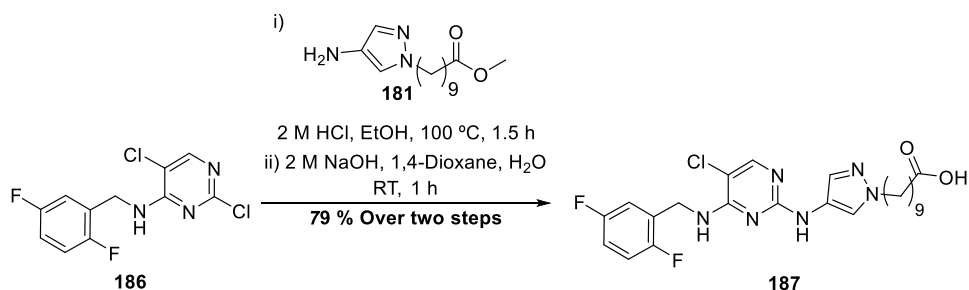
The initial step in the synthesis of the 10C and 4EG pyrimidine-H PROTACs **79 – 84** was carried out in a similar fashion to the $\text{S}_{\text{N}}\text{Ar}$ in the synthesis of pyrimidine-OH **118**; however, (2,5-

difluorophenyl)methanamine **185** was employed as the nucleophile (Scheme 23). Reaction between (2,5-difluorophenyl)methanamine **185** and trichloropyrimidine **114** afforded the substituted pyrimidine **186** in 69 % yield.



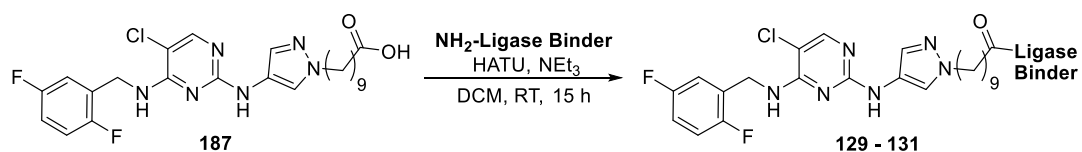
Scheme 23 The synthesis of pyrimidine **186**, via an S_NAr reaction.

Subsequent S_NAr reactions with various aminopyrazoles were carried out to install a variety of different linker lengths and linker types. An aminopyrazole appended to a 10C ester **181** was joined to pyrimidine **186**, and the ester hydrolysed to afford 10C acid **187** in 79 % yield (Scheme 24), significantly higher than that of the analogous 10C pyrimidine-OH acid **182** (24 % yield).



Scheme 24 The union of aminopyrazole **181** with pyrimidine **186**, followed by ester hydrolysis to provide acid **187**.

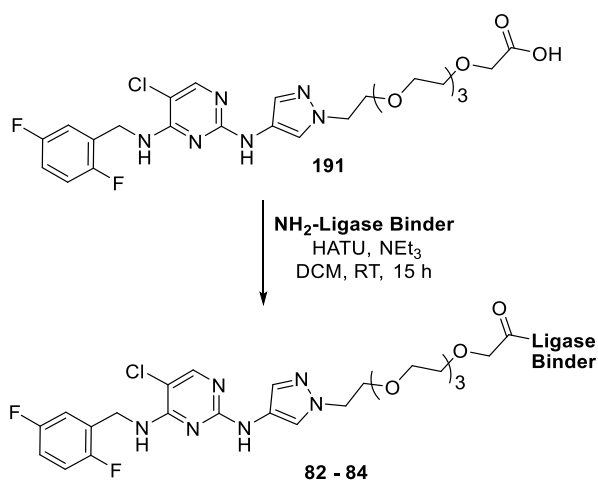
To explore differing linker compositions and lengths from the pyrazole vector of the pyrimidine-H core, nitropyrazole **175** was alkylated with a 4-ethylene glycol (4EG)-ester **188** to afford pyrazole **189** in a 63 % yield (Scheme 25). Subsequent reduction of the nitro group produced the aminopyrazole **190** which was installed onto the pyrimidine-H core **186** via an



NH ₂ -Ligase Binder	PROTAC	Linker Length	Yield (%)
<p>184</p>	<p>79</p>	10C	30*
<p>29</p>	<p>80</p>	10C	31
<p>65</p>	<p>81</p>	10C	29

Table 39 The synthesis of 10C linked pyrimidine-H PROTACs **79** – **81**, and their respective yields. TFA was added to the IAP PROTAC reaction mixtures, following amide coupling to effect Boc-deprotection. * = Yield over two steps (amide coupling, followed by Boc deprotection).

Similar amide couplings to the 10C acid were carried out on the 4EG-acid **191**, with each of the three ligase binders, providing the products **82** – **84** in a slightly elevated range of yields, from 29 – 47 % (Table 40). Exploring vectors from the pyrazole position was concluded at this stage, pending Western blot data to determine whether such PROTACs could induce JAK degradation.

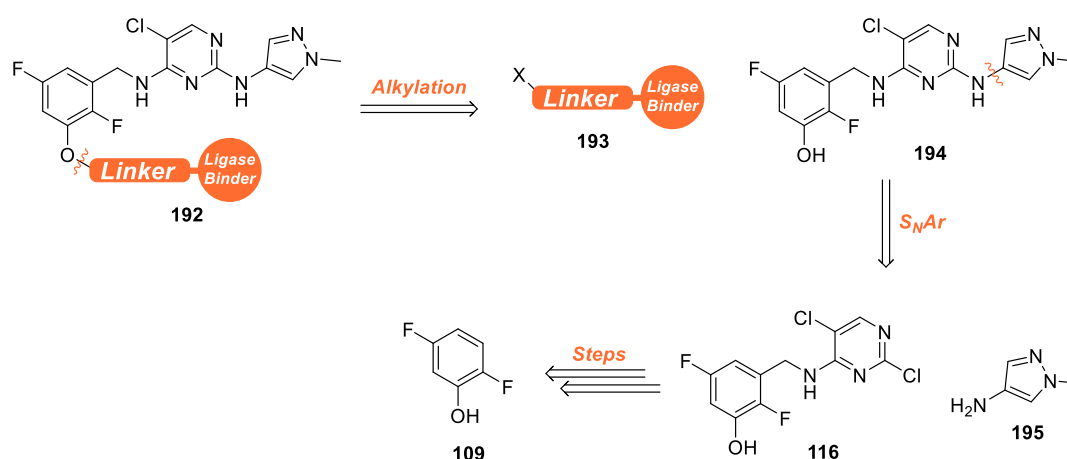


NH ₂ -Ligase Binder	Ligase Binder	Linker Length	Yield (%)
<p style="text-align: center;">184</p>	<p style="text-align: center;">82</p>	4EG	36*
<p style="text-align: center;">49</p>	<p style="text-align: center;">83</p>	4EG	47
<p style="text-align: center;">65</p>	<p style="text-align: center;">84</p>	4EG	29

Table 40 The synthesis of 4EG pyrimidine-H PROTACs **82 – 84**, and their respective yields. TFA was added to the IAP PROTAC reaction mixture following amide coupling to effect Boc-deprotection. * = Yield over two steps (amide coupling, followed by Boc deprotection).

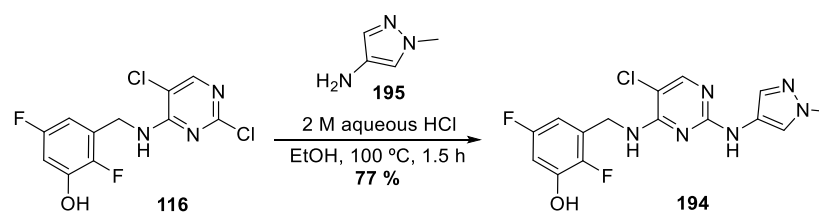
2.5.12 Pyrimidine-Bn PROTAC Synthesis

Changing the vector for which two proteins would be brought together could potentially result in increased PPIs, and more efficient JAK ubiquitination and degradation. As such, PROTACs generated from the benzyl substituent of the pyrimidine series were evaluated. The rationale behind the exploitation of the benzylic vector is discussed in more detail within Section 2.4.6. It was envisaged that an array of simple S_N2 reactions from phenol **194** could provide access to a variety of different linkers and ligase binders in quick succession (Scheme 26). An S_NAr reaction with pyrimidine **116** and methyl aminopyrazole **195** could give the core **194**, and pyrimidine **116** could be generated from the tried-and-tested route outlined in Scheme 1.



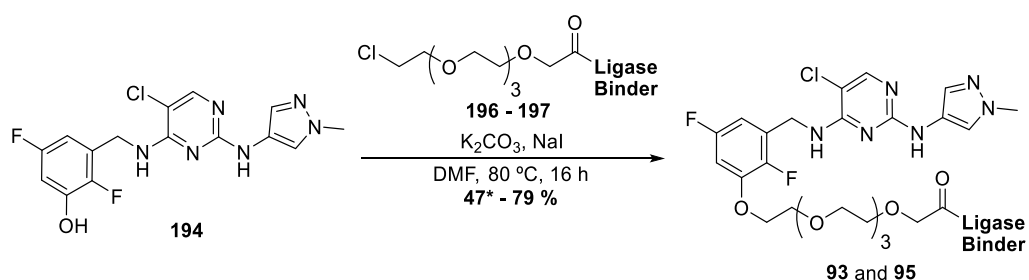
Scheme 26 A retrosynthetic analysis of the synthesis of pyrimidine-Bn PROTACs **192**. X = Leaving group.

The pyrimidine intermediate **116** was subjected to an S_NAr displacement with methyl aminopyrazole **195**, producing the pyrimidine core **194** in 77 % yield (Scheme 27).



Scheme 27 An S_NAr between methylpyrazole **195** and pyrimidine core **116**.

With the pyrimidine core **194** to hand, a series of alkylations with GSK-supplied Boc-IAP **196** and VHL **197** appended to a 4EG linker was carried out, affording the IAP PROTAC **93** in 47 % yield and the analogous VHL PROTAC **95** in 79 % yield (Table 41). Unfortunately, due to the inherent instability of the cyclic imide present in CRBN under basic conditions at elevated temperatures, alkylations could not be performed to achieve the analogous CRBN PROTAC. As such, amide coupling conditions were sought to install the 4EG-CRBN portion.

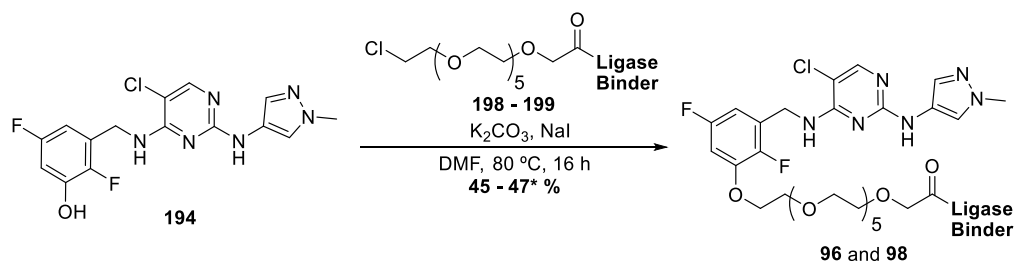


Compound Number	PROTAC	Linker Length	Yield (%)
93		4EG	47*
95			79

Table 41 Alkylations to the pyrimidine-Bn core, using 4EG IAP **196** and 4EG VHL **197**. * = Yield over two steps (amide coupling followed by Boc deprotection).

Identical alkylation conditions used within the 4EG PROTAC synthesis were employed to assemble the equivalent 6EG IAP **96** and VHL PROTACs **98**. Whilst the IAP yield was equal to that of the 4EG-IAP PROTAC **93** (47 %), the observed 6EG-VHL **98** yield (45 %) was diminished

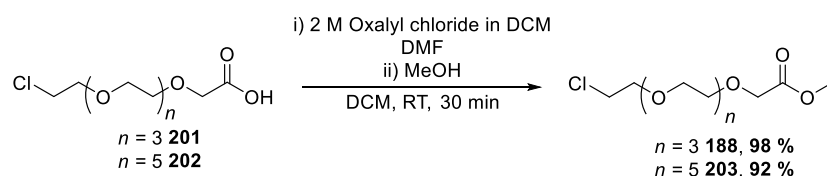
as compared to the analogous 4EG-VHL PROTAC **95** (79 %). The lower yield likely resulted from the poorer conversion and increased unknown by-product formation.



Compound Number	PROTAC	Linker Length	Yield (%)
96		6EG	47*
98			45

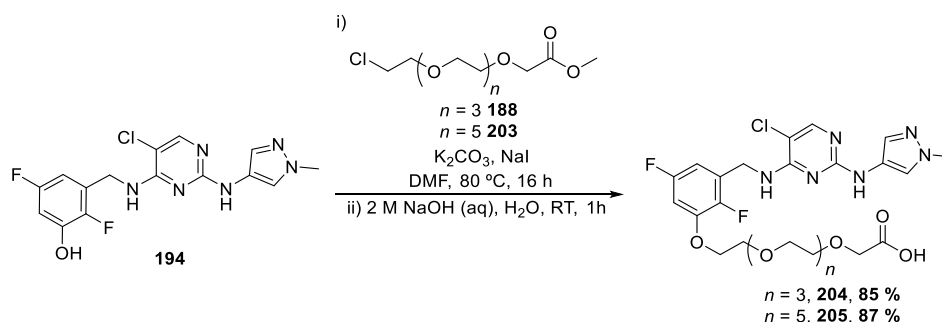
Table 42 Alkylations to the pyrimidine-Bn core **194**, using 6EG IAP **198** and 6EG VHL **199**. * = Yield over two steps (amide coupling followed by Boc deprotection).

To prevent the acids **201** and **202** reacting with themselves under alkylating conditions, the acids were protected through conversion to their corresponding methyl esters **203** and **188**. The reactions proceeded rapidly with oxalyl chloride and DMF, followed by MeOH addition to afford the methyl esters in 92 – 98 % yields (Scheme 28).



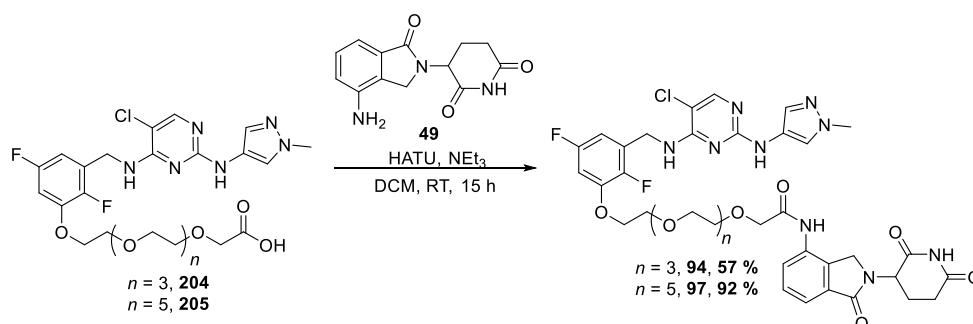
Scheme 28 The conversion of acids **201** – **202** to the corresponding methyl esters **188** and **203**.

The methyl esters **188** and **203** were attached to the pyrimidine-Bn core **194** under the previously used alkylating conditions (Scheme 29). The esters were partially hydrolysed under the alkylating conditions, and 2 M aqueous NaOH was added to provide acids **204** and **205** in 85 and 87 % yields.



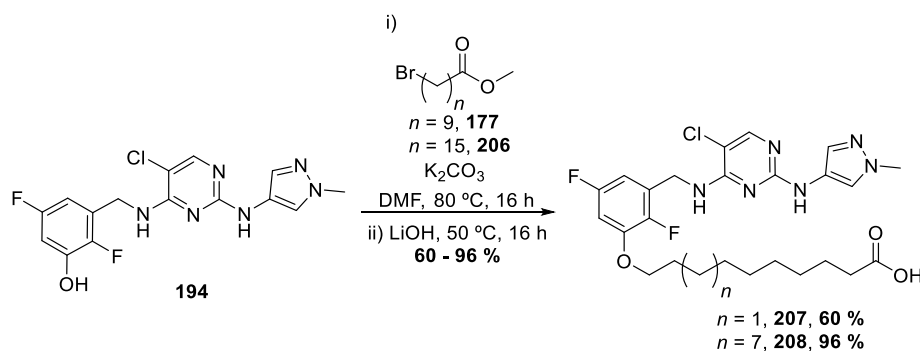
Scheme 29 The alkylation of pyrimidine-Bn core **194** with esters **188** and **203**, and their subsequent hydrolysis.

Both the carboxylic acids **204** and **205** were then subjected to amide couplings with CRBN **49**, to afford the corresponding 4EG and 6EG CRBN PROTACs **94** and **97** (Scheme 30).



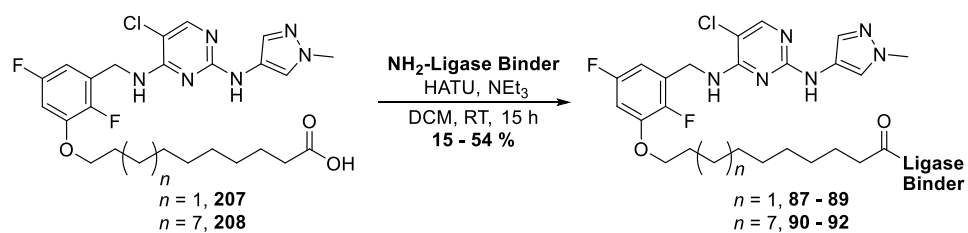
Scheme 30 The amide couplings of CRBN **49** to pyrimidine-Bn 4EG and 6EG acids **94** and **97**.

In addition to the pyrimidine-Bn ethylene glycol linked PROTACs, carbon-linked pyrimidine-Bn PROTACs **87** – **92** were also prepared, to provide a direct comparison to the analogous 10C and 16C pyrimidine-H PROTACs. The pyrimidine-Bn core was alkylated with the 10C and 16C esters **177** and **206** and subsequently hydrolysed to afford acids **207** and **208** (Scheme 31).



Scheme 31 The alkylation of pyrimidine-Bn core **194**, with 10C and 16C esters **177** and **206**.

The 10C and 16C pyrimidine-Bn acids **207** and **208** were exposed to the HATU amide coupling conditions, with the three ligase binders, IAP **184**, VHL **65** and CRBN **49**. As with all amide couplings described herein, the 10C and 16C PROTACs were generated in variable yields (15 – 54 %).



$\text{NH}_2\text{-Ligase Binder}$	Ligase Binder	Linker Length	Yield (%)
		10C	54*
		16C	15*
		10C	28
		16C	45
		10C	40
		16C	36

Table 43 The synthesis of 10C and 16C pyrimidine-Bn PROTACs **87 - 92**, and their respective yields. TFA was added to the IAP PROTAC reaction mixtures, following amide coupling to effect Boc-deprotection. * = Yield over two steps (amide coupling followed by Boc deprotection).

With the library of pyrimidine-Bn PROTACs available, they were then assessed biologically in their ability to engage JAK, which is discussed in Section 2.6.

2.5.13 On The Synthesis of Quinoxaline Series PROTACs

To rapidly and efficiently synthesise a library of quinoxaline PROTACs, the Novartis route was consulted.¹⁷⁹ However, prior to synthesising quinoxaline PROTACs, a parent quinoxaline compound was sought, which expressed a more pan-JAK profile within our JAK assays, than JAK2 selectivity. As such, two quinoxaline compounds were identified, and their synthesis executed (Fig 73).

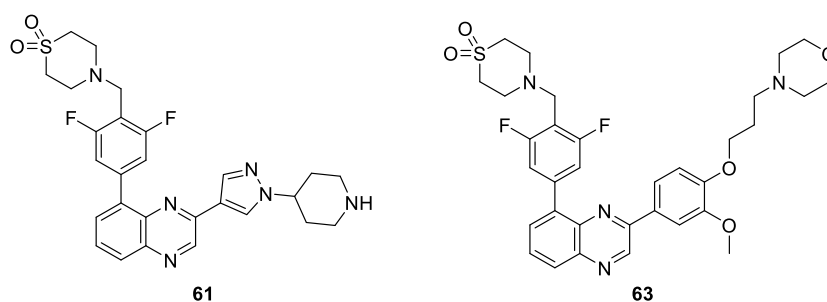
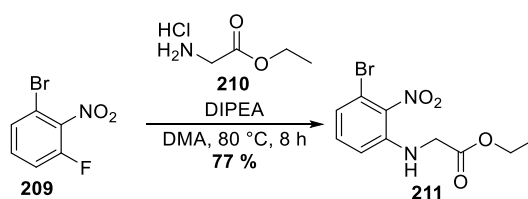


Fig 73 The selected quinoxaline warheads **61** and **63**.

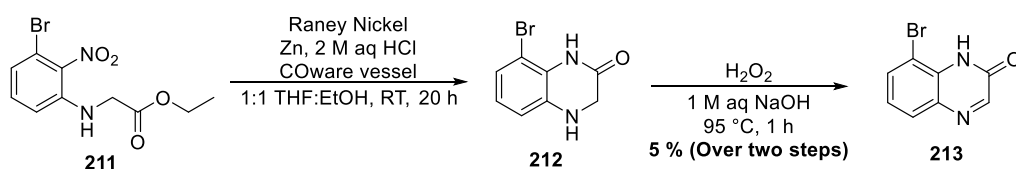
Since both quinoxalines **61** and **63** consist of the same core, and differ only in the 2-position substituent, the initial steps followed the same route. The first step consisted of an S_NAr reaction with bromofluoronitrobenzene **209** and ethyl glycinate **210** to afford the 3-position-substituted aniline **211** in 77 % yield (Scheme 32).



Scheme 32 An S_NAr reaction between bromofluoronitrobenzene **209** and ethyl glycinate **210** to generate substituted aniline **211**.

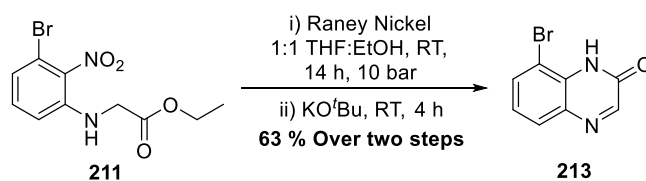
As per the Novartis patent,¹⁷⁹ a two-step batch procedure was employed to reduce the nitro group, cyclise and to generate quinoxaline **213**.

Recently, Skrydstrup developed a dual-chambered, commercially available glassware (COWare) that allows for the generation of hydrogen *in situ*, from zinc and HCl, whereby the amount of HCl generated may be controlled.²¹⁵ This negates the requirement for hydrogen storage, or *ex situ* generation of hydrogen as produced by the electrolysis of water. This system was utilised when reducing the nitro group within bromofluoronitrobenzene **211** to the substituted aniline **212** (Scheme 33). During the reduction step, minor quantities of cyclised quinoxalinone **213** were observed (15 % by LCMS). As such, the crude material was telescoped into the cyclisation and oxidation step, using hydrogen peroxide. This step was particularly low yielding (5 % over two steps), and a significant pressure build up was observed, raising safety concerns.



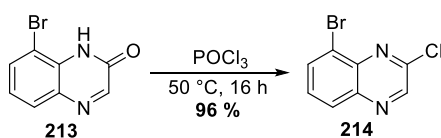
Scheme 33 the COWare-mediated reduction and cyclisation followed by the published step to access quinoxalinone **213** in poor yield.

In attempts to optimise this two-step procedure, it was proposed that increasing the pressure during the reduction would encourage cyclisation and thus dihydroquinoxalinone formation, and the addition of a base under air would furnish the desired oxidised quinoxalinone within a one-pot method. Accordingly, the reduction was carried out in flow, within a H-cube at 10 bar to predominantly afford the cyclised dihydroquinoxalinone **212** (77 % by LCMS) and the addition of KO^tBu under air produced quinoxalinone **213** in 63 % yield over the two steps (Scheme 34). This optimised method provided a significantly higher yield than the previously reported procedure, and removed the safety issues associated with pressurised, sealed vessels.



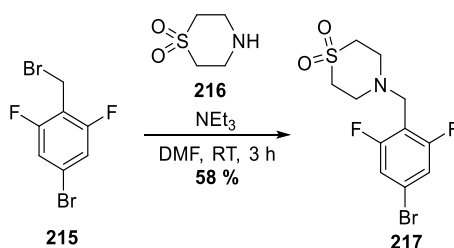
Scheme 34 The optimised synthetic sequence within a H-cube to access quinoxalinone **213** in good yield, removing the use of pressurised H₂O₂.

To provide a means to functionalise the 2-position of quinoxalinone **213**, quinoxalinone **213** was subjected to POCl₃ to afford 2-chloroquinoxaline **214** in an excellent yield (96 %) (Scheme 35).



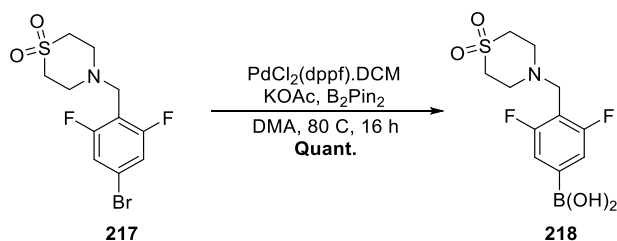
Scheme 35 Conversion of quinoxalinone **213** to 2-chloroquinoxaline **214** via POCl₃.

With the quinoxaline core to hand, the groups for incorporating into the 2- and 8-positions were synthesised. The 8-position substituent was identical in both parent compounds, **61** and **63**, and was prepared via an S_N2 reaction with thiomorpholinedioxide **216** and benzyl bromide **215** to afford benzylthiomorpholinedioxide **217** in 58 % yield (Scheme 36).



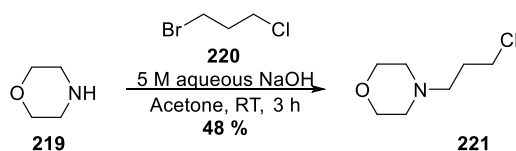
Scheme 36 An S_N2 reaction between thiomorpholinedioxide **216** and benzyl bromide **215** to afford benzylthiomorpholinedioxide **217**.

A Miyaura borylation was subsequently carried out on benzylthiomorpholinedioxide **217** to generate the boronic acid **218**, which was used without purification in a Suzuki-Miyaura cross-coupling reaction (Scheme 37).



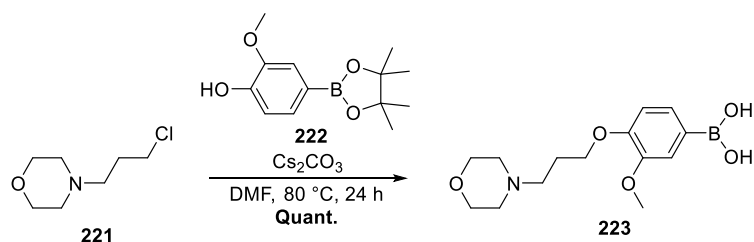
Scheme 37 The Miyaura borylation of benzylthiomorpholinedioxide **217** providing boronic acid **218** in quantitative yield.

The 2-position group of quinoxaline **63** was synthesised by installing morpholine **219** onto 1-bromo-3-chloropropane **220**, ejecting bromide, to produce chloropropylmorpholine **221** in a 48 % yield (Scheme 38).



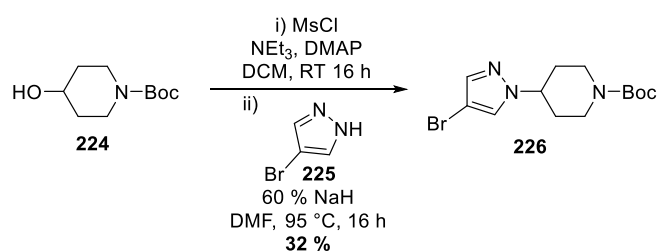
Scheme 38 The union of morpholine **219** and 1-bromo-3-chloropropane **220** to afford chloropropylmorpholine **221**.

A second $\text{S}_{\text{N}}2$ reaction with phenol **222** and chloropropylmorpholine **221** was conducted to afford the substituted phenylboronic acid **223** which was used without purification in the following Suzuki-Miyaura reaction (Scheme 39).



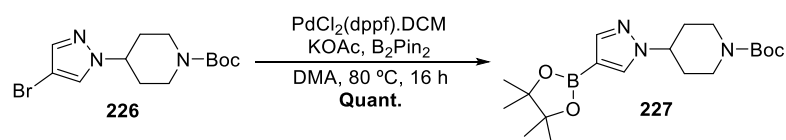
Scheme 39 An $\text{S}_{\text{N}}2$ reaction to append chloropropylmorpholine **221** to phenol **222** affording boronic acid **223** in quantitative yield.

To synthesise the 2-position substituent on quinoxaline **62**, Boc-hydroxypiperidine **224** was mesylated to generate the corresponding piperidine mesylate which was used directly into an $\text{S}_{\text{N}}2$ reaction with bromopyrazole **225** to afford the substituted bromopyrazole **226** in 32 % yield (Scheme 40).



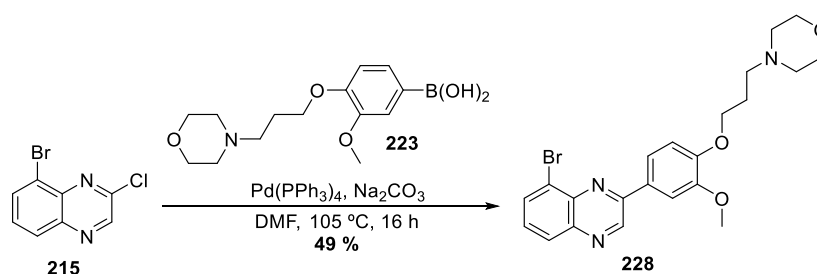
Scheme 40 The mesylation of Boc-hydroxypiperidine **224** followed by an $\text{S}_{\text{N}}2$ reaction with bromopyrazole **225** to give pyrazole **226**.

A Miyaura borylation was performed on bromopyrazole **226** affording the corresponding boronic ester **227** (Scheme 41), which was used without purification in the following Suzuki-Miyaura reaction.



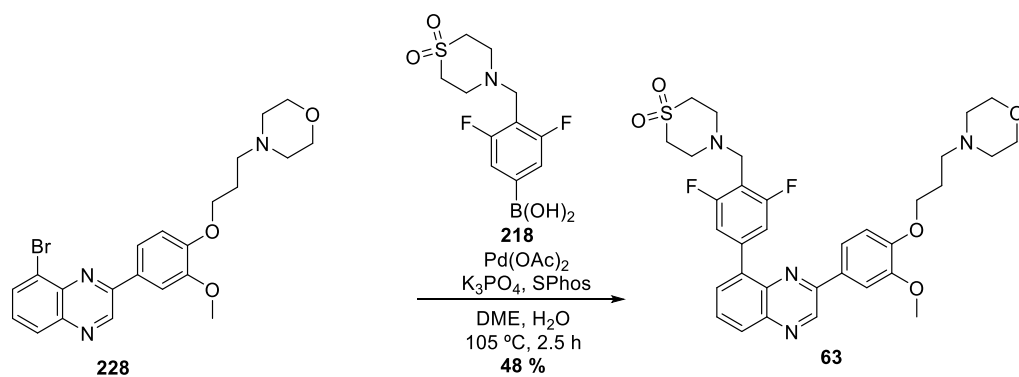
Scheme 41 The Miyaura borylation of bromopyrazole **226** affording boronic ester **227** in quantitative yield.

Following generation of the core, and the required coupling partners **218**, **223** and **227**, the various groups were united to provide parent compounds **61** and **63**. Due to the inherent enhanced reactivity of the chloro substituent at the 2-position, alpha to *N*, over the 8-Br substituent, the 2-position substituents were introduced first. This presents an inefficiency in the route, since the group at the 8-position remains constant whilst the substituent at the 2-position is varied resulting in the 8-position Suzuki-Miyaura reaction needing to be carried out multiple times after the 2-position group has been altered. To access the morpholine-containing intermediate **228**, a Suzuki-Miyaura cross coupling was employed between the quinoxaline core **215** and phenylboronic ester **223**, affording the desired intermediate in 49 % yield (Scheme 42).



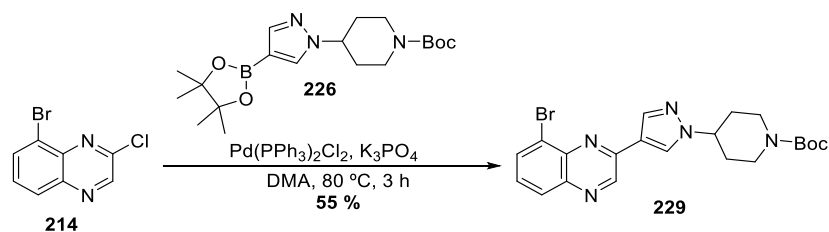
Scheme 42 The initial Suzuki-Miyaura reaction to append the 2-position substituent **223** to the quinoxaline core **215**.

Finally, a second Suzuki-Miyaura cross-coupling was achieved, appending thiomorpholinedioxide **218** to bromoquinoxaline **228** to produce the desired parent quinoxaline **63** in 48 % yield (Scheme 43).



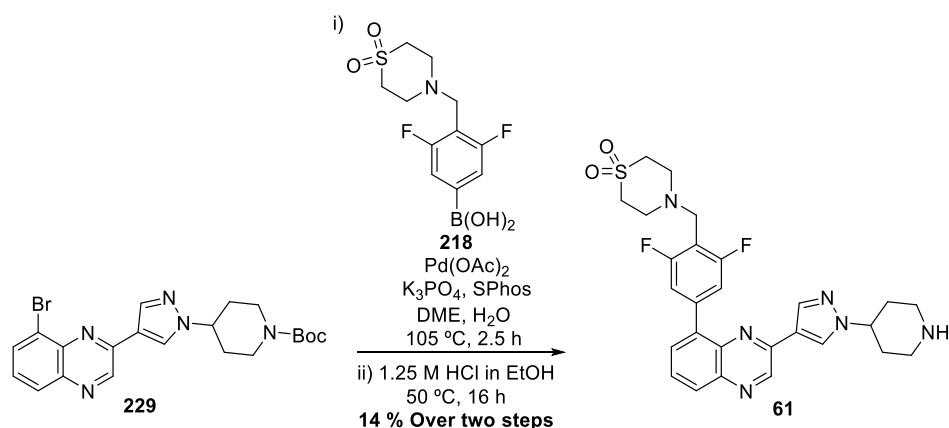
Scheme 43 The second Suzuki-Miyaura reaction furnishing parent quinoxaline warhead **63** in 48 % yield.

In a similar fashion to the synthesis of parent quinoxaline **63**, an initial Suzuki-Miyaura cross-coupling using pyrazole **226** and the quinoxaline core **214** afforded the pyrazole intermediate **229** in 55 % yield (Scheme 44).



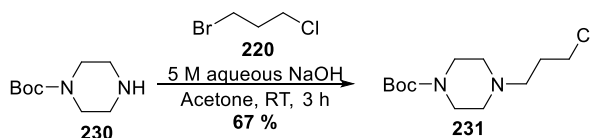
Scheme 44 The initial Suzuki-Miyaura reaction in the synthesis towards parent quinoxaline **61**.

This was followed by an additional Suzuki-Miyaura reaction with thiomorpholinedioxide **218** and subsequent Boc-deprotection furnishing the parent compound **61** in 14 % yield (Scheme 45).



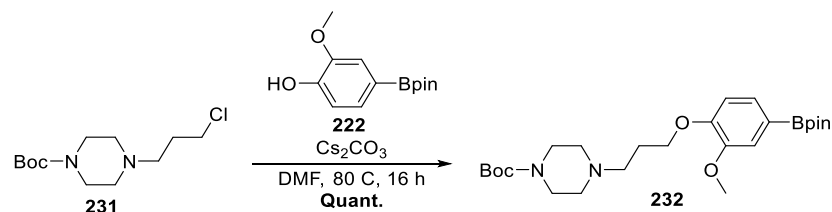
Scheme 45 The second Suzuki-Miyaura reaction, followed by Boc-deprotection, furnishing quinoxaline warhead **61** in 14 % yield over the two steps.

Both parent compounds **61** and **63** were evaluated within GSK-developed assays, with respect to their JAK biochemical and cell potencies, in addition to their physicochemical attributes. It was determined that compound **63** better suited to the requirements of this study with regards to the aforementioned properties (further discussed in Section 2.4.11). However, the morpholine moiety presented poor ligation opportunities due to *O* lacking the ability to undergo further substitution. As such, it was proposed that replacing the morpholine by a piperazine would allow ligation via *N*-alkylation. Therefore, the synthesis of the analogous methylated piperazine quinoxaline **235** was executed to determine whether the piperazine is tolerated. The 2-position piperazine substituent was prepared in a similar vein to the analogous morpholine moiety, beginning with the union between Boc-piperazine **230** and 1-bromo-3-chloropropane **220** in the presence of 5 M aqueous NaOH to afford alkylated piperazine **231** in a 67 % yield (Scheme 46).



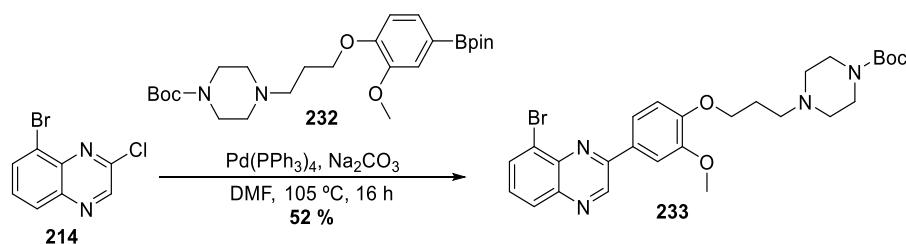
Scheme 46 The initial $\text{S}_{\text{N}}2$ reaction in steps towards piperidine quinoxaline **235**.

A second S_N2 with phenol **222**, displacing chloroalkane **231** afforded the boronic ester **232** in quantitative yield (Scheme 47).



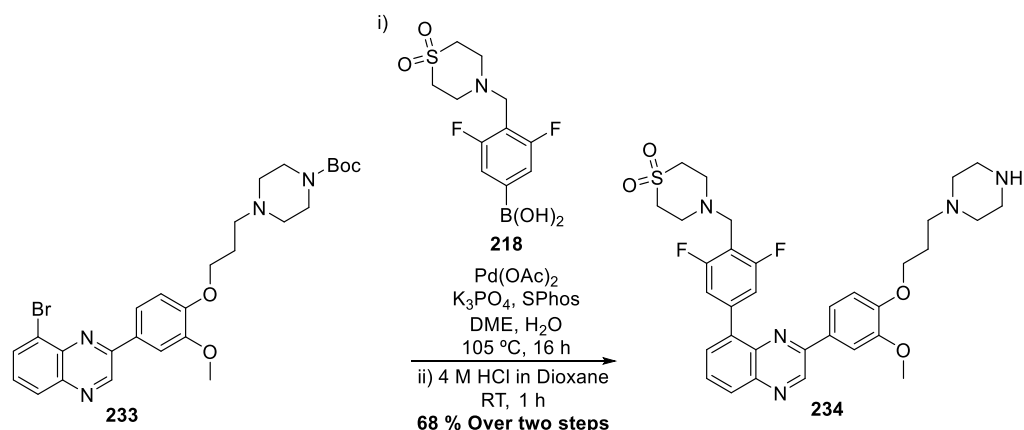
Scheme 47 The second S_N2 reaction affording boronic ester **232** in quantitative yield.

The phenylboronic ester **232** was then appended to the quinoxaline core **214** via a Suzuki-Miyaura cross-coupling reaction, affording Boc-piperazine intermediate **233** in 52 % yield (Scheme 48).



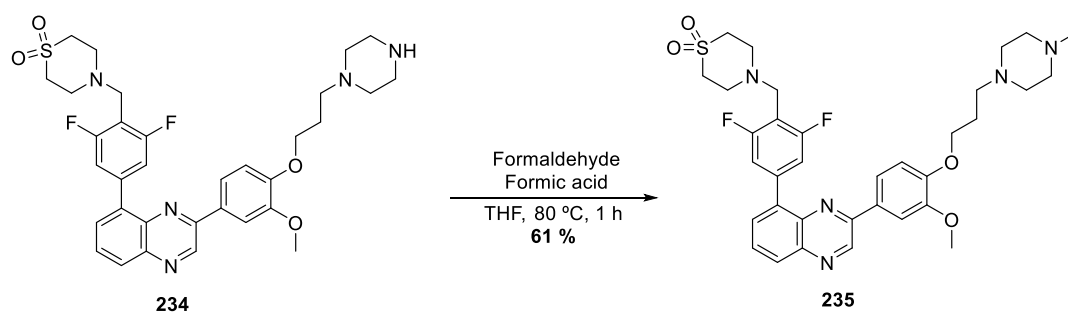
Scheme 48 Addition of phenylboronic ester **232** to the quinoxaline core **214** via a Suzuki-Miyaura reaction affording piperidine intermediate **233**.

A second Suzuki-Miyaura reaction was performed to append the thiomorpholinedioxide group **218**, producing the Boc-protected parent compound, which was subsequently telescoped into the Boc-deprotection using 4 M HCl in dioxane, to furnish free amine **234**, following basic work-up, in 68 % yield over the two steps (Scheme 49).



Scheme 49 The second Suzuki-Miyaura reaction, followed by Boc-deprotection, to afford piperazine **234** in 68 % yield over two steps.

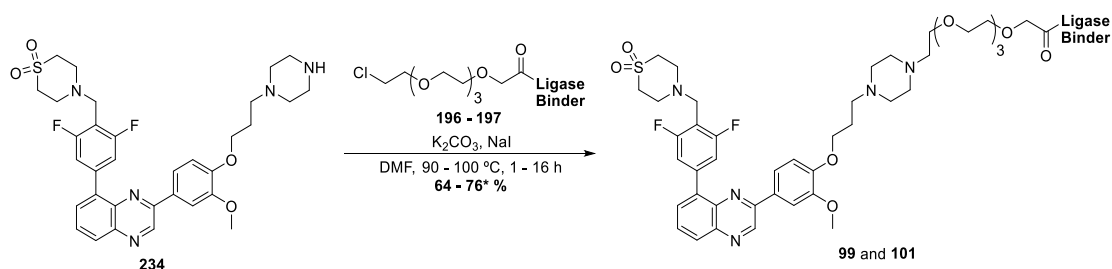
The free amine of compound **234** was subjected to a reductive amination furnishing the desired parent compound **235** in 61 % yield (Scheme 50).



Scheme 50 A reductive amination to generate methylated piperidine **235** in 61 % yield.

Two synthetic strategies were employed to derive PROTACs from quinoxaline **234**. The first was to carry out alkylations to linkers of varying lengths and compositions, appended to pre-existing ligase binders, readily available within our labs. And the second was attachment of a linker exhibiting a masked carboxylic acid on the terminal end of the linker, followed by a series of amide couplings with the appropriate ligase binders.

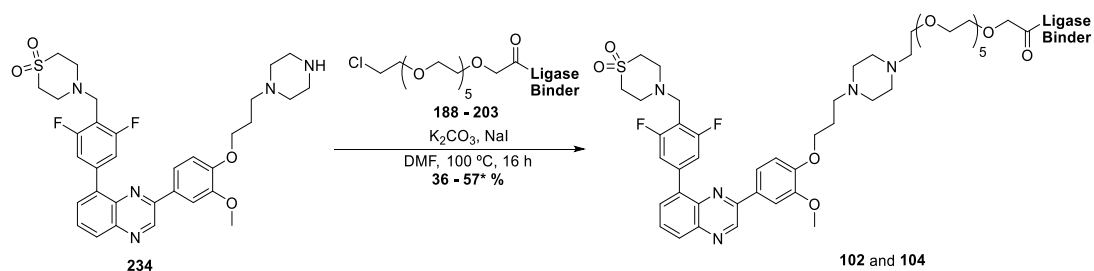
Due to the success of linker/ligase binder alkylations on the pyrimidine template, similar conditions were employed to attach the linker/ligase binders to the quinoxaline core **234**. Using temperatures ranging from 90 – 100 °C and 1 – 16 h, the 4EG linked IAP **196** and VHL binders **197** were attached in high yield (64 – 76 %), to afford quinoxaline 4EG IAP **99**, and quinoxaline 4EG VHL **101**, respectively (Table 44).



Compound Number	Ligase Binder	Linker Length	Yield (%)
99		4EG	76*
101		4EG	64

Table 44 Alkylations of the quinoxaline core **234**, using 4EG IAP **196** and 4EG VHL **197**. * = Yield over two steps (amide coupling followed by Boc deprotection).

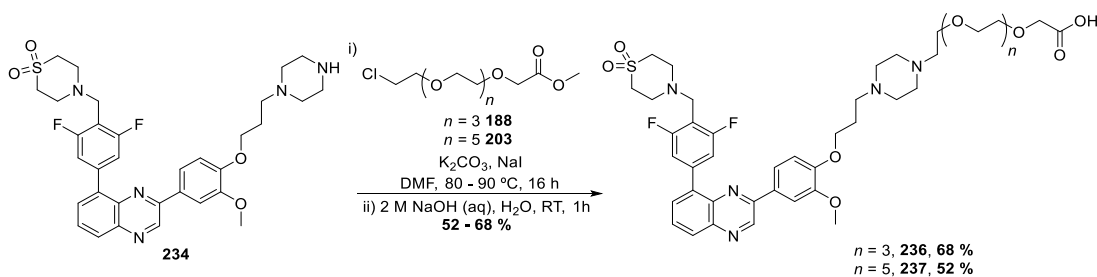
A similar strategy was employed to append 6EG IAP **188** and 6EG VHL **203**, to the quinoxaline core **234**, at 100 °C for 16 h to afford quinoxaline 6EG IAP **102**, and quinoxaline 6EG VHL **104** in low to moderate yield (36 – 57 %).



Compound Number	Ligase Binder	Linker Length	Yield (%)
102		6EG	57*
104			36

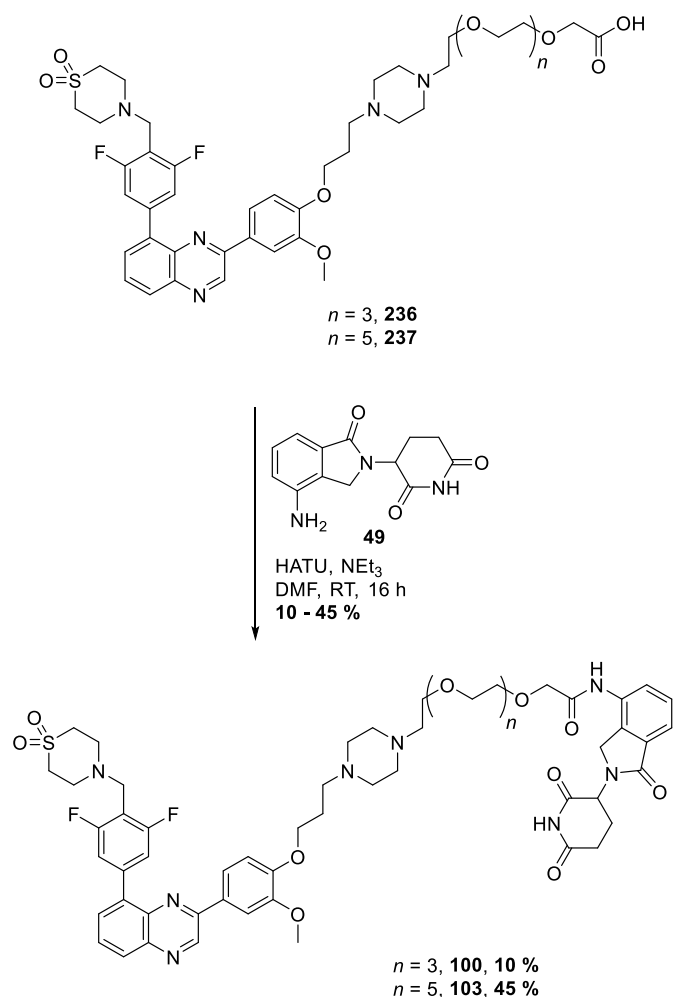
Table 45 Alkylations of the quinoxaline core **234**, using 4EG IAP **188** and 4EG VHL **203**. * = Yield over two steps (amide coupling followed by Boc deprotection).

To complete the 4EG and 6EG quinoxaline sets, the linker attachment, followed by amide coupling strategy, was employed. The 4EG and 6EG esters, previously prepared, were appended to the quinoxaline core. Subsequent ester hydrolysis afforded the quinoxaline 4EG **236** and 6EG **237** acids in 52 – 68 % yields, respectively, over the two steps (Scheme 51).



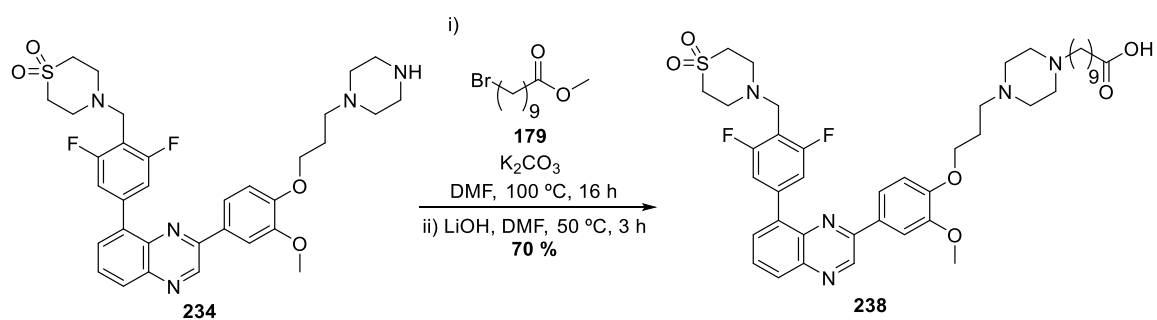
Scheme 51 The synthesis of 4EG and 6EG quinoxaline acids **236** and **237**.

Both the quinoxaline carboxylic acids **236** and **237** were then subjected to amide couplings with CRBN **49**, to afford the corresponding 4EG and 6EG quinoxaline CRBN PROTACs **100** in 10 % yield and **102** in 45 % yield (Scheme 52).



Scheme 52 Amide couplings with CRBN **49** onto the 4EG and 6EG quinoxaline acids **236** and **100** to afford 4EG and 6EG quinoxaline CRBN PROTACs **100** and **102**.

With the quinoxaline-ethylene glycol PROTACs synthesised, the carbon-linked 10C linked quinoxaline PROTACs were also sought. As with the pyrimidine PROTACs, a 10C chain linked to the quinoxaline core, with a terminal acid was prepared through an alkylation of quinoxaline **234** and ester **179** (Scheme 53). Following alkylation, the ester was hydrolysed *in situ* to afford acid **238** in a 70 % yield.

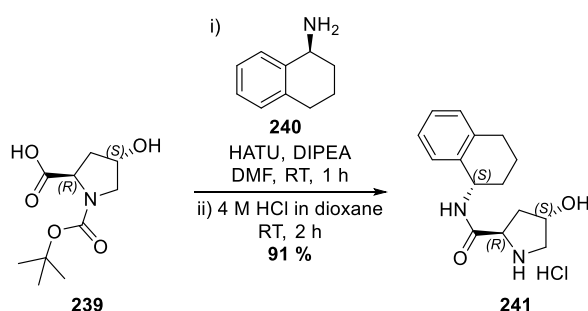


Scheme 53 The alkylation of quinoxaline **234**, with 10C ester **179** followed by ester hydrolysis to afford acid **238**.

The 10C quinoxaline acid **238** was subjected to the HATU amide coupling conditions, with the three ligase binders, IAP **184**, VHL **65** and CRBN **49** (Scheme 54). As with the amide couplings carried out on the pyrimidine series, the 10C quinoxaline PROTACs **105 - 107** were generated in varying yields (15 – 54 %).

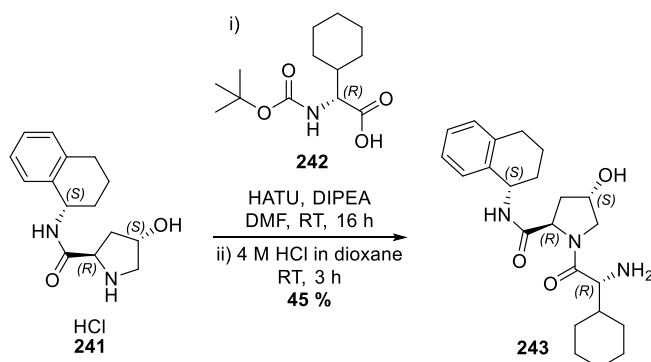
2.5.14 Synthesis of JP-6 Inverse; A Negative Control

To confirm that PROTAC-mediated degradation was occurring, a negative control was required (further discussed in Section 2.8.4). To this end, all of the stereocenters with the IAP portion of PROTAC **105** were inverted in the hopes that the IAP portion would no longer recruit IAP thus rendering it incapable of inducing JAK degradation. The synthesis was initiated by a HATU-mediated union of Boc-proline **239** and tetrahydronaphthalene amine **240** to afford the amide which was subsequently treated with 4 M HCl in dioxane to afford pyrrolidine **241** as the HCl salt in 91 % yield over two steps (Scheme 55).



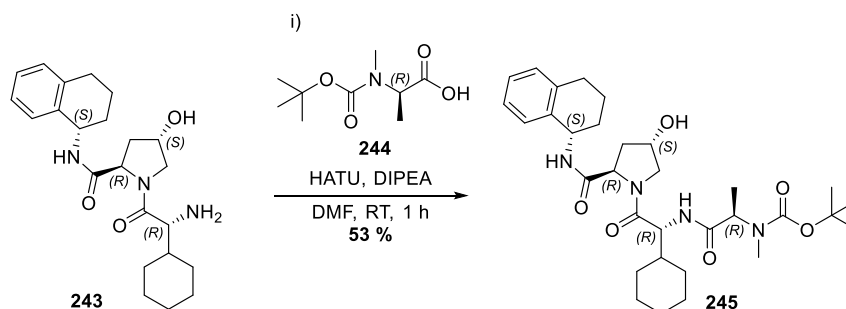
Scheme 55 An amide coupling between acid **239** and amine **240** to afford amide **241** in excellent yield.

A second amide bond was forged between pyrrolidine **241** and amino acid **242** to afford amide, which was exposed to 4 M HCl in dioxane to afford amine **243** in a 45 % yield over two steps (Scheme 56).



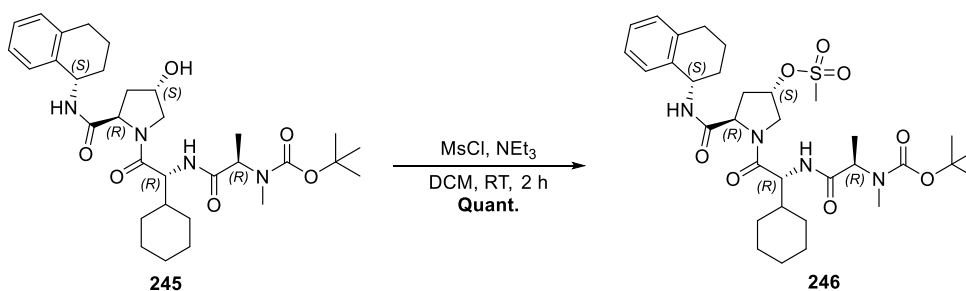
Scheme 56 The second amide bond formation between pyrrolidine **241** and amino acid **242** to provide amide **243** following Boc deprotection.

To conclude the series of amide couplings towards the inverted IAP compound, amine **243** was coupled via HATU to alanine **244** to furnishing amide **245** in a 53 % yield (Scheme 57).



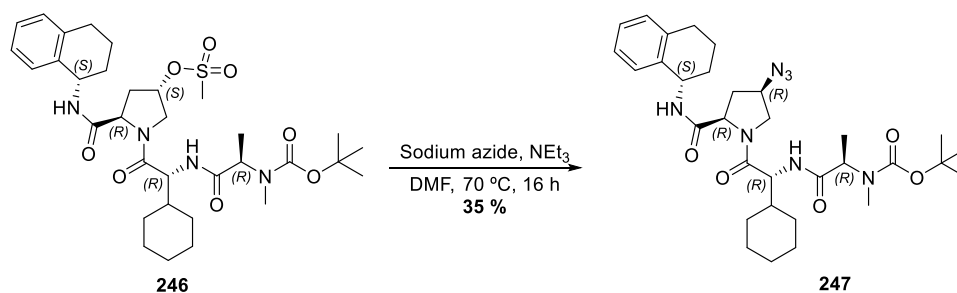
Scheme 57 The final amide coupling to afford amide **245** in 53 % yield.

The hydroxy group of hydroxyproline **245** was activated by mesyl-Cl to generate mesylate **246** in quantitative yield (Scheme 58).



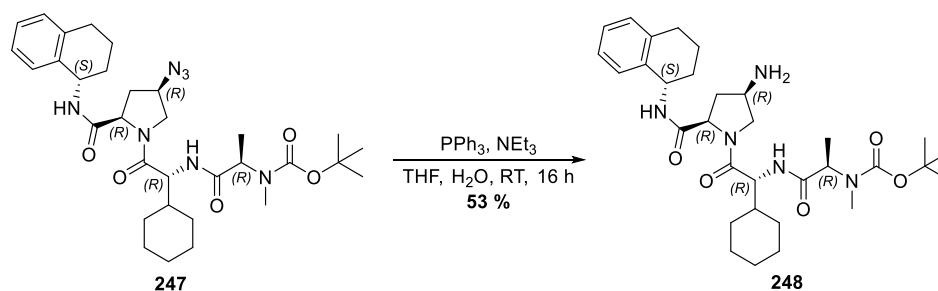
Scheme 58 Mesylation of alcohol **245** generating mesylate **246** in quantitative yield.

The mesylate **246** was subjected to a S_N2 reaction with sodium azide to provide azide **247** in 35 % yield (Scheme 59).



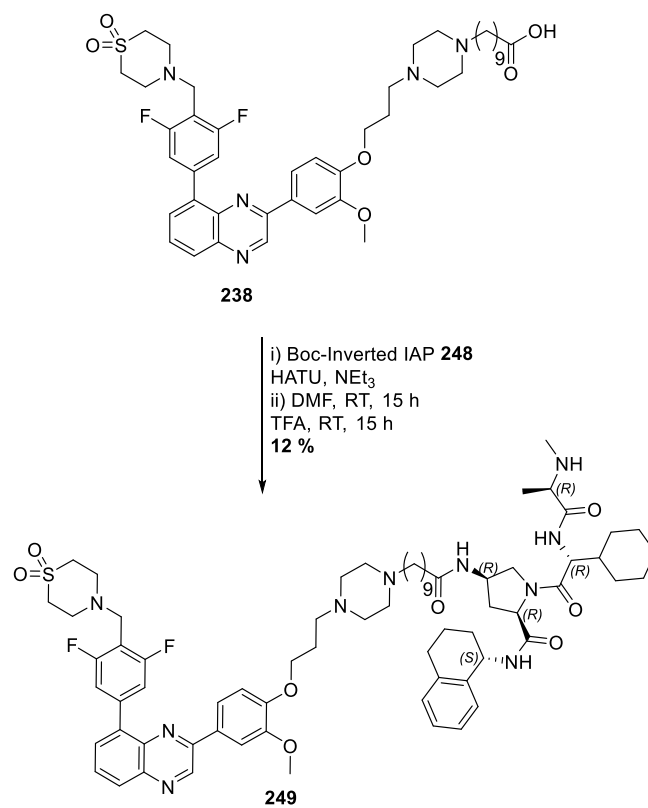
Scheme 59 Generation of azide **247** from mesylate **246** with sodium azide.

The azide **247** was converted to Boc-inverted IAP **248** in 53 % yield, under reductive conditions using PPh_3 (Scheme 60).



Scheme 60 Reduction of azide **247** with PPh_3 to afford Boc-inverted IAP **248**.

Finally, to achieve the inactive IAP-PROTAC **249**, a final amide coupling was conducted between 10C-quinoxaline acid **238** and Boc-inverted IAP **248**, and addition of TFA cleaved the Boc group to furnish 10C-linked inverted IAP PROTAC **249** as the free base in a 12 % yield over two steps (Scheme 61). With this final inactive PROTAC the synthesis was concluded, and efforts focused towards biological and cellular screening.



Scheme 61 The synthesis of inverted IAP quinoxaline PROTAC **249**.

2.6 Medicinal Chemistry of Pyrimidine Series PROTACs

2.6.1 The Pyrimidine-OH PROTAC Medicinal Chemistry

Following generation of the initial set of triazole pyrimidine series PROTACs, the compounds were profiled within biochemical and IL2 PBMC assays (Table 46). At this stage, the compounds were assessed in relation to function rather than protein degradation since the Western blot assay was yet to be developed. If the PROTACs failed to elicit protein degradation, they should still exhibit cell activity based on the inhibitory ability of the JAK warhead portion of the PROTACs. In addition, if protein degradation occurs within the incubation period (1 h) in the IL2 PBMC assay, it may be possible to observe greater cell potency than the parent compound. However, it is possible protein degradation may be slow and thus additional potency attributed to JAK degradation may not be observed within the timescale of the IL2 PBMC assay.

In order to determine whether the triazole was tolerated within the JAKs, the truncated PROTAC **163** was also assessed in both the biochemical and IL2 PBMC assay. In comparison to the parent compound **58**, a drop-off was observed in potency within the biochemical assay for truncated PROTAC **163** across the JAKs (JAK1 = 5-fold, JAK2 = > 100-fold, JAK3 = > 8-fold, TYK2 = 250-fold). Interestingly, enhanced selectivity over TYK2 against JAK1 was observed (160-fold) through the incorporation of the triazole, beyond what is seen in the parent compound. Whilst the biochemical potencies were lower as compared to the parent compound, truncated PROTAC **163** was still considered sufficiently potent across the JAKs. Unsurprisingly, a similar trend was displayed within the IL2 PBMC assay, whereby the truncated PROTAC was 30-fold less potent within the cell when compared to the parent compound **58**. Although the truncated PROTAC exhibited a significant drop-off in the PBMC assay, JAK binding was deemed sufficient to facilitate ternary complex formation. As a result, complete PROTACs were still prepared to ascertain whether a further drop in cell potency was displayed, or if the cell potency might increase due to JAK degradation. Unfortunately, further decreases in potency within both the biochemical and IL2 PBMC assays were observed across all triazole PROTACs **68 – 71**. The IAP triazole PROTAC **68** displayed the most

significant loss of potency within both the IL2 PBMC and biochemical assays, across the JAK isoforms. Most disappointingly, it displayed a pIC_{50} of < 4.7 within the IL2 PBMC. CRBN triazole PROTAC **69** exhibited greater potency within the biochemical assay across the JAKs in comparison to IAP PROTAC **68**. However, as with IAP triazole PROTAC **68**, poor IL2 PBMC potency was achieved ($pIC_{50} = 4.8$). The VHL and VHLII triazole PROTACs **70** and **71** displayed similar biochemical activity, however VHL triazole PROTAC **70** was the most potent ($pIC_{50} = 5.3$) of the set, and slightly more potent than the analogous VHLII triazole PROTAC **71** ($pIC_{50} = 4.9$) within the IL2 PBMC assay. The considerable drop in activity within the cell, as compared to their respective biochemical activity and the parent compounds' profile, was attributed to the triazoles being too polar in addition to their increased molecular weight (MW), thus conferring poor cell permeability and low intracellular concentration of the PROTACs. Consequently, it was proposed that modification of the linker to confer more favourable physicochemical properties may lead to increased cellular activity.

Compound	HBD	ChromLogD _{7.4}	MW	pIC_{50}				
								IL2
				JAK1	JAK2	JAK3	TYK2	PBMC
58	4	2.75	440	9.8	>9.8	>9.8	9.3	7.5
163	3	2.89	536	9.1	7.8	8.9	6.9	6.0
68	7	4.25	1148	7.7	6.7	8.1	6.1	< 4.7
69	5	3.39	910	8.6	7.4	8.7	6.4	4.8
70	6	4.03	1095	8.0	7.1	8.4	6.3	5.3
71	5	N/D	1199	7.9	7.3	8.3	6.2	4.9

Table 46 The physicochemical properties and the biochemical and cell potencies associated with the pyrimidine-OH triazole PROTACs. pIC_{50} values are quoted as a mean of multiple test occasions ($n \geq 3$).¹

¹ Pages to which the structures in Table 46 are located: **58** on page 101, **163** on page 153, **68 – 71** on page 116.

The generation of analogous PROTACs to the first iteration, but with all-carbon linkers, was proposed to circumvent the poor permeability conferred by the triazole. Shorter linkers than the triazole linkers, such as 7C and 10C chains were initially produced, which resulted in PROTACs **72** – **74**. As seen in

Table 47, the 7C-linked IAP PROTAC **72** displays a loss in JAK1 (10-fold) and JAK3 (6-fold) activity as compared to the analogous triazole-linked PROTAC **68**. However, 7C-linked IAP PROTAC **72** is more potent within the IL2 PBMC assay than the triazole-linked SMAP IAP PROTAC **68**. Similarly, 10C-linked IAP PROTAC **75** shows a loss in potency at JAK3 (3-fold) when compared to triazole-linked IAP PROTAC **68**, albeit less significant. 10C-linked IAP PROTAC **75** is however, equipotent within the IL2 PBMC assay to the analogous 7C-linked IAP PROTAC **72**. The increased potency within the cell exhibited by carbon-linked IAP PROTACs **72** and **75** may be attributed to increased cell permeability. Conversely, the triazole-linked CRBN PROTAC **69** is equipotent (within the error of the assay) to both the 7C-linked and the 10C-linked CRBN PROTACs **73** and **76** within the IL2 PBMC assay. Interestingly, the 7C-linked CRBN PROTAC **73** is 13-fold more potent at JAK2 than the corresponding triazole-linked CRBN PROTAC **69**. This could be a result of CRBN or the linker forming favourable interactions with JAK2. The VHL pyrimidine PROTACs **74** and **77** are somewhat equipotent across the JAKs, however 7C-linked PROTAC **74** provides a 16-fold increase in potency at JAK2 as compared to triazole-linked VHL PROTAC **70** and a 5-fold increase over 10C-linked PROTAC **77**. Similarly, to 7C-linked CRBN PROTAC **73**, the increased activity of 7C-linked VHL PROTAC **74** may also be attributed to more favourable interactions between VHL and JAK2 when closer to the protein. All VHL PROTACs **70**, **74** and **77** displayed the greatest potency of the set within the cell, with pIC_{50} s of 5.3 for the triazole-linked **70** and 7C-linked **74** PROTACs and 5.7 for the 10C-linked PROTAC **77**. Again, the increase in cellular potency from the triazole-linked VHL PROTAC **70** to the 10C-linked VHL PROTAC **77** may be a result of increased permeability resulting from increased lipophilicity reflected by their respective $ChromLogD_{7.4}$ values (**70** $ChromLogD_{7.4} = 4.03$, **77** $ChromLogD_{7.4} = 5.30$). Interestingly, the 7C-linked VHL PROTAC **74** and the analogous triazole-linked PROTAC **70** displayed equipotent IL2 PBMC activity.



Ligase Binder (R)	Linker	HBD	Chrom LogD _{7.4}	pIC ₅₀		
				JAK1	JAK2	JAK3 IL2 PBMC
IAP 64	 68	7	4.52	7.7/ 6.7 8.1		<4.7
	 72	7	4.76	6.7 6.8 7.3		5.2
	 75	7	5.64	7.4 7.0 7.6		5.1
CRBN* 49 or 48	 69	5	3.39	8.6 7.4 8.7		4.8
	 73	5	3.38	8.5 8.5 9.3		4.8
	 76	5	4.34	8.2 7.8 8.7		5.0
VHL 65	 70	6	4.03	8.0 7.1 8.4		5.3
	 74	6	4.79	8.1 8.3 8.8		5.3

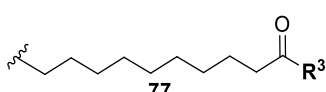
Linker	HBD	Chrom LogD _{7.4}	pIC ₅₀	
			JAK1 JAK2 JAK3	IL2 PBMC
 77	6	5.30	8.1 7.7 8.6	5.7

Table 47 The physicochemical properties and the biochemical and cell potencies associated with the triazole and all-carbon pyrimidine-OH PROTACs. * = Lenalidomide **49** was used in 7 and 10C-linked CRBN PROTACs, whereas pomalidomide **48** was present in the triazole-linked CRBN PROTAC. pIC₅₀ values are quoted as a mean of multiple test occasions (n = ≥ 3).

To obtain an understanding of the physicochemical space occupied by the current set of PROTACs **68 – 77**, HBD count and ChromLogD_{7.4} was plotted. As shown by Fig 74, six of the ten PROTACs fall within an undesired physicochemical space, with respect to their HBD count, which was proposed to have impacted negatively on their cell permeability. As a result, this could also diminish their cell potency due to reduced intracellular concentrations of PROTACs.

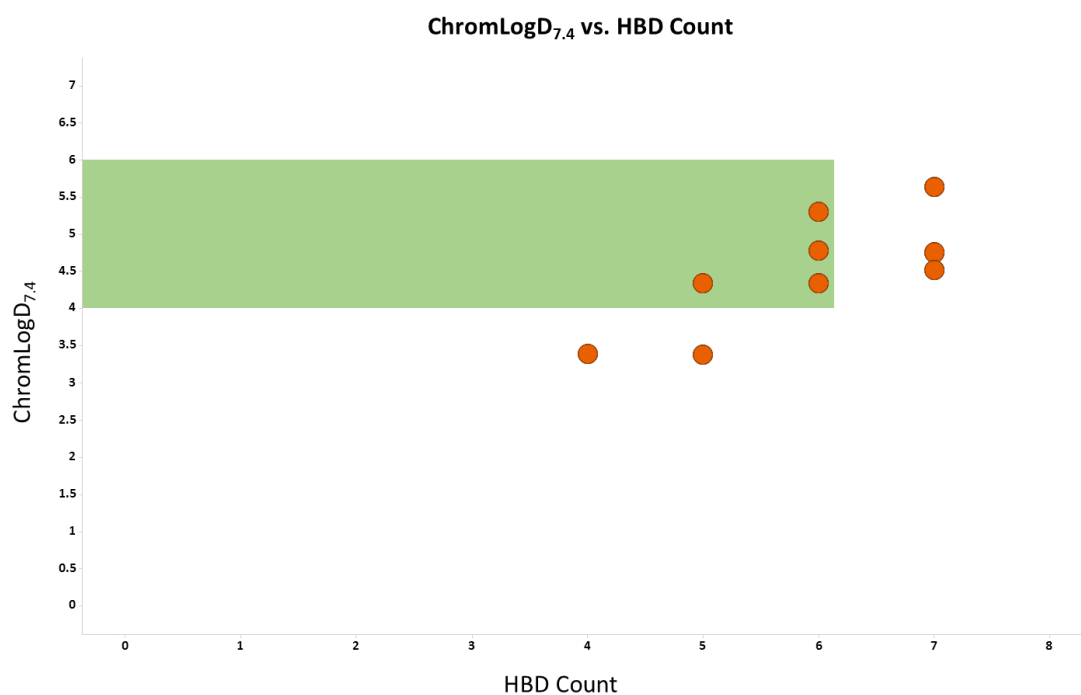


Fig 74 A graph illustrating the pyrimidine-OH PROTACs ChromLogD_{7.4} against their HBD, highlighting the favoured physicochemical space in relation to ChromLogD_{7.4} and HBD count in green.

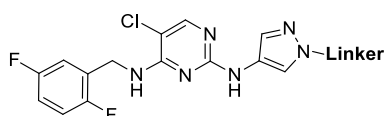
2.6.2 The Medicinal Chemistry of the Pyrimidine-H PROTACs

It was concluded that the poor physicochemical space occupied by the initial iteration of PROTACs may be limiting their cell permeation. Therefore, PROTACs with the modified JAK warhead **79 – 84** were synthesised to facilitate profiling to assess if the physicochemical modifications did indeed improve permeability.

Unsurprisingly, JAK biochemical potency confirmed the PROTACs were engaging each isoform, however the expected drop-off was observed across the JAKs (Table 48). Interestingly, pyrimidine-H 4EG-IAP PROTAC **82** displayed approximately a 10-fold increase in potency at each JAK isoform as compared to the analogous 10C PROTAC **79**. A similar trend was observed for the pyrimidine-H VHL PROTACs, in that the 4EG VHL PROTAC **84** was 2.5-fold more potent at JAK1, approximately 10-fold more potent at JAK2 and JAK3 than the analogous 10C VHL PROTAC **81**. The increased biochemical potency observed by the 4EG IAP

and VHL PROTACs **82** and **84** may be attributed to the increased flexibility and longer linker than the 10C linker, which may allow the ligase binders to form more favourable interactions with the external surface of the protein. The pyrimidine-H CRBN PROTACs **80** and **83** experienced similar biochemical potencies, with 10C CRBN PROTAC **80** exhibiting a slight increase at JAK1 (2.5-fold). The 10C PROTACs **79** – **81** experienced an increase in IL2 PBMC potency when compared to the analogous 4EG PROTACs **82** – **84**, which can be attributed to the 10C linker increasing the PROTACs lipophilicity and therefore increasing their cell permeability.

Intriguingly, the pyrimidine-H 10C PROTAC **79** – **81**, when compared to the analogous pyrimidine-OH 10C PROTACs **75** – **77**, did not display an increase in IL2 PBMC potency, as predicted, despite the decrease in HBD count and increase in lipophilicity. However, this maybe a result of the short incubation time (1 h) within the IL-2 PBMC assay, being insufficient for JAK PROTACs, rather than no improvement in cell penetration.



Ligase Binder (R)	Linker	HBD	ChromLogD _{7.4}	pIC ₅₀	
				JAK1 JAK2 JAK3	IL2 PBMC
R ¹ = IAP	 82	6	5.31	8.0	4.7
				8.2	
				7.8	
64	 79	6	7.26	7.2	5.1
			7.1		
			6.8		

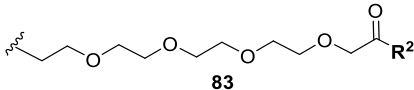
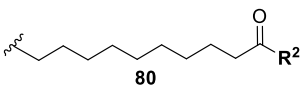
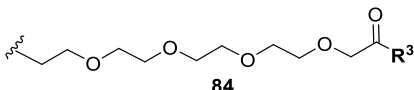
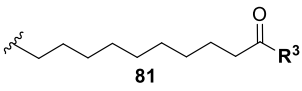
Ligase Binder (R)	Linker	HBD	ChromLogD _{7.4}	pIC ₅₀	
				JAK1 JAK2 JAK3	IL2 PBMC
R ² = CRBN 49		4	3.69	8.3	4.4
	83			8.1	
	8.1				
49		4	5.38	8.7	5.0
	80			8.0	
	8.2				
R ³ = VHL 65		5	4.70	7.9	4.7
	84			8.2	
	8.0				
65		5	6.31	7.5	5.0
	81			7.1	
	7.2				

Table 48 The physicochemical properties and the biochemical and cell potencies associated with the 10C and 4EG pyrimidine-H PROTACs. pIC₅₀ values are quoted as a mean of multiple test occasions (n = ≥ 3).

2.6.2 The Medicinal Chemistry of the Pyrimidine-Bn PROTACs: Exploiting an Alternative Vector

Exploiting alternative ligation vectors from the pyrimidine series could potentially result in more favourable PPIs between the JAKs and the E3 ligase binder, upon forming the ternary complex. This may have the result of achieving more efficient JAK ubiquitination and increased degradation. Therefore, PROTACs generated from the benzyl substituent of the pyrimidine series **85** were synthesised (Fig 75).

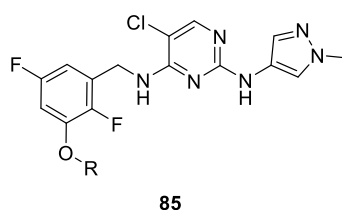


Fig 75 The Markush structure of pyrimidine-Bn PROTACs **85**, illustrating the ligation vector as R.

The benzylic PROTACs synthesised in Section 2.5.12 were profiled *in vitro* to assess whether ligating off the benzyl substituent was tolerated by JAK, and if they were cell penetrant. The biochemical data of the pyrimidine-Bn 4EG, 6EG and 10C demonstrated that growing off the phenol was well tolerated by the JAKs, as pIC_{50} values of > 6 were observed across each isoform with the 4EG, 6EG and 10C linkers (Table 49). The pyrimidine-Bn 4EG and 6EG IAP PROTACs **93** and **96** were equipotent and possessed the greatest potency across each isoform within the pyrimidine-Bn IAP set. Interestingly, the pyrimidine-Bn 10C IAP PROTAC **87** experienced diminished potencies across the JAKs, as compared to the pyrimidine-Bn 4EG and 6EG IAP PROTACs (**87** JAK1 \approx 6-fold reduction, JAK2 \approx 5-fold reduction, JAK3 \approx 36-fold reduction), however maintained a slightly higher IL2 PBMC signal (**93** pIC_{50} = 4.9, **96** pIC_{50} = 4.7, **87** pIC_{50} = 5.1). This is likely due to its increased lipophilicity as compared to the 4EG and 6EG IAP PROTACs **93** and **96**, aiding its cell penetration.

As with pyrimidine-Bn 4EG and 6EG IAP PROTACs **93** and **96**, the pyrimidine-Bn 4EG and 6EG CRBN PROTACs **94** and **97** were equipotent within the biochemical assay but possessed increased JAK3 activity in comparison to the analogous IAP PROTACs (\sim 4-fold). However,

whilst the pyrimidine-Bn 10C IAP PROTAC **87** maintained lower potencies across the JAKs, the pyrimidine-Bn 10C CRBN PROTAC **88** was equipotent at JAK1 and JAK2 to its analogous 4EG and 6EG PROTACs **94** and **97**, but was ~6-fold down at JAK3. Similarly, the pyrimidine-Bn 10C CRBN PROTAC **88** possessed greater IL2 PBMC activity to its PEG counterparts, likely due to a marked increase in lipophilicity and maintaining its JAK1 activity. The pyrimidine-Bn 16C CRBN PROTAC **91**, surprisingly displayed poor activity in both the biochemical and IL2 PBMC assays, which could potentially arise from the increased lipophilicity resulting in the PROTAC linker suffering from hydrophobic collapse in an aqueous environment, preventing binding to the JAKs.

Additionally, the pyrimidine-Bn VHL PEG PROTACs **95** and **98** were equipotent across the JAKs, highlighting that moving from 4EG to a 6EG linker growing from the phenol has no additional effect on tolerance. Likewise, the pyrimidine-Bn 10C VHL PROTAC **89** experienced a decrease in JAK2 and JAK3 potency (**89** JAK2 \approx 8-fold down, JAK3 \approx 25-fold down), however possessed a fairly similar IL2 PBMC potency to the analogous pyrimidine-Bn PEG VHL PROTACs **95** and **98**. As with the pyrimidine-Bn 16C CRBN PROTAC **91**, the corresponding 16C VHL PROTAC **92** possibly suffers hydrophobic collapse, resulting in poor JAK biochemical and IL2 PBMC activity.



Ligase Binder (R)	Linker	HBD	ChromLogD _{7.4}	pIC ₅₀	
				JAK1 JAK2 JAK3	IL2 PBMC
R ¹ = IAP 64	 93	6	5.19	8.6 7.6 7.7	4.9
	 96	6	5.18	8.4 7.4 7.6	4.7
	 87	6	7.54	7.7 6.8 6.1	5.1
	 90	6	10.62	6.2 7.0 5.1	< 4
R ² = CRBN 49	 94	4	3.61	8.5 7.6 8.3	4.7
	 97	4	3.68	8.7 7.6 8.1	4.7

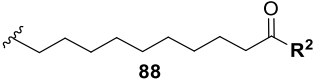
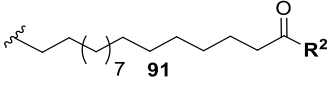
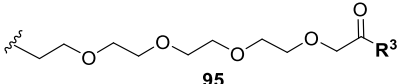
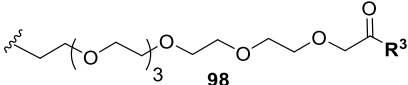
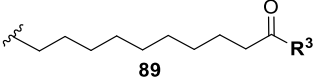
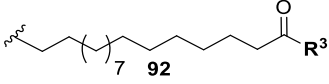
Linker	HBD	ChromLogD _{7.4}	pIC ₅₀	
			JAK1 JAK2 JAK3	IL2 PBMC
 88	4	5.64	8.7 7.2 7.4	5.1
 91	4	8.15	N/D 5.0 4.2	< 4.0
 95	5	4.52	8.5 7.7 8.0	5.3
R ³ = VHL 65  98	5	4.62	8.5 7.6 7.8	5.0
 89	5	6.49	8.2 6.7 6.5	5.0
 92	5	8.92	5.2 5.4 < 4.4	< 4.0

Table 49 The measured biological and physicochemical properties associated with the 10C, 16C, 4EG and 6EG pyrimidine-Bn PROTACs. pIC₅₀ values are quoted as a mean of multiple test occasions (n ≥ 3).

Comparatively, the pyrimidine-Bn 4EG IAP **93** and pyrimidine-H 4EG IAP PROTACs **82** display fairly similar ChromLogD_{7.4} values (**82** = 5.31, **93** = 5.19) and share the same HBD count. The pyrimidine-Bn 4EG IAP PROTAC **93**, however exhibits a slight increase in IL2 PBMC activity

(**82** = 4.7, **93** = 4.9). Whilst equipotent at JAK2, the increased activity may be attributed to pyrimidine-Bn 4EG IAP **93** being ~4-fold more active at JAK1. The pyrimidine-H 4EG IAP **82** is ~4-fold more potent at JAK2 than the analogous pyrimidine-Bn 4EG IAP PROTAC **93**, which reflects the pyrimidine-H parent compound **78** exhibiting higher JAK2 inhibition than the pyrimidine-Bn parent compound **86**. The pyrimidine-H and pyrimidine-Bn 10C IAP PROTACs **79** and **87**, on the other hand are equipotent within the IL2 PBMC assay. Whilst the pyrimidine-Bn 10C IAP PROTAC **87** is ~3-fold more active at JAK1 than pyrimidine-H 4EG IAP **82**, the pyrimidine-H PROTAC displays a ~5-fold increase at JAK3 resulting in equal activity within the IL2 PBMC assay.

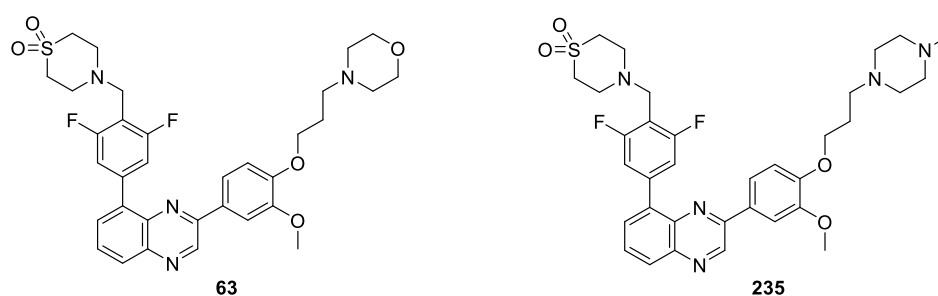
A dissimilar situation was observed for the pyrimidine-H and pyrimidine-Bn CRBN 4EG PROTACs **83** and **94**, in that they differed in IL2 PBMC activity (**83** = 4.4, **94** = 4.7). Whilst they exhibit similar lipophilicity, (**83** = 3.69, **94** = 3.61), they somewhat differ at JAK1 and JAK3. The pyrimidine-Bn 4EG CRBN PROTAC **94**, which displays greater cell potency, is ~2-fold more potent at JAK1 and JAK3. The minor difference may be significant enough to elicit a slight increase in IL2 PBMC activity. Similar to the pyrimidine-H and pyrimidine-Bn 10C IAP PROTACs, the analogous CRBN PROTACs **80** and **88** are equipotent within the IL2 PBMC assay. However, whilst equipotent at JAK1, pyrimidine-Bn **88** is ~6-fold more active at JAK3. The increased lipophilicity of pyrimidine-H 10C CRBN PROTAC **80** would increase permeability, thus increasing its cell potency.

The small difference in lipophilicity between the pyrimidine-H and pyrimidine-Bn 4EG VHL PROTACs (**84** = 4.70, **95** = 4.52) likely has little impact on cell penetration. The marked increase in JAK1 activity of pyrimidine-Bn 10C VHL (~4-fold) results in a significant IL2 PBMC potency increase in contrast to pyrimidine-H 4EG VHL (**84** = 4.7, **95** = 5.3). As with the other pyrimidine-H and pyrimidine-Bn 10C PROTACs, the comparative 10C VHL PROTACs **81** and **89** both exhibit a pIC₅₀ of 5.0 within the cellular assay. The similar activity can be attributed to pyrimidine-Bn 10C VHL **89** being ~5-fold more potent at JAK1 and ~5-fold less active at JAK3 in comparison to pyrimidine-H 10C VHL **81**.

Pleasingly, both expansion from both vectors of the pyrimidine series warheads with the addition of linkers and ligase binders was tolerated by the JAKs and did not impact on essential binding interactions. Clearly the lipophilicity and HBD count modulated by each constituent of the PROTAC impacts cell permeability.

2.6.4 The Medicinal Chemistry of the Quinoxaline Series

To assess whether the morpholine vector was a viable ligation point, the methylated piperidine was synthesised and analysed within our biochemical and cellular assays (Table 50). Interestingly, the methylated piperidine displayed an increase in potency across JAK1, JAK2 and JAK3, as compared to the morpholine analogue. However, the increase in potency at JAK1/JAK3 did not translate to an increase in activity within the IL-2 PBMC assay, and a ~3-fold decrease in activity was observed. This was likely a result of the additional basic centre which decreased the ChromLogD_{7.4} to 4.59 (~25-fold decrease), and thus likely reduced access to JAK1/JAK3 within the intracellular compartment. Pleasingly, however, the methylated piperidine was well tolerated by the JAKs, thereby green-lighting the synthesis of piperidine-ligated quinoxaline PROTACs.

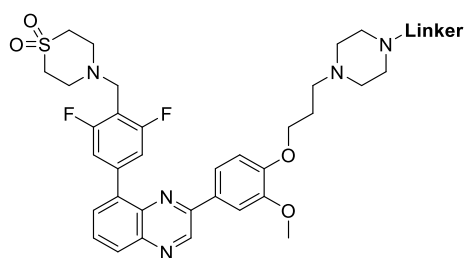


Compound	HBD	ChromLogD _{7.4}	MW	pIC ₅₀				
				IL2				
				JAK1	JAK2	JAK3	TYK2	PBMC
63	0	5.99	638.73	8.1	9.6	8.1	7.9	6.5
235	0	4.59	651.77	8.3	> 9.8	8.3	N/D	6.0

Table 50 The biological and physicochemical properties of quinoxaline **63** and **235**. pIC₅₀ values are quoted as a mean of multiple test occasions (n = ≥ 3). quinoxaline **63** tested as a formic acid salt.

Following the quinoxaline PROTAC library synthesis, the PROTACs were profiled within the JAK biochemical and cellular assays. Biochemical evaluation of the library indicated that the

4EG, 6EG and 10C linkers tethered to all three ligase binders were well tolerated, with all pIC_{50} values at each isoform ≥ 6.6 . The selectivity profile of all the quinoxaline PROTACs **99** – **107** mirrored that of the parent warhead **63**, in that activity at JAK1 and JAK3 was relatively equipotent, and a distinct JAK2 bias of ~ 13 – 25-fold was observed, for a given quinoxaline PROTAC. Furthermore, the diminished JAK1/JAK3 biochemical potency translated to a drop in IL-2 PBMC potency, as observed by the parent warhead **63**. A drop-off of ~ 6 – 20-fold was observed from the quinoxaline piperidine warhead **235** to the quinoxaline PROTACs **99** – **107**. Whilst this resulted in poor cellular activity, it proved encouraging since the PROTACs were penetrating the cell membrane and engaging with intracellular JAK1 and JAK3, and it was expected that IL-2 PBMC potency readout would be low due to decreased activity at JAK1 and JAK3 as detected by the biochemical assays. No major difference was observed between the IAP, CRBN and VHL quinoxaline PROTAC sets, in relation to IL-2 PBMC potency, despite significant differences in physicochemical properties.



Ligase Binder (R)	Linker	HBD	ChromLogD _{7,4}	pIC ₅₀	
				JAK1 JAK2 JAK3	IL2 PBMC
	 99	4	6.0	7.1 8.7 7.3	5.1
R ¹ = IAP 64	 102	4	5.8	7.0 8.5 7.3	4.9
	 105	4	7.7	6.6 8.7 6.6	5.2
	 100	2	4.5	7.9 9.4 8.1	5.0
R ² = CRBN 49	 103	2	4.5	7.6 8.9 7.7	4.7

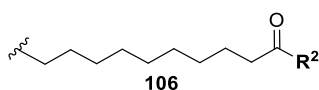
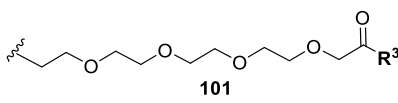
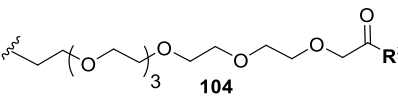
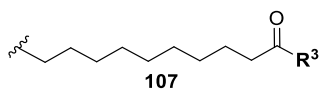
Linker	HBD	ChromLogD _{7.4}	pIC ₅₀	
			JAK1 JAK2 JAK3	IL2 PBMC
 106	2	5.7	7.2 8.4 7.4	4.9
 101	3	5.2	6.9 8.3 7.1	4.8
R ³ = VHL  104 65	3	5.3	7.3 8.4 7.3	5.0
 107	3	6.5	7.1 8.7 7.1	4.7

Table 51 The measured biological and physicochemical properties associated with the 10C, 4EG and 6EG quinoxaline PROTACs. pIC₅₀ values are quoted as a mean of multiple test occasions (n ≥ 3).

2.7 Physicochemical Property Impact on Permeability

To assess the impact of the PROTAC library's physicochemical properties on cell permeability, a permeability measure was required. Typically for small molecule inhibitors, moving from the isolated biochemical assay to a cellular environment such as the IL2 PBMC assay results in a drop-off in potency.²¹⁶ Since classic permeability assays designed for oral bioavailability did not provide useful data from a cellular context, the drop-off in potencies of JAK1 and JAK3 biochemical assay to the cellular assay was used as a permeability surrogate. This is

based on the assumption that a particularly large drop-off would be, at least in part, derived from poor access to the required intracellular compartment due to low membrane permeability.²¹⁷ As significant JAK degradation was unlikely to occur within the 1 h incubation period within the IL2 PBMC assay, and therefore unable to positively impact the potency readout, the drop-off from the biochemical assay to the cellular assay was deemed suitable as a permeability surrogate.

The pyrimidine-OH and 16C pyrimidine series were excluded from any further analysis due to their poor occupied physicochemical space, and inability to gain a handle on the 16C PROTAC's potency. Analysis of our JAK PROTAC library revealed PROTACs derived from the pyrimidine-H and pyrimidine-Bn series typically exhibited a greater drop-off from the isolated JAK1 and JAK3 biochemical assays to the cell as compared to analogous quinoxaline-based PROTACs possessing fewer HBDs (HBD count ≤ 5) than their pyrimidine counterparts (HBD count ≤ 6), and always expressed a higher ChromLogD_{7,4}, thereby increasing permeability.

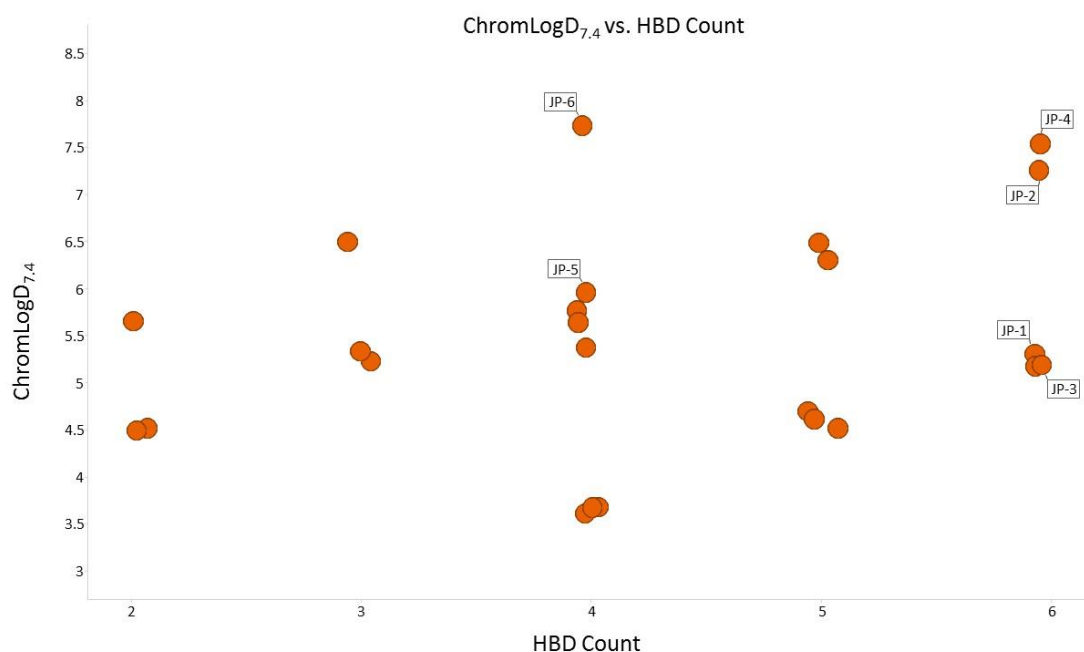
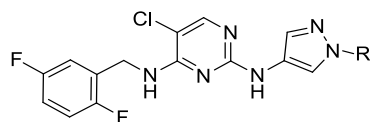


Fig 76 A plot of ChromLogD_{7,4} vs. HBD count of the JAK PROTAC library. PROTACs JP-1 – JP-6 (six PROTACs capable of inducing JAK1/JAK2 degradation) are labelled.



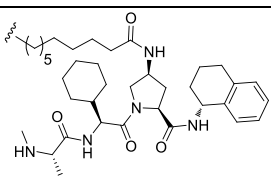
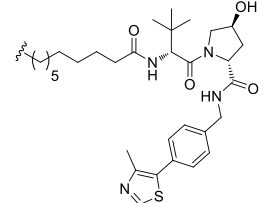
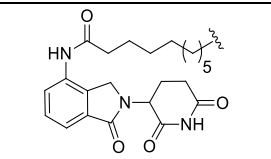
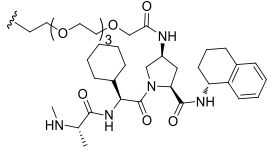
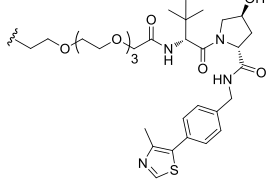
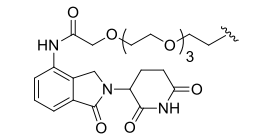
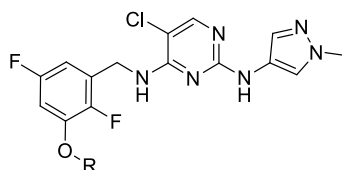
R	HBD	ChromLogD _{7.4}	pIC ₅₀		Fold	
			JAK1 JAK2 JAK3	IL2 PBMC	JAK1 Drop- Off	JAK3 Drop- Off
	6	7.3	7.2 7.1 6.8	5.1	126	50
	5	6.3	7.5 7.1 7.2	5	316	159
	4	5.4	8.7 8.0 8.2	5	5012	1585
	6	5.3	8.0 8.2 7.8	4.7	1995	1259
	5	4.7	7.9 8.2 8.0	4.7	1585	1995
	4	3.7	8.3 8.1 8.1	4.4	7943	5012

Table 52 The physicochemical and biological data associated with the pyrimidine-H series PROTACs, growing from the pyrazole vector. The potency drop-off from the biochemical JAK1 and JAK3 assays to the cellular IL2

PBMC assay were used as a surrogate for cell permeability. pIC₅₀ values are quoted as a mean of multiple, separate experiments (n ≥ 2).



R	HBD	ChromLogD _{7.4}	pIC ₅₀		Fold	
			JAK1 JAK2 JAK3	IL2 PBMC	JAK1 Drop- Off	JAK3 Drop- Off
	6	7.5	7.7 7.2 6.7	5.1	398	40
	5	6.5	8.1 6.6 6.6	5	1259	40
	4	5.6	8.6 7.1 7.3	5.3	1995	100
	6	5.2	8.6 7.6 7.7	4.9	5012	631

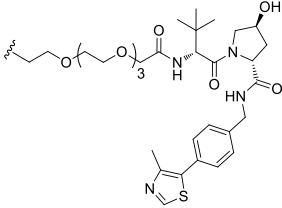
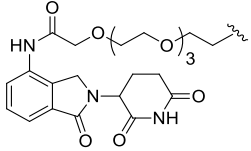
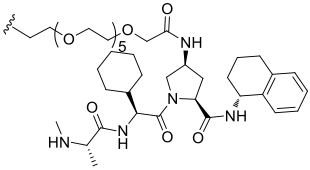
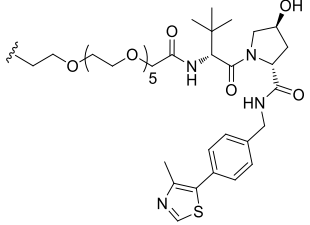
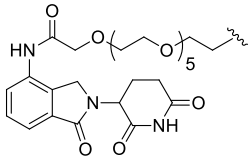
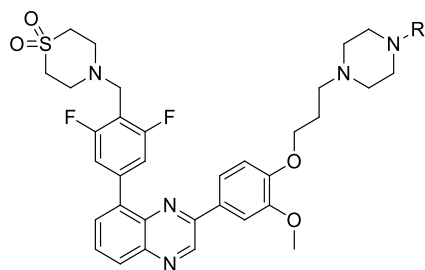
	5	4.5	8.5 7.7 8.0	5.3	1585	501
	4	3.6	8.5 7.6 8.3	4.7	6310	3981
	6	5.2	8.4 7.4 7.6	4.7	5012	794
	5	4.6	8.5 7.6 7.8	5	3162	631
	4	3.7	8.7 7.6 8.1	4.7	10000	2512

Table 53 The physicochemical and biological data associated with the pyrimidine-Bn series PROTACs, growing from the benzylic vector. The potency drop-off from the biochemical JAK1 and JAK3 assays to the cellular IL2 PBMC assay were used as a surrogate for cell permeability. pIC_{50} values are quoted as a mean of multiple, separate experiments ($n \geq 2$).



R	HBD	ChromLogD _{7.4}	pIC ₅₀		Fold	
			JAK1	JAK2	JAK1 IL2 Drop- Off	JAK3 Drop- Off
	4	7.7	6.6 8.7 6.6	5.2	25	25
	3	6.5	7.1 8.7 7.1	4.8	200	200
	2	5.7	7.2 8.4 7.4	4.9	200	316
	4	6.0	7.1 8.7 7.3	5.1	100	159

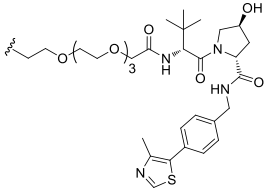
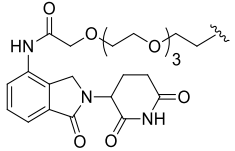
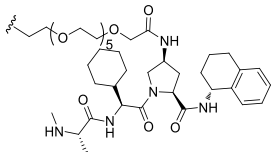
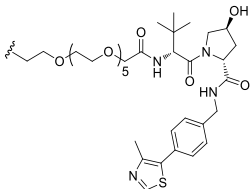
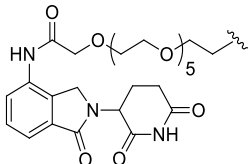
	3	5.3	7.3 8.4 7.3	5.1	159	159
	2	4.5	7.9 9.4 8.1	5	794	1259
	4	5.8	7 8.5 7.3	4.9	126	251
	3	5.2	6.9 8.3 7.1	4.8	126	199
	2	4.5	7.6 8.9 7.7	4.7	794	1000

Table 54 The physicochemical and biological data associated with the quinoxaline series PROTACs. The potency drop-off from the biochemical JAK1 and JAK3 assays to the cellular IL2 PBMC assay were used as a surrogate for cell permeability. pIC₅₀ values are quoted as a mean of multiple, separate experiments ($n \geq 2$).

Across the two series, it was identified that IAP-recruiting PROTACs tended to demonstrate a reduced cellular drop-off from either JAK1 or JAK3, in comparison to the equivalent VHL and CRBN PROTACs. Within the pyrimidine series, HBD count decreases from IAP- (HBD count = 6) to VHL- (HBD count = 5) to CRBN-recruiting (HBD count = 4) PROTACs. However, it is plausible to consider that a HBD within IAP is concealed via an Intramolecular HB, and this concurred with IAP molecular modelling observations. As such, this may mask additional polarity, and IAP may behave as if it exhibits 5 HBDs rather than 6. Conversely, an increase

in ChromLogD_{7.4} was observed from CRBN- to VHL- to IAP-recruiting PROTACs. The increased ChromLogD_{7.4} and potentially masked HBD count of IAP, translates to increased cell permeability, which is evident by the reduced potency drop-off from the biochemical to cellular assay. A similar trend was observed within the quinoxaline series in relation to the correlation between ChromLogD_{7.4} and HBD count, and reduced potency drop-off between the *in vitro* biochemical assay and cellular assay. As expected, switching a 4-PEG linker for a 10C linker had a profound effect on the PROTACs' physicochemical properties, typically increasing the ChromLogD_{7.4} by approximately 170-fold, and reducing the biochemical to cell drop-off.

2.8 Cellular Screening of JAK PROTACs

2.8.1 Initial Degradation Screen

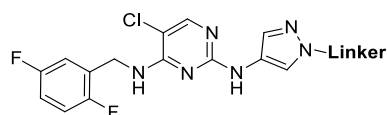
A panel of PROTACs was tested for their ability to degrade endogenous JAK1 and JAK2 by automated western blotting. A human leukemia monocytic cell line, THP-1 cells, was chosen to probe the JAK PROTAC library's degradation aptitude as they are known to express IAP, VHL and CRBN.²¹⁸ Additionally, both literature and GSK precedent identified THP-1 cells to be amenable to PROTAC activity screens.²¹⁹ THP-1 cells express JAK1 and JAK2, however, JAK3 is not expressed.

Due to the time-consuming nature of western blotting, and limited resource it was not feasible to screen each PROTAC against JAK1 and JAK2 to assess their degradation aptitude. Rather, 17 JAK PROTACs were selected based on structural diversity of the JAK warhead, ligation vector, linker composition and length, and ligase binder. Interestingly, of the PROTACs tested, degradation (> 20 % JAK1 and/or JAK2) was observed with PROTACs bearing an IAP E3 ligase binders. VHL- and CRBN-based PROTACs failed to induce JAK1 and/or JAK2 degradation within THP-1 cells (Table 55 – Table 57).

It was hypothesised that IAP-specific JAK degradation could be driven by, amongst others, three variables; differences in binding affinities of the three E3 ligases, expression levels of IAP, VHL and CRBN within THP-1 cells, or more favourable PPIs between JAK and IAP. Differences in binding affinities of the three E3 ligase binders was ruled out as degradation of differing proteins has been established with each of the differing E3 ligase binders.

Furthermore, IAP, CRBN and VHL proteins are expressed similarly within THP-1, which rules out increased IAP expression levels (XIAP within THP-1 cells NX 6.5;²²⁰ CRBN within THP-1 cells NX 13.4;²²¹ VHL within THP-1 cells 20.7;²²² where NX is the normalised expression level, and values > 1 are considered expressed).

Finally, the observed degradation selectivity with IAP is potentially due to formation of more favourable PPIs within the JAK-IAP ternary complex, than PPIs between JAK and CRBN, and JAK and VHL. The more favourable PPI interactions between JAK and IAP could result in more efficient ubiquitination, and thus more efficient target degradation.



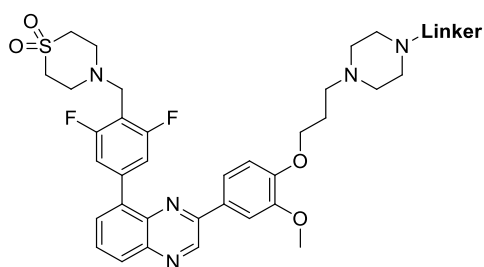
Ligase Binder (R)	Linker	JAK1 and/or JAK2 Degradation
<p>R¹ =</p>		✓
		✓
<p>R² =</p>		✗
		✗
<p>R³ =</p>		✗

Table 55 Identification of JAK1 and/or JAK2 degradation by selected pyrazole vector PROTACs. THP-1 cells were treated 3 μ M of PROTACs and degradation was determined by western blot analysis. Green tick indicates JAK1 and/or JAK2 degradation observed. Red cross indicates no JAK1 or JAK2 degradation observed. n \geq 1; western blots not shown.



Ligase Binder (R)	Linker	JAK1 and/or JAK2 Degradation
<p>R¹ =</p>		✓
		✓
<p>R² =</p>		✗
<p>R² =</p>		✗
		✗

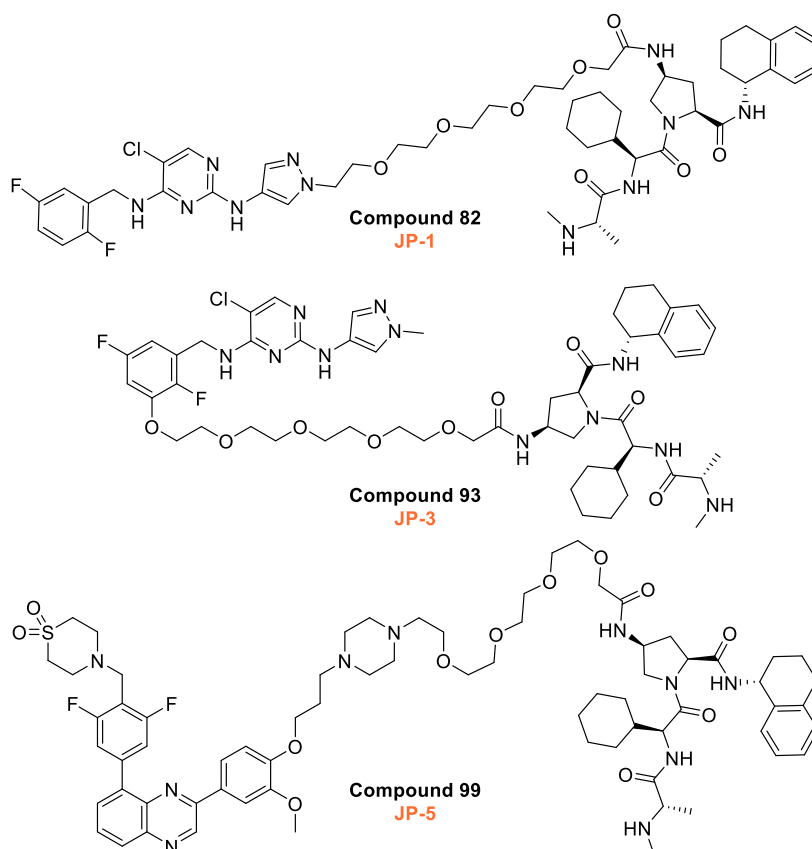
Table 56 Identification of JAK1 and/or JAK2 degradation by selected benzylic vector PROTACs. THP-1 cells were treated 3 μ M of PROTACs and degradation was determined by western blot analysis. Green tick indicates JAK1 and/or JAK2 degradation observed. Red cross indicates no JAK1 or JAK2 degradation observed. $n \geq 1$; western blots not shown.



Ligase Binder (R)	Linker	JAK1 and/or JAK2 Degradation
<p>R¹ =</p>		✓
		✓
<p>R² =</p>		✗
		✗
		✗
<p>R³ =</p>		✗
		✗

Table 57 Identification of JAK1 and/or JAK2 degradation by selected quinoxaline PROTACs. THP-1 cells were treated 3 μ M of PROTACs and degradation was determined by western blot analysis. Green tick indicates JAK1 and/or JAK2 degradation observed. Red cross indicates no JAK1 or JAK2 degradation observed. $n \geq 1$; western blots not shown.

Of our PROTAC library screened, we identified six PROTACs, from here on referred to as JP-1 – JP-6, capable of inducing significant JAK1 and/or JAK2 degradation (Fig 77). Furthermore, significant degradation was observed with both JAK warhead-derived PROTACs, and both vectors from PROTACs derived from the pyrimidine-H and pyrimidine-Bn series. With the initial set of IAP PROTACs identified as capable of inducing JAK1 and/or JAK2, further cellular screening was carried out to explore their degradation aptitude.



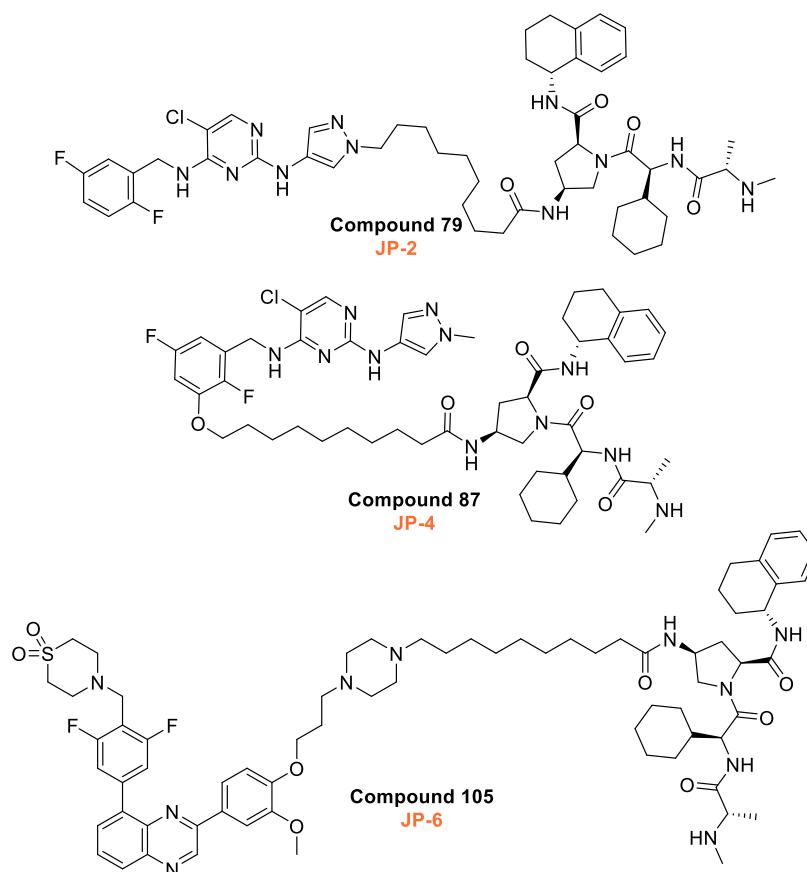


Fig 77 The six PROTACs, JP-1 – JP-6 capable of inducing significant JAK1 and/or JAK2 degradation.

2.8.2 Exploring PROTAC-Mediated JAK Degradation

Interestingly, all six active PROTACs, JP-1 – JP-6, displayed enhanced degradation activity against JAK2 when compared to JAK1 (up to 35 %) (Fig 78). Whilst quinoxaline **63** exhibited a JAK2-biased profile in the biochemical assays, the bias seems unlikely to be the sole cause of enhanced degradation activity at JAK2, since the pyrimidine-H and pyrimidine-Bn derived PROTACs, which exhibit a more pan-JAK profile, also invoked greater JAK2 degradation. The differences in the number and availability of ubiquitination sites can result in an observed difference in activity. However, multiple predicted and experimentally verified ubiquitination sites are present in both JAK1 and JAK2.^{223,224,225,226} Furthermore, differential activity of deubiquitinating enzymes on the target proteins can also contribute to this bias.

The half-life of the POI has a significant impact on the degradation efficiency of PROTACs. Proteins with short a half-life < 6 h are not amenable to PROTAC-mediated degradation since the fast turnover would compensate for any degradation. The experimentally verified half-life of JAK1 in THP-1 cells is 10.6 h and JAK2 is 14.7 h.²²⁷ The 24 h immunoblotting assay format we employed may favour the higher half-life of JAK2, thereby resulting in greater observed JAK2 degradation. Additionally, published findings on JAK1 and JAK2 propose both isoforms are localised exclusively in their proximal membrane-bound states,²²⁸ therefore reducing the likelihood that differential localisation of JAK1 and JAK2 plays a role in the enhanced JAK2 degradation efficiency. However, isoform selectivity has been observed through PROTAC generation of non-selective warheads with PROTACs targeting the BET family,¹⁷³ and protein kinases,^{229,230} through modulation of linker length, E3 ligase binders and ligation point, thus altering the nature of PPIs and the cooperativity of the formed ternary complex.²³¹ As such, the increased degradation of JAK2 over JAK1 could be a result of isoform-specific PPIs resulting in more positive cooperativity of the ternary complex involving JAK2 and IAP, over that of JAK1 and IAP.¹⁷³

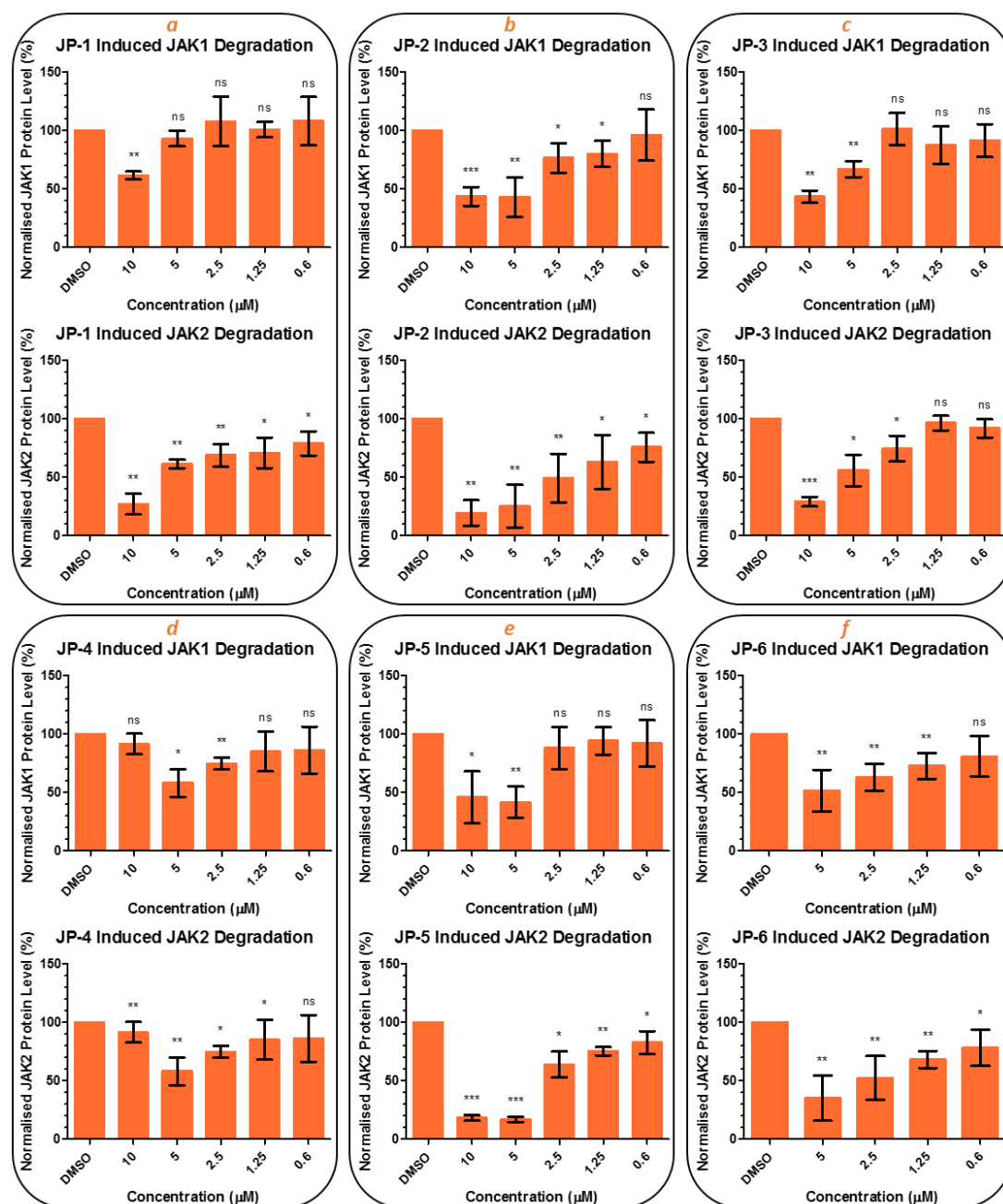


Fig 78 Quantification of JAK1 and JAK2 degradation by PROTACs JP1 – JP6. THP-1 cells were treated with a range of concentrations of PROTACs (0.6 – 10 μ M). Following a 24 h incubation period, the levels of JAK1/JAK2 degradation was determined by automated western blot analysis. % Degradation are quoted as a mean of multiple, separate experiments ($n \geq 3$). One-tailed, student's t-test was performed to assess the significance of JAK1 or JAK2 degradation at individual PROTAC concentrations when compared to the basal JAK1 or JAK2 levels in DMSO, *** = $P < 0.001$; ** = $P < 0.01$; * = $P < 0.05$; ns = non-significant. Individual western blot visualisations are displayed in Appendix Figures 84 – 89.

2.8.3 Implications of Physicochemical Properties on Degradation Efficiency

Within our immunoblotting assays, each PROTAC was tested across a wide range of concentrations (0.6 – 10 μ M) per condition to comprehend the impact of subtle differences of the linker, ligation vector and physicochemical properties between the PROTACs on degradation efficiency.

In relation to HBD count, the most efficient degraders of our library, JP-1 – JP-6, all possessed a HBD count within our targeted physicochemical space for enhanced cell penetration; HBD count ≤ 6 (1 HBD was concealed via an intramolecular HBD if the count was greater than 5). However, the ChromLogD_{7.4} values resided within the upper range and exceeded our initial ChromLogD_{7.4} guideline of 4 – 6. As such, the initial ChromLogD_{7.4} guidelines were deemed suboptimal for cell penetrant JAK PROTACs, and thus were re-evaluated and adjusted. Our data set suggested a ChromLogD_{7.4} range of 5 – 8 for cell penetrant JAK PROTACs (Fig 79).

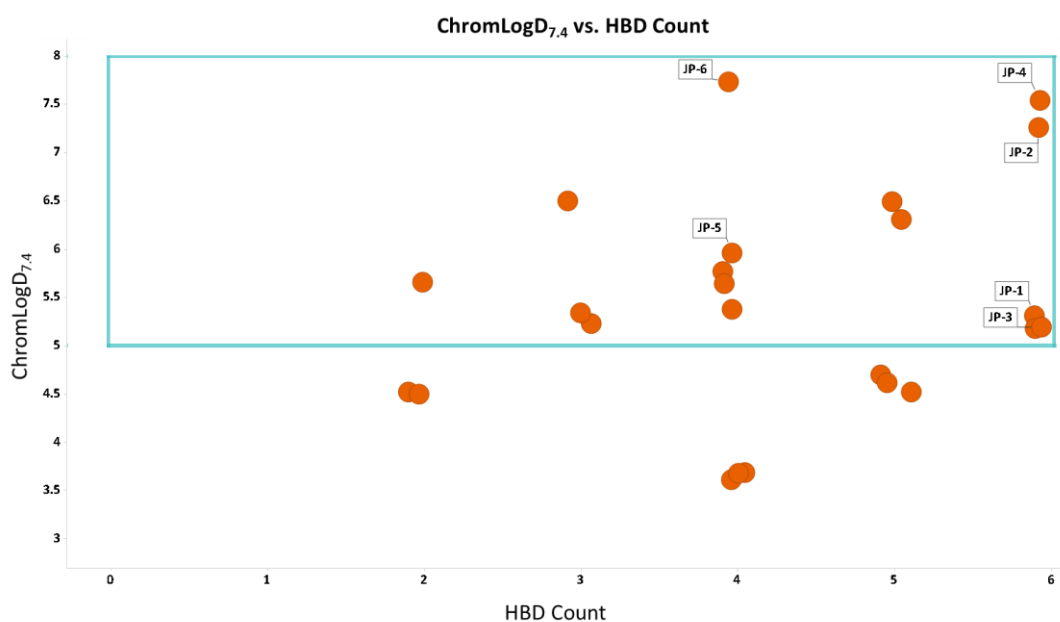


Fig 79 A plot of ChromLogD_{7.4} vs. HBD count of the JAK PROTAC library. JP-1 – JP-6 are labelled. The blue box indicates our preferred physicochemical space for cell penetrant JAK PROTACs.

Perhaps unsurprisingly, JP-1 – JP-6 possessed some of the smallest drop-off in potency values from the JAK1 and JAK3 biochemical assays to the cell (Fig 80). Interestingly, JP-4 was the only PROTAC of the set to exhibit the ‘hook effect’ at 10 μ M at both JAK1 and JAK2. This phenomenon is observed when the state of equilibrium no longer favours ternary complex formation, but rather binary complex formation.¹¹⁴

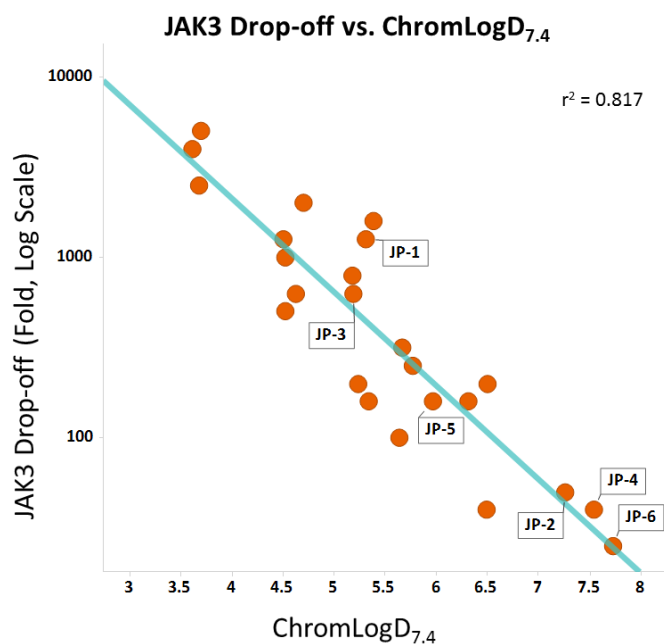
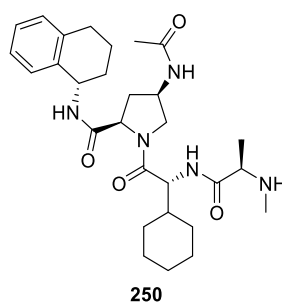


Fig 80 A plot of JAK3 drop-off (fold, log scale) vs. ChromLogD_{7,4} of the JAK PROTAC library. JP-1 – JP-6 are labelled. Blue line indicates straight line fit; $r^2 = 0.817$.

2.8.4 JAK PROTACs Mechanism of Action

To confirm JAK degradation was IAP-dependent, we synthesised negative control JP-6-Inverse, whereby all stereocenters within the IAP moiety had been inverted, thus rendering the PROTAC unable to bind IAP and form the ternary complex required for ubiquitination to occur (Table 58). The inverted IAP enantiomeric analogue was confirmed to be unable to bind IAP within our biochemical IAP assays (BIR2 XIAP $pIC_{50} < 4$, BIR3 XIAP $pIC_{50} < 4$, BIR3 cIAP $pIC_{50} < 4$).



Compound	BIR2 XIAP (pIC ₅₀)	BIR3 XIAP (pIC ₅₀)	BIR3 cIAP1 (pIC ₅₀)
250	< 4	< 4	< 4

Table 58 The binding affinities of IAP associated with inverted acetylated-IAP **250**, displaying a lack of affinity for IAP. pIC₅₀ values are quoted as a mean of multiple, separate experiments (n ≥ 2).

At the highest concentration tested (5 μM), where the analogous active PROTAC, JP-6, could induce JAK1 degradation by 48 % and JAK2 degradation by 65 %, JP-6-Inverse did not significantly decrease JAK1 or JAK2 protein levels (Fig 81a; Fig 81b), thus, indicating IAP-dependent JAK degradation. Additionally, co-treatment of THP-1 cells with JP-6, and increasing concentrations of the free, active IAP ligand dose-dependently ameliorated the ability of JP-6 to reduce JAK1 and JAK2 protein levels (Fig 81a; Fig 81b), conclusively demonstrating the IAP-dependent nature of PROTAC-mediated JAK degradation.

The requirement for the JAK PROTACs to facilitate ternary complex formation between JAK and IAP, to induce JAK degradation, was also investigated. Treatment of THP-1 cells with quinoxaline **63**, (the parent JAK ligand of JP-6), either alone or in combination with the free IAP ligand, had no marked effect on JAK1 or JAK2 protein levels (Fig 81; Fig 81d). This highlights the necessity of ternary complex formation, to induce JAK degradation. Moreover, the inability of quinoxaline **63** to impact JAK1 or JAK2 protein levels contrasts previous reports indicating that JAK inhibitors may cause a downregulation of JAK2 expression.²³²

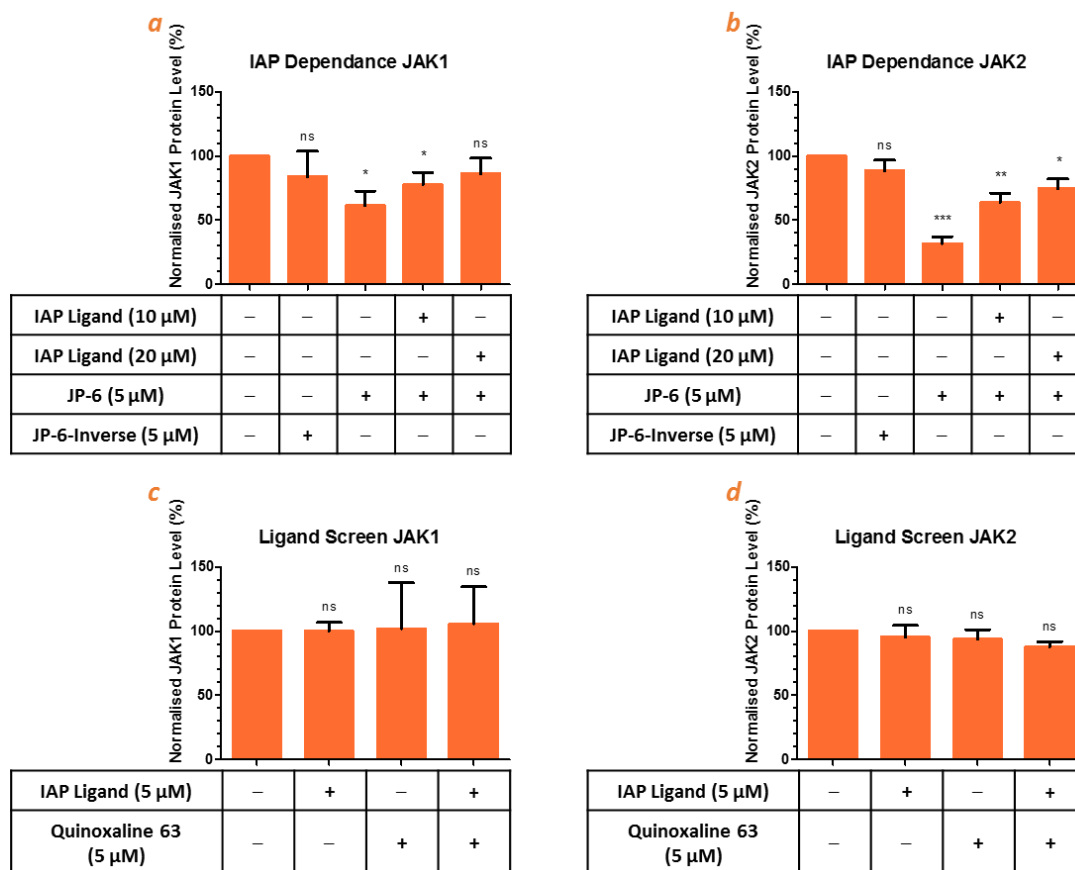


Fig 81 IAP dependence of PROTAC activity. a) and b) JAK1 and JAK2 protein levels determined by automated western blot analysis of JP-6-Inverse, which failed to elicit JAK degradation. Competition between JP-6 with increasing free IAP ligand restores basal JAK protein levels at JAK1 and JAK2. c) and d) JAK1 and JAK2 protein levels determined by automated western blot analysis of the free IAP ligand and Quinoxaline **63**, which failed to illicit JAK degradation. % Degradation values are quoted as a mean of multiple, separate experiments ($n \geq 3$). One-tailed, student's t-test was performed to assess the significance of JAK1 or JAK2 degradation at individual PROTAC concentrations when compared to the basal JAK1 or JAK2 levels in DMSO, *** = $P < 0.001$; ** = $P < 0.01$; * = $P < 0.05$; ns = non-significant. Individual western blot visualisations are displayed in Appendix Figures 90 – 95.

The ubiquitination state of JAK2 in response to JAK PROTAC exposure was next investigated through immunoprecipitation experiments. The proteasome inhibitor, MG132, was employed to facilitate the accumulation of ubiquitinated JAK, and enable its visualisation by immunoblotting. Treatment with JP-6 induced a greater extent of JAK2 ubiquitination compared to DMSO treatment, confirming the ubiquitin-mediated, and proteasome-dependent mechanism of PROTAC-induced JAK2 degradation (Fig 82). Proteasome dependence of PROTAC-mediated JAK1 and JAK2 degradation was further elucidated through co-treatment experiments with JP-6 and MG132 within THP-1 cells. Co-treatment

with MG132 resulted in complete abrogation of PROTAC-mediated JAK1 and JAK2 degradation, resulting in basal protein levels (Fig 83).

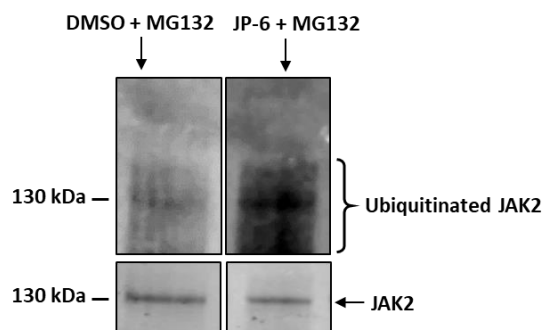


Fig 82 PROTAC JP-6 enhances ubiquitination of JAK2. JP-6 induced a greater extent of JAK2 ubiquitination compared to that of the DMSO-treated control. JAK2 was immunoprecipitated from THP-1 cells and treated with a combination of MG132 and DMSO, or MG132 and JP-6 for 16 h. The blot was probed with antibodies against ubiquitin and JAK2.

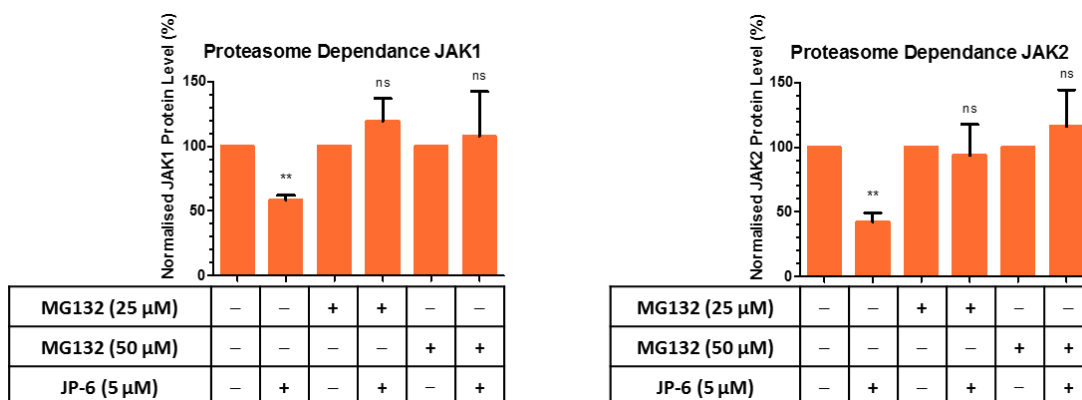


Fig 83 Effect of proteasome inhibitor, MG132, on PROTAC activity. Co-treatment of JP-6 and MG132 failed to elicit JAK1/2 degradation within THP-1 cells. % Degradation values are quoted as a mean of multiple, separate experiments ($n \geq 3$). One-tailed, student's t-test was performed to assess the significance of JAK1 or JAK2 degradation at individual PROTAC concentrations when compared to the basal JAK1 or JAK2 levels in DMSO, *** = $P < 0.001$; ** = $P < 0.01$; * = $P < 0.05$; ns = non-significant. Individual western blot visualisations are displayed in Appendix Figures 96 – 97.

3 Conclusions

In conclusion, literature and GSK-developed JAK inhibitors were evaluated for warhead selection and PROTAC generation, based on target potency, physicochemical properties and structural binding information. The initial set of warheads was triaged based on physicochemical properties, structural binding information, target potency and synthetic tractability. Compounds placed within the 'go' category were further reviewed and two warheads were selected, pyrimidine-OH **58** and quinoxaline **61** with the pyrimidine series possessing multiple ligation vectors. The quinoxaline series was further investigated to identify a more pan-JAK inhibitor which resulted in the identification of quinoxaline **63**. The PROTACs were enumerated with various linkers, ranging in composition and length and the three selected E3 ligase binders, IAP **64**, CRBN **49** and VHL **65**. The overall PROTACs were evaluated *in silico* with respect to their calculated physicochemical properties so as to explore the inner and outer guidelines of the preferred physicochemical space, and were shown to occupy wide physicochemical space.

A novel, significantly shorter route (seven steps decreased to four steps) towards pyrimidine series-PROTACs has been presented, which utilises more recently disclosed chemistries to bypass numerous steps. The decrease in steps removes a number of protection and deprotection steps in addition to the removal of reactions requiring cryogenic control. Furthermore, the overall yield towards the common intermediate **118** was higher within the shorter, novel route (12 %) than the previous route (11 %). Optimisation of the novel route through reversing the order of the etherification and cyanation was achieved, and the overall yield across the two steps was increased. The optimised route allowed for rapid generation of a subset of the JAK PROTAC library, which would have not been possible had the previous route been executed. Cu-catalysed 'click' chemistry proved successful in generating a truncated-PROTAC-like compound, and such technology could provide numerous PROTACs in an array format through the use of the linker-ligase binder toolbox. A linker alkylation followed by amide coupling strategy was employed to furnish the pyrimidine series PROTACs.

The quinoxaline parent compounds were synthesised according to literature precedent; however, the cyclisation step was significantly optimised, providing an increased yield and

bypassing the hazardous H₂O₂ step. Furthermore, a similar synthetic strategy to the pyrimidine PROTACs was utilised to rapidly access a library of quinoxaline PROTACs.

Novel PROTACs derived from pyrimidine-OH **162** were synthesised and profiled within both the JAK biochemical, and cellular assays. The initial set of triazole-linked PROTACs demonstrated poor cell potency which, in part, was hypothesised to be due to the incorporation of the polar triazole group which increased PSA and MW, and decreased ChromLogD_{7.4} resulting in inadequate cell permeability. Modulation of the physicochemical properties to enhance cell permeation was achieved through altering the linker type. Further optimisation efforts were carried out, which were based around pyrimidine-H **78** and pyrimidine-Bn **86** which displayed greater cell potency than pyrimidine-OH **58** and more favoured physicochemical properties in terms of HBD count. Interestingly, all PROTACs synthesised, from each ligation vector were well tolerated by the JAKs.

A vast physicochemical space encompassing and exceeding our initial target space was explored. JP-1 – JP-6 possessed the greatest degradation efficiency and displayed relatively minor drop-off values from the biochemical assays to the cellular assay. The physicochemical properties of these active PROTACs, along with data derived from our PROTAC library suggested ChromLogD_{7.4} guidelines of 5 – 8 for cell penetrant JAK PROTACs. Adopting such guidelines in the design of PROTACs targeting proximal membrane-bound proteins, in combination with a HBD count of ≤ 6 (if one or more HBDs are masked via an intramolecular HB), would likely result in PROTACs with enhanced cellular permeation, and so this work could directly influence the design of PROTACs targeting different proteins.

Significant degradation of JAK1 and JAK2 was achieved across both JAK chemotypes and all explored vectors, documenting the first PROTACs capable of degrading JAK and proximal membrane-bound proteins, thus greatly advancing the PROTAC technology to an unprecedented class of proteins.

Substantial mechanistic work was undertaken to determine the JAK PROTACs mechanism of action. A comparison of JP-6 and JP-6-Inverse within our Western blot assay determined PROTAC-mediated JAK degradation to be IAP-dependent. The IAP-dependent nature of JP-1 – JP-6 mediated JAK degradation was further confirmed via significant reduction of degradation in the presence of a competitive small molecule IAP inhibitor. In addition, it was

confirmed that JAK degradation was proteasome-dependent through co-treatments of JP-6 and MG132. Accumulation of ubiquitinated JAK2 was observed when cells were co-treated with JP-6 and MG132, illustrating enhanced ubiquitination of JAK2 in the presence of JP-6. As such, the mechanistic action of JAK-PROTACs was elucidated.

4 Future Work

Since the JAK PROTAC library displayed enhanced JAK2 degradation over JAK1, a JAK2 cellular assay could be employed, with greater incubation times than the current IL-2 PBMC assay, to probe whether JAK2 degradation has a functional effect.

One of the most exciting and beneficial properties of PROTACs is their ability to induce target protein degradation in a catalytic fashion,¹⁰⁹ and as such, the catalytic nature of the JAK PROTACs could be elucidated to ascertain how many molecules of JAK one PROTAC molecule could degrade.

Whilst significant JAK2 degradation was observed, understanding the cooperativity of the ternary complex could present opportunities to increase degradation potency through generation of more efficient ternary complexes. As such, a JAK cooperativity assay could be developed to determine the cooperativity between the JAK-PROTACs, IAP and JAK. Additionally, a cooperativity assay may provide insights into the observed enhanced JAK2 degradation over JAK1.

Furthermore, the crystal structure of the ternary complex could be solved to provide structural insights into the nature of PPIs within the ternary complex. The crystal structure would allow for structure-enabled modifications of the linker and vectors to enhance the efficiency of the ternary complex.

Further optimisation could be carried out on the JAK PROTAC library through adhering to the entire physicochemical guidelines in attempts to further increase cell penetration. This could be carried out through rigidification of the linker to reduce the number of rotatable bonds, and the removal of PEG linkers to reduce the HBA count. In addition, alternative JAK warheads discussed herein could be functionalised into PROTACs.

It is anticipated that the cell permeable optimisation studies documented herein would be of great use when attempting to design and synthesis cell penetrant PROTACs, regardless of the target. The physicochemical guidelines developed herein have already positively impacted on ongoing GSK PROTAC projects. The JAK PROTACs would also be of wider interests to scientist wanting to utilise these PROTACs to explore the chemical knockdown of JAK, and also to further develop them into therapeutics.

5 Experimental

5.1 Biological Methods

Cell line

THP-1 cells (monocytic cell line derived from an acute monocytic leukaemia patient) were obtained from GSK cell bank and cultured in RPMI-1640 (Gibco) containing 10 % foetal bovine serum, 1 % L-glutamine (Gibco) and 1 % penicillin-streptomycin (Gibco), and grown in a humidified incubator at 37 °C, 5 % CO₂.

Assessment of PROTAC-induced JAK degradation

To determine the effect of PROTACs on JAK protein levels, 5×10^4 THP-1 cells were plated in flat-bottom 96-well plates, treated with the specified concentrations of PROTAC/IAP ligand/JAK ligand in DMSO or an appropriate percentage of DMSO alone (negative control) for the indicated time, then washed twice in PBS to remove any residual compound and harvested in RIPA lysis buffer (Sigma) supplemented with Halt protease inhibitor cocktail (Thermo Fisher Scientific). The lysate was incubated on ice for 30 min prior to centrifugation at 13200 rpm for 10 min at 4 °C. Total protein concentrations of cell lysates were quantitated using the Pierce Bradford assay kit (Thermo Fisher Scientific) and protein concentration was equalised across samples using lysis buffer. The lysates were stored at –80 °C. Protein separation and detection were performed using an automated capillary electrophoresis system (Simple Western system and Compass software; ProteinSimple). Wes separation capillary cartridges 12 - 230 kDa were used. List of antibodies and dilutions used: JAK1, 1:50 (Merck Millipore, cat # 05-154), JAK2, 1:50 (Cell Signalling Technology, cat #3230), β -actin, 1:400 (Sigma-Aldrich, cat # A5441). HRP conjugated secondary antibodies and chemiluminescent substrate were used as per the manufacturer's instructions.

The chemiluminescent signal/peak obtained from each capillary, corresponding to a specific condition, was interpreted and analysed with the Compass software (Protein Simple v3.0.8). For each sample, the signal/peak corresponding to the protein of interest was normalised to that of the loading control, and reported as a ratio. The individual ratios of the compound-

treated samples were normalised to that of the negative control (DMSO treatment), and the data expressed as a percentage. GraphPad Prism 5.0.4 was used for all data analysis. One-tailed Student's t-test was the statistical test performed, and 95 % confidence intervals were used for all statistical analysis.

Immunoprecipitation and Immunoblotting

THP-1 cells were treated with 5 μ M of PROTAC and 50 μ M of the proteasome inhibitor, MG132 (Sigma) for 16 h. Cells treated with MG132 alone were used as the control in this experiment. After 16 h of treatment, the cells were lysed in RIPA before JAK2 was immunoprecipitated. For immunoprecipitation experiments, protein G Dynabeads (Invitrogen) were coupled with 7.5 μ g of JAK2 antibody (JAK2, Merck-Millipore #06-1310) using a 10 min incubation at room temperature, then washed in PBS with Tween-20 (0.05 %) to remove any non-specifically bound protein, and subsequently incubated with the pre-cleared THP-1 lysates overnight, at 4 °C with rotation. After the incubation, the Dynabeads were washed three times in PBS with Tween-20 (0.05 %), resuspended in NuPAGE LDS Sample Buffer (Thermo Fisher Scientific) with 40 mM dithiothreitol (DTT) and then heated at 95 °C for 5 min to elute the immunoprecipitated protein off the beads.

Protein samples were size separated by PAGE and transferred to a nitrocellulose membrane. Membranes were probed with the following antibodies: Ubiquitin (CST #3933S) at 1:1000 dilution, and JAK2 (JAK2: CST #3230) at 1:500 dilution. Secondary anti-mouse (#925-68020) and anti-rabbit (#926-68073, #925-32211) were used, at 1:5000 dilution – Detection was carried out using the Odyssey scanner (Li-COR Biosciences) and the data interpreted and analysed with the 'Image Studio' software (Li-COR Biosciences, v3.2).

5.2 Synthetic Chemistry

5.2.1 General Methods

Nuclear Magnetic Resonance Spectroscopy (NMR)

NMR spectra were recorded using a Bruker AV-400 (^1H = 400 MHz, ^{13}C = 101 MHz, ^{19}F = 376 MHz), AV-500 (^1H = 500 MHz, ^{13}C = 126 MHz) or AV-600 (^1H = 600 MHz, ^{13}C = 151 MHz). Chemical shifts (δ) are reported in parts per million (ppm) relative to tetramethylsilane, DMSO, CHCl_3 or CH_3OD and coupling constants (J) in Hz. The following abbreviations are used for multiplicities: s = singlet; br. s = broad singlet; d = doublet; t = triplet; q = quartet; app. q = apparent quartet; m = multiplet; dd = doublet of doublets; dt = doublet of triplets; spt = septet. If not specifically stated, the NMR experiments were run at 30 °C and ^{19}F and ^{13}C NMR experiments were run in $\{^1\text{H}\}$ -decoupled mode.

Liquid Chromatography Mass Spectrometry (LCMS)

Reaction progress and final LCMS analyses were conducted using one of the three methods below.

LCMS Method A

The liquid chromatography (LC) analysis was conducted on an Acquity UPLC CSH C_{18} column (50 mm \times 2.1 mm internal diameter, 1.7 μm packing diameter) at 40 °C using a 0.5 μL injection volume.

The solvents employed were:

A = 0.1 % v/v solution of formic acid in water.

B = 0.1 % v/v solution of formic acid in acetonitrile.

The gradient employed was:

Time (min)	Flow Rate (mL min ⁻¹)	% A	% B
0.00	1	97	3
1.50	1	5	95
1.90	1	5	95
2.00	1	97	3

The UV detection was a summed signal from a wavelength of 210 nm to 350 nm. Mass spectra were recorded on a Waters ZQ mass spectrometer using alternate-scan positive and negative electrospray ionisation (ES⁺ and ES⁻) with a scan range of 100 to 1000 amu, scan time of 0.27 s and an inter-scan delay of 0.10 s.

LCMS Method B

The liquid chromatography (LC) analysis was conducted on an Acquity UPLC CSH C₁₈ column (50 mm × 2.1 mm internal diameter, 1.7 μm packing diameter) at 40 °C using a 0.3 μL injection volume.

The solvents employed were:

A = 10 mM ammonium bicarbonate in water adjusted to pH 10 with ammonia solution.

B = Acetonitrile.

The gradient employed was:

Time (min)	Flow Rate (mL min ⁻¹)	% A	% B
0.00	1	97	3
0.05	1	97	3
1.50	1	5	95
1.90	1	5	95
2.00	1	97	3

The UV detection was a summed signal from a wavelength of 210 nm to 350 nm. Mass spectra were recorded on a Waters ZQ mass spectrometer using alternate-scan positive and negative electrospray ionisation (ES⁺ and ES⁻) with a scan range of 100 to 1000 amu, scan time of 0.27 s and an inter-scan delay of 0.10 s.

LCMS Method C

The liquid chromatography (LC) analysis was conducted on an Acquity UPLC CSH C₁₈ column (50 mm × 2.1 mm internal diameter, 1.7 µm packing diameter) at 40 °C using a 0.5 µL injection volume.

The solvents employed were:

A = 0.1 % v/v solution of trifluoroacetic acid in water.

B = 0.1 % v/v solution of trifluoroacetic acid in acetonitrile.

The gradient employed was:

Time (min)	Flow Rate (mL min ⁻¹)	% A	% B
0.00	1	95	3
1.50	1	5	95
1.90	1	5	95
2.00	1	95	3

The UV detection was a summed signal from a wavelength of 210 nm to 350 nm. Mass spectra were recorded on a Waters ZQ mass spectrometer using positive electrospray ionisation (ES⁺) with a scan range of 100 to 1000 amu, scan time of 0.27 s and an inter-scan delay of 0.05 s.

High Resolution Mass Spectrometry (HRMS)

High-resolution mass spectra were recorded on a Micromass Q-ToF Ultima hybrid quadrupole time-of-flight mass spectrometer, with analytes separated on an Agilent 1100 Liquid Chromatography equipped with a Phenomenex Luna C₁₈ (2) reversed phase column (100 mm × 2.1 mm, 3 μm packing diameter). LC conditions were 0.5 mL·min⁻¹ flow rate, 35 °C, injection volume 2 – 5 μL. Gradient elution with (A) water containing 0.1 % (v/v) formic acid and (B) acetonitrile containing 0.1% (v/v) formic acid. Gradient conditions were initially 5 % B, increasing linearly to 100% B over 6 min, remaining at 100 % B for 2.5 min then decreasing linearly to 5 % B over 1 min followed by an equilibration period of 2.5 min prior to the next injection. Mass to charge ratios (*m/z*) are reported in Daltons.

Mass Directed Automated Preparative HPLC (MDAP)

MDAP purifications were conducted on a Waters FractionLynx system comprising of a Waters 600 pump with extended pump heads, Waters 2700 autosampler, Waters 996 diode array and Gilson 202 fraction collector. The high performance liquid chromatography (HPLC) separation was conducted on an Xselect C₁₈ column (150 mm × 30 mm internal diameter, 5 μm packing diameter) at ambient temperature, utilising an appropriate solvent system and

elution gradient as determined by analytical LCMS (i.e. formic acid, ammonium bicarbonate, or trifluoroacetic acid modifier). Mass spectra were recorded on a Waters ZQ mass spectrometer using alternate-scan positive and negative electrospray ionisation (ES^+ and ES^-) with a scan range of 150 to 1500 amu, scan time of 0.50 s and an inter-scan delay of 0.25 s. The software used was MassLynx 3.5 with FractionLynx 4.1.

Column Chromatography

Automated column chromatography was conducted on a Teledyne Isco Combiflash Rf system using RediSep Rf Silica cartridges (for normal phase), or Biotage KP-C₁₈-HS cartridges (for reverse phase) of the correct size. Elution utilised standard HPLC grade solvents provided by Sigma Aldrich, with the desired modifier (for reverse phase) added in-house, unless otherwise stated.

Infrared Spectroscopy (IR)

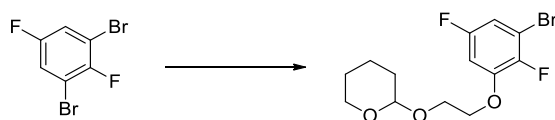
IR spectra were recorded using a Perkin Elmer Spectrum One spectrometer. Absorption frequencies (ν_{\max}) are reported in wavenumbers (cm^{-1}).

Melting Point

Melting points were measured on a Stuart SMP10 melting point apparatus

5.2.2 Synthesis of Novel Compounds

2-(2-(3-Bromo-2,5-difluorophenoxy)ethoxy)tetrahydro-2H-pyran (130)



1,3-Dibromo-2,5-difluorobenzene **128** (200 mg, 0.736 mmol), $[\text{Ir}\{\text{dF}(\text{CF}_3)\text{ppy}\}_2(\text{dtbpy})]\text{PF}_6$ (8 mg, 7.13 μmol), K_2CO_3 (102 mg, 0.736 mmol), and quinuclidine (8 mg, 0.072 mmol) were sealed within a vial and acetonitrile (3 mL) was added. A solution of $\text{Ni}(\text{glyme})\text{Cl}_2$ (8 mg, 0.036 mmol) and 4,4'-di-*tert*-butyl-2,2'-dipyridyl (10 mg, 0.037 mmol) in acetonitrile (1.5 mL) was

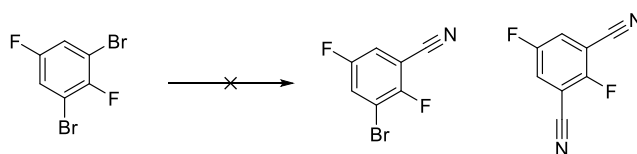
subsequently added and the reaction mixture was placed under nitrogen before the addition of 2-((tetrahydro-2H-pyran-2-yl)oxy)ethan-1-ol (0.110 mL, 0.809 mmol). The reaction mixture was then cooled to $-78\text{ }^{\circ}\text{C}$ and degassed via vacuum evacuation (5 min), backfilled with nitrogen, and then warmed to room temperature. This process was repeated three times and the sealed reaction mixture was irradiated with two 23 W, 1500 lumens, 6500K CFLs placed approximately 1 cm away from the reaction vessel at room temperature for 7 h, whilst being fan-cooled. Further $[\text{Ir}\{\text{dF}(\text{CF}_3)\text{ppy}\}_2(\text{dtbpy})]\text{PF}_6$ (8 mg, 3.57 μmol) and quinuclidine (4 mg, 0.036 mmol) within acetonitrile (1.5 mL) was sealed within a vial. A solution of $\text{Ni}(\text{glyme})\text{Cl}_2$ (4 mg, 0.018 mmol) and 4,4'-di-*tert*-butyl-2,2'-dipyridyl (5 mg, 0.019 mmol) in acetonitrile (1 mL) was subsequently added to the Ir catalyst solution and was placed under nitrogen before the addition of 2-((tetrahydro-2H-pyran-2-yl)oxy)ethan-1-ol (0.110 mL, 0.809 mmol). The mixture was then cooled to $-78\text{ }^{\circ}\text{C}$ and degassed via vacuum evacuation (5 min), backfilled with nitrogen, and then warmed to room temperature. This process was repeated three times and the sealed mixture was transferred to the reaction mixture. The irradiated mixture was stirred at room temperature for 18 h. Further 2-((tetrahydro-2H-pyran-2-yl)oxy)ethan-1-ol (0.110 mL, 0.809 mmol) was added and the irradiated reaction mixture was stirred for a further 2 h. Further $[\text{Ir}\{\text{dF}(\text{CF}_3)\text{ppy}\}_2(\text{dtbpy})]\text{PF}_6$ (8 mg, 3.57 μmol) and quinuclidine (4 mg, 0.036 mmol) were sealed within a vial and acetonitrile (1.5 mL) was added. A solution of $\text{Ni}(\text{glyme})\text{Cl}_2$ (4 mg, 0.018 mmol) and 4,4'-di-*tert*-butyl-2,2'-dipyridyl (5 mg, 0.019 mmol) in acetonitrile (1 mL) was subsequently added to the Ir catalyst mixture placed under nitrogen before the addition of 2-((tetrahydro-2H-pyran-2-yl)oxy)ethan-1-ol (0.110 mL, 0.809 mmol). The catalyst mixture was then cooled to $-78\text{ }^{\circ}\text{C}$ and degassed via vacuum evacuation (5 min), backfilled with nitrogen, and then warmed to room temperature. This process was repeated three times and the mixture was added to the irradiated reaction mixture and stirred at room temperature for 48 h. The reaction mixture was diluted with water (10 mL) and extracted with ethyl acetate ($3 \times 15\text{ mL}$). The organic layers were combined, passed through a hydrophobic frit and the solvent was removed *in vacuo*. The residue was purified by normal phase column chromatography (0 – 50 % ethyl acetate in cyclohexane, 120 g SiO_2 , 10 column volumes) to afford 2-(2-(3-bromo-2,5-difluorophenoxy)ethoxy)tetrahydro-2H-pyran **130** (83 mg, 0.246 mmol, 34 % yield) as a colourless oil. $^1\text{H NMR}$ (400 MHz, $\text{DMSO-}d_6$) = ppm 7.16 - 7.32 (2H, m), 4.57 - 4.72 (1H, m), 4.24 - 4.29 (2H, m), 3.88 - 3.95 (1H, m), 3.69 - 3.79 (2H, m), 3.40 - 3.47 (1H, m), 1.57 - 1.73

(2H, m), 1.40 - 1.51 (4H, m); LCMS (Method B): $t_R = 1.35$ min, $[M+H]^+$ No ionisation, (92 % purity).

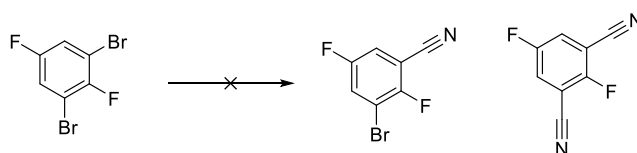
2,5-Difluoro-3-(2-((tetrahydro-2H-pyran-2-yl)oxy)ethoxy)benzonitrile (144)



2-(2-(3-Bromo-2,5-difluorophenoxy)ethoxy)tetrahydro-2H-pyran **130** (368 mg, 1.091 mmol), potassium acetate (11 mg, 0.112 mmol), t BuXPhos (14 mg, 0.033 mmol), t BuXPhos Pd G1 (23 mg, 0.033 mmol) and potassium hexacyanoferrate (II) trihydrate (231 mg, 0.546 mmol) were stirred together in ethanol (2 mL) and water (2 mL) within a sealed vial. The vial was evacuated and purged with nitrogen three times and the reaction mixture was heated to 90 °C for 16 h. Further t BuXPhos (14 mg, 0.033 mmol), t BuXPhos Pd G1 (23 mg, 0.033 mmol) and potassium hexacyanoferrate (II) trihydrate (231 mg, 0.546 mmol) were added and the vial was evacuated and purged with nitrogen three times and the reaction mixture was heated to 90 °C for 5 h. The solvent was removed *in vacuo* and the residue was diluted with water (20 mL) and extracted with ethyl acetate (3 × 20 mL). The organic layers were combined, dried over a hydrophobic frit and the solvent was removed *in vacuo*. The residue was purified by normal phase column chromatography (0 – 20 % ethyl acetate in cyclohexane, 40 g SiO₂, 10 column volumes) to yield 2,5-difluoro-3-(2-((tetrahydro-2H-pyran-2-yl)oxy)ethoxy)benzonitrile **144** (280 mg, 0.988 mmol, 91 % yield) as a colourless oil. ¹H NMR (400 MHz, DMSO-*d*₆) = ppm 7.63 (1H, ddd, $J = 10.4, 7.2, 2.9$ Hz), 7.42 - 7.48 (1H, m), 4.65 (1H, app. t, $J = 3.2$ Hz), 4.33 - 4.22 (2H, m), 3.90 - 3.97 (1H, m), 3.70 - 3.78 (2H, m), 3.40 - 3.48 (1H, m), 1.57 - 1.70 (2H, m), 1.41 - 1.54 (4H, m); LCMS (Method B): $t_R = 1.17$ min, $[M+H]^+$ No ionisation, (97 % purity).

2,5-Difluoroisophthalonitrile (146)

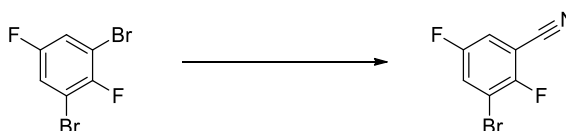
1,3-Dibromo-2,5-difluorobenzene **128** (200 mg, 0.736 mmol), potassium acetate (7.22 mg, 0.074 mmol), ^tBuXPhos (9.37 mg, 0.022 mmol), ^tBuXPhos Pd G1 (25.3 mg, 0.037 mmol) and potassium hexacyanoferrate (II) trihydrate (155 mg, 0.368 mmol) were stirred together in ethanol (1.400 mL) and water (1.4 mL) within a sealed vial. The vial was evacuated and purged with nitrogen three times and the reaction mixture was heated in a Biotage Initiator microwave for 1 h at 90 °C using a very high absorption setting. The reaction mixture was allowed to cool to room temperature. Further ^tBuXPhos Pd G1 (25.3 mg, 0.037 mmol) was added and the vial was evacuated and purged with nitrogen three times and the reaction mixture was heated in a Biotage Initiator microwave for 2 h at 90 °C using a very high absorption setting. The reaction mixture was allowed to cool to room temperature. The solvent was removed *in vacuo* and the residue was diluted with water (20 mL) and extracted with ethyl acetate (3 × 20 mL). The organic layers were combined, passed through a hydrophobic frit and the solvent was removed *in vacuo*. The residue was purified by normal phase column chromatography (0 – 20 % ethyl acetate in cyclohexane, 40 g SiO₂, 10 column volumes) to yield 2,5-difluoroisophthalonitrile **146** (158 mg, 0.963 mmol, quantitative yield) as a white solid. ¹H NMR (400 MHz, DMSO-*d*₆) δ = 8.43 (2H, dd, *J* = 8.1, 5.1 Hz); LCMS (Method B): *t*_R = 0.84 min, [M-H]⁻ 163, (100 % purity).

2,5-Difluoroisophthalonitrile (146)

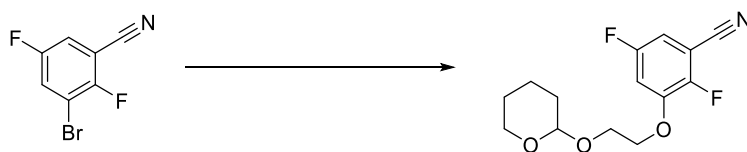
1,3-Dibromo-2,5-difluorobenzene **128** (100 mg, 0.368 mmol), ^tBuXPhos Pd G1 (5 mg, 7.28 μmol), Zn(CN)₂ (29 mg, 0.247 mmol), THF (0.2 mL) and water (1 mL) were sealed within a vial and the vial was evacuated and purged three times with nitrogen. The reaction mixture was

stirred rapidly (such that the two phases appeared homogenous and the vortex was clearly visible) at room temperature. LCMS analysis indicated formation of 2,5-difluoroisophthalonitrile **146**, but no desired product formation and so the reaction was abandoned.

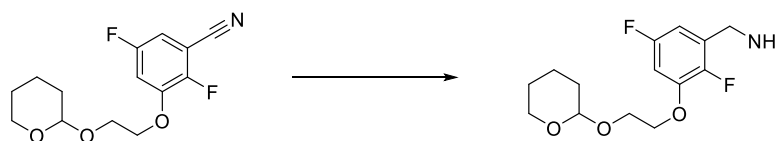
3-Bromo-2,5-difluorobenzonitrile (**145**)



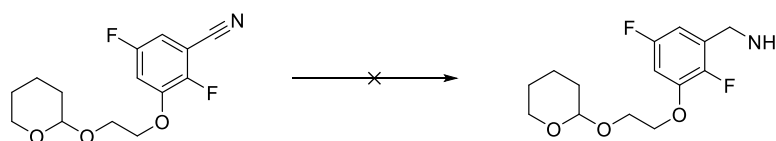
i PrMgCl·LiCl (3.11 mL of 1.3 M solution in THF, 4.05 mmol) in THF (4 mL) was stirred at -20 °C for 5 min under a nitrogen atmosphere. 1,3-Dibromo-2,5-difluorobenzene **128** (1 g, 3.68 mmol) in THF (1 mL) was added dropwise and the reaction mixture was stirred for 20 min. DMF (0.427 mL, 5.51 mmol) was added dropwise and the reaction mixture was stirred for 2 h at 0 °C. 28 % Ammonium hydroxide (2.86 mL, 25.7 mmol) and iodine (1.867 g, 7.36 mmol) were added and the reaction mixture was stirred for 1 h at room temperature. The reaction mixture was poured onto 28 % aqueous sodium thiosulfate (30 mL) and extracted with DCM (2 \times 30 mL). The organic layers were combined, passed through a hydrophobic frit and the solvent was removed *in vacuo*. The residue was purified by normal phase column chromatography (0 – 80 % EtOAc in cyclohexane, 80 g SiO₂, 15 column volumes) to afford 3-bromo-2,5-difluorobenzonitrile **145** (533 mg, 67 % yield) as a white solid. M.pt.: 49 - 51 °C; ν_{\max} (neat): 3268, 2110, 1547 cm^{-1} ; ^1H NMR (400 MHz, CDCl₃) δ = 7.58 (1H, ddd, J = 7.2, 4.4, 3.1 Hz), 7.32 (1H, ddd, J = 7.2, 4.2, 3.1 Hz); ^{13}C NMR (101 MHz, CDCl₃) δ = 157.5 (dd, J = 251.6, 3.7 Hz), 156.7 (dd, J = 256.0, 2.9 Hz), 126.0 (d, J = 26.4 Hz), 118.8 (d, J = 27.1 Hz), 111.9 (d, J = 2.9 Hz), 111.1 (dd, J = 22.7, 10.3 Hz), 103.2 (dd, J = 19.1, 10.3 Hz); ^{19}F NMR (376 MHz, CDCl₃) δ = -105.43 (d, J = 13.9 Hz), -113.58 (d, J = 13.9 Hz); LCMS (Method B): t_{R} = 1.08 min, $[\text{M}+\text{H}]^+$ No ionisation, (100 % purity).

2,5-Difluoro-3-(2-((tetrahydro-2H-pyran-2-yl)oxy)ethoxy)benzonitrile (144)

3-Bromo-2,5-difluorobenzonitrile **145** (200 mg, 0.771 mmol), [Ir{dF(CF₃)ppy}₂(dtbpy)]PF₆ (9 mg, 8.02 μmol), K₂CO₃ (107 mg, 0.771 mmol) and quinuclidine (9 mg, 0.081 mmol) were sealed within a vial and acetonitrile (3 mL) was added. A solution of Ni(glyme)Cl₂ (9 mg, 0.041 mmol) and 4,4'-di-*tert*-butyl-2,2'-dipyridyl (11 mg, 0.041 mmol) in acetonitrile (2.6 mL) was subsequently added and the reaction mixture was placed under nitrogen before the addition of 2-((tetrahydro-2H-pyran-2-yl)oxy)ethan-1-ol (0.157 mL, 1.156 mmol). The reaction mixture was cooled to -78 °C and degassed via vacuum evacuation (5 min), backfilled with nitrogen, and then warmed to room temperature. This process was repeated three times and the sealed reaction mixture was irradiated with two 23 W, 1500 lumens, 6500K CFLs placed approximately 1 cm away from the reaction vessel at room temperature for 23 h, whilst being fan-cooled. The reaction mixture was diluted with water (30 mL) and extracted with ethyl acetate (3 × 30 mL). The organic layers were combined, passed through a hydrophobic frit and the solvent was removed *in vacuo*. The residue was dissolved in methanol:DMSO 1:1 (3 mL) and purified by reverse phase column chromatography (30 – 95 % MeCN in H₂O + 0.1% (NH₄)₂CO₃, 60 g C₁₈, 10 column volumes) to afford 2,5-difluoro-3-(2-((tetrahydro-2H-pyran-2-yl)oxy)ethoxy)benzonitrile **144** (133 mg, 61 % yield) as a pale orange oil. ν_{\max} (neat): 3091, 2944, 2873, 2240, 1593, 1495, 1034 cm⁻¹; ¹H NMR (400 MHz, CDCl₃) δ = 7.07 (1H, ddd, *J* = 9.7, 6.5, 2.9 Hz), 6.89 (1H, ddd, *J* = 7.2, 4.0, 2.9 Hz), 4.71 (1H, t, *J* = 3.2 Hz), 4.24 - 4.33 (2H, m), 4.07 - 4.15 (1H, m), 3.81 - 3.93 (2H, m), 3.51 - 3.60 (1H, m), 1.71 - 1.87 (2H, m), 1.57 - 1.68 (4H, m); ¹³C NMR (101 MHz, CDCl₃) δ = 158.0 (dd, *J* = 246.1, 3.3 Hz), 150.6 (dd, *J* = 257.1, 3.3 Hz), 148.7 (t, *J* = 10.6 Hz), 112.9 (d, *J* = 2.9 Hz), 109.6 (d, *J* = 27.1 Hz), 108.5 (dd, *J* = 27.5, 2.6 Hz), 102.1 (dd, *J* = 15.3, 12.1 Hz), 99.2, 69.9, 65.5, 62.2, 30.4, 25.3, 19.3; ¹⁹F NMR (376 MHz, CDCl₃) δ = -113.27 (d, *J* = 13.9 Hz), -131.54 (d, *J* = 13.9 Hz); LCMS (Method B): *t*_R = 1.18 min, [M+H]⁺ No ionisation, (95 % purity).

(2,5-Difluoro-3-(2-((tetrahydro-2H-pyran-2-yl)oxy)ethoxy)phenyl)methanamine 150

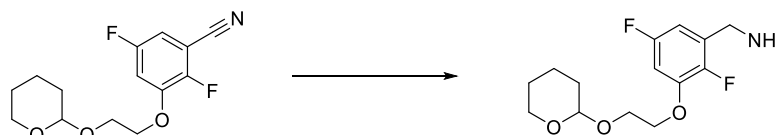
2,5-Difluoro-3-(2-((tetrahydro-2H-pyran-2-yl)oxy)ethoxy)benzonitrile **144** (160 mg, 0.565 mmol) was stirred in THF (8 mL) over an NaCl-ice-water bath for 5 min under a nitrogen atmosphere. LiAlH₄ (1.3 mL of a 2.2 M solution in 2-MeTHF, 2.86 mmol) was added dropwise over 2 min and the reaction mixture was stirred for 16 h. The reaction mixture was slowly diluted with water (5 mL) and 2 M aqueous NaOH (2.5 mL). After 5 min, further water (5 mL) was added and the reaction mixture was stirred at room temperature for 30 min under a nitrogen atmosphere. The reaction mixture was filtered, and the filtrate was collected and concentrated *in vacuo*. The residue was purified by reverse phase column chromatography (15 – 55 % MeCN in H₂O + 0.1% (NH₄)₂CO₃, 30 g C₁₈, 12 column volumes) to afford (2,5-difluoro-3-(2-((tetrahydro-2H-pyran-2-yl)oxy)ethoxy)phenyl)methanamine **150** (44 mg, 0.153 mmol, 27 % yield) as a yellow gum. ¹H NMR (400 MHz, DMSO-*d*₆) δ = 6.98 (1H, ddd, *J* = 10.2, 7.0, 2.9 Hz), 6.84 - 6.92 (1H, m), 4.63 - 4.69 (1H, m), 4.18 - 4.23 (2H, m), 3.88 - 3.95 (1H, m), 3.68 - 3.81 (4H, m), 3.41 - 3.48 (1H, m), 2.04 (2H, br s), 1.58 - 1.75 (2H, m), 1.41 - 1.54 (4H, m); LCMS (Method B): *t*_R = 0.93 min, [M+H]⁺ 288, (95 % purity).

(2,5-Difluoro-3-(2-((tetrahydro-2H-pyran-2-yl)oxy)ethoxy)phenyl)methanamine 150

To a COWare tube, 10 % Pd/C (9.02 mg, 8.47 μmol) and 2,5-difluoro-3-(2-((tetrahydro-2H-pyran-2-yl)oxy)ethoxy)benzonitrile **144** (240 mg, 0.847 mmol) in cyclohexane (17 mL) were added to one tube under nitrogen and that tube was sealed to the atmosphere. 2 M aqueous HCl (6.35 mL, 25.4 mmol) and zinc (554 mg, 8.47 mmol) were added under a flow of nitrogen to the other tube which was subsequently sealed to the atmosphere. The reaction mixture

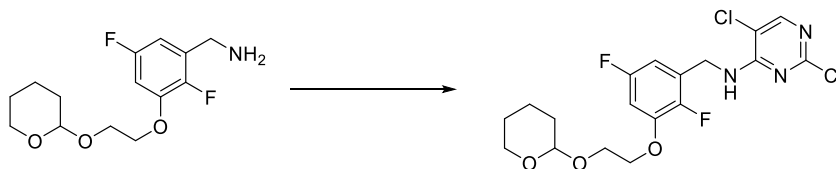
was left to stir at room temperature for 16 h. The reaction mixture was filtered over Celite and washed with ethyl acetate (20 mL). The solvent was removed *in vacuo* and dissolved in cyclohexane (20 mL). The solution was looped through a H-Cube (1 mL/ min, 50 bar, 70 °C, Pd/C cat cart) for 1 h. The reaction was abandoned due to lack of product formation.

(2,5-Difluoro-3-(2-((tetrahydro-2H-pyran-2-yl)oxy)ethoxy)phenyl)methanamine 150



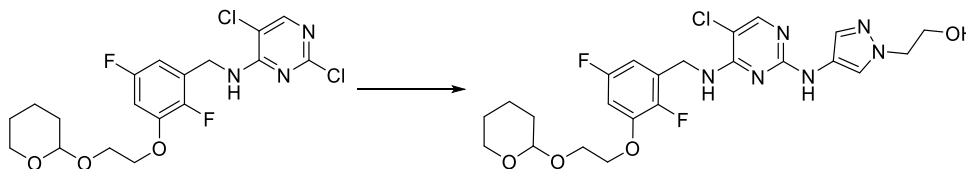
2,5-Difluoro-3-(2-((tetrahydro-2H-pyran-2-yl)oxy)ethoxy)benzonitrile **144** (100 mg, 0.353 mmol) in THF (3.53 mL) was added borane-THF complex (1.412 mL, 1.412 mmol) dropwise over 2 min followed by NaBH₄ (53.4 mg, 1.412 mmol) and the reaction mixture stirred for 16 h at room temperature under a nitrogen atmosphere. The reaction mixture was quenched with MeOH (5 mL) and solvent removed *in vacuo*. The residue was purified by reverse phase prep column chromatography (30 - 85 % MeCN in H₂O + 0.1% (NH₄)₂CO₃, Xbridge C₁₈, 25 mL/min, 45 min) to afford (2,5-difluoro-3-(2-((tetrahydro-2H-pyran-2-yl)oxy)ethoxy)phenyl)methanamine (58 mg, 0.202 mmol, 57 % yield) **150** as an colourless oil. ¹H NMR (400 MHz, CDCl₃) δ = 6.92 (1H, ddd, *J* = 11.1, 9.2, 5.4 Hz), 6.60 - 6.76 (1H, m), 4.68 (1H, t, *J* = 3.6 Hz), 4.28 - 4.42 (2H, m), 3.97 - 4.07 (1H, m), 3.82 - 3.89 (1H, m), 3.70 - 3.79 (1H, m), 3.49 - 3.56 (1H, m), 1.70 - 1.88 (2H, m), 1.49 - 1.66 (6H, m); ¹³C NMR (101 MHz, CDCl₃) δ = 156.6 (dd, *J* = 241.4, 2.2 Hz), 151.5 (dd, *J* = 242.1, 2.9 Hz), 145.2 (dd, *J* = 11.7, 8.1 Hz), 125.5 (dd, *J* = 19.1, 1.5 Hz), 115.0 (dd, *J* = 22.0, 10.3 Hz), 109.8 (dd, *J* = 25.7, 7.3 Hz), 98.9, 73.2, 73.1, 66.4, 62.2, 30.5, 25.4, 19.3; ¹⁹F NMR (376 MHz, CDCl₃) δ = -123.28 (d, *J* = 15.6 Hz), -134.57 (d, *J* = 15.6 Hz); LCMS (Method B): *t_R* = 0.98 min, [M+H]⁺ 288, (100 % purity); HRMS: (C₁₄H₁₉F₂NO₃) [M+H]⁺ requires 288.1411, found [M+H]⁺ 288.1420.

2,5-Dichloro-*N*-(2,5-difluoro-3-(2-((tetrahydro-2*H*-pyran-2-yl)oxy)ethoxy)benzyl)-pyrimidin-4-amine (118)



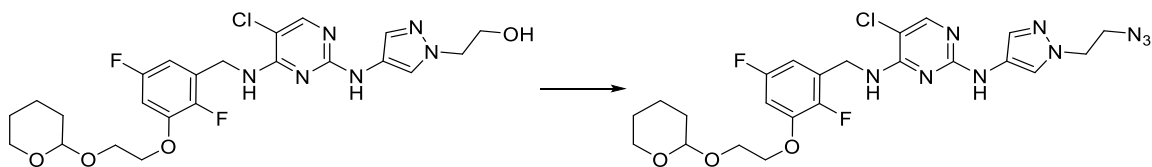
(2,5-Difluoro-3-(2-((tetrahydro-2*H*-pyran-2-yl)oxy)ethoxy)phenyl)methanamine **150** (42 mg, 0.146 mmol), 2,4,5-trichloropyrimidine (20 μ L, 0.175 mmol) and DIPEA (38.3 μ L, 0.219 mmol) were stirred together in isopropanol (0.4 mL) under a nitrogen atmosphere at room temperature for 2 h. The solvent was removed *in vacuo* and the residue was diluted with aqueous saturated sodium hydrogen carbonate solution (10 mL) and extracted with DCM (3 \times 10 mL). The organic layers were combined, passed through a hydrophobic frit and the solvent was removed *in vacuo*. The residue was purified by normal phase column chromatography (0 – 100 % TBME in cyclohexane, 12 g SiO₂, 10 column volumes) to yield 2,5-dichloro-*N*-(2,5-difluoro-3-(2-((tetrahydro-2*H*-pyran-2-yl)oxy)ethoxy)benzyl)-pyrimidin-4-amine **118** (49 mg, 0.073 mmol, 50 % yield) as a yellow solid. ¹H NMR (400 MHz, CDCl₃) δ = 8.06 (1H, s), 6.65 - 6.77 (2H, m), 5.77 - 5.92 (1H, m), 4.74 (2H, d, *J* = 5.4 Hz), 4.69 - 4.72 (1H, m), 4.19 - 4.24 (2H, m), 4.02 - 4.12 (1H, m), 3.80 - 3.92 (2H, m), 3.46 - 3.61 (1H, m), 1.70 - 1.88 (2H, m), 1.50 - 1.66 (4H, m); LCMS (Method B): *t*_R = 1.29 min, [M+H]⁺ 434, 436 & 438, (65 % purity). The material was used crude in the subsequent reaction.

2-(4-((5-Chloro-4-((2,5-difluoro-3-(2-((tetrahydro-2H-pyran-2-yl)oxy)ethoxy)benzyl)pyrimidin-2-yl)amino)-1H-pyrazol-1-yl)ethanol (156)



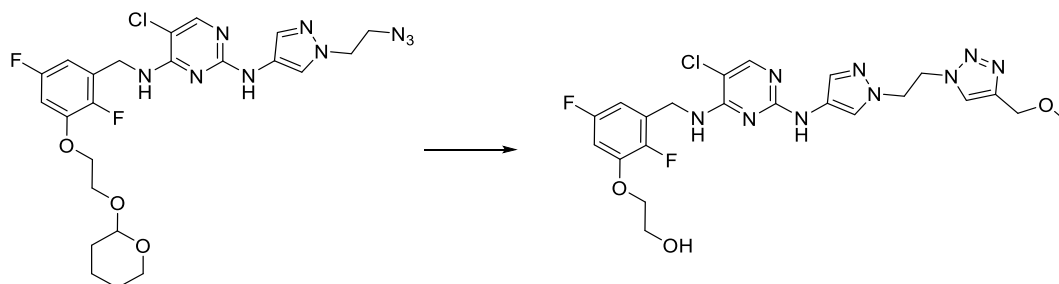
2,5-Dichloro-*N*-(2,5-difluoro-3-(2-((tetrahydro-2*H*-pyran-2-yl)oxy)ethoxy)benzyl)pyrimidin-4-amine **118** (625 mg, 1.439 mmol), DIPEA (1.508 mL, 8.64 mmol) and 2-(4-amino-1*H*-pyrazol-1-yl)ethan-1-ol (274 mg, 2.159 mmol) were sealed within a vessel and heated in a Biotage Initiator microwave for 6 h at 150 °C using a very high absorption setting. The reaction mixture was allowed to cool to room temperature. The solvent was removed *in vacuo* and the residue was diluted with saturated aqueous sodium bicarbonate solution (30 mL) and extracted with ethyl acetate (3 × 30 mL). The organic layers were combined, passed through a hydrophobic frit and the solvent was removed *in vacuo*. The residue was dissolved in methanol:DMSO 1:1 (2 mL) and purified by reverse phase chromatography (30 – 95% MeCN in H₂O + 0.1% (NH₄)₂CO₃, 60 g C₁₈, 10 column volumes) to afford 2-(4-((5-chloro-4-((2,5-difluoro-3-(2-((tetrahydro-2*H*-pyran-2-yl)oxy)ethoxy)benzyl)amino)-pyrimidin-2-yl)amino)-1*H*-pyrazol-1-yl)ethanol **156** (344 mg, 0.655 mmol, 46 % yield) as a white solid. M.pt.: 158 - 160 °C; ν_{\max} (neat): 3450, 3273, 2950, 2871 cm⁻¹; ¹H NMR (400 MHz, CDCl₃) δ = 7.90 (1H, s), 7.64 (1H, br s), 7.42 (1H, s), 6.66 - 6.75 (2H, m), 6.58 (1H, ddd, *J* = 8.2, 5.0, 2.9 Hz), 5.64 (1H, br t, *J* = 5.9 Hz), 4.68 - 4.77 (3H, m), 4.05 - 4.25 (6H, m), 3.80 - 4.02 (4H, m), 3.49 - 3.58 (1H, m), 1.72 - 1.85 (2H, m), 1.50 - 1.64 (4H, m); ¹³C NMR (151 MHz, MeOD) δ = 158.4, 158.6 (dd, *J* = 241.0, 2.8 Hz), 153.3, 152.1, 147.7 (t, *J* = 11.6 Hz), 146.4 (dd, *J* = 241.3, 1.9 Hz), 130.8, 128.2 (dd, *J* = 13.8, 8.8 Hz), 122.9, 121.4, 104.9 (d, *J* = 23.8 Hz), 103.4, 101.1 (d, *J* = 28.2 Hz), 99.0, 68.9, 65.6, 61.8, 60.6, 54.1, 37.6 (d, *J* = 4.4 Hz), 30.2, 25.1, 19.0; ¹⁹F NMR (376 MHz, CDCl₃) δ = -115.77 (s), -145.58 (s); LCMS (Method B): *t_r* = 1.07 min, [M+H]⁺ 525 & 527, (96 % purity); HRMS: (C₂₃H₂₈ClF₂N₆O₄) [M+H]⁺ requires 525.1827, found [M+H]⁺ 525.1827.

***N2*-(1-(2-Azidoethyl)-1*H*-pyrazol-4-yl)-5-chloro-*N4*-(2,5-difluoro-3-(2-((tetrahydro-2*H*-pyran-2-yl)oxy)ethoxy)benzyl)pyrimidine-2,4-diamine (157)**



A solution of 2-(4-((5-chloro-4-((2,5-difluoro-3-(2-((tetrahydro-2*H*-pyran-2-yl)oxy)ethoxy)benzyl)-amino)pyrimidin-2-yl)amino)-1*H*-pyrazol-1-yl)ethan-1-ol **156** (122 mg, 0.232 mmol) in triethylamine (0.1 mL, 0.717 mmol) and DCM (1.2 mL) was cooled to 0 °C and mesyl chloride (0.022 mL, 0.279 mmol) was added dropwise and stirred for 1 h under a nitrogen atmosphere and allowed to reach room temperature. The reaction mixture was washed with saturated aqueous sodium hydrogen carbonate (10 mL) and the organic extract was passed through a hydrophobic frit and the solvent removed *in vacuo*. To the residue was added sodium azide (25 mg, 0.385 mmol) and DMF (0.600 mL) and the reaction mixture was stirred at 90 °C for 1 h under a nitrogen atmosphere. The reaction mixture was diluted with water (10 mL) and extracted with ethyl acetate (2 × 20 mL). The organic extracts were combined, passed through a hydrophobic frit and the solvent removed *in vacuo*. The residue was purified by normal phase column chromatography (0 – 80 % EtOH in EtOAc (3:1) in EtOAc, 24 g SiO₂, 12 column volumes) to provide *N2*-(1-(2-azidoethyl)-1*H*-pyrazol-4-yl)-5-chloro-*N4*-(2,5-difluoro-3-(2-((tetrahydro-2*H*-pyran-2-yl)oxy)ethoxy)benzyl)pyrimidine-2,4-diamine **157** (80 mg, 0.145 mmol, 63 % yield) as a white solid. ¹H NMR (400 MHz, MeOD-*d*₄) δ = 7.88 (1H, s), 7.67 (1H, s), 7.45 (1H, s), 6.88 (1H, ddd, *J* = 9.9, 6.7, 2.9 Hz), 6.54 - 6.63 (1H, m), 4.78 (2H, s), 4.73 (1H, t, *J* = 3.4 Hz), 4.23 - 4.28 (2H, m), 4.15 - 4.20 (2H, m), 4.04 - 4.11 (1H, m), 3.89 - 3.96 (1H, m), 3.81 - 3.88 (1H, m), 3.61 - 3.66 (2H, m), 3.51 - 3.58 (1H, m), 1.69 - 1.90 (2H, m), 1.49 - 1.66 (4H, m); ¹³C NMR (101 MHz, MeOD-*d*₄) δ = 130.8, 123.8, 120.6, 101.1, 100.9, 99.1, 68.9, 65.6, 61.9, 50.9, 50.9, 30.3, 25.1, 19.0 (weak spectrum); LCMS (Method B): *t*_R = 1.23 min, [M+H]⁺ 550 & 552, (100 % purity).

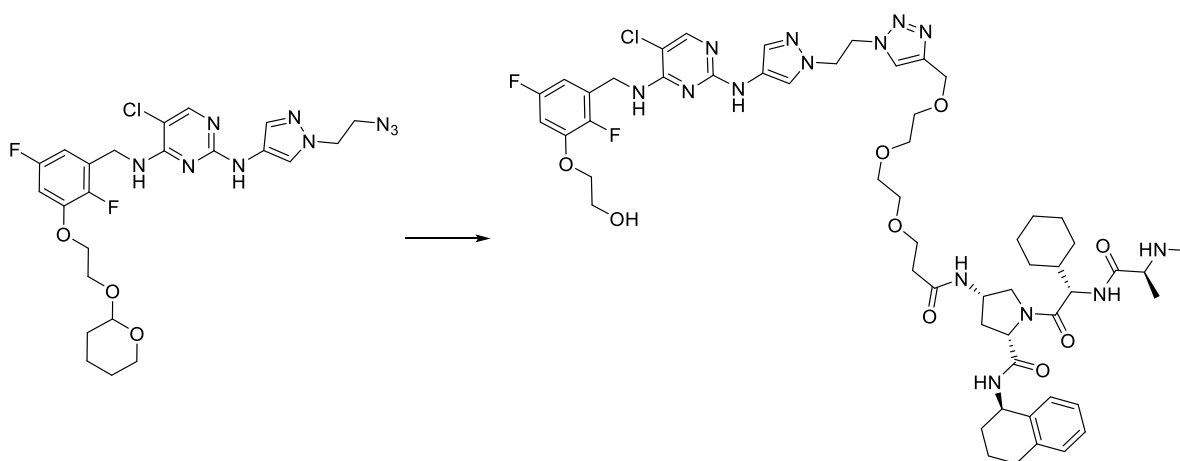
2-(3-(((5-Chloro-2-((1-(2-(4-(methoxymethyl)-1H-1,2,3-triazol-1-yl)ethyl)-1H-pyrazol-4-yl)amino)pyrimidin-4-yl)amino)methyl)-2,5-difluorophenoxy)ethanol (163)



To a 50 mM DMSO solution of *N*2-(1-(2-azidoethyl)-1*H*-pyrazol-4-yl)-5-chloro-*N*4-(2,5-difluoro-3-(2-((tetrahydro-2*H*-pyran-2-yl)oxy)ethoxy)benzyl)pyrimidine-2,4-diamine **157** (364 μ L, 0.018 mmol) was added a 50 mM DMSO solution of 3-methoxyprop-1-yne (364 μ L, 0.018 mmol), a 100 mM aqueous solution of copper(II) sulfate (36.4 μ L, 3.64 μ mol), a 200 mM aqueous solution of sodium (*R*)-2-((*S*)-1,2-dihydroxyethyl)-4-hydroxy-5-oxo-2,5-dihydrofuran-3-olate (91 μ L, 0.018 mmol) and a 50 mM solution of 3,3',3''-((nitrilotris(methylene))tris(1*H*-1,2,3-triazole-4,1-diyl))tris(propan-1-ol) (145 μ L, 7.27 μ mol). The reaction mixture was stirred for 20 min at room temperature. 1.25 M HCl in ethanol (29.1 μ L, 0.036 mmol) was added and the reaction mixture was stirred for 16 h at room temperature. The reaction mixture was purified directly by MDAP (ammonium carbonate modifier). The solvent was removed *in vacuo* to afford 2-(3-(((5-chloro-2-((1-(2-(4-(methoxymethyl)-1*H*-1,2,3-triazol-1-yl)ethyl)-1*H*-pyrazol-4-yl)amino)pyrimidin-4-yl)amino)methyl)-2,5-difluorophenoxy)ethan-1-ol **163** (7 mg, 0.013 mmol, 72 % yield) as a white solid. ν_{\max} (neat): 3320, 2931, 2882, 1600, 1490 cm^{-1} ; ^1H NMR (600 MHz, MeOD-*d*₄) δ = 7.86 (1H, br s), 7.44 (1H, s), 7.41 (1H, s), 7.38 (1H, br s), 6.84 (1H, ddd, *J* = 9.7, 6.6, 3.1 Hz), 6.54 - 6.58 (1H, m), 4.84 - 4.86 (2H, m), 4.71 (2H, s), 4.50 (2H, t, *J* = 5.5 Hz), 4.44 (2H, s), 4.15 (2H, t, *J* = 4.8 Hz), 3.93 (2H, t, *J* = 4.8 Hz), 3.24 (3H, s), exchangeable hydrogens not observed; ^{13}C NMR (151 MHz, MeOD-*d*₄) δ = 161.1, 159.8, 159.3, 154.4, 149.2, 149.1, 145.9, 132.8, 130.0, 129.9, 125.3, 122.1, 111.6, 102.5, 102.3, 72.5, 66.2, 61.6, 58.2, 52.8, 51.3, 39.1 (weak spectrum); ^{19}F NMR (376 MHz, MeOD-*d*₄) δ = -117.82 (br s), -147.46 (d, *J* = 15.6 Hz); LCMS

(Method B): $t_R = 0.85$ min, $[M+H]^+$ 536 & 538, (100 % purity); HRMS: $(C_{22}H_{25}ClF_2N_9O_3)$ $[M+H]^+$ requires 536.1737, found $[M+H]^+$ 536.1737.

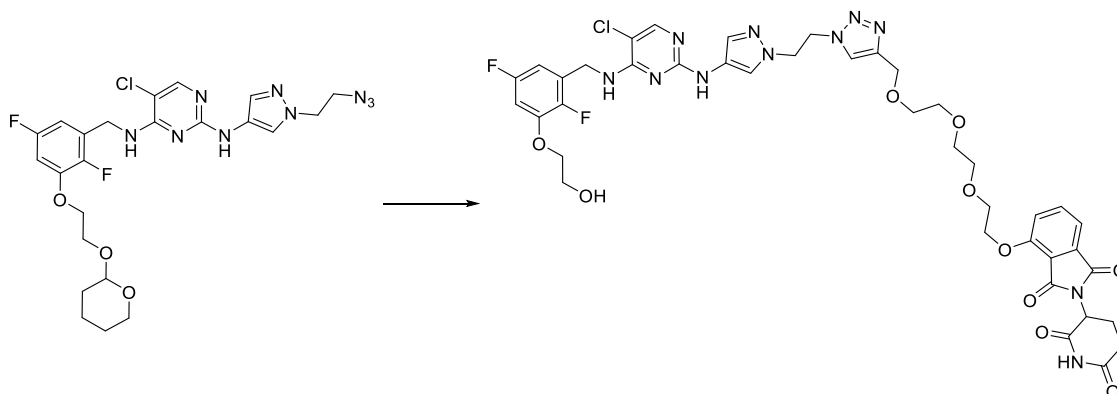
(2S,4S)-4-(3-(2-(2-((1-(2-(4-((5-Chloro-4-((2,5-difluoro-3-(2-hydroxyethoxy)benzyl)amino)-pyrimidin-2-yl)amino)-1H-pyrazol-1-yl)ethyl)-1H-1,2,3-triazol-4-yl)methoxy)ethoxy)ethoxy)-propana-mido)-1-((S)-2-cyclohexyl-2-((S)-2-(methylamino)propanamido)-acetyl)-N-((R)-1,2,3,4-tetrahydronaphthalen-1-yl)pyrrolidine-2-carboxamide (68)



To a mixture of a 200 mM aqueous solution of sodium (*R*)-2-((*S*)-1,2-dihydroxyethyl)-4-hydroxy-5-oxo-2,5-dihydrofuran-3-olate (91 μ L, 0.018 mmol), a 50 mM aqueous solution of 3,3',3''-((nitriлотris(methylene))tris(1*H*-1,2,3-triazole-4,1-diyl))tris(propan-1-ol) (145 μ L, 7.27 μ mol), a 50 mM DMSO solution of *N*2-(1-(2-azidoethyl)-1*H*-pyrazol-4-yl)-5-chloro-*N*4-(2,5-difluoro-3-(2-((tetrahydro-2*H*-pyran-2-yl)oxy)ethoxy)benzyl)pyrimidine-2,4-diamine **157** (364 μ L, 0.018 mmol) and a 100 mM DMSO solution of (2*S*,4*S*)-1-((*S*)-2-cyclohexyl-2-((*S*)-2-(methylamino)propanamido)acetyl)-4-(3-(2-(2-(prop-2-yn-1-yloxy)ethoxy)ethoxy)ethoxy)propanamido)-*N*-((*R*)-1,2,3,4-tetrahydronaphthalen-1-yl)pyrrolidine-2-carboxamide hydrochloride (182 μ L, 0.018 mmol) was a 100 mM aqueous solution of added copper(II) sulfate (36.4 μ L, 3.64 μ mol). The reaction mixture was stirred for 20 min at room temperature. 1.25 M HCl in ethanol (29.1 μ L, 0.036 mmol) was added and the reaction mixture was stirred at room temperature for 16 h. The sample was directly purified by MDAP (formic acid modifier). The solvent was removed *in vacuo* to afford (2*S*,4*S*)-4-(3-(2-(2-((1-(2-(4-((5-chloro-4-((2,5-difluoro-3-(2-hydroxyethoxy)benzyl)-amino)-pyrimidin-2-yl)amino)-1*H*-pyrazol-1-yl)ethyl)-1*H*-1,2,3-triazol-4-yl)methoxy)ethoxy)ethoxy)-propana-mido)-1-((*S*)-2-cyclohexyl-2-((*S*)-2-

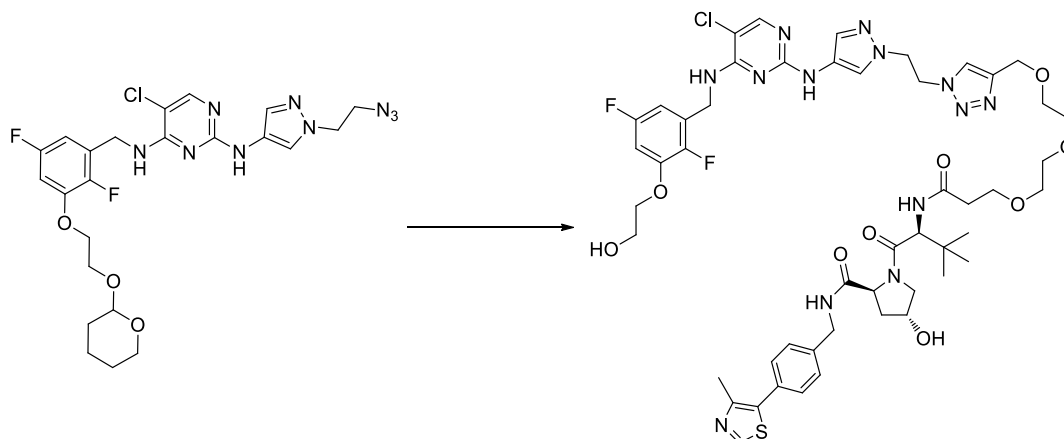
(methylamino)-propanamido)-acetyl)-*N*-((*R*)-1,2,3,4-tetrahydronaphthalen-1-yl)pyrrolidine-2-carboxamide **68** (5 mg, 4.36 μmol , 24 % yield) as a white solid. ^1H NMR (600 MHz, $\text{DMSO-}d_6$) δ = 9.03 (1H, br s), 8.35 (1H, d, J = 8.8 Hz), 8.21 (1H, br s), 8.17 (1H, d, J = 7.3 Hz), 7.96 (1H, br d, J = 8.8 Hz), 7.92 (1H, s), 7.70 (1H, br s), 7.54 - 7.68 (1H, m), 7.35 (1H, br s), 7.31 (1H, d, J = 7.3 Hz), 7.06 - 7.16 (3H, m), 7.00 (1H, ddd, J = 10.1, 6.8, 2.9 Hz), 6.55 (1H, br s), 4.84 - 5.00 (1H, m), 4.73 (2H, t, J = 5.9 Hz), 4.62 (2H, br d, J = 5.9 Hz), 4.45 (4H, s), 4.38 (1H, t, J = 8.1 Hz), 4.20 - 4.35 (2H, m), 4.09 - 4.18 (1H, m), 4.07 (2H, t, J = 4.8 Hz), 3.72 (3H, t, J = 5.0 Hz), 3.59 (2H, t, J = 6.6 Hz), 3.44 (9H, d, J = 9.5 Hz), 3.27 - 3.31 (2H, m), 3.03 (1H, q, J = 6.7 Hz), 2.65 - 2.77 (2H, m), 2.34 - 2.46 (1H, m), 2.30 (2H, t, J = 6.6 Hz), 2.22 (1H, d, J = 11.7 Hz), 2.19 (2H, s), 1.79 - 1.91 (3H, m), 1.57 - 1.75 (8H, m), 1.12 - 1.20 (2H, m), 1.11 (3H, d, J = 6.6 Hz), 0.92 - 1.01 (2H, m); ^{13}C NMR (151 MHz, $\text{DMSO-}d_6$) δ = 173.8, 170.6 (2C), 169.9, 169.7, 157.3 (2C), 157.8 (2C, d, J = 239.4 Hz), 147.3 (app. t, J = 11.9 Hz), 143.6, 137.2, 136.8, 130.4, 128.4 (d, J = 14.4 Hz), 126.5 (2C), 125.5 (2C), 123.9 (2C), 123.4 (2C), 101.1 (2C, d, J = 28.2 Hz), 71.0, 69.5 (2C), 69.5, 69.4, 68.5, 66.5, 63.2, 59.2, 58.7, 58.3, 54.2, 52.0, 50.8, 49.2, 47.6, 46.6, 40.0, 36.1, 34.2, 33.8, 29.7, 28.7, 28.6, 27.8, 25.8, 25.6, 25.4, 20.1, 18.7, all F-couplings not identified due to complexity of spectrum; ^{19}F NMR (376 MHz, $\text{DMSO-}d_6$) δ = -116.12 (s), -145.31 (s); LCMS (Method A): t_R = 0.74 min, $[(M+2H)/2]^+$ 575, (99 % purity); HRMS: ($\text{C}_{55}\text{H}_{74}\text{ClF}_2\text{N}_{14}\text{O}_9$) $[M+H]^+$ requires 1147.5420, found $[M+H]^+$ 1147.5399.

4-(2-(2-(2-((1-(2-(4-((5-Chloro-4-((2,5-difluoro-3-(2-hydroxyethoxy)benzyl)amino)-pyrimidin-2-yl)amino)-1H-pyrazol-1-yl)ethyl)-1H-1,2,3-triazol-4-yl)methoxy)ethoxy)-ethoxy)ethoxy)-2-(2,6-dioxopiperidin-3-yl)isoindoline-1,3-dione (69)



To a mixture of a 200 mM aqueous solution of sodium (*R*)-2-((*S*)-1,2-dihydroxyethyl)-4-hydroxy-5-oxo-2,5-dihydrofuran-3-olate (91 μ L, 0.018 mmol), a 50 mM aqueous solution of 3,3',3''-((nitrilotris(methylene))tris(1*H*-1,2,3-triazole-4,1-diyl))tris(propan-1-ol) (145 μ L, 7.27 μ mol), a 50 mM DMSO solution of *N*2-(1-(2-azidoethyl)-1*H*-pyrazol-4-yl)-5-chloro-*N*4-(2,5-difluoro-3-(2-((tetrahydro-2*H*-pyran-2-yl)oxy)ethoxy)benzyl)pyrimidine-2,4-diamine (364 μ L, 0.018 mmol) **157** and a 100 mM DMSO solution of 2-(2,6-dioxopiperidin-3-yl)-4-(2-(2-(2-(prop-2-yn-1-yloxy)ethoxy)ethoxy)ethoxy)-isoindoline-1,3-dione (182 μ L, 0.018 mmol) was added a 100 mM aqueous solution of copper(II) sulfate (36.4 μ L, 3.64 μ mol). The reaction mixture was stirred for 20 min at room temperature. 1.25 M HCl in ethanol (29.1 μ L, 0.036 mmol) was added and the reaction mixture was stirred at room temperature for 16 h. The sample was directly purified by MDAP (formic acid modifier). The solvent was removed *in vacuo* to afford 4-(2-(2-(2-((1-(2-(4-((5-chloro-4-((2,5-difluoro-3-(2-hydroxyethoxy)benzyl)amino)pyrimidin-2-yl)amino)-1*H*-pyrazol-1-yl)ethyl)-1*H*-1,2,3-triazol-4-yl)methoxy)ethoxy)ethoxy)ethoxy)-2-(2,6-dioxopiperidin-3-yl)isoindoline-1,3-dione **69** (16 mg, 0.018 mmol, 97 % yield) as a white solid. ^1H NMR (400 MHz, DMSO-*d*₆) δ = 11.06 (1H, br s), 9.02 (1H, br s), 8.18 - 8.51 (1H, m), 7.92 (1H, s), 7.79 (1H, dd, *J* = 8.3, 7.3 Hz), 7.70 (1H, br s), 7.51 (1H, d, *J* = 8.8 Hz), 7.44 (1H, d, *J* = 7.3 Hz), 7.36 (1H, br s), 6.99 (1H, ddd, *J* = 10.0, 6.6, 2.9 Hz), 6.52 - 6.60 (1H, m), 5.08 (1H, dd, *J* = 12.7, 5.4 Hz), 4.73 (2H, t, *J* = 5.9 Hz), 4.62 (2H, br s), 4.42 - 4.48 (4H, m), 4.30 - 4.35 (2H, m), 4.07 (2H, t, *J* = 4.9 Hz), 3.77 - 3.82 (2H, m), 3.72 (2H, t, *J* = 4.6 Hz), 3.58 - 3.65 (2H, m), 3.48 (2H, dd, *J* = 5.9, 3.9 Hz), 3.40 - 3.45 (4H, m), 2.82 - 2.94 (1H, m), 2.52 - 2.64 (2H, m), 2.45 - 2.49 (1H, m), 1.97 - 2.08 (1H, m); ^{13}C NMR (101 MHz, DMSO-*d*₆) δ = 173.1, 170.3, 167.3, 165.7 (2C), 157.8 (2C), 156.3 (2C), 147.9 (app. t, *J* = 11.7 Hz), 144.3, 137.4, 133.7, 131.0 (2C), 130.9, 128.9, 124.4, 123.9, 120.5 (2C), 116.8, 115.8, 101.7 (2C, d, *J* = 27.9 Hz), 71.6, 70.6 (2C), 70.3, 70.1, 69.3, 69.2, 69.1, 63.8, 59.7, 51.4, 49.8, 49.2, 31.4, 22.5 all F-couplings not identified due to complexity of spectrum; ^{19}F NMR (376 MHz, DMSO-*d*₆) δ = -116.13 (s), -145.35 (s); LCMS (Method A): *t*_R = 0.73 min, [M+H]⁺ 910, (99 % purity); HRMS: (C₄₀H₄₃ClF₂N₁₁O₁₀) [M+H]⁺ requires 910.2851, found [M+H]⁺ 910.2830.

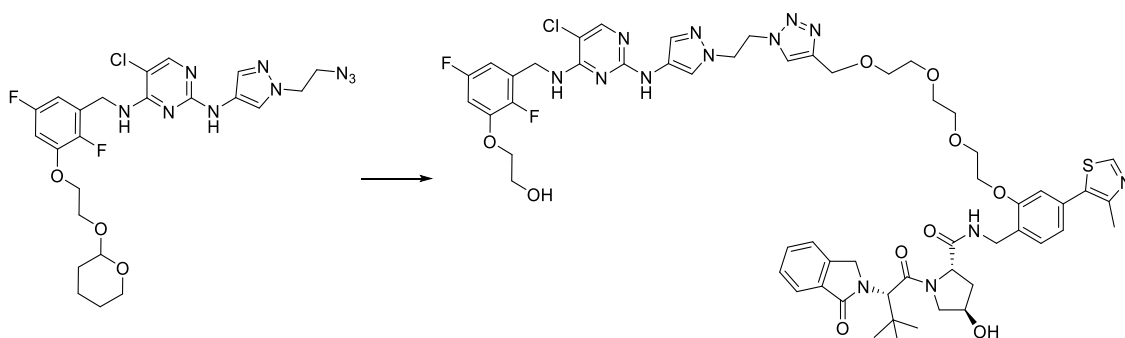
(2*S*,4*R*)-1-((*S*)-13-(*tert*-Butyl)-1-(1-(2-(4-((5-chloro-4-((2,5-difluoro-3-(2-hydroxyethoxy)benzyl)-amino)pyrimidin-2-yl)amino)-1*H*-pyrazol-1-yl)ethyl)-1*H*-1,2,3-triazol-4-yl)-11-oxo-2,5,8-trioxa-12-azatetradecan-14-oyl)-4-hydroxy-*N*-(4-(4-methylthiazol-5-yl)benzyl)-pyrrolidine-2-carboxamide (70)



To a mixture of a 200 mM aqueous solution of sodium (*R*)-2-((*S*)-1,2-dihydroxyethyl)-4-hydroxy-5-oxo-2,5-dihydrofuran-3-olate (91 μ L, 0.018 mmol), a 50 mM aqueous solution of 3,3',3''-((nitriлотris(methylene))tris(1*H*-1,2,3-triazole-4,1-diyl))tris(propan-1-ol) (145 μ L, 7.27 μ mol), a 50 mM DMSO solution of *N*2-(1-(2-azidoethyl)-1*H*-pyrazol-4-yl)-5-chloro-*N*4-(2,5-difluoro-3-(2-((tetrahydro-2*H*-pyran-2-yl)oxy)ethoxy)benzyl)pyrimidine-2,4-diamine (364 μ L, 0.018 mmol) **157** and a 100 mM solution of (2*S*,4*R*)-1-((*S*)-2-(*tert*-butyl)-4-oxo-7,10,13-trioxa-3-azahexadec-15-ynoyl)-4-hydroxy-*N*-(4-(4-methylthiazol-5-yl)benzyl)pyrrolidine-2-carboxamide (182 μ L, 0.018 mmol) was added a 100 mM aqueous solution of copper(II) sulfate (36.4 μ L, 3.64 μ mol). The reaction mixture was stirred for 20 min at room temperature. 1.25 M HCl in ethanol (29.1 μ L, 0.036 mmol) was added and the reaction mixture was stirred at room temperature for 16 h. The sample was directly purified by MDAP (formic acid modifier). The solvent was removed in vacuo to afford (2*S*,4*R*)-1-((*S*)-13-(*tert*-butyl)-1-(1-(2-(4-((5-chloro-4-((2,5-difluoro-3-(2-hydroxyethoxy)benzyl)-amino)pyrimidin-2-yl)amino)-1*H*-pyrazol-1-yl)ethyl)-1*H*-1,2,3-triazol-4-yl)-11-oxo-2,5,8-trioxa-12-azatetradecan-14-oyl)-4-hydroxy-*N*-(4-(4-methylthiazol-5-yl)benzyl)-pyrrolidine-2-carboxamide **70** (5 mg, 4.57 μ mol, 25 % yield) as a white solid. ^1H NMR (600 MHz, DMSO- d_6) δ = 9.04 (1H, br s), 8.97 (1H, s), 8.55 (1H, t, J = 6.1 Hz), 8.44 (2H, br s), 7.87 - 7.93 (2H, m), 7.71 (1H, br s), 7.66

(1H, br s), 7.35 - 7.44 (5H, m), 6.99 (1H, ddd, $J = 9.9, 6.6, 2.9$ Hz), 6.55 (1H, br s), 5.75 (1H, s), 4.73 (3H, m), 4.62 (2H, br d, $J = 5.9$ Hz), 4.55 (2H, d, $J = 9.5$ Hz), 4.39 - 4.50 (7H, m), 4.30 - 4.39 (2H, m), 4.22 (1H, dd, $J = 15.8, 5.5$ Hz), 4.07 (2H, t, $J = 4.8$ Hz), 3.72 (3H, t, $J = 5.0$ Hz), 3.17 (6H, s), 2.44 (3H, s), 2.30 - 2.39 (1H, m), 2.00 - 2.06 (1H, m), 1.90 (1H, ddd, $J = 12.8, 8.4, 4.8$ Hz), 0.93 (10H, s); ^{13}C NMR (151 MHz, $\text{DMSO-}d_6$) $\delta = 172.4, 170.4, 170.0, 157.9, 158.4$ (d, $J = 238.8$ Hz), 151.9 (2C), 148.2, 147.9 (app. t, $J = 12.2$ Hz), 144.2, 144.2, 140.0, 131.6 (2C), 130.9, 130.1 (2C), 129.1, 127.9 (2C), 124.4 (2C), 124.0, 110.0, 101.7 (2C, d, $J = 27.6$ Hz), 71.6, 70.1, 70.1, 69.9, 69.3, 69.1, 67.4, 63.8, 59.8, 59.2, 56.8, 55.4, 51.4, 49.8, 49.1, 42.1, 40.6, 38.4, 36.1, 35.8, 26.8 (3C), 16.4, all F-couplings not identified due to complexity of spectrum; ^{19}F NMR (376 MHz, $\text{DMSO-}d_6$) $\delta = -116.08$ (s), -145.29 (s); LCMS (Method A): $t_R = 0.80$ min, $[(M+2H)/2]^+ 548$, (92 % purity); HRMS: ($\text{C}_{50}\text{H}_{63}\text{ClF}_2\text{N}_{13}\text{O}_9\text{S}$) $[M+H]^+$ requires 1094.4249, found $[M+H]^+ 1094.4227$.

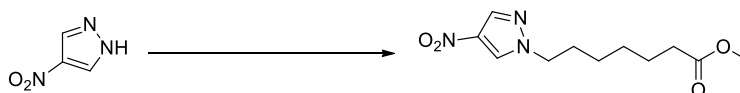
(2*S*,4*R*)-*N*-(2-(2-(2-(2-((1-(2-(4-((5-Chloro-4-((2,5-difluoro-3-(2-hydroxyethoxy)-benzyl)amino)-pyrimidin-2-yl)amino)-1*H*-pyrazol-1-yl)ethyl)-1*H*-1,2,3-triazol-4-yl)methoxy)ethoxy)ethoxy)-ethoxy)-4-(4-methylthiazol-5-yl)benzyl)-1-((*S*)-3,3-dimethyl-2-(1-oxoisoindolin-2-yl)butanoyl)-4-hydroxypyrrolidine-2-carboxamide (71)



To a mixture of a 200 mM aqueous solution of sodium (*R*)-2-((*S*)-1,2-dihydroxyethyl)-4-hydroxy-5-oxo-2,5-dihydrofuran-3-olate (91 μL , 0.018 mmol), a 50 mM aqueous solution of 3,3',3''-((nitriлотris(methylene))tris(1*H*-1,2,3-triazole-4,1-diyl))tris(propan-1-ol) (145 μL , 7.27 μmol), a 50 mM DMSO solution of *N*2-(1-(2-azidoethyl)-1*H*-pyrazol-4-yl)-5-chloro-*N*4-(2,5-difluoro-3-(2-((tetrahydro-2*H*-pyran-2-yl)oxy)ethoxy)benzyl)pyrimidine-2,4-diamine **157** (364 μL , 0.018 mmol) and a 100 mM DMSO solution of (2*S*,4*R*)-1-((*S*)-3,3-dimethyl-2-(1-oxoisoindolin-2-yl)butanoyl)-4-hydroxy-*N*-(4-(4-methylthiazol-5-yl)-2-(2-(2-(2-(prop-2-yn-1-

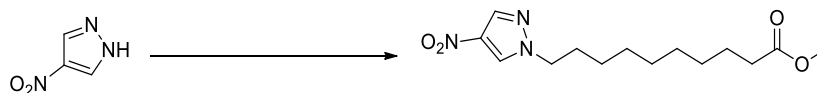
loxy)ethoxy)ethoxy)-ethoxy)benzyl)pyrrolidine-2-carboxamide (182 μL , 0.018 mmol) was added a 100 mM aqueous solution of copper(II) sulfate (36.4 μL , 3.64 μmol). The reaction mixture was stirred for 20 min at room temperature. 1.25 M HCl in ethanol (29.1 μL , 0.036 mmol) was added and the reaction mixture was stirred at room temperature for 16 h. The sample was directly purified by MDAP (formic acid modifier). The solvent was removed *in vacuo* to afford (2*S*,4*R*)-*N*-(2-(2-(2-(2-((1-(2-(4-((5-chloro-4-((2,5-difluoro-3-(2-hydroxyethoxy)benzyl)amino)pyrimidin-2-yl)amino)-1*H*-pyrazol-1-yl)ethyl)-1*H*-1,2,3-triazol-4-yl)methoxy)ethoxy)ethoxy)ethoxy)-4-(4-methylthiazol-5-yl)benzyl)-1-((*S*)-3,3-dimethyl-2-(1-oxoisindolin-2-yl)butanoyl)-4-hydroxypyrrolidine-2-carboxamide **71** (4 mg, 3.34 μmol , 18 % yield) as a white solid. ^1H NMR (600 MHz, DMSO- d_6) δ = 9.03 (1H, br s), 8.97 (1H, s), 8.51 (1H, br s), 8.39 (1H, t, J = 6.1 Hz), 7.91 (1H, s), 7.72 (2H, d, J = 7.7 Hz), 7.56 - 7.69 (4H, m), 7.46 - 7.56 (1H, m), 7.44 (2H, d, J = 7.7 Hz), 7.31 - 7.39 (1H, m), 7.04 (1H, d, J = 1.5 Hz), 6.92 - 7.03 (2H, m), 6.55 (1H, br s), 5.07 (1H, br s), 5.03 (1H, s), 4.92 (1H, br s), 4.78 (2H, d, J = 3.7 Hz), 4.72 (2H, br t, J = 5.7 Hz), 4.62 (2H, br d, J = 5.9 Hz), 4.44 (3H, s), 4.30 - 4.35 (1H, m), 4.28 (1H, d, J = 5.9 Hz), 4.25 (1H, d, J = 5.9 Hz), 4.17 - 4.19 (2H, m), 4.07 (2H, t, J = 5.0 Hz), 3.77 - 3.79 (2H, m), 3.70 - 3.77 (3H, m), 3.60 (2H, dd, J = 5.7, 3.9 Hz), 3.54 - 3.59 (1H, m), 3.50 (2H, dd, J = 5.7, 3.9 Hz), 3.41 - 3.47 (4H, m), 2.46 (3H, s), 1.98 - 2.06 (1H, m), 1.92 (1H, m), 1.11 (1H, s), 1.07 (8H, s); ^{13}C NMR (151 MHz, DMSO- d_6) δ = 171.8, 168.1, 167.6, 157.3, 157.0 (2C), 155.7, 151.3 (2C), 147.8, 147.3, 143.7, 142.4, 131.5 (2C), 131.2, 130.8 (d, J = 12.7 Hz), 127.7 (3C), 127.7, 127.1, 123.9, 123.8, 123.4, 123.3, 122.8, 120.9, 112.0, 101.1 (dd, J = 27.6, 1.7 Hz), 71.0, 69.9, 69.7, 69.5, 68.9, 68.6, 68.6, 67.8, 63.2, 59.2, 58.6, 58.1, 56.0, 50.8, 49.5, 49.2, 48.6, 40.0, 37.9, 37.2, 37.1, 36.1, 27.3 (3C), 26.7, 15.9 all F-couplings not identified due to complexity of spectrum; ^{19}F NMR (376 MHz, DMSO- d_6) δ = -116.10 (s), -145.29 (s); LCMS (Method A): t_{R} = 0.93 min, [($\text{M}+2\text{H}$)/2] $^+$ 600, (100 % purity); HRMS: ($\text{C}_{57}\text{H}_{67}\text{ClF}_2\text{N}_{13}\text{O}_{10}\text{S}$) [$\text{M}+\text{H}$] $^+$ requires 1198.4486, found [$\text{M}+\text{H}$] $^+$ 1198.4511.

Methyl 7-(4-nitro-1*H*-pyrazol-1-yl)heptanoate (109)



4-Nitro-1*H*-pyrazole **175** (2.000 g, 17.69 mmol), methyl 7-bromoheptanoate (4.71 mL, 26.5 mmol) and potassium carbonate (3.67 g, 26.5 mmol) were sealed within a vessel and *N,N*-dimethylformamide (DMF) (20.10 mL) was added. The reaction mixture was heated for 1.5 h at 50 °C. The reaction mixture was diluted with water (50 mL) and extracted with DCM (3 × 50 mL). The organic layers were combined, passed through a hydrophobic frit and the solvent was removed *in vacuo*. The residue dissolved in DCM (5 mL) and purified by normal phase column chromatography (0 – 100 % EtOAc in cyclohexane, 120 g SiO₂) to afford methyl 7-(4-nitro-1*H*-pyrazol-1-yl)heptanoate **178** (4.282 g, 16.77 mmol, 95 % yield) as a white solid. M.pt.: 65 - 67 °C; ν_{\max} (neat): 3130, 2938, 1718, 1535 cm⁻¹; ¹H NMR (400 MHz, DMSO-*d*₆) δ = 8.89 (1H, s), 8.24 (1H, s), 4.16 (2H, t, *J* = 6.8 Hz), 3.29 (3H, s), 2.27 (2H, t, *J* = 7.3 Hz), 1.79 (2H, app. quin, *J* = 7.2 Hz), 1.50 (2H, app. quin, *J* = 7.5 Hz), 1.17 - 1.32 (4H, m); ¹³C NMR (101 MHz, DMSO-*d*₆) δ = 173.2, 135.4, 134.7, 130.2, 52.2, 51.1, 33.1, 28.9, 27.7, 25.3, 24.1; LCMS (Method B): *t*_R = 1.02 min, [M+H]⁺ 256, (100 % purity); HRMS: (C₁₁H₁₈N₃O₄) [M+H]⁺ requires 256.1297, found [M+H]⁺ 256.1298;

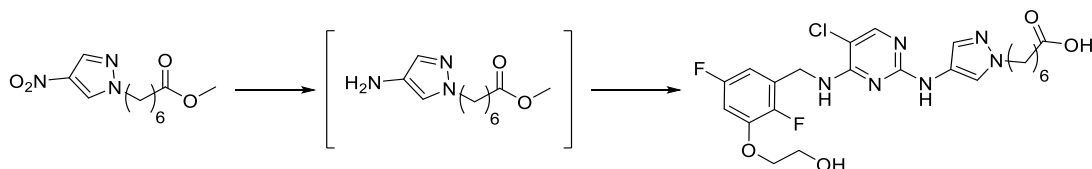
Methyl 10-(4-nitro-1*H*-pyrazol-1-yl)decanoate (**179**)



4-Nitro-1*H*-pyrazole **175** (1 g, 8.84 mmol), methyl 10-bromodecanoate (3.09 mL, 13.27 mmol) and potassium carbonate (1.833 g, 13.27 mmol) were sealed within a vessel and *N,N*-dimethylformamide (DMF) (10.05 mL) was added. The reaction mixture was heated in for 1.5 h at 50 °C. The reaction mixture was diluted with water (30 mL) and extracted with DCM (3 × 30 mL). The organic layers were combined, passed through a hydrophobic frit and the solvent was removed *in vacuo*. The residue was taken into DCM (5 mL) and purified by normal phase column chromatography (0 – 100 % EtOAc in cyclohexane, 80 g SiO₂) to afford methyl 10-(4-nitro-1*H*-pyrazol-1-yl)decanoate **179** (2.2 g, 7.40 mmol, 84 % yield) as a white solid. M.pt.: 69 - 71 °C; ν_{\max} (neat): 3151, 3123, 2928, 2855, 1722, 1533 cm⁻¹; ¹H NMR (400 MHz, DMSO-*d*₆) δ = 8.89 (1H, s), 8.24 (1H, s), 4.16 (2H, t, *J* = 7.1 Hz), 3.58 (3H, s), 2.27 (2H, t, *J* = 7.3 Hz), 1.75 - 1.86 (2H, m), 1.45 - 1.54 (2H, m), 1.15 - 1.29 (10H, m); ¹³C NMR (101 MHz, DMSO-

d_6) δ = 173.8, 135.9, 135.2, 130.8, 52.8, 51.6, 33.7, 29.5, 29.1, 29.0, 28.9, 28.7, 26.1, 24.9; LCMS (Method A): t_R = 1.28 min, $[M+H]^+$ 298, (100 % purity); HRMS: ($C_{14}H_{24}N_3O_4$) $[M+H]^+$ requires 298.1767, found $[M+H]^+$ 298.1767.

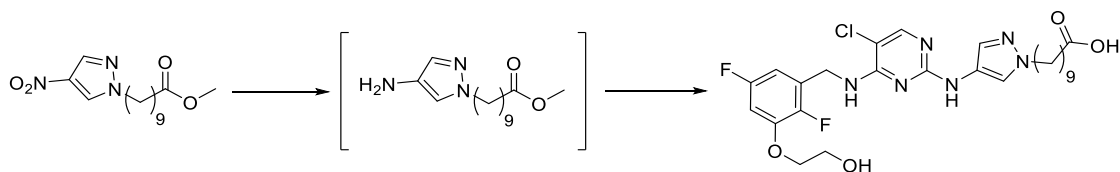
7-(4-((5-Chloro-4-((2,5-difluoro-3-(2-hydroxyethoxy)-benzyl)amino)pyrimidin-2-yl)amino)-1H-pyrazol-1-yl)heptanoic acid (182)



To a COWare tube, palladium on carbon (0.177 g, 0.167 mmol) and methyl 7-(4-nitro-1H-pyrazol-1-yl)heptanoate **178** (4.252 g, 16.66 mmol) in ethanol (49.6 mL) were added to one tube under nitrogen and that tube was sealed to the atmosphere. 2 M aqueous HCl (250 mL, 500 mmol) and zinc (10.89 g, 167 mmol) were added under nitrogen to the other tube which was subsequently sealed to the atmosphere. The reaction mixture was stirred at room temperature for 16 h. The reaction mixture was filtered over Celite and washed with ethyl acetate (30 mL). The solvent was removed *in vacuo* and the residue was dissolved in DMSO (5 mL) and purified by reverse phase column chromatography (0 – 25 % MeCN + 0.1 % HCO₂H in H₂O + 0.1 % HCO₂H, 12 g C₁₈) to afford methyl 7-(4-amino-1H-pyrazol-1-yl)heptanoate (1.621 g, 7.20 mmol, 43 % yield) as a purple oil. 2,5-Dichloro-*N*-(2,5-difluoro-3-(2-((tetrahydro-2H-pyran-2-yl)oxy)ethoxy)-benzyl)pyrimidin-4-amine (1.89 g, 4.35 mmol), methyl 7-(4-amino-1H-pyrazol-1-yl)heptanoate (1.368 g, 5.22 mmol) and 2 M aqueous HCl (4.35 mL, 8.70 mmol) in ethanol (8.72 mL) were sealed within a vessel and heated in a Biotage Initiator microwave for 1.5 h at 100 °C using a high absorption setting. The reaction mixture was allowed to cool to room temperature. The solvent was removed *in vacuo* and 2 M aqueous NaOH (21.76 mL, 43.5 mmol), 1,4-dioxane (8.72 mL) and water (3.49 mL) were added and the reaction mixture was stirred for 1 h at room temperature. The solvent was concentrated *in vacuo* and purified directly by reverse phase column chromatography (15 – 35 % MeCN + 0.1 % HCO₂H in H₂O + 0.1 % HCO₂H, 120 g C₁₈) to afford 7-(4-((5-chloro-4-((2,5-difluoro-3-(2-hydroxyethoxy)-benzyl)amino)pyrimidin-2-yl)amino)-1H-pyrazol-1-yl)heptanoic acid **182** (536 mg, 1.021 mmol, 24 % yield) as a brown gum. ¹H NMR (400 MHz, DMSO-*d*₆) δ = 9.05 (1H, br s), 7.94 (1H, s), 7.66 (1H, br s), 7.44 - 7.62 (1H, m), 7.32 (1H, br s),

7.02 (1H, ddd, $J = 10.1, 6.8, 2.9$ Hz), 6.51 - 6.62 (1H, m), 4.67 (2H, br d, $J = 5.4$ Hz), 4.09 (2H, t, $J = 4.9$ Hz), 3.88 - 3.94 (2H, m), 3.75 (2H, t, $J = 4.9$ Hz), 2.17 (2H, t, $J = 7.3$ Hz), 1.61 - 1.70 (2H, m), 1.46 (3H, m), 1.09 - 1.30 (5H, m); ^{13}C NMR (101 MHz, $\text{DMSO-}d_6$) $\delta = 175.0, 158.1, 158.0, 158.4$ (d, $J = 239.2$ Hz), 154.0, 147.9 (app. t, $J = 11.7$ Hz), 146.2 (d, $J = 239.2$ Hz), 129.9, 128.9 (dd, $J = 13.9, 8.8$ Hz), 123.6, 119.3, 105.1 (d, $J = 28.6$ Hz), 101.6 (d, $J = 27.9$ Hz), 91.1, 71.6, 66.8, 59.8, 51.7, 34.2, 30.3, 28.5, 26.2, 24.9; ^{19}F NMR (376 MHz, $\text{DMSO-}d_6$) $\delta = -116.1$ (br s), -145.6 (br s); LCMS (Method A): $t_R = 0.70$ min, $[\text{M}+\text{H}]^+$ 525 & 527, (94 % purity); HRMS: ($\text{C}_{23}\text{H}_{28}\text{ClF}_2\text{N}_6\text{O}_4$) $[\text{M}+\text{H}]^+$ requires 525.1838, found $[\text{M}+\text{H}]^+$ 525.1833.

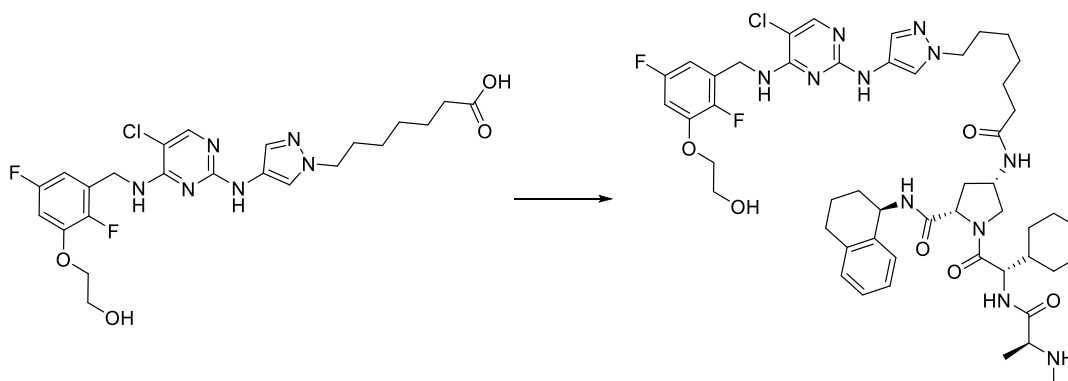
10-(4-((5-Chloro-4-((2,5-difluoro-3-(2-hydroxyethoxy)benzyl)amino)pyrimidin-2-yl)amino)-1H-pyrazol-1-yl)decanoic acid (183)



To a COware tube, palladium on carbon (4 mg, 3.76 μmol) and methyl 10-(4-nitro-1H-pyrazol-1-yl)decanoate **179** (100 mg, 0.336 mmol) in ethanol (1 mL) were added to one tube under nitrogen and that tube was sealed to the atmosphere. 2 M aqueous HCl (5.04 mL, 10.09 mmol) and zinc (220 mg, 3.36 mmol) were added under nitrogen to the other tube, which was subsequently sealed to the atmosphere. The reaction mixture was stirred at room temperature for 3 h. The reaction mixture was filtered over Celite and washed with ethyl acetate (30 mL). The solvent was removed *in vacuo* and the residue was dissolved in methanol:DMSO 1:1 (0.5 mL) and purified by reverse phase column chromatography (15 – 55 % MeCN + 0.1 % HCO_2H in H_2O + 0.1 % HCO_2H , 12 g C_{18}). The appropriate fractions were combined, and the solvent was removed *in vacuo*. The residue was taken into DCM (20 mL) and washed with 2 M aqueous NaOH (20 mL). The organic layer was passed through a hydrophobic frit and the solvent removed *in vacuo* to afford methyl 10-(4-amino-1H-pyrazol-1-yl)decanoate (68 mg, 0.254 mmol, 76 % yield) as a purple solid. 2,5-Dichloro-N-(2,5-difluoro-3-(2-((tetrahydro-2H-pyran-2-yl)oxy)ethoxy)benzyl)pyrimidin-4-amine (340 mg, 0.783 mmol), methyl 10-(4-amino-1H-pyrazol-1-yl)decanoate (502 mg, 0.940 mmol) and 2 M aqueous HCl (0.783 mL, 1.566 mmol) in ethanol (1.568 mL) were sealed within a vessel

and heated in a Biotage Initiator microwave for 1.5 h at 100 °C using a high absorption setting. The reaction mixture was allowed to cool to room temperature. The solvent was removed *in vacuo* and 2 M aqueous NaOH (3.91 mL, 7.83 mmol), 1,4-dioxane (1.568 mL) and water (0.627 mL) were added and the reaction mixture was stirred for 1 h at room temperature. The solvent was removed *in vacuo*. The residue was dissolved in DMSO (5 mL) and purified by reverse phase column chromatography (15 – 35 % MeCN + 0.1 % HCO₂H in H₂O + 0.1 % HCO₂H, 120 g C₁₈) to afford 10-(4-((5-chloro-4-((2,5-difluoro-3-(2-hydroxyethoxy)-benzyl)amino)pyrimidin-2-yl)amino)-1H-pyrazol-1-yl)decanoic acid **183** (257 mg, 0.453 mmol, 58 % yield) as a pale pink solid. M.pt.: 117 - 119 °C; ν_{\max} (neat): 3441, 2921, 2853, 1425 cm⁻¹; ¹H NMR (400 MHz, DMSO-*d*₆) δ = 9.05 (1H, br s), 7.94 (1H, s), 7.65 (1H, br s), 7.46 - 7.61 (1H, m), 7.30 (1H, br s), 7.02 (1H, ddd, *J* = 10.1, 6.8, 3.1 Hz), 6.52 - 6.65 (1H, m), 4.66 (2H, br d, *J* = 5.6 Hz), 4.08 (2H, t, *J* = 5.0 Hz), 3.84 - 3.96 (2H, m), 3.74 (2H, t, *J* = 4.9 Hz), 2.17 (2H, t, *J* = 7.3 Hz), 1.56 - 1.74 (2H, m), 1.41 - 1.52 (2H, m), 1.21 - 1.11 (10H, m); ¹³C NMR (101 MHz, DMSO-*d*₆) δ = 174.9, 158.1, 158.0, 158.4 (d, *J* = 241.4 Hz), 154.1, 147.9 (app. t, *J* = 11.4 Hz), 146.2 (d, *J* = 239.2 Hz), 129.9, 129.0 (d, *J* = 9.5 Hz), 123.6, 119.3, 105.1 (d, *J* = 27.9 Hz), 101.6 (d, *J* = 28.6 Hz), 91.1, 71.6, 59.8, 51.8, 34.2 (2C), 30.4, 29.3, 29.1, 29.0, 28.9, 26.4, 25.0; ¹⁹F NMR (376 MHz, DMSO-*d*₆) δ = -116.18 (s), -145.55 (s); LCMS (Method A): *t*_R = 0.84 min, [M+H]⁺ 567 & 569 (96 % purity); HRMS: (C₂₆H₃₄ClF₂N₆O₄) [M+H]⁺ requires 567.2298, found [M+H]⁺ 567.2302.

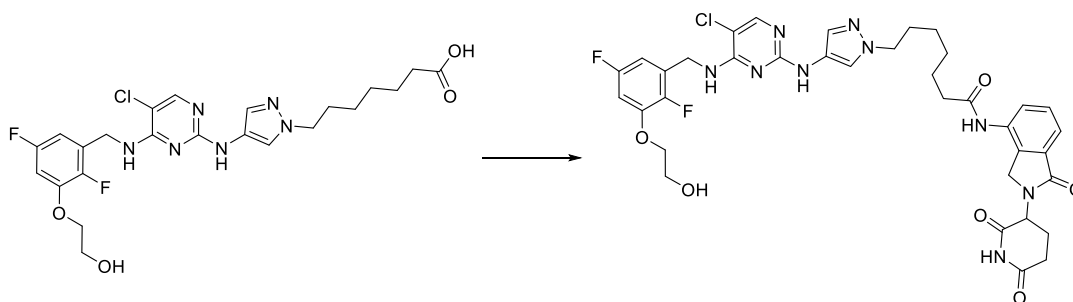
(2S,4S)-4-(7-(4-((5-Chloro-4-((2,5-difluoro-3-(2-hydroxyethoxy)benzyl)amino)pyrimidin-2-yl)amino)-1H-pyrazol-1-yl)heptanamido)-1-((S)-2-cyclo-hexyl-2-((S)-2-(methylamino)propanamido)acetyl)-N-((R)-1,2,3,4-tetrahydronaphthalen-1-yl)pyrro-lidine-2-carboxamide (72)



7-(4-((5-Chloro-4-((2,5-difluoro-3-(2-hydroxyethoxy)benzyl)amino)pyrimidin-2-yl)amino)-1H-pyrazol-1-yl)heptanoic acid **182** (140 mg, 0.267 mmol), *tert*-butyl ((S)-1-(((S)-2-((2S,4S)-4-amino-2-(((R)-1,2,3,4-tetrahydronaphthalen-1-yl)carbamoyl)pyrrolidin-1-yl)-1-cyclohexyl-2-oxoethyl)amino)-1-oxopropan-2-yl)(methyl)carbamate (187 mg, 0.320 mmol), triethylamine (112 μ L, 0.800 mmol) and HATU (152 mg, 0.400 mmol) were stirred together in *N,N*-dimethylformamide (DMF) (5.334 mL) for 15 h at room temperature. TFA (205 μ L, 2.67 mmol) was added and the reaction mixture was stirred at room temperature for 16 h. The reaction mixture was diluted with DMSO (0.2 mL) and purified directly by MDAP (formic acid modifier). The solvent was removed *in vacuo* to afford (2S,4S)-4-(7-(4-((5-chloro-4-((2,5-difluoro-3-(2-hydroxyethoxy)benzyl)amino)pyrimidin-2-yl)amino)-1H-pyrazol-1-yl)heptanamido)-1-((S)-2-cyclo-hexyl-2-((S)-2-(methylamino)propanamido)acetyl)-N-((R)-1,2,3,4-tetrahydronaphthalen-1-yl)pyrro-lidine-2-carboxamide **72** (31 mg, 0.031 mmol, 12 % yield) as a colourless, hard gum. ν_{\max} (neat): 3265, 2929, 2865, 1573, 1025 cm^{-1} ; ^1H NMR (600 MHz, DMSO- d_6) δ = 9.08 (1H, s), 8.38 (1H, d, J = 8.4 Hz), 8.12 (1 H, d, J = 7.7 Hz), 7.89 - 7.98 (1H, m), 7.67 (1H, br s), 7.27 - 7.33 (1H, m), 7.12 - 7.16 (1H, m), 7.05 - 7.11 (2H, m), 7.02 (1H, ddd, J = 9.8, 6.7, 2.9 Hz), 6.55 (1H, br s), 4.88 - 4.98 (1H, m), 4.66 (1H, br d, J = 4.8 Hz), 4.54 - 4.63 (1H, m), 4.45 - 4.54 (1H, m), 4.35 - 4.41 (1H, m), 4.23 - 4.34 (2H, m), 4.10 - 4.21 (1H, m), 4.08 (1H, t, J = 5.0 Hz), 4.01 - 4.06 (1H, m), 3.90 (1H, br s), 3.74 (2H, t, J = 5.0 Hz), 3.28 - 3.35 (1H, m), 2.92 (2H, s), 2.74 (4H, br s), 2.37 - 2.41 (1H, m), 2.03 (1H, t, J = 7.5 Hz), 1.76 - 1.90 (3H, m), 1.42 - 1.76 (12H, m), 1.31 - 1.49 (7H, m), 1.18 - 1.26 (4H, m), 1.28 - 1.14 (5H, m), 0.89

- 1.02 (2H, m); ^{13}C NMR (151 MHz, $\text{DMSO-}d_6$) δ = 172.4, 171.8, 171.4, 170.2, 165.5, 160.9, 158.0, 148.0, 147.9, 147.8, 137.8, 137.7, 137.4, 129.0, 129.0, 128.8, 127.1, 127.1, 126.1, 123.6, 101.7, 101.5, 71.6, 59.8, 58.9, 55.4, 55.3, 52.8, 51.7, 48.2, 47.4, 47.2, 40.6, 35.9, 34.9, 30.5, 30.3, 30.3, 29.2, 29.2, 29.2, 28.7, 28.5, 26.4, 26.3, 26.2, 26.0, 25.5, 20.8, 20.7, F-coupling not identified due to complexity of spectrum; LCMS (Method B): t_R = 1.38 min, $[(M+2H)/2]^+$ 496, (96 % purity); HRMS: ($\text{C}_{50}\text{H}_{67}\text{ClF}_2\text{N}_{11}\text{O}_6$) $[M+H]^+$ requires 989.4854, found $[M+H]^+$ 990.4920.

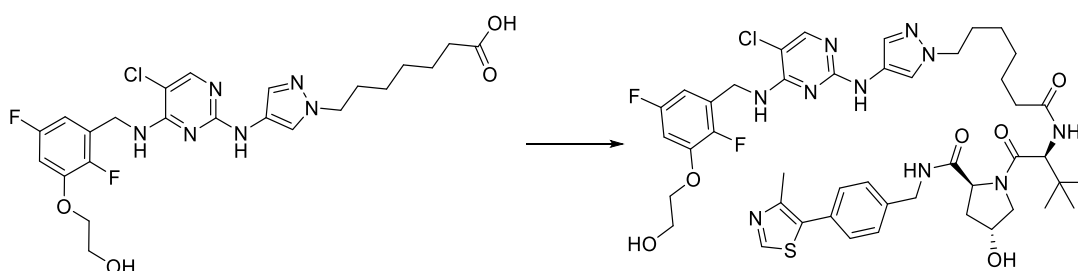
7-(4-((5-Chloro-4-((2,5-difluoro-3-(2-hydroxyethoxy)benzyl)amino)pyrimidin-2-yl)amino)-1H-pyrazol-1-yl)-N-(2-(2,6-dioxopiperidin-3-yl)-1-oxoisindolin-4-yl)heptanamide (73)



7-(4-((5-Chloro-4-((2,5-difluoro-3-(2-hydroxyethoxy)benzyl)amino)pyrimidin-2-yl)amino)-1H-pyrazol-1-yl)heptanoic acid **182** (140 mg, 0.267 mmol), 3-(4-amino-1-oxoisindolin-2-yl)piperidine-2,6-dione (83 mg, 0.320 mmol), triethylamine (112 μL , 0.800 mmol) and HATU (152 mg, 0.400 mmol) were stirred together in *N,N*-dimethylformamide (DMF) (5.334 mL) for 15 h at room temperature. The reaction mixture was concentrated *in vacuo* and split into two equal portions. Each portion was diluted with added DMSO (0.2 mL) and purified directly by MDAP (formic acid modifier). The solvent was removed *in vacuo* to afford 7-(4-((5-chloro-4-((2,5-difluoro-3-(2-hydroxyethoxy)-benzyl)amino)pyrimidin-2-yl)amino)-1H-pyrazol-1-yl)-N-(2-(2,6-dioxopiperidin-3-yl)-1-oxoisindolin-4-yl)heptanamide **73** (32 mg, 0.042 mmol, 16 % yield) as a colourless, hard gum. ν_{max} (neat): 3259, 2936, 2856, 1639 cm^{-1} ; ^1H NMR (600 MHz, $\text{DMSO-}d_6$) δ = 11.00 (1H, s), 10.11 (1H, br s), 9.74 (1H, s), 9.17 (1H, br s), 8.19 (1H, br s), 7.95 (1H, s), 7.81 (1H, d, J = 7.3 Hz), 7.62 (1H, br s), 7.46 - 7.53 (2H, m), 7.44 (1H, br s), 7.06 (1H, ddd, J = 10.1, 6.8, 2.9 Hz), 6.64 (1H, br s), 5.14 (1H, dd, J = 13.2, 5.1 Hz), 4.72 (2H, br d, J = 5.9 Hz), 4.32 - 4.42 (2H, m), 4.09 (2H, t, J = 4.8 Hz), 4.00 (2H, br s), 3.74 (2H, t, J = 4.8 Hz),

2.90 - 2.96 (1H, m), 2.58 - 2.65 (1H, m), 2.30 - 2.37 (3H, m), 2.01 - 2.06 (1H, m), 1.66 - 1.78 (2H, m), 1.53 - 1.62 (2H, m), 1.17 - 1.35 (4H, m); ^{13}C NMR (151 MHz, DMSO- d_6) δ = 171.7, 170.2, 169.9, 166.7, 161.9, 161.2, 157.5, 157.2, 157.0, 156.8 (dd, J = 239.9, 2.2 Hz), 146.4 (app. t, J = 11.6 Hz), 144.7 (dd, J = 240.5, 2.8 Hz), 132.7, 132.6, 131.5, 127.5, 125.2, 124.1, 117.9, 116.9, 115.0, 100.6 (d, J = 28.2 Hz), 70.0, 58.2, 50.5, 45.4, 37.1, 34.7, 34.6, 30.1, 29.7, 28.6, 27.1, 24.6, 23.8, 21.5, all F-couplings not identified due to complexity of spectrum; LCMS (Method B): t_R = 0.92 min, $[\text{M}+\text{H}]^+$ 766 & 768, (94 % purity); HRMS: ($\text{C}_{36}\text{H}_{39}\text{ClF}_2\text{N}_9\text{O}_6$) $[\text{M}+\text{H}]^+$ requires 766.2680, found $[\text{M}+\text{H}]^+$ 766.2683.

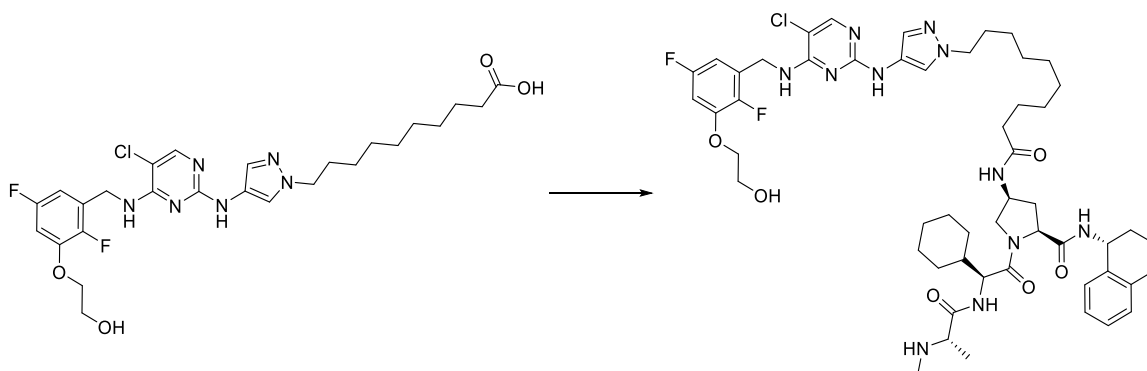
(2*S*,4*R*)-1-((*S*)-2-(7-(4-((5-Chloro-4-((2,5-difluoro-3-(2-hydroxyethoxy)benzyl)amino)pyrimidin-2-yl)amino)-1*H*-pyrazol-1-yl)heptanami-do)-3,3-dimethylbutanoyl)-4-hydroxy-*N*-(4-(4-methylthiazol-5-yl)benzyl)pyrrolidine-2-carboxamide (74)



7-(4-((5-Chloro-4-((2,5-difluoro-3-(2-hydroxyethoxy)benzyl)amino)pyrimidin-2-yl)amino)-1*H*-pyrazol-1-yl)heptanoic acid **182** (140 mg, 0.267 mmol), (2*S*,4*R*)-1-((*S*)-2-amino-3,3-dimethylbutanoyl)-4-hydroxy-*N*-(4-(4-methylthiazol-5-yl)benzyl)pyrrolidine-2-carboxamide hydrochloride (149 mg, 0.320 mmol), triethylamine (112 μL , 0.800 mmol) and HATU (152 mg, 0.400 mmol) were stirred together in *N,N*-Dimethylformamide (DMF) (5.334 mL) for 16 h at room temperature. The reaction mixture was concentrated *in vacuo*, diluted with DMSO (0.5 mL), split into two equal portions and purified directly by MDAP (formic acid modifier). The solvent was removed *in vacuo* to afford (2*S*,4*R*)-1-((*S*)-2-(7-(4-((5-chloro-4-((2,5-difluoro-3-(2-hydroxyethoxy)benzyl)amino)pyrimidin-2-yl)amino)-1*H*-pyrazol-1-yl)heptanami-do)-3,3-dimethylbutanoyl)-4-hydroxy-*N*-(4-(4-methylthiazol-5-yl)benzyl)-pyrrolidine-2-carboxamide **74** (149 mg, 0.159 mmol, 60 % yield) as a yellow solid. M.pt.: 108 - 110 $^{\circ}\text{C}$; ν_{max} (neat): 3279, 2935, 1630, 1570, 837, 557 cm^{-1} ; ^1H NMR (400 MHz, DMSO- d_6) δ = 9.66 (1H, br s), 8.98 (1H,

s), 8.62 (1H, br d, $J = 5.6$ Hz), 8.53 (1H, t, $J = 6.1$ Hz), 8.06 (1H, br s), 7.81 (1H, d, $J = 9.3$ Hz), 7.35 - 7.46 (5H, m), 7.05 (1H, ddd, $J = 10.1, 6.8, 3.1$ Hz), 6.62 (1H, br s), 4.70 (2H, br d, $J = 5.6$ Hz), 4.55 (1H, d, $J = 9.3$ Hz), 4.40 - 4.48 (2H, m), 4.37 (1H, br s), 4.23 (1H, dd, $J = 15.9, 5.6$ Hz), 4.09 (2H, t, $J = 4.8$ Hz), 3.96 (2H, br s), 3.75 (2H, t, $J = 4.9$ Hz), 3.62 - 3.71 (2H, m), 2.45 (3H, s), 2.18 - 2.33 (1H, m), 2.00 - 2.16 (5H, m), 1.87 - 1.98 (1H, m), 1.68 (2H, br s), 1.35 - 1.55 (2H, m), 1.09 - 1.31 (4H, m), 0.90 - 0.98 (9H, m); ^{13}C NMR (101 MHz, $\text{DMSO-}d_6$) $\delta = 170.9, 170.8, 168.6, 161.8, 157.3, 156.8$ (dd, $J = 240.3, 1.8$ Hz), 150.3, 146.5 (2C), 146.4 (app. t, $J = 11.7$ Hz), 144.7 (d, $J = 240.0$ Hz), 138.4, 130.1 (2C), 128.5, 127.7, 127.5 (2C), 126.9 (2C), 126.3, 116.9, 104.0, 100.4 (2C, br d, $J = 27.9$ Hz), 70.0, 67.8, 58.2, 57.6, 55.2, 50.4 (2C), 40.6, 36.8, 34.1, 33.7 (2C), 28.6, 27.1, 25.3, 24.6, 24.2 (3C), 14.8; ^{19}F NMR (376 MHz, $\text{DMSO-}d_6$) $\delta = -69.23$ (s), -71.11 (s); LCMS (Method A): $t_R = 0.90$ min, $[(M+2H)/2]^+$ 470, (95 % purity); HRMS: ($\text{C}_{45}\text{H}_{56}\text{ClF}_2\text{N}_{10}\text{O}_6\text{S}$) $[(M+2H)/2]^+$ requires 469.1919, found $[(M+2H)/2]^+$ 469.1927.

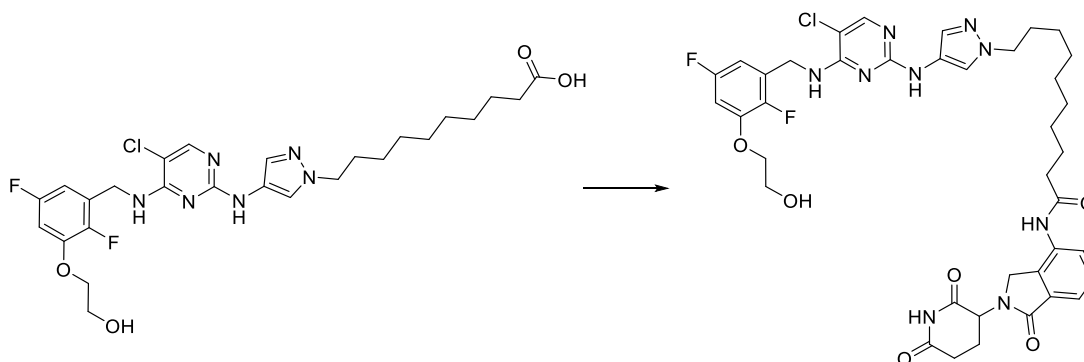
(2S,4S)-4-(10-(4-((5-Chloro-4-((2,5-difluoro-3-(2-hydroxyethoxy)benzyl)amino)pyrimidin-2-yl)amino)-1H-pyrazol-1-yl)decanamido)-1-((S)-2-cyclohexyl-2-((S)-2-(methylamino)propanamido)acet-yl)-N-((R)-1,2,3,4-tetrahydronaphthalen-1-yl)pyrrolidine-2-carboxamide (75)



10-(4-((5-Chloro-4-((2,5-difluoro-3-(2-hydroxyethoxy)benzyl)amino)pyrimidin-2-yl)amino)-1H-pyrazol-1-yl)decanoic acid **183** (151 mg, 0.229 mmol), *tert*-butyl ((S)-1-(((S)-2-((2S,4S)-4-amino-2-(((R)-1,2,3,4-tetrahydronaphthalen-1-yl)carbamoyl)pyrrolidin-1-yl)-1-cyclohexyl-2-oxoethyl)amino)-1-oxopropan-2-yl)(methyl)carbamate (160 mg, 0.275 mmol), triethylamine (96 μL , 0.687 mmol) and HATU (131 mg, 0.344 mmol) were stirred together in *N,N*-dimethylformamide (DMF) (4.580 mL) for 16 h at room temperature. TFA (176 μL , 2.290

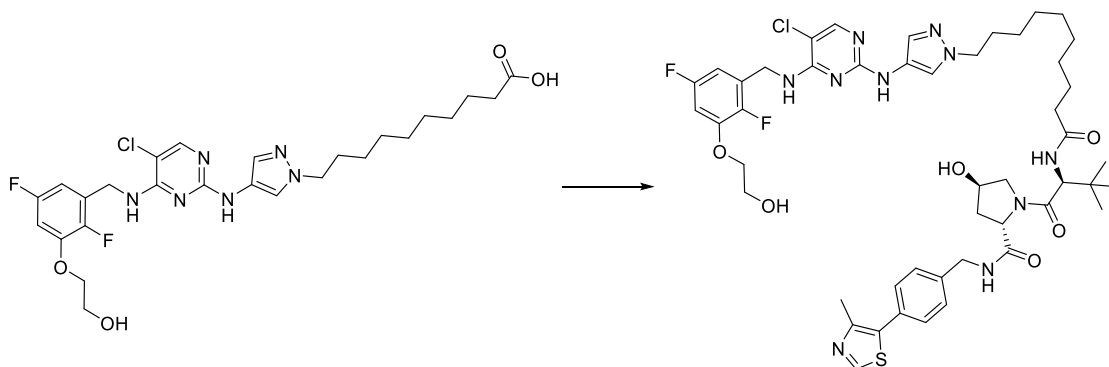
mmol) was added and the reaction mixture was stirred for a further 1 h. The reaction mixture was concentrated *in vacuo*; DMSO (1 mL) was added, split into two equal portions and purified directly by MDAP (ammonium carbonate modifier). The solvent was removed *in vacuo* to afford (2*S*,4*S*)-4-(10-(4-((5-chloro-4-((2,5-difluoro-3-(2-hydroxyethoxy)-benzyl)amino)pyrimidin-2-yl)amino)-1*H*-pyrazol-1-yl)decanamido)-1-((*S*)-2-cyclohexyl-2-((*S*)-2-(methylamino)propanamido)acetyl)-*N*-((*R*)-1,2,3,4-tetrahydronaphthalen-1-yl)pyrrolidine-2-carboxamide **75** (19 mg, 0.018 mmol, 8 % yield) as a brown, hard gum. ν_{\max} (neat): 3278, 2926, 2854, 1634, 1574, 1538, 1025 cm^{-1} ; ^1H NMR (600 MHz, DMSO- d_6) δ = 9.07 (1H, br s), 8.40 (1H, d, J = 8.4 Hz), 8.11 (1H, d, J = 7.7 Hz), 7.84 - 7.98 (2H, m), 7.66 (1H, br s), 7.32 (2H, br d, J = 7.7 Hz), 7.06 - 7.17 (3H, m), 7.02 (1H, br s), 6.56 (1H, br s), 4.87 - 5.00 (2H, m), 4.66 (2H, br d, J = 5.5 Hz), 4.39 (1H, t, J = 8.1 Hz), 4.25 - 4.33 (2H, m), 4.02 - 4.10 (3H, m), 3.90 (2H, br s), 3.70 - 3.82 (2H, m), 2.93 - 3.01 (1H, m), 2.66 - 2.80 (2H, m), 2.32 - 2.49 (1H, m), 2.18 (3H, s), 2.04 - 2.11 (8H, m), 1.97 - 1.98 (1H, m), 1.79 - 1.90 (1H, m), 1.61 - 1.75 (8H, m), 1.47 (2H, s), 1.08 - 1.26 (16H, m); ^{13}C NMR (151 MHz, DMSO- d_6) δ = 173.2, 170.9, 169.8 (2C), 168.8, 156.4, 156.8 (dd, J = 239.1, 1.9 Hz), 150.6, 146.3 (app. t, J = 11.6 Hz), 144.6 (dd, J = 237.7, 1.7 Hz), 140.0, 136.2, 135.8, 127.3 (d, J = 15.5 Hz), 125.5, 124.5, 122.0 (2C), 116.9, 100.0 (2C, d, J = 28.2 Hz), 89.1, 70.0, 58.2, 58.0, 57.3, 53.7, 53.1, 51.2, 50.2, 46.6, 45.6, 38.9, 34.4, 33.1 (2C), 29.5, 28.8, 28.6, 27.7, 27.6, 27.6, 27.5, 27.4, 26.8, 25.8, 24.8, 24.8, 24.6, 24.4, 24.0, 19.1, 17.9; LCMS (Method A): t_R = 0.88 min, $[(M+2H)/2]^+$ 517, (100 % purity); HRMS: ($\text{C}_{53}\text{H}_{74}\text{ClF}_2\text{N}_{11}\text{O}_6$) $[(M+2H)/2]^+$ requires 516.7751, found $[(M+2H)/2]^+$ 516.7745.

10-(4-((5-Chloro-4-((2,5-difluoro-3-(2-hydroxyethoxy)benzyl)amino)pyrimidin-2-yl)-amino)-1*H*-pyrazol-1-yl)-*N*-(2-(2,6-dioxopiperidin-3-yl)-1-oxoisindolin-4-yl)decanamide (76)



10-(4-((5-Chloro-4-((2,5-difluoro-3-(2-hydroxyethoxy)benzyl)amino)pyrimidin-2-yl)amino)-1H-pyrazol-1-yl)decanoic acid **183** (100 mg, 0.152 mmol), 3-(4-amino-1-oxoisindolin-2-yl)piperidine-2,6-dione (47.2 mg, 0.182 mmol), triethylamine (63.4 μ L, 0.455 mmol) and HATU (87 mg, 0.227 mmol) were stirred together in *N,N*-dimethylformamide (DMF) (3.033 mL) for 16 h at room temperature. The reaction mixture was concentrated *in vacuo*, diluted with DMSO (0.5 mL) and purified directly by MDAP (ammonium carbonate modifier). The solvent was removed *in vacuo* to afford 10-(4-((5-chloro-4-((2,5-difluoro-3-(2-hydroxyethoxy)benzyl)amino)pyrimidin-2-yl)amino)-1H-pyrazol-1-yl)-*N*-(2-(2,6-dioxopiperidin-3-yl)-1-oxoisindolin-4-yl)decanamide **76** (18 mg, 0.022 mmol, 15 % yield) as a brown hard gum. ν_{\max} (neat): 3039, 2928, 2855, 1674, 1199 cm^{-1} ; ^1H NMR (600 MHz, DMSO- d_6) δ = 11.01 (1H, s), 9.78 (1H, s), 9.07 - 9.45 (1H, m), 7.97 (1H, s), 7.82 (1H, dd, J = 7.5, 0.9 Hz), 7.45 - 7.54 (2H, m), 7.29 (1H, s), 7.21 (1H, s), 7.12 (1H, s), 7.02 (1H, ddd, J = 9.9, 6.8, 2.8 Hz), 6.53 - 6.65 (1H, m), 5.14 (1H, dd, J = 13.2, 5.1 Hz), 4.67 (2H, br d, J = 5.5 Hz), 4.08 (2H, t, J = 4.8 Hz), 3.91 (2H, br s), 3.74 (2H, t, J = 5.0 Hz), 2.88 - 2.97 (1H, m), 2.59 - 2.65 (1H, m), 2.55 (1H, s), 2.33 - 2.37 (2H, m), 2.08 (2H, s), 2.00 - 2.06 (1H, m), 1.56 - 1.69 (4H, m), 1.12 - 1.33 (11H, m); ^{13}C NMR (151 MHz, DMSO- d_6) δ = 171.7, 170.3, 169.9, 166.7, 161.8, 156.8 (d, J = 238.0 Hz), 152.7, 151.3, 146.3 (app. t, J = 11.6 Hz), 144.6 (dd, J = 237.7, 1.1 Hz), 132.7, 132.6, 131.5, 127.4, 127.1 (dd, J = 14.4, 9.4 Hz), 124.1, 121.6, 117.8, 116.9 (d, J = 4.4 Hz), 114.9, 105.7, 100.1 (d, J = 27.6 Hz), 70.0, 61.4, 58.2, 50.4, 50.2, 45.4, 39.3, 34.7, 30.1, 28.8, 27.7, 27.6, 27.5, 27.4, 24.8, 24.0, 21.5; LCMS (Method A): t_{R} = 1.04 min, $[\text{M}+\text{H}]^+$ 808 & 810, (92 % purity); HRMS: ($\text{C}_{39}\text{H}_{45}\text{ClF}_2\text{N}_9\text{O}_6$) $[\text{M}+\text{H}]^+$ requires 808.3149, found $[\text{M}+\text{H}]^+$ 808.3154.

(2*S*,4*R*)-1-((*S*)-2-(10-(4-((5-Chloro-4-((2,5-difluoro-3-(2-hydroxyethoxy)benzyl)amino)pyrimidin-2-yl)amino)-1*H*-pyrazol-1-yl)decanamido)-3,3-dimethylbutanoyl)-4-hydroxy-*N*-(4-(4-methylthiazol-5-yl)benzyl)pyrrolidine-2-carboxamide (77)



10-(4-((5-Chloro-4-((2,5-difluoro-3-(2-hydroxyethoxy)benzyl)amino)pyrimidin-2-yl)amino)-1*H*-pyrazol-1-yl)decanoic acid **183** (65 mg, 0.086 mmol), (2*S*,4*R*)-1-((*S*)-2-amino-3,3-dimethylbutanoyl)-4-hydroxy-*N*-(4-(4-methylthiazol-5-yl)benzyl)pyrrolidine-2-carboxamide hydrochloride (48.2 mg, 0.103 mmol), triethylamine (36.0 μ L, 0.258 mmol) and HATU (49.0 mg, 0.129 mmol) were stirred together in *N,N*-dimethylformamide (DMF) (1.719 mL) for 15 h at room temperature. The reaction mixture was diluted with added DMSO (0.2 mL) and purified directly by MDAP (formic acid modifier). The solvent was removed *in vacuo* to afford (2*S*,4*R*)-1-((*S*)-2-(10-(4-((5-chloro-4-((2,5-difluoro-3-(2-hydroxyethoxy)benzyl)amino)pyrimidin-2-yl)amino)-1*H*-pyrazol-1-yl)decanamido)-3,3-dimethyl-butanoyl)-4-hydroxy-*N*-(4-(4-methylthiazol-5-yl)benzyl)pyrrolidine-2-carboxamide **77** (12 mg, 0.012 mmol, 14 % yield) as a brown, hard gum. ν_{\max} (neat): 3285, 2927, 2851, 1625, 1576 cm^{-1} ; ^1H NMR (400 MHz, DMSO- d_6) δ = 9.05 (1H, s), 8.97 (1H, s), 8.53 (1H, t, J = 6.0 Hz), 7.93 (1H, s), 7.79 (1H, d, J = 9.3 Hz), 7.65 (1H, br s), 7.36 - 7.44 (4H, m), 7.29 (1H, br s), 7.01 (1H, ddd, J = 10.1, 6.8, 3.1 Hz), 6.50 - 6.60 (1H, m), 5.10 (1H, d, J = 3.4 Hz), 4.91 (1H, t, J = 5.4 Hz), 4.65 (2H, br d, J = 5.9 Hz), 4.54 (1H, d, J = 9.5 Hz), 4.39 - 4.48 (2H, m), 4.31 - 4.39 (1H, m), 4.22 (1H, dd, J = 15.9, 5.4 Hz), 4.01 - 4.13 (4H, m), 3.90 (1H, br s), 3.73 (2H, q, J = 4.9 Hz), 3.17 (4H, d, J = 5.1 Hz), 2.44 (3H, s), 1.99 - 2.15 (2H, m), 1.58 - 1.71 (2H, m), 1.35 - 1.58 (2H, m), 1.08 - 1.32 (10H, m), 0.93 (9H, s); ^{13}C NMR (101 MHz, DMSO- d_6) δ = 172.6, 172.4, 170.2, 158.1, 158.0, 151.9 (2C), 148.2 (4C), 140.0, 131.6 (2C), 130.1 (2C), 129.1 (2C), 127.9 (2C), 123.6, 119.6, 101.8, 101.5 (2C), 71.6, 69.3, 59.8, 59.2, 56.8, 51.8, 49.1, 42.1, 38.4, 35.7, 35.4 (2C), 30.4, 29.3, 29.2, 29.1, 29.0,

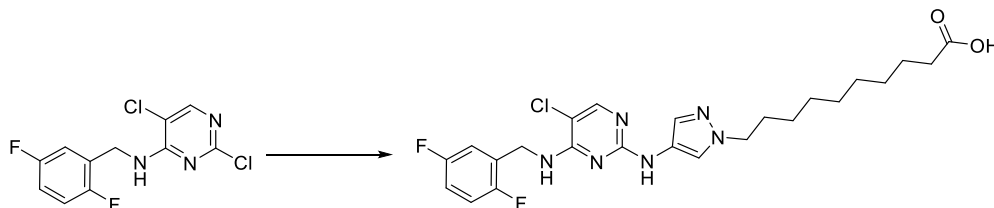
26.8, 26.4, 25.9 (3C), 16.4, F-couplings not identified due to complexity of spectrum; LCMS (Method A): $t_R = 1.17$ min, $[M+H]^+$ 979 & 981, (100 % purity); HRMS: ($C_{48}H_{63}ClF_2N_{10}O_6S$) $[(M+2H)/2]^+$ requires 490.2154, found $[(M+2H)/2]^+$ 490.2165. N.B. Characterising data obtained from separate batch.

2,5-Dichloro-*N*-(2,5-difluorobenzyl)pyrimidin-4-amine (186)



(2,5-Difluorophenyl)methanamine **185** (1.637 mL, 13.97 mmol), 2,4,5-trichloropyrimidine (1.917 mL, 16.73 mmol) and DIPEA (6.10 mL, 34.9 mmol) were stirred together in isopropanol (100 mL) under an atmosphere of nitrogen at room temperature for 2 h. The solvent was removed *in vacuo* and the residue was diluted with aqueous saturated sodium hydrogen carbonate (40 mL) and extracted with DCM (4 × 40 mL). The organic layers were combined, passed through a hydrophobic frit and the solvent was removed *in vacuo*. The resultant brown solid was triturated with ether (4 × 5 mL) to yield 2,5-dichloro-*N*-(2,5-difluorobenzyl)pyrimidin-4-amine **186** (2.779 g, 9.58 mmol, 69 % yield) as a white solid. M.pt.: 108 – 110 °C; ν_{max} (neat): 3049, 1544, 1106, 756 cm^{-1} ; 1H NMR (400 MHz, DMSO- d_6) $\delta = 8.47$ (1H, br t, $J = 6.0$ Hz), 8.23 (1H, s), 7.22 - 7.31 (1H, m), 7.12 - 7.20 (2H, m), 4.64 (2H, d, $J = 5.9$ Hz); ^{13}C NMR (101 MHz, DMSO- d_6) $\delta = 159.2$, 158.8 (dd, $J = 193.7$, 2.2 Hz), 157.7, 156.4 (dd, $J = 194.4$, 2.2 Hz), 154.6, 127.7 (dd, $J = 17.2$, 7.7 Hz), 117.1 (dd, $J = 24.2$, 8.8 Hz), 116.1 (dd, $J = 24.9$, 5.1 Hz), 115.7 (dd, $J = 24.2$, 8.8 Hz), 113.6, 38.2 (d, $J = 3.7$ Hz); LCMS (Method A): $t_R = 1.19$ min, $[M+H]^+$ 290 & 292 (99 % purity); HRMS: ($C_{11}H_8Cl_2F_2N_3$) $[M+H]^+$ requires 290.0063, found $[M+H]^+$ 290.0066.

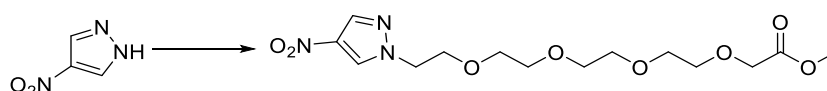
10-(4-((5-Chloro-4-((2,5-difluorobenzyl)amino)pyrimidin-2-yl)amino)-1H-pyrazol-1-yl)decanoic acid (187)



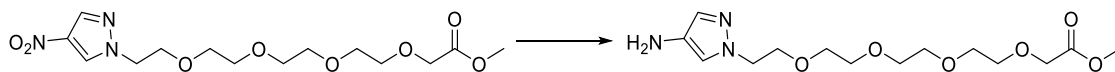
2,5-Dichloro-*N*-(2,5-difluorobenzyl)pyrimidin-4-amine **186** (340 mg, 1.172 mmol), methyl 10-(4-amino-1*H*-pyrazol-1-yl)decanoate (689 mg, 1.289 mmol) and 2 M aqueous HCl (1.172 mL, 2.344 mmol) in ethanol (2.348 mL) were sealed within a vessel and heated in a Biotage Initiator microwave for 1.5 h at 100 °C using a high absorption setting. The reaction mixture was allowed to cool to room temperature. The solvent was removed *in vacuo* and 2 M aqueous NaOH (5.86 mL, 11.72 mmol), 1,4-dioxane (2.348 mL) and water (0.939 mL) was added and the reaction mixture was stirred for 1 h at room temperature. The solvent was removed *in vacuo*. The residue purified by reverse phase chromatography (15 – 35 % MeCN + 0.1 % HCO₂H in H₂O + 0.1 % HCO₂H, 120 g C₁₈) to afford 10-(4-((5-chloro-4-((2,5-difluorobenzyl)amino)pyrimidin-2-yl)amino)-1*H*-pyrazol-1-yl)decanoic acid **187** (470 mg, 0.927 mmol, 79 % yield) as a brown gum. M.pt.: 86 – 88 °C; ν_{\max} (neat): 3267, 3027, 2854, 2926, 1918, 1724, 1359 cm⁻¹; ¹H NMR (400 MHz, DMSO-*d*₆) δ = 12.30 (1H, br s), 9.05 (1H, br s), 7.94 (1H, s), 7.66 (1H, br s), 7.53 (1H, br s), 7.23 - 7.34 (2H, m), 7.09 - 7.17 (1H, m), 6.98 - 7.08 (1H, m), 4.67 (2H, br d, *J* = 5.6 Hz), 3.90 (2H, t, *J* = 5.7 Hz), 2.17 (2H, t, *J* = 7.3 Hz), 1.59 - 1.70 (2H, m), 1.41 - 1.53 (2H, m), 1.16 - 1.25 (10H, m); ¹³C NMR (101 MHz, DMSO-*d*₆) δ = 173.3, 161.9, 156.5, 156.5, 157.1 (dd, *J* = 239.9, 1.5 Hz), 153.6 (dd, *J* = 236.2, 2.2 Hz), 152.5, 128.3 (2C), 127.5 (dd, *J* = 17.6, 7.3 Hz), 122.0, 115.4 (2C, dd, *J* = 24.2, 8.8 Hz), 113.7 (dd, *J* = 24.2, 8.8 Hz), 50.2, 36.4 (dd, *J* = 4.8, 1.8 Hz), 32.5, 28.8, 27.6, 27.5, 27.4, 27.3, 24.8, 23.3; ¹⁹F NMR (376 MHz, DMSO-*d*₆) δ = -118.60 (s), -124.50 (s); LCMS (Method A): *t*_R = 0.99 min, [M+H]⁺ 507 & 509 (97 % purity); HRMS: (C₂₄H₃₀ClF₂N₆O₂) [M+H]⁺ requires 507.2113, found [M+H]⁺ 507.2100.

Methyl 14-chloro-3,6,9,12-tetraoxatetradecanoate (188)

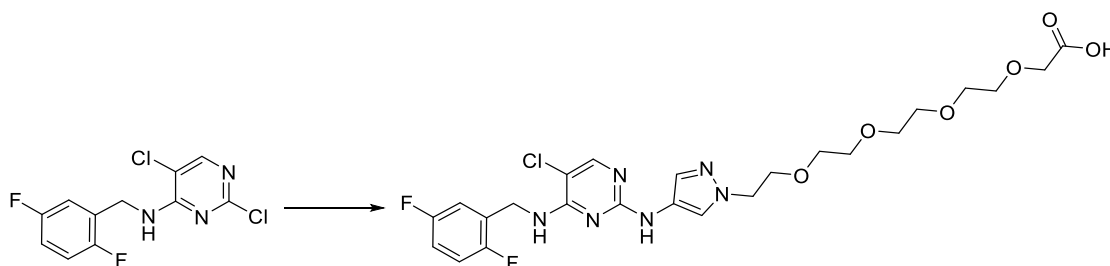
14-Chloro-3,6,9,12-tetraoxatetradecanoic acid **201** (1.5 g, 5.54 mmol) was dissolved in DMF (0.021 mL, 0.277 mmol) and DCM (16.15 mL), and was added 2 M oxalyl chloride in DCM (3.32 mL, 6.65 mmol) dropwise and the reaction mixture was stirred at room temperature for 15 min. MeOH (1.939 mL, 47.9 mmol) was added and the reaction mixture was stirred at room temperature for a further 15 min. The reaction mixture was diluted with saturated aqueous NaHCO₃ (50 mL) the layers were separated using a hydrophobic frit. The organic layer was evaporated *in vacuo* to afford methyl 14-chloro-3,6,9,12-tetraoxatetradecanoate **188** (1.497 g, 5.26 mmol, 95 % yield) as a brown oil. Used crude in the next reaction.

14-(4-Nitro-1H-pyrazol-1-yl)-3,6,9,12-tetraoxatetradecanoate (191)

4-Nitro-1H-pyrazole **175** (100 mg, 0.884 mmol), methyl 14-chloro-3,6,9,12-tetraoxatetradecanoate (378 mg, 1.327 mmol) and potassium carbonate (183 mg, 1.327 mmol) were sealed within a vessel and DMF (1.005 mL) was added. The reaction mixture was heated in for 1.5 h at 50 °C. The reaction mixture was diluted with water (50 mL) and extracted with DCM (3 × 50 mL). The organic layers were combined, passed through a hydrophobic frit and the solvent was removed *in vacuo*. The residue was purified by reverse phase column chromatography (5 - 30 % MeCN in H₂O + 0.1 % (NH₄)₂CO₃, 30 g C₁₈) to afford methyl 14-(4-nitro-1H-pyrazol-1-yl)-3,6,9,12-tetraoxatetradecanoate **191** (202 mg, 0.559 mmol, 63 % yield) a colourless oil. ¹H NMR (400 MHz, DMSO-*d*₆) δ = 8.83 (1H, d, *J* = 0.5 Hz), 8.26 (1H, d, *J* = 0.7 Hz), 4.35 (2H, t, *J* = 5.3 Hz), 4.12 (2H, s), 3.82 (2H, t, *J* = 5.3 Hz), 3.65 (3H, s), 3.56 - 3.62 (6H, m), 3.47 - 3.51 (6H, m); ¹³C NMR (101 MHz, DMSO-*d*₆) δ = 171.0, 135.9, 135.3, 131.3, 71.0, 70.5, 70.5, 70.2, 70.2, 68.5, 68.1, 68.1, 52.8, 51.8; LCMS (Method B): t_R = 0.76 min, [M+H]⁺ 362 (96 % purity).

Methyl 14-(4-amino-1H-pyrazol-1-yl)-3,6,9,12-tetraoxatetradecanoate (190)

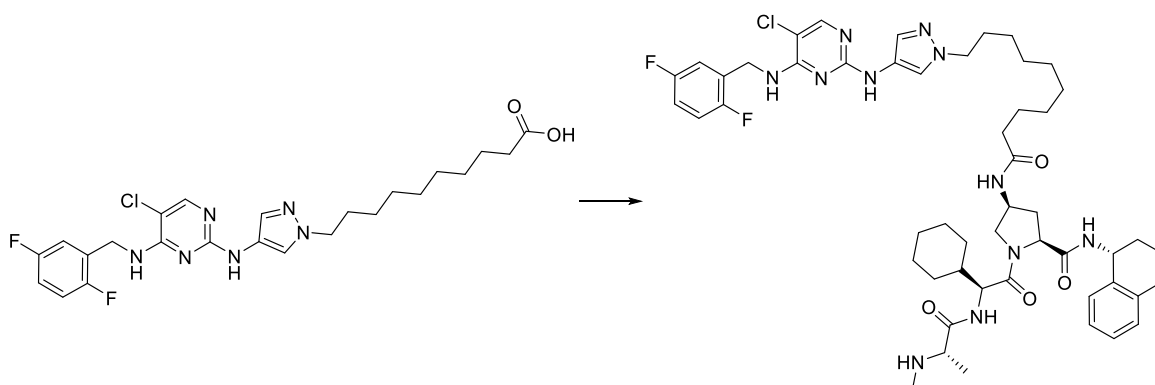
To a COWare tube, palladium on carbon (3.83 mg, 3.60 μmol) and methyl 14-(4-nitro-1H-pyrazol-1-yl)-3,6,9,12-tetraoxatetradecanoate **189** (130 mg, 0.360 mmol) in ethanol (1.077 mL) were added to one tube under nitrogen and that tube was sealed to the atmosphere. 2 M aqueous HCl (5.396 mL, 10.79 mmol) and zinc (353 mg, 5.40 mmol) were added under nitrogen to the other tube which was subsequently sealed to the atmosphere. The reaction mixture stirred at room temperature for 16 h. The reaction mixture was filtered over Celite and washed with ethyl acetate (30 mL). The solvent was removed *in vacuo* and the residue was dissolved in methanol:DMSO 1:1 (0.5 mL) and purified by reverse phase column chromatography (5 - 30 % MeCN in H₂O + 0.1 % (NH₄)₂CO₃, 30 g C₁₈) to afford methyl 14-(4-amino-1H-pyrazol-1-yl)-3,6,9,12-tetraoxatetradecanoate **190** (153 mg, 0.462 mmol, 128 % yield) as an orange oil. LCMS (Method B): t_R = 0.53 min, [M+H]⁺ 332 (42 % purity). Used crude in the next reaction.

14-(4-((5-Chloro-4-((2,5-difluorobenzyl)amino)pyrimidin-2-yl)amino)-1H-pyrazol-1-yl)-3,6,9,12-tetraoxatetradecanoic acid (191)

2,5-Dichloro-*N*-(2,5-difluorobenzyl)pyrimidin-4-amine **186** (185 mg, 0.638 mmol), methyl 14-(4-amino-1H-pyrazol-1-yl)-3,6,9,12-tetraoxatetradecanoate (894 mg, 0.701 mmol) and 2 M aqueous HCl (638 μL 1.275 mmol) in ethanol (1.284 mL) were sealed within a vessel and heated in a Biotage Initiator microwave for 1.5 h at 100 °C using a high absorption setting. The reaction mixture was allowed to cool to room temperature. The solvent was removed *in*

vacuo and 2 M aqueous NaOH (3.189 mL, 6.38 mmol), 1,4-dioxane (1.284 mL) and water (513 μ L) was added and the reaction mixture was stirred for 1 h at room temperature. The solvent was removed *in vacuo*. The residue was dissolved in DMSO (5 mL) and purified by reverse phase chromatography (2 - 55 % MeCN + 0.1 % HCO₂H in H₂O + 0.1 % HCO₂H, 30 g C₁₈) to afford 14-(4-((5-chloro-4-((2,5-difluorobenzyl)amino)pyrimidin-2-yl)amino)-1H-pyrazol-1-yl)-3,6,9,12-tetraoxatetradecanoic acid **191** (355 mg, 0.491 mmol, 77 % yield) as a light pink solid. LCMS (Method A): t_R = 0.69 min, [M+H]⁺ 571 & 573 (79 % purity). Used crude in the next reaction.

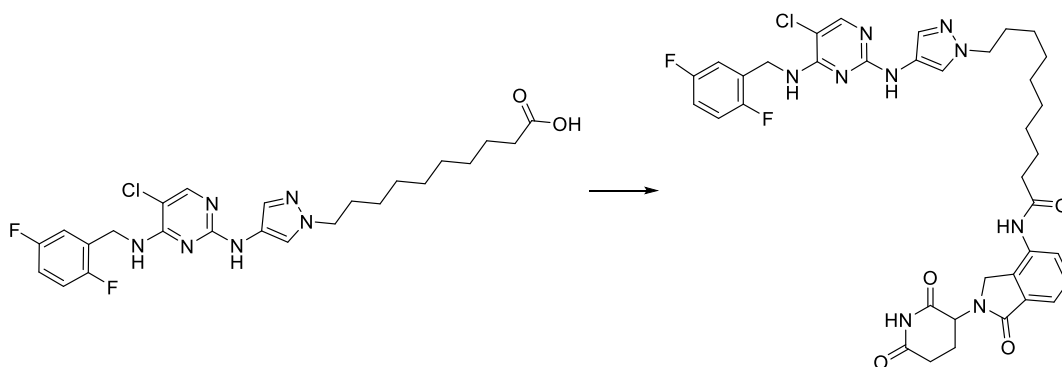
(2S,4S)-4-(10-(4-((5-Chloro-4-((2,5-difluorobenzyl)amino)pyrimidin-2-yl)amino)-1H-pyrazol-1-yl)decanamido)-1-((S)-2-cyclohexyl-2-((S)-2-(methylamino)propanamido)-acetyl)-N-((R)-1,2,3,4-tetrahydronaphthalen-1-yl)pyrrolidine-2-carboxamide (79)



10-(4-((5-Chloro-4-((2,5-difluorobenzyl)amino)pyrimidin-2-yl)amino)-1H-pyrazol-1-yl)decanoic acid **187** (141 mg, 0.278 mmol), *tert*-butyl ((S)-1-(((S)-2-((2S,4S)-4-amino-2-(((R)-1,2,3,4-tetrahydronaphthalen-1-yl)carbamoyl)pyrrolidin-1-yl)-1-cyclohexyl-2-oxoethyl)-amino)-1-oxopropan-2-yl)(methyl)carbamate (195 mg, 0.334 mmol), triethylamine (116 μ L, 0.834 mmol) and HATU (159 mg, 0.417 mmol) were stirred together in DMF (5.562 mL) for 16 h at room temperature. TFA (214 μ L, 2.78 mmol) was added and the reaction mixture was stirred for a further 16 h. The reaction mixture was concentrated *in vacuo* and DMSO (1 mL) was added, split into two equal portions and purified directly by MDAP (ammonium carbonate modifier). The solvent was removed *in vacuo*. The residue was purified by reverse phase column chromatography (50 – 95 % MeCN in H₂O + 0.1 % (NH₄)₂CO₃, 120 g C₁₈) to afford (2S,4S)-4-(10-(4-((5-chloro-4-((2,5-difluorobenzyl)amino)pyrimidin-2-yl)amino)-1H-

pyrazol-1-yl)decanamido)-1-((S)-2-cyclohexyl-2-((S)-2-(methylamino)propanamido)acetyl)-N-((R)-1,2,3,4-tetrahydronaphthalen-1-yl)pyrrolidine-2-carboxamide **79** (82 mg, 0.084 mmol, 30 % yield) as a white solid. M.pt.: 100 - 102 °C; ν_{\max} (neat): 3281, 2927, 2854, 1645, 1574, 1490 cm^{-1} ; ^1H NMR (400 MHz, DMSO- d_6) δ = 9.06 (1H, br s), 8.40 (1H, d, J = 8.6 Hz), 8.11 (1H, d, J = 7.8 Hz), 7.94 (1H, s), 7.90 (1H, d, J = 8.6 Hz), 7.67 (1H, br s), 7.53 (1H, br s), 7.22 - 7.37 (3H, m), 7.01 - 7.19 (5H, m), 5.75 (1H, s), 4.89 - 4.98 (1H, m), 4.67 (2H, br d, J = 5.6 Hz), 4.39 (1H, br t, J = 8.1 Hz), 4.23 - 4.34 (2H, m), 4.02 - 4.10 (1H, m), 3.90 (2H, br s), 3.33 - 3.41 (1H, m), 2.96 (1H, q, J = 6.8 Hz), 2.64 - 2.80 (2H, m), 2.33 - 2.43 (1H, m), 2.18 (2H, s), 2.05 (2H, br t, J = 7.5 Hz), 1.79 - 1.90 (3H, m), 1.55 - 1.78 (10H, m), 1.40 - 1.55 (2H, m), 1.22 (9H, br s), 1.12 - 1.18 (4H, m), 1.10 (3H, m), 0.85 - 1.08 (3H, m); ^{13}C NMR (101 MHz, DMSO- d_6) δ = 174.8, 172.4, 171.4, 170.4, 158.2, 158.1, 158.7 (d, J = 239.2 Hz), 156.4 (br d, J = 239.6 Hz), 154.1, 137.8, 137.4, 129.9, 129.2 (d, J = 7.3 Hz), 129.1, 128.9 (d, J = 7.3 Hz), 127.1, 126.1, 123.6, 117.0 (dd, J = 24.2, 8.8 Hz), 115.3 (dd, J = 24.2, 8.8 Hz), 59.6, 58.9, 55.4, 54.7, 52.9, 51.8, 48.2, 47.2, 38.1 (2C), 36.0, 34.9, 34.7, 30.4 (2C), 30.3 (2C), 29.3 (2C), 29.2, 29.2, 29.1, 29.0, 28.4, 26.5, 26.4, 26.2, 26.0, 25.6, 20.7, 19.5; ^{19}F NMR (376 MHz, DMSO- d_6) δ = -118.56 (s), -124.50 (s); LCMS (Method B): t_{R} = 1.42 min, $[\text{M}+\text{H}]^+$ 973 & 975 (100 % purity); HRMS: ($\text{C}_{51}\text{H}_{69}\text{ClF}_2\text{N}_{11}\text{O}_4$) $[\text{M}+\text{H}]^+$ requires 972.5190, found $[\text{M}+\text{H}]^+$ 972.5232.

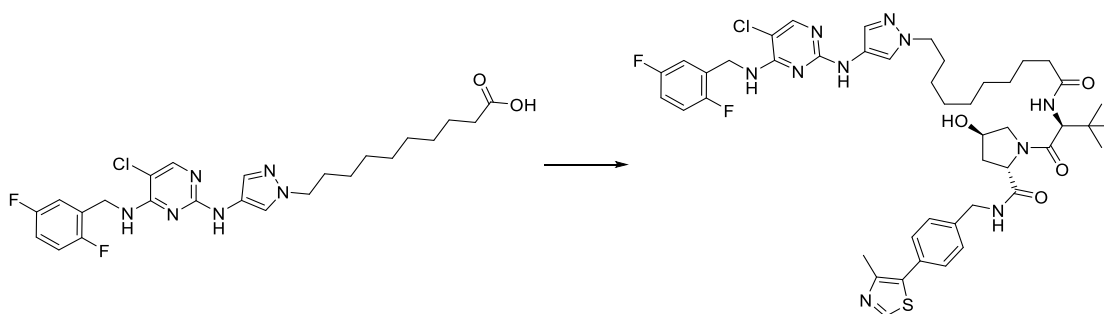
10-(4-((5-Chloro-4-((2,5-difluorobenzyl)amino)pyrimidin-2-yl)amino)-1H-pyrazol-1-yl)-N-(2-(2,6-dioxopiperidin-3-yl)-1-oxoisoindolin-4-yl)decanamide (80)



10-(4-((5-Chloro-4-((2,5-difluorobenzyl)amino)pyrimidin-2-yl)amino)-1H-pyrazol-1-yl)decanoic acid **187** (141 mg, 0.278 mmol), 3-(4-amino-1-oxoisoindolin-2-yl)piperidine-2,6-dione (87 mg, 0.334 mmol), triethylamine (116 μL , 0.834 mmol) and HATU (159 mg, 0.417

mmol) were stirred together in DMF (5.562 mL) for 16 h at room temperature. The reaction mixture was concentrated *in vacuo* and diluted with DMSO (0.5 mL) and purified directly by MDAP (ammonium carbonate modifier). The residue was purified by reverse phase column chromatography (30 - 55 % H₂O + 0.1 % (NH₄)₂CO₃ in MeCN, 12 g C₁₈) to afford 10-(4-((5-chloro-4-((2,5-difluorobenzyl)amino)pyrimidin-2-yl)amino)-1H-pyrazol-1-yl)-N-(2-(2,6-dioxopiperidin-3-yl)-1-oxoisindolin-4-yl)decanamide **79** (64 mg, 0.086 mmol, 30.8 % yield) as a colourless gum. ν_{\max} (neat): 3280, 2927, 2863, 1679, 1488 cm⁻¹; ¹H NMR (400 MHz, DMSO-*d*₆) δ = 11.01 (1H, s), 9.73 (1H, s), 9.06 (1H, br s), 7.95 (1H, s), 7.82 (1H, dd, *J* = 7.5, 1.6 Hz), 7.67 (1H, br s), 7.46 - 7.54 (2H, m), 7.32 (1H, br s), 7.23 - 7.30 (1H, m), 7.09 - 7.16 (1H, m), 7.04 (1H, br s), 5.16 (1H, dd, *J* = 13.2, 5.1 Hz), 4.68 (2H, br d, *J* = 5.6 Hz), 4.38 (2H, d, *J* = 6.6 Hz), 3.91 (2H, br s), 2.87 - 2.98 (1H, m), 2.58 - 2.67 (1H, m), 2.33 - 2.38 (3H, m), 2.08 (2H, s), 2.00 - 2.07 (1H, m), 1.56 - 1.68 (4H, m), 1.17 - 1.34 (9H, m); ¹³C NMR (101 MHz, DMSO-*d*₆) δ = 171.7, 170.2, 169.9, 166.7, 157.1 (br d, *J* = 238.4 Hz), 154.7 (d, *J* = 237.0 Hz), 152.5, 132.7, 132.5, 131.5, 128.3, 127.6 (d, *J* = 7.3 Hz), 127.4, 127.4, 124.1, 122.0, 117.8, 116.8, 115.4 (dd, *J* = 24.2, 8.1 Hz), 113.7 (dd, *J* = 23.8, 8.4 Hz), 101.0, 53.7, 50.4, 50.2, 45.4, 36.4, 34.7, 30.1, 28.8, 27.7, 27.6, 27.5, 27.4, 24.8, 23.9, 21.5; ¹⁹F NMR (376 MHz, DMSO-*d*₆) δ = -118.54 (s), -124.47 (s); LCMS (Method B): *t*_R = 1.16 min, [M+H]⁺ 749 & 750 (100 % purity); HRMS: (C₃₇H₄₁ClF₂N₉O₄) [M+H]⁺ requires 748.2938, found [M+H]⁺ 748.2941.

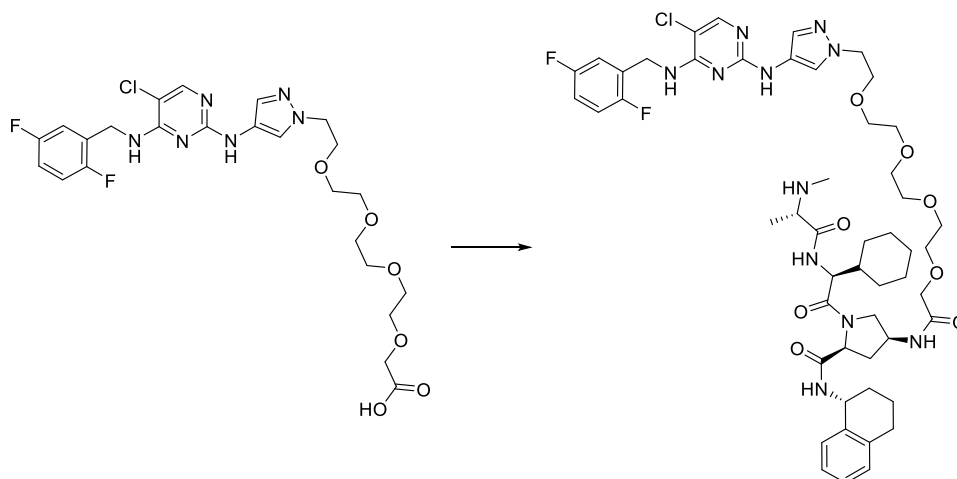
(2S,4R)-1-((S)-2-(10-(4-((5-chloro-4-((2,5-difluorobenzyl)amino)pyrimidin-2-yl)amino)-1H-pyrazol-1-yl)decanamido)-3,3-dimethylbutanoyl)-4-hydroxy-N-(4-(4-methylthiazol-5-yl)benzyl)pyrrolidine-2-carboxamide (81)



10-(4-((5-Chloro-4-((2,5-difluorobenzyl)amino)pyrimidin-2-yl)amino)-1H-pyrazol-1-yl)-decanoic acid **187** (141 mg, 0.278 mmol), (2S,4R)-1-((S)-2-amino-3,3-dimethylbutanoyl)-4-

hydroxy-*N*-(4-(4-methylthiazol-5-yl)benzyl)pyrrolidine-2-carboxamide, triethylamine (116 μ L, 0.834 mmol) and HATU (159 mg, 0.417 mmol) were stirred together in DMF (5.562 mL) for 15 h at room temperature. The reaction mixture was diluted with added DMSO (0.2 mL) and purified directly by MDAP (ammonium carbonate modifier). The solvent was removed *in vacuo* to afford (2*S*,4*R*)-1-((*S*)-2-(10-(4-((5-chloro-4-((2,5-difluorobenzyl)amino)pyrimidin-2-yl)amino)-1*H*-pyrazol-1-yl)decanamido)-3,3-dimethyl-butanoyl)-4-hydroxy-*N*-(4-(4-methylthiazol-5-yl)benzyl)pyrrolidine-2-carboxamide **131** (74 mg, 0.080 mmol, 29 % yield) as a white gum. ν_{\max} (neat): 3275, 2928, 2856, 1611 cm^{-1} ; ^1H NMR (400 MHz, $\text{DMSO-}d_6$) δ = 9.06 (1H, br s), 8.98 (1H, s), 8.54 (1H, t, J = 6.0 Hz), 7.95 (1H, s), 7.80 (1H, d, J = 9.3 Hz), 7.67 (1H, br s), 7.36 - 7.45 (4H, m), 7.31 (1H, br s), 7.23 - 7.30 (1H, m), 7.08 - 7.17 (1H, m), 7.00 - 7.08 (1H, m), 5.11 (1H, d, J = 3.2 Hz), 4.68 (2H, br d, J = 5.9 Hz), 4.56 (1H, d, J = 9.5 Hz), 4.40 - 4.48 (2H, m), 4.33 - 4.40 (1H, m), 4.23 (1H, dd, J = 15.9, 5.6 Hz), 4.05 - 4.12 (2H, m), 3.88 - 3.92 (2H, m), 3.62 - 3.72 (2H, m), 3.18 (4H, d, J = 5.1 Hz), 2.45 (3H, s), 2.19 - 2.31 (1H, m), 2.00 - 2.15 (3H, m), 1.88 - 2.00 (1H, m), 1.64 (2H, br s), 1.37 - 1.58 (2H, m), 1.22 (4H, br s), 0.94 (9H, s); ^{13}C NMR (101 MHz, $\text{DMSO-}d_6$) δ = 171.0, 170.8, 168.6, 156.5, 156.5, 157.1 (d, J = 237.7 Hz), 154.7 (d, J = 238.4 Hz), 152.5, 150.2, 146.6, 138.4 (2C), 130.0, 128.5 (2C), 128.3 (2C), 127.5 (2C), 127.4, 126.3, 122.0, 117.6, 115.4 (dd, J = 24.2, 8.8 Hz), 113.7 (dd, J = 24.2, 8.1 Hz), 67.8, 57.6, 55.2, 50.2, 47.5, 40.6, 36.8, 36.5, 34.1, 33.8, 28.8, 27.7, 27.6, 27.5, 27.4, 25.2 (3C), 24.9, 24.3, 14.8; ^{19}F NMR (376 MHz, $\text{DMSO-}d_6$) δ = -118.54 (s), -124.47 (s); LCMS (Method B): t_{R} = 1.26 min, $[\text{M}+\text{H}]^+$ 920 & 922 (99 % purity); HRMS: ($\text{C}_{46}\text{H}_{58}\text{ClF}_2\text{N}_{10}\text{O}_4\text{S}$) $[\text{M}+\text{H}]^+$ requires 919.4020, found $[\text{M}+\text{H}]^+$ 919.4043.

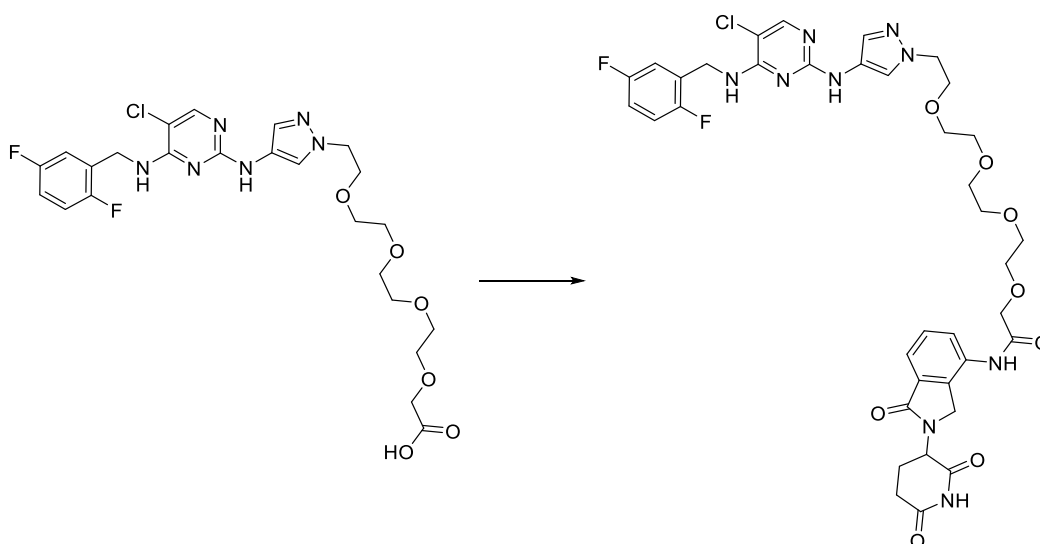
(2S,4S)-4-(14-(4-((5-Chloro-4-((2,5-difluorobenzyl)amino)pyrimidin-2-yl)amino)-1H-pyrazol-1-yl)-3,6,9,12-tetraoxatetradecanamido)-1-((S)-2-cyclohexyl-2-((S)-2-(methylamino)propanamido)-acetyl)-N-((R)-1,2,3,4-tetrahydronaphthalen-1-yl)pyrrolidine-2-carboxamide (82)



14-(4-((5-Chloro-4-((2,5-difluorobenzyl)amino)pyrimidin-2-yl)amino)-1H-pyrazol-1-yl)-3,6,9,12-tetraoxatetradecanoic acid **191** (122 mg, 0.175 mmol), *tert*-butyl ((S)-1-(((S)-2-((2S,4S)-4-amino-2-(((R)-1,2,3,4-tetrahydronaphthalen-1-yl)carbamoyl)pyrrolidin-1-yl)-1-cyclohexyl-2-oxoethyl)amino)-1-oxopropan-2-yl)(methyl)carbamate (123 mg, 0.210 mmol), triethylamine (73.3 μ L, 0.526 mmol) and HATU (100 mg, 0.263 mmol) were stirred together in DMF (3.504 mL) for 15 h at room temperature. The reaction mixture was diluted with water (10 mL) and extracted with DCM (3 \times 10 mL). The solvent was concentrated *in vacuo* and TFA (135 μ L, 1.752 mmol) was added and the reaction mixture was stirred at room temperature for 16 h. The reaction mixture was diluted with added DMSO (0.2 mL) and purified directly by MDAP (ammonium carbonate modifier). The solvent was removed *in vacuo* to afford (2S,4S)-4-(14-(4-((5-chloro-4-((2,5-difluorobenzyl)amino)pyrimidin-2-yl)amino)-1H-pyrazol-1-yl)-3,6,9,12-tetraoxatetradecanamido)-1-((S)-2-cyclohexyl-2-((S)-2-(methylamino)propanamido)-acetyl)-N-((R)-1,2,3,4-tetrahydronaphthalen-1-yl)pyrrolidine-2-carboxamide **82** (65 mg, 0.063 mmol, 36 % yield) as a white solid. M.pt.: 90 - 92 $^{\circ}$ C; ν_{\max} (neat): 3263, 3061, 2927, 2855, 1608, 1574, 1490 cm^{-1} ; ^1H NMR (400 MHz, DMSO- d_6) δ = 9.03 (1H, br s), 8.44 (1H, d, J = 8.8 Hz), 8.32 (1H, br d, J = 8.6 Hz), 8.28 (1H, s), 8.09 (1H, d, J = 8.3 Hz), 7.94 (1H, s), 7.60 - 7.70 (1H, m), 7.22 - 7.38 (3H, m), 7.01 - 7.17 (5H, m), 4.90 - 5.00 (2H, m), 4.66 (2H, br d, J = 5.9 Hz), 4.33 - 4.49 (3H, m), 3.99 - 4.12 (3H, m), 3.88 (2H, s), 3.66 (2H,

br t, $J = 5.4$ Hz), 3.43 - 3.59 (12H, m), 2.65 - 2.79 (2H, m), 2.34 - 2.43 (1H, m), 2.20 - 2.29 (3H, m), 2.07 (2H, s), 1.77 - 1.89 (4H, m), 1.55 - 1.77 (7H, m), 0.93 - 1.21 (8H, m); ^{13}C NMR (101 MHz, DMSO- d_6) $\delta = 172.0, 169.9, 168.7, 167.9, 163.1, 156.5, 157.1$ (d, $J = 239.9$ Hz), 154.8 (d, $J = 239.9$ Hz), 152.4, 136.2, 135.8, 128.7 (2C), 127.3 (dd, $J = 16.1, 4.4$ Hz), 125.5 (2C), 124.5 (2C), 122.1, 118.4, 115.5 (dd, $J = 24.2, 8.8$ Hz), 113.7 (dd, $J = 24.6, 8.4$ Hz), 69.3, 68.8, 68.6, 68.6, 68.5, 68.5, 68.4, 68.1, 57.4, 57.2, 56.8, 53.4, 51.8, 50.2, 46.3, 45.6, 36.3, 33.1, 32.3, 32.1, 28.6, 27.6, 26.9, 24.7, 24.6, 24.4, 19.1, 17.2, 17.0; ^{19}F NMR (376 MHz, DMSO- d_6) $\delta = -118.66$ (s), -124.35 (s); LCMS (Method B): $t_R = 1.22$ min, $[(M+2H)/2]^+$ 519 (99 % purity); HRMS: ($\text{C}_{51}\text{H}_{70}\text{ClF}_2\text{N}_{11}\text{O}_8$) $[(M+2H)/2]^+$ requires 518.7532, found $[(M+2H)/2]^+$ 518.7541.

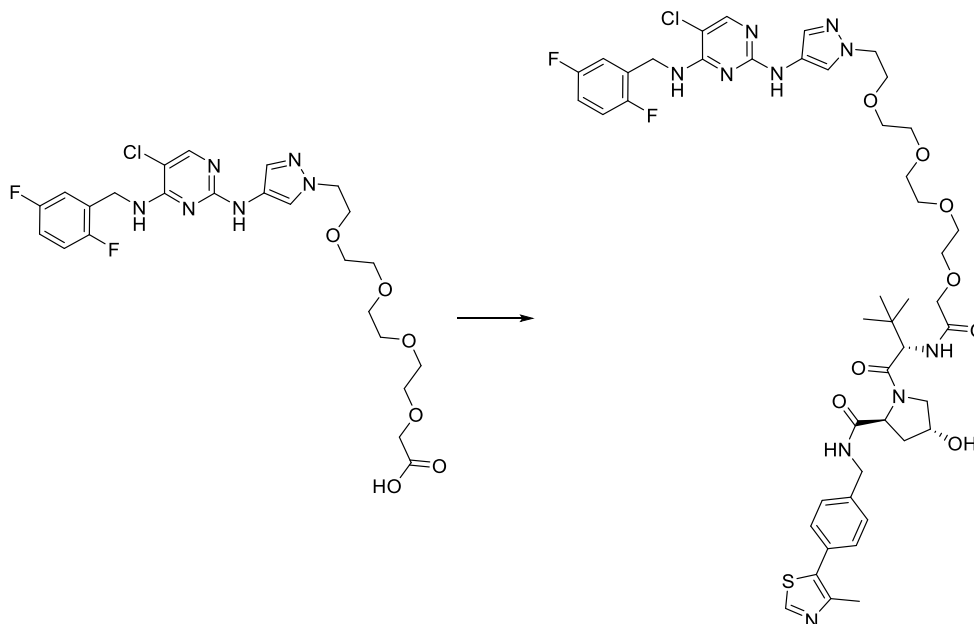
14-(4-((5-Chloro-4-((2,5-difluorobenzyl)amino)pyrimidin-2-yl)amino)-1H-pyrazol-1-yl)-N-(2-(2,6-dioxopiperidin-3-yl)-1-oxoisindolin-4-yl)-3,6,9,12-tetraoxatetradecanamide (83)



14-(4-((5-Chloro-4-((2,5-difluorobenzyl)amino)pyrimidin-2-yl)amino)-1H-pyrazol-1-yl)-3,6,9,12-tetra-oxatetradecanoic acid **191** (122 mg, 0.175 mmol), 3-(4-amino-1-oxoisindolin-2-yl)piperidine-2,6-dione (54.5 mg, 0.210 mmol), triethylamine (73.3 μL , 0.526 mmol) and HATU (100 mg, 0.263 mmol) were stirred together in DMF (3.504 mL) for 15 h at room temperature. The reaction mixture was diluted with water (10 mL) and extracted with DCM (3 \times 10 mL). The solvent was removed *in vacuo* and diluted with DMSO (1.4 mL) and purified directly by MDAP (ammonium carbonate modifier). The solvent was removed *in vacuo* to afford 14-(4-((5-chloro-4-((2,5-difluorobenzyl)amino)pyrimidin-2-yl)amino)-1H-pyrazol-1-

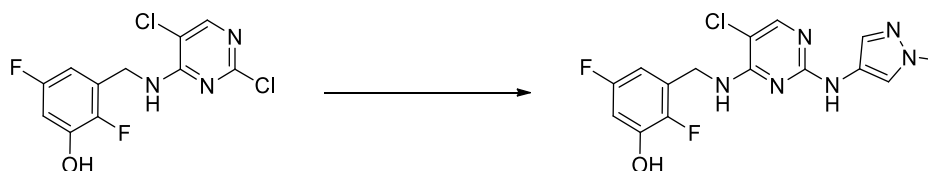
yl)-*N*-(2-(2,6-dioxopiperidin-3-yl)-1-oxoisindolin-4-yl)-3,6,9,12-tetraoxate-tradecanamide **83** (68 mg, 0.084 mmol, 48 % yield) as a brown gum. ν_{\max} (neat): 3295, 2869, 1685, 1576, 1489, 1431 cm^{-1} ; ^1H NMR (400 MHz, $\text{DMSO-}d_6$) δ = 10.99 (1H, s), 9.64 (1H, s), 9.03 (1H, br s), 7.94 (1H, s), 7.74 (1H, dd, J = 7.7, 1.1 Hz), 7.61 - 7.71 (1H, m), 7.55 - 7.59 (1H, m), 7.48 - 7.54 (1H, m), 7.35 (1H, br s), 7.22 - 7.31 (1H, m), 7.09 - 7.16 (1H, m), 6.99 - 7.09 (1H, m), 5.14 (1H, dd, J = 13.4, 5.1 Hz), 4.66 (2H, br d, J = 5.6 Hz), 4.30 - 4.46 (2H, m), 4.13 (2H, s), 4.08 (1H, br s), 3.63 - 3.69 (3H, m), 3.56 - 3.61 (2H, m), 3.44 - 3.53 (3H, m), 3.39 - 3.42 (3H, m), 2.85 - 2.97 (1H, m), 2.56 - 2.65 (1H, m), 2.30 - 2.45 (1H, m), 2.17 - 2.17 (5H, m), 1.97 - 2.05 (1H, m); ^{13}C NMR (101 MHz, $\text{DMSO-}d_6$) δ = 171.7, 169.8, 167.3, 166.6, 156.5, 156.4, 157.1 (d, J = 239.9 Hz), 154.8 (dd, J = 239.5, 1.8 Hz), 152.4, 133.7, 131.8, 131.6, 128.7, 128.7, 127.6, 127.5, 127.4 (d, J = 7.3 Hz), 125.2, 122.1, 118.6, 116.9, 115.5 (dd, J = 24.2, 8.8 Hz), 113.7 (dd, J = 24.2, 8.8 Hz), 69.3, 68.8, 68.6, 68.6, 68.5, 68.5 (2C), 68.1, 50.4, 50.2, 45.3, 36.4, 30.1, 21.4; LCMS (Method B): t_R = 0.96 min, 812 & 814 (95 % purity); HRMS: ($\text{C}_{37}\text{H}_{41}\text{ClF}_2\text{N}_9\text{O}_8$) $[\text{M}+\text{H}]^+$ requires 812.2734, found $[\text{M}+\text{H}]^+$ 812.2747.

(2*S*,4*R*)-1-((*S*)-2-(*tert*-Butyl)-17-(4-((5-chloro-4-((2,5-difluorobenzyl)amino)pyrimidin-2-yl)amino)-1*H*-pyrazol-1-yl)-4-oxo-6,9,12,15-tetraoxa-3-azaheptadecanoyl)-4-hydroxy-*N*-(4-(4-methylthiazol-5-yl)benzyl)pyrrolidine-2-carboxamide (84**)**



14-(4-((5-Chloro-4-((2,5-difluorobenzyl)amino)pyrimidin-2-yl)amino)-1*H*-pyrazol-1-yl)-3,6,9,12-tetraoxatetradecanoic acid **191** (122 mg, 0.175 mmol), (2*S*,4*R*)-1-((*S*)-2-amino-3,3-dimethylbutanoyl)-4-hydroxy-*N*-(4-(4-methylthiazol-5-yl)benzyl)pyrrolidine-2-carboxamide (91 mg, 0.210 mmol), triethylamine (73.3 μ L, 0.526 mmol) and HATU (100 mg, 0.263 mmol) were stirred together in DMF (3.504 mL) for 15 h at room temperature. The reaction mixture was diluted with DMSO (0.2 mL) and purified directly by MDAP (ammonium carbonate modifier) to afford (2*S*,4*R*)-1-((*S*)-2-(*tert*-butyl)-17-(4-((5-chloro-4-((2,5-difluorobenzyl)amino)pyrimidin-2-yl)amino)-1*H*-pyrazol-1-yl)-4-oxo-6,9,12,15-tetraoxa-3-azaheptadecanoyl)-4-hydroxy-*N*-(4-(4-methylthiazol-5-yl)benzyl)pyrrolidine-2-carboxamide **84** (50 mg, 0.051 mmol, 29 % yield) as a beige solid. M.pt.: 84 - 87 °C; ν_{max} (neat): 3295, 2924, 2872, 1626, 1575, 1490 cm^{-1} ; ^1H NMR (400 MHz, $\text{DMSO-}d_6$) δ = 9.03 (1H, br s), 8.97 (1H, s), 8.58 (1H, t, J = 6.0 Hz), 7.94 (1H, s), 7.66 (2H, br s), 7.32 - 7.47 (7H, m), 7.20 - 7.31 (1H, m), 7.08 - 7.17 (1H, m), 7.05 (1H, br s), 4.67 (2H, br d, J = 5.6 Hz), 4.57 (1H, d, J = 9.5 Hz), 4.46 (1H, t, J = 8.1 Hz), 4.34 - 4.43 (2H, m), 4.22 - 4.30 (1H, m), 4.09 (2H, br s), 3.96 (2H, s), 3.46 - 3.71 (15H, m), 3.18 (1H, s), 2.44 (3H, s), 2.03 - 2.11 (1H, m), 1.92 (1H, ddd, J = 12.9, 8.6, 4.6 Hz), 0.95 (9H, s); ^{13}C NMR (101 MHz, $\text{DMSO-}d_6$) δ = 172.2, 169.6, 169.1, 165.2, 158.1, 158.7 (d, J = 239.9 Hz), 156.4 (d, J = 241.4 Hz), 154.0, 151.9, 148.2 (2C), 139.9, 131.6, 130.3, 130.2, 129.3, 129.1, 129.0 (d, J = 7.3 Hz), 127.9, 123.7 (2C), 120.0, 117.1 (dd, J = 24.2, 8.8 Hz), 115.3 (dd, J = 23.8, 8.4 Hz), 70.9, 70.3, 70.2, 70.1, 70.1, 70.0, 69.7, 69.3 (2C), 59.2, 57.0, 56.2, 51.8, 49.1, 42.2, 38.4, 38.0, 36.2, 26.6 (3C), 16.4; ^{19}F NMR (376 MHz, $\text{DMSO-}d_6$) δ = -118.62 (s), -124.32 (s); LCMS (Method B): t_{R} = 1.09 min, $[\text{M}+\text{H}]^+$ 934 & 936 (100 % purity); HRMS: ($\text{C}_{46}\text{H}_{58}\text{ClF}_2\text{N}_{10}\text{O}_8\text{S}$) $[\text{M}+\text{H}]^+$ requires 983.3816, found $[\text{M}+\text{H}]^+$ 983.3844.

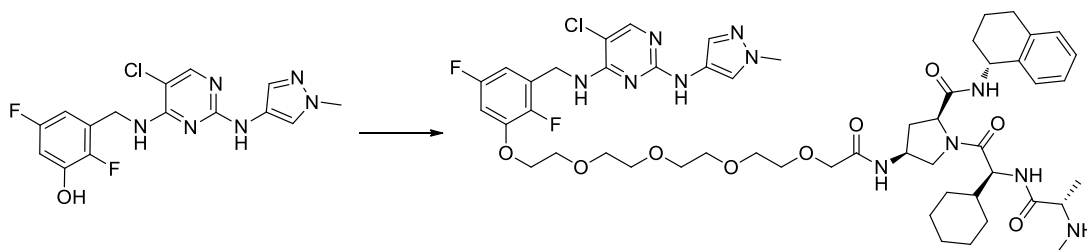
3-(((5-Chloro-2-((1-methyl-1*H*-pyrazol-4-yl)amino)pyrimidin-4-yl)amino)methyl)-2,5-difluorophenol (194)



3-(((2,5-Dichloropyrimidin-4-yl)amino)methyl)-2,5-difluorophenol **226** (2 g, 6.53 mmol), 1-methyl-1*H*-pyrazol-4-amine (0.952 g, 9.80 mmol) and 2 M aqueous HCl (6.53 ml, 13.07

mmol) in ethanol (13.15 mL) were sealed within a vessel and heated in a Biotage Initiator microwave for 1.5 h at 100 °C using a high absorption setting. The reaction mixture was allowed to cool to room temperature. Water (30 mL) was added and the reaction mixture was filtered under vacuum. The solid was washed with water (10 mL) followed by DCM (10 mL). The solid was collected and dried in a vacuum oven for 16 h at 40 °C to afford 3-(((5-chloro-2-((1-methyl-1*H*-pyrazol-4-yl)amino)pyrimidin-4-yl)amino)methyl)-2,5-difluorophenol **194** (1.848 g, 5.04 mmol, 77 % yield) as a white solid. M.pt.: 206 - 210 °C; ν_{\max} (neat): 3445, 3321, 2945, 1603, 1577 1551, 1445, 752 cm^{-1} ; ^1H NMR (400 MHz, $\text{DMSO-}d_6$) δ = 10.57 (1H, br s), 10.21 (1H, br s), 8.84 (1H, br s), 8.07 - 8.20 (1H, m), 7.56 (1H, br s), 7.38 (1H, s), 6.76 (1H, ddd, J = 9.8, 6.8, 3.2 Hz), 6.40 - 6.53 (1H, m), 4.68 (2H, br d, J = 5.9 Hz), 3.75 (3H, s); ^{13}C NMR (101 MHz, $\text{DMSO-}d_6$) δ = 159.0, 159.0, 159.0, 158.2 (dd, J = 239.2, 2.2 Hz), 146.5 (t, J = 12.8 Hz), 145.9 (dd, J = 236.6, 2.6 Hz), 130.9 (d, J = 6.6 Hz), 130.7, 127.6, 120.9, 104.2, 103.9, 103.9 (dd, J = 26.4, 2.2 Hz), 39.2, 38.9; ^{19}F NMR (376 MHz, $\text{DMSO-}d_6$) δ = -117.36 (s), -147.05 (s); LCMS (Method A): t_R = 0.57 min, $[\text{M}+\text{H}]^+$ 367 & 369 (97 % purity); HRMS: ($\text{C}_{15}\text{H}_{14}\text{ClF}_2\text{N}_6\text{O}$) $[\text{M}+\text{H}]^+$ requires 367.0885, found $[\text{M}+\text{H}]^+$ 367.0891.

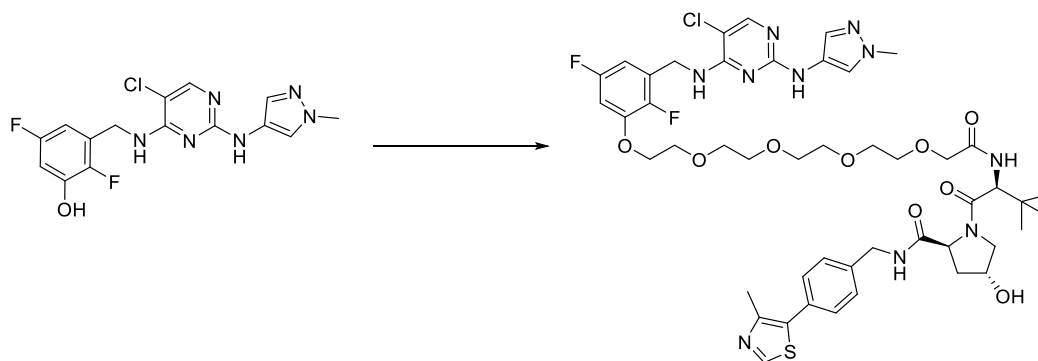
(2*S*,4*S*)-4-(14-(3-(((5-Chloro-2-((1-methyl-1*H*-pyrazol-4-yl)amino)pyrimidin-4-yl)amino)methyl)-2,5-difluorophenoxy)-3,6,9,12-tetraoxatetradecanamido)-1-((*S*)-2-cyclohexyl-2-((*S*)-2-(methylamino)-propanamido)acetyl)-*N*-((*R*)-1,2,3,4-tetrahydronaphthalen-1-yl)pyrrolidine-2-carboxamide (93)



3-(((5-Chloro-2-((1-methyl-1*H*-pyrazol-4-yl)amino)pyrimidin-4-yl)amino)methyl)-2,5-difluorophenol **194** (50 mg, 0.136 mmol) was added to a stirred mixture of *tert*-butyl ((*S*)-1-(((*S*)-2-((2*S*,4*S*)-4-(14-chloro-3,6,9,12-tetraoxatetradecanamido)-2-(((*R*)-1,2,3,4-tetrahydronaphthalen-1-yl)carbamoyl)pyrrolidin-1-yl)-1-cyclohexyl-2-oxoethyl)amino)-1-oxopropan-2-yl)(methyl)carbamate (114 mg, 0.136 mmol) and potassium carbonate (37.7

mg, 0.273 mmol) in DMF (418 μ L). The reaction mixture was heated to 80 $^{\circ}$ C for 16 h under a nitrogen atmosphere. The reaction mixture was cooled to room temperature and diluted with water (10 mL) and extracted with DCM (3 \times 10 mL). The organic layers were combined, passed through a hydrophobic frit and the solvent was removed *in vacuo*. TFA (105 μ L, 1.363 mmol) was added and the reaction mixture was stirred at room temperature for 1 h. The solvent was removed *in vacuo* and dissolved in 1:1 MeOH:DMSO (2 mL) and purified by MDAP (ammonium carbonate modifier). The solvent was removed *in vacuo* to afford (2*S*,4*S*)-4-(14-(3-(((5-chloro-2-((1-methyl-1*H*-pyrazol-4-yl)amino)pyrimidin-4-yl)amino)methyl)-2,5-difluorophenoxy)-3,6,9,12-tetraoxatetradecanamido)-1-((*S*)-2-cyclohexyl-2-((*S*)-2-(methylamino)propanamido)acetyl)-*N*-((*R*)-1,2,3,4-tetrahydronaphthalen-1-yl)pyrrolidine-2-carboxamide **93** (68 mg, 0.064 mmol, 46.8 % yield) as a white gum. ν_{\max} (neat): 3280, 2928, 2856, 1630, 1607, 1574, 1490 cm^{-1} ; ^1H NMR (400 MHz, $\text{DMSO-}d_6$) δ = 9.04 (1H, br s), 8.45 (1H, d, J = 8.6 Hz), 8.25 - 8.38 (2H, m), 7.90 - 8.00 (2H, m), 7.69 (1H, br s), 7.24 - 7.35 (2H, m), 7.05 - 7.20 (4H, m), 7.01 (1H, ddd, J = 10.0, 6.7, 3.1 Hz), 6.53 - 6.62 (1H, m), 4.90 - 4.99 (1H, m), 4.65 (2H, br d, J = 5.9 Hz), 4.42 - 4.49 (1H, m), 4.32 - 4.41 (2H, m), 4.14 - 4.22 (2H, m), 4.03 (1H, dd, J = 10.0, 6.4 Hz), 3.90 (2H, s), 3.73 - 3.78 (3H, m), 3.68 - 3.73 (3H, m), 3.56 - 3.60 (6H, m), 3.47 - 3.50 (3H, m), 3.02 (1H, q, J = 6.8 Hz), 2.67 - 2.78 (2H, m), 2.35 - 2.44 (1H, m), 2.20 (3H, s), 1.62 - 1.88 (12H, m), 0.95 - 1.22 (10H, m); ^{13}C NMR (101 MHz, $\text{DMSO-}d_6$) δ = 174.5, 171.6, 170.4, 169.5, 158.0, 158.4 (d, J = 238.4 Hz), 154.0, 147.6 (app. t, J = 11.7 Hz), 144.9, 137.8, 137.4, 129.9 (2C), 129.0, 128.9, 127.1, 126.1 (2C), 123.9, 105.0, 101.6 (d, J = 27.1 Hz), 70.9 (2C), 70.5 (2C), 70.4, 70.3, 70.2, 70.1, 69.3, 69.2, 59.3, 59.0, 54.8, 53.4, 47.9, 47.2, 38.9 (2C), 38.0, 34.7, 34.4 (3C), 30.2, 29.2, 28.5, 26.4, 26.2, 26.0, 20.7, 19.3, all F-couplings not identified due to complexity of spectrum; ^{19}F NMR (376 MHz, $\text{DMSO-}d_6$) δ = -116.10 (s), -145.60 (s); LCMS (Method B): t_{R} = 1.21 min, $[\text{M}+\text{H}]^+$ 1067 & 1069 (99 % purity); HRMS: ($\text{C}_{52}\text{H}_{72}\text{ClF}_2\text{N}_{11}\text{O}_9$) $[(\text{M}+2\text{H})/2]^+$ requires 533.7586, found $[(\text{M}+2\text{H})/2]^+$ 533.7592.

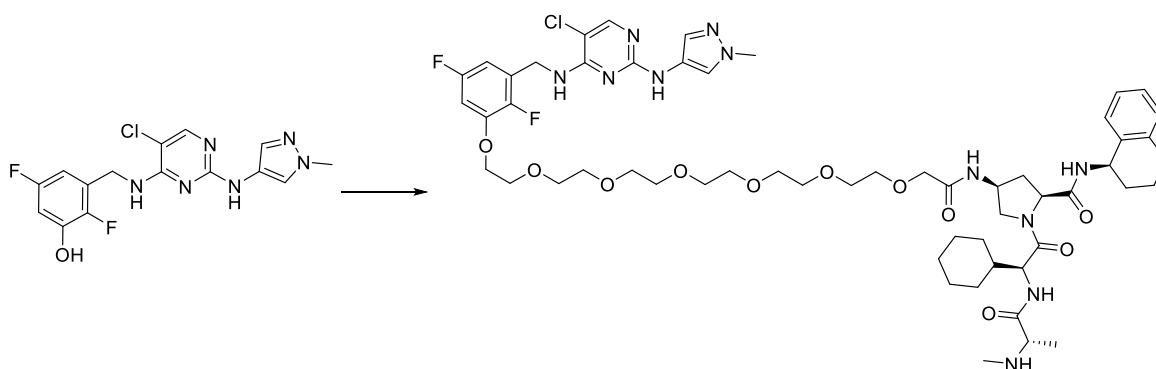
(2*S*,4*R*)-1-((*S*)-2-(*tert*-Butyl)-17-(3-(((5-chloro-2-((1-methyl-1*H*-pyrazol-4-yl)amino)pyrimidin-4-yl)-amino)methyl)-2,5-difluorophenoxy)-4-oxo-6,9,12,15-tetraoxa-3-azaheptadecanoyl)-4-hydroxy-*N*-(4-(4-methylthiazol-5-yl)benzyl)pyrrolidine-2-carboxamide (95)



3-(((5-Chloro-2-((1-methyl-1*H*-pyrazol-4-yl)amino)pyrimidin-4-yl)amino)methyl)-2,5-difluorophenol **194** (55 mg, 0.132 mmol) was added to a stirred mixture of (2*S*,4*R*)-1-((*S*)-2-(*tert*-butyl)-17-chloro-4-oxo-6,9,12,15-tetraoxa-3-azaheptadecanoyl)-4-hydroxy-*N*-(4-(4-methylthiazol-5-yl)benzyl)pyrrolidine-2-carboxamide (108 mg, 0.158 mmol) and potassium carbonate (36.5 mg, 0.264 mmol) in DMF (0.405 mL). The reaction mixture was heated to 70 °C for 16 h. The reaction mixture was heated to 80 °C for a further 16 h. The reaction mixture was cooled to room temperature and diluted with water (5 mL) and extracted with ethyl acetate (3 × 10 mL). The organic layers were combined, passed through a hydrophobic frit and the solvent was removed *in vacuo*. The residue was purified by reverse phase column chromatography (30 - 85 % MeCN in H₂O + 0.1 % (NH₄)₂CO₃, 30 g C₁₈) to afford (2*S*,4*R*)-1-((*S*)-2-(*tert*-butyl)-17-(3-(((5-chloro-2-((1-methyl-1*H*-pyrazol-4-yl)amino)pyrimidin-4-yl)amino)methyl)-2,5-difluorophenoxy)-4-oxo-6,9,12,15-tetraoxa-3-azaheptadecanoyl)-4-hydroxy-*N*-(4-(4-methyl-thiazol-5-yl)benzyl)pyrrolidine-2-carboxamide **95** (105 mg, 0.104 mmol, 79 % yield) as a beige solid. M.pt.: 67 - 69 °C; ν_{max} (neat): 3294, 2921, 2872, 1629, 1575 cm⁻¹; ¹H NMR (400 MHz, DMSO-*d*₆) δ = 9.00 - 9.17 (1H, m), 8.96 - 8.99 (1H, m), 8.58 (1H, t, *J* = 6.1 Hz), 7.93 (1H, s), 7.69 (1H, br s), 7.37 - 7.47 (4H, m), 7.29 (1H, br s), 7.01 (1H, ddd, *J* = 10.1, 6.8, 2.9 Hz), 6.54 - 6.61 (1H, m), 4.65 (2H, br d, *J* = 4.2 Hz), 4.58 (1H, d, *J* = 9.5 Hz), 4.36 - 4.49 (3H, m), 4.16 - 4.30 (3H, m), 3.97 (2H, s), 3.51 - 3.78 (19H, m), 3.29 - 3.36 (3H, m), 3.18 (3H, s), 2.01 - 2.11 (1H, m), 1.88 - 1.96 (1H, m), 0.95 (9H, s); ¹³C NMR (101 MHz, DMSO-*d*₆) δ = 172.2, 169.6, 169.0, 158.1, 158.0, 158.4 (d, *J* = 241.4 Hz), 154.0, 151.8, 148.2 (2C), 147.6 (app. t, *J* =

11.7 Hz), 139.9, 131.6 (2C), 130.2 (2C), 129.1, 129.0 (d, $J = 4.4$ Hz), 127.9 (2C), 123.9 (2C), 105.4, 101.6 (d, $J = 27.9$ Hz), 70.9, 70.4, 70.3, 70.3, 70.1, 70.1, 69.3, 69.3, 69.1, 59.2, 57.0, 56.2, 55.4, 49.1, 42.2, 38.9, 38.4, 38.0 (d, $J = 9.5$ Hz), 36.2, 26.6 (3C), 16.4, all F-couplings not identified due to complexity of spectrum; ^{19}F NMR (376 MHz, $\text{DMSO-}d_6$) $\delta = -116.10$ (s), -145.57 (s); LCMS (Method B): $t_R = 1.08$ min, $[\text{M}+\text{H}]^+$ 1014 & 1016 (96 % purity); HRMS: ($\text{C}_{47}\text{H}_{60}\text{ClF}_2\text{N}_{10}\text{O}_9\text{S}$) $[\text{M}+\text{H}]^+$ requires 1013.3958, found $[\text{M}+\text{H}]^+$ 1013.3962.

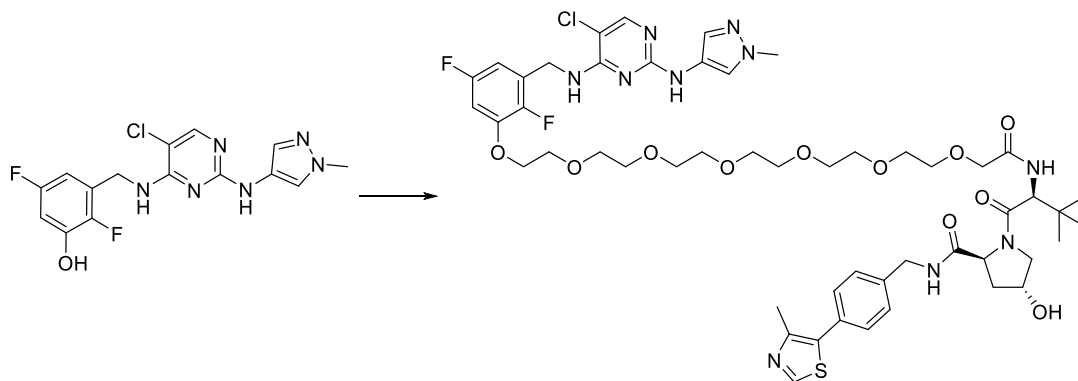
(2S,4S)-4-(20-(3-(((5-Chloro-2-((1-methyl-1H-pyrazol-4-yl)amino)pyrimidin-4-yl)amino)-methyl)-2,5-difluorophenoxy)-3,6,9,12,15,18-hexaoxaicosanamido)-1-((S)-2-cyclohexyl-2-((S)-2-(methyl-amino)propanamido)acetyl)-N-((R)-1,2,3,4-tetrahydronaphthalen-1-yl)pyrrolidine-2-carboxamide (96)



3-(((5-Chloro-2-((1-methyl-1H-pyrazol-4-yl)amino)pyrimidin-4-yl)amino)methyl)-2,5-difluorophenol **194** (50 mg, 0.136 mmol) was added to a stirred mixture of *tert*-butyl ((S)-1-(((S)-2-((2S,4S)-4-(20-chloro-3,6,9,12,15,18-hexaoxaicosanamido)-2-(((R)-1,2,3,4-tetrahydronaphthalen-1-yl)carbamoyl)pyrrolidin-1-yl)-1-cyclohexyl-2-oxoethyl)amino)-1-oxopropan-2-yl)(methyl)carbamate (151 mg, 0.164 mmol) and potassium carbonate (37.7 mg, 0.273 mmol) in DMF (418 μL). The reaction mixture was heated to 80 $^{\circ}\text{C}$ for 16 h under a nitrogen atmosphere. The reaction mixture was cooled to room temperature and diluted with water (10 mL) and extracted with DCM (2 \times 30 mL). The organic layers were combined, passed through a hydrophobic frit and the solvent was removed *in vacuo*. TFA (105 μL , 1.363 mmol) was added and the reaction mixture was stirred at room temperature for 1 h. The solvent was removed *in vacuo* and the residue was purified by MDAP (ammonium carbonate modifier) to afford (2S,4S)-4-(20-(3-(((5-chloro-2-((1-methyl-1H-pyrazol-4-

yl)amino)pyrimidin-4-yl)amino)methyl)-2,5-difluorophenoxy)-3,6,9,12,15,18-hexaoxaicosanamido)-1-((*S*)-2-cyclohexyl-2-((*S*)-2-(methylamino)-propanamido)acetyl)-*N*-((*R*)-1,2,3,4-tetrahydronaphthalen-1-yl)pyrrolidine-2-carboxamide **96** (74 mg, 0.064 mmol, 47 % yield) as a colourless gum. ν_{\max} (neat): 3289, 3060, 2927, 2856, 1574, 1631, 1490, 1107 cm^{-1} ; ^1H NMR (400 MHz, $\text{DMSO-}d_6$) δ = 9.04 (1H, br s), 8.45 (1H, d, J = 8.6 Hz), 8.34 (1H, d, J = 8.3 Hz), 7.86 - 8.01 (2H, m), 7.25 - 7.35 (1H, m), 7.23 - 7.35 (2H, m), 7.06 - 7.20 (4H, m), 7.02 (1H, ddd, J = 10.1, 6.8, 2.9 Hz), 6.54 - 6.62 (1H, m), 4.90 - 4.99 (1H, m), 4.66 (2H, br d, J = 5.6 Hz), 4.33 - 4.49 (4H, m), 4.16 - 4.22 (2H, m), 3.99 - 4.06 (1H, m), 3.89 (2H, s), 3.75 - 3.78 (2H, m), 3.70 (3H, s), 3.48 - 3.62 (19H, m), 3.00 (1H, q, J = 6.8 Hz), 2.65 - 2.81 (3H, m), 2.35 - 2.44 (1H, m), 2.19 (3H, s), 1.62 - 1.87 (11H, m), 1.06 - 1.18 (7H, m), 0.91 - 1.06 (2H, m); ^{13}C NMR (101 MHz, $\text{DMSO-}d_6$) δ = 174.6, 171.6, 170.4, 169.5, 165.0, 158.1, 158.0, 158.4 (d, J = 239.2 Hz), 154.0, 147.7 (app. t, J = 11.7 Hz), 144.9, 137.8, 137.4, 129.9, 129.0, 128.9, 127.1, 126.1 (2C), 123.9, 120.1, 105.2, 101.7 (2C, d, J = 27.9 Hz), 70.9, 70.5, 70.4, 70.3 (3C), 70.2, 70.2, 70.1 (3C), 69.3, 69.2, 59.4, 59.0, 54.7, 53.4, 47.9, 47.2, 38.9, 38.0, 34.7, 34.6, 30.2, 29.2, 29.2, 28.5, 26.4, 26.2, 26.0, 20.7, 19.4, all F-couplings not identified due to complexity of spectrum; ^{19}F NMR (376 MHz, $\text{DMSO-}d_6$) δ = -116.10 (s), -145.60 (s); LCMS (Method B): t_{R} = 1.21 min, $[(\text{M}+2\text{H})/2]^+$ 578 (96 % purity); HRMS: ($\text{C}_{56}\text{H}_{80}\text{ClF}_2\text{N}_{11}\text{O}_{11}$) $[(\text{M}+2\text{H})/2]^+$ requires 577.7847, found $[(\text{M}+2\text{H})/2]^+$ 577.7854.

(2*S*,4*R*)-1-((*S*)-2-(*tert*-Butyl)-23-(3-(((5-chloro-2-((1-methyl-1*H*-pyrazol-4-yl)amino)-pyrimidin-4-yl)amino)methyl)-2,5-difluorophenoxy)-4-oxo-6,9,12,15,18,21-hexaoxa-3-azatricosanoyl)-4-hydroxy-*N*-(4-(4-methylthiazol-5-yl)benzyl)pyrrolidine-2-carboxamide (98)



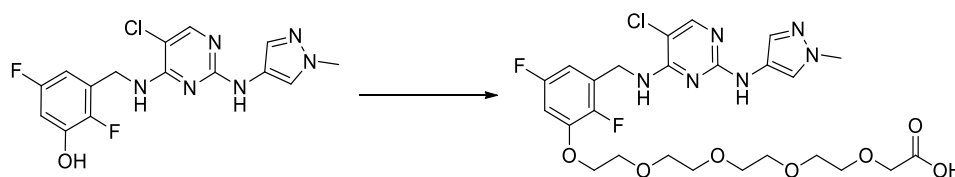
3-(((5-Chloro-2-((1-methyl-1*H*-pyrazol-4-yl)amino)pyrimidin-4-yl)amino)methyl)-2,5-difluorophenol **194** (50 mg, 0.136 mmol) was added to a stirred mixture of (2*S*,4*R*)-1-((*S*)-2-(*tert*-butyl)-23-chloro-4-oxo-6,9,12,15,18,21-hexaoxa-3-azatricosanoyl)-4-hydroxy-*N*-(4-(4-methylthiazol-5-yl)benzyl)-pyrrolidine-2-carboxamide (126 mg, 0.164 mmol) and potassium carbonate (37.7 mg, 0.273 mmol) in DMF (418 μ L). The reaction mixture was heated to 80 °C for 16 h under a nitrogen atmosphere. The reaction mixture was cooled to room temperature and diluted with water (10 mL) and extracted with DCM (3 \times 10 mL). The organic layers were combined, passed through a hydrophobic frit and the solvent was concentrated *in vacuo*. The residue was purified by MDAP (ammonium carbonate modifier) to afford (2*S*,4*R*)-1-((*S*)-2-(*tert*-butyl)-23-(3-(((5-chloro-2-((1-methyl-1*H*-pyrazol-4-yl)amino)pyrimidin-4-yl)amino)methyl)-2,5-difluorophenoxy)-4-oxo-6,9,12,15,18,21-hexaoxa-3-azatricosanoyl)-4-hydroxy-*N*-(4-(4-methylthiazol-5-yl)benzyl)pyrrolidine-2-carboxamide **98** (68 mg, 0.062 mmol, 45 % yield) as white foam. M.pt.: 65 - 68 °C; ν_{max} (neat): 3300, 2872, 2919, 1607, 1575, 1490, 1089 cm^{-1} ; ^1H NMR (400 MHz, CDCl_3) δ = 8.67 (1H, s), 7.87 (1H, s), 7.56 (2H, br t, J = 5.4 Hz), 7.39 (1H, d, J = 0.5 Hz), 7.34 (4H, d, J = 1.7 Hz), 7.28 - 7.33 (1H, m), 7.16 - 7.24 (1H, m), 6.66 (1H, ddd, J = 9.7, 6.6, 3.1 Hz), 6.56 (1H, ddd, J = 8.3, 4.8, 3.1 Hz), 5.77 (1H, br t, J = 5.6 Hz), 4.68 - 4.75 (3H, m), 4.50 - 4.57 (3H, m), 4.33 (1H, dd, J = 14.9, 5.4 Hz), 4.13 - 4.17 (2H, m), 3.90 - 4.04 (3H, m), 3.86 (2H, dd, J = 5.4, 4.2 Hz), 3.81 (3H, s), 3.69 - 3.72 (2H, m), 3.60 - 3.66 (21H, m), 2.50 (3H, s), 2.08 - 2.15 (1H, m), 0.96 (9H, s); ^{13}C NMR (101 MHz, CDCl_3) δ = 171.2, 171.0, 170.4, 157.9, 157.9, 158.4 (2C, d, J = 242.8 Hz), 153.4, 150.3, 148.5, 147.6 (app. t, J = 11.7 Hz), 138.2, 131.6 (2C), 130.9, 129.5 (2C), 128.1 (2C), 127.4 (dd, J = 13.9, 8.8 Hz), 122.9, 121.3, 106.2 (d, J = 25.7 Hz), 104.0, 101.9 (d, J = 27.9 Hz), 71.1, 71.0 (3C), 70.6, 70.6, 70.5, 70.4 (3C), 70.4, 70.1, 69.5, 69.3, 58.6, 57.1, 56.8, 43.2, 39.1, 38.5 (d, J = 4.4 Hz), 36.2, 35.2, 26.4 (3C), 16.0; ^{19}F NMR (376 MHz, CDCl_3) δ = -115.71 (s), -145.41 (s); LCMS (Method B): t_{R} = 1.08 min, $[(\text{M}+2\text{H})/2]^+$ 551 (98 % purity); HRMS: ($\text{C}_{51}\text{H}_{69}\text{ClF}_2\text{N}_{10}\text{O}_{11}\text{S}$) $[(\text{M}+2\text{H})/2]^+$ requires 551.2271, found $[(\text{M}+2\text{H})/2]^+$ 551.2272.

Methyl 20-chloro-3,6,9,12,15,18-hexaoxaicosanoate (203)



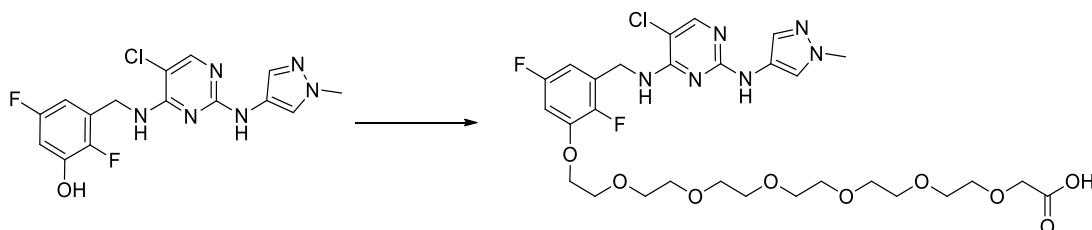
20-Chloro-3,6,9,12,15,18-hexaoxaicosanoic acid **202** (1.5 g, 4.18 mmol) in DMF (0.016 mL, 0.209 mmol) and DCM (12.19 mL was added 2 M oxalyl chloride in DCM (2.508 mL, 5.02 mmol) dropwise and the reaction mixture was stirred at room temperature for 15 min. MeOH (1.463 mL, 36.2 mmol) was added and the reaction mixture was stirred at room temperature for a further 15 min. The reaction mixture was saturated aqueous NaHCO₃ (50 mL) the layers were separated using a hydrophobic frit. The organic layer was evaporated *in vacuo* to afford methyl 20-chloro-3,6,9,12,15,18-hexaoxaicosanoate **203** (1.438 g, 3.86 mmol, 92 % yield) as a brown oil. ¹H NMR (400 MHz, CDCl₃) δ = 4.17 (3H, s), 3.61 - 3.77 (26H, m); ¹³C NMR (101 MHz, CDCl₃) δ = 170.8, 71.4, 70.9, 70.7 (6C), 70.6, 70.6, 70.6, 68.6, 51.7, 42.7.

14-(3-(((5-Chloro-2-((1-methyl-1H-pyrazol-4-yl)amino)pyrimidin-4-yl)amino)methyl)-2,5-difluorophenoxy)-3,6,9,12-tetraoxatetradecanoic acid (204)



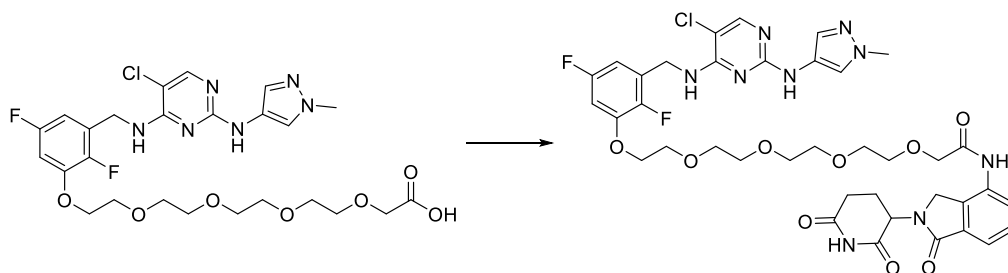
Methyl 14-chloro-3,6,9,12-tetraoxatetradecanoate (69.9 mg, 0.245 mmol) was added to a stirred mixture of 3-(((5-chloro-2-((1-methyl-1H-pyrazol-4-yl)amino)pyrimidin-4-yl)amino)methyl)-2,5-difluorophenol **194** (75 mg, 0.204 mmol) and potassium carbonate (56.5 mg, 0.409 mmol) in DMF (627 μL). The reaction mixture was heated to 80 °C for 16 h under a nitrogen atmosphere. 2 M aqueous NaOH (102 μL, 0.204 mmol) and Water (251 μL) was added and the reaction mixture was stirred at room temperature for 1 h. The solvent was removed *in vacuo* and the residue was purified by reverse phase column chromatography (15 - 55 % MeCN in H₂O + 0.1 % (NH₄)₂CO₃, 30 g C₁₈) to afford 14-(3-(((5-chloro-2-((1-methyl-1H-pyrazol-4-yl)amino)pyrimidin-4-yl)amino)methyl)-2,5-difluorophenoxy)-3,6,9,12-tetraoxatetradecanoic acid **204** (104 mg, 0.173 mmol, 85 % yield) as a white solid. LCMS (Method A): t_R = 0.68 min, [M+H]⁺ 601 & 603 (77 % purity). Used crude in the next reaction.

20-(3-(((5-Chloro-2-((1-methyl-1*H*-pyrazol-4-yl)amino)pyrimidin-4-yl)amino)methyl)-2,5-difluoro-phenoxy)-3,6,9,12,15,18-hexaoxaicosanoic acid (205)



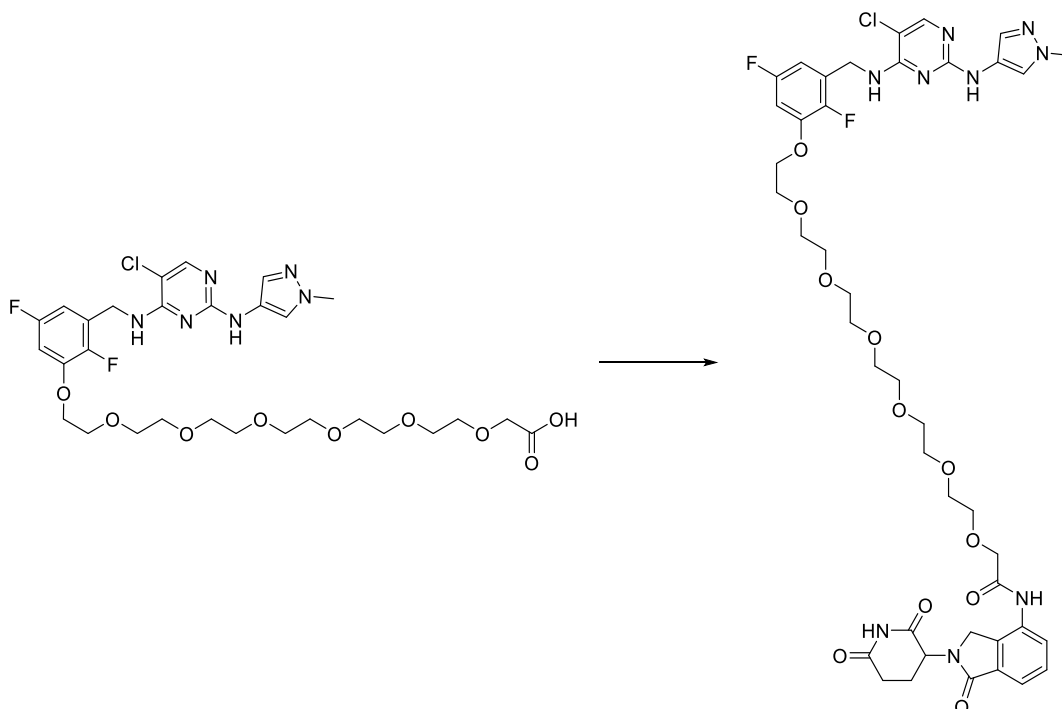
Methyl 20-chloro-3,6,9,12,15,18-hexaoxaicosanoate (91 mg, 0.245 mmol) was added to a stirred mixture of 3-(((5-chloro-2-((1-methyl-1*H*-pyrazol-4-yl)amino)pyrimidin-4-yl)amino)methyl)-2,5-difluorophenol **194** (75 mg, 0.204 mmol) and potassium carbonate (56.5 mg, 0.409 mmol) in DMF (627 μ L). The reaction mixture was heated to 80 $^{\circ}$ C for 16 h under a nitrogen atmosphere. 2 M aqueous NaOH (1.022 μ L, 2.045 mmol) and water (251 μ L) was added and the reaction mixture was stirred at room temperature for 1 h. The solvent was removed *in vacuo* and the residue was purified by reverse phase column chromatography (15 - 55 % MeCN in H₂O + 0.1 % (NH₄)₂CO₃, 30 g C₁₈) to afford 20-(3-(((5-chloro-2-((1-methyl-1*H*-pyrazol-4-yl)amino)pyrimidin-4-yl)amino)methyl)-2,5-difluorophenoxy)-3,6,9,12,15,18-hexaoxaicosanoic acid **205** (123 mg, 0.178 mmol, 87 % yield) as a white solid. LCMS (Method A): t_R = 0.71 min, [M+H]⁺ 689 & 691 (76 % purity). Used crude in the next reaction.

14-(3-(((5-Chloro-2-((1-methyl-1*H*-pyrazol-4-yl)amino)pyrimidin-4-yl)amino)methyl)-2,5-difluoro-phenoxy)-*N*-(2-(2,6-dioxopiperidin-3-yl)-1-oxoisindolin-4-yl)-3,6,9,12-tetraoxatetradecanamide (94)



14-(3-(((5-Chloro-2-((1-methyl-1*H*-pyrazol-4-yl)amino)pyrimidin-4-yl)amino)methyl)-2,5-difluoro-phenoxy)-3,6,9,12-tetraoxatetradecanoic acid **204** (104 mg, 0.133 mmol), 3-(4-amino-1-oxoisindolin-2-yl)piperidine-2,6-dione (41.5 mg, 0.160 mmol), triethylamine (55.7 μ L, 0.400 mmol) and HATU (76 mg, 0.200 mmol) were stirred together in DMF (2.665 mL) for 15 h at room temperature. The reaction mixture was diluted with water (10 mL) and extracted with DCM (3 \times 10 mL). The organic layers were combined, passed through a hydrophobic frit and the solvent removed *in vacuo*. The residue was purified by MDAP (ammonium carbonate modifier). The solvent was removed *in vacuo* to afford 14-(3-(((5-chloro-2-((1-methyl-1*H*-pyrazol-4-yl)amino)pyrimidin-4-yl)amino)methyl)-2,5-difluoro-phenoxy)-*N*-(2-(2,6-dioxopiperidin-3-yl)-1-oxoisindolin-4-yl)-3,6,9,12-tetraoxatetradecanamide **94** (64 mg, 0.076 mmol, 57 % yield) as a white solid. M.pt.: 82 - 84 °C; ν_{\max} (neat): 3280, 2874, 1681, 1605, 1488, 1412, 1089 cm^{-1} ; ^1H NMR (400 MHz, DMSO- d_6) δ = 11.00 (1H, s), 9.66 (1H, s), 9.04 (1H, br s), 7.94 (1H, s), 7.76 (1H, dd, J = 7.6, 1.0 Hz), 7.68 (1H, s), 7.55 - 7.59 (1H, m), 7.46 - 7.55 (2H, m), 7.29 (1H, br s), 7.01 (1H, ddd, J = 10.1, 6.8, 2.9 Hz), 6.53 - 6.63 (1H, m), 5.15 (1H, dd, J = 13.4, 5.1 Hz), 4.66 (2H, br d, J = 5.9 Hz), 4.32 - 4.47 (2H, m), 4.16 - 4.19 (2H, m), 4.15 (2H, s), 3.73 - 3.76 (2H, m), 3.68 - 3.71 (4H, m), 3.60 - 3.65 (2H, m), 3.50 - 3.56 (7H, m), 2.85 - 2.98 (1H, m), 2.30 - 2.45 (1H, m), 1.99 - 2.09 (4H, m); ^{13}C NMR (151 MHz, MeOD) δ = 174.7, 172.1, 171.3, 171.0, 160.9 (d, J = 2.8 Hz), 159.7, 159.3, 159.3, 149.0 (app. t, J = 11.6 Hz), 147.7 (dd, J = 239.4, 3.3 Hz), 137.0, 134.0, 133.7, 131.4, 130.2, 129.8 (dd, J = 13.8, 8.8 Hz), 128.4, 124.9, 122.6, 122.0, 111.4, 106.2 (d, J = 23.8 Hz), 104.7, 102.3 (d, J = 28.2 Hz), 72.2, 71.8, 71.6, 71.6, 71.4, 71.3, 70.6, 70.3, 53.7, 48.4, 39.1, 39.0 (d, J = 3.9 Hz), 32.4, 24.2, all F-couplings not identified due to complexity of spectrum; ^{19}F NMR (376 MHz, DMSO- d_6) δ = -116.08 (s), -145.57 (s); LCMS (Method B): t_{R} = 0.95 min, $[\text{M}+\text{H}]^+$ 842 & 844 (93 % purity); HRMS: ($\text{C}_{38}\text{H}_{43}\text{ClF}_2\text{N}_9\text{O}_9$) $[\text{M}+\text{H}]^+$ requires 842.2840, found $[\text{M}+\text{H}]^+$ 842.2839.

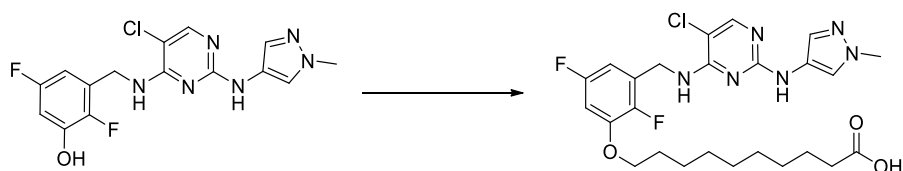
20-(3-(((5-Chloro-2-((1-methyl-1*H*-pyrazol-4-yl)amino)pyrimidin-4-yl)amino)methyl)-2,5-difluoro-phenoxy)-*N*-(2-(2,6-dioxopiperidin-3-yl)-1-oxoisindolin-4-yl)-3,6,9,12,15,18-hexaoxaicosanamide (97)



20-(3-(((5-Chloro-2-((1-methyl-1*H*-pyrazol-4-yl)amino)pyrimidin-4-yl)amino)methyl)-2,5-difluoro-phenoxy)-3,6,9,12,15,18-hexaoxaicosanoic acid **205** (123 mg, 0.107 mmol), 3-(4-amino-1-oxoisindolin-2-yl)piperidine-2,6-dione (33.3 mg, 0.129 mmol), triethylamine (44.8 μ L, 0.321 mmol) and HATU (61.1 mg, 0.161 mmol) were stirred together in DMF (2.142 mL) for 15 h at room temperature. The reaction mixture was concentrated *in vacuo* and diluted with water (10 mL). The aqueous was extracted with DCM (3 \times 10 mL) and the organic layers were combined, passed through a hydrophobic frit and the solvent concentrated *in vacuo*. The residue was purified by MDAP (ammonium carbonate modifier). The solvent was removed *in vacuo* to afford 20-(3-(((5-chloro-2-((1-methyl-1*H*-pyrazol-4-yl)amino)pyrimidin-4-yl)amino)methyl)-2,5-difluorophenoxy)-*N*-(2-(2,6-dioxopiperidin-3-yl)-1-oxoisindolin-4-yl)-3,6,9,12,15,18-hexaoxaicosanamide **97** (92 mg, 0.099 mmol, 92 % yield) as a white solid. M.pt.: 90 - 92 $^{\circ}$ C; ν_{\max} (neat): 3298, 2914, 2874, 1682, 1606, 1575, 1411, 1089 cm^{-1} ; ^1H NMR (400 MHz, DMSO- d_6) δ = 10.99 (1H, br s), 9.65 (1H, s), 9.03 (1H, br s), 7.93 (1H, s), 7.75 (1H, dd, J = 7.7, 1.1 Hz), 7.68 (1H, br s), 7.46 - 7.59 (3H, m), 7.28 (1H, br s), 7.01 (1H, ddd, J = 10.1, 6.8, 3.2 Hz), 6.52 - 6.63 (1H, m), 5.14 (1H, dd, J = 13.2, 5.1 Hz), 4.65 (2H, br d, J = 5.9 Hz), 4.31

- 4.47 (2H, m), 4.16 - 4.21 (2H, m), 4.14 (2H, s), 3.73 - 3.79 (2H, m), 3.67 - 3.73 (5H, m), 3.45 - 3.64 (16H, m), 2.85 - 2.97 (1H, m), 2.57 - 2.66 (1H, m), 2.30 - 2.46 (1H, m), 2.07 (3H, s); ^{13}C NMR (101 MHz, DMSO- d_6) δ = 171.7, 169.8, 167.3, 166.6, 156.5, 156.4, 156.8 (d, J = 239.9 Hz), 152.5 (d, J = 3.7 Hz), 146.0 (app. t, J = 11.7 Hz), 144.5 (dd, J = 239.9, 3.7 Hz), 133.7, 131.8, 131.6, 128.3, 128.3 (dd, J = 4.0, 1.8 Hz), 127.5, 125.2 (2C), 122.3, 118.6, 103.8 (d, J = 4.4 Hz), 103.7, 100.1 (d, J = 27.1 Hz), 69.3, 68.8 (4C), 68.8, 68.7, 68.6, 68.6, 68.6, 68.5, 67.7, 67.5, 50.4, 45.3, 37.3, 36.4 (d, J = 7.3 Hz), 30.1, 21.4; ^{19}F NMR (376 MHz, DMSO- d_6) δ = -116.10 (s), -145.69 (s); LCMS (Method A): t_{R} = 0.96 min, $[\text{M}+\text{H}]^+$ 931 & 933 (91 % purity); HRMS: ($\text{C}_{42}\text{H}_{51}\text{ClF}_2\text{N}_9\text{O}_{11}$) $[\text{M}+\text{H}]^+$ requires 930.3364, found $[\text{M}+\text{H}]^+$ 930.3372.

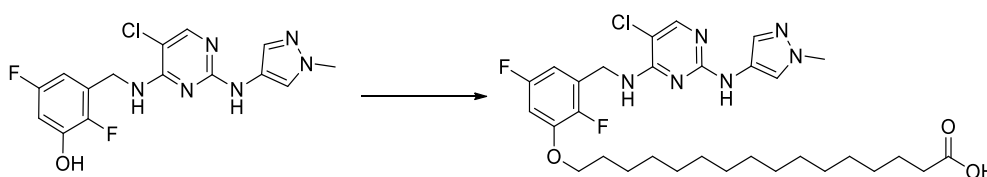
10-(3-(((5-Chloro-2-((1-methyl-1H-pyrazol-4-yl)amino)pyrimidin-4-yl)amino)methyl)-2,5-difluorophenoxy)decanoic acid (207)



Methyl 10-bromodecanoate (347 mg, 1.309 mmol) was added to a stirred mixture of 3-(((5-chloro-2-((1-methyl-1H-pyrazol-4-yl)amino)pyrimidin-4-yl)amino)methyl)-2,5-difluorophenol **194** (400 mg, 1.091 mmol) and potassium carbonate (301 mg, 2.181 mmol) in DMF (3.343 mL). The reaction mixture was heated to 80 °C for 3.5 h under a nitrogen atmosphere. The reaction mixture was cooled to room temperature and diluted with water (10 mL) and extracted with DCM (2 × 10 mL). The organic layers were combined, passed through a hydrophobic frit and the solvent was concentrated *in vacuo*. The reaction mixture was added LiOH (261 mg, 10.91 mmol) and heated to 50 °C for 16 h under a nitrogen atmosphere. The reaction mixture was filtered hot and the filtrate solvent removed *in vacuo* to afford 10-(3-(((5-chloro-2-((1-methyl-1H-pyrazol-4-yl)amino)pyrimidin-4-yl)amino)methyl)-2,5-difluorophenoxy)decanoic acid **207** (352 mg, 0.655 mmol, 60 % yield) as a white solid. M.pt.: 105 - 107 °C; ν_{max} (neat): 3440, 2913, 2851, 1637, 1551, 1489 cm^{-1} ; ^1H NMR (400 MHz, DMSO- d_6) δ = 9.04 (1H, br s), 7.93 (1H, s), 7.67 (1H, br s), 7.51 (1H, br s), 7.29 (1H, br s), 6.98 (1H, ddd, J = 10.1, 6.8, 2.9 Hz), 6.50 - 6.60 (1H, m), 4.65 (2H, br d, J = 5.9 Hz), 4.04 (2H, t, J = 6.5 Hz), 3.70 (3H, s), 2.19 (2H, t, J = 7.3 Hz), 1.65 - 1.77 (2H, m), 1.49 (2H, m),

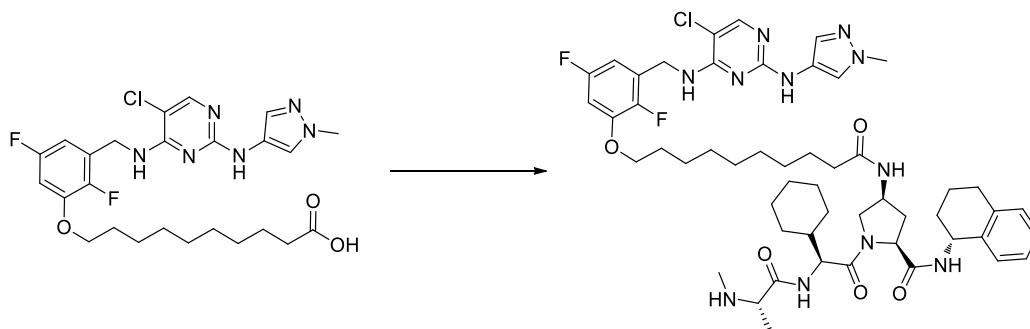
1.25 - 1.42 (11H, m); ^{13}C NMR (101 MHz, $\text{DMSO-}d_6$) δ = 175.0, 158.1, 158.0, 158.5 (dd, J = 239.9, 2.2 Hz), 154.0 (d, J = 5.1 Hz), 147.8 (app. t, J = 11.7 Hz), 146.2 (dd, J = 239.5, 2.6 Hz), 129.9, 128.9 (dd, J = 13.9, 8.8 Hz), 123.9, 120.1, 105.0 (2C), 101.5 (d, J = 27.1 Hz), 69.6, 38.8, 38.0 (dd, J = 5.5, 2.6 Hz), 34.2, 29.3, 29.1, 29.1, 29.0, 28.9, 25.8, 25.0; ^{19}F NMR (376 MHz, $\text{DMSO-}d_6$) δ = -116.2 (s), -145.9 (s); LCMS (Method A): t_R = 1.02 min, $[\text{M}+\text{H}]^+$ 537 & 539 (99 % purity); HRMS: ($\text{C}_{25}\text{H}_{32}\text{ClF}_2\text{N}_6\text{O}_3$) $[\text{M}+\text{H}]^+$ requires 537.2192, found $[\text{M}+\text{H}]^+$ 537.2196.

16-(3-(((5-Chloro-2-((1-methyl-1*H*-pyrazol-4-yl)amino)pyrimidin-4-yl)amino)methyl)-2,5-difluoro-phenoxy)hexadecanoic acid (208)



Methyl 16-bromohexadecanoate (457 mg, 1.309 mmol) was added to a stirred mixture of 3-(((5-chloro-2-((1-methyl-1*H*-pyrazol-4-yl)amino)pyrimidin-4-yl)amino)methyl)-2,5-difluorophenol **194** (400 mg, 1.091 mmol) and potassium carbonate (301 mg, 2.181 mmol) in DMF (3.343 mL). The reaction mixture was heated to 80 °C for 3.5 h under a nitrogen atmosphere. The reaction mixture was filtered hot and LiOH (261 mg, 10.91 mmol) was added to the filtrate and the reaction mixture was heated at 50 °C for 16 h. The reaction mixture was heated with a heat gun and filtered hot. The filtrate was collected, and the solvent removed *in vacuo* to afford 16-(3-(((5-chloro-2-((1-methyl-1*H*-pyrazol-4-yl)amino)pyrimidin-4-yl)amino)methyl)-2,5-difluorophenoxy)hexadecanoic acid **208** (649 mg, 1.045 mmol, 96 % yield) as a white solid. Full characterisation not carried out as sample likely contains unknown quantities of inorganics.

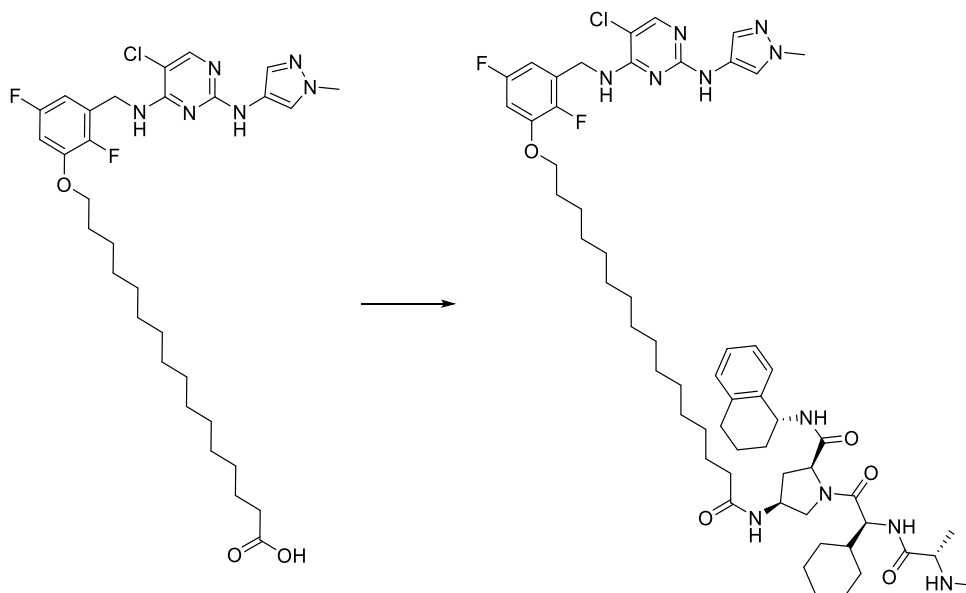
(2S,4S)-4-(10-(3-(((5-Chloro-2-((1-methyl-1H-pyrazol-4-yl)amino)pyrimidin-4-yl)amino)methyl)-2,5-difluorophenoxy)decanamido)-1-((S)-2-cyclohexyl-2-((S)-2-(methylamino)propanamido)acetyl)-N-((R)-1,2,3,4-tetrahydronaphthalen-1-yl)pyrrolidine-2-carboxamide (87)



10-(3-(((5-Chloro-2-((1-methyl-1H-pyrazol-4-yl)amino)pyrimidin-4-yl)amino)methyl)-2,5-difluoro-phenoxy)decanoic acid **207** (100 mg, 0.186 mmol), *tert*-butyl ((S)-1-(((S)-2-((2S,4S)-4-amino-2-(((R)-1,2,3,4-tetrahydronaphthalen-1-yl)carbamoyl)pyrrolidin-1-yl)-1-cyclohexyl-2-oxoethyl)amino)-1-oxopropan-2-yl)(methyl)carbamate (130 mg, 0.223 mmol), triethylamine (78 μ L, 0.559 mmol) and HATU (106 mg, 0.279 mmol) were stirred together in *N,N*-Dimethylformamide (DMF) (3.724 mL) for 16 h at room temperature. The reaction mixture was diluted with water (10 mL) and extracted with DCM (3 \times 10 mL). The solvent was removed *in vacuo* and TFA (143 μ L, 1.862 mmol) was added and the reaction mixture was stirred at room temperature for 16 h. The reaction mixture was diluted with water (10 mL) and extracted with DCM (3 \times 10 mL). The solvent was concentrated *in vacuo* and purified by reverse phase prep column chromatography (40 - 95 % MeCN in H₂O + 0.1 % (NH₄)₂CO₃, Xbridge C₁₈, 42 mL/ min, 45 min) to afford (2S,4S)-4-(10-(3-(((5-chloro-2-((1-methyl-1H-pyrazol-4-yl)amino)pyrimidin-4-yl)amino)methyl)-2,5-difluorophenoxy)decanamido)-1-((S)-2-cyclohexyl-2-((S)-2-(methylamino)propanamido)acetyl)-N-((R)-1,2,3,4-tetrahydronaphthalen-1-yl)pyrrolidine-2-carboxamide **87** (100 mg, 0.100 mmol, 54 % yield) as a white solid. M.pt.: 103 - 105 °C; ν_{\max} (neat): 3296, 2927, 2854, 1634, 1574, 1430, 778 cm⁻¹; ¹H NMR (400 MHz, MeOD) δ = 7.83 (1H, s), 7.55 (1H, s), 7.35 - 7.40 (1H, m), 7.34 (1H, s), 7.08 - 7.15 (2H, m), 7.01 - 7.06 (1H, m), 6.72 (1H, ddd, *J* = 9.9, 6.7, 2.9 Hz), 6.49 - 6.56 (1H, m), 5.02 - 5.07 (1H, m), 4.71 (2H, s), 4.42 - 4.55 (3H, m), 4.12 - 4.20 (1H, m), 3.97 (2H, t, *J* = 6.4 Hz), 3.75 (3H, s), 3.60 (1H, dd, *J* = 10.4, 5.3 Hz), 3.09 - 3.16 (1H, m), 2.67 - 2.83 (2H, m), 2.50 (1H, ddd, *J* =

13.2, 8.8, 6.6 Hz), 2.29 (2H, s), 2.28 (1H, s), 2.19 (2H, t, $J = 7.6$ Hz), 1.69 - 2.03 (14H, m), 1.57 - 1.68 (4H, m), 1.38 - 1.55 (3H, m), 1.34 (8H, s), 0.99 - 1.31 (10H, m); ^{13}C NMR (101 MHz, MeOD) $\delta = 175.8, 174.3, 172.0, 171.3, 158.3, 157.8, 158.7$ (dd, $J = 241.0, 2.6$ Hz), 152.8, 147.8 (dd, $J = 11.7, 10.3$ Hz), 146.2 (dd, $J = 238.4, 2.2$ Hz), 137.1, 136.1, 129.9, 128.5, 128.4, 128.3, 128.2, 128.2, 126.7, 125.7, 123.6, 121.1, 104.3 (dd, $J = 24.9, 2.2$ Hz), 103.2, 100.5 (d, $J = 27.9$ Hz), 69.2, 59.4, 58.9, 55.5, 53.2, 48.6, 47.8, 40.1, 37.6, 36.0, 34.2, 33.5 (dd, $J = 6.6, 2.2$ Hz), 33.2, 29.8, 29.2, 29.1, 29.0, 28.9, 28.9, 28.8, 28.6, 28.5, 25.9, 25.7, 25.5, 20.2, 17.9, all F-couplings not identified due to complexity of spectrum; LCMS (Method B): $t_R = 1.49$ min, $[\text{M}+\text{H}]^+$ 1003 & 1005 (100 % purity); HRMS: ($\text{C}_{52}\text{H}_{71}\text{ClF}_2\text{N}_{11}\text{O}_5$) $[\text{M}+\text{H}]^+$ requires 1002.5296, found $[\text{M}+\text{H}]^+$ 1002.5303.

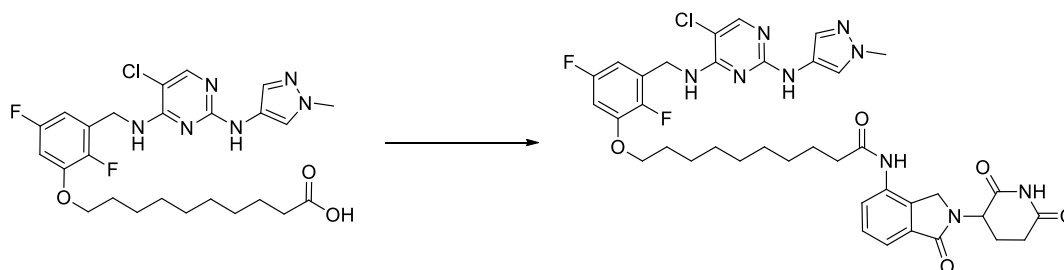
(2S,4S)-4-(16-(3-(((5-Chloro-2-((1-methyl-1H-pyrazol-4-yl)amino)pyrimidin-4-yl)amino)methyl)-2,5-difluorophenoxy)hexadecanamido)-1-((S)-2-cyclohexyl-2-((S)-2-(methyl-amino)propanamido)-acetyl)-N-((R)-1,2,3,4-tetrahydronaphthalen-1-yl)pyrrolidine-2-carboxamide (90)



16-(3-(((5-Chloro-2-((1-methyl-1H-pyrazol-4-yl)amino)pyrimidin-4-yl)amino)methyl)-2,5-difluoro-phenoxy)hexadecanoic acid **208** (150 mg, 0.241 mmol), *tert*-butyl ((S)-1-(((S)-2-

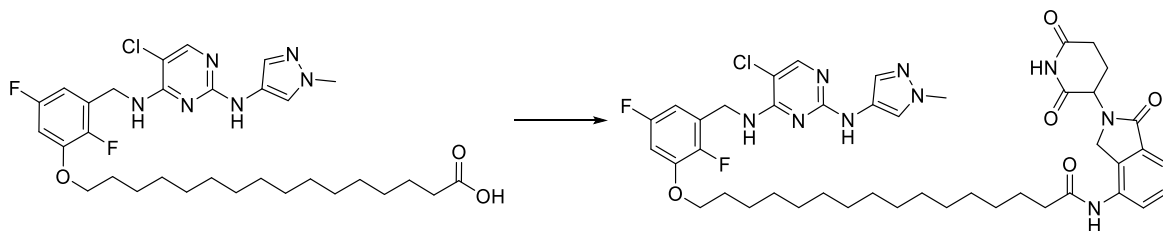
((2S,4S)-4-amino-2-(((R)-1,2,3,4-tetrahydronaphthalen-1-yl)carbamoyl)pyrrolidin-1-yl)-1-cyclohexyl-2-oxoethyl-amino)-1-oxopropan-2-yl)(methyl)carbamate (169 mg, 0.290 mmol), triethylamine (101 μ L, 0.724 mmol) and HATU (138 mg, 0.362 mmol) were stirred together in DMF (4.830 mL) for 16 h at room temperature. The reaction mixture was diluted with water (10 mL) and extracted with DCM (3 \times 10 mL). The solvent was concentrated *in vacuo* and TFA (186 μ L, 2.415 mmol) was added and the reaction mixture was stirred at room temperature for 16 h. The reaction was neutralised with 2 M aqueous HCl and extracted with DCM (2 \times 10 mL) The solvent was removed *in vacuo* and purified by reverse phase prep column chromatography (40 - 95 % MeCN in H₂O + 0.1 % (NH₄)₂CO₃, Xbridge C₁₈, 42 mL/ min, 45 min) to afford (2S,4S)-4-(16-(3-(((5-chloro-2-((1-methyl-1H-pyrazol-4-yl)amino)pyrimidin-4-yl)amino)methyl)-2,5-difluorophenoxy)hexadecanamido)-1-((S)-2-cyclohexyl-2-((S)-2-(methylamino)-propanamido)acetyl)-N-((R)-1,2,3,4-tetrahydronaphthalen-1-yl)pyrrolidine-2-carboxamide **90** (38 mg, 0.035 mmol, 15 % yield) as an off white solid. M.pt.: 95 - 97 °C; ν_{\max} (neat): 3448, 3274, 3065, 2924, 2853, 1636, 1547, 1490, 728 cm⁻¹; ¹H NMR (400 MHz, CDCl₃) δ = 7.94 (1H, d, *J* = 6.6 Hz), 7.89 (1H, s), 7.84 - 7.88 (1H, m), 7.49 - 7.64 (2H, m), 7.38 (1H, d, *J* = 0.7 Hz), 7.12 (2H, t, *J* = 7.3 Hz), 6.99 - 7.10 (3H, m), 6.60 (1H, ddd, *J* = 9.7, 6.5, 3.1 Hz), 6.55 (1H, ddd, *J* = 8.3, 4.9, 2.9 Hz), 5.70 (1H, br t, *J* = 5.9 Hz), 5.29 (2H, s), 5.09 - 5.16 (1H, m), 4.69 - 4.76 (3H, m), 4.54 - 4.64 (1H, m), 4.36 (1H, t, *J* = 8.2 Hz), 4.01 - 4.13 (1H, m), 3.98 (2H, t, *J* = 6.6 Hz), 3.82 (3H, s), 3.68 (1H, d, *J* = 11.0 Hz), 3.03 (1H, t, *J* = 6.8 Hz), 2.69 - 2.82 (2H, m), 2.37 (1H, s), 2.33 (2H, s), 2.17 - 2.24 (3H, m), 1.97 - 2.06 (2H, m), 1.78 - 1.88 (5H, m), 1.68 (2H, br s), 1.52 - 1.59 (2H, m), 1.41 - 1.51 (3H, m), 1.22 - 1.35 (25H, m), 1.05 - 1.13 (3H, m), 0.87 - 1.01 (2H, m); ¹³C NMR (101 MHz, CDCl₃) δ = 173.3, 173.1, 171.3, 158.0, 157.9, 158.6 (dd, *J* = 242.5, 2.6 Hz), 153.5, 147.9 (app. t, *J* = 11.4 Hz), 145.6 (d, *J* = 2.2 Hz), 137.2, 136.1, 136.1, 130.8, 129.2, 128.2, 127.2, 126.0, 122.9, 121.3, 105.6 (d, *J* = 25.7 Hz), 104.0, 101.3 (dd, *J* = 27.9, 1.5 Hz), 69.6, 60.2, 60.2, 60.1, 60.0, 55.9, 54.9, 54.8, 53.4, 49.4, 48.0, 40.6, 39.1, 38.5 (d, *J* = 5.1 Hz), 36.9, 35.3, 35.0, 31.2, 30.0, 29.6, 29.6, 29.5, 29.5, 29.4, 29.3, 29.3, 29.1, 29.0, 28.7, 26.1, 26.0, 25.9, 25.7, 20.1, 19.4, all F-couplings not identified due to complexity of spectrum; ¹⁹F NMR (376 MHz, CDCl₃) δ = -115.9 (s), -146.1 (s); LCMS (Method B): *t*_R = 1.81 min, [M+H]⁺ 1087 & 1089 (100 % purity); HRMS: (C₅₈H₈₃ClF₂N₁₁O₅) [M+H]⁺ requires 1086.6255, found [M+H]⁺ 1086.6262.

10-(3-(((5-Chloro-2-((1-methyl-1H-pyrazol-4-yl)amino)pyrimidin-4-yl)amino)methyl)-2,5-difluoro-phenoxy)-N-(2-(2,6-dioxopiperidin-3-yl)-1-oxoisindolin-4-yl)decanamide (88)



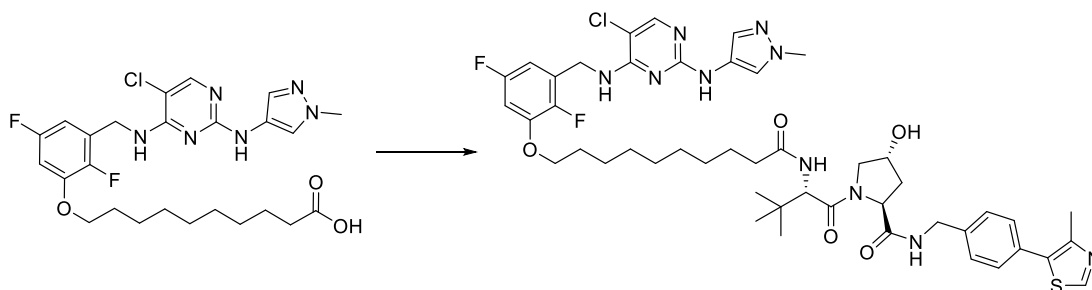
10-(3-(((5-Chloro-2-((1-methyl-1H-pyrazol-4-yl)amino)pyrimidin-4-yl)amino)methyl)-2,5-difluoro-phenoxy)decanoic acid **207** (100 mg, 0.186 mmol), 3-(4-amino-1-oxoisindolin-2-yl)piperidine-2,6-dione (57.9 mg, 0.223 mmol), triethylamine (78 μ L, 0.559 mmol) and HATU (106 mg, 0.279 mmol) were stirred together in DMF (3.724 mL) for 16 h at room temperature. The reaction mixture was diluted with water (10 mL) and extracted with DCM (3 \times 10 mL). The solvent was concentrated *in vacuo* and purified by reverse phase prep column chromatography (50 - 95 % MeCN in H₂O + 0.1 % (NH₄)₂CO₃, Xbridge C₁₈, 42 mL/ min, 45 min) to afford 10-(3-(((5-chloro-2-((1-methyl-1H-pyrazol-4-yl)amino)pyrimidin-4-yl)amino)methyl)-2,5-difluorophenoxy)-N-(2-(2,6-dioxopiperidin-3-yl)-1-oxoisindolin-4-yl)decanamide **88** (40 mg, 0.051 mmol, 28 % yield) as a white gum. ν_{\max} (neat): 3270, 2928, 2854, 1683, 1488, 1025, 992, 751 cm^{-1} ; ¹H NMR (400 MHz, DMSO-*d*₆) δ = 11.01 (1H, br s), 9.77 (1H, s), 9.04 (1H, br s), 7.93 (1H, s), 7.83 (1H, ddd, *J* = 7.2, 4.5, 1.6 Hz), 7.68 (1H, br s), 7.42 - 7.55 (2H, m), 7.29 (1H, br s), 6.98 (1H, ddd, *J* = 10.0, 6.7, 3.1 Hz), 6.49 - 6.63 (1H, m), 5.15 (1H, dd, *J* = 13.4, 5.1 Hz), 4.65 (2H, br s), 4.29 - 4.45 (2H, m), 4.04 (2H, t, *J* = 6.5 Hz), 3.70 - 3.77 (1H, m), 3.23 - 3.44 (1H, m), 2.92 (1H, ddd, *J* = 17.5, 13.6, 5.4 Hz), 2.56 - 2.67 (1H, m), 2.25 - 2.41 (3H, m), 1.98 - 2.10 (1H, m), 1.66 - 1.76 (2H, m), 1.56 - 1.65 (2H, m), 1.11 - 1.54 (12H, m); ¹³C NMR (101 MHz, DMSO-*d*₆) δ = 173.2, 171.9, 171.8, 171.5, 168.3, 158.0, 157.9, 158.5 (d, *J* = 241.4 Hz), 154.1, 147.8 (app. t, *J* = 11.7 Hz), 146.1 (dd, *J* = 236.2, 3.7 Hz), 134.3, 134.2, 134.2, 134.1, 133.1, 129.9, 129.1, 125.7, 125.6, 123.9, 123.8, 119.4, 101.5 (d, *J* = 27.1 Hz), 69.6, 52.0, 47.0, 38.9, 38.0, 36.3 (d, *J* = 3.7 Hz), 31.7, 29.4, 29.2, 29.1, 28.9, 25.8, 25.6, 23.1; ¹⁹F NMR (376 MHz, DMSO-*d*₆) δ = -116.17 (s), -145.94 (s); LCMS (Method B): *t*_R = 1.21 min, [M+H]⁺ 779 & 781 (95 % purity); HRMS: (C₃₈H₄₃ClF₂N₉O₅) [M+H]⁺ requires 778.3046, found [M+H]⁺ 778.3050.

16-(3-(((5-Chloro-2-((1-methyl-1H-pyrazol-4-yl)amino)pyrimidin-4-yl)amino)methyl)-2,5-difluorophenoxy)-N-(2-(2,6-dioxopiperidin-3-yl)-1-oxoisindolin-4-yl)hexadecanamide (91)



16-(3-(((5-Chloro-2-((1-methyl-1H-pyrazol-4-yl)amino)pyrimidin-4-yl)amino)methyl)-2,5-difluoro-phenoxy)hexadecanoic acid **208** (150 mg, 0.241 mmol), 3-(4-amino-1-oxoisindolin-2-yl)piperidine-2,6-dione (75 mg, 0.290 mmol), triethylamine (101 μ L, 0.724 mmol) and HATU (138 mg, 0.362 mmol) were stirred together in DMF (4.830 mL) for 16 h at room temperature. The reaction mixture was diluted with water (10 mL) and extracted with DCM (3 \times 10 mL). The solvent was concentrated *in vacuo* reverse phase prep column chromatography (50 - 95 % MeCN in H₂O + 0.1 % (NH₄)₂CO₃, Xbridge C₁₈, 42 mL/min, 25 min) to afford 16-(3-(((5-chloro-2-((1-methyl-1H-pyrazol-4-yl)amino)pyrimidin-4-yl)amino)methyl)-2,5-difluorophenoxy)-N-(2-(2,6-dioxopiperidin-3-yl)-1-oxoisindolin-4-yl)hexadecanamide **91** (94 mg, 0.109 mmol, 45 % yield) as a white solid. M.pt.: 134 - 136 $^{\circ}$ C; ν_{\max} (neat): 3453, 3274, 3060, 2924, 2852, 1636, 1576, 1488, 1165, 775 cm^{-1} ; ^1H NMR (400 MHz, DMSO-*d*₆) δ = 11.00 (1H, s), 9.73 (1H, s), 9.04 (1H, br s), 7.93 (1H, s), 7.81 (1H, dd, J = 7.1, 2.0 Hz), 7.69 (1H, br s), 7.40 - 7.59 (3H, m), 7.28 (1H, br s), 6.98 (1H, ddd, J = 10.1, 6.8, 2.9 Hz), 6.52 - 6.58 (1H, m), 5.14 (1H, dd, J = 13.2, 5.1 Hz), 4.64 (2H, br d, J = 5.9 Hz), 4.29 - 4.43 (2H, m), 4.04 (2H, t, J = 6.5 Hz), 3.69 (3H, s), 2.92 (1H, ddd, J = 17.4, 13.6, 5.4 Hz), 2.56 - 2.67 (1H, m), 2.31 - 2.38 (3H, m), 1.98 - 2.08 (1H, m), 1.67 - 1.77 (2H, m), 1.55 - 1.65 (2H, m), 1.35 - 1.42 (2H, m), 1.23 - 1.33 (20H, m); ^{13}C NMR (151 MHz, DMSO-*d*₆) δ = 172.6, 171.2, 170.8, 167.7, 157.4, 157.3, 157.9 (br d, J = 239.4 Hz), 153.4 (br s), 147.3 (t, J = 11.1 Hz), 145.6 (dd, J = 237.5, 3.0 Hz), 133.7, 133.6, 133.5, 132.6, 129.3, 128.5, 125.0 (2C), 123.2, 118.8, 101.0 (2C, d, J = 28.2 Hz), 69.0, 51.4, 46.4, 38.3 (br s), 37.4, 35.7 (d, J = 6.6 Hz), 31.1, 29.0, 28.9, 28.9 (3C), 28.9, 28.9, 28.9, 28.7, 28.6, 28.6, 28.3, 25.2, 25.0, 22.6; ^{19}F NMR (376 MHz, DMSO-*d*₆) δ = -116.2 (s), -146.0 (s); LCMS (Method B): t_{R} = 1.37 min, $[\text{M}+\text{H}]^+$ 863 & 865 (100 % purity); HRMS: (C₄₄H₅₅ClF₂N₉O₅) $[\text{M}+\text{H}]^+$ requires 862.3982, found $[\text{M}+\text{H}]^+$ 862.3976.

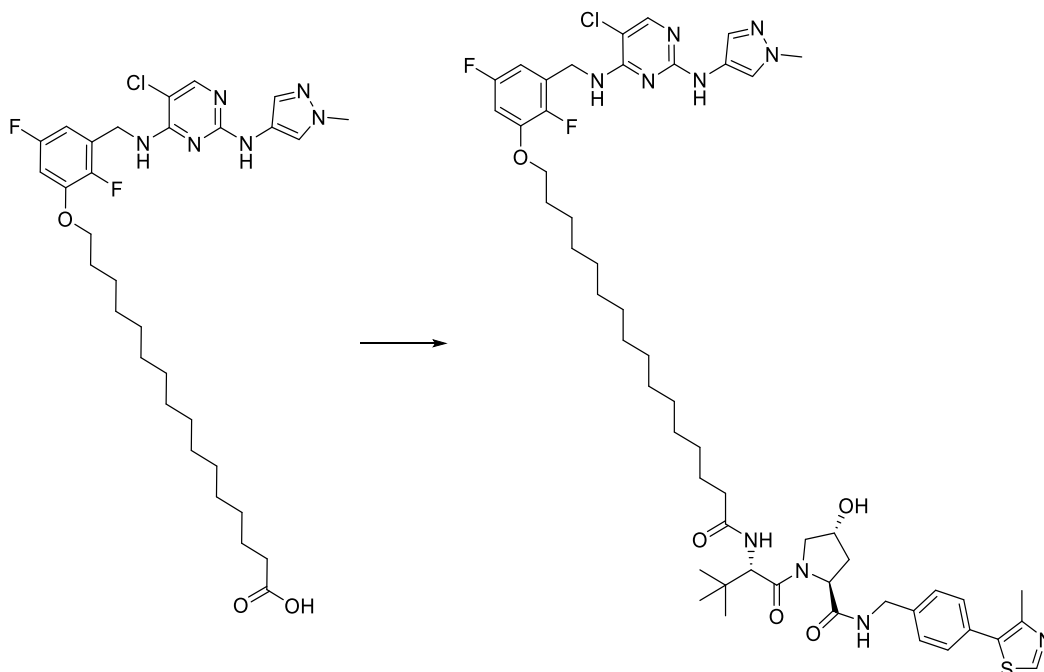
(2*S*,4*R*)-1-((*S*)-2-(10-(3-(((5-chloro-2-((1-methyl-1*H*-pyrazol-4-yl)amino)pyrimidin-4-yl)amino)methyl)-2,5-difluorophenoxy)decanamido)-3,3-dimethylbutanoyl)-4-hydroxy-*N*-(4-(4-methylthiazol-5-yl)benzyl)pyrrolidine-2-carboxamide (89)



10-(3-(((5-Chloro-2-((1-methyl-1*H*-pyrazol-4-yl)amino)pyrimidin-4-yl)amino)methyl)-2,5-difluoro-phenoxy)decanoic acid **207** (100 mg, 0.186 mmol), (2*S*,4*R*)-1-((*S*)-2-amino-3,3-dimethylbutanoyl)-4-hydroxy-*N*-(4-(4-methylthiazol-5-yl)benzyl)pyrrolidine-2-carboxamide (96 mg, 0.223 mmol), triethylamine (78 μ L, 0.559 mmol) and HATU (106 mg, 0.279 mmol) were stirred together in DMF (3.724 mL) for 16 h at room temperature. The reaction mixture was diluted with water (10 mL) and extracted with DCM (3 \times 10 mL). The organic layers were combined, passed through a hydrophobic frit and the solvent removed *in vacuo*. The residue was purified by reverse phase column chromatography (50 - 95 % H₂O + 0.1 % (NH₄)₂CO₃ in MeCN, Xbridge column C₁₈, 42 mL/ min, 35 min) to afford (2*S*,4*R*)-1-((*S*)-2-(10-(3-(((5-chloro-2-((1-methyl-1*H*-pyrazol-4-yl)amino)pyrimidin-4-yl)amino)methyl)-2,5-difluorophenoxy)-decanamido)-3,3-dimethylbutanoyl)-4-hydroxy-*N*-(4-(4-methylthiazol-5-yl)benzyl)-pyrrolidine-2-carboxamide **89** (71 mg, 0.075 mmol, 40 % yield) as an off white solid. M.pt.: 127 – 129 °C; ν_{max} (neat): 3283, 2929, 2854, 1667, 1631, 1518, 1128, 726 cm⁻¹; ¹H NMR (400 MHz, MeOD-*d*₄) δ = 8.85 (1H, s), 7.85 (1H, s), 7.56 (1H, br s), 7.35 - 7.48 (6H, m), 6.75 (1H, ddd, *J* = 9.7, 6.7, 2.9 Hz), 6.49 - 6.58 (1H, m), 4.72 (2H, s), 4.47 - 4.70 (5H, m), 4.36 (1H, d, *J* = 15.4 Hz), 4.00 (2H, t, *J* = 6.4 Hz), 3.93 (1H, br d, *J* = 11.2 Hz), 3.82 (1H, dd, *J* = 11.0, 3.9 Hz), 3.77 (3H, s), 2.47 (3H, s), 2.20 - 2.31 (3H, m), 2.11 (1H, ddd, *J* = 13.3, 8.9, 4.5 Hz), 1.73 - 1.83 (2H, m), 1.61 (2H, br s), 1.43 - 1.51 (2H, m), 1.33 (11H, br s), 1.05 (9H, s); ¹³C NMR (101 MHz, MeOD) δ = 174.6, 173.0, 171.0, 158.3, 157.8, 158.7 (dd, *J* = 241.4, 2.2 Hz), 152.8, 151.3, 147.8 (t, *J* = 11.9 Hz), 147.6, 146.2 (dd, *J* = 239.9, 2.9 Hz), 138.8, 132.0 (2C), 130.1, 129.9, 128.9 (2C), 127.6 (2C), 123.5, 121.1, 104.3 (d, *J* = 25.7 Hz), 103.3, 100.5 (d, *J* = 27.9 Hz), 69.7, 69.2, 59.4, 57.6, 56.6, 42.3, 37.5 (d, *J* = 9.5 Hz), 35.3, 35.2 (2C), 29.1 (3C), 28.9, 28.9, 28.8, 25.7, 25.6 (3C), 25.6, 14.5; ¹⁹F NMR (376 MHz, MeOD-*d*₄) δ = -117.7 (s), -147.9 (s); LCMS (Method B): *t*_R =

1.40 min, $[M+H]^+$ 950 & 952 (94 % purity); HRMS: $(C_{47}H_{60}ClF_2N_{10}O_5S)$ $[M+H]^+$ requires 949.4125, found $[M+H]^+$ 949.4134.

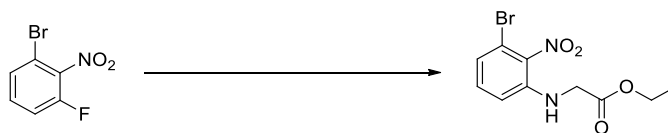
(2S,4R)-1-((S)-2-(16-(3-(((5-Chloro-2-((1-methyl-1H-pyrazol-4-yl)amino)pyrimidin-4-yl)amino)methyl)-2,5-difluorophenoxy)hexadecanamido)-3,3-dimethylbutanoyl)-4-hydroxy-N-(4-(4-methylthiazol-5-yl)benzyl)pyrrolidine-2-carboxamide (92)



16-(3-(((5-Chloro-2-((1-methyl-1H-pyrazol-4-yl)amino)pyrimidin-4-yl)amino)methyl)-2,5-difluoro-phenoxy)hexadecanoic acid **208** (150 mg, 0.241 mmol), (2S,4R)-1-((S)-2-amino-3,3-dimethylbutanoyl)-4-hydroxy-N-(4-(4-methylthiazol-5-yl)benzyl)pyrrolidine-2-carboxamide (125 mg, 0.290 mmol), triethylamine (101 μ L, 0.724 mmol) and HATU (138 mg, 0.362 mmol) were stirred together in DMF (4.830 mL) for 3 h at room temperature. The reaction mixture was concentrated *in vacuo* and purified by reverse phase prep column chromatography (80 - 95 % MeCN in H_2O + 0.1 % $(NH_4)_2CO_3$, Xbridge C_{18} , 42 mL/ min, 25 min) to afford (2S,4R)-1-((S)-2-(16-(3-(((5-chloro-2-((1-methyl-1H-pyrazol-4-yl)amino)pyrimidin-4-yl)amino)methyl)-2,5-difluorophenoxy)hexadecanamido)-3,3-dimethylbutan-oyl)-4-hydroxy-N-(4-(4-methylthiazol-5-yl)benzyl)pyrrolidine-2-carboxamide **92** (90 mg, 0.087 mmol, 36 % yield) as a yellow solid. M.pt.: 99 - 101 $^{\circ}C$; ν_{max} (neat): 3448, 3274, 3060, 2923, 2853, 1634, 1548, 1489, 1412, 771 cm^{-1} ; 1H NMR (400 MHz, $CDCl_3$) δ = 8.67 (1H, s), 7.87 (1H, s), 7.56 (1H, br s), 7.49

(1H, br t, $J = 5.9$ Hz), 7.39 (1H, d, $J = 0.7$ Hz), 7.31 - 7.37 (5H, m), 6.60 (1H, ddd, $J = 9.7, 6.7, 2.9$ Hz), 6.54 (1H, ddd, $J = 8.4, 5.0, 3.1$ Hz), 6.32 (1H, d, $J = 8.8$ Hz), 5.72 (1H, br t, $J = 5.9$ Hz), 4.69 - 4.74 (3H, m), 4.50 - 4.59 (3H, m), 4.33 (1H, dd, $J = 14.9, 5.1$ Hz), 4.07 (1H, br d, $J = 11.5$ Hz), 3.98 (2H, t, $J = 6.5$ Hz), 3.81 (3H, s), 3.62 (1H, dd, $J = 11.2, 3.7$ Hz), 2.44 - 2.53 (4H, m), 2.14 (3H, t, $J = 7.7$ Hz), 1.77 - 1.85 (2H, m), 1.42 - 1.51 (2H, m), 1.22 - 1.34 (23H, m), 0.94 (9H, s); ^{13}C NMR (101 MHz, CDCl_3) $\delta = 173.8, 171.9, 170.9, 157.9, 157.9, 158.6$ (dd, $J = 242.8, 2.9$ Hz), 153.4, 150.3, 148.5, 147.9 (app. t, $J = 11.7$ Hz), 145.5 (d, $J = 3.7$ Hz), 138.1, 131.6, 130.9, 130.8 (2C), 129.5, 128.1, 127.2 (dd, $J = 14.3, 9.2$ Hz), 123.0 (2C), 121.3, 105.5 (dd, $J = 25.7, 2.9$ Hz), 103.9, 101.3 (d, $J = 26.4$ Hz), 70.0, 69.6, 58.7, 57.5, 56.8, 43.3, 39.0, 38.5 (d, $J = 5.1$ Hz), 36.5, 36.1, 35.0, 29.6, 29.6, 29.5, 29.4 (3C), 29.3 (2C), 29.2, 29.2, 29.0, 26.5, 25.9 (3C), 25.7, 16.0, all F-couplings not identified due to complexity of spectrum; ^{19}F NMR (376 MHz, CDCl_3) $\delta = -115.9$ (br s), -146.1 (d, $J = 14.7$ Hz); LCMS (Method B): $t_R = 1.59$ min, $[\text{M}+\text{H}]^+ 1034$ & 1035 (97 % purity); HRMS: ($\text{C}_{53}\text{H}_{72}\text{ClF}_2\text{N}_{10}\text{O}_5\text{S}$) $[\text{M}+\text{H}]^+$ requires 1033.5065, found $[\text{M}+\text{H}]^+ 1033.5077$.

Ethyl (3-bromo-2-nitrophenyl)glycinate (211)



1-Bromo-3-fluoro-2-nitrobenzene **209** (10.25 g, 46.6 mmol), ethyl glycinate hydrochloride (7.15 g, 51.3 mmol), DIPEA (24.45 mL, 140 mmol) in DMA (116 mL) were sealed within a vessel and heated to 80 °C for 8 h. The reaction mixture was diluted with DCM (400 mL) and washed with water (4 × 200 mL). The organic layers were combined, passed through a hydrophobic frit and the solvent was removed *in vacuo*. The residue was dissolved in DCM (10 mL) and split into two equal portions. Each portion was purified by normal phase chromatography (0 – 70 % EtOAc in cyclohexane, 120 g SiO_2) and combined to afford ethyl (3-bromo-2-nitrophenyl)glycinate **211** (10.90 g, 36.0 mmol, 77 % yield) as an orange solid. M.pt.: 83 – 85 °C; ν_{max} (neat): 3409, 2993, 1728, 1522, 1501 cm^{-1} ; ^1H NMR (400 MHz, $\text{DMSO}-d_6$) $\delta = 7.24$ (1H, t, $J = 8.1$ Hz), 7.00 (1H, d, $J = 7.8$ Hz), 6.78 (1H, d, $J = 8.3$ Hz), 6.52 (1H, t, $J = 6.1$ Hz), 4.12 (2H, q, $J = 7.0$ Hz), 4.03 (2H, d, $J = 5.9$ Hz), 1.19 (3H, t, $J = 7.1$ Hz); ^{13}C NMR (101 MHz, $\text{DMSO}-d_6$) $\delta = 170.5, 142.2, 137.9, 133.1, 120.8, 114.1, 113.6, 61.1, 44.7, 14.5$; LCMS

(Method A): $t_R = 1.19$ min, $[M+H]^+$ 303 & 305 (99 % purity); HRMS: $(C_{10}H_{11}BrN_2O_4)$ $[M+H]^+$ requires 302.9980, found $[M+H]^+$ 302.9976.

8-Bromoquinoxalin-2(1H)-one (213)



Ethyl (3-bromo-2-nitrophenyl)glycinate **211** (6.168 g, 20.35 mmol) in ethanol (127 mL) and THF (127 mL) was looped through a 30 mm Raney Ni Catcart 2800 at 1 mL/min, 10 bar, 25 °C for 14 h within a H-cube. KO^tBu (3.43 g, 30.5 mmol) was added and the reaction mixture was stirred under air at room temperature for 4 h. The solvent was removed *in vacuo* and diluted with water (60 mL) and extracted with ethyl acetate (3 × 60 mL). The organic layers were combined, passed through a hydrophobic frit and the solvent removed *in vacuo*. The residue was purified by reverse phase column chromatography (5 – 55 % MeCN + 0.1 % HCO_2H in H_2O + 0.1 % HCO_2H , 120 g C_{18}) to afford 8-bromoquinoxalin-2(1H)-one **213** (2.889 g, 12.84 mmol, 63 % yield) as an off-white solid. M.pt.: 208 – 210 °C; ν_{max} (neat): 3120, 3036, 1670 cm^{-1} ; 1H NMR (400 MHz, $DMSO-d_6$) $\delta = 11.73$ (1H, br s), 8.22 (1H, s), 7.86 (1H, dd, $J = 7.8, 1.0$ Hz), 7.81 (1H, dd, $J = 8.1, 1.2$ Hz), 7.28 (1H, t, $J = 7.9$ Hz); ^{13}C NMR (101 MHz, $DMSO-d_6$) $\delta = 156.1, 152.2$ (br s), 134.5, 134.2 (br s), 131.6 (br s), 129.2, 124.8, 109.6 (br s); LCMS (Method A): $t_R = 0.68$ min, $[M+H]^+$ 225 & 227, (95 % purity); HRMS: $(C_8H_5BrN_2O)$ $[M+H]^+$ requires 224.9642, found $[M+H]^+$ 224.9660.

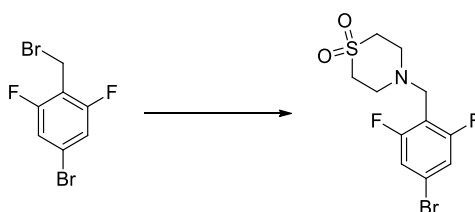
8-Bromo-2-chloroquinoxaline (214)



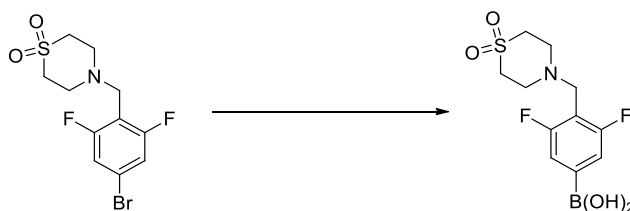
8-Bromoquinoxalin-2(1H)-one **213** (600 mg, 2.67 mmol) in $POCl_3$ (11 mL, 118 mmol) was heated to 50 °C for 16 h under a nitrogen atmosphere. The solvent was removed *in vacuo* and the residue was diluted with water (50 mL). The aqueous was extracted with DCM (3 ×

50 mL) and the organic layers were combined, passed through a hydrophobic frit and the solvent was removed *in vacuo*. The residue was purified by normal phase column chromatography (0 – 70 % EtOAc in cyclohexane, 120 g SiO₂) to afford 8-bromo-2-chloroquinoxaline **214** (622 mg, 2.55 mmol, 96 % yield) as a white solid. M.pt.: 98 – 101 °C; ν_{\max} (neat): 3049, 978 cm⁻¹; ¹H NMR (400 MHz, CDCl₃) δ = 8.81 (1H, s), 8.07 - 8.14 (2H, m), 7.66 (1H, dd, *J* = 8.3, 7.6 Hz); ¹³C NMR (101 MHz, CDCl₃) δ = 148.3, 145.8, 141.9, 140.0, 134.7, 130.4, 129.1, 122.9; LCMS (Method A): *t*_R = 1.13 min, [M+H]⁺ 243 & 245 (98 % purity); HRMS: (C₈H₄BrClN₂) [M+H]⁺ requires 242.9325, found [M+H]⁺ 242.9323.

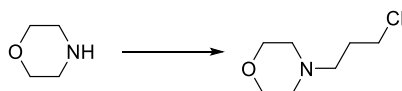
4-(4-Bromo-2,6-difluorobenzyl)thiomorpholine 1,1-dioxide (**217**)



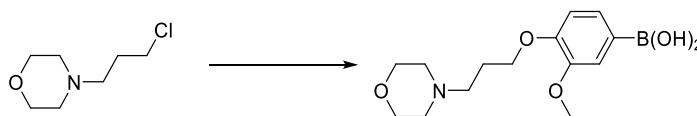
To a mixture of 5-bromo-2-(bromomethyl)-1,3-difluorobenzene **215** (5 g, 17.49 mmol), thiomorpholine 1,1-dioxide (2.60 g, 19.24 mmol) and triethylamine (7.56 mL, 54.2 mmol) was added DMF (58.3 mL) and the reaction mixture was stirred at room temperature for 3 h. The reaction mixture was diluted with water (20 mL) and extracted with DCM (3 × 20 mL). The organic layers were combined, passed through a hydrophobic frit and the solvent was removed *in vacuo*. The residue was purified by normal phase column chromatography (0 – 100 % EtOAc in cyclohexane, 120 g SiO₂) to afford 4-(4-bromo-2,6-difluorobenzyl)thiomorpholine 1,1-dioxide **217** (3.42 g, 10.05 mmol, 58 % yield) as a white solid. M.pt.: 154 – 156 °C; ν_{\max} (neat): 2943, 2822, 1328, 1117 cm⁻¹; ¹H NMR (400 MHz, CDCl₃) δ = 7.10 - 7.17 (2H, m), 3.78 - 3.81 (2H, m), 3.02 - 3.08 (8H, m); ¹³C NMR (101 MHz, CDCl₃) δ = 161.7 (2C, dd, *J* = 252.4, 8.8 Hz), 122.0 (t, *J* = 12.8 Hz), 115.52 (2C, dd, *J* = 27.9, 2.2 Hz), 111.5 (t, *J* = 19.8 Hz), 51.4 (2C), 50.1 (2C), 47.8; ¹⁹F NMR (376 MHz, CDCl₃) δ = -111.86 (s); LCMS (Method A): *t*_R = 0.99 min, [M+H]⁺ 340 & 342, (100 % purity); HRMS: (C₁₁H₁₂BrF₂NO₂S) [M+H]⁺ requires 339.9818, found [M+H]⁺ 339.9821.

4-((1,1-Dioxidothiomorpholino)methyl)-3,5-difluorophenyl)boronic acid (218)

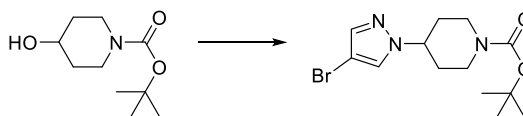
4-(4-Bromo-2,6-difluorobenzyl)thiomorpholine 1,1-dioxide **217** (1.721 g, 5.06 mmol), bis(pinacolato)diboron (1.413 g, 5.56 mmol) and PdCl₂(dppf)-CH₂Cl₂ adduct (0.124 g, 0.152 mmol) were sealed within a vessel and the reaction mixture was evacuated and purged three times with nitrogen. DMA (5.81 mL) was added and the reaction mixture was evacuated and purged three times with nitrogen and heated at 80 °C for 16 h. The reaction mixture was diluted with water (40 mL) and extracted with EtOAc (3 × 50 mL). The organic layers were combined, passed through a hydrophobic frit and the solvent was removed *in vacuo*. The residue was dried under vacuum for 16 h to afford 4-((1,1-dioxidothiomorpholino)methyl)-3,5-difluorophenyl)boronic acid **218** (1.543 g, 5.06 mmol, 100 % yield) as a brown solid. Partially characterised, used Crude in next reaction. LCMS (Method A): t_R = 0.56 min, [M+H]⁺ 306, (63 % purity).

4-(3-Chloropropyl)morpholine (221)

Morpholine **219** (1.004 mL, 11.48 mmol), 1-bromo-3-chloropropane (1.135 mL, 11.48 mmol) and 5 M NaOH Aq (2.75 mL, 13.77 mmol) were stirred together in acetone (43 mL) for 2 h at room temperature under a nitrogen atmosphere. The solvent was removed *in vacuo* and diluted with water (40 mL) and extracted with ethyl acetate (3 × 30 mL). The organic layers were combined, and the solvent removed *in vacuo* to afford 4-(3-chloropropyl)morpholine **221** (902 mg, 5.51 mmol, 48 % yield) as a colourless oil. R_f = 0.33, (50 % EtOAc in cyclohexane); ¹H NMR (400 MHz, CDCl₃) δ = 3.68 - 3.73 (4H, m), 3.61 (2H, t, J = 6.4 Hz), 2.49 (2H, t, J = 7.1 Hz), 2.42 - 2.46 (4H, m), 1.89 - 2.00 (2H, m); ¹³C NMR (101 MHz, CDCl₃) δ = 67.0 (2C), 55.8, 53.7 (2C), 43.0, 29.6.

(3-Methoxy-4-(3-morpholinopropoxy)phenyl)boronic acid (223)

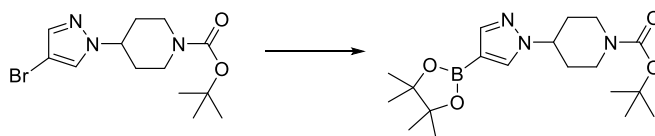
2-Methoxy-4-(4,4,5,5-tetramethyl-1,3,2-dioxaborolan-2-yl)phenol **221** (1.33 g, 5.32 mmol) and cesium carbonate (3.118 g, 9.57 mmol) in DMF (29 mL) was added 4-(3-chloropropyl)morpholine (0.87 g, 5.32 mmol). The reaction mixture was heated to 80 °C for 16 h. The solvent was removed *in vacuo* and diluted with water (120 mL). The aqueous was extracted with ethyl acetate (3 × 120 mL), the organic layers were combined, passed through a hydrophobic frit and the solvent removed *in vacuo* and the residue was dried under vacuum for 16 h to afford (3-methoxy-4-(3-morpholinopropoxy)phenyl)boronic acid **223** (1.828 g, 6.19 mmol, 117 % yield) as a brown solid. LCMS (Method B): $t_R = 0.69$ min, $[M+H]^+$ 296, (67 % purity). Used crude in next reaction.

***Tert*-butyl 4-(4-bromo-1H-pyrazol-1-yl)piperidine-1-carboxylate (226)**

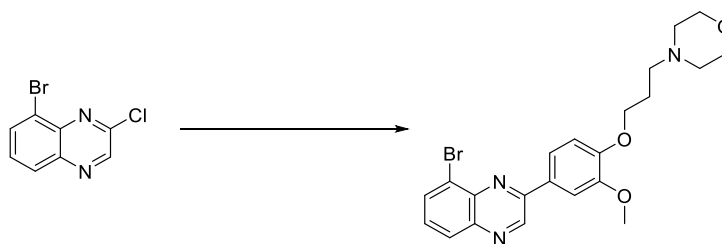
Tert-butyl 4-hydroxypiperidine-1-carboxylate **224** (3.8 g, 18.88 mmol) and DMAP (0.023 g, 0.189 mmol) in DCM (38.4 mL) was stirred over an ice-water bath, and triethylamine (3.95 mL, 28.3 mmol) was added followed by cautious addition of mesyl-Cl (1.765 mL, 22.66 mmol). The reaction mixture was stirred at room temperature for 16 h under a nitrogen atmosphere. The reaction mixture was diluted with water (40 mL) and extracted with DCM (3 × 50 mL). The organic layers were combined and passed through a hydrophobic frit to afford *tert*-butyl 4-((methylsulfonyl)oxy)piperidine-1-carboxylate (6.288 g, 22.51 mmol, 119 % yield) as a pale yellow solid. Used directly in the next reaction. NaH (0.988 g, 24.70 mmol, 60 % in mineral oil) was added portionwise to a stirred solution of 4-bromo-1H-pyrazole (3.30 g, 22.45 mmol) in DMF (14.53 mL) over an ice-water bath, under a nitrogen atmosphere for 1 h. *tert*-Butyl 4-((methylsulfonyl)oxy)piperidine-1-carboxylate (6.27 g, 22.45 mmol) was added and the reaction mixture was heated to 95 °C for 16 h under a nitrogen atmosphere.

The reaction mixture was diluted with water (60 mL) and extracted with ethyl acetate (3 × 60 mL). The organic layers were combined and passed through a hydrophobic frit. The solvent was removed *in vacuo* and purified by reverse phase column chromatography (50 - 95 % H₂O + 0.1% (NH₄)₂CO₃ in MeCN, 120 g C₁₈) to afford *tert*-butyl 4-(4-bromo-1*H*-pyrazol-1-yl)piperidine-1-carboxylate **226** (2.356 g, 7.13 mmol, 32 % yield) as a white solid. M.pt.: 78 - 80 °C; ν_{\max} (neat): 3122, 2933, 2858, 1681 cm⁻¹; ¹H NMR (400 MHz, CDCl₃) δ = ppm 7.46 (1H, s), 7.43 (1H, s), 4.14 - 4.34 (3H, m), 2.80 - 2.94 (2H, m), 2.06 - 2.13 (2H, m), 1.81 - 1.93 (2H, m), 1.47 (9H, s); ¹³C NMR (101 MHz, CDCl₃) δ = 154.5, 139.5, 127.0, 92.8, 80.0, 59.9, 42.7 (2C, br s), 32.2 (2C), 28.4 (3C); LCMS (Method B): t_R = 1.18 min, [M+H]⁺ 330 & 332 (100 % purity).

***Tert*-butyl 4-(4-(4,4,5,5-tetramethyl-1,3,2-dioxaborolan-2-yl)-1*H*-pyrazol-1-yl)piperidine-1-carboxylate (227)**

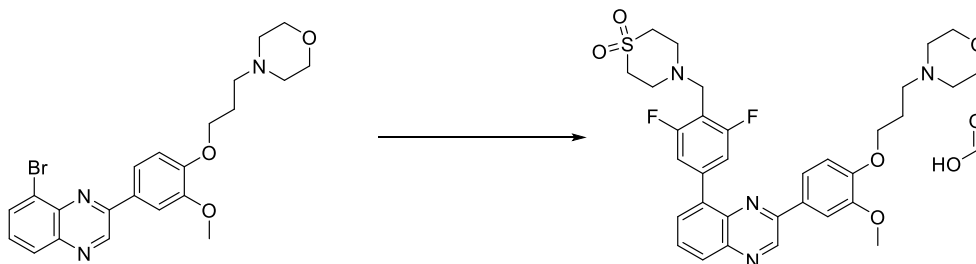


Tert-butyl 4-(4-bromo-1*H*-pyrazol-1-yl)piperidine-1-carboxylate **226** (2.264 g, 6.86 mmol), bis(pinacolato)diboron (1.915 g, 7.54 mmol), potassium acetate (1.346 g, 13.71 mmol) and PdCl₂(dppf)-CH₂Cl₂ adduct (0.168 g, 0.206 mmol) were sealed within a vessel which was evacuated and purged three times with nitrogen. DMA (7.88 mL) was added and the reaction mixture was evacuated and purged three times with nitrogen and heated to 80 °C for 16 h. The reaction mixture was diluted with water (40 mL) and extracted with ethyl acetate (3 × 40 mL). The organic layers were combined, passed through a hydrophobic frit and the solvent was removed *in vacuo* to afford *tert*-butyl 4-(4-(4,4,5,5-tetramethyl-1,3,2-dioxaborolan-2-yl)-1*H*-pyrazol-1-yl)piperidine-1-carboxylate **227** (2.921 g, 7.74 mmol, 113 % yield) as a brown solid. LCMS (Method B): t_R = 1.22 min, [M+H]⁺ 378 (59 % purity). Used crude in the next reaction.

4-(3-(4-(8-Bromoquinoxalin-2-yl)-2-methoxyphenoxy)propyl)morpholine (228)

8-Bromo-2-chloroquinoxaline **215** (493 mg, 2.025 mmol), (3-methoxy-4-(3-morpholinopropoxy)phenyl)boronic acid (679 mg, 2.025 mmol), Pd(PPh₃)₄ (70.2 mg, 0.061 mmol) and Na₂CO₃ (644 mg, 6.07 mmol) were sealed within a vial and the reaction mixture was evacuated and purged three times with nitrogen. DMF (25 mL) was added and the reaction mixture was evacuated and purged three times with nitrogen. The reaction mixture was heated to 105 °C for 16 h. The reaction mixture was filtered over Celite and washed with ethyl acetate (30 mL). The solvent was removed *in vacuo* and the residue was purified by normal phase column chromatography (0 – 100 % EtOAc in cyclohexane, 120 g SiO₂, 10 column volumes). The appropriate fractions were combined, and the solvent removed *in vacuo* to afford 4-(3-(4-(8-bromoquinoxalin-2-yl)-2-methoxyphenoxy)propyl)morpholine **228** (457 mg, 0.997 mmol, 49.2 % yield) as a beige solid. M.pt.: 110 - 112 °C; ν_{\max} (neat): 2949, 2823, 1515, 1598, 1227, 761 cm⁻¹; ¹H NMR (400 MHz, CDCl₃) δ = 9.31 (1H, s), 8.00 - 8.08 (3H, m), 7.80 (1H, dd, *J* = 8.4, 2.1 Hz), 7.54 (1H, dd, *J* = 8.4, 7.5 Hz), 7.05 (1H, d, *J* = 8.3 Hz), 4.19 (2H, t, *J* = 6.6 Hz), 4.03 (3H, s), 3.70 - 3.75 (6H, m), 2.53 - 2.59 (2H, m), 2.46 - 2.50 (4H, m); ¹³C NMR (101 MHz, CDCl₃) δ = 151.1, 150.2, 145.9, 143.3, 142.1, 139.9, 139.8, 133.6, 129.2, 129.0, 128.9, 124.4, 120.6, 112.8, 110.9, 106.1, 67.4, 67.0, 56.1, 55.4, 53.8, 26.3; LCMS (Method A): *t_R* = 0.76 min, [M+H]⁺ 458 & 460 (95 % purity); HRMS: (C₂₂H₂₄BrN₃O₃) [M+H]⁺ requires 458.1079, found [M+H]⁺ 458.1078.

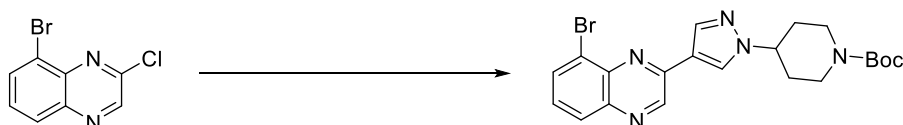
4-(2,6-Difluoro-4-(3-(3-methoxy-4-(3-morpholinopropoxy)phenyl)quinoxalin-5-yl)benzyl)thiomorpholine 1,1-dioxide, formic acid salt (63)



4-(3-(4-(8-Bromoquinoxalin-2-yl)-2-methoxyphenoxy)propyl)morpholine **228** (410 mg, 0.895 mmol), (4-((1,1-dioxidothiomorpholino)methyl)-3,5-difluorophenyl)boronic acid (358 mg, 0.939 mmol), PdOAc₂ (6.02 mg, 0.027 mmol), potassium phosphate tribasic (570 mg, 2.68 mmol) and SPhos (33 mg, 0.081 mmol) were sealed in a vial which was then evacuated and purged three times with nitrogen. DME (84.5 mL) and water (0.203 mL) was added and the reaction mixture was evacuated and purged three times with nitrogen and then heated to 105 °C under a nitrogen atmosphere for 2.5 h. The reaction mixture was filtered over Celite, washed with ethyl acetate (30 mL) and the solvent was removed *in vacuo*. The residue was purified by normal phase column chromatography (0 - 100% 3:1 ethyl acetate:ethanol in ethyl acetate, 80 g Si, 15 column volumes) to afford a yellow solid. The residue was purified by Mass Directed AutoPrep on an Xselect CSH column using acetonitrile water with a formic acid modifier to afford 4-(2,6-difluoro-4-(3-(3-methoxy-4-(3-morpholinopropoxy)phenyl)quinoxalin-5-yl)benzyl)thiomorpholine 1,1-dioxide, formic acid salt **63** (293 mg, 0.428 mmol, 48 % yield) as a yellow solid. M.pt.: 70 - 72 °C; ν_{\max} (neat): 2949, 2832, 1132, 1124 cm⁻¹; ¹H NMR (400 MHz, DMSO-*d*₆) δ = 9.57 (1H, s), 8.19 (1H, s), 8.09 (1H, br d, *J* = 8.1 Hz), 7.97 (1H, br d, *J* = 6.8 Hz), 7.79 - 7.90 (3H, m), 7.60 (2H, br d, *J* = 8.8 Hz), 7.03 - 7.09 (1H, m), 4.07 (2H, br t, *J* = 6.2 Hz), 3.88 (2H, s), 3.84 (3H, s), 3.57 - 3.64 (4H, m), 3.12 - 3.23 (4H, m), 2.89 - 3.06 (4H, m), 2.40 - 2.54 (6H, m), 1.87 - 1.97 (2H, m) (N.B. additional peak due to formic acid salt); ¹³C NMR (101 MHz, DMSO-*d*₆) δ = 162.0, 159.6 (2C, dd, *J* = 245.0, 9.5 Hz), 149.4, 148.7, 148.3, 142.0, 139.7, 138.9 (t, *J* = 10.6 Hz), 137.3, 135.3 (d, *J* = 1.5 Hz), 129.6, 128.3, 127.9, 127.2, 119.3, 112.7 (2C, dd, *J* = 19.8, 7.3 Hz), 111.6, 109.9 (t, *J* = 20.5 Hz), 108.8, 65.5, 65.0, 53.8 (2C), 53.6 (2C), 52.2, 49.2 (2C), 48.8 (2C), 45.8, 24.7; (N.B. additional peak due to formic acid salt); ¹⁹F NMR (376 MHz, DMSO-*d*₆) δ = -114.82 (s); LCMS (Method A): *t*_R = 0.80 min, [M+H]⁺

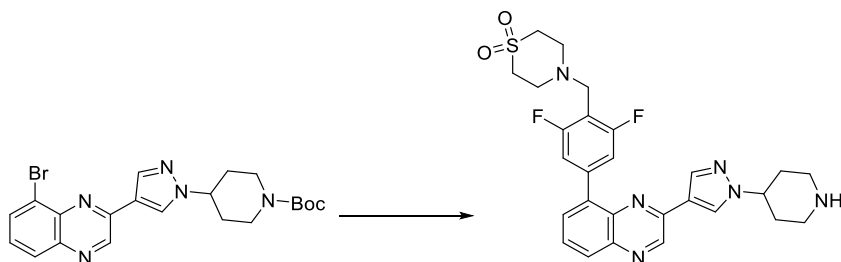
639, (97 % purity); HRMS: (C₃₃H₃₆F₂N₄O₅S) [M+H]⁺ requires 639.2452, found [M+H]⁺ 639.2449.

4-(4-(8-Bromoquinoxalin-2-yl)-1H-pyrazol-1-yl)piperidine-1-carboxylate (**229**)

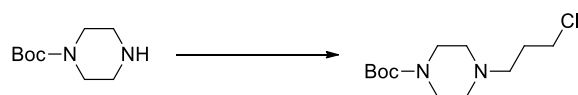


8-Bromo-2-chloroquinoxaline **214** (446 mg, 1.832 mmol), *tert*-butyl 4-(4-(4,4,5,5-tetramethyl-1,3,2-dioxaborolan-2-yl)-1H-pyrazol-1-yl)piperidine-1-carboxylate (760 mg, 2.015 mmol), potassium phosphate tribasic (1283 mg, 6.04 mmol) and Pd(PPh₃)₂Cl₂ (38.6 mg, 0.055 mmol) were sealed within a vial and the reaction mixture was evacuated and purged three times with nitrogen. DMA (2.476 mL) and water (0.108 mL) were added and the reaction mixture was evacuated and purged three times with nitrogen. The reaction mixture was heated to 80 °C for 3 h. The reaction mixture was filtered over Celite and washed with EtOAc (40 mL). The reaction mixture was diluted with water (30 mL) and extracted with EtOAc (3 × 40 mL). The organic layers were combined, passed through a hydrophobic frit and the solvent removed *in vacuo*. The residue was purified by normal phase column chromatography (0 - 100 % EtOAc in cyclohexane, 120 g SiO₂, 13 column volumes) to afford *tert*-butyl 4-(4-(8-bromoquinoxalin-2-yl)-1H-pyrazol-1-yl)piperidine-1-carboxylate **229** (461 mg, 1.006 mmol, 55 % yield) as a yellow gum. ν_{\max} (neat): 3380, 2940, 2832, 1631, 1025 cm⁻¹; ¹H NMR (400 MHz, DMSO-*d*₆) δ = 9.35 (1H, s), 8.76 (1H, s), 8.33 (1H, s), 8.16 (1H, dd, *J* = 7.6, 1.2 Hz), 8.05 (1H, dd, *J* = 8.3, 1.0 Hz), 7.65 (1H, t, *J* = 7.9 Hz), 4.37 - 4.65 (1H, m), 4.09 (2H, br d, *J* = 13.0 Hz), 2.96 (2H, br s), 2.11 (2H, br dd, *J* = 12.2, 2.2 Hz), 1.81 - 1.94 (2H, m), 1.08 (9H, s); ¹H NMR (400 MHz, DMSO-*d*₆) δ = 9.35 (1H, s), 8.76 (1H, s), 8.33 (1H, s), 8.16 (1H, dd, *J* = 7.6, 1.2 Hz), 8.05 (1H, dd, *J* = 8.3, 1.0 Hz), 7.62 - 7.68 (1H, m), 4.52 (1H, tt, *J* = 11.4, 3.9 Hz), 4.02 - 4.16 (2H, m), 2.85 - 3.05 (2H, m), 2.04 - 2.17 (2H, m), 1.80 - 1.95 (2H, m), 1.44 (9H, s); ¹³C NMR (101 MHz, DMSO-*d*₆) δ ppm 154.3, 148.3, 145.2, 141.8, 139.6, 138.6, 134.2, 129.7, 129.4, 123.1 (2C), 120.0, 79.4, 59.1, 32.3 (2C), 28.6 (2C), 25.4 (3C); LCMS (Method B): *t*_R = 1.34 min, [M+H]⁺ 458 & 460 (96 % purity).

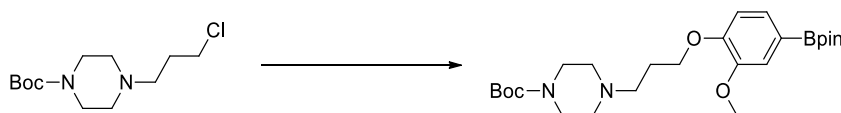
4-(2,6-Difluoro-4-(3-(1-(piperidin-4-yl)-1H-pyrazol-4-yl)quinoxalin-5-yl)benzyl)thiomorpholine 1,1-dioxide (61)



Tert-butyl 4-(4-(8-bromoquinoxalin-2-yl)-1H-pyrazol-1-yl)piperidine-1-carboxylate **229** (150 mg, 0.327 mmol), 4-((1,1-dioxidothiomorpholino)methyl)-3,5-difluorophenyl)boronic acid (131 mg, 0.344 mmol), PdOAc₂ (2.204 mg, 9.82 μmol), potassium phosphate tribasic (208 mg, 0.982 mmol) and SPhos (12.09 mg, 0.029 mmol) were sealed in a vial and evacuated and purged three times with nitrogen. DME (30.916 mL) and water (0.074 mL) was added and the reaction mixture was evacuated and purged three times with nitrogen and heated to 105 °C under a nitrogen atmosphere for 2.5 h. The reaction mixture was filtered over Celite, washed with ethyl acetate (30 mL) and the solvent was removed *in vacuo*. The residue was purified by reverse phase column chromatography (55 - 95 % H₂O + 0.1 % (NH₄)₂CO₃ in MeCN, 30 g C₁₈, 12 column volumes) to afford a yellow solid. 1.25 M HCl in EtOH (4.19 mL, 5.24 mmol) was added and the reaction mixture was heated to 50 °C for 16 h. The solvent was removed *in vacuo* and the residue was purified by reverse phase column chromatography (55 - 95 % H₂O + 0.1 % (NH₄)₂CO₃ in MeCN, 30 g C₁₈, 10 column volumes) to afford 4-(2,6-difluoro-4-(3-(1-(piperidin-4-yl)-1H-pyrazol-4-yl)quinoxalin-5-yl)benzyl)thiomorpholine 1,1-dioxide **61** (27 mg, 0.046 mmol, 14 % yield) as a yellow solid. M.pt.: 141 - 142 °C; ν_{\max} (neat): 3380, 2940, 2832, 1330, 1128 cm⁻¹; ¹H NMR (400 MHz, DMSO-*d*₆) δ = 9.35 (1H, s), 8.58 (1H, s), 8.12 (1H, s), 8.08 (1H, dd, *J* = 8.3, 1.2 Hz), 7.96 (1H, dd, *J* = 7.3, 1.5 Hz), 7.81 (1H, dd, *J* = 8.3, 7.3 Hz), 7.53 - 7.59 (2H, m), 4.32 - 4.43 (1H, m), 3.89 (2H, s), 3.13 - 3.18 (6H, m), 2.96 - 3.05 (4H, m), 2.89 (1H, s), 2.71 - 2.78 (2H, m), 2.00 - 2.16 (2H, m), 1.86 - 1.99 (2H, m); ¹³C NMR (101 MHz, DMSO-*d*₆) δ = 161.2 (2C, dd, *J* = 245.8, 9.5 Hz), 147.2, 144.3, 141.0, 140.6 (t, *J* = 10.6 Hz), 139.3, 138.3, 136.6, 135.6, 131.2, 130.0, 128.9, 128.7, 114.1 (2C, dd, *J* = 19.1, 6.6 Hz), 111.4 (t, *J* = 20.5 Hz), 59.1, 50.8 (2C), 50.5 (2C), 47.4, 44.7 (2C), 32.7 (2C); ¹⁹F NMR (376 MHz, DMSO-*d*₆) δ = -114.7 (s); LCMS (Method B): t_R = 1.00 min, [M+H]⁺ 539 (100 % purity); HRMS: (C₂₇H₂₈F₂N₆O₂S) [M+H]⁺ requires 539.2040, found [M+H]⁺ 539.2035.

***tert*-Butyl 4-(3-chloropropyl)piperazine-1-carboxylate (231)**

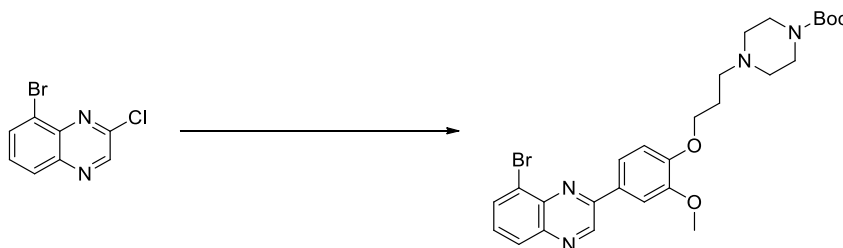
tert-Butyl piperazine-1-carboxylate **230** (5 g, 26.8 mmol), 5 M aqueous NaOH (6.44 mL, 32.2 mmol) and 1-bromo-3-chloropropane (2.65 mL, 26.8 mmol) were stirred together in acetone (100 mL) under a nitrogen atmosphere at room temperature for 3 h. The solvent was removed *in vacuo* and diluted with water (70 mL). The aqueous phase was extracted with DCM (3 × 70 mL) and the combined organic layers were passed through a hydrophobic frit and the solvent was removed *in vacuo* to afford *tert*-butyl 4-(3-chloropropyl)piperazine-1-carboxylate **231** (4.731 g, 18.00 mmol, 67 % yield) as a colourless oil. $R_f = 0.33$, 50 % EtOAc in cyclohexane; ν_{\max} (neat): 2933, 2611, 1691, 1166, 1122, 1004 cm^{-1} ; ^1H NMR (400 MHz, CDCl_3) $\delta = 3.60$ (2H, t, $J = 6.5$ Hz), 3.40 - 3.46 (4H, m), 2.50 (2H, t, $J = 7.1$ Hz), 2.34 - 2.46 (4H, m), 1.91 - 2.00 (2H, m), 1.46 (9H, s); ^{13}C NMR (101 MHz, CDCl_3) $\delta = 154.7$, 79.6, 55.4 (2C), 53.0, 44.2, 43.0 (2C), 29.7, 28.4 (3C); HRMS: ($\text{C}_{12}\text{H}_{23}\text{ClN}_2\text{O}_2$) $[\text{M}+\text{H}]^+$ requires 263.1534, found $[\text{M}+\text{H}]^+$ 263.1523.

4-(3-(2-Methoxy-4-(4,4,5,5-tetramethyl-1,3,2-dioxaborolan-2-yl)phenoxy)propyl)piperazine-1-carboxylate (232)

2-Methoxy-4-(4,4,5,5-tetramethyl-1,3,2-dioxaborolan-2-yl)phenol **231** (4.50 g, 18.00 mmol) and cesium carbonate (10.52 g, 32.3 mmol) in DMF (98 mL) was added *tert*-butyl 4-(3-chloropropyl)piperazine-1-carboxylate (4.731 g, 18.00 mmol). The reaction mixture was heated to 80 °C for 16 h. The solvent was removed *in vacuo* and diluted with water (120 mL). The aqueous was extracted with ethyl acetate (3 × 120 mL), the organic layers were combined, passed through a hydrophobic frit and the solvent removed *in vacuo* to afford *tert*-butyl 4-(3-(2-methoxy-4-(4,4,5,5-tetramethyl-1,3,2-dioxaborolan-2-yl)phenoxy)propyl)piperazine-1-carboxylate **232** (8.580 g, 18.01 mmol, 100 % yield) as a brown solid. The

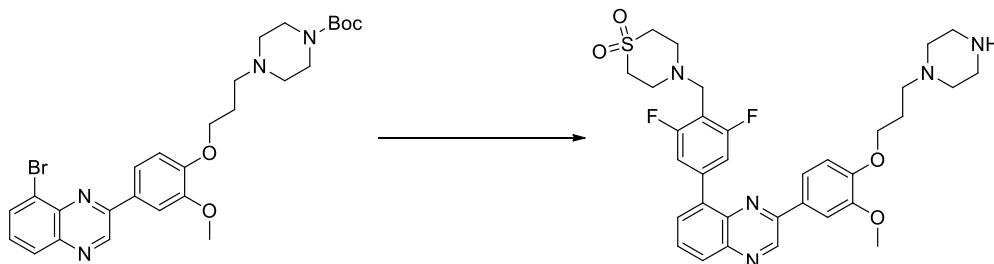
material was used crude in the next reaction. Partially characterised. LCMS (Method B): $t_R = 1.40$ min, $[M+H]^+$ 477, (67 % purity).

4-(3-(4-(8-Bromoquinoxalin-2-yl)-2-methoxyphenoxy)propyl)piperazine-1-carboxylate (233)



8-Bromo-2-chloroquinoxaline **214** (4.385 g, 18.01 mmol), *tert*-butyl 4-(3-(2-methoxy-4-(4,4,5,5-tetramethyl-1,3,2-dioxaborolan-2-yl)phenoxy)propyl)piperazine-1-carboxylate (8.58 g, 18.01 mmol), $\text{Pd}(\text{PPh}_3)_4$ (0.624 g, 0.540 mmol) and Na_2CO_3 (5.73 g, 54.0 mmol) were sealed within a vial and the reaction mixture was evacuated and purged three times with nitrogen. DMF (222 mL) was added and the reaction mixture was evacuated and purged three times with nitrogen. The reaction mixture was heated to 105 °C for 16 h. The reaction mixture was filtered over Celite and washed with ethyl acetate (30 mL). The solvent was removed *in vacuo* and the residue was purified by normal phase column chromatography (0 – 100 % EtOAc in cyclohexane, 120 g SiO_2) to afford *tert*-butyl 4-(3-(4-(8-bromoquinoxalin-2-yl)-2-methoxyphenoxy)propyl)piperazine-1-carboxylate **233** (5.183 g, 9.30 mmol, 52 % yield) as a beige solid. Partially characterised, used crude in next reaction. ^1H NMR (400 MHz, $\text{DMSO}-d_6$) $\delta = 9.64$ (1H, s), 8.20 (1H, dd, $J = 7.6, 1.2$ Hz), 8.10 (1H, dd, $J = 8.3, 1.2$ Hz), 7.99 - 8.05 (2H, m), 7.70 (1H, dd, $J = 8.3, 7.6$ Hz), 7.15 - 7.22 (1H, m), 4.12 (2H, t, $J = 6.5$ Hz), 3.93 (3H, s), 3.31 - 3.36 (4H, m), 2.47 (2H, t, $J = 7.2$ Hz), 2.31 - 2.37 (4H, m), 1.90 - 1.97 (2H, m), 1.40 (9H, s); LCMS (Method A): $t_R = 0.84$ min, $[M+H]^+$ 557 & 559 (85 % purity).

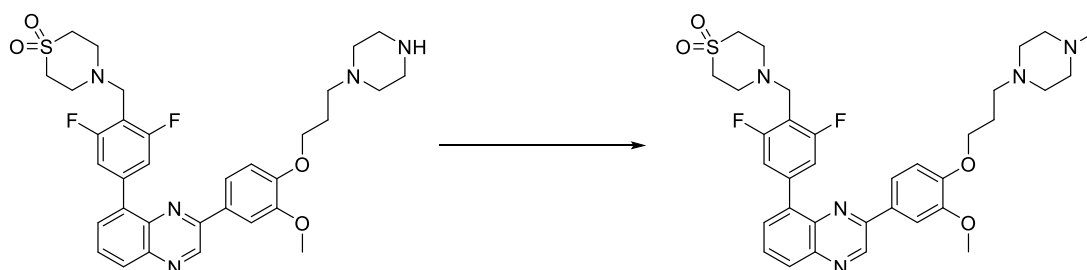
4-(2,6-Difluoro-4-(3-(3-methoxy-4-(3-(piperazin-1-yl)propoxy)phenyl)quinoxalin-5-yl)benzyl)thiomorpholine 1,1-dioxide (234)



Tert-butyl 4-(3-(4-(8-bromoquinoxalin-2-yl)-2-methoxyphenoxy)propyl)piperazine-1-carboxylate **233** (2.1 g, 3.77 mmol), 4-((1,1-dioxidothiomorpholino)methyl)-3,5-difluorophenyl)boronic acid (1.508 g, 3.96 mmol), PdOAc₂ (0.025 g, 0.113 mmol), K₃PO₄ (2.399 g, 11.30 mmol) and SPhos (0.139 g, 0.339 mmol) were sealed in a vial and evacuated and purged three times with nitrogen. DME (300 mL) and water (0.720 mL) were added and the reaction mixture was evacuated and purged three times with nitrogen and heated to 105 °C under a nitrogen atmosphere for 16 h. The reaction mixture was filtered over Celite, washed with ethyl acetate (30 mL) and the solvent was concentrated *in vacuo*. 4 M HCl in 1,4-dioxane (4.71 mL, 18.83 mmol) was added and the reaction mixture was stirred at room temperature for 1 h. The solvent was concentrated *in vacuo* and diluted with water (30 mL) and extracted with DCM (3 × 30 mL). The organic layers were combined, passed through a hydrophobic frit and the solvent concentrated *in vacuo*. The residue was purified by reverse phase column chromatography (30 – 85 % MeCN in H₂O + 0.1 % (NH₄)₂CO₃, 130 g C₁₈) to afford 4-(2,6-difluoro-4-(3-(3-methoxy-4-(3-(piperazin-1-yl)propoxy)phenyl)quinoxalin-5-yl)benzyl)thiomorpholine 1,1-dioxide **234** (1.633 g, 2.56 mmol, 68 % yield) as a yellow solid. ¹H NMR (400 MHz, DMSO-*d*₆) δ = 9.58 (1H, s), 8.10 (1H, dd, *J* = 8.3, 1.5 Hz), 7.98 (1H, dd, *J* = 7.2, 1.3 Hz), 7.81 - 7.90 (3H, m), 7.57 - 7.65 (2H, m), 7.04 - 7.09 (1H, m), 4.06 (2H, t, *J* = 6.4 Hz), 3.88 (2H, s), 3.84 (3H, s), 3.14 - 3.19 (4H, m), 2.96 - 3.02 (4H, m), 2.67 - 2.72 (4H, m), 2.50 - 2.53 (1H, m), 2.39 (2H, t, *J* = 7.1 Hz), 2.23 - 2.36 (4H, m), 1.84 - 1.94 (2H, m); ¹³C NMR (101 MHz, DMSO-*d*₆) δ = 161.2 (2C, dd, *J* = 245.8, 9.5 Hz), 151.0, 150.2, 149.9, 143.5, 141.3, 140.4 (t, *J* = 10.6 Hz), 138.9, 136.8, 131.1, 129.9, 129.4, 128.7, 120.9, 114.2 (2C, dd, *J* = 20.5, 7.3 Hz), 113.1, 111.4 (t, *J* = 20.9 Hz), 110.3, 67.2, 55.6, 55.4, 54.8 (2C), 50.8 (2C), 50.4 (2C), 49.1, 47.4, 46.1, 26.5; ¹⁹F NMR (376 MHz, DMSO-*d*₆) δ = -114.8 (s); LCMS (Method B): *t*_R = 1.23

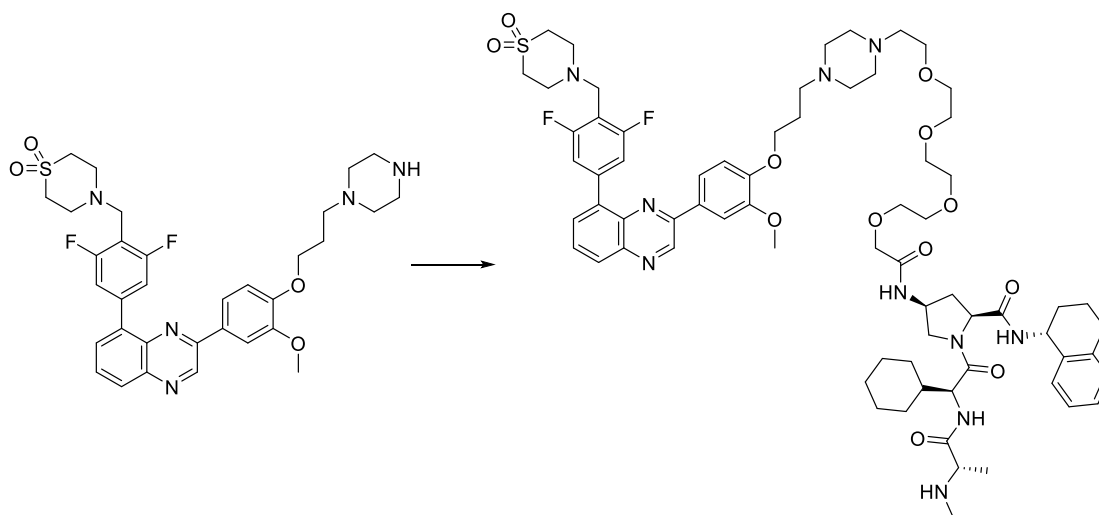
min, $[M+H]^+$ 639 (98 % purity); HRMS: ($C_{33}H_{37}F_2N_5O_4S$) $[M+H]^+$ requires 638.2612, found $[M+H]^+$ 638.2617.

4-(2,6-Difluoro-4-(3-(3-methoxy-4-(3-(4-methylpiperazin-1-yl)propoxy)phenyl)quinoxalin-5-yl)benzyl)thiomorpholine 1,1-dioxide (235)



4-(2,6-Difluoro-4-(3-(3-methoxy-4-(3-(piperazin-1-yl)propoxy)phenyl)quinoxalin-5-yl)benzyl)thiomorpholine 1,1-dioxide **234** (80 mg, 0.125 mmol) was added to a sealed mixture of formaldehyde (18.68 μ L, 0.251 mmol) and formic acid (9.62 μ L, 0.251 mmol) in THF (2201 μ L). The sealed reaction mixture was heated to 80 $^{\circ}$ C for 1 h. The reaction mixture was cooled to room temperature and diluted with water (10 mL) and extracted with DCM (3 \times 10 mL). The organic layers were combined, passed through a hydrophobic frit and the solvent was removed *in vacuo*. The residue was purified by reverse phase prep column chromatography (40 - 95 % H_2O + 0.1 % $(NH_4)_2CO_3$ in MeCN, Xbridge C_{18} , 42 mL/ min, 35 min) to afford 4-(2,6-difluoro-4-(3-(3-methoxy-4-(3-(4-methylpiperazin-1-yl)propoxy)phenyl)quinoxalin-5-yl)benzyl)thiomorpholine 1,1-dioxide **235** (50 mg, 0.077 mmol, 61 % yield) as an orange solid. M.pt.: 68 - 70 $^{\circ}$ C; ν_{max} (neat): 3370, 2937, 2800, 1633, 1600, 1490, 1286 cm^{-1} ; 1H NMR (400 MHz, $CDCl_3$) δ = 9.38 (1H, s), 8.15 (1H, dd, J = 8.3, 1.5 Hz), 7.75 - 7.89 (3H, m), 7.71 (1H, dd, J = 8.3, 2.0 Hz), 7.46 - 7.54 (2H, m), 7.03 (1H, d, J = 8.3 Hz), 4.17 (2H, t, J = 6.7 Hz), 3.95 (3H, s), 3.93 (2H, s), 3.07 - 3.17 (8H, m), 2.40 - 2.65 (10H, m), 2.31 (3H, s), 2.02 - 2.12 (2H, m); ^{13}C NMR (101 MHz, $CDCl_3$) δ = 161.3 (2C, dd, J = 246.5, 9.5 Hz), 151.0, 150.5, 150.2, 142.7, 141.5, 140.8 (t, J = 10.6 Hz), 139.4, 137.3, 130.5, 129.9, 129.1, 128.8, 120.2, 114.0 (2C, dd, J = 20.5, 6.6 Hz), 112.7, 110.8 (t, J = 20.2 Hz), 110.4, 67.5, 55.7, 55.1 (2C), 54.9, 53.1 (2C), 51.5 (2C), 50.1 (2C), 48.0, 46.0, 26.6; ^{19}F NMR (376 MHz, $CDCl_3$) δ = -115.2 (s); LCMS (Method B): t_R = 1.22 min, $[M+H]^+$ 652 (100 % purity); HRMS: ($C_{34}H_{39}F_2N_5O_4S$) $[M+H]^+$ requires 652.2769, found $[M+H]^+$ 652.2767.

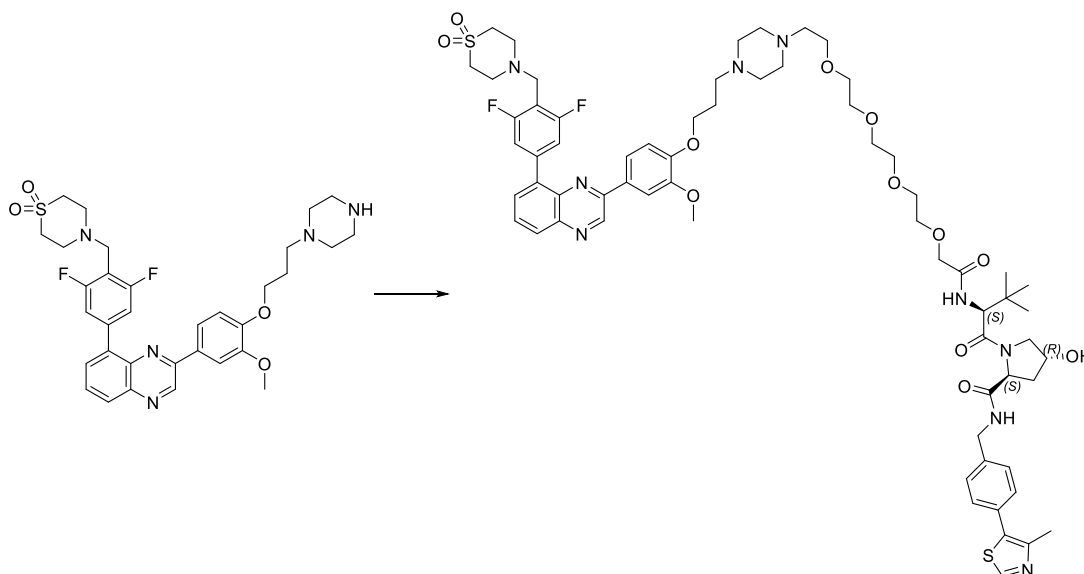
(2S,4S)-1-((S)-2-Cyclohexyl-2-((S)-2-(methylamino)propanamido)acetyl)-4-(14-(4-(3-(4-(8-(4-((1,1-dioxidothiomorpholino)methyl)-3,5-difluorophenyl)quinoxalin-2-yl)-2-methoxyphenoxy)propyl)-piperazin-1-yl)-3,6,9,12-tetraoxatetradecanamido)-N-((R)-1,2,3,4-tetrahydronaphthalen-1-yl)-pyrrolidine-2-carboxamide (99, JP-5)



4-(2,6-Difluoro-4-(3-(3-methoxy-4-(3-(piperazin-1-yl)propoxy)phenyl)quinoxalin-5-yl)benzyl)thio-morpholine 1,1-dioxide **234** (80 mg, 0.125 mmol) was added to a stirred mixture of *tert*-butyl ((S)-1-(((S)-2-((2S,4S)-4-(14-chloro-3,6,9,12-tetraoxatetradecanamido)-2-(((R)-1,2,3,4-tetrahydronaphthalen-1-yl)carbamoyl)pyrrolidin-1-yl)-1-cyclohexyl-2-oxoethyl)amino)-1-oxopropan-2-yl)(methyl)carbamate (126 mg, 0.151 mmol), sodium iodide (23 mg, 0.153 mmol) and potassium carbonate (35 mg, 0.253 mmol) in DMF (385 μ L). The reaction mixture was heated to 100 $^{\circ}$ C for 1 h under a nitrogen atmosphere. The reaction mixture was cooled to room temperature and diluted with water (10 mL) and extracted with DCM (3 \times 10 mL). The organic layers were combined, passed through a hydrophobic frit and the solvent was concentrated *in vacuo*. TFA (97 μ L, 1.254 mmol) was added and the reaction mixture was stirred for 16 h at room temperature. The reaction mixture was diluted with water (10 mL) and extracted with DCM (3 \times 10 mL). The organic layers were combined, passed through a hydrophobic frit and the solvent was concentrated *in vacuo*. The residue was purified by reverse phase prep column chromatography (30 – 95 % MeCN in H₂O + 0.1 % NH₄HCO₃, XBridge C₁₈, 42 mL/min, 45 min) to afford (2S,4S)-1-((S)-2-cyclohexyl-2-((S)-2-(methylamino)propanamido)acetyl)-4-(14-(4-(3-(4-(8-(4-((1,1-dioxidothiomorpholino)-methyl)-3,5-difluorophenyl)quinoxalin-2-yl)-2-methoxyphenoxy)-propyl)piperazin-1-yl)-

3,6,9,12-tetraoxatetradecanamido)-*N*-((*R*)-1,2,3,4-tetrahydronaphthalen-1-yl)pyrrolidine-2-carboxamide **99** (127 mg, 0.095 mmol, 76 % yield) as an orange solid. M.pt.: 69 – 71 °C; ν_{\max} (neat): 3319, 2928, 2851, 1634, 1517, 1429, 1124 cm^{-1} ; ^1H NMR (400 MHz, CDCl_3) δ = 9.38 (1H, s), 8.53 (1H, d, J = 7.1 Hz), 8.15 (1H, dd, J = 8.2, 1.6 Hz), 7.88 (1H, d, J = 2.2 Hz), 7.84 (1H, dd, J = 7.3, 1.7 Hz), 7.75 - 7.80 (1H, m), 7.71 (1H, dd, J = 8.4, 2.1 Hz), 7.63 (1H, d, J = 8.3 Hz), 7.47 - 7.55 (3H, m), 7.10 - 7.16 (2H, m), 7.00 - 7.08 (3H, m), 5.07 - 5.16 (1H, m), 4.72 - 4.77 (1H, m), 4.61 - 4.69 (1H, m), 4.37 (1H, t, J = 8.2 Hz), 4.13 - 4.21 (3H, m), 4.05 (2H, s), 3.95 (3H, s), 3.93 (2H, s), 3.67 - 3.74 (4H, m), 3.56 - 3.66 (12H, m), 3.06 - 3.16 (8H, m), 2.99 - 3.05 (1H, m), 2.65 - 2.85 (3H, m), 2.45 - 2.62 (12H, m), 2.35 (3H, s), 2.16 - 2.26 (1H, m), 1.97 - 2.11 (4H, m), 1.76 - 1.90 (4H, m), 1.47 - 1.62 (4H, m), 1.27 (3H, d, J = 6.8 Hz), 1.03 - 1.14 (3H, m), 0.86 - 1.03 (2H, m); ^{13}C NMR (101 MHz, CDCl_3) δ = 174.9, 173.1, 170.6, 170.1, 161.3 (2C, dd, J = 246.9, 9.2 Hz), 151.0, 150.5, 150.2, 142.7, 141.5, 140.7 (t, J = 10.6 Hz), 139.4, 137.3 (t, J = 2.2 Hz), 137.2, 136.4, 130.5, 129.9, 129.1, 129.1, 128.8, 128.3, 127.2, 126.1, 120.2, 114.0 (2C, dd, J = 20.5, 7.3 Hz), 112.7, 110.8 (t, J = 20.2 Hz), 110.4, 71.3, 70.9, 70.7, 70.6, 70.5, 70.5, 70.3, 68.9, 67.5, 60.3, 60.0, 57.8, 55.7, 55.5, 54.9, 54.7, 53.6 (2C), 53.1 (2C), 51.5 (2C), 50.1 (2C), 48.9, 48.0, 47.7, 40.5, 35.1, 31.1, 30.1, 29.4, 29.2, 28.5, 26.6, 26.0, 26.0, 25.8, 20.2, 19.5; ^{19}F NMR (376 MHz, CDCl_3) δ = -115.2 (s); LCMS (Method B): t_{R} = 1.36 min, $[(\text{M}+2\text{H})/2]^+$ 670 (100 % purity); HRMS: ($\text{C}_{70}\text{H}_{94}\text{F}_2\text{N}_{10}\text{O}_{12}\text{S}$) $[(\text{M}+2\text{H})/2]^+$ requires 669.3449, found $[(\text{M}+2\text{H})/2]^+$ 669.3454.

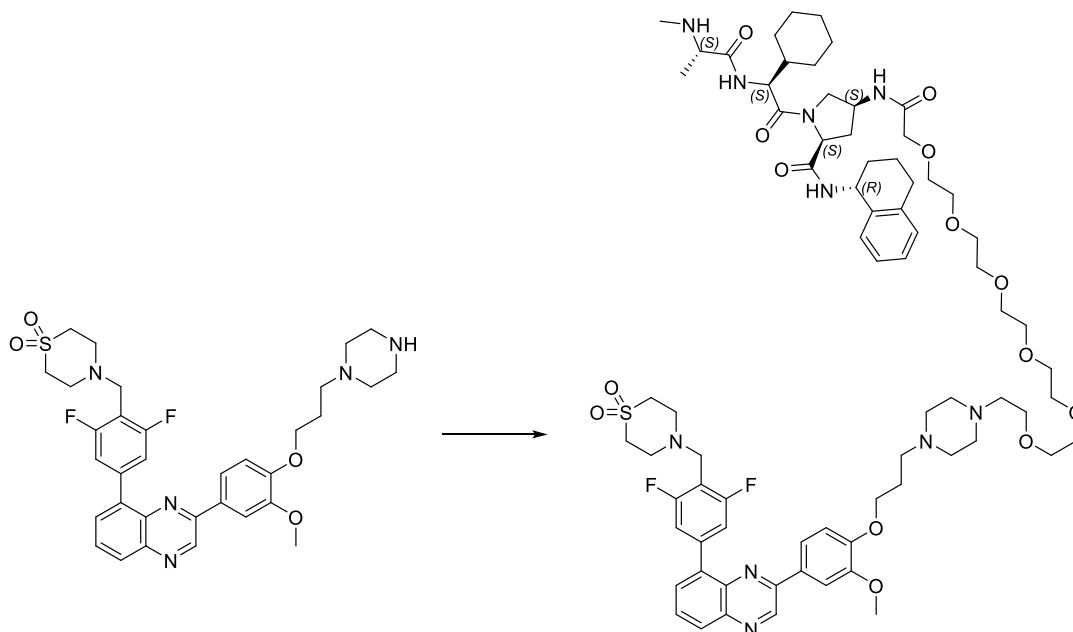
(2*S*,4*R*)-1-((*S*)-2-(*tert*-Butyl)-17-(4-(3-(4-(8-(4-((1,1-dioxidothiomorpholino)methyl)-3,5-difluorophenyl)quinoxalin-2-yl)-2-methoxyphenoxy)propyl)piperazin-1-yl)-4-oxo-6,9,12,15-tetraoxa-3-azaheptadecanoyl)-4-hydroxy-*N*-(4-(4-methylthiazol-5-yl)benzyl)pyrrolidine-2-carboxamide (101)



4-(2,6-Difluoro-4-(3-(3-methoxy-4-(3-(piperazin-1-yl)propoxy)phenyl)quinoxalin-5-yl)benzyl)thiomorpholine 1,1-dioxide **234** (80 mg, 0.125 mmol) was added to a stirred mixture of (2*S*,4*R*)-1-((*S*)-2-(*tert*-butyl)-17-chloro-4-oxo-6,9,12,15-tetraoxa-3-azaheptadecanoyl)-4-hydroxy-*N*-(4-(4-methylthiazol-5-yl)benzyl)pyrrolidine-2-carboxamide (103 mg, 0.151 mmol), sodium iodide (23 mg, 0.153 mmol) and potassium carbonate (35 mg, 0.253 mmol) in DMF (385 μ L). The reaction mixture was heated to 90 $^{\circ}$ C for 16 h under a nitrogen atmosphere. The reaction mixture was cooled to room temperature and diluted with water (10 mL) and extracted with DCM (3 \times 10 mL). The organic layers were combined, passed through a hydrophobic frit and the solvent was concentrated *in vacuo*. The residue was purified by reverse phase prep column chromatography (30 - 95 % H₂O + 0.1 % (NH₄)₂CO₃ in MeCN, Xbridge C18, 42 mL/ min, 40 min) to afford (2*S*,4*R*)-1-((*S*)-2-(*tert*-butyl)-17-(4-(3-(4-(8-(4-((1,1-dioxidothiomorpholino)methyl)-3,5-difluorophenyl)quinoxalin-2-yl)-2-methoxyphenoxy)propyl)piperazin-1-yl)-4-oxo-6,9,12,15-tetraoxa-3-azaheptadecanoyl)-4-hydroxy-*N*-(4-(4-methylthiazol-5-yl)benzyl)pyrrolidine-2-carboxamide **101** (103 mg, 0.080 mmol, 64 % yield) as a yellow solid. M.pt.: 65 - 67 $^{\circ}$ C; ν_{\max} (neat): 3389, 2935, 2877, 2930, 1634, 1517, 1429, 1124 cm^{-1} ; ^1H NMR (400 MHz, CDCl₃) δ = 9.38 (1H, s), 8.67 (1H, s), 8.14

(1H, dd, $J = 8.2, 1.6$ Hz), 7.88 (1H, d, $J = 2.2$ Hz), 7.84 (1H, dd, $J = 7.3, 1.7$ Hz), 7.76 - 7.80 (1H, m), 7.71 (1H, dd, $J = 8.4, 2.1$ Hz), 7.46 - 7.52 (2H, m), 7.43 (1H, t, $J = 6.0$ Hz), 7.32 - 7.38 (4H, m), 7.26 - 7.31 (1H, m), 7.02 (1H, d, $J = 8.6$ Hz), 4.73 (1H, t, $J = 7.9$ Hz), 4.50 - 4.58 (3H, m), 4.35 (1H, dd, $J = 14.9, 5.4$ Hz), 4.16 (2H, t, $J = 6.6$ Hz), 3.98 - 4.07 (3H, m), 3.95 (3H, s), 3.93 (2H, s), 3.58 - 3.69 (16H, m), 3.06 - 3.17 (8H, m), 2.48 - 2.62 (15H, m), 2.02 - 2.16 (3H, m), 0.99 - 1.12 (1H, m), 0.96 (9H, s); ^{13}C NMR (101 MHz, CDCl_3) $\delta = 171.3, 170.8, 170.3, 161.3$ (2C, dd, $J = 246.5, 8.8$ Hz), 150.9, 150.5, 150.3, 150.1, 148.5, 142.7, 141.4, 140.7 (t, $J = 10.6$ Hz), 139.4, 138.2, 137.3 (t, $J = 2.2$ Hz), 131.6, 130.9, 130.5, 129.9, 129.5 (2C), 129.1, 128.8, 128.1 (2C), 120.2, 114.0 (2C, dd, $J = 20.5, 6.6$ Hz), 112.7, 110.8 (t, $J = 20.5$ Hz), 110.4, 71.2, 70.6, 70.6, 70.5, 70.4, 70.3, 70.0, 68.8, 67.5, 58.6, 57.7, 57.1, 56.7, 55.7, 54.9, 53.6 (2C), 53.4, 53.1 (2C), 51.5 (2C), 50.1 (2C), 48.0, 43.2, 36.0, 35.1, 26.6, 26.4 (3C), 16.1; ^{19}F NMR (376 MHz, CDCl_3) $\delta = -115.17$ (s); LCMS (Method B): $t_R = 1.23$ min, $[(M+2H)/2]^+ 643$ (100 % purity); HRMS: ($\text{C}_{65}\text{H}_{83}\text{F}_2\text{N}_9\text{O}_{12}\text{S}_2$) $[M+H]^+$ requires 642.7861, found $[M+H]^+ 642.7872$.

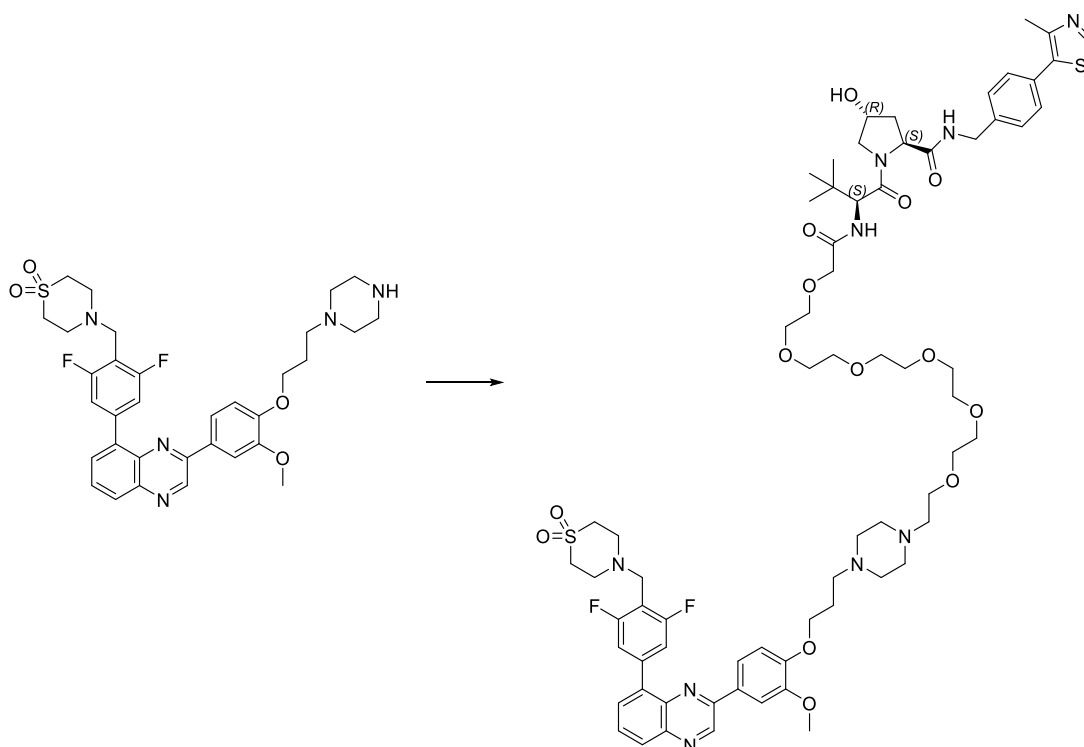
(2S,4S)-1-((S)-2-Cyclohexyl-2-((S)-2-(methylamino)propanamido)acetyl)-4-(20-(4-(3-(4-(8-(4-((1,1-dioxidothiomorpholino)methyl)-3,5-difluorophenyl)quinoxalin-2-yl)-2-methoxyphenoxy)propyl)piperazin-1-yl)-3,6,9,12,15,18-hexaoxaicosanamido)-N-((R)-1,2,3,4-tetrahydronaphthalen-1-yl)pyrrolidine-2-carboxamide (102)



4-(2,6-Difluoro-4-(3-(3-methoxy-4-(3-(piperazin-1-yl)propoxy)phenyl)quinoxalin-5-yl)benzyl)thiomorpholine 1,1-dioxide **234** (80 mg, 0.125 mmol) was added to a stirred mixture of *tert*-butyl ((*S*)-1-(((*S*)-2-((2*S*,4*S*)-4-(20-chloro-3,6,9,12,15,18-hexaoxaicosanamido)-2-(((*R*)-1,2,3,4-tetrahydronaphthalen-1-yl)carbamoyl)pyrrolidin-1-yl)-1-cyclohexyl-2-oxoethyl)amino)-1-oxopropan-2-yl)(methyl)carbamate (139 mg, 0.151 mmol), sodium iodide (22.56 mg, 0.151 mmol) and potassium carbonate (34.7 mg, 0.251 mmol) in DMF (385 μ L). The reaction mixture was heated to 100 °C for 16 h under a nitrogen atmosphere. The reaction mixture was cooled to room temperature and diluted with water (10 mL) and extracted with DCM (3 \times 10 mL). The organic layers were combined, passed through a hydrophobic frit and the solvent was concentrated *in vacuo*. TFA (97 μ L, 1.254 mmol) was added and the reaction mixture was stirred at room temperature for 1 h. The residue was purified by reverse phase column chromatography (30 - 95 % H₂O + 0.1 % HCO₂H in MeCN + 0.1 % HCO₂H, Xbridge C₁₈, 42 mL/ min, 40 min) to afford (2*S*,4*S*)-1-(((*S*)-2-cyclohexyl-2-(((*S*)-2-(methylamino)propanamido)acetyl)-4-(20-(4-(3-(4-(8-(4-(((1,1-dioxidothiomorpholino)methyl)-3,5-difluorophenyl)quinoxalin-2-yl)-2-methoxyphenoxy)-propyl)piperazin-1-yl)-3,6,9,12,15,18-hexaoxaicosanamido)-*N*-(((*R*)-1,2,3,4-tetrahydronaphthalen-1-yl)pyrrolidine-2-carboxamide **102** (102 mg, 0.072 mmol, 57 % yield) as a yellow solid. M.pt.: 57 - 59 °C; ν_{\max} (neat): 3302, 2927, 2856, 1633, 1517, 1429, 1124 cm⁻¹; ¹H NMR (400 MHz, CDCl₃) δ = 9.38 (1H, s), 8.53 (1H, d, *J* = 7.1 Hz), 8.15 (1H, dd, *J* = 8.2, 1.6 Hz), 7.75 - 7.91 (3H, m), 7.71 (1H, dd, *J* = 8.4, 2.1 Hz), 7.63 (1H, d, *J* = 8.3 Hz), 7.47 - 7.54 (3H, m), 7.09 - 7.16 (2H, m), 7.00 - 7.08 (3H, m), 5.09 - 5.16 (1H, m), 4.75 (1H, d, *J* = 7.8 Hz), 4.61 - 4.69 (1H, m), 4.37 (1H, t, *J* = 8.2 Hz), 4.13 - 4.20 (3H, m), 4.05 (2H, s), 3.95 (3H, s), 3.93 (2H, s), 3.69 - 3.74 (4H, m), 3.57 - 3.66 (20H, m), 3.07 - 3.16 (8H, m), 2.99 - 3.05 (1H, m), 2.68 - 2.85 (2H, m), 2.45 - 2.63 (13H, m), 2.35 (3H, s), 2.18 - 2.26 (1H, m), 1.96 - 2.11 (4H, m), 1.77 - 1.89 (4H, m), 1.64 - 1.68 (1H, m), 1.47 - 1.60 (3H, m), 1.27 (3H, d, *J* = 6.8 Hz), 1.02 - 1.15 (3H, m), 0.86 - 1.02 (2H, m); ¹³C NMR (101 MHz, CDCl₃) δ = 174.9, 173.1, 170.6, 170.1, 161.3 (2C, dd, *J* = 246.9, 9.2 Hz), 151.0, 150.5, 150.2, 142.7, 141.5, 140.7 (t, *J* = 10.6 Hz), 139.3, 137.3 (d, *J* = 2.2 Hz), 137.2, 136.4, 130.5, 129.9, 129.1, 129.1, 128.8, 128.3, 127.2, 126.1, 120.2, 114.0 (2C, dd, *J* = 20.5, 7.3 Hz), 112.7, 110.8 (t, *J* = 20.5 Hz), 110.4, 71.3, 70.9, 70.7, 70.6 (2C), 70.5 (2C), 70.5, 70.4, 68.9, 67.5, 60.3, 60.0, 57.8, 55.7, 55.5, 54.9, 54.7, 53.6 (2C), 53.1 (2C), 51.5 (2C), 50.1 (2C), 48.9, 48.0, 47.7, 40.5, 35.1, 31.2 (2C), 30.0, 29.4, 29.2, 28.5, 26.6, 26.0, 26.0, 25.8 (2C), 20.2, 19.5; ¹⁹F NMR (376 MHz, CDCl₃-d) δ = -115.18 (s); LCMS (Method B): *t*_R = 1.35 min,

$[(M+2H)/2]^+$ 714 (100 % purity); HRMS: (C₇₄H₁₀₂F₂N₁₀O₁₄S) $[M+H]^+$ requires 713.3711, found $[M+H]^+$ 713.3723.

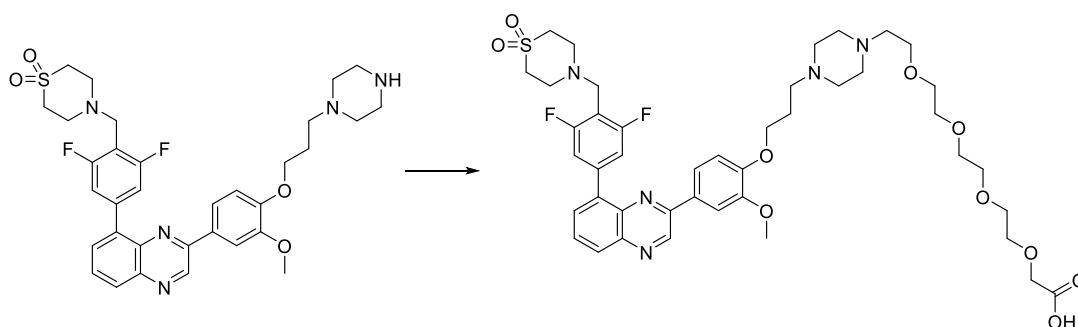
(2S,4R)-1-((S)-2-(tert-butyl)-23-(4-(3-(4-(8-(4-((1,1-dioxidothiomorpholino)methyl)-3,5-difluorophenyl)quinoxalin-2-yl)-2-methoxyphenoxy)propyl)piperazin-1-yl)-4-oxo-6,9,12,15,18,21-hexaoxa-3-azatricosanoyl)-4-hydroxy-N-(4-(4-methylthiazol-5-yl)benzyl)pyrrolidine-2-carboxamide (104)



4-(2,6-Difluoro-4-(3-(3-methoxy-4-(3-(piperazin-1-yl)propoxy)phenyl)quinoxalin-5-yl)benzyl)thiomorpholine 1,1-dioxide **234** (55 mg, 0.086 mmol) was added to a stirred mixture of (2S,4R)-1-((S)-2-(tert-butyl)-23-chloro-4-oxo-6,9,12,15,18,21-hexaoxa-3-azatricosanoyl)-4-hydroxy-N-(4-(4-methylthiazol-5-yl)benzyl)pyrrolidine-2-carboxamide (80 mg, 0.103 mmol), sodium iodide (12.93 mg, 0.086 mmol) and potassium carbonate (24 mg, 0.174 mmol) in DMF (265 μ L). The reaction mixture was heated to 100 °C for 16 h under a nitrogen atmosphere. The reaction mixture was cooled to room temperature and diluted with water (10 mL) and extracted with DCM (3 \times 10 mL). The organic layers were combined, passed through a hydrophobic frit and the solvent was concentrated *in vacuo*. The residue

was purified by reverse phase column chromatography (30 - 95 % H₂O + 0.1 % (NH₄)₂CO₃ in MeCN, Xbridge C₁₈, 42 mL/ min, 40 min) to afford (2*S*,4*R*)-1-((*S*)-2-(*tert*-butyl)-23-(4-(3-(4-(8-(4-((1,1-dioxidothiomorpholino)methyl)-3,5-difluorophenyl)quinoxalin-2-yl)-2-methoxyphenoxy)propyl)piperazin-1-yl)-4-oxo-6,9,12,15,18,21-hexaoxa-3-azatricosanoyl)-4-hydroxy-*N*-(4-(4-methylthiazol-5-yl)benzyl)pyrrolidine-2-carboxamide **104** (42 mg, 0.031 mmol, 35.5 % yield) as a yellow solid. M.pt.: 65 - 67 °C; ν_{\max} (neat): 3319, 2873, 2940, 1633, 1517, 1429, 1126, 728 cm⁻¹; ¹H NMR (400 MHz, CDCl₃) δ = 9.38 (1H, s), 8.67 (1H, s), 8.14 (1H, dd, J = 8.3, 1.5 Hz), 7.74 - 7.89 (3H, m), 7.71 (1H, dd, J = 8.4, 2.1 Hz), 7.45 - 7.54 (3H, m), 7.28 (1H, s), 7.02 (1H, d, J = 8.3 Hz), 4.71 (1H, t, J = 7.9 Hz), 4.50 - 4.58 (3H, m), 4.36 (1H, dd, J = 14.9, 5.4 Hz), 4.16 (2H, t, J = 6.6 Hz), 3.99 - 4.07 (3H, m), 3.92 - 3.97 (5H, m), 3.57 - 3.68 (24H, m), 3.08 - 3.17 (8H, m), 2.47 - 2.60 (20H, m), 2.02 - 2.18 (3H, m), 0.97 (9H, s); ¹³C NMR (101 MHz, CDCl₃) δ = 171.2, 171.1, 170.4, 161.3 (2C, dd, J = 246.5, 9.5 Hz), 150.9, 150.5, 150.3, 150.1, 148.4, 142.7, 141.4, 140.7 (t, J = 10.4 Hz), 139.4, 138.3, 137.3 (d, J = 2.2 Hz), 131.6, 130.8, 130.5, 129.9, 129.5 (2C), 129.1, 128.8, 128.1 (2C), 120.2, 114.0 (2C, dd, J = 20.3, 7.3 Hz), 112.7, 110.8 (t, J = 20.5 Hz), 110.3, 71.1, 70.6, 70.5 (6C), 70.4, 70.4, 70.3, 70.0, 68.6, 67.5, 58.7, 57.8, 57.0, 56.8, 55.7, 54.9, 53.5 (2C), 53.0 (2C), 51.5 (2C), 50.1 (2C), 48.0, 43.2, 36.2, 35.3, 26.6, 26.4 (3C), 16.0; ¹⁹F NMR (376 MHz, CDCl₃) δ = -115.16 (s); LCMS (Method B): t_R = 1.23 min, [(M+2H)/2]⁺ 687 (96 % purity); HRMS: (C₆₉H₉₁F₂N₉O₁₄S₂) [(M+2H)/2]⁺ requires 686.8125, found [(M+2H)/2]⁺ 686.8132.

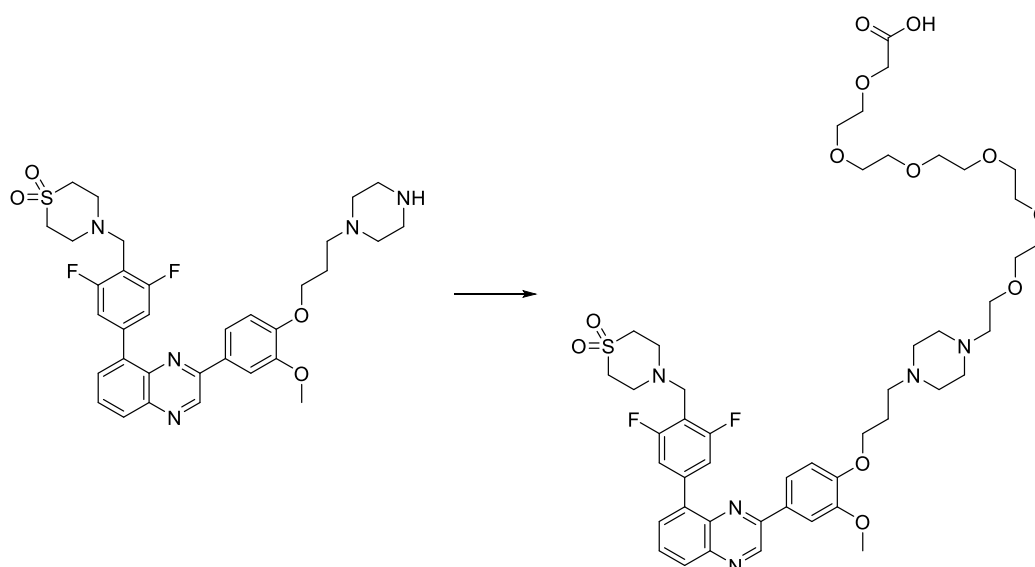
14-(4-(3-(4-(8-(4-((1,1-Dioxidothiomorpholino)methyl)-3,5-difluorophenyl)quinoxalin-2-yl)-2-methoxyphenoxy)propyl)piperazin-1-yl)-3,6,9,12-tetraoxatetradecanoic acid (236)



4-(2,6-Difluoro-4-(3-(3-methoxy-4-(3-(piperazin-1-yl)propoxy)phenyl)quinoxalin-5-yl)benzyl)thiomorpholine 1,1-dioxide **234** (118 mg, 0.185 mmol) was added to a stirred

mixture of methyl 14-chloro-3,6,9,12-tetraoxatetradecanoate (63.2 mg, 0.222 mmol), sodium iodide (33.3 mg, 0.222 mmol) and potassium carbonate (51.1 mg, 0.370 mmol) in DMF (568 μ L). The reaction mixture was heated to 90 $^{\circ}$ C for 16 h under a nitrogen atmosphere. The reaction mixture was cooled to room temperature and diluted with water (10 mL) and extracted with DCM (3 \times 10 mL). The organic layers were combined, passed through a hydrophobic frit and the solvent was concentrated *in vacuo*. 2 M aqueous NaOH (925 μ L, 1.850 mmol) was added and the reaction mixture was stirred at room temperature for 16 h under an atmosphere of nitrogen. The reaction mixture was concentrated *in vacuo* and purified by reverse phase prep column chromatography (30 - 85 % H₂O + 0.1 % HCO₂H in MeCN + 0.1 % HCO₂H, Sunfire C₁₈, 42 mL/ min, 45 min) to afford 14-(4-(3-(4-(8-(4-((1,1-dioxidothiomorpholino)methyl)-3,5-difluorophenyl)quinoxalin-2-yl)-2-methoxyphenoxy)propyl)piperazin-1-yl)-3,6,9,12-tetraoxatetradecanoic acid **236** (109 mg, 0.125 mmol, 68 % yield) as a yellow solid. LCMS (Method A): t_R = 0.76 min, [(M+2H)/2]⁺ 872 (88 % purity). The material was used crude directly in next the reaction.

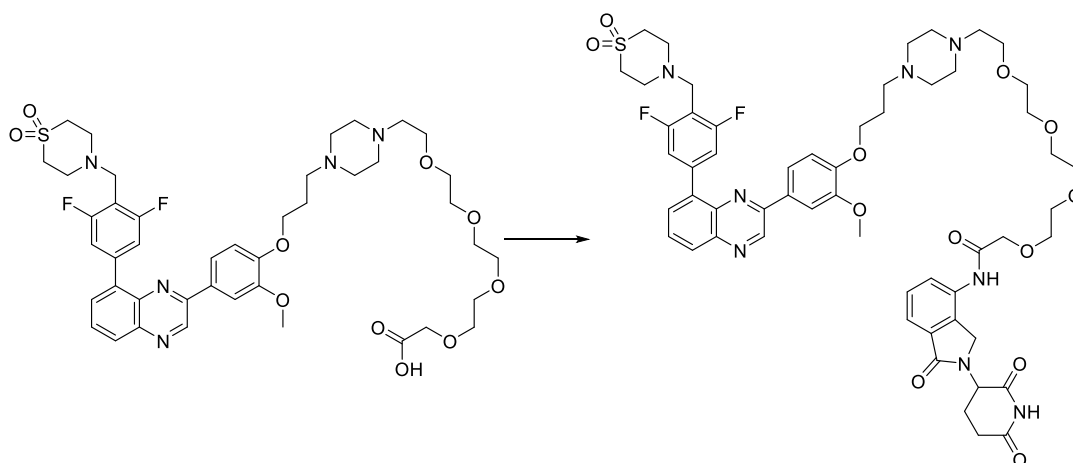
20-(4-(3-(4-(8-(4-((1,1-Dioxidothiomorpholino)methyl)-3,5-difluorophenyl)quinoxalin-2-yl)-2-methoxyphenoxy)propyl)piperazin-1-yl)-3,6,9,12,15,18-hexaoxaicosanoic acid (237)



4-(2,6-Difluoro-4-(3-(3-methoxy-4-(3-(piperazin-1-yl)propoxy)phenyl)quinoxalin-5-yl)benzyl)thiomorpholine 1,1-dioxide **234** (118 mg, 0.185 mmol) was added to a stirred mixture of methyl 20-chloro-3,6,9,12,15,18-hexaoxaicosanoate (83 mg, 0.222 mmol),

sodium iodide (33.3 mg, 0.222 mmol) and potassium carbonate (51.1 mg, 0.370 mmol) in DMF (568 μ L). The reaction mixture was heated to 80 $^{\circ}$ C for 16 h under a nitrogen atmosphere. The reaction mixture was cooled to room temperature and diluted with water (10 mL) and extracted with DCM (3 \times 10 mL). The organic layers were combined, passed through a hydrophobic frit and the solvent was concentrated *in vacuo*. 2 M aqueous NaOH (925 μ L, 1.850 mmol) was added and the reaction mixture was stirred at room temperature for 2 h under an atmosphere of nitrogen. The reaction mixture was concentrated *in vacuo* and purified by reverse phase prep column chromatography (30 - 95 % H₂O + 0.1 % HCO₂H in MeCN + 0.1 % HCO₂H, Sunfire C₁₈, 42 mL/ min, 45 min) to afford 20-(4-(3-(4-(8-(4-((1,1-dioxidothiomorpholino)methyl)-3,5-difluorophenyl)quinoxalin-2-yl)-2-methoxyphenoxy)propyl)piperazin-1-yl)-3,6,9,12,15,18-hexaoxaicosanoic acid **237** (93 mg, 0.097 mmol, 52 % yield) as a yellow solid. LCMS (Method A): t_R = 0.79 min, [M+H]⁺ 961 (72 % purity). The material was used crude directly in next the reaction.

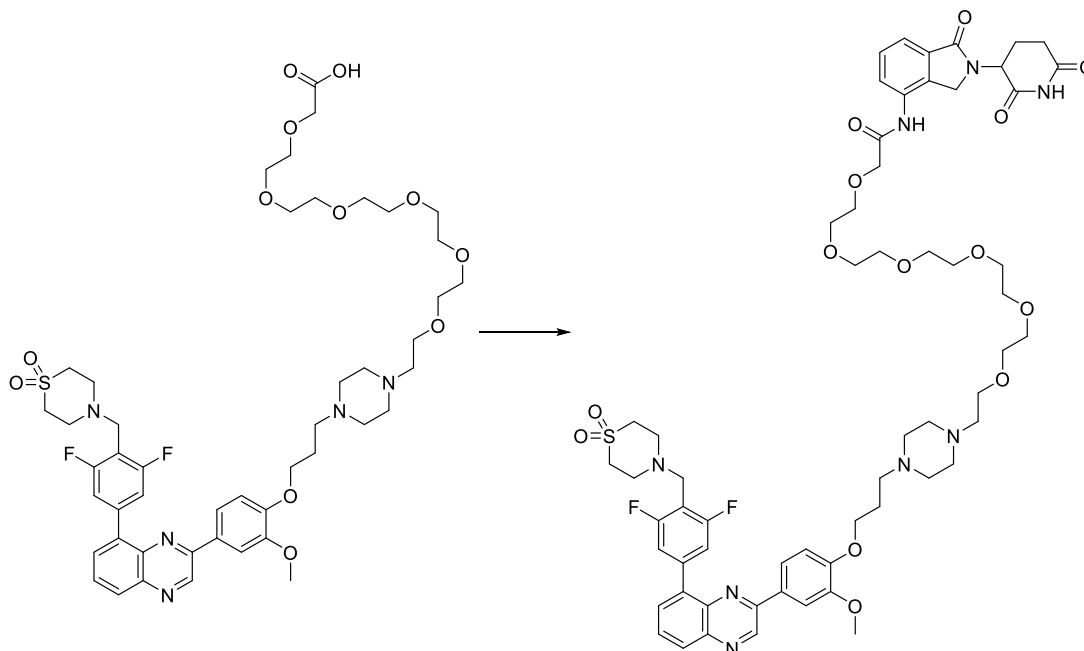
14-(4-(3-(4-(8-(4-((1,1-Dioxidothiomorpholino)methyl)-3,5-difluorophenyl)quinoxalin-2-yl)-2-methoxyphenoxy)propyl)piperazin-1-yl)-N-(2-(2,6-dioxopiperidin-3-yl)-1-oxoisoindolin-4-yl)-3,6,9,12-tetraoxatetradecanamide (100)



14-(4-(3-(4-(8-(4-((1,1-Dioxidothiomorpholino)methyl)-3,5-difluorophenyl)quinoxalin-2-yl)-2-methoxyphenoxy)propyl)piperazin-1-yl)-3,6,9,12-tetraoxatetradecanoic acid **234** (109 mg, 0.110 mmol), 3-(4-amino-1-oxoisoindolin-2-yl)piperidine-2,6-dione (34.2 mg, 0.132 mmol), triethylamine (46.0 μ L, 0.330 mmol) and HATU (62.7 mg, 0.165 mmol) were stirred together

in DMF (2200 μ L) for 16 h at room temperature. The reaction mixture was diluted with water (10 mL) and extracted with DCM (3 \times 10 mL). The solvent was concentrated *in vacuo* and submitted to reverse phase prep column chromatography (15 - 95 % H₂O + 0.1 % (NH₄)₂CO₃ in MeCN, Xbridge C₁₈, 45 min, 42 mL/ min) to afford a yellow gum. The residue was further purified by reverse phase prep column chromatography (15 - 85 % H₂O + 0.1% (NH₄)₂CO₃ in MeCN, Xbridge C₁₈, 60 min, 42 mL/ min) to afford 14-(4-(3-(4-(8-(4-((1,1-dioxidothiomorpholino)methyl)-3,5-difluorophenyl)quinoxalin-2-yl)-2-methoxyphenoxy)propyl)piperazin-1-yl)-N-(2-(2,6-dioxopiperidin-3-yl)-1-oxoisindolin-4-yl)-3,6,9,12-tetraoxatetradecanamide **100** (12 mg, 10.78 μ mol, 9.80 % yield) as a yellow gum. ¹H NMR (600 MHz, DMSO-*d*₆) δ = 9.61 (1H, s), 8.12 (1H, dd, *J* = 8.3, 1.3 Hz), 8.01 (1H, dd, *J* = 7.3, 1.5 Hz), 7.88 - 7.91 (2H, m), 7.86 (1H, dd, *J* = 8.1, 7.3 Hz), 7.77 (1H, dd, *J* = 7.7, 0.7 Hz), 7.62 - 7.67 (2H, m), 7.57 (1H, dd, *J* = 7.7, 0.8 Hz), 7.51 (1H, t, *J* = 7.7 Hz), 7.10 (1H, d, *J* = 8.8 Hz), 5.15 (1H, dd, *J* = 13.2, 5.1 Hz), 4.34 - 4.45 (2H, m), 4.15 (2H, s), 4.07 (2H, t, *J* = 6.4 Hz), 4.03 (4H, s), 3.89 (2H, s), 3.70 (2H, dd, *J* = 5.5, 3.7 Hz), 3.60 - 3.64 (2H, m), 3.54 - 3.58 (2H, m), 3.50 - 3.54 (2H, m), 3.41 - 3.49 (6H, m), 3.36 (1H, br s), 3.11 - 3.19 (4H, m), 2.96 - 3.03 (4H, m), 2.92 (1H, ddd, *J* = 17.5, 13.7, 5.5 Hz), 2.57 - 2.66 (1H, m), 2.55 (1H, s), 2.22 - 2.48 (12H, m), 1.98 - 2.06 (1H, m), 1.85 - 1.92 (2H, m); ¹³C NMR (151 MHz, DMSO-*d*₆) δ = 173.2, 171.3, 168.8, 168.2, 161.2 (2C, dd, *J* = 245.5, 9.4 Hz), 151.0, 150.3, 149.9, 143.6, 141.3, 140.5 (t, *J* = 10.8 Hz), 138.9, 136.9 (d, *J* = 2.2 Hz), 135.1, 133.2, 133.2, 131.2, 129.9, 129.5, 129.1, 128.8, 126.6, 120.9, 120.2, 114.3 (2C, dd, *J* = 22.7, 5.0 Hz), 113.2, 111.5 (t, *J* = 20.7 Hz), 110.4, 70.9, 70.4, 70.3, 70.2, 70.1, 70.1, 68.7, 67.2, 57.7, 55.4, 54.8, 53.6 (2C), 53.3 (2C), 52.0, 50.8 (2C), 50.4 (2C), 47.4, 46.9, 40.8, 31.6, 26.7, 23.0; ¹⁹F NMR (376 MHz, DMSO-*d*₆) δ = -114.86 (s); LCMS (Method B): *t*_R = 1.13 min, [M+H]⁺ 1114 (92 % purity); HRMS: (C₅₆H₆₆F₂N₈O₁₂S) [M+H]⁺ requires 1113.4567, found [M+H]⁺ 1113.4551.

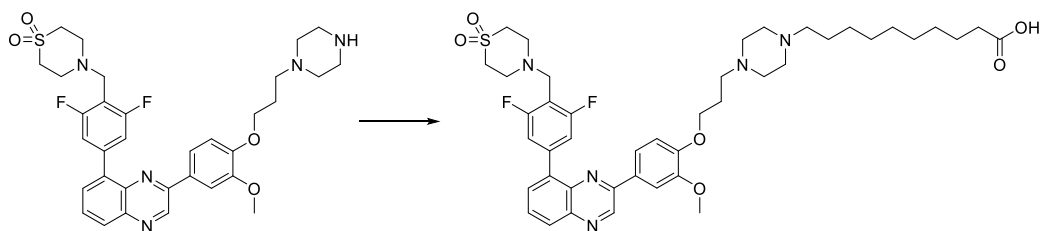
20-(4-(3-(4-(8-(4-((1,1-Dioxidothiomorpholino)methyl)-3,5-difluorophenyl)quinoxalin-2-yl)-2-methoxyphenoxy)propyl)piperazin-1-yl)-N-(2-(2,6-dioxopiperidin-3-yl)-1-oxoisoindolin-4-yl)-3,6,9,12,15,18-hexaoxaicosanamide (103)



20-(4-(3-(4-(8-(4-((1,1-Dioxidothiomorpholino)methyl)-3,5-difluorophenyl)quinoxalin-2-yl)-2-methoxyphenoxy)propyl)piperazin-1-yl)-3,6,9,12,15,18-hexaoxaicosanoic acid **234** (93 mg, 0.070 mmol), 3-(4-amino-1-oxoisoindolin-2-yl)piperidine-2,6-dione (21.70 mg, 0.084 mmol), triethylamine (29.2 μ l, 0.209 mmol) and HATU (39.8 mg, 0.105 mmol) were stirred together in DMF (1395 μ L) for 16 h at room temperature. The reaction mixture was diluted with water (10 mL) and extracted with DCM (3 \times 10 mL). The solvent was removed *in vacuo* and diluted with DMSO (1.4 mL) and submitted to reverse phase prep column chromatography (15 - 95 % H₂O + 0.1% (NH₄)₂CO₃ in MeCN, Xbridge C₁₈, 45 min, 42 mL/ min) to afford a yellow gum. The residue was further purified by reverse phase prep column chromatography (15 - 85 % H₂O + 0.1 % (NH₄)₂CO₃ in MeCN, Xbridge C₁₈, 60 min, 42 mL/ min) to afford 20-(4-(3-(4-(8-(4-((1,1-dioxidothiomorpholino)methyl)-3,5-difluorophenyl)quinoxalin-2-yl)-2-methoxyphenoxy)propyl)piperazin-1-yl)-N-(2-(2,6-dioxopiperidin-3-yl)-1-oxoisoindolin-4-yl)-3,6,9,12,15,18-hexaoxaicosanamide **103** (38 mg, 0.032 mmol, 45.4 % yield) as a yellow gum. ¹H NMR (600 MHz, MeOD-*d*₄) δ = 9.36 (1H, s), 8.35 (2H, br s), 8.04 (1H, d, *J* = 8.1 Hz), 7.83 - 7.87 (2H, m), 7.78 (1H, t, *J* = 7.7 Hz), 7.72 - 7.76 (2H, m), 7.65 (1H, d, *J* = 7.7 Hz), 7.51 (1H, t, *J* = 7.7 Hz), 7.44 (2H, d, *J* = 8.8 Hz), 7.02 (1H, d, *J* = 8.4 Hz), 5.13 (1H, dd, *J* = 13.2, 5.1

Hz), 4.45 - 4.52 (2H, m), 4.16 (2H, s), 4.13 (2H, t, $J = 5.7$ Hz), 3.93 (2H, s), 3.87 (3H, s), 3.74 - 3.77 (2H, m), 3.67 - 3.73 (4H, m), 3.62 - 3.65 (2H, m), 3.59 (3H, s), 3.57 (4H, dd, $J = 8.8, 5.1$ Hz), 3.52 - 3.55 (2H, m), 3.49 (3H, s), 3.12 (5H, s), 3.04 - 3.09 (7H, m), 3.00 (5H, br t, $J = 5.1$ Hz), 2.92 - 2.96 (3H, m), 2.82 - 2.91 (1H, m), 2.73 - 2.78 (1H, m), 2.39 - 2.49 (1H, m), 2.07 - 2.18 (3H, m), 2.03 (2H, s); ^{13}C NMR (151 MHz, MeOD- d_4) $\delta = 173.8, 171.3, 170.4, 170.1, 161.8$ (2C, dd, $J = 246.0, 9.4$ Hz), 151.1, 150.9, 150.4, 142.9, 141.4, 141.3 (t, $J = 10.5$ Hz), 139.7, 137.8, 136.1, 133.2, 133.0, 131.1, 129.8, 129.5, 129.4, 127.5, 121.1, 120.8, 114.2 (2C, dd, $J = 22.7, 5.5$ Hz), 113.2, 111.6 (t, $J = 20.5$ Hz), 110.5, 71.4, 70.8 (2C), 70.7, 70.7 (2C), 70.7, 70.6, 70.6, 70.5, 70.5, 70.5, 67.2, 66.7, 56.7, 55.5, 55.0, 52.9 (2C), 51.9 (2C), 51.4 (2C), 51.4, 50.7 (2C), 47.6, 31.6, 25.7, 23.4; ^{19}F NMR (376 MHz, MeOD- d_4) $\delta = -116.40$ (s); LCMS (Method A): $t_R = 0.78$ min, $[\text{M}+\text{H}]^+$ 1202 (99 % purity); HRMS: ($\text{C}_{60}\text{H}_{74}\text{F}_2\text{N}_8\text{O}_{14}\text{S}$) $[\text{M}+\text{H}]^+$ requires 1201.5091, found $[\text{M}+\text{H}]^+$ 1201.5089.

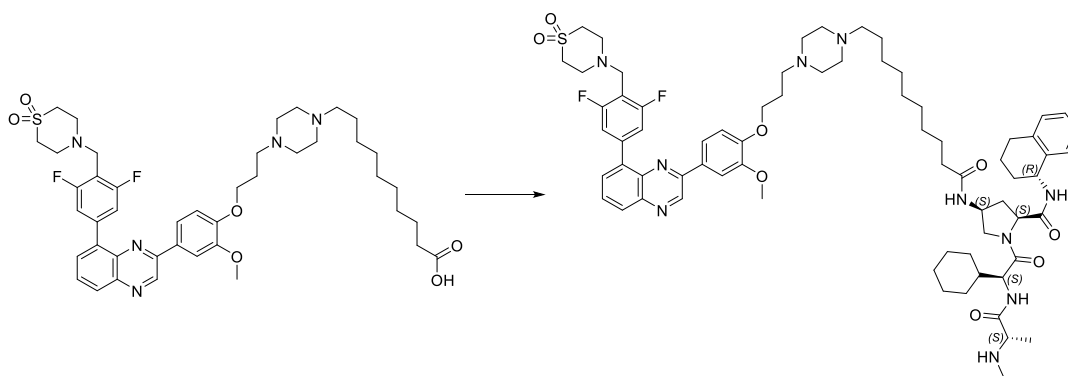
10-(4-(3-(4-(8-(4-((1,1-Dioxidothiomorpholino)methyl)-3,5-difluorophenyl)quinoxalin-2-yl)-2-methoxyphenoxy)propyl)piperazin-1-yl)decanoic acid (238)



4-(2,6-Difluoro-4-(3-(3-methoxy-4-(3-(piperazin-1-yl)propoxy)phenyl)quinoxalin-5-yl)benzyl)thiomorpholine 1,1-dioxide **234** (400 mg, 0.627 mmol) was added to a stirred mixture of methyl 10-bromodecanoate (200 mg, 0.753 mmol) and potassium carbonate (173 mg, 1.254 mmol) in DMF (1924 μL). The reaction mixture was heated to 100 $^\circ\text{C}$ for 16 h under a nitrogen atmosphere. The reaction mixture was cooled to room temperature and diluted with water (10 mL) and extracted with DCM (3 \times 10 mL). The organic layers were combined, passed through a hydrophobic frit and the solvent was concentrated *in vacuo*. LiOH (150 mg, 6.27 mmol) was added and the reaction mixture was heated at 50 $^\circ\text{C}$ for 3 h under a nitrogen atmosphere. The reaction mixture was filtered and purified by reverse phase prep column chromatography (30 - 95 % H_2O + 0.1 % HCO_2H in MeCN + 0.1 % HCO_2H , Sunfire C_{18} , 42 mL/min, 45 min) to afford 10-(4-(3-(4-(8-(4-((1,1-dioxidothiomorpholino)methyl)-3,5-

difluorophenyl)quinoxalin-2-yl)-2-methoxyphenoxy)propyl)piperazin-1-yl)decanoic acid **238** (354 mg, 0.438 mmol, 70 % yield) as a yellow solid. LCMS (Method B): t_R = 1.01 min, $[M+H]^+$ 809 (89 % purity). The material was used crude directly in next the reaction.

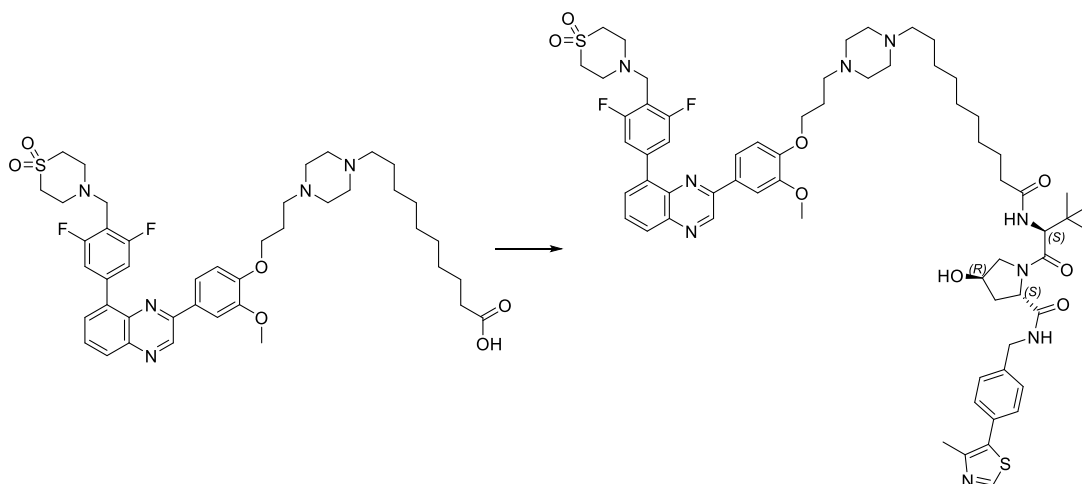
(2S,4S)-1-((S)-2-cyclohexyl-2-((S)-2-(methylamino)propanamido)acetyl)-4-(10-(4-(3-(4-(8-(4-((1,1-dioxidothiomorpholino)methyl)-3,5-difluorophenyl)quinoxalin-2-yl)-2-methoxyphenoxy)propyl)piperazin-1-yl)decanamido)-N-((R)-1,2,3,4-tetrahydronaphthalen-1-yl)pyrrolidine-2-carboxamide (105)



10-(4-(3-(4-(8-(4-((1,1-Dioxidothiomorpholino)methyl)-3,5-difluorophenyl)quinoxalin-2-yl)-2-methoxyphenoxy)propyl)piperazin-1-yl)decanoic acid **234** (100 mg, 0.124 mmol), *tert*-butyl ((S)-1-(((S)-2-((2S,4S)-4-amino-2-(((R)-1,2,3,4-tetrahydronaphthalen-1-yl)carbamoyl)pyrrolidin-1-yl)-1-cyclohexyl-2-oxoethyl)amino)-1-oxopropan-2-yl)(methyl)carbamate (87 mg, 0.149 mmol), triethylamine (51.8 μ L, 0.371 mmol) and HATU (70.6 mg, 0.186 mmol) were stirred together in DMF (2475 μ L) for 15 h at room temperature. The reaction mixture was diluted with water (10 mL) and extracted with DCM (3 \times 10 mL). The solvent was concentrated *in vacuo* and TFA (95 μ L, 1.238 mmol) was added and the reaction mixture was stirred at room temperature for 16 h. The reaction mixture was diluted with water (10 mL) and extracted with DCM (3 \times 10 mL). The solvent was concentrated *in vacuo* and purified by reverse phase prep column chromatography (70 - 95 % H₂O + 0.1 % (NH₄)₂CO₃ in MeCN, Xbridge C₁₈, 42 mL/ min, 45 min) to afford (2S,4S)-1-((S)-2-cyclohexyl-2-((S)-2-(methylamino)propanamido)acetyl)-4-(10-(4-(3-(4-(8-(4-((1,1-dioxidothiomorpholino)methyl)-3,5-difluorophenyl)quinoxalin-2-yl)-2-methoxyphenoxy)-propyl)piperazin-1-yl)decanamido)-N-((R)-1,2,3,4-tetrahydronaphthalen-1-yl)pyrrolidine-2-carboxamide **105**

(85 mg, 0.067 mmol, 53.9 % yield) as a yellow solid. M.pt.: 100 - 102 °C; ν_{\max} (neat): 3315, 2928, 2853, 1632, 1469, 1126 cm^{-1} ; ^1H NMR (400 MHz, CDCl_3) δ = 9.38 (1H, s), 8.14 (1H, dd, J = 8.2, 1.6 Hz), 7.88 - 8.00 (1H, m), 7.85 (1H, d, J = 1.5 Hz), 7.85 (1H, dd, J = 18.2, 1.8 Hz), 7.79 - 7.81 (1H, m), 7.75 - 7.79 (1H, m), 7.70 (1H, dd, J = 8.4, 2.1 Hz), 7.49 (2H, d, J = 9.0 Hz), 7.11 - 7.16 (2H, m), 7.05 - 7.09 (2H, m), 7.02 (1H, d, J = 8.3 Hz), 5.08 - 5.16 (1H, m), 4.74 (1H, d, J = 8.8 Hz), 4.56 - 4.62 (1H, m), 4.36 (1H, t, J = 8.2 Hz), 4.17 (2H, t, J = 6.7 Hz), 4.07 (1H, dd, J = 11.2, 5.1 Hz), 3.95 (3H, s), 3.93 (2H, s), 3.68 (1H, d, J = 10.8 Hz), 3.07 - 3.16 (8H, m), 3.00 - 3.04 (1H, m), 2.70 - 2.85 (2H, m), 2.47 - 2.63 (9H, m), 2.30 - 2.43 (7H, m), 1.99 - 2.24 (8H, m), 1.78 - 1.90 (4H, m), 1.67 - 1.73 (2H, m), 1.36 - 1.63 (7H, m), 1.25 - 1.35 (12H, m), 1.23 (1H, d, J = 6.8 Hz), 1.09 (3H, br s), 0.88 - 1.05 (2H, m); ^{13}C NMR (101 MHz, CDCl_3) δ = 175.0, 173.3, 173.1, 171.2, 161.3 (2C, dd, J = 246.5, 9.5 Hz), 150.9, 150.5, 150.2, 142.7, 141.4, 140.7 (t, J = 11.0 Hz), 139.4, 137.3, 137.3, 136.1, 130.5, 129.9, 129.2, 129.1, 128.8, 128.2, 127.3, 126.0, 120.1, 114.0 (2C, dd, J = 19.8, 5.9 Hz), 112.7, 110.8 (t, J = 20.2 Hz), 110.4, 67.5, 60.2, 60.1, 60.1, 60.0, 58.8, 55.9, 55.7, 55.0, 54.7, 53.2 (2C), 53.1 (2C), 51.5 (2C), 50.1 (2C), 49.4, 48.0, 40.6, 36.9, 35.1, 31.1, 30.0, 29.6, 29.4, 29.3, 29.2, 29.1, 28.6, 27.6, 26.8, 26.6, 26.1, 26.0, 25.9, 25.7, 20.1, 19.4; ^{19}F NMR (376 MHz, CDCl_3) δ = -115.18 (s); LCMS (Method B): t_{R} = 1.62 min, $[(\text{M}+2\text{H})/2]^+$ 637 (100 % purity); HRMS: ($\text{C}_{70}\text{H}_{94}\text{F}_2\text{N}_{10}\text{O}_8\text{S}$) $[\text{M}+\text{H}]^+$ requires 1273.7023, found $[\text{M}+\text{H}]^+$ 1273.7014.

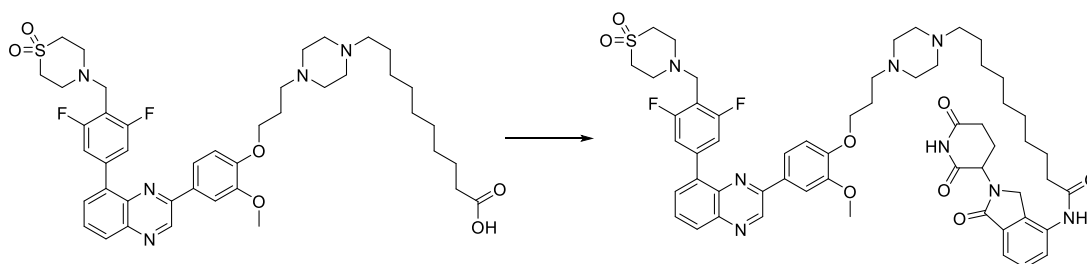
(2S,4R)-1-((S)-2-(10-(4-(3-(4-(8-(4-((1,1-Dioxidothiomorpholino)methyl)-3,5-difluorophenyl)quinoxalin-2-yl)-2-methoxyphenoxy)propyl)piperazin-1-yl)decanamido)-3,3-dimethylbutanoyl)-4-hydroxy-N-(4-(4-methylthiazol-5-yl)benzyl)pyrrolidine-2-carboxamide (238)



10-(4-(3-(4-(8-(4-((1,1-Dioxidothiomorpholino)methyl)-3,5-difluorophenyl)quinoxalin-2-yl)-2-methoxyphenoxy)propyl)piperazin-1-yl)decanoic acid **234** (100 mg, 0.124 mmol), (2S,4R)-1-((S)-2-amino-3,3-dimethylbutanoyl)-4-hydroxy-N-(4-(4-methylthiazol-5-yl)benzyl)-pyrrolidine-2-carboxamide (64 mg, 0.149 mmol), triethylamine (52 μ L, 0.373 mmol) and HATU (71 mg, 0.187 mmol) were stirred together in DMF (2500 μ L) for 16 h at room temperature. The reaction mixture was diluted with water (10 mL) and extracted with DCM (3 \times 10 mL). The organic layers were combined, passed through a hydrophobic frit and the solvent concentrated *in vacuo*. The residue was purified by reverse phase prep column chromatography (40 - 95 % H₂O + 0.1 % (NH₄)₂CO₃ in MeCN, Xbridge C₁₈, 42 mL/ min, 40 min) to afford (2S,4R)-1-((S)-2-(10-(4-(3-(4-(8-(4-((1,1-dioxidothiomorpholino)methyl)-3,5-difluorophenyl)quinoxalin-2-yl)-2-methoxyphenoxy)propyl)piperazin-1-yl)decanamido)-3,3-dimethylbutanoyl)-4-hydroxy-N-(4-(4-methylthiazol-5-yl)benzyl)pyrrolidine-2-carboxamide **107** (53 mg, 0.043 mmol, 35 % yield) as a yellow solid. M.pt.: 80 - 82 $^{\circ}$ C; ν_{\max} (neat): 3313, 2929, 2858, 1631, 1469, 1148 cm^{-1} ; ^1H NMR (400 MHz, CDCl₃) δ = 9.37 (1H, s), 8.67 (1H, s), 8.14 (1H, dd, J = 8.2, 1.3 Hz), 7.87 (1H, d, J = 2.0 Hz), 7.84 (1H, dd, J = 7.4, 1.5 Hz), 7.75 - 7.80 (1H, m), 7.70 (1H, dd, J = 8.6, 2.0 Hz), 7.46 - 7.52 (2H, m), 7.43 (1H, br t, J = 5.9 Hz), 7.31 - 7.36 (1H, m), 7.02 (1H, d, J = 8.6 Hz), 6.28 (1H, d, J = 9.0 Hz), 4.70 (1H, t, J = 7.9 Hz), 4.58 (1H, s), 4.56 (1H, t, J = 3.2 Hz), 4.53 (1H, br d, J = 6.1 Hz), 4.35 (1H, dd, J = 15.2, 5.4 Hz), 4.16 (2H, t, J

= 6.6 Hz), 4.03 - 4.04 (1H, m), 4.05 (1H, br d, $J = 11.5$ Hz), 3.95 (3H, s), 3.93 (2H, s), 3.64 (1H, dd, $J = 11.1, 3.5$ Hz), 3.06 - 3.16 (9H, m), 2.61 (2H, s), 2.41 - 2.60 (14H, m), 2.27 - 2.35 (3H, m), 2.15 - 2.21 (2H, m), 2.02 - 2.12 (2H, m), 1.43 - 1.63 (5H, m), 1.26 (10H, s), 0.95 (8H, s); ^{13}C NMR (101 MHz, CDCl_3) $\delta = 173.7, 171.7, 171.0, 161.3$ (2C, dd, $J = 246.9, 9.2$ Hz), 150.9, 150.5, 150.3, 150.1, 148.4, 142.7, 141.4, 140.7 (t, $J = 11.0$ Hz), 139.3, 138.2, 137.3 (t, $J = 2.2$ Hz), 131.6, 130.9, 130.5 (2C), 129.8 (2C), 129.4, 129.0, 128.8, 128.0, 120.1, 114.0 (2C, dd, $J = 20.5, 8.1$ Hz), 112.7, 110.7 (t, $J = 20.2$ Hz), 110.3, 69.9, 67.5, 58.8, 57.3, 56.8, 55.6, 54.9, 53.2 (2C), 53.1 (2C), 51.4 (2C), 50.1 (2C), 48.0, 43.2, 40.9, 36.5, 36.2, 35.2, 29.3, 29.2, 29.1, 29.1, 27.5, 26.7, 26.6, 26.4 (3C), 25.6, 16.0; ^{19}F NMR (376 MHz, CDCl_3) $\delta = -115.18$ (s); LCMS (Method B): $t_R = 1.44$ min, $[\text{M}+\text{H}]^+$ 1221 (100 % purity); HRMS: ($\text{C}_{65}\text{H}_{83}\text{F}_2\text{N}_9\text{O}_8\text{S}_2$) $[\text{M}+\text{H}]^+$ requires 1220.5852, found $[\text{M}+\text{H}]^+$ 1220.5847.

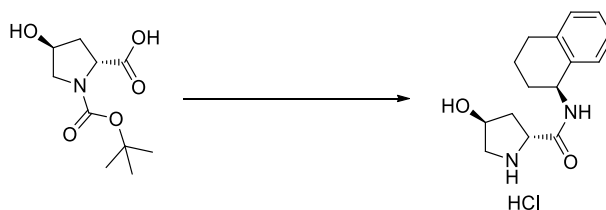
10-(4-(3-(4-(8-(4-((1,1-Dioxidothiomorpholino)methyl)-3,5-difluorophenyl)quinoxalin-2-yl)-2-methoxyphenoxy)propyl)piperazin-1-yl)-N-(2-(2,6-dioxopiperidin-3-yl)-1-oxoisoindolin-4-yl)decanamide (238)



10-(4-(3-(4-(8-(4-((1,1-dioxidothiomorpholino)methyl)-3,5-difluorophenyl)quinoxalin-2-yl)-2-methoxyphenoxy)propyl)piperazin-1-yl)decanoic acid **238** (100 mg, 0.124 mmol), 3-(4-amino-1-oxoisoindolin-2-yl)piperidine-2,6-dione (38.5 mg, 0.149 mmol), triethylamine (51.8 μL , 0.371 mmol) and HATU (70.6 mg, 0.186 mmol) were stirred together in DMF (2475 μL) for 16 h at room temperature. The reaction mixture was diluted with water (10 mL) and extracted with DCM (3×10 mL). The solvent was concentrated *in vacuo* and purified by reverse phase prep column chromatography (40 - 95 % H_2O + 0.1% $(\text{NH}_4)_2\text{CO}_3$ in MeCN, XSelect C_{18} , 42 mL/min, 45 min) to afford 10-(4-(3-(4-(8-(4-((1,1-dioxidothiomorpholino)methyl)-3,5-difluorophenyl)quinoxalin-2-yl)-2-methoxyphenoxy)-propyl)piperazin-1-yl)-N-(2-(2,6-dioxopiperidin-3-yl)-1-oxoisoindolin-4-yl)decanamide **106**

(46 mg, 0.044 mmol, 35 % yield) as a yellow solid. M.pt.: 133 - 135 °C; ν_{\max} (neat): 3320, 2928, 2853, 1670, 1517, 1126, 726 cm^{-1} ; ^1H NMR (400 MHz, CDCl_3) δ = 9.37 (1H, s), 8.38 (1H, br s), 8.14 (1H, dd, J = 8.1, 1.5 Hz), 7.84 (1H, d, J = 1.5 Hz), 7.84 (1H, dd, J = 17.5, 1.6 Hz), 7.74 - 7.79 (1H, m), 7.70 (1H, dd, J = 8.6, 2.0 Hz), 7.65 (2H, br d, J = 7.6 Hz), 7.46 - 7.52 (2H, m), 7.42 (1H, t, J = 7.8 Hz), 7.01 (1H, d, J = 8.3 Hz), 5.10 (1H, br dd, J = 13.1, 5.0 Hz), 4.26 - 4.44 (2H, m), 4.15 (2H, br t, J = 6.5 Hz), 3.94 (3H, s), 3.92 (2H, s), 3.04 - 3.17 (9H, m), 2.50 - 2.75 (10H, m), 2.41 (3H, br t, J = 7.1 Hz), 2.33 (2H, br t, J = 7.7 Hz), 2.02 - 2.10 (3H, m), 2.00 (2H, s), 1.61 - 1.78 (2H, m), 1.41 - 1.52 (2H, m), 1.23 - 1.38 (10H, m); ^{13}C NMR (101 MHz, CDCl_3) δ = 172.1 (2C), 170.5, 169.1, 161.3 (2C, dd, J = 246.9, 9.2 Hz), 150.9, 150.5, 150.1, 142.7, 141.4, 140.7 (t, J = 10.6 Hz), 139.3, 137.2, 134.5, 133.1 (d, J = 2.9 Hz), 132.7, 130.5, 129.8, 129.1, 129.0, 128.8, 126.3, 120.8, 120.2, 114.0 (2C, dd, J = 19.8, 6.6 Hz), 112.7, 110.7 (t, J = 20.2 Hz), 110.3, 67.4, 58.4, 55.6, 54.8, 52.9 (2C), 52.8 (2C), 51.8, 51.5 (2C), 50.1 (2C), 48.0, 46.6, 36.8, 31.6, 29.3, 29.3, 29.2, 29.2, 27.4, 26.5, 26.2, 25.6, 23.4; ^{19}F NMR (376 MHz, CDCl_3) δ = -115.15 (s); LCMS (Method B): t_{R} = 1.35 min, $[\text{M}+\text{H}]^+$ 1050 (93 % purity); HRMS: ($\text{C}_{56}\text{H}_{66}\text{F}_2\text{N}_8\text{O}_8\text{S}$) $[\text{M}+\text{H}]^+$ requires 1049.4770, found $[\text{M}+\text{H}]^+$ 1049.4781.

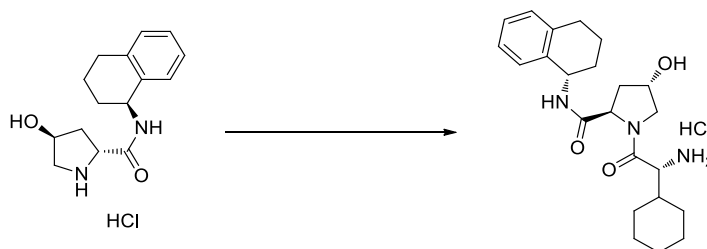
(2R,4S)-4-Hydroxy-N-((S)-1,2,3,4-tetrahydronaphthalen-1-yl)pyrrolidine-2-carboxamide HCl (241)



To a stirred solution of (2R,4S)-1-(*tert*-butoxycarbonyl)-4-hydroxypyrrolidine-2-carboxylic acid **239** (3 g, 12.97 mmol), (S)-1,2,3,4-tetrahydronaphthalen-1-amine (2.080 mL, 14.27 mmol) and DIPEA (6.80 mL, 38.9 mmol) in DMF (36 mL) was added HATU (5.43 g, 14.27 mmol), and the reaction mixture stirred at room temperature for 1 h. The reaction mixture was diluted with water (100 mL) and extracted with EtOAc (100 mL). The organic layer was sequentially washed with 5 % aqueous citric acid (100 mL), saturated aqueous NaHCO_3 (100 mL) and passed through a hydrophobic frit. The solvent was removed *in vacuo*. DCM (5 mL) was added followed by 4 M HCl in dioxane (12.97 mL, 51.9 mmol) and the reaction mixture

was stirred for 2 h at room temperature to afford a white precipitate. The reaction mixture was concentrated *in vacuo* and filtered under vacuum. The solid was washed with DCM (20 mL) and collected. The solid was dried in a vacuum oven at 40 °C for 16 h to afford (2*R*,4*S*)-4-hydroxy-*N*-((*S*)-1,2,3,4-tetrahydronaphthalen-1-yl)pyrrolidine-2-carboxamide, HCl **241** (2.704 g, 9.11 mmol, 70 % yield) as a white solid. M.pt.: 284 – 286 °C; ν_{\max} (neat): 3341, 3230, 2983, 2857, 2701, 1662, 1550, 1076, 744 cm^{-1} ; ^1H NMR (400 MHz, $\text{DMSO-}d_6$) δ = 10.30 (1H, br s), 9.01 (1H, d, J = 8.3 Hz), 8.70 (1H, br s), 7.01 - 7.28 (4H, m), 5.58 (1H, br s), 4.94 - 5.05 (1H, m), 4.43 (1H, br s), 4.34 (1H, dd, J = 10.3, 7.3 Hz), 3.35 - 3.43 (1H, m), 3.11 (1H, d, J = 12.0 Hz), 2.66 - 2.82 (2H, m), 2.26 - 2.34 (1H, m), 1.81 - 1.95 (3H, m), 1.65 - 1.80 (2H, m); ^{13}C NMR (101 MHz, $\text{DMSO-}d_6$) δ = 167.7, 137.6, 136.8, 129.3, 128.9, 127.5, 126.3, 69.5, 58.4, 53.7, 47.5, 39.3, 29.9, 29.1, 20.0; LCMS (Method A): t_R = 0.42 min, $[\text{M}+\text{H}]^+$ 261 (100 % purity); HRMS: ($\text{C}_{15}\text{H}_{20}\text{N}_2\text{O}_2$) $[\text{M}+\text{H}]^+$ requires 261.1603, found $[\text{M}+\text{H}]^+$ 261.1613.

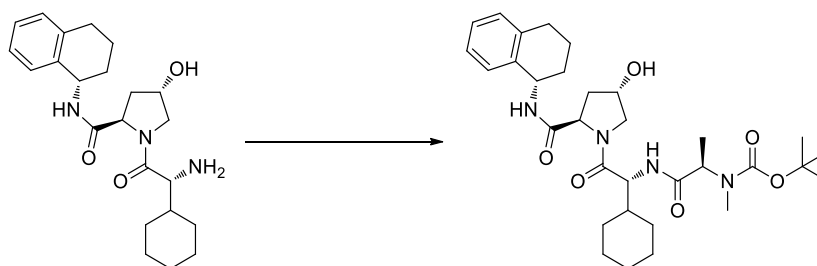
(2*R*,4*S*)-1-((*R*)-2-Amino-2-cyclohexylacetyl)-4-hydroxy-*N*-((*S*)-1,2,3,4-tetrahydronaphthalen-1-yl)pyrrolidine-2-carboxamide, HCl (243)



To a stirred solution of (2*R*,4*S*)-4-hydroxy-*N*-((*S*)-1,2,3,4-tetrahydronaphthalen-1-yl)pyrrolidine-2-carboxamide HCl **241** (2 g, 6.74 mmol), (*R*)-2-((*tert*-butoxycarbonyl)amino)-2-cyclohexylacetic acid (1.907 g, 7.41 mmol) and DIPEA (4.71 mL, 27.0 mmol) in DMF (32.2 mL) was added HATU (3.07 g, 8.09 mmol). The mixture stirred at room temperature for 16 h. The reaction mixture was diluted water (100 mL) and extracted with DCM (100 mL). The organic layer was sequentially washed with 5 % aqueous citric acid (100 mL), saturated aqueous NaHCO_3 (100 mL), passed through a hydrophobic frit and the solvent was removed *in vacuo*. The residue was dissolved in DCM (40 mL) and added 4 M HCl in dioxane (20.22 mL, 81 mmol). The reaction mixture was stirred at room temperature for 3 h. The solvent was removed *in vacuo* and the residue was diluted with water (70 mL) and extracted with DCM

(70 mL) and the organic layer was discarded. The aqueous layer was adjusted to pH 2 using 2 M aqueous HCl and the acidic aqueous media was extracted with DCM (70 mL) and the organic layer was discarded. The aqueous was neutralised with saturated aqueous sodium bicarbonate solution and the aqueous media was extracted with *n*-BuOH (3 × 70 mL). The organic layers were combined, passed through a hydrophobic frit and the solvent removed *in vacuo* to afford (2*R*,4*S*)-1-((*R*)-2-amino-2-cyclohexylacetyl)-4-hydroxy-*N*-((*S*)-1,2,3,4-tetrahydronaphthalen-1-yl)pyrrolidine-2-carboxamide, HCl **243** (1.333 g, 3.06 mmol, 45 % yield) as a white solid. LCMS (Method A): $t_R = 0.61$ min, $[M+H]^+$ 400 (75 % purity).

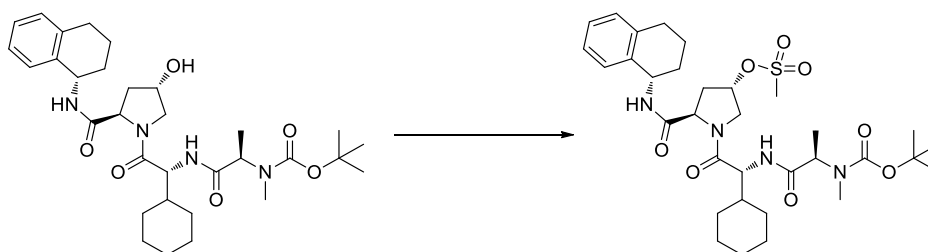
Tert-butyl ((*R*)-1-(((*R*)-1-cyclohexyl-2-((2*R*,4*S*)-4-hydroxy-2-(((*S*)-1,2,3,4-tetrahydronaphthalen-1-yl)carbamoyl)pyrrolidin-1-yl)-2-oxoethyl)amino)-1-oxopropan-2-yl)(methyl)carbamate (245)



To a stirred solution of (2*R*,4*S*)-1-((*R*)-2-amino-2-cyclohexylacetyl)-4-hydroxy-*N*-((*S*)-1,2,3,4-tetrahydronaphthalen-1-yl)pyrrolidine-2-carboxamide **243** (1.3 g, 3.25 mmol), *N*-(*tert*-butoxycarbonyl)-*N*-methyl-*D*-alanine (0.794 g, 3.90 mmol) and DIPEA (2.273 mL, 13.02 mmol) in DMF (24 mL) was added HATU (1.485 g, 3.90 mmol). The mixture stirred at room temperature for 1 h. The solvent was removed *in vacuo* and the residue was diluted with water (60 mL) and extracted with ethyl acetate (60 mL). The organic layer was sequentially washed with 5 % aqueous citric acid (100 mL) and saturated aqueous NaHCO₃ (100 mL), passed through a hydrophobic frit and the solvent was removed *in vacuo* to afford *tert*-butyl ((*R*)-1-(((*R*)-1-cyclohexyl-2-((2*R*,4*S*)-4-hydroxy-2-(((*S*)-1,2,3,4-tetrahydronaphthalen-1-yl)carbamoyl)pyrrolidin-1-yl)-2-oxoethyl)amino)-1-oxopropan-2-yl)(methyl)carbamate **245** (1.001 g, 1.712 mmol, 53 % yield) as a white solid. M.pt.: 76 – 78 °C; ν_{\max} (neat): 3314, 2928, 2854, 1661, 1628, 1520, 1553 cm⁻¹; ¹H NMR (400 MHz, DMSO-*d*₆) δ = 8.22 (1H, d, J = 8.6 Hz), 7.31 (1H, d, J = 7.3 Hz), 7.03 - 7.19 (3H, m), 5.06 (1H, d, J = 3.7 Hz), 4.88 - 4.98 (1H, m), 4.49 -

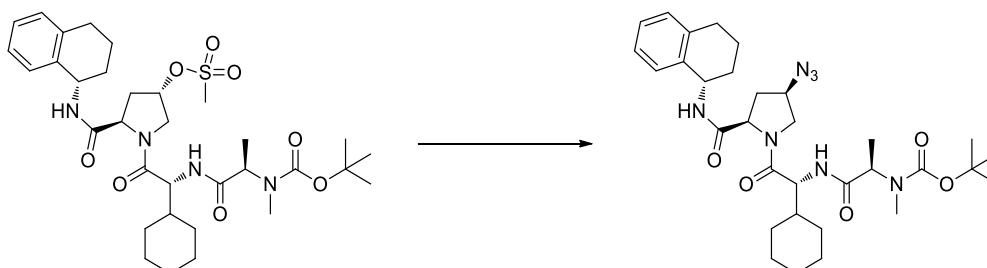
4.64 (1H, m), 4.31 - 4.46 (3H, m), 3.64 - 3.73 (1H, m), 3.57 (1H, br d, $J = 10.5$ Hz), 2.68 - 2.79 (6H, m), 2.07 (1H, s), 1.97 - 2.05 (1H, m), 1.79 - 1.94 (4H, m), 1.54 - 1.76 (9H, m), 1.29 - 1.51 (14H, m); ^{13}C NMR (101 MHz, $\text{DMSO-}d_6$) $\delta = 171.4$ (2C), 170.1, 155.5, 138.2, 137.3, 128.9, 128.7, 127.0, 126.1, 79.5, 69.3, 59.3, 56.0, 55.0 (2C), 47.0, 40.4, 38.3 (2C), 30.4 (2C), 29.4, 29.3, 28.5 (3C), 26.4, 26.2, 26.1, 20.9, 14.0; LCMS (Method B): $t_R = 1.25$ min, $[\text{M}+\text{H}]^+$ 585 (95 % purity); HRMS: ($\text{C}_{32}\text{H}_{48}\text{N}_4\text{O}_6$) $[\text{M}+\text{H}]^+$ requires 585.3652, found $[\text{M}+\text{H}]^+$ 585.3659.

(3S,5R)-1-((R)-2-((R)-2-((Tert-butoxycarbonyl)(methyl)amino)propanamido)-2-cyclohexylacetyl)-5-(((S)-1,2,3,4-tetrahydronaphthalen-1-yl)carbamoyl)pyrrolidin-3-yl methanesulfonate (246)



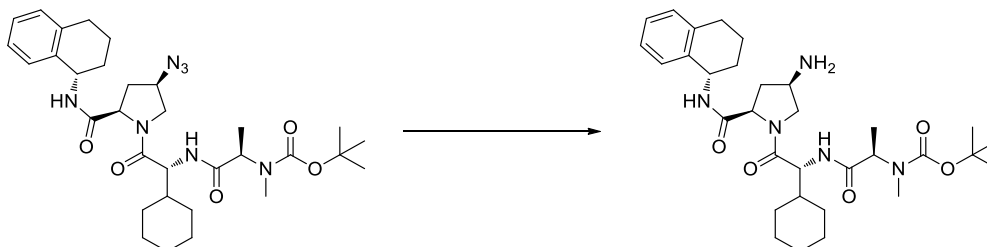
To a solution of *tert*-butyl ((*R*)-1-(((*R*)-1-cyclohexyl-2-((2*R*,4*S*)-4-hydroxy-2-(((*S*)-1,2,3,4-tetrahydronaphthalen-1-yl)carbamoyl)pyrrolidin-1-yl)-2-oxoethyl)amino)-1-oxopropan-2-yl)(methyl)carbamate **245** (915 mg, 1.565 mmol) and triethylamine (0.436 mL, 3.13 mmol) in DCM (37 mL) was added methanesulfonyl chloride (0.244 mL, 3.13 mmol) over an ice-water bath under a nitrogen atmosphere and the reaction mixture was allowed to reach room temperature over 2 h. The reaction mixture was diluted with saturated aqueous sodium hydrogen carbonate (40 mL) and extracted with DCM (2 × 40 mL). The combined organic layers were passed through a hydrophobic frit and the solvent was removed *in vacuo* to afford (3*S*,5*R*)-1-((*R*)-2-((*R*)-2-((*tert*-butoxycarbonyl)(methyl)amino)propanamido)-2-cyclohexylacetyl)-5-(((*S*)-1,2,3,4-tetrahydronaphthalen-1-yl)carbamoyl)pyrrolidin-3-yl methanesulfonate **246** (1.035 g, 1.561 mmol, 100 % yield) as a white solid. Partially characterised, used crude in next reaction. LCMS (Method A): $t_R = 1.30$ min, $[\text{M}+\text{H}]^+$ 664 (62 % purity).

***Tert*-butyl ((*R*)-1-(((*R*)-2-((2*R*,4*R*)-4-azido-2-(((*S*)-1,2,3,4-tetrahydronaphthalen-1-yl)carbamoyl)pyrrolidin-1-yl)-1-cyclohexyl-2-oxoethyl)amino)-1-oxopropan-2-yl)(methyl)carbamate (**247**)**



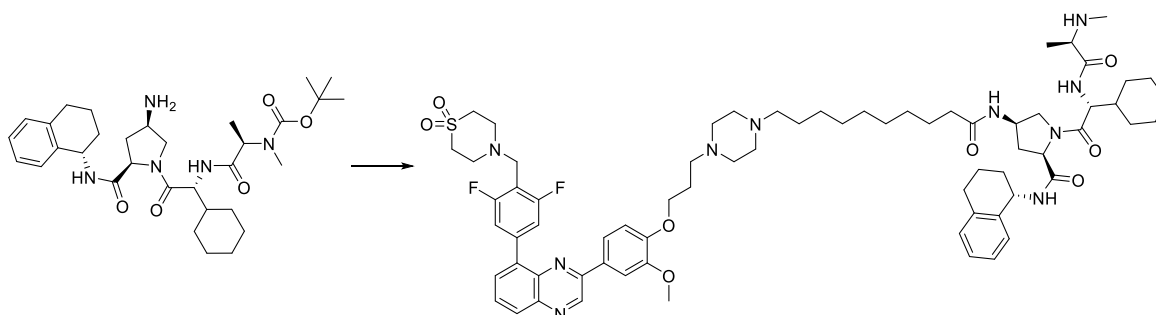
To a stirred solution of (*3S,5R*)-1-((*R*)-2-((*R*)-2-((*tert*-butoxycarbonyl)(methyl)amino)propanamido)-2-cyclohexylacetyl)-5-(((*S*)-1,2,3,4-tetrahydronaphthalen-1-yl)carbamoyl)pyrrolidin-3-yl methane-sulfonate **246** (1.020 g, 1.539 mmol) in DMF (30.8 mL) was added sodium azide (0.200 g, 3.08 mmol) and the reaction mixture was heated at 70 °C for 16 h under a nitrogen atmosphere. The reaction mixture was diluted with water (50 mL) and extracted with ethyl acetate (3 × 50 mL), and the organic layers were combined, passed through a hydrophobic frit and the solvent removed *in vacuo*. The residue was purified by normal phase column chromatography (0 – 100 % EtOAc in cyclohexane, 120 g SiO₂) to afford *tert*-butyl ((*R*)-1-(((*R*)-2-((2*R*,4*R*)-4-azido-2-(((*S*)-1,2,3,4-tetrahydronaphthalen-1-yl)carbamoyl)pyrrolidin-1-yl)-1-cyclohexyl-2-oxoethyl)amino)-1-oxopropan-2-yl)(methyl)carbamate **247** (328 mg, 0.538 mmol, 35 % yield) as a white solid. M.pt.: 70 – 72 °C; ν_{\max} (neat): 3314, 2928, 2854, 2103, 1652, 1515, 1153 cm⁻¹; ¹H NMR (400 MHz, DMSO-*d*₆) δ = 8.04 (1H, d, *J* = 8.6 Hz), 7.24 (1H, d, *J* = 8.1 Hz), 7.05 - 7.17 (4H, m), 4.89 - 4.97 (2H, m), 4.45 - 4.62 (2H, m), 4.25 - 4.45 (4H, m), 4.12 (1H, dd, *J* = 10.5, 6.6 Hz), 3.43 (1H, dd, *J* = 10.5, 5.9 Hz), 2.73 (4H, s), 1.80 - 1.90 (4H, m), 1.56 - 1.77 (10H, m), 1.39 (9H, s), 0.86 - 1.08 (4H, m); ¹³C NMR (101 MHz, DMSO-*d*₆) δ = 170.6, 170.4, 170.1 (2C), 154.4, 137.8, 137.4, 129.1, 128.7, 127.1, 126.1, 79.5, 60.2, 59.0, 58.8, 55.5, 53.8, 52.0, 47.1, 34.4, 30.5, 30.3, 29.3, 29.2, 28.5, 26.8, 26.3, 26.2, 26.0, 21.2, 20.6, 14.6; LCMS (Method A): *t*_R = 1.38 min, [M+H]⁺ 611 (90 % purity); HRMS: (C₃₂H₄₇N₇O₅) [M+H]⁺ requires 610.3717, found [M+H]⁺ 610.3724.

***Tert*-butyl ((*R*)-1-(((*R*)-2-((2*R*,4*R*)-4-amino-2-(((*S*)-1,2,3,4-tetrahydronaphthalen-1-yl)carbamoyl)pyrrolidin-1-yl)-1-cyclohexyl-2-oxoethyl)amino)-1-oxopropan-2-yl)(methyl)carbamate (**248**)**



Triphenylphosphine (275 mg, 1.050 mmol) and *tert*-butyl ((*R*)-1-(((*R*)-2-((2*R*,4*R*)-4-azido-2-(((*S*)-1,2,3,4-tetrahydronaphthalen-1-yl)carbamoyl)pyrrolidin-1-yl)-1-cyclohexyl-2-oxoethyl)amino)-1-oxopropan-2-yl)(methyl)carbamate **247** (320 mg, 0.525 mmol) in THF (8 mL) and water (0.8 mL) were stirred together at room temperature under a nitrogen atmosphere for 16 h. The solvent was removed *in vacuo* and the residue purified by reverse phase column chromatography (30 - 95 % MeCN in H₂O + 0.1 % NH₄HCO₃, Xbridge C₁₈, 32 mL/min, 40 min) to afford *tert*-butyl ((*R*)-1-(((*R*)-2-((2*R*,4*R*)-4-amino-2-(((*S*)-1,2,3,4-tetrahydronaphthalen-1-yl)carbamoyl)pyrrolidin-1-yl)-1-cyclohexyl-2-oxoethyl)amino)-1-oxopropan-2-yl)(methyl)carbamate **248** (162 mg, 0.278 mmol, 53 % yield) as a white hard gum. ν_{\max} (neat): 3313, 2928, 2854, 2467, 1635, 1439, 1152 cm⁻¹; ¹H NMR (400 MHz, MeOD) δ = 7.39 (1H, dd, *J* = 5.3, 3.8 Hz), 7.10 - 7.16 (2H, m), 7.04 - 7.10 (1H, m), 5.03 (1H, t, *J* = 5.9 Hz), 4.56 (1H, s), 4.46 (1H, d, *J* = 8.1 Hz), 4.37 (1H, dd, *J* = 8.8, 6.4 Hz), 4.03 - 4.13 (1H, m), 3.43 - 3.54 (2H, m), 3.34 (1H, s), 2.84 (3H, s), 2.64 - 2.83 (2H, m), 2.43 - 2.51 (1H, m), 1.73 - 2.00 (10H, m), 1.60 - 1.73 (2H, m), 1.48 - 1.51 (1H, m), 1.47 (9H, s), 1.09 - 1.35 (8H, m), 0.97 - 1.08 (1H, m); ¹³C NMR (101 MHz, MeOD) δ = 172.1, 171.2, 156.0, 137.1, 136.3, 128.5, 128.5, 126.7, 125.7, 80.4, 59.9, 55.8, 55.6, 50.9 (2C), 40.1, 37.1 (2C), 29.9 (2C), 29.6, 29.2, 28.9, 27.3 (3C), 25.9 (2C), 25.8, 25.6 (2C), 20.2; LCMS (Method B): *t*_R = 1.22 min, [M+H]⁺ 584 (99 % purity); HRMS: (C₃₂H₄₉N₅O₅) [M+H]⁺ requires 584.3812, found [M+H]⁺ 584.3816.

(2*R*,4*R*)-1-((*R*)-2-Cyclohexyl-2-((*R*)-2-(methylamino)propanamido)acetyl)-4-(10-(4-(3-(4-(8-(4-((1,1-dioxidothiomorpholino)methyl)-3,5-difluorophenyl)quinoxalin-2-yl)-2-methoxyphenoxy)propyl)piperazin-1-yl)decanamido)-*N*-((*S*)-1,2,3,4-tetrahydronaphthalen-1-yl)pyrrolidine-2-carboxamide (249)



10-(4-(3-(4-(8-(4-((1,1-Dioxidothiomorpholino)methyl)-3,5-difluorophenyl)quinoxalin-2-yl)-2-methoxyphenoxy)propyl)piperazin-1-yl)decanoic acid **248** (63 mg, 0.078 mmol), *tert*-butyl ((*R*)-1-(((*R*)-2-((2*R*,4*R*)-4-amino-2-((*S*)-1,2,3,4-tetrahydronaphthalen-1-yl)carbamoyl)pyrrolidin-1-yl)-1-cyclohexyl-2-oxoethyl)amino)-1-oxopropan-2-yl)(methyl)carbamate (50.1 mg, 0.086 mmol), triethylamine (32.6 μ L, 0.234 mmol) and HATU (44.5 mg, 0.117 mmol) were stirred together in DMF (1.559 mL) for 15 h at room temperature. The reaction mixture was diluted with water (10 mL) and extracted with DCM (3 \times 10 mL). The solvent was concentrated *in vacuo* and TFA (60.1 μ L, 0.780 mmol) was added and the reaction mixture was stirred at room temperature for 16 h. The reaction mixture was diluted with water (10 mL) and extracted with DCM (3 \times 10 mL). The solvent was concentrated *in vacuo* and the residue was purified by reverse phase prep column chromatography (70 – 95 % H₂O + 0.1 % NH₄HCO₃ in MeCN, Xbridge C₁₈, 42 mL/min, 45 min) to afford (2*R*,4*R*)-1-((*R*)-2-cyclohexyl-2-((*R*)-2-(methylamino)propanamido)acetyl)-4-(10-(4-(3-(4-(8-(4-((1,1-dioxidothiomorpholino)methyl)-3,5-difluorophenyl)quinoxalin-2-yl)-2-methoxyphenoxy)propyl)piperazin-1-yl)decanamido)-*N*-((*S*)-1,2,3,4-tetrahydronaphthalen-1-yl)pyrrolidine-2-carboxamide **249** (12 mg, 9.42 μ mol, 12 % yield) as a yellow solid. M.pt.: 98 – 100 °C; ν_{\max} (neat): 3277, 2928, 2854, 1664, 1518, 1124 cm⁻¹; ¹H NMR (600 MHz, CDCl₃) δ = 9.38 (1H, s), 8.15 (1H, dd, *J* = 8.4, 1.5 Hz), 8.00 (1H, br d, *J* = 8.8 Hz), 7.88 (1H, d, *J* = 2.2 Hz), 7.83 - 7.85 (1H, m), 7.79 (1H, t, *J* = 7.6 Hz), 7.70 (1H, dd, *J* = 8.4, 1.8 Hz), 7.46 - 7.50 (2H, m), 7.16 (1H, d, *J* = 7.3 Hz), 6.94 - 7.06 (4H, m), 5.19 (1H, br s), 4.73 - 4.79 (1H, m), 4.55 (1H, br t, *J* = 8.8 Hz), 4.35 (1H, br d, *J* = 9.5 Hz), 4.16 (2H, t, *J* = 6.1 Hz), 3.99 - 4.06 (1H, m), 3.94 (2H,

br s), 3.94 (3H, s), 3.75 - 3.82 (2H, m), 3.48 (1H, s), 3.08 - 3.15 (10H, m), 2.86 - 2.96 (5H, m), 2.66 - 2.77 (2H, m), 2.61 (1H, s), 2.41 - 2.50 (1H, m), 2.13 - 2.21 (4H, m), 2.02 - 2.09 (1H, m), 1.97 - 2.02 (1H, m), 1.90 - 1.96 (3H, m), 1.82 - 1.90 (4H, m), 1.73 - 1.82 (4H, m), 1.68 (4H, br s), 1.60 - 1.64 (2H, m), 1.25 - 1.34 (18H, m), 1.05 - 1.14 (2H, m), 0.99 - 1.04 (2H, m), 0.83 - 0.92 (1H, m), exchangeable protons not observed; ^{13}C NMR (151 MHz, CDCl_3) δ = 172.7, 171.8, 171.7, 168.2, 161.3 (2C, dd, J = 246.6, 9.4 Hz), 150.4, 150.3, 150.2, 142.7, 141.5, 140.7 (t, J = 10.5 Hz), 139.4, 138.0, 137.4, 137.0, 130.5, 129.9, 129.7, 129.3, 128.9, 128.8, 127.1, 125.8, 120.1, 119.4, 118.9, 117.5, 115.5, 114.0 (2C, dd, J = 22.7, 5.0 Hz), 113.1, 110.7 (t, J = 20.5 Hz), 110.4, 66.6, 59.7, 57.2, 55.6, 54.4, 51.5 (2C), 50.8, 50.6, 50.1 (2C), 49.9, 48.4 (2C), 48.0 (2C), 45.7, 41.0, 40.8, 36.9, 31.9, 30.9, 29.4, 29.1, 29.0, 29.0, 28.9, 26.6, 26.3, 26.1, 25.9, 25.6, 22.7, 19.3, 14.1, 8.5; LCMS (Method B): t_R = 1.66 min, $[(M+2H)/2]^+$ 638 (100 % purity); HRMS: ($\text{C}_{70}\text{H}_{94}\text{F}_2\text{N}_{10}\text{O}_8\text{S}$) $[M+H]^+$ requires 1273.7023, found $[M+H]^+$ 1273.7015.

8 References

- (1) Lightfoot, H. L.; Goldberg, F. W.; Sedelmeier, J. Evolution of Small Molecule Kinase Drugs. *ACS Med. Chem. Lett.* **2019**, *10* (2), 153–160. <https://doi.org/10.1021/acsmchemlett.8b00445>.
- (2) Roskoski, R. FDA-approved small molecule protein kinase inhibitors <http://www.brimr.org/PKI/PKIs.htm>.
- (3) Fabbro, D.; Cowan-Jacob, S. W.; Moebitz, H. Ten Things You Should Know about Protein Kinases: IUPHAR Review 14. *Br. J. Pharmacol.* **2015**, *172* (11), 2675–2700. <https://doi.org/10.1111/bph.13096>.
- (4) Ferguson, F. M.; Gray, N. S. Kinase Inhibitors: The Road Ahead. *Nat. Rev. Drug Discov.* **2018**, *17* (5), 353–376. <https://doi.org/10.1038/nrd.2018.21>.
- (5) Van Rompay, A. R.; Johansson, M.; Karlsson, A. Phosphorylation of Nucleosides and Nucleoside Analogs by Mammalian Nucleoside Monophosphate Kinases. *Pharmacol. Ther.* **2000**, *87* (2–3), 189–198. [https://doi.org/10.1016/S0163-7258\(00\)00048-6](https://doi.org/10.1016/S0163-7258(00)00048-6).
- (6) Cohen, P.; Alessi, D. R. Kinase Drug Discovery - What's next in the Field? *ACS Chem. Biol.* **2013**, *8* (1), 96–104. <https://doi.org/10.1021/cb300610s>.
- (7) Modi, V.; Dunbrack, R. L. Defining a New Nomenclature for the Structures of Active and Inactive Kinases. *Proc. Natl. Acad. Sci. U. S. A.* **2019**, *116* (14), 6818–6827. <https://doi.org/10.1073/pnas.1814279116>.
- (8) Vazquez, M. L.; Kaila, N.; Strohbach, J. W.; Trzuppek, J. D.; Brown, M. F.; Flanagan, M. E.; Mitton-Fry, M. J.; Johnson, T. A.; Tenbrink, R. E.; Arnold, E. P.; et al. Identification of N-{cis-3-[Methyl(7H-Pyrrolo[2,3-d]Pyrimidin-4-yl)Amino]Cyclobutyl}propane-1-Sulfonamide (PF-04965842): A Selective JAK1 Clinical Candidate for the Treatment of Autoimmune Diseases. *J. Med. Chem.* **2018**, *61* (3), 1130–1152. <https://doi.org/10.1021/acs.jmedchem.7b01598>.
- (9) Roskoski, R. Classification of Small Molecule Protein Kinase Inhibitors Based upon the Structures of Their Drug-Enzyme Complexes. *Pharmacol. Res.* **2016**, *103*, 26–48. <https://doi.org/10.1016/j.phrs.2015.10.021>.
- (10) Kontzias, A.; Kotlyar, A.; Laurence, A.; Changelian, P.; O'Shea, J. J. Jakinibs: A New

- Class of Kinase Inhibitors in Cancer and Autoimmune Disease. *Curr. Opin. Pharmacol.* **2012**, *12* (4), 464–470. <https://doi.org/10.1016/j.coph.2012.06.008>.
- (11) Laurence, A. JAK Kinases in Health and Disease: An Update. *Open Rheumatol. J.* **2012**, *6* (1), 232–244. <https://doi.org/10.2174/1874312901206010232>.
- (12) Pesu, M.; Laurence, A.; Kishore, N.; Zwillich, S. H.; Chan, G.; O’Shea, J. J. Therapeutic Targeting of Janus Kinases. *Immunol. Rev.* **2008**, *223* (1), 132–142. <https://doi.org/10.1111/j.1600-065X.2008.00644.x>.
- (13) Riedy, M. C.; Dutra, A. S.; Blake, T. B.; Modi, W.; Lal, B. K.; Davis, J.; Bosse, A.; O’Shea, J. J.; Johnston, J. A. Genomic Sequence, Organization, and Chromosomal Localization of Human JAK3. *Genomics* **1996**, *37* (1), 57–61. <https://doi.org/10.1006/geno.1996.0520>.
- (14) O’Shea, J. J.; Schwartz, D. M.; Villarino, A. V.; Gadina, M.; McInnes, I. B.; Laurence, A. The JAK-STAT Pathway: Impact on Human Disease and Therapeutic Intervention. *Annu. Rev. Med.* **2015**, *66* (1), 311–328. <https://doi.org/10.1146/annurev-med-051113-024537>.
- (15) Stark, G. R.; Darnell, J. E. The JAK-STAT Pathway at Twenty. *Immunity* **2012**, *36* (4), 503–514. <https://doi.org/10.1016/j.immuni.2012.03.013>.
- (16) O’Shea, J. J.; Holland, S. M.; Staudt, L. M. Mechanisms of Disease JAKs and STATs in Immunity, Immunodeficiency, and Cancer. *N. Engl. J. Med.* **2013**, *368* (2), 161–170. <https://doi.org/10.1056/NEJMra1202117>.
- (17) Hacein-Bey-Abina, S.; Le Deist, F.; Carlier, F.; Bouneaud, C.; Hue, C.; De Villartay, J.-P.; Thrasher, A. J.; Wulffraat, N.; Sorensen, R.; Dupuis-Girod, S.; et al. Sustained Correction of X-Linked Severe Combined Immunodeficiency by Ex Vivo Gene Therapy. *N. Engl. J. Med.* **2002**, *346* (16), 1185–1193. <https://doi.org/10.1056/NEJMoa012616>.
- (18) Clark, J. D.; Flanagan, M. E.; Telliez, J. B. Discovery and Development of Janus Kinase (JAK) Inhibitors for Inflammatory Diseases. *J. Med. Chem.* **2014**, *57* (12), 5023–5038. <https://doi.org/10.1021/jm401490p>.
- (19) Baker, S. J.; Rane, S. G.; Reddy, E. P. Hematopoietic Cytokine Receptor Signaling. *Oncogene* **2007**, *26* (47), 6724–6737. <https://doi.org/10.1038/sj.onc.1210757>.
- (20) H., P.; M., M.; E.M., R. Intracellular Signal Pathways: Potential for Therapies. *Curr.*

- Rheumatol. Rep.* **2009**, *11* (5), 378–385. <https://doi.org/10.1007/s11926-009-0054-9>.
- (21) Leonard, W. J.; O’Shea, J. J. JAKS AND STATS: Biological Implications. *Annu. Rev. Immunol.* **1998**, *16* (1), 293–322. <https://doi.org/10.1146/annurev.immunol.16.1.293>.
- (22) Gadina, M.; Hilton, D.; Johnston, J. A.; Morinobu, A.; Lighvani, A.; Zhou, Y. J.; Visconti, R.; O’Shea, J. J. Signaling by Type I and II Cytokine Receptors: Ten Years After. *Curr. Opin. Immunol.* **2001**, *13* (3), 363–373. [https://doi.org/10.1016/S0952-7915\(00\)00228-4](https://doi.org/10.1016/S0952-7915(00)00228-4).
- (23) Shuai, K.; Liu, B. Regulation of JAK-STAT Signalling in the Immune System. *Nat. Rev. Immunol.* **2003**, *3* (11), 900–911. <https://doi.org/10.1038/nri1226>.
- (24) Leonard, W. J.; O’Shea, J. J. Jaks and STATs: Biological Implications. *Annu. Rev. Immunol.* **1998**, *16* (1), 293–322. <https://doi.org/10.1146/annurev.immunol.16.1.293>.
- (25) Ihle, J. N. The Stat Family in Cytokine Signaling. *Curr. Opin. Cell Biol.* **2001**, *13* (2), 211–217. [https://doi.org/10.1016/S0955-0674\(00\)00199-X](https://doi.org/10.1016/S0955-0674(00)00199-X).
- (26) Yeh, T. C.; Dondi, E.; Uze, G.; Pellegrini, S. A Dual Role for the Kinase-like Domain of the Tyrosine Kinase Tyk2 in Interferon-Alpha Signaling. *Proc. Natl. Acad. Sci. U. S. A.* **2000**, *97* (16), 8991–8996. <https://doi.org/10.1073/pnas.160130297>.
- (27) Kisseleva, T.; Bhattacharya, S.; Braunstein, J.; Schindler, C. W. Signaling through the JAK/STAT Pathway, Recent Advances and Future Challenges. *Gene* **2002**, *285* (1–2), 1–24. [https://doi.org/10.1016/S0378-1119\(02\)00398-0](https://doi.org/10.1016/S0378-1119(02)00398-0).
- (28) Wallweber, H. J. A.; Tam, C.; Franke, Y.; Starovasnik, M. A.; Lupardus, P. J. Structural Basis of Recognition of Interferon- α Receptor by Tyrosine Kinase 2. *Nat. Struct. Mol. Biol.* **2014**, *21* (5), 443–448. <https://doi.org/10.1038/nsmb.2807>.
- (29) Girault, J.-A.; Labesse, G.; Mornon, J.-P.; Callebaut, I. Janus Kinases and Focal Adhesion Kinases Play in the 4.1 Band: A Superfamily of Band 4.1 Domains Important for Cell Structure and Signal Transduction. *Mol. Med.* **1998**, *4* (12), 751–769. <https://doi.org/10.1007/BF03401769>.
- (30) Frank, S. J.; Gilliland, G.; Kraft, A. S.; Arnold, C. S. Interaction of the Growth Hormone Receptor Cytoplasmic Domain with the JAK2 Tyrosine Kinase. *Endocrinology* **1994**,

- 135 (5), 2228–2239. <https://doi.org/0.1210/endo.135.5.7956946>.
- (31) Luo, H.; Rose, P.; Barber, D.; Hanratty, W. P.; Lee, S.; Roberts, T. M.; D’Andrea, A. D.; Dearolf, C. R. Mutation in the Jak Kinase JH2 Domain Hyperactivates Drosophila and Mammalian Jak-Stat Pathways. *Mol. Cell. Biol.* **1997**, *17* (3), 1562–1571. <https://doi.org/10.1128/mcb.17.3.1562>.
- (32) Chrencik, J. E.; Patny, A.; Leung, I. K.; Korniski, B.; Emmons, T. L.; Hall, T.; Weinberg, R. A.; Gormley, J. A.; Williams, J. M.; Day, J. E.; et al. Structural and Thermodynamic Characterization of the TYK2 and JAK3 Kinase Domains in Complex with CP-690550 and CMP-6. *J. Mol. Biol.* **2010**, *400* (3), 413–433. <https://doi.org/10.1016/j.jmb.2010.05.020>.
- (33) Schwartz, D. M.; Bonelli, M.; Gadina, M.; O’Shea, J. J. Type I/II Cytokines, JAKs, and New Strategies for Treating Autoimmune Diseases. *Nat. Rev. Rheumatol.* **2016**, *12* (1), 25–36. <https://doi.org/10.1038/nrrheum.2015.167>.
- (34) Singh, J. A.; Hossain, A.; Tanjong Ghogomu, E.; Mudano, A. S.; Tugwell, P.; Wells, G. A. Biologic or Tofacitinib Monotherapy for Rheumatoid Arthritis in People with Traditional Disease-Modifying Anti-Rheumatic Drug (DMARD) Failure: A Cochrane Systematic Review and Network Meta-Analysis (NMA). *Cochrane Database Syst. Rev.* **2016**, *2016* (11), 1–71. <https://doi.org/10.1002/14651858.CD012437>.
- (35) Schwartz, D. M.; Kanno, Y.; Villarino, A.; Ward, M.; Gadina, M.; O’Shea, J. J. JAK Inhibition as a Therapeutic Strategy for Immune and Inflammatory Diseases. *Nat. Rev. Drug Discov.* **2017**, *16* (12), 843–862. <https://doi.org/10.1038/nrd.2017.201>.
- (36) Levy, R. S.; Gupta, V.; Dipersio, J. F.; Catalano, J. V; Deininger, M.; Miller, C.; Silver, R. T.; Talpaz, M.; Winton, E. F.; Harvey, J. H.; et al. A Double-Blind, Placebo-Controlled Trial of Ruxolitinib for Myelofibrosis. *N. Engl. J. Med.* **2012**, *366* (9), 799–807. <https://doi.org/10.1056/NEJMoa1110557>.
- (37) Waltzman, R.; Stalbovskaya, V.; Mcquitty, M.; Hunter, D. S.; Levy, R.; Knoops, L.; Cervantes, F.; Vannucchi, A. M.; Barbui, T.; Barosi, G. JAK Inhibition with Ruxolitinib versus Best Available Therapy for Myelofibrosis. *N. Engl. J. Med.* **2012**, *366* (9), 787–798. <https://doi.org/10.1056/NEJMoa1110556>.
- (38) Bradley, E. C.; Erickson-Viitanen, S.; Vaddi, K.; Levy, R.; Tefferi, A. Safety and Efficacy

- of INCB018424, a JAK1 and JAK2 Inhibitor, in Myelofibrosis. *N. Engl. J. Med.* **2010**, *363* (12), 1117–1127. <https://doi.org/10.1056/NEJMoa1002028>.
- (39) Vaddi, K.; Liu, P.; Manshour, T.; Li, J.; Scherle, P. A.; Caulder, E.; Wen, X.; Li, Y.; Waeltz, P.; Rupa, M.; et al. Preclinical Characterization of the Selective JAK1 / 2 Inhibitor INCB018424 : Therapeutic Implications for the Treatment of Myeloproliferative Neoplasms. *Blood* **2010**, *115* (15), 3109–3117. <https://doi.org/10.1182/blood-2009-04-214957>.The.
- (40) Kesarwani, M.; Huber, E.; Kincaid, Z.; Evelyn, C. R.; Biesiada, J.; Rance, M.; Thapa, M. B.; Shah, N. P.; Meller, J.; Zheng, Y.; et al. Targeting Substrate-Site in Jak2 Kinase Prevents Emergence of Genetic Resistance. *Sci. Rep.* **2015**, *5* (14538), 1–19. <https://doi.org/10.1038/srep14538>.
- (41) Lucet, I. S.; Fantino, E.; Styles, M.; Bamert, R.; Patel, O.; Broughton, S. E.; Walter, M.; Burns, C. J.; Treutlein, H.; Wilks, A. F.; et al. The Structural Basis of Janus Kinase 2 Inhibition by a Potent and Specific Pan-Janus Kinase Inhibitor. *Blood* **2006**, *107* (1), 176–183. <https://doi.org/10.1182/blood-2005-06-2413>.Supported.
- (42) Rowland, P. GSK Unpublished Work.
- (43) Punwani, N.; Burn, T.; Scherle, P.; Flores, R.; Shi, J.; Collier, P.; Hertel, D.; Haley, P.; Lo, Y.; Waeltz, P.; et al. Downmodulation of Key Inflammatory Cell Markers with a Topical Janus Kinase 1/2 Inhibitor. *Br. J. Dermatol.* **2015**, *173* (4), 989–997. <https://doi.org/10.1111/bjd.13994>.
- (44) Treatment, A.; Topical, W.; Craiglow, B. G.; Tavares, D.; King, B. A. Topical Ruxolitinib for the Treatment of Alopecia Universalis Misdiagnosed Periocular Pyoderma Gangrenosum Requiring Ectropion Repair With Development of Second Lesion of Pyoderma Gangrenosum at Graft Site. *JAMA Dermatology* **2019**, *60* (12), 2015–2016. <https://doi.org/10.1001/jamadermatol.2015.4445>.jamadermatology.com.
- (45) Lee, E. B.; Fleischmann, R.; Hall, S.; Wilkinson, B.; Bradley, J. D.; Gruben, D.; Koncz, T.; Krishnaswami, S.; Wallenstein, G. V.; Zang, C.; et al. Tofacitinib versus Methotrexate in Rheumatoid Arthritis. *N. Engl. J. Med.* **2014**, *370* (25), 2377–2386. <https://doi.org/10.1056/NEJMoa1310476>.
- (46) Burmester, G. R.; Blanco, R.; Charles-schoeman, C.; Wollenhaupt, J.; Zerbini, C.;

- Benda, B.; Gruben, D.; Wallenstein, G. Tofacitinib (CP-690 ,550) in Combination with Methotrexate in Patients with Active Rheumatoid Arthritis with an Inadequate Response to Tumour Necrosis Factor Inhibitors : A Randomised Phase 3 Trial. *Lancet* **2013**, *381* (9865), 451–460. [https://doi.org/10.1016/S0140-6736\(12\)61424-X](https://doi.org/10.1016/S0140-6736(12)61424-X).
- (47) Cohen, S.; Lee, E. B.; Meijide, J. A. G.; Gruben, D.; Koncz, T.; Wallenstein, G. V.; Krishnaswami, S.; Bradley, J. D. Tofacitinib or Adalimumab versus Placebo in Rheumatoid Arthritis. *Am. J. Transplant.* **2012**, *367* (6), 508–519. <https://doi.org/10.1056/NEJMoa1112072>.
- (48) Lee, E. B.; Fleischmann, R.; Hall, S.; Vollenhoven, R. F. van; Bradley, J.; Gruben, D.; Koncz, T.; Krishnaswami, S.; Wallenstein, G.; Zwillich, S. H.; et al. Radiographic, Clinical and Functional Comparison of Tofacitinib Monotherapy Versus Methotrexate in Methotrexate-Naïve Patients with Rheumatoid Arthritis. *Arthritis Rheumatol.* **2012**, *64* (12), S1049. <https://doi.org/10.1002/art.37735>.
- (49) Kremer, J. M.; Russell, A. S.; Emery, P.; Abud-mendoza, C.; Szechinski, J.; Westhovens, R.; Li, T.; Zhou, X.; Becker, J.; Aranda, R.; et al. Long-Term Safety, Efficacy and Inhibition of Radiographic Progression with Abatacept Treatment in Patients with Rheumatoid Arthritis and an Inadequate Response to Methotrexate: 3-Year Results from the AIM Trial. *Annu. Rheum. Dis.* **2011**, *36* (10), 1826–1830. <https://doi.org/10.1136/ard.2010.139345>.
- (50) Flanagan, M. E.; Blumenkopf, T. A.; Brissette, W. H.; Brown, M. F.; Casavant, J. M.; Shang-poa, C.; Doty, J. L.; Elliott, E. A.; Fisher, M. B.; Hines, M.; et al. Discovery of CP-690, 550 A Potent and Selective Janus Kinase (JAK) Inhibitor for the Treatment of Autoimmune Diseases and Organ Transplant Rejection. *J. Med. Chem.* **2010**, *53* (24), 8468–8484. <https://doi.org/10.1021/jm1004286>.
- (51) Karaman, M. W.; Herrgard, S.; Treiber, D. K.; Gallant, P.; Atteridge, C. E.; Campbell, B. T.; Chan, K. W.; Ciceri, P.; Davis, M. I.; Edeen, P. T.; et al. A Quantitative Analysis of Kinase Inhibitor Selectivity. *Nat. Biotechnol.* **2008**, *26* (1), 127–132. <https://doi.org/10.1038/nbt1358>.
- (52) Wollenhaupt, J.; Silverfield, J.; Lee, E. B.; Curtis, J. R.; Wood, S. P.; Soma, K.; Nduaka, C. I.; Benda, B.; Gruben, D.; Nakamura, H.; et al. Safety and Efficacy of Tofacitinib , an Oral Janus Kinase Inhibitor , for the Treatment of Rheumatoid Arthritis in Open-Label

- , Longterm Extension Studies Safety and Efficacy of Tofacitinib , an Oral Janus Kinase Inhibitor , for the Treatment of Rheumatoid Arthritis. *J. Rheumatol.* **2014**, *41* (5). <https://doi.org/10.3899/jrheum.130683>.
- (53) Vincenti, F.; Silva, H. T.; Busque, S.; Connell, O.; Friedewald, J.; Cibrik, D.; Budde, K.; Yoshida, A.; Cohney, S.; Weimar, W.; et al. Randomized Phase 2b Trial of Tofacitinib (CP-690 , 550) in De Novo Kidney Transplant Patients : Efficacy , Renal Function and Safety at 1 Year. *Am. J. Transplant.* **2012**, *12* (7), 2446–2456. <https://doi.org/10.1111/j.1600-6143.2012.04127.x>.
- (54) Vincenti, F.; Silva, H. T.; Busque, S.; Connell, P. J. O.; Russ, G.; Budde, K.; Yoshida, A.; Tortorici, M. A.; Lamba, M. Evaluation of the Effect of Tofacitinib Exposure on Outcomes in Kidney Transplant Patients. *Am. J. Transplant.* **2015**, *15* (6), 1644–1653. <https://doi.org/10.1111/ajt.13181>.
- (55) Sivaraman, P.; Cohen, S. B. Malignancy and Janus Kinase Inhibition. *Rheum. Dis. Clin. NA* **2017**, *43* (1), 79–93. <https://doi.org/10.1016/j.rdc.2016.09.008>.
- (56) Shi, J. G.; Chen, X.; Lee, F.; Emm, T.; Scherle, P. A.; Lo, Y.; Punwani, N.; Williams, W. V.; Yeleswaram, S. The Pharmacokinetics, Pharmacodynamics, and Safety of Baricitinib, an Oral JAK 1/2 Inhibitor, in Healthy Volunteers. *J. Clin. Pharmacol.* **2014**, *52* (12), 1354–1361. <https://doi.org/10.1002/jcph.354>.
- (57) Fala, L. Olumiant (Baricitinib) Once-Daily Oral Drug Approved for the Treatment of Patients with Moderately to Severely Active Rheumatoid Arthritis. *Am. Heal. Drug Benefits* **2019**, *12*, 68–70.
- (58) Dougados, M.; Heijde, D. Van Der; Chen, Y.; Greenwald, M.; Drescher, E.; Liu, J.; Beattie, S.; Witt, S.; Torre, I. De; Gaich, C.; et al. Baricitinib in Patients with Inadequate Response or Intolerance to Conventional Synthetic DMARDs : Results from the RA-BUILD Study. *Ann. Rheum. Dis.* **2017**, *76* (1), 88–95. <https://doi.org/10.1136/annrheumdis-2016-210094>.
- (59) Fleischmann, R.; Schiff, M.; Heijde, V. Der; Ramos-remus, C.; Spindler, A.; Stanislav, M.; Zerbini, C. A. F.; Gurbuz, S.; Dickson, C.; Bono, S. De; et al. Baricitinib, Methotrexate, or Combination in Patients With Rheumatoid Arthritis and No or Limited Prior Disease-Modifying Antirheumatic Drug Treatment. *Arthritis Rheumatol.* **2017**, *69* (3), 506–517. <https://doi.org/10.1002/art.39953>.

- (60) Shea, J. J. O.; Schwartz, D. M.; Villarino, A. V; Gadina, M.; McInnes, I. B.; Laurence, A. The JAK-STAT Pathway : Impact on Human Disease and Therapeutic Intervention. *Annu. Rev. Med.* **2015**, *66* (1), 311–328. <https://doi.org/10.1146/annurev-med-051113-024537>.
- (61) Hamaguchi, H.; Amano, Y.; Moritomo, A.; Shirakami, S.; Nakajima, Y. Bioorganic & Medicinal Chemistry Discovery and Structural Characterization of Peficitinib (ASP015K) as a Novel and Potent JAK Inhibitor. *Bioorg. Med. Chem.* **2018**, *26* (18), 4971–4983. <https://doi.org/10.1016/j.bmc.2018.08.005>.
- (62) Markham, A.; Keam, S. J. Peficitinib: First Global Approval. *Drugs* **2019**, *79* (8), 887–891. <https://doi.org/10.1007/s40265-019-01131-y>.
- (63) Menet, C. J.; Fletcher, S. R.; Lommen, G. Van; Geney, R.; Blanc, J.; Smits, K.; Jouannigot, N.; Deprez, P.; Aar, E. M. Van Der; Clement-lacroix, P.; et al. Triazolopyridines as Selective JAK1 Inhibitors: From Hit Identification to GLPG0634. *J. Med. Chem.* **2014**, *57* (22), 9323–9342. <https://doi.org/10.1021/jm501262q>.
- (64) Zak, M.; Hurley, C. A.; Ward, S. I.; Bergeron, P.; Barrett, K.; Balazs, M.; Blair, W. S.; Bull, R.; Chakravarty, P.; Chang, C.; et al. Identification of C-2 Hydroxyethyl Imidazopyrrolopyridines as Potent JAK1 Inhibitors with Favorable Physicochemical Properties and High Selectivity over JAK2. *J. Med. Chem.* **2013**, *56* (11), 4764–4785. <https://doi.org/10.1021/jm4004895>.
- (65) Inhibitors, K.; Schenkel, L. B.; Huang, X.; Cheng, A.; Deak, H. L.; Doherty, E.; Emkey, R.; Gu, Y.; Gunaydin, H.; Kim, J. L.; et al. Discovery of Potent and Highly Selective Thienopyridine Janus Kinase 2 Inhibitors. *J. Med. Chem.* **2011**, *54* (24), 8440–8450. <https://doi.org/10.1021/jm200911r>.
- (66) Parmentier, J. M.; Voss, J.; Graff, C.; Schwartz, A.; Argiriadi, M.; Friedman, M.; Camp, H. S.; Padley, R. J.; George, J. S.; Hyland, D.; et al. In Vitro and in Vivo Characterization of the JAK1 Selectivity of Upadacitinib (ABT-494). *BMC Rheumatol.* **2018**, *2* (1), 23. <https://doi.org/10.1186/s41927-018-0031-x>.
- (67) AbbVie Receives FDA Approval of RINVOQ™ (upadacitinib), an Oral JAK Inhibitor For The Treatment of Moderate to Severe Rheumatoid Arthritis <https://news.abbvie.com/news/press-releases/abbvie-receives-fda-approval-rinvoq-upadacitinib-an-oral-jak-inhibitor-for-treatment-moderate-to-severe->

rheumatoid-arthritis.htm.

- (68) Friedman, M.; Frank, K. E.; Aguirre, A.; Argiriadi, M. A.; Davis, H.; Edmunds, J. J.; George, D. M.; George, J. S.; Goedken, E.; Fiamengo, B.; et al. [4,3-a] Pyrazines as Jak1 Kinase Inhibitors. *Bioorg. Med. Chem. Lett.* **2015**, *25* (20), 4399–4404. <https://doi.org/10.1016/j.bmcl.2015.09.020>.
- (69) Macchi, P.; Ii, A. V.; Gilianit, S.; Sacco, M. G.; Frattini, A.; Portat, F.; Ugaziot, A. G.; Johnstont, J. A.; Candotti, F.; Sheat, J. J. O.; et al. Mutations of Jak-3 Gene in Patients with Autosomal Severe Combined Immune Deficiency (SCID). *Nature* **1995**, *377* (6544), 65–68. <https://doi.org/10.1038/377065a0>.
- (70) Farmer, L. J.; Ledebor, M. W.; Hooek, T.; Arnost, M. J.; Bethiel, R. S.; Bennani, Y. L.; Black, J. J.; Brummel, C. L.; Chakilam, A.; Dorsch, W. A.; et al. Discovery of VX-509 (Decernotinib): A Potent and Selective Janus Kinase 3 Inhibitor for the Treatment of Autoimmune Diseases. *J. Med. Chem.* **2015**, *58* (18), 7195–7726. <https://doi.org/10.1021/acs.jmedchem.5b00301>.
- (71) Genovese, M. C.; Vollenhoven, R. F. Van; Zhang, Y.; Kinnman, N. VX-509 (Decernotinib), an Oral Selective JAK-3 Inhibitor, in Combination With Methotrexate in Patients With Rheumatoid Arthritis. *Arthritis Rheumatol.* **2016**, *68* (1), 46–55. <https://doi.org/10.1002/art.39473>.
- (72) Genovese, M. C.; Yang, F.; Østergaard, M.; Kinnman, N. Efficacy of VX-509 (Decernotinib) in Combination with a Disease-Modifying Antirheumatic Drug in Patients with Rheumatoid Arthritis : Clinical and MRI Findings. *Annu. Rheum. Dis.* **2016**, *75* (11), 1979–1983. <https://doi.org/10.1136/annrheumdis-2015-208901>.
- (73) Huang, J.; Yang, F.; Yogaratnam, J.; Shen, J. SAT0227 The Effect of Deuteration of VX-509 (Decernotinib) on Drug-Drug Interactions (DDI) with Midazolam. *Ann. Rheum. Dis.* **2015**, *74*, (Suppl 2):740.2-740. <https://doi.org/10.1136/annrheumdis-2015-eular.1810>.
- (74) Ghosh, A. K.; Samanta, I.; Mondal, A.; Liu, W. R. Covalent Inhibition in Drug Discovery. *ChemMedChem* **2019**, *14* (9), 889–906. <https://doi.org/10.1002/cmdc.201900107>.
- (75) Telliez, J.; Dowty, M. E.; Wang, L.; Jussif, J.; Lin, T.; Li, L.; Moy, E.; Balbo, P.; Li, W.; Zhao, Y.; et al. Discovery of a JAK3-Selective Inhibitor: Functional Differentiation of

- JAK3-Selective Inhibition over Pan-JAK or JAK1-Selective Inhibition. *ACS Chem. Biol.* **2016**, *11* (12), 3442–3451. <https://doi.org/10.1021/acscchembio.6b00677>.
- (76) Goedken, E. R.; Argiriadi, M. A.; Banach, D. L.; Fiamengo, B. A.; Foley, S. E.; Frank, K. E.; George, J. S.; Harris, C. M.; Hobson, A. D.; Ihle, D. C.; et al. Tricyclic Covalent Inhibitors Selectively Target Jak3 through an Active Site Thiol. *J. Biol. Chem.* **2015**, *290* (8), 4573–4589. <https://doi.org/10.1074/jbc.M114.595181>.
- (77) Tan, L.; Akahane, K.; McNally, R.; Reyskens, K. M. S. E.; Ficarro, S. B.; Liu, S.; Hertersprie, G. S.; Koyama, S.; Pattison, M. J.; Labella, K.; et al. Development of Selective Covalent Janus Kinase 3 Inhibitors. *J. Med. Chem.* **2015**, *58* (16), 6589–6606. <https://doi.org/10.1021/acs.jmedchem.5b00710>.
- (78) Thorarensen, A.; Dowty, M. E.; Banker, M. E.; Juba, B.; Jussif, J.; Lin, T.; Vincent, F.; Czerwinski, R. M.; Casimiro-garcia, A.; Unwalla, R.; et al. Design of a Janus Kinase 3 (JAK3) Specific Inhibitor 1-((2S,5R)-5-((7H-Pyrrolo[2,3-d]Pyrimidin-4-Yl)Amino)-2-Methylpiperidin-1- Yl)Prop-2-En-1-One (PF-06651600) Allowing for the Interrogation of JAK3 Signaling in Humans. *J. Med. Chem.* **2017**, *60* (5), 1971–1993. <https://doi.org/10.1021/acs.jmedchem.6b01694>.
- (79) Thorarensen, A.; Banker, M. E.; Fensome, A.; Telliez, J.; Juba, B.; Vincent, F.; Czerwinski, R. M.; Casimiro-garcia, A. ATP-Mediated Kinome Selectivity: The Missing Link in Understanding the Contribution of Individual JAK Kinase Isoforms to Cellular Signaling. *ACS Chem. Biol.* **2014**, *9* (7), 1552–1558. <https://doi.org/10.1021/cb5002125>.
- (80) Field, S. D.; Arkin, J.; Li, J.; Jones, L. H. Selective Downregulation of JAK2 and JAK3 by an ATP-Competitive Pan-JAK Inhibitor. *ACS Chem. Biol.* **2017**, *12* (5), 1183–1187. <https://doi.org/10.1021/acscchembio.7b00116>.
- (81) Pickart, C. M. Back to the Future with Ubiquitin. *Cell* **2004**, *116* (2), 181–190. [https://doi.org/10.1016/S0092-8674\(03\)01074-2](https://doi.org/10.1016/S0092-8674(03)01074-2).
- (82) Hershko, A.; Ciechanover, A.; Varshavsky, A. Basic Medical Research Award. The Ubiquitin System. *Nat. Med.* **2000**, *6* (10), 1073–1081. <https://doi.org/10.1038/80384>.
- (83) Nedelsky, N. B.; Todd, P. K.; Taylor, J. P. Autophagy and the Ubiquitin-Proteasome

- System: Collaborators in Neuroprotection. *Biochim. Biophys. Acta - Mol. Basis Dis.* **2008**, *1782* (12), 691–699. <https://doi.org/10.1016/j.bbadis.2008.10.002>.
- (84) Vijay-Kumar, S.; Bugg, C. E.; Cook, W. J. Structure of Ubiquitin Refined at 1.8 Å Resolution. *J. Mol. Biol.* **1987**, *194* (3), 531–544. [https://doi.org/10.1016/0022-2836\(92\)90903-W](https://doi.org/10.1016/0022-2836(92)90903-W).
- (85) Pickart, C. M. Ubiquitin in Chains. *Trends Biochem. Sci.* **2000**, *25* (11), 544–548. [https://doi.org/10.1016/S0968-0004\(00\)01681-9](https://doi.org/10.1016/S0968-0004(00)01681-9).
- (86) Gregori, L.; Poosch, M. S.; Cousins, G.; Chau, V. A Uniform Isopeptide-Linked Multiubiquitin Chain Is Sufficient to Target Substrate for Degradation in Ubiquitin-Mediated Proteolysis. *J. Biol. Chem.* **1990**, *265* (15), 8354–8357. <https://doi.org/265.8354-8357>.
- (87) Nalepa, G.; Rolfe, M.; Harper, J. W. Drug Discovery in the Ubiquitin–Proteasome System. *Nat. Rev. Drug Discov.* **2006**, *5* (7), 596–613. <https://doi.org/10.1038/nrd2056>.
- (88) Reischl, D.; Zimmer, A. Drug Delivery of siRNA Therapeutics: Potentials and Limits of Nanosystems. *Nanomedicine NBM* **2009**, *5* (1), 8–20. <https://doi.org/10.1016/j.nano.2008.06.001>.
- (89) Bertrand, J.-R.; Pottier, M.; Vekris, A.; Opolon, P.; Maksimenko, A.; Malvy, C. Comparison of Antisense Oligonucleotides and siRNAs in Cell Culture and in Vivo. *Biochem. Biophys. Res. Commun.* **2002**, *296* (4), 1000–1004. [https://doi.org/10.1016/S0006-291X\(02\)02013-2](https://doi.org/10.1016/S0006-291X(02)02013-2).
- (90) Elbashir, S. M.; Lendeckel, W.; Tuschl, T. RNA Interference Is Mediated 21- and 22-Nucleotide RNAs. *Genes Dev.* **2000**, *15* (2), 188–200. <https://doi.org/10.1101/gad.862301.vents>.
- (91) Akhtar, S.; Benter, I. F. Nonviral Delivery of Synthetic siRNAs in Vivo. *J. Clin. Invest.* **2007**, *117* (12), 3623–3632. <https://doi.org/10.1172/JCI33494>.
- (92) Tokatlian, T.; Segura, T. siRNA Applications in Nanomedicine. *Wiley Interdiscip. Rev. Nanomedicine Nanobiotechnology* **2010**, *2* (3), 305–315. <https://doi.org/10.1002/wnan.81>.
- (93) Moullick, K.; Ahn, J. H.; Zong, H.; Rodina, A.; Cerchietti, L.; Gomes DaGama, E. M.;

- Caldas-Lopes, E.; Beebe, K.; Perna, F.; Hatzi, K.; et al. Affinity-Based Proteomics Reveal Cancer-Specific Networks Coordinated by Hsp90. *Nat. Chem. Biol.* **2011**, *7* (11), 818–826. <https://doi.org/10.1038/nchembio.670>.
- (94) Schneider, C.; Sepp-Lorenzino, L.; Nimmesgern, E.; Ouerfelli, O.; Danishefsky, S.; Rosen, N.; Hartl, F. U. Pharmacologic Shifting of a Balance between Protein Refolding and Degradation Mediated by Hsp90. *Proc. Natl. Acad. Sci. U. S. A.* **1996**, *93* (25), 14536–14541. <https://doi.org/10.1073/pnas.93.25.14536>.
- (95) Mimnaugh, E. P185erB2 Binds to GRP94 in Vivo. *J. Biol. Chem.* **1996**, *271* (9), 4974–4977. <https://doi.org/10.1074/jbc.271.9.4974>.
- (96) Samuni, Y.; Ishii, H.; Hyodo, F.; Samuni, U.; Krishna, M. C.; Goldstein, S.; Mitchell, J. B. Reactive Oxygen Species Mediate Hepatotoxicity Induced by the Hsp90 Inhibitor Geldanamycin and Its Analogs. *Free Radic. Biol. Med.* **2010**, *48* (11), 1559–1563. <https://doi.org/10.1016/j.freeradbiomed.2010.03.001>.
- (97) Banerji, U.; O'Donnell, A.; Scurr, M.; Pacey, S.; Stapleton, S.; Asad, Y.; Simmons, L.; Maloney, A.; Raynaud, F.; Campbell, M.; et al. Phase I Pharmacokinetic and Pharmacodynamic Study of 17-Allylamino, 17-Demethoxygeldanamycin in Patients with Advanced Malignancies. *J. Clin. Oncol.* **2005**, *23* (18), 4152–4161. <https://doi.org/10.1200/JCO.2005.00.612>.
- (98) Taldone, T.; Gozman, A.; Maharaj, R.; Chiosis, G. Targeting Hsp90: Small-Molecule Inhibitors and Their Clinical Development. *Curr. Opin. Pharmacol.* **2008**, *8* (4), 370–374. <https://doi.org/10.1016/j.coph.2008.06.015>.
- (99) Wells, J. A.; McClendon, C. L. Reaching for High-Hanging Fruit in Drug Discovery at Protein-Protein Interfaces. *Nature* **2007**, *450* (7172), 1001–1009. <https://doi.org/10.1038/nature06526>.
- (100) Kim, J.; Kim, H.; Park, S. B. Privileged Structures: Efficient Chemical “Navigators” toward Unexplored Biologically Relevant Chemical Spaces. *J. Am. Chem. Soc.* **2014**, *136* (42), 14629–14638. <https://doi.org/10.1021/ja508343a>.
- (101) Toure, M.; Crews, C. M. Small-Molecule PROTACS: New Approaches to Protein Degradation. *Angew. Chem. Int. Ed.* **2016**, *55* (6), 1966–1973. <https://doi.org/10.1002/anie.201507978>.

- (102) Neklesa, T. K.; Tae, H. S.; Schneekloth, A. R.; Stulberg, M. J.; Corson, T. W.; Sundberg, T. B.; Raina, K.; Holley, S. A.; Crews, C. M. Small-Molecule Hydrophobic Tagging-Induced Degradation of HaloTag Fusion Proteins. *Nat. Chem. Biol.* **2011**, *7* (8), 538–543. <https://doi.org/10.1038/nchembio.597>.
- (103) Tae, H. S.; Sundberg, T. B.; Neklesa, T. K.; Noblin, D. J.; Gustafson, J. L.; Roth, A. G.; Raina, K.; Crews, C. M. Identification of Hydrophobic Tags for the Degradation of Stabilized Proteins. *Chembiochem* **2013**, *13* (4), 538–541. <https://doi.org/10.1002/cbic.201100793>.Identification.
- (104) Los, G. V.; Encell, L. P.; Mcdougall, M. G.; Hartzell, D. D.; Karassina, N.; Zimprich, C.; Wood, M. G.; Learish, R.; Ohana, R. F.; Urh, M.; et al. HaloTag: A Novel Protein Labeling Technology for Cell Imaging and Protein Analysis. *ACS Chem. Biol.* **2008**, *3* (6), 373–382. <https://doi.org/10.1021/cb800025k>.
- (105) Long, M. J. C.; Gollapalli, D. R.; Hedstrom, L. Inhibitor Mediated Protein Degradation. *Chem. Biol.* **2012**, *19* (5), 629–637. <https://doi.org/10.1016/j.chembiol.2012.04.008>.
- (106) Teutsch, G.; Goubet, F.; Battmann, T.; Bonfils, A.; Bouchoux, F.; Cerede, E.; Gofflo, D.; Gaillard-Kelly, M.; Philibert, D. Non-Steroidal Antiandrogens: Synthesis and Biological Profile of High-Affinity Ligands for the Androgen Receptor. *J. Steroid Biochem. Mol. Biol.* **1994**, *48* (1), 111–119. [https://doi.org/10.1016/0960-0760\(94\)90257-7](https://doi.org/10.1016/0960-0760(94)90257-7).
- (107) Gustafson, J. L.; Neklesa, T. K.; Cox, C. S.; Roth, A. G.; Buckley, D. L.; Tae, H. S.; Sundberg, T. B.; Stagg, D. B.; Hines, J.; McDonnell, D. P.; et al. Small Molecule Mediated Degradation of the Androgen Receptor Through Hydrophobic Tagging. *Angew. Chem. Int. Ed.* **2015**, *54* (33), 9659–9662. <https://doi.org/10.1126/scisignal.274pe36>.Insulin.
- (108) Schneekloth, A. R.; Pucheault, M.; Tae, H. S.; Crews, C. M. Targeted Intracellular Protein Degradation Induced by a Small Molecule: En Route to Chemical Proteomics. *Bioorg. Med. Chem. Lett.* **2008**, *18* (22), 5904–5908. <https://doi.org/10.1016/j.bmcl.2008.07.114>.
- (109) Bondeson, D. P.; Mares, A.; Smith, I. E.; Ko, E.; Campos, S.; Miah, A. H.; Mulholland, K. E.; Routly, N.; Buckley, D. L.; Gustafson, J. L.; et al. Catalytic in Vivo Protein Knockdown by Small-Molecule PROTACs. *Nat. Chem. Biol.* **2015**, *11* (8), 611–617. <https://doi.org/10.1038/nchembio.1858>.

- (110) Johnson, D. S.; Weerapana, E.; Cravatt, B. F. Strategies for Discovering and Derisking Covalent, Irreversible Enzyme Inhibitors. *Future Med. Chem.* **2010**, *2* (6), 949–964. <https://doi.org/10.4155/fmc.10.21>.
- (111) Zengerle, M.; Chan, K.-H.; Ciulli, A. Selective Small Molecule Induced Degradation of the BET Bromodomain Protein BRD4. *ACS Chem. Biol.* **2015**, *10* (8), 1770–1777. <https://doi.org/10.1021/acscchembio.5b00216>.
- (112) Lipinski, C. A.; Lombardo, F.; Dominy, B. W.; Feeney, P. J. Experimental and Computational Approaches to Estimate Solubility and Permeability in Drug Discovery and Development Settings. *Adv. Drug Deliv. Rev.* **1997**, *23* (1–3), 3–25. <https://doi.org/10.1016/j.addr.2012.09.019>.
- (113) Komander, D.; Clague, M. J.; Urbé, S. Breaking the Chains: Structure and Function of the Deubiquitinases. *Nat. Rev. Mol. Cell Biol.* **2009**, *10* (8), 550–563. <https://doi.org/10.1038/nrm2731>.
- (114) Douglass, E. F.; Miller, C. J.; Sparer, G.; Shapiro, H.; Spiegel, D. A. A Comprehensive Mathematical Model for Three-Body Binding Equilibria. *J. Am. Chem. Soc.* **2013**, *135* (16), 6092–6099. <https://doi.org/10.1021/ja311795d>.
- (115) Sakamoto, K. M.; Kim, K. B.; Kumagai, A.; Mercurio, F.; Crews, C. M.; Deshaies, R. J. Protacs: Chimeric Molecules That Target Proteins to the Skp1-Cullin-F Box Complex for Ubiquitination and Degradation. *Proc. Natl. Acad. Sci. U. S. A.* **2001**, *98* (15), 8554–8559. <https://doi.org/10.1073/pnas.141230798>.
- (116) Lai, A. C.; Crews, C. M. Induced Protein Degradation: An Emerging Drug Discovery Paradigm. *Nat. Rev. Drug Discov.* **2016**, *16* (2), 101–114. <https://doi.org/10.1038/nrd.2016.211>.
- (117) Hon, W.; Wilson, M.; Harlos, K.; Claridge, T.; Schofield, C.; Pugh, C.; Maxwell, P.; Ratcliffe, P.; Stuart, D.; Jones, E. Structural Basis for the Recognition of Hydroxyproline in HIF-1 Alpha by PVHL. *Nature* **2002**, *417* (June), 975–978. <https://doi.org/10.1038/nature00767>.
- (118) Min, J.-H.; Yang, H.; Ivan, M.; Gertler, F.; Kaelin, W. G.; Pavletich, N. P. Structure of an HIF-1alpha -PVHL Complex: Hydroxyproline Recognition in Signaling. *Science* **2002**, *296* (5574), 1886–1889. <https://doi.org/10.1126/science.1073440>.

- (119) Wender, P. A.; Mitchell, D. J.; Pattabiraman, K.; Pelkey, E. T.; Steinman, L.; Rothbard, J. B. The Design, Synthesis, and Evaluation of Molecules That Enable or Enhance Cellular Uptake: Peptoid Molecular Transporters. *Proc. Natl. Acad. Sci. U. S. A.* **2000**, *97* (24), 13003–13008. <https://doi.org/10.1073/pnas.97.24.13003>.
- (120) Schneekloth, J. S.; Fonseca, F. N.; Koldobskiy, M.; Mandal, A.; Deshaies, R.; Sakamoto, K.; Crews, C. M. Chemical Genetic Control of Protein Levels : Selective in Vivo Targeted Degradation. *J. Am. Chem. Soc.* **2004**, *126* (12), 3748–3754. <https://doi.org/10.1021/ja039025z>.
- (121) Bargagna-Mohan, P.; Baek, S. H.; Lee, H.; Kim, K.; Mohan, R. Use of PROTACS as Molecular Probes of Angiogenesis. *Bioorg. Med. Chem. Lett.* **2005**, *15* (11), 2724–2727. <https://doi.org/10.1016/j.bmcl.2005.04.008>.
- (122) Zhang, D.; Baek, S. H.; Ho, A.; Kim, K. Degradation of Target Protein in Living Cells by Small-Molecule Proteolysis Inducer. *Bioorg. Med. Chem. Lett.* **2004**, *14* (3), 645–648. <https://doi.org/10.1016/j.bmcl.2003.11.042>.
- (123) Henning, R. K.; Varghese, J. O.; Das, S.; Nag, A.; Tang, G.; Tang, K.; Sutherland, A. M.; Heath, J. R. Degradation of Akt Using Protein-Catalyzed Capture Agents. *J. Pept. Sci.* **2016**, *22* (4), 196–200. <https://doi.org/10.1002/psc.2858>.
- (124) Pfeilsticker, J. A.; Umeda, A.; Farrow, B.; Hsueh, C. L.; Deyle, K. M.; Kim, J. T.; Lai, B. T.; Heath, J. R. A Cocktail of Thermally Stable, Chemically Synthesized Capture Agents for the Efficient Detection of Anti-Gp41 Antibodies from Human Sera. *PLoS One* **2013**, *8* (10), 4–8. <https://doi.org/10.1371/journal.pone.0076224>.
- (125) Vassilev, L. T.; Vu, B. T.; Craves, B.; Carvajal, D.; Podlaski, F.; Filipovic, Z.; Kong, N.; Kammlott, U.; Lukacs, C.; Klein, C.; et al. In Vivo Activation of the P53 Pathway by Small-Molecule Antagonists of MDM2. *Science (80-.)*. **2004**, *303* (5659), 844–848. <https://doi.org/10.1126/science.1092472>.
- (126) Ding, Q.; Zhang, Z.; Liu, J.; Jiang, N.; Zhang, J.; Ross, T. M.; Chu, X.; Bartkovitz, D.; Podlaski, F.; Janson, C.; et al. Discovery of RG7388, a Potent and Selective P53 – MDM2 Inhibitor in Clinical Development. *J. Med. Chem.* **2013**, *56* (14), 5979–5983. <https://doi.org/10.1021/jm400487c>.
- (127) Vu, B.; Wovkulich, P.; Pizzolato, G.; Lovey, A.; Ding, Q.; Jiang, N.; Liu, J. J.; Zhao, C.;

- Glenn, K.; Wen, Y.; et al. Discovery of RG7112: A Small-Molecule MDM2 Inhibitor in Clinical Development. *ACS Med. Chem. Lett.* **2013**, *4* (5), 466–469. <https://doi.org/10.1021/ml4000657>.
- (128) Itoh, Y.; Ishikawa, M.; Naito, M.; Hashimoto, Y. Protein Knockdown Using Methyl Bestatin-Ligand Hybrid Molecules: Design and Synthesis of Inducers of Ubiquitination-Mediated Degradation of Cellular Retinoic Acid-Binding Proteins. *J. Am. Chem. Soc.* **2010**, *132* (16), 5820–5826. <https://doi.org/10.1021/ja100691p>.
- (129) Umezawa, H.; Aoyagi, T.; Suda, H.; Hamada, M.; Takeuchi, T. Bestatin, An Inhibitor of Aminopeptidase B, Produced by Actinomycetes. *J. Antibiot. (Tokyo)*. **1979**, *XXIX* (1), 97–99. <https://doi.org/10.7164/antibiotics.29.97>.
- (130) Orning, L.; Krivi, G.; Fitzpatrick, F. A. Leukotriene A4 Hydrolase: Inhibition by Bestatin and Intrinsic Aminopeptidase Activity Establish Its Functional Resemblance to Metallohydrolase Enzymes. *J. Biol. Chem.* **1991**, *266* (3), 1375–1378. <https://doi.org/10.1074/jbc.266.3.1375>.
- (131) Sekine, K.; Takubo, K.; Kikuchi, R.; Nishimoto, M.; Kitagawa, M.; Abe, F.; Nishikawa, K.; Tsuruo, T.; Naito, M. Small Molecules Destabilize CIAP1 by Activating Auto-Ubiquitylation. *J. Biol. Chem.* **2008**, *283* (14), 8961–8968. <https://doi.org/10.1074/jbc.M709525200>.
- (132) Itoh, Y.; Ishikawa, M.; Kitaguchi, R.; Okuhira, K.; Naito, M.; Hashimoto, Y. Double Protein Knockdown of CIAP1 and CRABP-II Using a Hybrid Molecule Consisting of ATRA and IAPs Antagonist. *Bioorg. Med. Chem. Lett.* **2012**, *22* (13), 4453–4457. <https://doi.org/10.1016/j.bmcl.2012.04.134>.
- (133) Demizu, Y.; Okuhira, K.; Motoi, H.; Ohno, A.; Shoda, T.; Fukuhara, K.; Okuda, H.; Naito, M.; Kurihara, M. Design and Synthesis of Estrogen Receptor Degradation Inducer Based on a Protein Knockdown Strategy. *Bioorg. Med. Chem. Lett.* **2012**, *22* (4), 1793–1796. <https://doi.org/10.1016/j.bmcl.2011.11.086>.
- (134) Itoh, Y.; Kitaguchi, R.; Ishikawa, M.; Naito, M.; Hashimoto, Y. Design, Synthesis and Biological Evaluation of Nuclear Receptor-Degradation Inducers. *Bioorg. Med. Chem.* **2011**, *19* (22), 6768–6778. <https://doi.org/10.1016/j.bmc.2011.09.041>.
- (135) Ohoka, N.; Nagai, K.; Hattori, T.; Okuhira, K.; Shibata, N.; Cho, N.; Naito, M. Cancer

- Cell Death Induced by Novel Small Molecules Degrading the TACC3 Protein via the Ubiquitin–Proteasome Pathway. *Cell Death Dis.* **2014**, *5* (11), 1–10. <https://doi.org/10.1038/cddis.2014.471>.
- (136) Buckley, D. L.; Van Molle, I.; Gareiss, P. C.; Tae, H. S.; Michel, J.; Noblin, D. J.; Jorgensen, W. L.; Ciulli, A.; Crews, C. M. Targeting the von Hippel-Lindau E3 Ubiquitin Ligase Using Small Molecules to Disrupt the VHL/HIF-1 α Interaction. *J. Am. Chem. Soc.* **2012**, *134* (10), 4465–4468. <https://doi.org/10.1021/ja209924v>.
- (137) Buckley, D. L.; Gustafson, J. L.; Van-Molle, I.; Roth, A. G.; Tae, H. S.; Gareiss, P. C.; Jorgensen, W. L.; Ciulli, A.; Crews, C. M. Small-Molecule Inhibitors of the Interaction between the E3 Ligase VHL and HIF1. *Angew. Chem. Int. Ed.* **2012**, *51* (46), 11463–11467. <https://doi.org/10.1002/anie.201206231>.
- (138) Van Molle, I.; Thomann, A.; Buckley, D. L.; So, E. C.; Lang, S.; Crews, C. M.; Ciulli, A. Dissecting Fragment-Based Lead Discovery at the von Hippel-Lindau Protein:Hypoxia Inducible Factor 1 α Protein-Protein Interface. *Chem. Biol.* **2012**, *19* (10), 1300–1312. <https://doi.org/10.1016/j.chembiol.2012.08.015>.
- (139) Galdeano, C.; Gadd, M. S.; Soares, P.; Sca, S.; Molle, I. Van; Birced, I.; Hewitt, S.; Dias, D. M.; Ciulli, A. Structure-Guided Design and Optimization of Small Molecules Targeting the Protein – Protein Interaction between the von Hippel – Lindau (VHL) E3 Ubiquitin Ligase and the Hypoxia Inducible Factor (HIF) Alpha Subunit with in Vitro Nanomolar Affinities. *J. Med. Chem.* **2014**, *57* (20), 8657–8663. <https://doi.org/10.1021/jm5011258>.
- (140) Filippakopoulos, P.; Qi, J.; Picaud, S.; Shen, Y.; Smith, W. B.; Fedorov, O.; Morse, E. M.; Keates, T.; Hickman, T. T.; Felletar, I.; et al. Selective Inhibition of BET Bromodomains. *Nature* **2010**, *468* (7327), 1067–1073. <https://doi.org/10.1038/nature09504>.
- (141) Gadd, M. .; Testa, A.; Lucas, X.; Chan, K. .; Chen, W.; Lamont, D. .; Zengerle, M.; Ciulli, A. Structural Basis of PROTAC Cooperative Recognition for Selective Protein Degradation. *Nat. Chem. Biol.* **2017**, *13* (5), 514–521. <https://doi.org/10.2210/PDB5T35/PDB>.
- (142) Whitty, A. Cooperativity and Biological Complexity. *Nat. Chem. Biol.* **2008**, *4* (8), 435–439. <https://doi.org/10.1038/nchembio0808-435>.

- (143) Buckley, D. L.; Raina, K.; Darricarrere, N.; Hines, J.; Gustafson, J. L.; Smith, I. E.; Miah, A. H.; Harling, J. D.; Crews, C. M. HaloPROTACS: Use of Small Molecule PROTACs to Induce Degradation of HaloTag Fusion Proteins. *ACS Chem. Biol.* **2015**, *10* (8), 1831–1837. <https://doi.org/10.1021/acscchembio.5b00442>.
- (144) Lai, A. C.; Toure, M.; Hellerschmied, D.; Salami, J.; Jaime-Figueroa, S.; Ko, E.; Hines, J.; Crews, C. M. Modular PROTAC Design for the Degradation of Oncogenic BCR-ABL. *Angew. Chem. Int. Ed.* **2016**, *55* (2), 807–810. <https://doi.org/10.1002/anie.201507634>.
- (145) Crew, A. P.; Raina, K.; Dong, H.; Qian, Y.; Wang, J.; Vigil, D.; Serebrenik, Y. V.; Hamman, B. D.; Morgan, A.; Ferraro, C.; et al. Identification and Characterization of von Hippel-Lindau-Recruiting Proteolysis Targeting Chimeras (PROTACs) of TANK-Binding Kinase 1. *J. Med. Chem.* **2018**, *61* (2), 583–598. <https://doi.org/10.1021/acs.jmedchem.7b00635>.
- (146) Gechijian, L. N.; Buckley, D. L.; Lawlor, M. A.; Reyes, J. M.; Paulk, J.; Ott, C. J.; Winter, G. E.; Erb, M. A.; Scott, T. G.; Xu, M.; et al. Functional TRIM24 Degradator via Conjugation of Ineffectual Bromodomain and VHL Ligands Article. *Nat. Chem. Biol.* **2018**, *14* (4), 405–412. <https://doi.org/10.1038/s41589-018-0010-y>.
- (147) Mahmood, T.; Yang, P. Western Blot: Technique, Theory, and Trouble Shooting. *N. Am. J. Med. Sci.* **2012**, *4* (9), 429–434. <https://doi.org/10.4103/1947-2714.100998>.
- (148) Miller, M. T.; Stromland, K. Teratogen Update: Thalidomide: A Review, with a Focus on Ocular Findings and New Potential Uses. *Teratology* **1999**, *60* (5), 306–321. [https://doi.org/10.1002/\(SICI\)1096-9926\(199911\)60:5<306::AID-TERA11>3.0.CO;2-Y](https://doi.org/10.1002/(SICI)1096-9926(199911)60:5<306::AID-TERA11>3.0.CO;2-Y).
- (149) Melchert, M.; List, A. The Thalidomide Saga. *Int. J. Biochem. Cell Biol.* **2007**, *39* (7–8), 1489–1499. <https://doi.org/10.1016/j.biocel.2007.01.022>.
- (150) Knobloch, J.; R  ther, U. Shedding Light on an Old Mystery: Thalidomide Suppresses Survival Pathways to Induce Limb Defects. *Cell Cycle* **2008**, *7* (9), 1121–1127. <https://doi.org/10.4161/cc.7.9.5793>.
- (151) Ito, T.; Ando, H.; Suzuki, T.; Ogura, T.; Hotta, K.; Imamura, Y.; Yamaguchi, Y.; Handa, H. Identification of a Primary Target Of. *Science (80-.)*. **2013**, *327* (2010), 1345–1350.

<https://doi.org/10.1126/science.1177319>.

- (152) Krönke, J.; Udeshi, N. D.; Narla, A.; Grauman, P.; Hurst, S. N.; McConkey, M.; Svinikina, T.; Heckl, D.; Comer, E.; Li, X.; et al. Lenalidomide Causes Selective Degradation of IKZF1 and IKZF3 in Multiple Myeloma Cells. *Science (80-.)*. **2014**, *343* (January), 301–306. <https://doi.org/10.1126/science.1244851>.
- (153) Lu, G.; Middleton, R. E.; Sun, H.; Naniong, M.; Christopher, J.; Mitsiades, C. S.; Wong, K.; Bradner, J. E.; William, G.; Chase, C. The Myeloma Drug Lenalidomide Promotes the Cereblon Dependent Destruction of Ikaros Proteins. *Science (80-.)*. **2014**, *343* (6168), 305–309. <https://doi.org/10.1126/science.1244917>.The.
- (154) Gandhi, A. K.; Kang, J.; Havens, C. G.; Conklin, T.; Ning, Y.; Wu, L.; Ito, T.; Ando, H.; Waldman, M. F.; Thakurta, A.; et al. Immunomodulatory Agents Lenalidomide and Pomalidomide Co-Stimulate T Cells by Inducing Degradation of T Cell Repressors Ikaros and Aiolos via Modulation of the E3 Ubiquitin Ligase Complex CRL4CRBN. *Br. J. Haematol.* **2014**, *164* (6), 811–821. <https://doi.org/10.1111/bjh.12708>.
- (155) Krönke, J.; Fink, E. C.; Hollenbach, P. W.; MacBeth, K. J.; Hurst, S. N.; Udeshi, N. D.; Chamberlain, P. P.; Mani, D. R.; Man, H. W.; Gandhi, A. K.; et al. Lenalidomide Induces Ubiquitination and Degradation of CK1 α in Del(5q) MDS. *Nature* **2015**, *523* (7559), 183–188. <https://doi.org/10.1038/nature14610>.
- (156) Petzold, G.; Fischer, E. S.; Thomä, N. H. Structural Basis of Lenalidomide-Induced CK1 α Degradation by the CRL4CRBN Ubiquitin Ligase. *Nature* **2016**, *532* (7597), 127–130. <https://doi.org/10.1038/nature16979>.
- (157) Matyskiela, M. E.; Lu, G.; Ito, T.; Pagarigan, B.; Lu, C.-C.; Miller, K.; Fang, W.; Wang, N.-Y.; Nguyen, D.; Houston, J.; et al. A Novel Cereblon Modulator Recruits GSPT1 to the CRL4CRBN Ubiquitin Ligase. *Nature* **2016**, *535* (7611), 252–257. <https://doi.org/10.1038/nature18611>.
- (158) Lu, J.; Qian, Y.; Altieri, M.; Dong, H.; Wang, J.; Raina, K.; Hines, J.; Winkler, J. D.; Crew, A. P.; Coleman, K.; et al. Hijacking the E3 Ubiquitin Ligase Cereblon to Efficiently Target BRD4. *Chem. Biol.* **2015**, *22* (6), 755–763. <https://doi.org/10.1016/j.chembiol.2015.05.009>.
- (159) Shimamura, T.; Chen, Z.; Soucheray, M.; Carretero, J.; Kikuchi, E.; Tchaicha, J. H.; Gao,

- Y.; Cheng, K. A.; Cohoon, T. J.; Qi, J.; et al. Efficacy of BET Bromodomain Inhibition in KRAS-Mutant Non-Small Cell Lung Cancer. *Clin. Cancer Res.* **2013**, *19* (22), 6183–6192. <https://doi.org/10.1158/1078-0432.CCR-12-3904>.
- (160) Winter, G. E.; Buckley, D. L.; Paulk, J.; Roberts, J. M.; Souza, A.; Dhe-Paganon, S.; Bradner, J. E. Phthalimide Conjugation as a Strategy for in Vivo Target Protein Degradation. *Science* **2015**, *348* (6241), 1376–1381. <https://doi.org/10.1126/science.aab1433>.
- (161) Lou, K.-J. PROTAC the Protein. *Sci. Exch.* **2012**, *5* (20). <https://doi.org/10.1038/scibx.2012.514>.
- (162) Chi, K. R. Drug Developers Delve into the Cell’s Trash-Disposal Machinery. *Nat. Rev. Drug Discov.* **2016**, *15* (5), 295–297. <https://doi.org/10.1038/nrd.2016.86>.
- (163) Guo, J.; Liu, J.; Wei, W. Degrading Proteins in Animals: “PROTAC”Tion Goes in Vivo. *Cell Res.* **2019**, *29* (3), 179–180. <https://doi.org/10.1038/s41422-019-0144-9>.
- (164) An, W. F.; Tolliday, N. J. *Introduction: Cell-Based Assays for High-Throughput Screening*; 2009; Vol. 486. https://doi.org/10.1007/978-1-60327-545-3_1.
- (165) LANCE Ultra TR-FRET Kinase Assays http://www.perkinelmer.com.cn/content/relatedmaterials/brochures/fly_lanceultraanew.pdf (accessed Oct 18, 2017).
- (166) Oshimi, K.; Oshimi, Y.; Satake, M.; Mizoguchi, H. Natural Killer-Mediated Target Lysis of Normal and Malignant Target Cells, and Its Regulation by Monocytes. *J. Exp. Med.* **1985**, *162* (2), 472–486. <https://doi.org/10.1084/jem.162.2.472>.
- (167) Sekar, R. B.; Periasamy, A. Fluorescence Resonance Energy Transfer (FRET) Microscopy Imaging of Live Cell Protein Localizations. *J. Cell Biol.* **2003**, *160* (5), 629–633. <https://doi.org/10.1083/jcb.200210140>.
- (168) Bar-Beris, C.; Carry, J.-C.; Doerflinger, G.; Barbalat-Damour, D.; Clerc, F.-F.; Minoux, H. Hydrazinocarbonyl-Thieno[2,3-c]Pyrazoles, Their Preparation, Compositions Containing Them and Their Use as Inhibitors of Protein Kinases. FR2882751B1, 2006.
- (169) Savitski, M. M.; Zinn, N.; Faelth-Savitski, M.; Poeckel, D.; Gade, S.; Becher, I.; Muelbaier, M.; Wagner, A. J.; Strohmmer, K.; Werner, T.; et al. Multiplexed Proteome Dynamics Profiling Reveals Mechanisms Controlling Protein Homeostasis Resource

- Multiplexed Proteome Dynamics Profiling Reveals Mechanisms Controlling Protein Homeostasis. *Cell* **2018**, *173* (1), 260-274.e25. <https://doi.org/10.1016/j.cell.2018.02.030>.
- (170) Overview of Western Blotting <https://www.thermofisher.com/uk/en/home/life-science/protein-biology/protein-biology-learning-center/protein-biology-resource-library/pierce-protein-methods/overview-western-blotting.html> (accessed Sep 25, 2019).
- (171) Kelder, J.; D. J. Grootenhuys, P.; M. Bayada, D.; P. C. Delbressine, L.; Ploemen, J.-P. Polar Molecular Surface as a Dominating Determinant for Oral Absorption and Brain Penetration of Drugs. *Pharm. Res.* **1999**, *16* (10), 1514–1519. <https://doi.org/10.1023/A:1015040217741>.
- (172) Churcher, I. Protac-Induced Protein Degradation in Drug Discovery: Breaking the Rules or Just Making New Ones? *J. Med. Chem.* **2018**, *61* (2), 444–452. <https://doi.org/10.1021/acs.jmedchem.7b01272>.
- (173) Gadd, M. S.; Testa, A.; Lucas, X.; Chan, K. H.; Chen, W.; Lamont, D. J.; Zengerle, M.; Ciulli, A. Structural Basis of PROTAC Cooperative Recognition for Selective Protein Degradation. *Nat. Chem. Biol.* **2017**, *13* (5), 514–521. <https://doi.org/10.1038/nchembio.2329>.
- (174) Chan, K. H.; Zengerle, M.; Testa, A.; Ciulli, A. Impact of Target Warhead and Linkage Vector on Inducing Protein Degradation: Comparison of Bromodomain and Extra-Terminal (BET) Degraders Derived from Triazolodiazepine (JQ1) and Tetrahydroquinoline (I-BET726) BET Inhibitor Scaffolds. *J. Med. Chem.* **2018**, *61* (2), 504–513. <https://doi.org/10.1021/acs.jmedchem.6b01912>.
- (175) Zimmermann, K.; Sang, X.; Mastalerz, H. A.; Johnson, W. L.; Zhang, G.; Liu, Q.; Batt, D.; Lombardo, L. J.; Vyas, D.; Trainor, G. L.; et al. 9H -Carbazole-1-Carboxamides as Potent and Selective JAK2 Inhibitors. *Bioorg. Med. Chem. Lett.* **2015**, *25* (14), 2809–2812. <https://doi.org/10.1016/j.bmcl.2015.04.101>.
- (176) Lim, J.; Taoka, B.; Otte, R. D.; Spencer, K.; Dinsmore, C. J.; Altman, M. D.; Chan, G.; Rosenstein, C.; Sharma, S.; Su, H.; et al. Discovery of 1-Amino-5H-Pyrido[4,3-b]Indol-4-Carboxamide Inhibitors of Janus Kinase 2 (JAK2) for the Treatment of Myeloproliferative Disorders. *J. Med. Chem.* **2011**, *54* (20), 7334–7349.

<https://doi.org/10.1021/jm200909u>.

- (177) Fazakerley, N.; Needham, D.; Wellaway, C.; Barker, M.; Tape, D.; Shah, R. R.; Redmond, J.; Coe, D. *GSK Unpublished Work*; GSK.
- (178) Almansa Rosales, C.; Salas Solana, J.; Solvia Coliva, R.; Rodriguez Escrich, S.; Sicre Gonzalez, M. C. N-Containing Heteroaryl Derivatives As JAK3 Kinase Inhibitors. WO 2011/051452 A1, 2011.
- (179) Gerspacher, M.; Furet, P.; Vangrevelinghe, E.; Pissot Soldermann, C.; Gaul, C.; Holzer, P. Preparation of Quinoxalines, Particularly Heterocyclyl-Substituted Diarylquinoxalines, as Inhibitors of the Tyrosine Kinase Activity of Janus Kinases for Use in the Treatment of Immune and Proliferative Disorders. WO 2008148867, 2008.
- (180) Coe, D.; Fazakerley, N.; Needham, D.; Redmond, J.; Shah, R. R.; Wellaway, C. *GSK Unpublished Work*.
- (181) Chung, C.-W.; Neu, M. *GSK Unpublished Work*.
- (182) Baffert, F.; Régnier, C. H.; De Pover, A.; Pissot-Soldermann, C.; Tavares, G. A.; Blasco, F.; Brueggen, J.; Chène, P.; Drucekes, P.; Erdmann, D.; et al. Potent and Selective Inhibition of Polycythemia by the Quinoxaline JAK2 Inhibitor NVP-BSK805. *Mol. Cancer Ther.* **2010**, *9* (7), 1945–1955. <https://doi.org/10.1158/1535-7163.MCT-10-0053>.
- (183) Buckley, D. L.; Raina, K.; Darricarrere, N.; Hines, J.; Gustafson, L. J.; Smith, I. E.; Miah, A. H.; Harling, J. D.; Crews, C. M. HaloPROTACS: Use of Small Molecule PROTACs to Induce Degradation of HaloTag Fusion Proteins. *ACS Chem. Biol.* **2015**, *10* (8), 1831–1837. <https://doi.org/10.1021/acscchembio.5b00442>.
- (184) Doak, B. C.; Over, B.; Giordanetto, F.; Kihlberg, J. Oral Druggable Space beyond the Rule of 5: Insights from Drugs and Clinical Candidates. *Chem. Biol.* **2014**, *21* (9), 1115–1142. <https://doi.org/10.1016/j.chembiol.2014.08.013>.
- (185) Harling, J. D.; Smith, I. E. D. Preparation of IAP E3 Ligase Directed Proteolysis Targeting Chimeric Molecules. WO 2016169989, 2016.
- (186) Galdeano, C.; Gadd, M. S.; Soares, P.; Scaffidi, S.; Van Molle, I.; Birced, I.; Hewitt, S.; Dias, D. M.; Ciulli, A. Structure-Guided Design and Optimization of Small Molecules Targeting the Protein–Protein Interaction between the von Hippel–Lindau (VHL) E3

- Ubiquitin Ligase and the Hypoxia Inducible Factor (HIF) Alpha Subunit with in Vitro Nanomolar Affinities. *J. Med. Chem.* **2014**, *57* (20), 8657–8663. <https://doi.org/10.1021/jm5011258>.
- (187) Rackham, M. *GSK Unpublished Work*; GSK.
- (188) Rostovtsev, V. V.; Green, L. G.; Fokin, V. V.; Sharpless, K. B. A Stepwise Huisgen Cycloaddition Process: Copper(I)-Catalyzed Regioselective “Ligation” of Azides and Terminal Alkynes. *Angew. Chem. Int. Ed.* **2002**, *41* (14), 2596–2599. [https://doi.org/10.1002/1521-3773\(20020715\)41:14<2596::AID-ANIE2596>3.0.CO;2-4](https://doi.org/10.1002/1521-3773(20020715)41:14<2596::AID-ANIE2596>3.0.CO;2-4).
- (189) Das, S.; Zhou, S.; Addis, D.; Enthaler, S.; Junge, K.; Beller, M. Selective Catalytic Reductions of Amides and Nitriles to Amines. *Top. Catal.* **2010**, *53* (15–18), 979–984. <https://doi.org/10.1007/s11244-010-9526-4>.
- (190) Nicewicz, D. A.; Macmillan, D. W. C. Merging Photoredox Catalysis with Organocatalysis: The Direct Asymmetric Alkylation of Aldehydes. *Science (80-.)*. **2008**, *105* (2005), 77–80. <https://doi.org/10.1126/science.1161976>.
- (191) Ischay, M. A.; Anzovino, M. E.; Du, J.; Yoon, T. P. Efficient Visible Light Photocatalysis of [2+2] Enone Cycloadditions. *J. Am. Chem. Soc.* **2008**, *130* (39), 12886–12887. <https://doi.org/10.1021/ja805387f>.
- (192) Cowell, J. J.; Lambert, R. M.; Santra, K.; Williams, F. J.; Cropley, R. L.; Palermo, A.; Lopez, N.; Illas, F.; Hartley, G. W.; Christopher, P.; et al. Photoredox Activation for the Direct β -Arylation of Ketones and Aldehydes. *Science (80-.)*. **2013**, *339* (6127), 1593–1596. <https://doi.org/10.1126/science.1232993>.
- (193) Hamilton, D. S.; Nicewicz, D. A. Direct Catalytic Anti-Markovnikov Hydroetherification of Alkenols. *J. Am. Chem. Soc.* **2012**, *134* (45), 18577–18580. <https://doi.org/10.1021/ja309635w>.
- (194) Narayanam, J. M. R.; Tucker, J. W.; Stephenson, C. R. J. Electron-Transfer Photoredox Catalysis: Development of a Tin-Free Reductive Dehalogenation Reaction. *J. Am. Chem. Soc.* **2009**, *131* (25), 8756–8757. <https://doi.org/10.1021/ja9033582>.
- (195) Terrett, J. A.; Cuthbertson, J. D.; Shurtleff, V. W.; MacMillan, D. W. C. Switching on Elusive Organometallic Mechanisms with Photoredox Catalysis. *Nature* **2015**, *524*

- (7565), 330–334. <https://doi.org/10.1038/nature14875>.
- (196) Matsunaga, P. T.; Hillhouse, G. L.; Rheingold, A. L. Oxygen-Atom Transfer from Nitrous Oxide to a Nickel Metallacycle. Synthesis, Structure, and Reactions of [Cyclic] (2,2'-Bipyridine)Ni(OCH₂CH₂CH₂CH₂). *J. Am. Chem. Soc.* **1993**, *5* (115), 2075–2077. <https://doi.org/10.1021/ja00058a085>.
- (197) Matsunaga, P. T.; Mavropoulos, J. C.; Hillhouse, G. L. Oxygen-Atom Transfer from Nitrous Oxide (N=N=O) to Nickel Alkyls. Syntheses and Reactions of Nickel(II) Alkoxides. *Polyhedron* **1995**, *14* (1), 175–185. [https://doi.org/10.1016/0277-5387\(94\)00330-H](https://doi.org/10.1016/0277-5387(94)00330-H).
- (198) Han, R.; Hillhouse, G. L. Carbon-Oxygen Reductive-Elimination from Nickel(II) Oxametallacycles and Factors That Control Formation of Ether, Aldehyde, Alcohol, or Ester Products. *J. Am. Chem. Soc.* **1997**, *119* (34), 8135–8136. <https://doi.org/10.1021/ja9714999>.
- (199) Lowry, M. S.; Goldsmith, J. I.; Slinker, J. D.; Pascal, R. A.; Malliaras, G. G.; Bernhard, S.; Rohl, R. Single-Layer Electroluminescent Devices and Photoinduced Hydrogen Production from an Ionic Iridium(III) Complex. *Chem. Mater.* **2005**, *17* (23), 5712–5719. <https://doi.org/10.1021/cm051312>.
- (200) Rosenmund, K. W.; Struck, E. Das Am Ringkohlenstoff Gebundene Halogen Und Sein Ersatz Durch Andere Substituenten. I. Mitteilung: Ersatz Des Halogens Durch Die Carboxylgruppe. *Berichte der Dtsch. Chem. Gesellschaft* **1919**, *52* (8), 1749–1756. <https://doi.org/10.1002/cber.19190520840>.
- (201) Ellis, G. P.; Romney-Alexander, T. M. Cyanation of Aromatic Halides. *Chem. Rev.* **1987**, *87* (4), 779–794. <https://doi.org/10.1021/cr00080a006>.
- (202) Sandmeyer, T. Ueber Die Ersetzung Der Amid-Gruppe Durch Chlor, Brom Und Cyan in Den Aromatischen Substanzen. *Berichte der Dtsch. Chem. Gesellschaft* **1884**, *17* (2), 2650–2653. <https://doi.org/10.1002/cber.188401702202>.
- (203) Hodgson, H. H. The Sandmeyer Reaction. *Chem. Rev.* **1947**, *40* (2), 251–277. <https://doi.org/10.1021/cr60126a003>.
- (204) Senecal, T. D.; Shu, W.; Buchwald, S. L. A General, Practical Palladium-Catalyzed Cyanation of (Hetero)Aryl Chlorides and Bromides. *Angew. Chem. Int. Ed.* **2013**, *52*

- (38), 10035–10039. <https://doi.org/10.1002/anie.201304188>.
- (205) Capello, C.; Fischer, U.; Hungerbühler, K. What Is a Green Solvent? A Comprehensive Framework for the Environmental Assessment of Solvents. *Green Chem.* **2007**, *9* (9), 927–934. <https://doi.org/10.1039/b617536h>.
- (206) Cohen, D. T.; Buchwald, S. L. Mild Palladium-Catalyzed Cyanation of (Hetero)Aryl Halides and Triflates in Aqueous Media. *Org. Lett.* **2015**, *17* (2), 202–205. <https://doi.org/10.1021/ol5032359>.
- (207) Ishii, G.; Harigae, R.; Moriyama, K.; Togo, H. Practical One-Pot Conversion of Aryl Bromides and β -Bromostyrenes into Aromatic Nitriles and Cinnamitriles. *Tetrahedron* **2013**, *69* (5), 1462–1469. <https://doi.org/10.1016/j.tet.2012.12.022>.
- (208) Kaisalo, L. H.; Hase, T. A. Cleavage of the THP Protecting Group under Pd/C-Catalyzed Hydrogenation Conditions. *Tetrahedron Lett.* **2001**, *42* (43), 7699–7701. [https://doi.org/10.1016/S0040-4039\(01\)01630-6](https://doi.org/10.1016/S0040-4039(01)01630-6).
- (209) Handy, S. T.; Zhang, Y. A Simple Guide for Predicting Regioselectivity in the Coupling of Polyhaloheteroaromatics. *Chem. Commun.* **2006**, *3* (1), 299–301. <https://doi.org/10.1039/b512948f>.
- (210) Almond-Thynne, J.; Blakemore, D. C.; Pryde, D. C.; Spivey, A. C. Site-Selective Suzuki-Miyaura Coupling of Heteroaryl Halides – Understanding the Trends for Pharmaceutically Important Classes. *Chem. Sci.* **2017**, *8* (1), 1–23. <https://doi.org/10.1039/C6SC02118B>.
- (211) Anderson, S. C.; Handy, S. T. One-Pot Double Suzuki Couplings of Dichloropyrimidines. *Synthesis (Stuttg.)* **2010**, *16* (2), 2721–2724. <https://doi.org/10.1016/j.pestbp.2011.02.012>. Investigations.
- (212) Himo, F.; Lovell, T.; Hilgraf, R.; Rostovtsev, V. V.; Noodleman, L.; Sharpless, K. B.; Fokin, V. V. Copper(I)-Catalyzed Synthesis of Azoles. DFT Study Predicts Unprecedented Reactivity and Intermediates. *J. Am. Chem. Soc.* **2005**, *127* (1), 210–216. <https://doi.org/10.1021/ja0471525>.
- (213) Rodionov, V. O.; Fokin, V. V.; Finn, M. G. Mechanism of the Ligand-Free CuI-Catalyzed Azide-Alkyne Cycloaddition Reaction. *Angew. Chem. Int. Ed.* **2005**, *44* (15), 2210–2215. <https://doi.org/10.1002/anie.200461496>.

- (214) Worrell, B. T.; Malik, J. a.; Fokin, V. V. Direct Evidence of a Dinuclear Copper Intermediate in Cu(I)-Catalyzed Azide-Alkyne Cycloadditions. *Science (80-.)*. **2013**, *340* (6131), 457–460. <https://doi.org/10.1126/science.1229506>.
- (215) Friis, S. D.; Lindhardt, A. T.; Skrydstrup, T. The Development and Application of Two-Chamber Reactors and Carbon Monoxide Precursors for Safe Carbonylation Reactions. *Acc. Chem. Res.* **2016**, *49* (4), 594–605. <https://doi.org/10.1021/acs.accounts.5b00471>.
- (216) Thorarensen, A.; Banker, M. E.; Fensome, A.; Telliez, J.-B.; Juba, B.; Vincent, F.; Czerwinski, R. M.; Casimiro-Garcia, A. ATP-Mediated Kinome Selectivity: The Missing Link in Understanding the Contribution of Individual JAK Kinase Isoforms to Cellular Signaling. *ACS Chem. Biol.* **2014**, *9* (7), 1552–1558. <https://doi.org/10.1021/cb5002125>.
- (217) Mateus, A.; Gordon, L. J.; Wayne, G. J.; Almqvist, H.; Axelsson, H.; Seashore-Ludlow, B.; Treyer, A.; Matsson, P.; Lundbäck, T.; West, A.; et al. Prediction of Intracellular Exposure Bridges the Gap between Target- and Cell-Based Drug Discovery. *Proc. Natl. Acad. Sci.* **2017**, *114* (30), E6231–E6239. <https://doi.org/10.1073/pnas.1701848114>.
- (218) Proteinatlas.org <https://www.proteinatlas.org/ENSG00000101966-XIAP/cell> (accessed Sep 27, 2018).
- (219) Bondeson, D. P.; Mares, A.; Smith, I. E. D.; Ko, E.; Campos, S.; Miah, A. H.; Mulholland, K. E.; Routly, N.; Buckley, D. L.; Gustafson, J. L.; et al. Catalytic in Vivo Protein Knockdown by Small-Molecule PROTACs. *Nat. Chem. Biol.* **2015**, *11* (8), 611–617. <https://doi.org/10.1038/nchembio.1858>.
- (220) XIAP <https://www.proteinatlas.org/ENSG00000101966-XIAP/tissue>.
- (221) CRBN <https://www.proteinatlas.org/ENSG00000113851-CRBN/tissue>.
- (222) VHL <https://www.proteinatlas.org/ENSG00000134086-VHL/tissue>.
- (223) Emanuele, M. J.; Elia, A. E. H.; Xu, Q.; Thoma, C. R.; Izhar, L.; Leng, Y.; Guo, A.; Chen, Y. N.; Rush, J.; Hsu, P. W. C.; et al. Global Identification of Modular Cullin-RING Ligase Substrates. *Cell* **2011**, *147* (2), 459–474. <https://doi.org/10.1016/j.cell.2011.09.019>.
- (224) Udeshi, N. D.; Svinkina, T.; Mertins, P.; Kuhn, E.; Mani, D. R.; Qiao, J. W.; Carr, S. A. Refined Preparation and Use of Anti-Diglycine Remnant (K-ε-GG) Antibody Enables

- Routine Quantification of 10,000s of Ubiquitination Sites in Single Proteomics Experiments. *Mol. Cell. Proteomics* **2013**, *12* (3), 825–831. <https://doi.org/10.1074/mcp.O112.027094>.
- (225) Wagner, S. A.; Beli, P.; Weinert, B. T.; Nielsen, M. L.; Cox, J.; Mann, M.; Choudhary, C. A Proteome-Wide, Quantitative Survey of In Vivo Ubiquitylation Sites Reveals Widespread Regulatory Roles. *Mol. Cell. Proteomics* **2011**, *10* (10), M111.013284. <https://doi.org/10.1074/mcp.M111.013284>.
- (226) Sarraf, S. A.; Raman, M.; Guarani-Pereira, V.; Sowa, M. E.; Huttlin, E. L.; Gygi, S. P.; Harper, J. W. Landscape of the PARKIN-Dependent Ubiquitylome in Response to Mitochondrial Depolarization. *Nature* **2013**, *496* (7445), 372–376. <https://doi.org/10.1038/nature12043>.
- (227) Zinn, N. *CellZome Unpublished Work*; Cellzome GmbH, GlaxoSmithKline, 2017.
- (228) Behrmann, I.; Smyczek, T.; Heinrich, P. C.; Schmitz-Van De Leur, H.; Komyod, W.; Giese, B.; Müller-Newen, G.; Haan, S.; Haan, C. Janus Kinase (Jak) Subcellular Localization Revisited: The Exclusive Membrane Localization of Endogenous Janus Kinase 1 by Cytokine Receptor Interaction Uncovers the Jak-receptor Complex to Be Equivalent to a Receptor Tyrosine Kinase. *J. Biol. Chem.* **2004**, *279* (34), 35486–35493. <https://doi.org/10.1074/jbc.M404202200>.
- (229) Bondeson, D. P.; Smith, B. E.; Burslem, G. M.; Buhimschi, A. D.; Hines, J.; Jaime-Figueroa, S.; Wang, J.; Hamman, B. D.; Ishchenko, A.; Crews, C. M. Lessons in PROTAC Design from Selective Degradation with a Promiscuous Warhead. *Cell Chem. Biol.* **2018**, *25* (1), 78-87.e5. <https://doi.org/10.1016/j.chembiol.2017.09.010>.
- (230) Huang, H. T.; Dobrovolsky, D.; Paulk, J.; Yang, G.; Weisberg, E. L.; Doctor, Z. M.; Buckley, D. L.; Cho, J. H.; Ko, E.; Jang, J.; et al. A Chemoproteomic Approach to Query the Degradable Kinome Using a Multi-Kinase Degradator. *Cell Chem. Biol.* **2018**, *25* (1), 88-99.e6. <https://doi.org/10.1016/j.chembiol.2017.10.005>.
- (231) Smith, B. E.; Wang, S. L.; Jaime-Figueroa, S.; Harbin, A.; Wang, J.; Hamman, B. D.; Crews, C. M. Differential PROTAC Substrate Specificity Dictated by Orientation of Recruited E3 Ligase. *Nat. Commun.* **2019**, *10* (1), 1–13. <https://doi.org/10.1038/s41467-018-08027-7>.

- (232) Field, S. D.; Arkin, J.; Li, J.; Jones, L. H. Selective Downregulation of JAK2 and JAK3 by an ATP-Competitive Pan-JAK Inhibitor. *ACS Chem. Biol.* **2017**, *12* (5), 1183–1187. <https://doi.org/10.1021/acscchembio.7b00116>.

9 Appendix

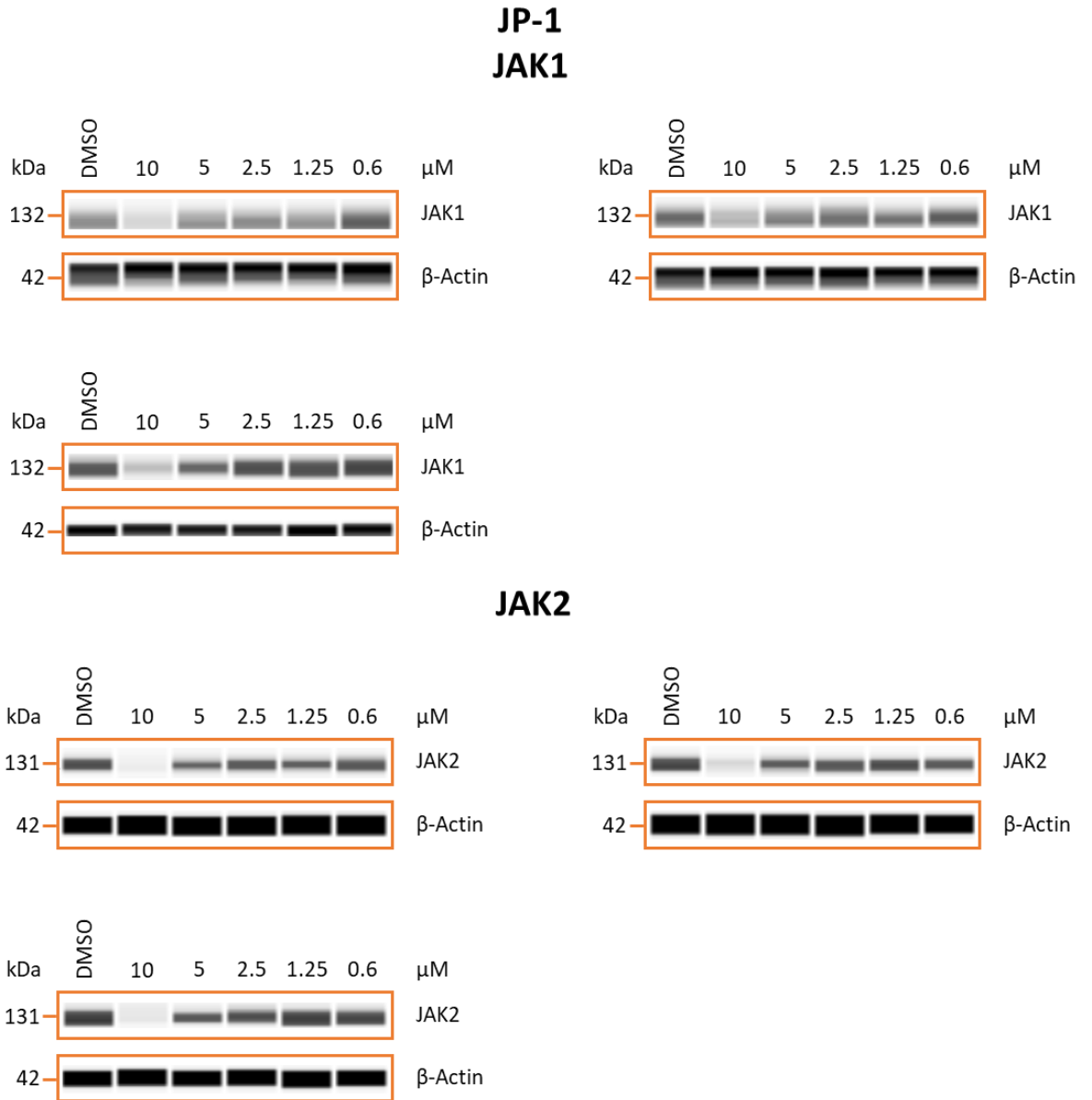


Fig 84 Western blot visualisations generated on a capillary-based Wes™ system of JAK1 and JAK2 protein levels in THP-1 cells treated with JP-1 on three independent test occasions.

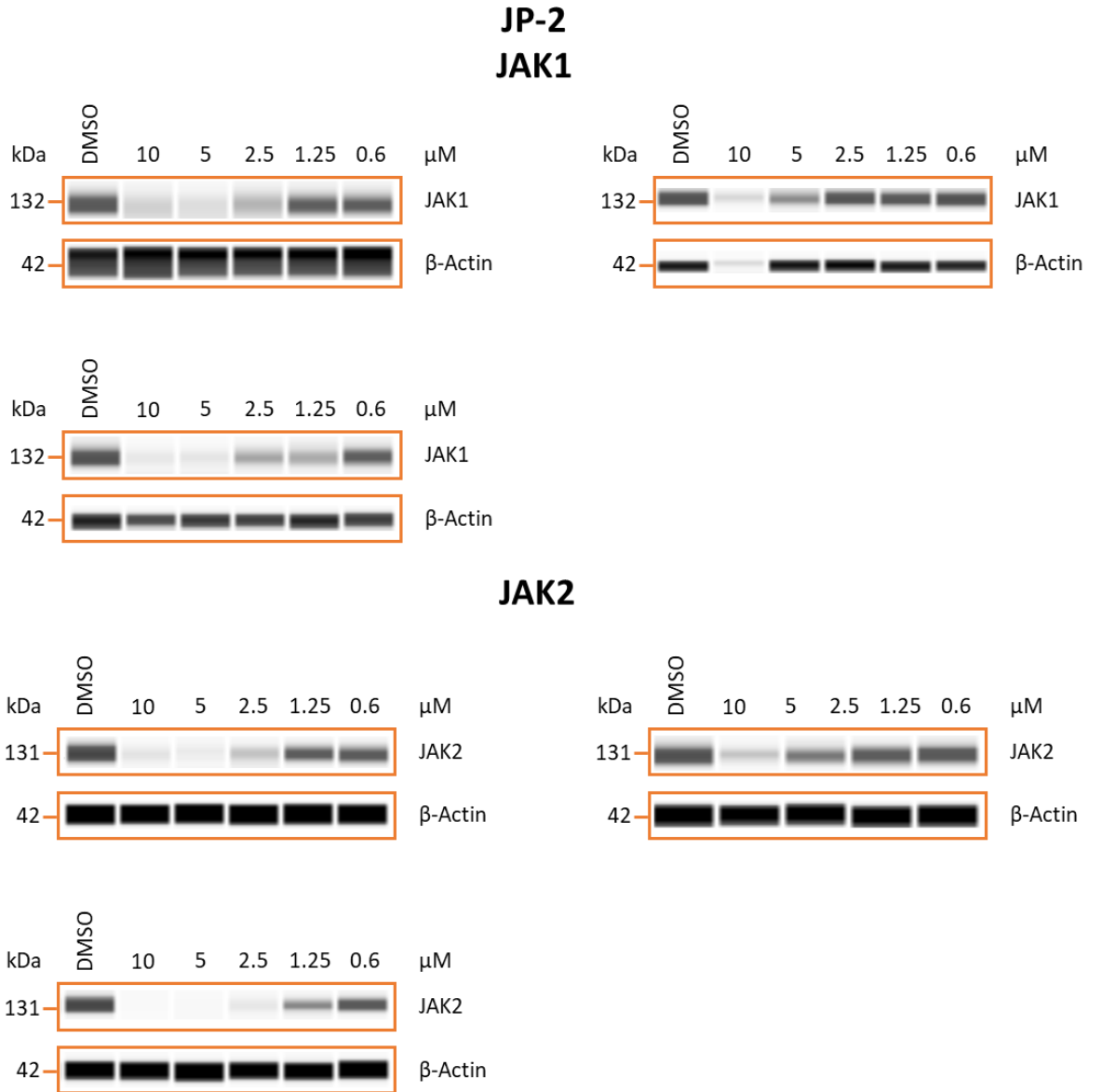


Fig 85 Western blot visualisations generated on a capillary-based Wes™ system of JAK1 and JAK2 protein levels in THP-1 cells treated with JP-2 on three independent test occasions.

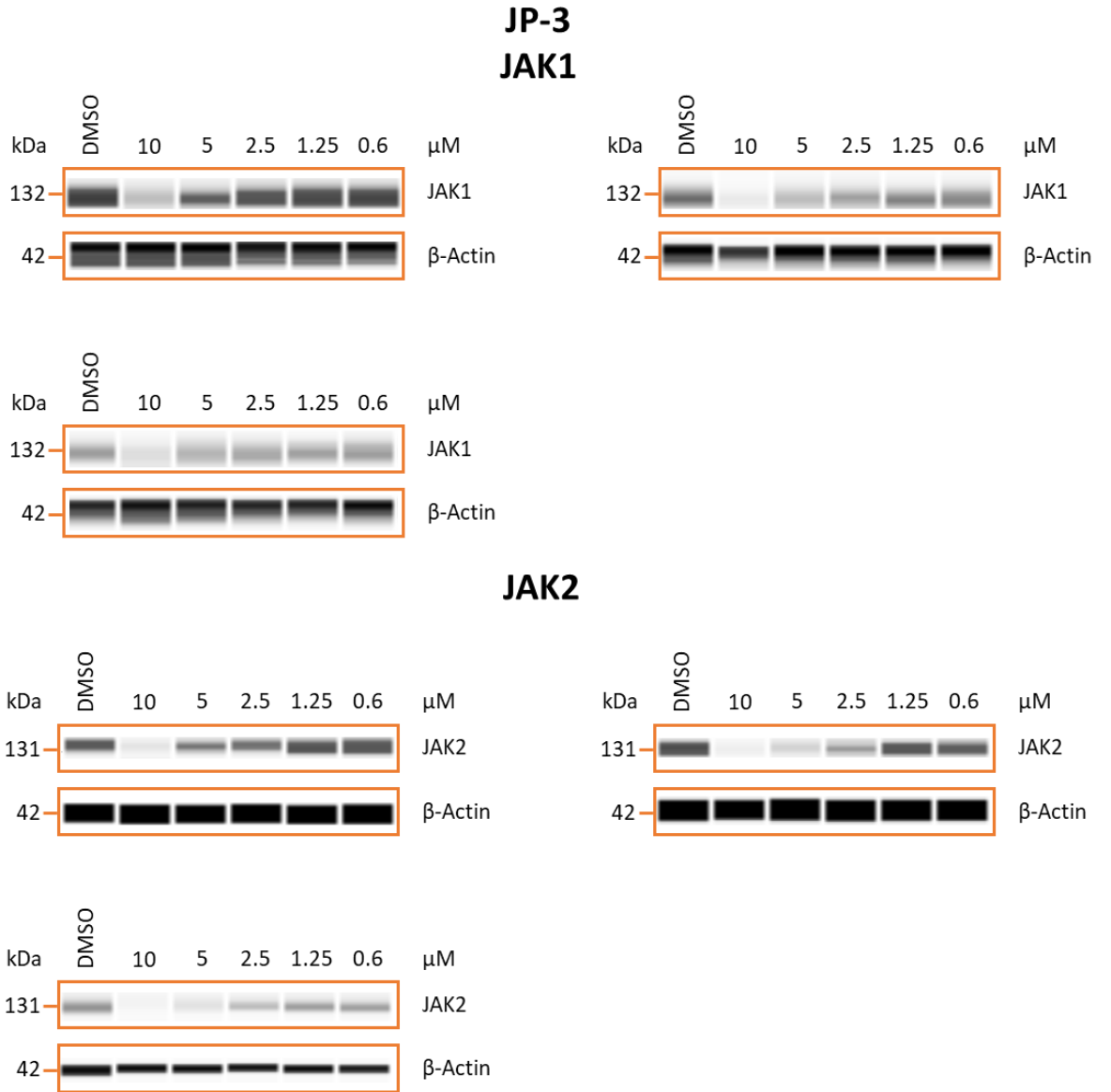


Fig 86 Western blot visualisations generated on a capillary-based Wes™ system of JAK1 and JAK2 protein levels in THP-1 cells treated with JP-3 on three independent test occasions.

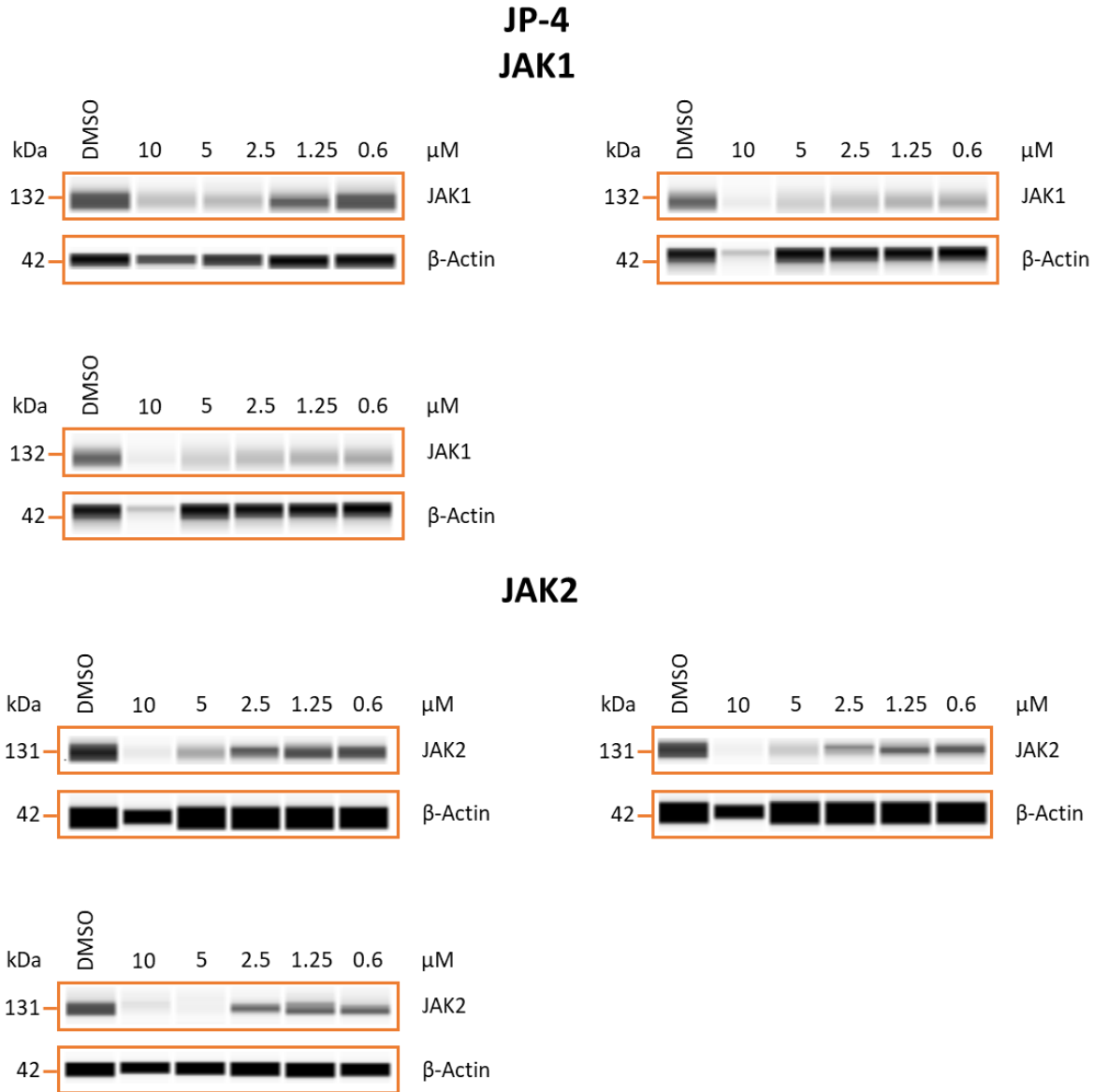


Fig 87 Western blot visualisations generated on a capillary-based Wes™ system of JAK1 and JAK2 protein levels in THP-1 cells treated with JP-4 on three independent test occasions. β

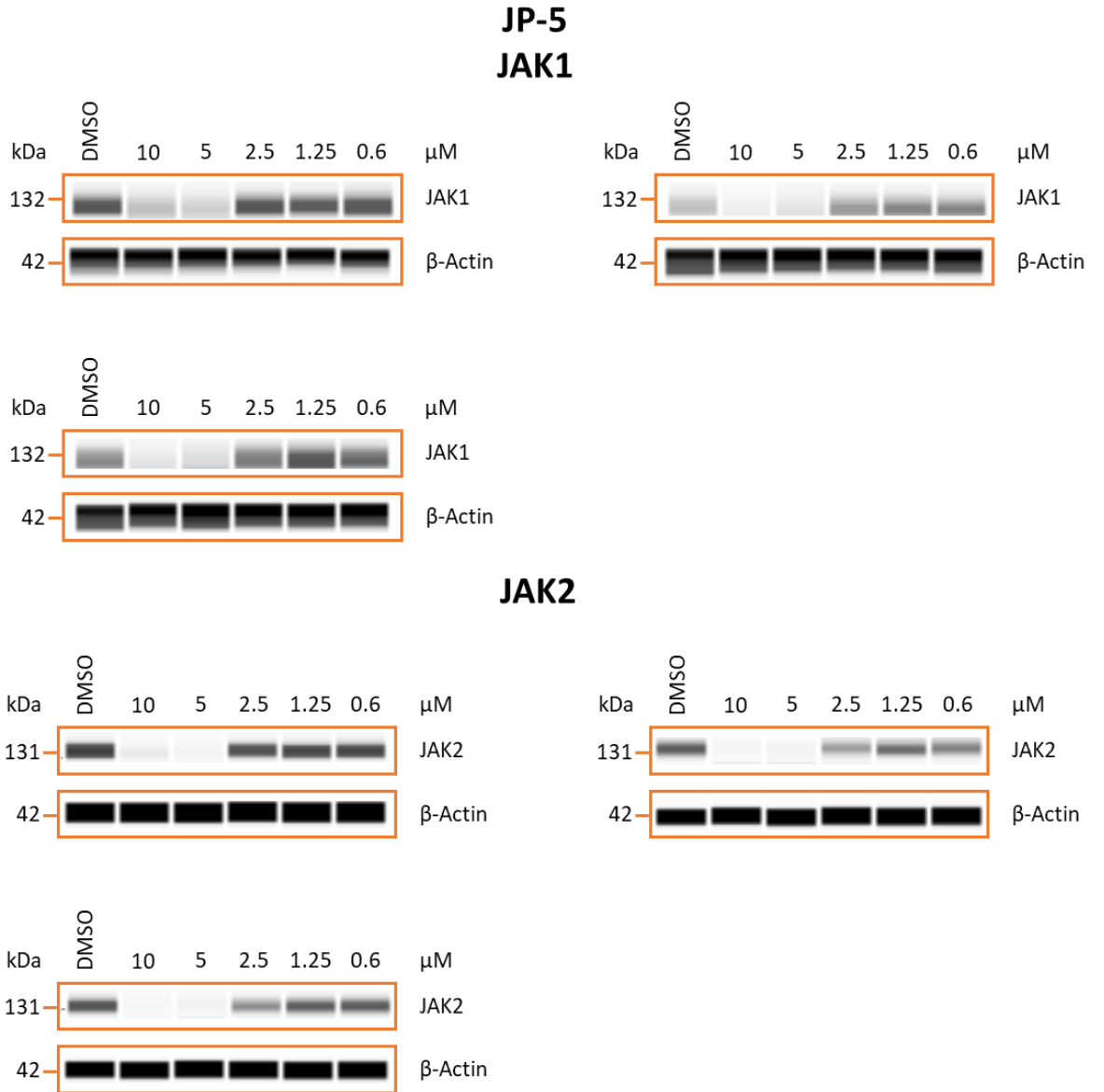
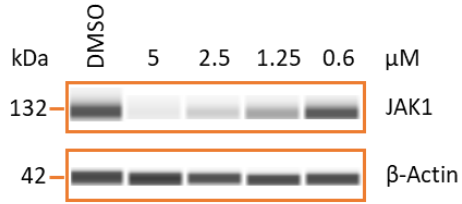
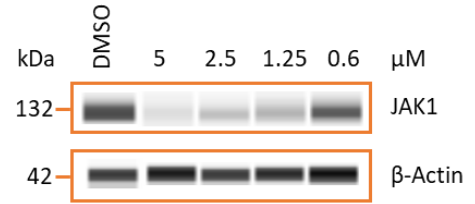
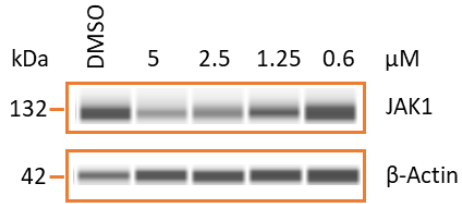


Fig 88 Western blot visualisations generated on a capillary-based Wes™ system of JAK1 and JAK2 protein levels in THP-1 cells treated with JP-5 on three independent test occasions.

**JP-6
JAK1**



JAK2

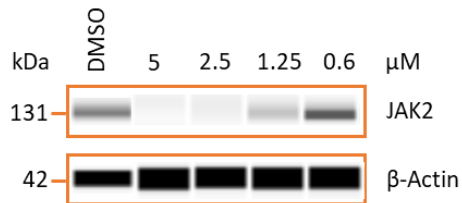
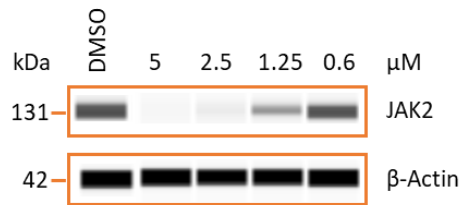
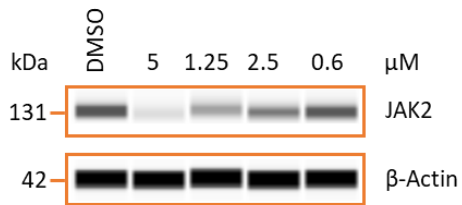


Fig 89 Western blot visualisations generated on a capillary-based Wes™ system of JAK1 and JAK2 protein levels in THP-1 cells treated with JP-6 on three independent test occasions.

JP-6 Inverse Blots JAK1

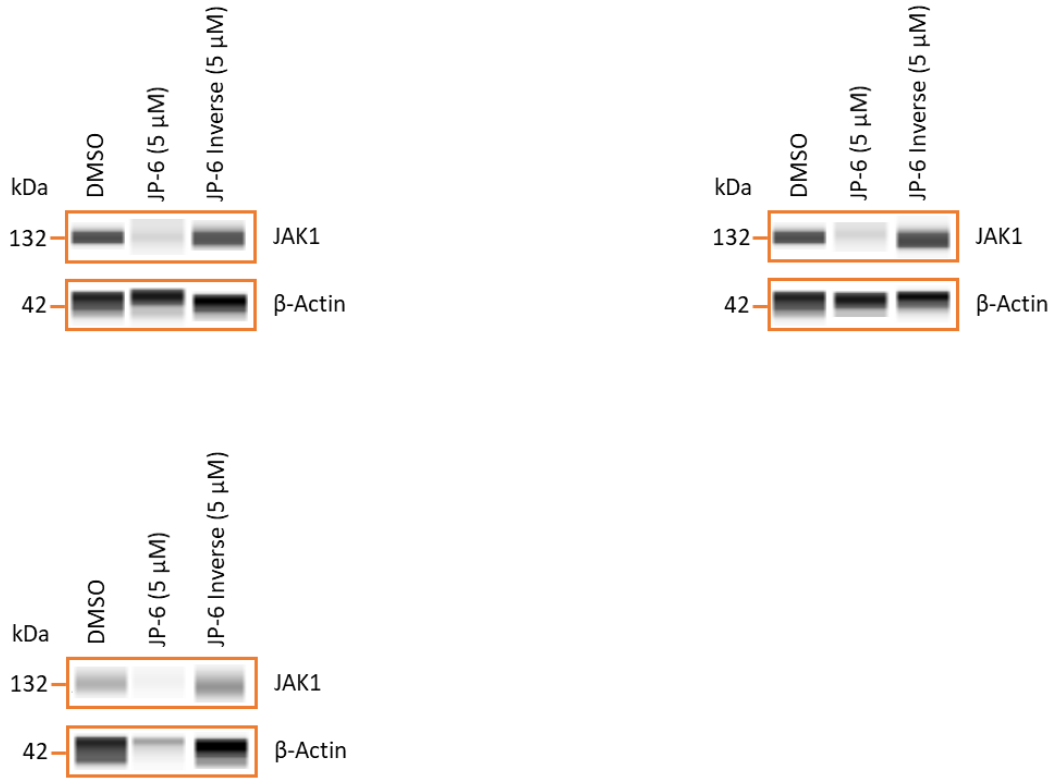


Fig 90 Western blot visualisations generated on a capillary-based Wes™ system of JAK1 protein levels in THP-1 cells treated with JP-6 and JP-6 Inverse (IAP-inactive PROTAC), on three independent test occasions.

JP-6 Inverse Blots JAK2

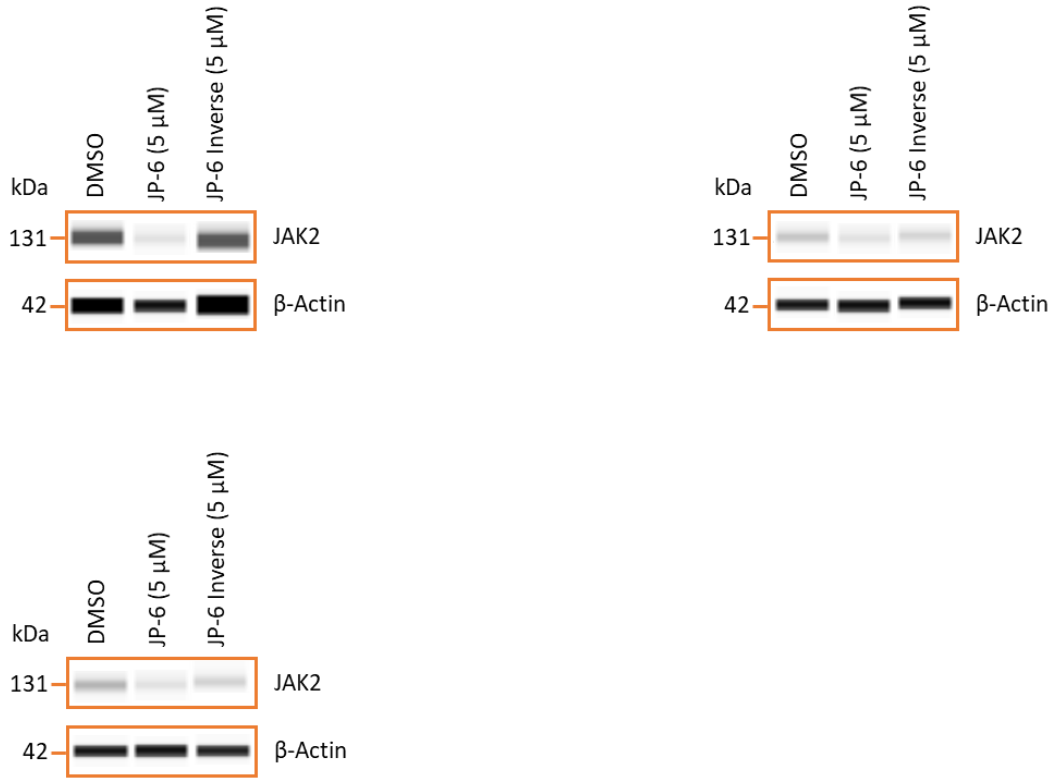


Fig 91 Western blot visualisations generated on a capillary-based Wes™ system of JAK2 protein levels in THP-1 cells treated with JP-6 and JP-6 Inverse (IAP-inactive PROTAC), on three independent test occasions.

IAP Competition Blots JAK1

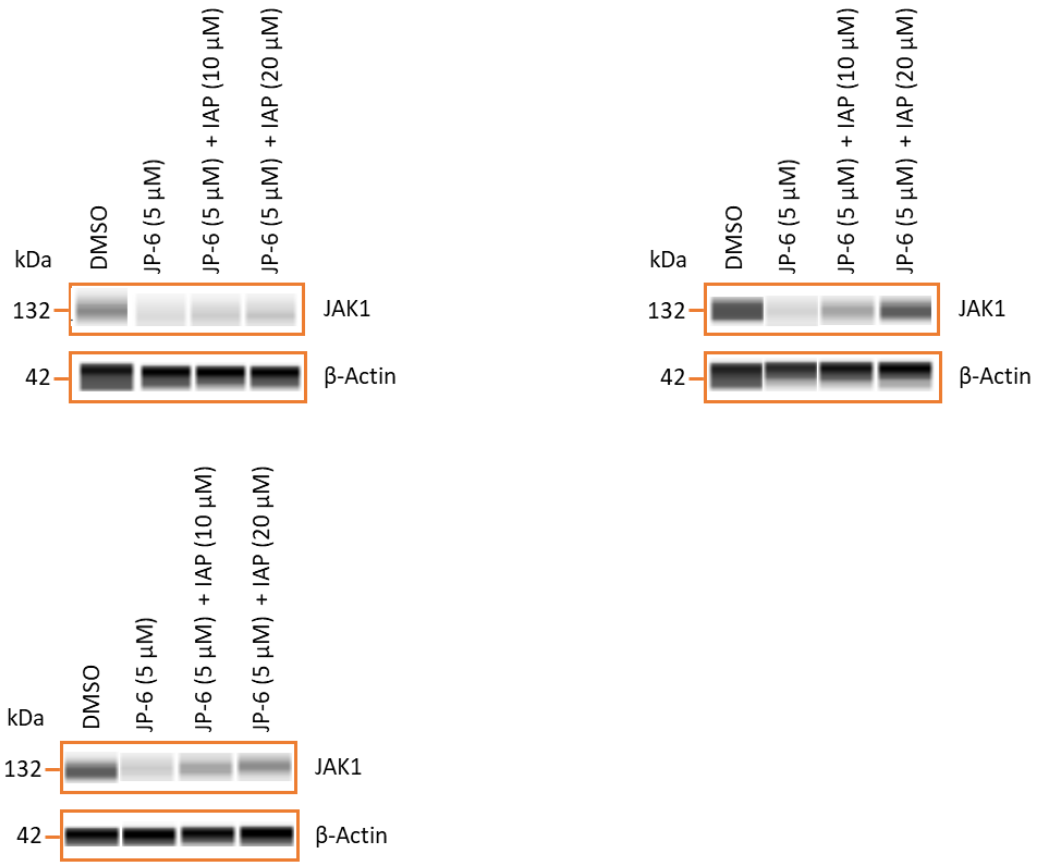


Fig 92 Western blot visualisations generated on a capillary-based Wes™ system of JAK1 protein levels in THP-1 cells treated with JP-6, and combinations of JP-6 and IAP at 10 and 20 μM, on three independent test occasions.

IAP Competition Blots JAK2



Fig 93 Western blot visualisations generated on a capillary-based Wes™ system of JAK2 protein levels in THP-1 cells treated with JP-6, and combinations of JP-6 and IAP at 10 and 20 μ M, on three independent test occasions.

IAP and Quinoxaline 2 Blots JAK1

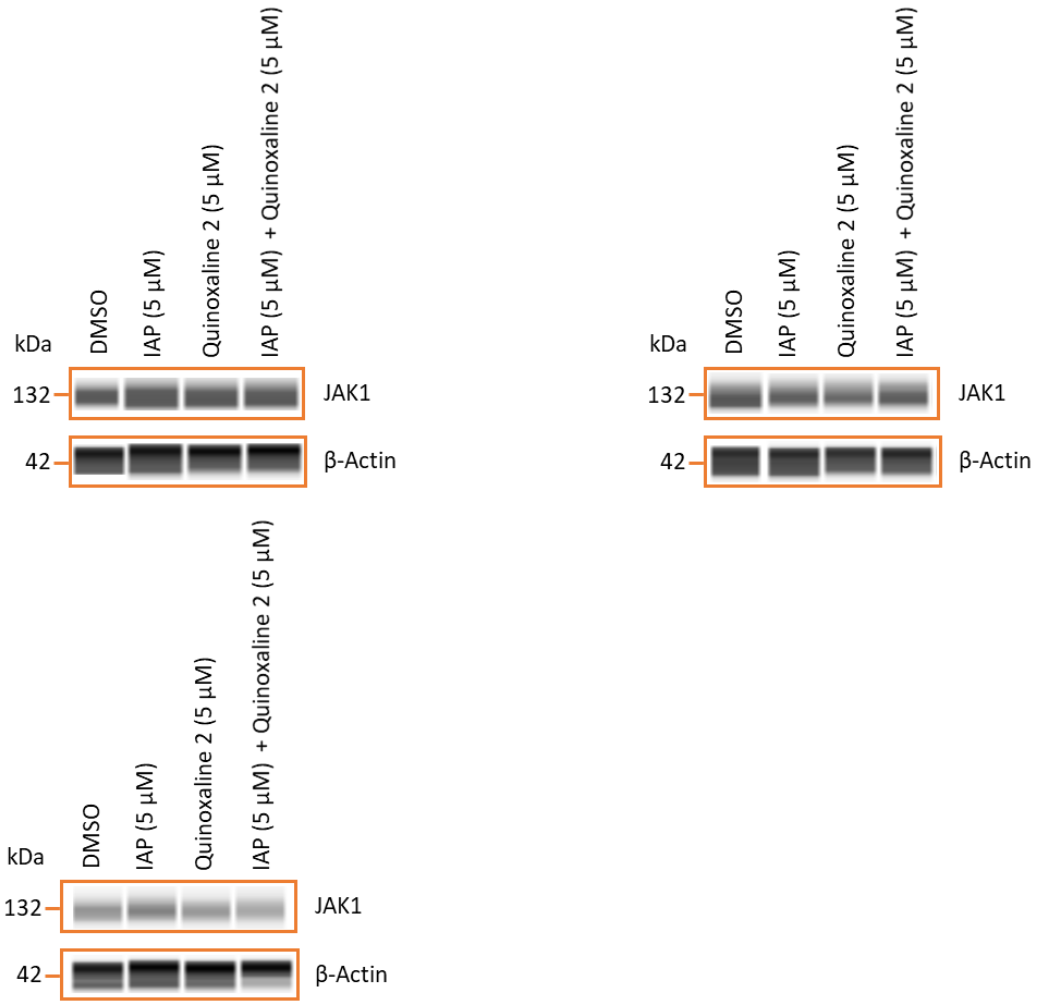


Fig 94 Western blot visualisations generated on a capillary-based Wes™ system of JAK1 protein levels in THP-1 cells treated with IAP, Quinoxaline 2 and a combination of IAP and Quinoxaline 2, on three independent test occasions.

IAP and Quinoxaline 2 Blots JAK2

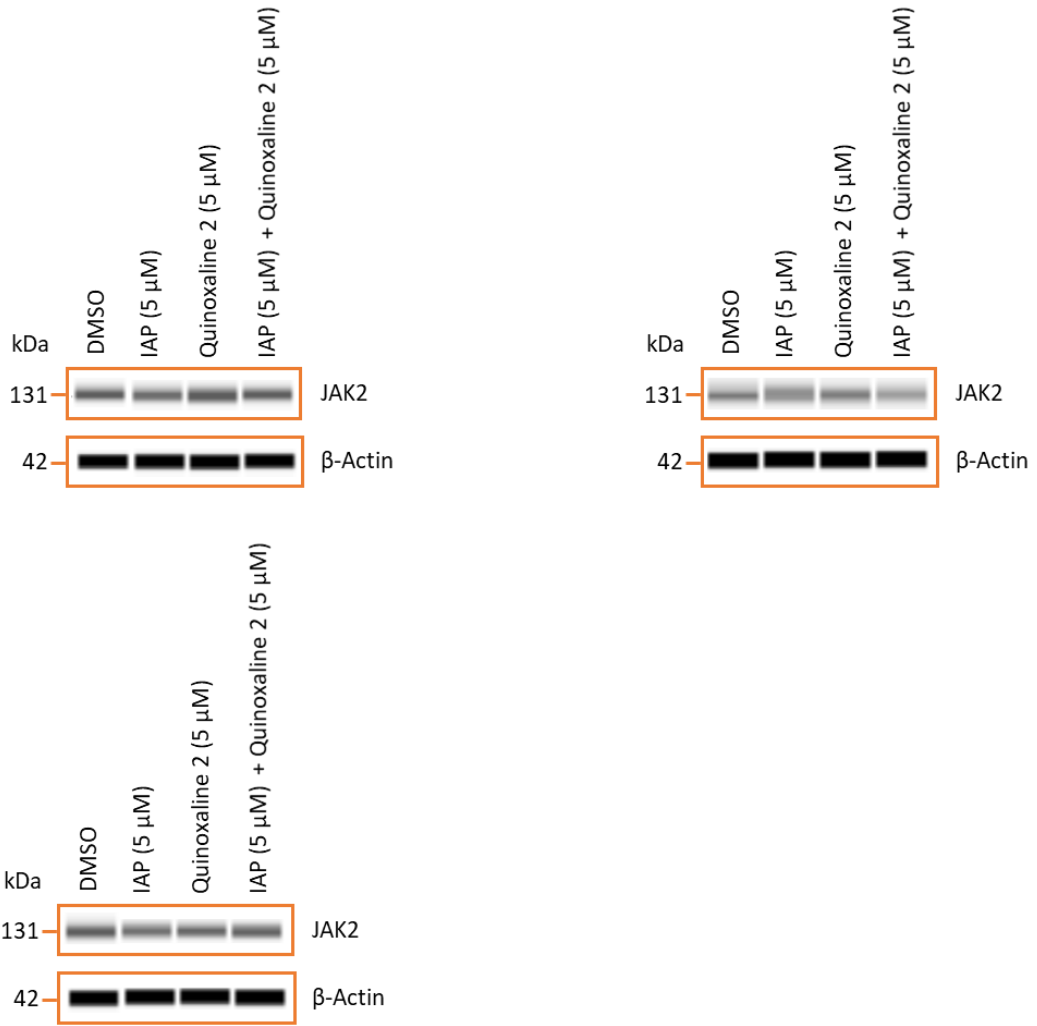


Fig 95 Western blot visualisations generated on a capillary-based Wes™ system of JAK2 protein levels in THP-1 cells treated with IAP, Quinoxaline 2 and a combination of IAP and Quinoxaline 2, on three independent test occasions.

MG132 Blots JAK1

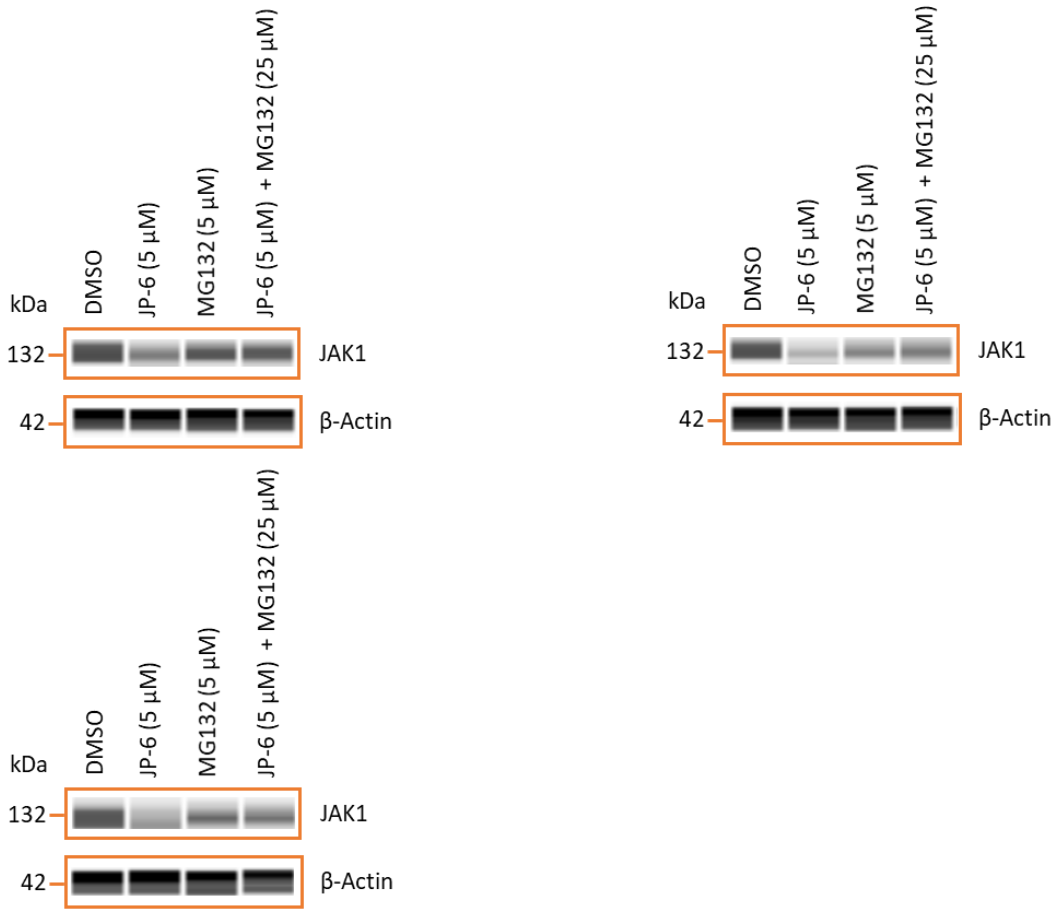


Fig 96 Western blot visualisations generated on a capillary-based Wes™ system of JAK1 protein levels in THP-1 cells treated with JP-6, proteasome inhibitor MG132, and a combination of JP-6 and MG132, on three independent test occasions.

MG132 Blots JAK2

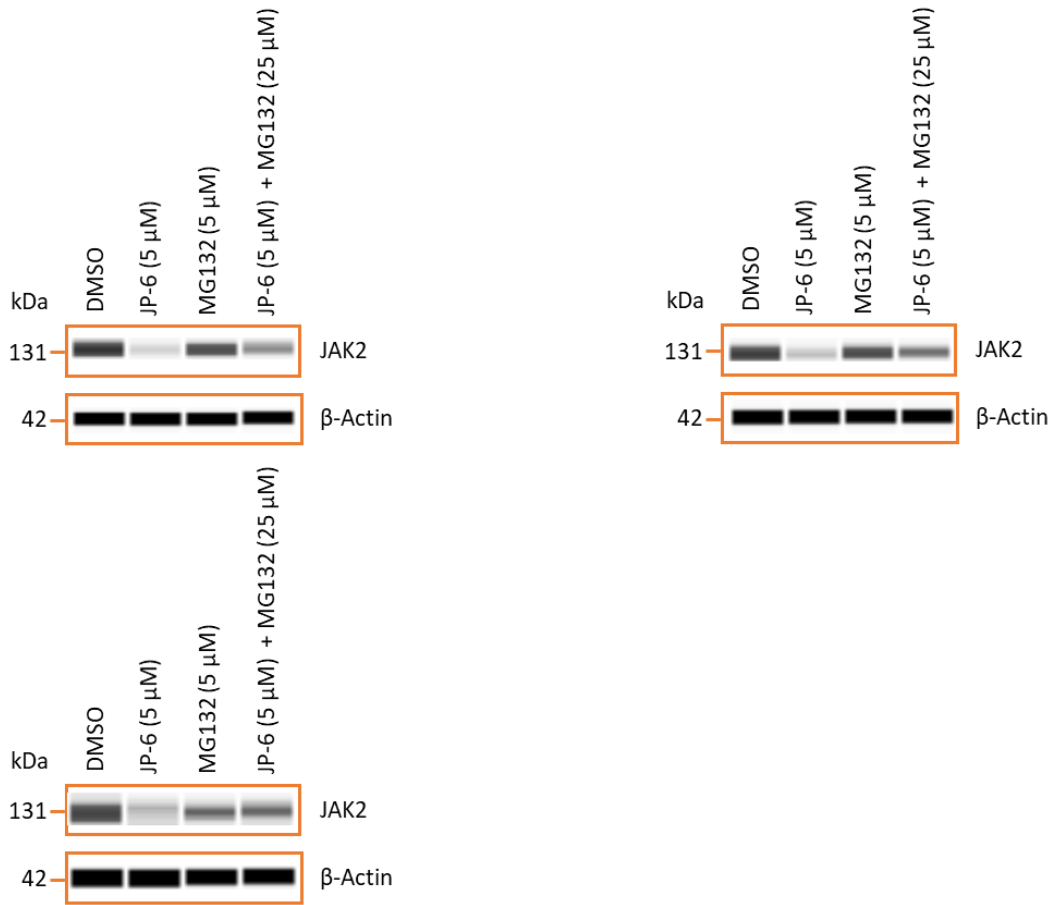


Fig 97 Western blot visualisations generated on a capillary-based Wes™ system of JAK2 protein levels in THP-1 cells treated with JP-6, proteasome inhibitor MG132, and a combination of JP-6 and MG132, on three independent test occasions.